DISS. ETH NO. 24190

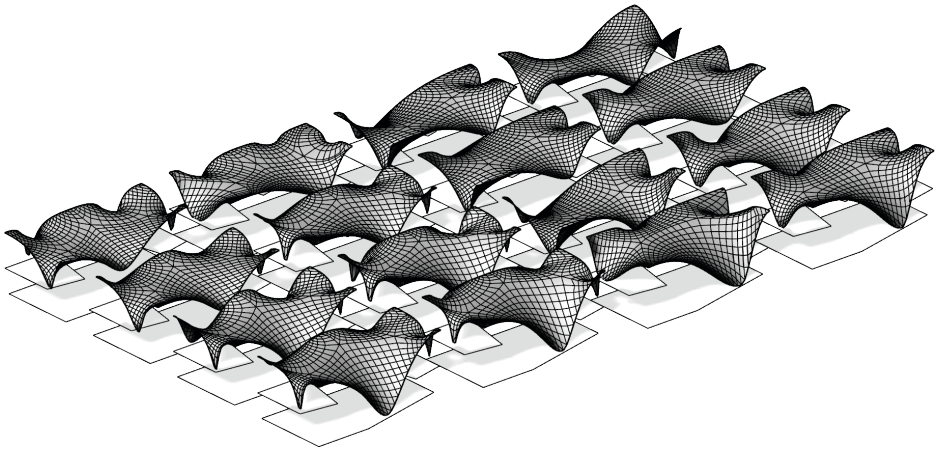

DESIGN AND FORM FINDING OF FLEXIBLY FORMED CONCRETE SHELL STRUCTURES

Diederik Veenendaal

DISS. ETH NO. 24190

DESIGN AND FORM FINDING OF FLEXIBLY FORMED CONCRETE SHELL STRUCTURES

A thesis submitted to attain the degree of

DOCTOR OF SCIENCES of ETH Zurich
(Dr. sc. ETH Zurich)

presented by

DIEDERIK VEENENDAAL

MSc., Delft University of Technology
born 05.02.1982
citizen of the Netherlands

accepted on the recommendation of

Prof. Dr. Philippe Block
Prof. Mark West
Prof. Dr.-Ing. Kai-Uwe Bletzinger
Prof. Dr. Kristina Shea
Dr. Bernhard Thomaszewski

2017

Thesis supervisor:

Prof. Dr. Philippe Block	ETH Zurich

Co-examiners:

Prof. Mark West	Massachusetts Institute of Technology
Prof. Dr.-Ing. Kai-Uwe Bletzinger	Technische Universität München
Prof. Dr. Kristina Shea	ETH Zurich
Dr. Bernhard Thomaszewski	Disney Research Zurich

Chair of doctoral exam:

Prof. Annette Spiro	ETH Zurich

A catalogue record for this doctoral thesis is available from ETH-Bibliothek.

ISBN: 978-3-906327-36-5
DOI: 10.3929/ethz-a-010831669

Typeset in Minion Pro and Myriad Pro. Printed and bound in the Netherlands by Proefschriftmaken.nl.

To you, dear reader.
May this work delight and enlighten, rather than confuse and frustrate you.

Preface

Several events have heavily shaped and directed the present work.

In 2010, I advised Zwarts & Jansma Architects in Amsterdam, on their competition entry for the ARC Wildlife Crossing. Their proposal, Landshape, was a large cable-net and fabric-formed, hyperbolic paraboloid, thin-shell bridge. Although I was invited for my knowledge on fabric formworks, the discussion soon turned to the shell itself. The structural engineers had designed it with six large, parallel arches, instead of relying on the double curvature of the shell with its inherent stiffness. Unable to objectively argue the point, I went home and resorted to the physical model in Figure 1: a Pringles potato chip. Without knowing the outcome for certain, the final result delighted and surprised myself and the architects as well. It immediately revealed the potential of good structural form.

Figure 1: Landshape competition entry (Torsing et al. 2015, 2012), and my physical model: a Pringles potato chip supporting 250 times its own weight through two point loads at its extremities.

When my supervisor, Prof. Philippe Block, invited me in 2011 to serve as co-editor for a book project with Prof. Sigrid Adriaenssens, I was essentially a layperson in its topic of shells. By the end, the book "Shell Structures for Architecture" became a joint effort of some thirty-seven authors, both architects and engineers, academics

and professionals (Adriaenssens et al. 2014*b*). The publication touches on many topics relevant to shells, and through my editorial work and co-authorship, I learned a great deal on these subjects. It deepened my understanding, but did not diminish my awe, of that simple Pringle model. By working on form-finding methods, for the book, and my own thesis, I was able to meet with authorities in this field, such as Prof. Klaus Linkwitz and Prof. Hans-Jörg Schek (Figure 2). Their pioneering work from the 1970s pervades this thesis, most noticeably in the use of their notation.

Figure 2: Awkward photos of the visits to the Block Research Group by Prof. Klaus Linkwitz, 2012, and Prof. Hans-Jörg Schek, 2013.

Back in 2010, at the annual symposium of the International Association for Shell and Spatial Structures (IASS) in Shanghai, Tom van Mele and Prof. Block presented a paper on fabric formworks for shells (Van Mele & Block 2010). The presented method calculates the required forces within a given discrete network for a set of applied loads i.e. the wet concrete, and is essential to this thesis. The practicality of producing a precise stress distribution within a fabric membrane became a point of debate. This strengthened the concept of using cables instead of fabric, as the individual cables can be more easily and precisely controlled, measured and corrected.

In late 2012, Prof. Block was, at the invitation of the Swiss Federal Institute of Technology (EMPA), then able to propose the actual implementation of this idea under real-life conditions. An apartment, called HiLo, featuring a cable-net and fabric-formed roof, will be built within EMPA's NEST building. During my tenure as project coordinator for its early and final design stages (2013–2015), I was also responsible for optimizing and analyzing the roof geometry. This would not have been possible without the knowledge that I had gained from my supervisor, our research group, the book's co-authors, and the many works produced by those in the IASS throughout the past decades.

The present thesis is my contribution to this great body of work, and our shared endeavour to produce elegant, expressive and efficient lightweight structural form.

Acknowledgements

Over the past few years, many people have contributed in some way to the present thesis.

First and foremost, I would like to thank my supervisor, Philippe Block. He gave me the wonderful opportunity to join his fledgeling research group. It was an honour to be part of these exciting beginnings; to see how the group grew and matured, embarking on increasingly ambitious endeavours, culminating in last year's participation in the Venice Biennale of Architecture. *Philippe, het was een genoegen om deze bijzondere jaren met je mee te maken. Mijn rollen als co-redacteur voor het boek en project-coördinator voor HiLo vormden enorme kansen met veel verantwoordelijkheid. Hiervoor, en voor je vertrouwen in mij, zal ik je altijd dankbaar blijven.*

I am equally thankful to all my colleagues who shared in this adventure. You are passionate, driven, inspirational and, quite simply, the best. Thank you for all the conversations, coffee breaks, lunches, dinners, barbecues, swimming as well as our memorable academic and recreational outings to London, Innsbruck, Istanbul, Wrocław, Brasília, Amsterdam, Iran, and throughout Switzerland.

Several colleagues and friends supported specific aspects of this thesis. I am grateful to Lara Davis, Tom Van Mele and Andrew Liew for proofreading publications during the course of this thesis, that now help inform it. Edyta Augustynowicz helped to process the data for Figure 10.8, and her husband, Wojciech Marcińczyk, gave a second opinion on Section 3.8.4, lending his financial expertise. On multiple occasions I had to correspond in Spanish and Portuguese. Here, I received help from my colleagues Juliana Felkner as well as *el guapos* – David López López, Tomás Méndez Echenagucia, and Cristián Calvo Barentin — and my friends; Ronnie Araya from CAST and Flávia Mota Mugglin. Romana Rust and Matthias Rippmann helped

with the German translation of my abstract. I enjoyed fruitlessly hunting with Tomás for the elusive or imaginary cable-net formed shell he once saw, and vigorously meditating at the funicular floor system I built with Masoud Akbarzadeh, David and Michael Stirnemann.

The prototypes in Chapter 9 were built with help from Ramon Weber, Masoud, David, *M&M* – Mariana and Maryanne –, Cristián, Lukáš Kurilla and Zhao Ma. I'd like to acknowledge Master students Paul Mayencourt and Mathias Amstad, who built an early cable-net prototype. Special thanks go out to two Master students who diligently worked on the second and third prototypes; Mile Bezbradica and Aike Steentoft. Others who have helped on construction and measurement are David Novák, Robert Presl, Konrad Schindler and Jonas Sundberg. Further advice and support from the workshops and labs was provided by Thomas Jaggi, Paul Fischlin, Heinz Richner, Dominik Werne and Oliver Zgraggen. Manuela Tan and Noah Nichols from Propex, and Kaloyana Kostova and John Orr from the University of Bath, each provided fabrics.

I haven't yet explicitly mentioned, but would like to thank and acknowledge, some of the other colleagues, assistants and interns from the Block Research Group: Marcel Aubert, Gianni Birindelli, Claudia Brunier-Ernst, Michaela Burch, Ursula Frick, Hannes Hofmann, Lorenz Lachauer, Juney Lee, Anna Maragkoudaki, Robin Oval, Noelle Paulson, Emma Radaelli, Michela Rossi, Jean-Marc Stadelmann and Simon Zemp.

The NEST HiLo project became a major preoccupation for a period of two years. Completing the final design and obtaining a building permit, was a milestone towards realizing the apartment and its innovations including the roof, described in Chapter 12. I'd like to thank the entire team, and particularly those team members whom I met with regularly and who shared in the coordination efforts: Gearóid Lydon, Anja Willman, Tomás, and Dave Pigram.

Many people that I met and corresponded with over the years provided me with valuable knowledge, rare publications, original datasets and wonderful images: Robert Barber, Michael Barnes, Alessio Bazzanella, Arielle Blonder, John Butcher, Tim Chen, John Chilton, Barbara Cutler, Renaud Danhaive, Falko Dieringer, Bernard Espion, Homayoon Estekanchi, Carlos Felippa, Miguel Fernández Ruiz, Lothar Gründig, Robert Haber, Wendy Hall, Frank Huijben, Axel Kilian, Carlos Lázaro, Wanda Lewis, Thouraya Nouri-Baranger, George Nez, Ruy Pauletti, Daniel Piker, William Plunkett, Arno Pronk, Hans-Jörg Schek, Paul Shepherd, Jennifer Stevenson, Dieter Ströbel, Gabriel Tang, Antonio Tomás Espín, Martha Tsigkari, Fruto Vivas, Rob Waller, Agnes

Weilandt, Brad Wells, and Chris Williams. I'd also like to refer to the specific acknowledgements contained in the co-authored books by Adriaenssens et al. (2014*b*) and West (2016). Prof. Linkwitz was especially supportive of my work, and allowed me to co-author and work with him on his chapter for the former book.

I'd like to acknowledge a few professionals and their companies that supported my work or collaborated with me: Kevin Lamyuktseung and Florian Idenburg from SOIL Architects in New York, US; Jack Bakker, Jochem Verbeek, and Rob Torsing from Zwarts & Jansma Architects in Amsterdam, Netherlands; Iain (Max) Maxwell and Dave from Supermanoeuvre in Sydney, Australia; Agnes Weilandt from Bollinger + Grohmann Ingenieure in Frankfurt, Germany; and, Hans Laagland and Theo Salet from Witteveen + Bos in Deventer, Netherlands.

Whether they realize it or not, a few people were highly influential for setting me on the path that I am today, some of whom I have mentioned already but would like to again. I am extremely grateful to Leo Wagemans, Chris Williams, Jan Vamberský, Jeroen Coenders, Theo Salet, Hans Laagland, Rein Jansma and Philippe Block for inspiring, supervising or guiding me during my professional and academic career.

Finally, I would like to thank my family and friends in the Netherlands, including my dad and my brother, Jan, for supporting me in this opportunity to go to Switzerland, and visiting me and Regine while we were there. Regine, you are the love of my life. You left everything to come and be at my side. You kept me sane, reminded me of life outside the PhD and took me on so many adventures in our new country. I love you and I am for ever grateful to you. I promise I will never do another PhD again.

Contents

Abstract

Concrete shells are efficient structural systems to cover large areas without the need for intermediate supports. Historically, their shapes were derived from mathematical equations, with some of the thinnest described by the hyperbolic paraboloid, or hypar. Unfortunately, the relative cost of formwork for shells has increased such that they are no longer built in any significant number.

The thesis explores the concept of casting large span, anticlastic concrete shell structures with the aid of a flexible formwork, specifically a prestressed cable-net and/or fabric formwork. Such a system consists of lightweight, inexpensive and widely available cables and fabrics, requires little to no falsework, allowing for unobstructed access underneath, and does not rely on skilled labour nor on the use of release agents for demoulding.

A flexible formwork allows a wider range of shapes to be constructed compared to traditional, mathematically described shells, with up to 25 to 40% lower cost than conventional timber formwork, independent of the span. This creates a potential to revive shells and design them such that they are structurally more efficient and architecturally less constrained.

A design process for flexibly formed shells is developed that consists of the followings steps: generating a shell through initial form finding and (possibly) subsequent shape and thickness optimization; patterning and flattening the corresponding formwork surface; calculating loads from the applied concrete; calculating the resulting stresses in the formwork due to those loads; materializing the formwork and calculating the prestresses prior to casting, including stress compensation of the cutting patterns; and, analyzing the formwork frame. The workflow aims to keep computational cost manageable, to allow for implementation in a parametric design or optimization model.

The process is informed by: an extensive review and comprehensive comparison of form-finding methods; an overview of constrained form-finding methods based on least squares; and, a full description of recommendations issued by the IASS, in order to deal with nonlinearities in the analysis of thin concrete shells by using simple reduction factors. The review of form-finding methods itself leads to the description of a generic form-finding method with linear finite elements that encompasses existing ones, and allows for the comparison of their computational performance.

Based on an implementation of the design process, a parametric study is carried out for a simple square hyperbolic paraboloid. It shows that, in this case, a fabric and a cable-net formwork can be applied for spans of up to almost 10 to 15 m and up to almost 20 to 40 m, respectively.

The computational work is verified through the construction and measurement of one fabric-formed, and two cable-net and fabric-formed shell prototypes. These are measured, which establishes that deviations for the cable-net and fabric-formed shells are well below accepted tolerances, while the fabric-formed shell reveals that further work is necessary on the detailing and fabrication of its cutting patterns, and methods to measure its stress state.

The main case study is the structural design of a flexibly formed shell roof of NEST HiLo, a duplex penthouse apartment to be completed in 2018 in Dübendorf, Switzerland. This unique shell has spans in the range of 6 to 9 m and a surface area of 157 m^2.

This work contributed to the approval of a building permit for this structure, slated to be the world's first computationally form-found, permanent thin concrete shell structure.

Zusammenfassung

Betonschalen sind hochleistungsfähige Tragwerke, die grosse Flächen ohne innenliegende Stützen überspannen können. Der Entwurf traditioneller Schalenarchitektur basiert auf mathematischen Flächen, wie etwa das hyperbolische Paraboloid (Hypar), welches zu den dünnwandigsten Schalentypen zählt. Bedauerlicherweise werden Betonschalen heute nur noch vereinzelt gebaut, da sich die relativen Kosten für deren Schalung erhöht haben.

Die vorliegende Dissertation untersucht flexible Schalungssysteme aus vorgespannten Seilnetzen und/oder Textilien zur Herstellung antiklastischer Betonschalen mit grossen Spannweiten. Ein solches System besteht aus leichtgewichtigen, kostengünstigen und weitgehend verfügbaren Drahtseilen und Textilien, ist weder auf spezielle Fachkräfte noch auf Trennmittel für die Entformung angewiesen und erfordert wenig bzw. gar kein Lehrgerüst, was den ungehinderten Zugang unterhalb der Schalung ermöglicht.

Im Vergleich zu traditionellen, mathematisch definierten Schalen erlaubt ein flexibles Schalungssystem zudem einen grösseren Spielraum in der Formgebung und weist, unabhängig von der Spannweite, etwa 25 bis zu 40% geringere Kosten als konventionelle Holzschalungen auf. Vor diesem Hintergrund gewinnen Betonschalen wieder an Bedeutung, sind tragstrukturell effizienter und erschliessen gleichzeitig ein vielfältigeres Formenspektrum.

Im Rahmen der vorliegenden Dissertation wurde ein Arbeitsablauf für den Entwurf und die Herstellung flexibel geformte Schalen entwickelt, welcher wie folgt aufgebaut ist: Erzeugung der Schalenform mittels Methoden zur Formfindung und gegebenenfalls anschliessender Form- und Querschnittsoptimierung; Zuschnittsermittlung und Abwicklung der entsprechenden Schalungsoberflächen; Berechnung der Lasteinwirkung des Betonauftrags und der resultierenden Spannungen in der Schalung infolge der Lasten; Dimensionierung der Schalung und Berechnung der

Vorspannungskräfte vor dem Betonierprozess unter Berücksichtigung der Spannungskompensation durch das Zuschnittmuster; und letztlich, Tragwerksanalyse und Bemessung des Schalungsrahmens. Dieser Arbeitsablauf zielt darauf ab den Rechenaufwand der Einzelschritte zu minimieren, um deren Anwendung innerhalb eines parametrischen Entwurfs- und Optimierungsmodels zu ermöglichen.

Die Entwicklungen entlang dieser Prozesskette basieren auf einer ausführlichen Literaturrecherche und einer umfangreichen Vergleichsstudie unterschiedlicher Formfindungsmethoden, einem Überblick über Formfindungsmethoden mit Zwangsbedingungen basierend auf der Methode der kleinsten Quadrate und Richtlinien der IASS hinsichtlich der Verwendung einfacher Reduktionsfaktoren bei nichtlinearen Analyseverfahren für dünnen Betonschalen. Die Gegenüberstellung von unterschiedlichen Formfindungsmethoden ermöglicht die Definition einer allgemein formulierten Formfindungsmethode mit linearen finiten Elementen, welche vorhandene Methoden inkludiert und einen Vergleich der jeweilig benötigten Computerrechenzeit erlaubt.

Basierend auf einer Implementierung des angeführten Entwurfs- und Analyseprozesses, wird eine parametrische Studie für ein einfaches quadratisches hyperbolisches Paraboloid durchgeführt. Damit wird exemplarisch demonstriert, dass die Textil- und Seilnetzschalung, für Spannweiten von 10 bis 15, beziehungsweise von 20 bis 40 m, verwendet werden kann.

Die entwickelten rechnergestützten Methoden werden durch die Konstruktion und Vermessung von drei prototypischen Betonschalen überprüft, wovon eine mittels Textilschalung und zwei mittels kombinierter Seilnetz-Textilschalung hergestellt werden. Die durchgeführten Messungen zeigen, dass die Toleranzen der Seilnetz-Textilschalung deutlich unter den üblichen Messwerten liegen, wohingegen die Messwerte für die reine Textilschalung auf weiteren Entwicklungsbedarf hinsichtlich der Detaillierung und der Herstellung des Schnittmusters und der Messverfahren zur Spannungsverteilung hinweisen.

Die Hauptfallstudie dieser Arbeit umfasst den Tragwerksentwurf der flexibel geformten Dachschale des NEST HiLo, einem zweigeschossigen Penthouse Apartment in Dübendorf in der Schweiz, welches 2018 fertiggestellt wird. Die Spannweite dieser einzigartigen Schale beträgt zwischen 6 und 9 m und hat eine Oberfläche von 157 m^2. Die vorliegende Dissertation hat zur Abnahme der Baugenehmigung dieses Flächentragwerks beigetragen, welche die weltweit erste, durch digitale Formfindungsmethoden entwickelte, Betonschale werden wird.

Part I

Introduction

There are no limits to the shape of concrete. Enormous freedom lies before the designer, an astonishingly vast field. It is astonishing that in fact very little use is made of this freedom. It is astonishing that the great majority of concrete buildings follow the typical shapes of wood and steel, namely the straight beam, the flat slab and the plane wall. [...] The problem of building technique is another impediment. Curved formwork is complicated and expensive, at least in the traditional sense.

— Heinz Isler, 1981

CHAPTER ONE

Introduction

"There are no limits to the shape of concrete." Isler (1981), a renowned builder of thin concrete shells, spoke of the potential of this initially fluid material. He singled out several reasons why this potential, to his mind, was not being realized, which included the complexity and cost of traditional formwork. In fact, concrete shells are no longer being built in any significant number. Isler himself was often referred to as an exception to this development, as he continued designing and engineering elegant shell structures through his methods of *form finding*. With his passing in 2009, the future and relevance for such structures has become even more uncertain.

1.1 Motivation

Several developments and advances in architecture and engineering could allow for concrete shells to return in greater numbers. At the same time, the structural efficiency of shells allows for savings in material use, leading to associated reductions in energy use and carbon emissions[1]. A major obstacle to shell construction is formwork complexity and cost. This could be addressed by a *flexible formwork*, specifically a prestressed cable-net and/or fabric formwork. Such a formwork offers greater freedom than conventional systems to construct and therefore design structural forms. As such, it can be a straightforward means to realize efficient shell geometries derived from form finding. The following section expands on these points in more detail.

[1]Subsection 1.1.5 is based on co-authored publications Hawkins et al. (2016) and Block et al. (2017).

1.1.1 Freeform design

Modern trends in architecture have led to forms that, in many ways, are more complicated than ever before. Advances in digital modelling have allowed for such complexity, as relatively simple operations can easily produce curves that in turn define three-dimensional shapes. Computer-based design has now become commonplace in architectural practice, a development since the early 1990s, referred to as the *digital turn* in architecture (Carpo 2012).

Early works in this period, often characterized by double curvature, were referred to as *blob architecture*. This style is said to have been initiated by Lars Spuybroek's and Kas Oosterhuis' Water Pavilion and epitomized by Frank Gehry's Guggenheim Museum (Figure 1.1). The term was coined by Greg Lynn in 1995, based on the acronym for "binary large objects", referring to the digital nature of such architecture. Often contracted to *blobitecture*, the word has become derogatory to some, alluding to shapeless masses devoid of meaning, instead of binary data (Safire 2002).

Figure 1.1: Water pavilion, designed in two connected parts, by Kas Oosterhuis, ONL and by Lars Spuybroek, NOX, Netherlands, 1993-1997, and the Guggenheim Museum Bilbao by Frank Gehry, Spain, 1997.

More recently, *Parametricism*, coined by Patrik Schumacher in 2008, is also applied to this style and period, including successive works. It can be seen as an attempt to provide a deeper rationale or logic for this type of architecture, but the term is even more controversial. It "is neither a style nor a movement, but merely a now ubiquitous 21st-century technology coupled with a stylistic preference for topologically derived (smooth) digital surfaces" (Gage 2016). Like blobitecture, the logic for such surfaces is not obvious to the critic, and becomes the source of their derision.

To realize these forms, whatever their reason, much time and effort is being invested in the development of new, often computer-controlled, fabrication strategies. The general digitization of manufacturing is said to constitute a *third industrial revolution* by Markillie (2012).

Figure 1.2: Heydar Aliyev Center by Zaha Hadid Architects, Azerbaijan, 2012, and Louis Vuitton Foundation by Frank Gehry, France, 2014.

The unconstrained nature of computer-aided design, now combined with digital fabrication, has given an apparent promise of complete geometrical freedom. Arguably, this has led to forms that are not only geometrically complex, they require awkward structural solutions, useful only to extravagant landmark or signature buildings.

For example, the 2012 Heydar Aliyev Center is said to require 5.500 tons of steel to cover 15.500 m^2 of surface area, or about 350 kg/m^2. The 2014 Louis Vuitton Foundation contains 15.000 tons of steel to cover 12.000 m^2, or about 1250 kg/m^2. Its sail-like glazed panels alone contain 300 kg/m^2 of steel (Figure 1.2).

By comparison, the shape of the gridshell covering the British Museum Great Court was derived by computational form finding. As a result of taking structural considerations in mind, it weighs a mere 130 kg/m^2, of which 80 kg/m^2 is the steel structure (Figure 1.3).

Moreover, while the latter steel and glass gridshell forms a transparant atrium roof, the steel structures of Heydar Aliyev Center and Louis Vuitton Foundation are mostly hidden from view, and clad with glass-fibre reinforced concrete or polymer. Block (2016) argues that "architecture has failed if it is merely a freeform skin with a substructure, like the flat building fronts propped up from behind on the set of a Western, where it is only an image lacking materiality".

1.1.2 Concrete shell structures

Thin-shell concrete structures are structurally efficient systems for covering large areas. They rely on double curvature to produce resistance to load by transferring forces perpendicular to their surface to in-plane stresses. The perceived wasteful nature of current architectural design has led to a review of the merits of such

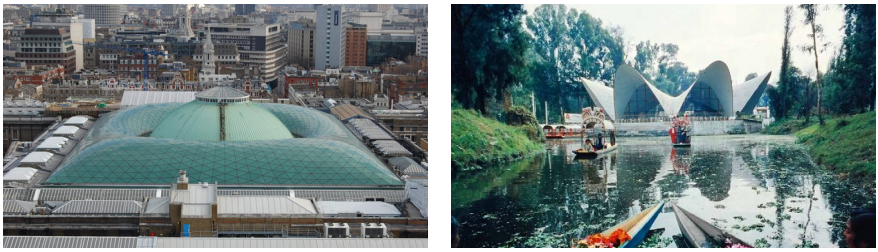

Figure 1.3: British Museum Great Court roof by Foster + Partners, London, UK, 2000, and Los Manantiales Restaurant by Félix Candela, Xochimilco, Mexico, 1958.

structures. Rippmann (2016) remarks that they "share a similar formal language of fluidity and curvilinearity [but despite this,] do not resemble each other in structural performance." However, this distinction may be at the verge of dissolving. At the 2012 Venice Biennale of Architecture, Zaha Hadid Architects displayed the works of shell builders Heinz Isler and Félix Candela, writing that "[the] more our design research and work evolved on the basis of algorithmic form generation, the more we learned to appreciate the work of [such] pioneers".

The 42 m span Los Manantiales restaurant by Candela, arguably one of the most elegant concrete shells, weighed 100 kg/m^2 for most of its surface (Figure 1.3). This is in the same order of magnitude as the weight of the aforementioned steel structures, but that excluded the cladding.

Any interest in concrete shells today appears to run counter to historical developments. The golden era of concrete shells, when tens of thousands were built around the world, was between the 1920s and 1960s. Since then, their construction has seen a sharp decline, with the minor exceptions of airformed concrete domes and slipformed concrete cooling towers. The wish among some engineers and scientists to revive them has been marked by publications such as "Do concrete shells have a future?" (Schlaich & Sobek 1986) and "Do concrete shells deserve another look?" (Meyer & Sheer 2005).

Commonly cited reasons for their disappearance are (Cassinello et al. 2010, Isler 1995, Meyer & Sheer 2005, Schlaich & Sobek 1986):

1. limitations of traditional shell geometries, and contrary architectural trends;
2. competition with prefabricated and mass-produced systems;
3. competition with new materials, tensioned membrane roofs and steel or timber gridshells; and,
4. the cost of concrete formwork and associated labour;

As argued, contemporary trends in architecture should allow for more concrete shells to be realized, where the concrete is not (only) the cladding, but the structural system as well. Clearly, the design space between traditional shells, which were limited to a specific set of mathematical shapes, and freeform design needs to be explored to arrive at forms that fit within these trends, yet display a structural logic as well.

Still, it should be accepted that concrete shells cannot fully regain their original dominance, and will have their place among other lightweight systems such as membrane roofs and gridshells. Instead, it should be clarified when a concrete shell is appropriate.

For example, membrane roofs are not always applicable due to requirements related to thermal or acoustical insulation, fire safety, daylight entry, integration and support of various building systems and so on. Both timber and steel gridshells are generally lighter than concrete shells. However, they are not always more economical, for example due to local buckling of the individual steel members and related sizing requirements (Muttoni et al. 2013). The carbon footprint of steel is substantially higher than that of concrete. Furthermore, architectural, spatial and/or functional constraints may require a monolithic, continuous, smooth surface that concrete naturally provides, while avoiding complicated detailing. A concrete shell can also integrate multiple functions in ways that a membrane roof or gridshell cannot. For example, the thermal mass of a large unobstructed internal concrete surface can be used to passively reduce heating and cooling demand (Aste et al. 2009), as well as actively as a radiant heating and cooling panel.

The final point, the cost of formwork, might be tackled by considering a *fabric formwork* instead of conventional timber formwork.

Figure 1.4: Columns, and carry-on travel bags holding their formwork, for Casa Dent in Culebra, Puerto Rico (West 2004). Free-standing 10 × 1.7 × 0.3 m fabric-formed wall, University of Sydney, Australia (Redjvani & Wheen 1995).

1.1.3 Fabric formworks

Fabric formwork is a building technology that involves the use of structural membranes as the main contact material for concrete moulds. Unlike traditional formworks, the material is highly flexible and can deflect under the pressures of fresh concrete. The resulting forms exhibit curvature as well as excellent surface finishes that are generally not associated with concrete structures.

The history of flexible formworks is more than a century long (Block & Veenendaal 2013, Veenendaal 2016, Veenendaal et al. 2011), with many recent and ongoing developments (Hawkins et al. 2016). However, no substantial work into their computational form finding exists (Veenendaal & Block 2012*a*).

A flexible formwork with fabric shuttering offers several immediate advantages (Veenendaal 2016). It has the appeal of simplicity, requiring nothing more than the application of fresh concrete to some kind of fabric or flexible membrane. By simply suspending or prestressing a cable net or fabric within a supporting frame, then either casting concrete, rendering or spraying mortar or concrete, a wide range of regular and irregular shapes can be cast quickly and cost-effectively. It can also be patterned and inflated by concrete pumping as in marine applications, or by air as in pneumatically formed shells.

The fabric is easy to strip, requiring no release agents, but can be left in place just as well, even protecting the concrete. The permeability of the fabric will affect the quality of the surface concrete, reducing the amount of air voids and blowholes, and therefore improve overall durability. In many examples, no skilled labour or sophisticated equipment are needed. As the fabric is lightweight, compact, cheap and reusable, fabric formworks offer savings in the amount of form- and falsework material and thus in terms of transportation, storage and labour. This is dramatically seen in column and wall formworks, which are able to resist up to 10 m of concrete pressure while requiring minimal material and limited stabilization (Figure 1.4).

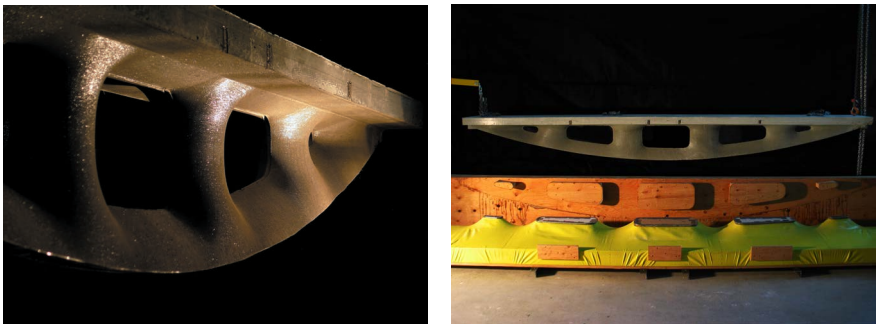

Figure 1.5: Fabric-formed, 4 m span, concrete truss (West 2006).

The sculptural possibilities of these methods can also be used to create structurally efficient concrete designs, thus leading to further savings in the amount of concrete, reinforcement, and subsequently in embodied energy and greenhouse gas emissions (Figure 1.5).

1.1.4 Flexibly formed shells

If the architectural program calls for a concrete shell, then a lightweight structure such as a tensioned membrane or a deployable gridshell could also serve as a formwork for a concrete shell; a *flexible formwork*. This would make sense if the cost of such a structure is less than that of conventional formwork. The cost of a large membrane roof is about 300 €/m^2 including design and engineering from personal experience, while Bavarel et al. (2012) describe a deployable GFRP gridshell with a material cost of 150 €/m^2. Assuming that such structures are generally designed for 1.0 kN/m^2 of live load with a load factor of 1.5, their use as temporary formwork would allow for an equivalent load of 60 mm of concrete. Even if the final design requires a thicker shell, this thickness should suffice for an intermediate, self-supporting shell structure in many cases. Given that conventional timber formworks for curved shells cost about 400-800 €/m^2, depending on the curvature, it seems that flexible formworks may be very competitive.

Prestressed fabrics have already been applied as formwork for anticlastic shell structures up to modest sizes. By combining a cable net with fabric, it is possible to scale the concept of fabric formworks to the size of large-span roofs and bridges (Torsing et al. 2015, 2012, Veenendaal & Block 2014*b*), especially when applying a thin coat of concrete or mortar to form a shell structure. By carefully designing the cable net and its topology, and calculating and controlling the prestressing forces, it is possible to form a wide range of anticlastic shell shapes beyond those of the traditional hyperbolic paraboloid (Van Mele & Block 2011). These lightweight formwork systems reduce the need for separate foundations of the formwork and allow unobstructed space underneath the shell during construction.

1.1.5 Embodied energy

Placed in a wider context, flexibly formed shells can offer a positive contribution to the challenge of climate change. The scientific consensus is that climate change is a result of man-made greenhouse gas emissions, and that these must be rapidly reduced in order to limit widespread and destructive effects (Cook et al. 2013, Hansen et al. 2013). In response, EU countries have agreed on a binding target of a 80% reduction of greenhouse gas emissions by 2050 (Hübler & Löschel 2013).

Buildings account for 40% of global energy consumption and up to 30% of global greenhouse gas emissions (UNEP 2013). A large share of this energy is locked in for long periods due to the life span of buildings. In fact, the superstructure of buildings alone, either steel or reinforced concrete, can account for up to 45% of

embodied energy (Kaethner & Burridge 2012). Concrete in particular is our most widely used construction material, and, meanwhile, worldwide consumption of cement is increasing. Cement manufacture alone is estimated to account for 5.2% of global CO_2 emissions (Boden et al. 2013). On the other hand, the embodied carbon of reinforced concrete is anywhere between 5 to 50 times lower than that of steel (Purnell 2013), possibly twice that when accounting for carbon uptake due to long-term carbonation of built concrete (Xi et al. 2016).

With clear targets for the reduction of carbon emissions, and with concrete for building construction representing a large share of current emissions, bringing about the revival of efficient, thin concrete shells, and reducing material waste of their formworks, are worthwhile pursuits.

1.2 Problem statement and objectives

The problem statement of the thesis is:

> Concrete shells, though appropriate for modern application and efficient structurally, ultimately suffer due to formal limitations as well as material and labour cost of conventional formwork systems.

The hypothesis is that a flexible formwork can mitigate or entirely remove the disadvantages mentioned in the problem statement, by allowing a wider range of geometries to be constructed in a more economical fashion than possible with conventional formworks.

The scope is limited to prestressed cable-net and fabric formworks, which necessarily produce only anticlastic, i.e. negatively curved shell structures. It is also limited to concrete as the most common material used for casting.

The primary objectives of this thesis are:

- to conceptualize a constructional flexible formwork system for thin concrete shells;
- to develop a workflow for the design of such a formwork system and resulting shell structure; and,
- to establish its technical feasibility, or limits thereof.

At the start of this thesis, the history of flexible formworks was not fully understood. A prior state-of-the-art review by Abdelgader et al. (2008) refers to a 1906 patent, one structure by Felix Candela (Figure 3.8), and developments mostly in 1970s and 80s. Shells cast on networks of wires in the 1960s (shown in Section 3.7) were not cited in contemporary literature, and a wider view of formworks using discrete elements such as wires, cables, chains or belts had not yet been taken.

Furthermore, it was clear that some method of form finding would be relevant to apply, should the shape of the formwork and/or the resulting shell be optimal in some way. Unfortunately, literature on existing form-finding methods did not reveal any thorough comparisons, making it unclear to what extent these methods differ and in which cases one may be preferable over another.

As a result, secondary objectives of this thesis, intended to contextualize the present work, are:

- to review and compare existing form-finding methods, limited to the basic case of self-stressed networks and surfaces;
- to review the history of fabric formworks and specifically flexible formworks applied to the construction of shells.

1.3 Outline

This thesis is divided into six parts. The present introduction forms the first part and chapter. The remaining parts are: a review of shell design and construction methods; a review and comparison of numerical methods for form finding, without and with constraints; a proposed design methodology and workflow for the fast generation of flexibly formed shells; results in the form of prototypes, a parametric study and a case study; and, conclusions.

Chapter 2 introduces the methods with which shells and other lightweight structure have traditionally been designed: mathematical equations, physical and numerical form finding and freeform design. It concludes by discussing conventional formworks, their cost, and potential developments in 3D printing.

Chapter 3 provides a review of flexible formworks for shell structures, including methods related or similar to the proposed cable-net and fabric formwork system. These developments are placed in a wider historical context. Any available information on cost is collected and compared to that of conventional systems in the previous chapter.

Chapter 4 discusses networks of linear and triangular finite elements commonly used in numerical form finding. These elements can be purely geometrical (line and triangle) or, including material properties, be mechanical (spring, bar and membrane). The elements and notation are used in subsequent chapters on numerical methods.

Chapter 5 provides a review of form-finding methods for prestressed networks and surfaces. A generic form-finding method is presented and explanations are given throughout, under what conditions it becomes a specific well known form-finding method. The resulting framework is then used to compare the performance of existing methods.

Chapter 6 is an introduction to least squares methods for solving form-finding problems that have additional constraints. It links variations of such methods as they have been applied in the 1970s, and more recently in the context of flexible formworks and this thesis.

Chapter 7 outlines a step-by-step workflow for the design and engineering of a flexibly formed shell and its formwork. A form-finding method, from Chapter 5, can be used for the generation of an initial form, and a constrained form-finding method, from Chapter 6, is necessary to compute forces or stresses in the formwork under load. The workflow aims to keep computational cost manageable, to allow for implementation in a parametric design tool or an optimization model.

Chapter 8 provides a complete description of recommendations given by the International Association of Shells and Spatial Structures, for the design of a concrete shell given the lack of guidance from building codes for such structures. This description allows one to quickly consider relevant aspects at an early stage of design, without the need for time-consuming nonlinear analyses or model testing until later on.

Chapter 9 presents three prototype shell structures that were made with flexible formworks. It offers photo documentation and additional information regarding detailing and construction.

Chapter 10 proceeds with the experimental results obtain from the prototypes. They served three purposes: as constructional proof of concepts; to test the design workflow from Chapter 7; and to investigate construction tolerances of flexible formworks.

Chapter 11 implements the workflow from Chapter 7 to explore the limits of flexibly formed shells in a parametric study, based on a simple hyperbolic paraboloid shape. Sensitivities to inaccuracies in material and load assumptions are investigated as well.

Chapter 12 describes the structural design of the flexibly formed shell roof of NEST HiLo, a duplex penthouse apartment to be completed in 2018 in Dübendorf, Switzerland. This work constitutes the final design, which was submitted in August 2015 and led to approval of the building permit.

Chapter 13 offers conclusions, recommendations and suggestions for future work regarding the concept and development of flexibly formed shell structures.

Part II

Review

[The shell] *is the prima donna among load-bearing structures: if it is used correctly, it is capable of maximum performance. It can, however, also be temperamental, therefore sensitive, if it is not properly treated.*

— Ekkehard Ramm, 2002

CHAPTER TWO

Shell design and construction

The most structurally efficient shells exploit double curvature to create stiffness. This makes it difficult to describe them geometrically, both for analysis and construction.

From the start of the golden era of shells, the 1920s, analytical functions were the method of choice to simplify both these tasks, and until the 1960s nearly all shells and their formworks were defined as such *mathematical shapes*.

In the 1960s and 70s, physical form finding was used to generate newer, potentially more efficient shell forms, or *natural shapes*. Both Heinz Isler and Frei Otto used hanging models for this purpose, and the latter and Sergio Musmeci used soap films as well. "However the shells almost vanished from the market[, with] Isler as the most encouraging exception of [sic] the rule" (Schlaich 1985).

The introduction of computer-aided design led to a proliferation of complex designs from the late 1990s onward. As a consequence, much of architecture and academia is preoccupied with technically rationalizing such *freeform shapes* through the studies of architectural geometry, structural geometry and structural optimization. The field of structural geometry includes computer simulations of earlier physical form-finding methods. Such numerical form-finding methods were already developed in the 1970s and have been in use, particularly for the design of tensioned membrane roofs, since the 1980s.

These three categories of shell shapes—mathematical, natural and freeform—also appear in the introduction by Adriaenssens, Block, Veenendaal & Williams (2014*b*). This chapter provides an overview of traditional methods to generate these three types shapes: mathematics, form finding and freeform design. In addition, an overview of existing and emerging formwork methods is given, with the exception of flexible formworks, which are discussed in Chapter 3.

Section 2.1 lists typical analytical functions as well as more recent trigonometric functions that were used to define shell geometries. Sections 2.2 and 2.3 explain the historical development of physical form finding and their subsequent numerical analogues. The mathematics of these numerical methods is described in detail in Chapter 5. Section 2.4 offers examples of early and recent freeform shells. Section 2.5 summarizes the types of formwork construction that have been used and mentions some recent developments as well. References on the cost of shell construction are summarized. The chapter ends with a discussion in Section 2.6, before drawing conclusions in Section 2.7.

2.1 Mathematical shapes

Early shell design was dictated by analytical expressions defining their geometry. Indeed, Heinz Isler remarked that "curiously, practically all such shells built at the time of the shell boom (until the 1960's) are characterised by a common distinguishing feature: they are all geometric forms, i.e. their form is dictated chiefly by the shapes of school geometry. Thus we find cylinders, sphere sections, cones, hyperboloids etc. It was the analytic thinking of the times that restricted the creators' thinking to the shapes easily defined" (Isler 1995).

Medwadowski et al. (1979) divides shell geometries into Catalan surfaces, translational and generalized translational surfaces, and helicoids. Quadric surfaces cover the first two categories, except for conoids and cylindroids. Distinctions between such shapes are often made on the basis of their generating curves: the *generatrix* and the *directrix*. A generatrix is a curve, that when moved along a given path, or directrix, generates a shape.

Beyond these types of surfaces, it is possible to perform affine transformations to deform them, aggregate multiple surfaces into new compound surfaces (Medwadowski et al. 1979), introduce damping in the case of sinusoidal surfaces, or superpose multiple surfaces.

The following sections give selected examples of analytically defined shells and their formworks. Section 2.1.1 deals with conic and quadric surfaces, which include ellipsoids, paraboloids and hyperboloids; Section 2.1.2 with conoids and cylindroids. Section 2.1.3 discusses generalized translational surfaces and other analytical surfaces. Apart from concrete shells, there are many brick vaults as well as steel and timber gridshells with such shapes. The reader is referred to Ochsendorf (2013), Schober (2015) and Chilton & Tang (2017) respectively.

2.1.1 Conics and quadrics

The definition of nearly all classical shells can be derived from conics or quadrics. Conics are curves that arise from intersections between a plane and a cone, i.e., conic sections. They are the circle, the ellipse, the parabola and the hyperbola.

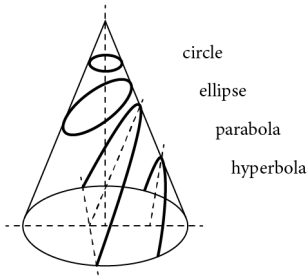

Figure 2.1: Conic sections, or conics, result from the intersections between a plane and a cone.

In three dimensions, the resulting surfaces are referred to as quadrics. The simplest are degenerate quadrics, such as cones or cylinders, which are extrusions of the conic sections. Shells based on cylinders are known as barrel vaults. Quadrics can also have double curvature, which is the case for the ellipsoid, elliptic paraboloid, hyperbolic paraboloid, elliptic hyperboloid of one sheet (also known as a hyperbolic hyperboloid), or elliptic hyperboloid of two sheets (also known as a elliptic hyperboloid). Table 2.1 gives an overview of their equations.

elliptic (circular if $a = b$)	**hyperbolic**	**parabolic**
ellipsoid (spheroid if $a = b$, sphere if $a = b = c$) $\frac{x^2}{a^2} + \frac{y^2}{b^2} + \frac{z^2}{c^2} > 0$ 		
(elliptic) cylinder $\frac{x^2}{a^2} + \frac{y^2}{b^2} > 0$ 	hyperbola ("hyperbolic curve") $\frac{x^2}{a^2} - \frac{y^2}{b^2} > 0$ 	parabola ("parabolic curve") $x^2 + 2ay = 0$ 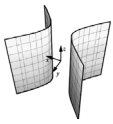
cone $\frac{x^2}{a^2} + \frac{y^2}{b^2} - \frac{z^2}{c^2} = 0$ 		
hyperboloid of two sheets ("elliptic hyperboloid") $\frac{x^2}{a^2} + \frac{y^2}{b^2} - \frac{z^2}{c^2} < 0$ 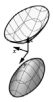	hyperboloid of one sheet ("hyperbolic hyperboloid") $\frac{x^2}{a^2} + \frac{y^2}{b^2} - \frac{z^2}{c^2} > 0$ 	see hyperbolic paraboloid ("parabolic hyperboloid")
elliptic paraboloid $\frac{x^2}{a^2} + \frac{y^2}{b^2} - \frac{z}{c} = 0$ 	hyperbolic paraboloid $\frac{x^2}{a^2} - \frac{y^2}{b^2} - \frac{z}{c} = 0$ 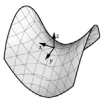	

Table 2.1: Quadrics used for the design of analytical shells.

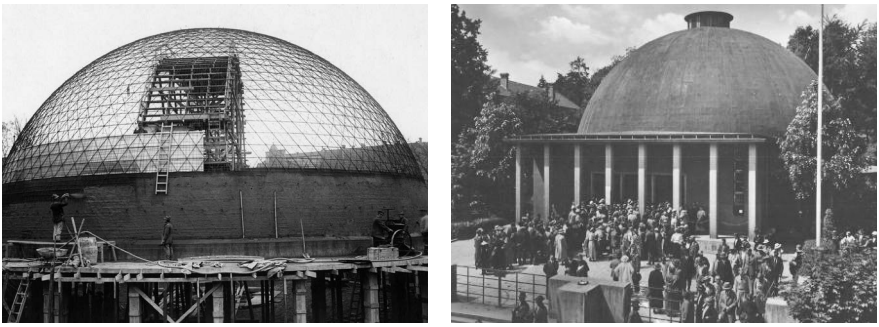

Figure 2.2: Construction and opening of the Zeiss Planetarium in Jena, Germany, 1926.

Ellipsoids

The most basic doubly curved geometry for shells is the semi-spherical dome, based on a spheroid. Seminal examples are the Pantheon in Rome, built in the second century BCE, and the 1926 Zeiss Planetarium in Jena, Germany (Figure 2.2). This planetarium was developed and designed by Walter Bauersfeld (1879-1959), an engineer with the client, Carl Zeiss Optical Industries, and Franz Dischinger and Ulrich Finsterwalder from the engineering firm Dyckerhoff & Widmann. Several models were built leading up to a 16 m span, 30 mm thick prototype, built on top of the Zeiss factory in 1924, and considered the first thin concrete shell of the modern era (Medwadowski 1998, Meyer & Sheer 2005). The final 25 m span, 60 mm thick dome was constructed using a rigid triangular steel grid, a geodesic dome, as a stay-in-place framework and reinforcement. Concrete was sprayed (Torkretbeton) from the outside onto curved timber panels, suspended from the steel grid (Figure 2.2) (Schmidt 2005).

The construction system was later patented under the name Zeiss-Dywidag, and exploited by Dyckerhoff & Widmann with considerable success, with c. 1'680'000 m^2 of licensed shell surface, mostly barrel vaults (cylinders) and domes, built between 1923 and 1944 (May 2015). Apart from the patent, the required engineering knowhow for these shells contributed to their competitive position in the market. The complexity of their calculations, considered "a sort of transcendental mystery only divested by the German school" (Pizzetti 1958), remained a source of frustration for others, as "the mathematical prowess of those who revel in the somewhat mystical approximations [...] is denied to many members of the profession." (Waller & Aston 1953). At the same time, the limited repertoire of shell geometries, led others to describe them as "plain (Zeiss-Dywidag) shells" (Billig 1951).

A recent ellipsoidal shell is the Centro Ovale in Chiasso, Switzerland (Figure 2.3) (Muttoni et al. 2013). This 93 × 52 m, 100 mm thick shell was constructed by spraying and pouring steel fibre-reinforced concrete onto traditional reinforcement and timber falsework with panels bent on site. The cost of falsework and formwork was reported to be 49 % of the total construction cost of the shell. Muttoni et al. (2013) concluded that traditional approaches to formwork and falsework can lead to excessively complicated and expensive systems, and that further research and innovation is needed.

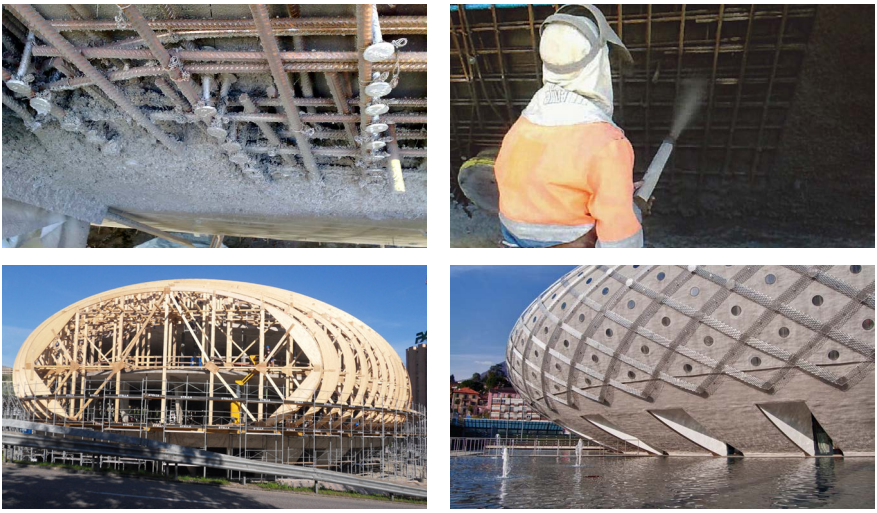

Figure 2.3: Construction and final structure of the Centro Ovale, Chiasso, Switzerland, 2013.

Paraboloids

Domes with an (elliptic) paraboloidal shape are less common than spherical domes. More well known examples include several concrete domes designed by Oscar Niemeyer, such as the 1960 National Congress of Brazil (Figure 2.4) and the 2006 Cultural Complex of the Republic, both in Brasilia, and the 2011 Centro Niemeyer in Avilés, Spain.

Figure 2.4: National Congress of Brazil, Brasilia, 1960.

Apart from the spherical dome, the hyperbolic paraboloid, also known as a *hypar* or HP shell, has been of great interest in shell design, and was popularized by renowned shell builder Félix Candela Outeriño (1910–1997). This shape is a ruled surface, described by a straight generatrix and straight directrices, which can be exploited for construction. For example, the shuttering of the formwork and reinforcement of the shell can both be built using straight elements.

Espion (2016) considers Fernand Aimond (1902–1984), a chief engineer with the French Ministry of Air, to be the "father of the hypar". The first built examples he designed are the 1933-1936 shelters for hydrogen bottles storage at the Cuers-Pierrefeu airship base in France (Figure 2.5). Aimond (1936) published a 112-page paper on the subject, which introduced Candela to this particular shape.

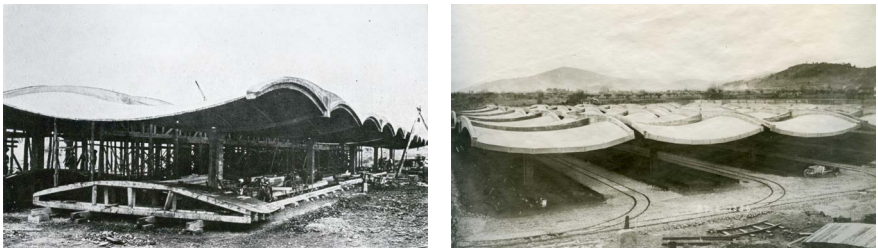

Figure 2.5: The first built hypar concrete shells: the hydrogen bottles storage at the Cuers-Pierrefeu airship base, France, 1933.

Candela started using the hypar for the 11 m span, 15 mm thick Cosmic Rays Laboratory, built in Mexico City in 1951 (Figure 8.4). His hypar shells were constructed on timber formworks, that made efficient use of straight timber boards, but also required substantial scaffolding (Figure 2.6).

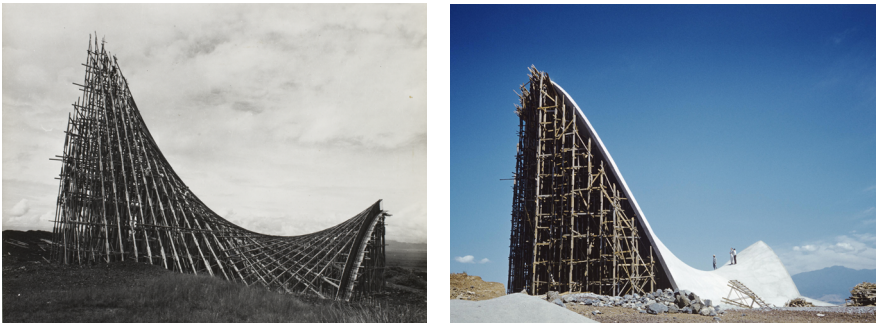

Figure 2.6: The 18 m span, 40 mm thick Chapel Lomas de Cuernavaca, Morelos, Mexico, 1959.

His last works were the hyperbolic paraboloid entrance and restaurant buildings of L'Oceanogràfic, an oceanarium in Valencia, Spain. The latter, a 35.5 m span, 60 mm thick shell, used steel fibre reinforced shotcrete along with traditional reinforcement. The formwork was still the same in principle, but used some modern, equivalent components, such as engineered timber beams for the shuttering as well as a standard modular, tubular shoring system (Figure 2.7) (Domingo et al. 2004).

Figure 2.7: Entrance and restaurant buildings of L'Oceanogràfic, also known as ACHypar and JCHypar, Valencia, Spain, 2003.

The Philips Pavilion, designed by Iannis Xenakis (1922–2001) while collaborating with Le Corbusier (1887–1965), built for the 1958 World Expo in Brussels, Belgium, is unique for several reasons. The entire envelope consisted of hyperbolic paraboloid surfaces, nine in total. The structure, 40 × 25 m in plan, and 22 m high, was further segmented into c. 1.5 m^2, 50 mm panels, that were prestressed by steel cables. These segments were prefabricated on an earthen mould (Figure 2.8) (Pronk et al. 2007*b*).

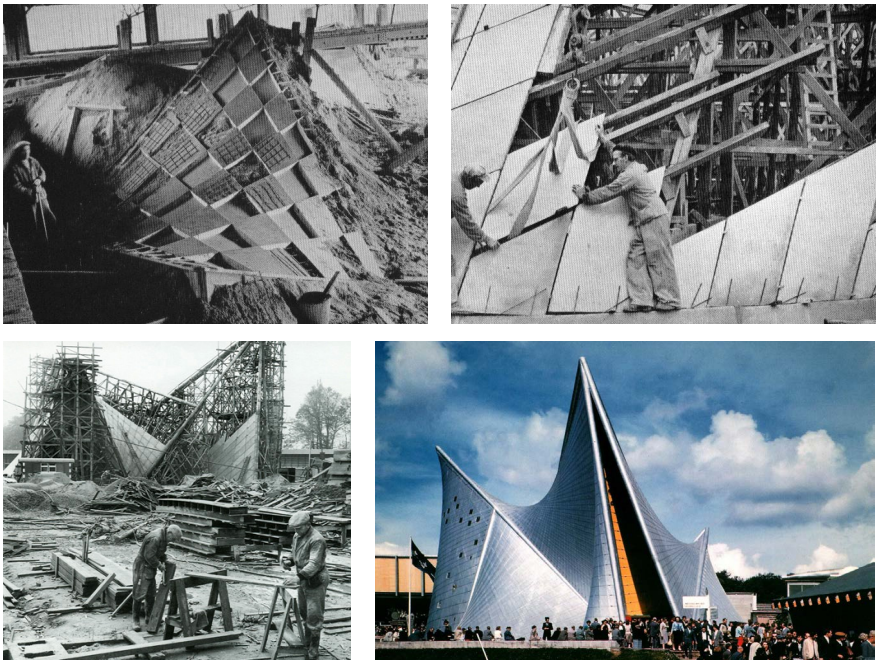

Figure 2.8: Philips Pavilion, World Exposition, Brussels, Belgium, 1958.

Hyperboloid of two sheets

Domes with an (elliptic) hyperboloidal shape are very rare. The only example found is the St. Maria Goretti Catholic Church in Scottsdale, Arizona, US, designed by Wendell E. Rossman. The central hyperboloid dome has a span of 17 m and is 100 mm thick consisting of foam with sprayed concrete (Gunite).

Hyperboloid of one sheet

The hyperboloid is the default shape for concrete, natural draught cooling towers, and has become associated in particular with nuclear power plants. The hyperboloid shape has a positive effect on air flow and cooling efficiency, and also allows straight reinforcement along its ruled surface. The idea of a concrete hyperboloid cooling tower was patented and executed by Van Iterson & Kuypers (1918), as an alternative to steel or timber cooling towers at the time. The first two were built in 1917-1918 as part of the Dutch state coal mining facility Emma in Heerlen (Figure 2.9). The second was 35 m high, with a wall thickness between 75 and 300 mm. The company Mouchel subsequently built 600 of such towers over a 40 year period (Damjakob & Tummers 2004).

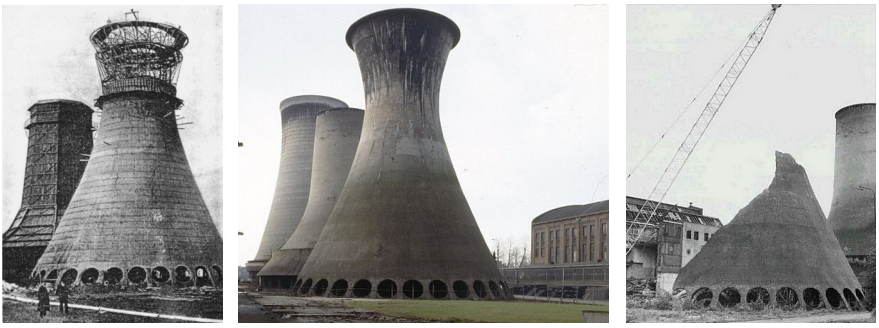

Figure 2.9: Van Iterson cooling tower during construction, operation and demolition, Staatskoolmijn Emma, Heerlen, Netherlands, 1918-1980.

A modern example is the tower for the RWE power station in Niederaussem, Germany (Busch et al. 2002), which was the worlds highest such cooling tower at 200 m, until the construction of two 202 m cooling towers (though they are smaller in surface area) for the Kalisindh thermal energy plant in Rajasthan, India completed in June 2012 (Asadzadeh & Alam 2014). Formwork systems have become standardized, self-climbing slipform systems, which allow variations in angle and diameter (Figure 2.10).

A wide-span shell roof using hyperboloids is the 2004 bus station in Casar de Cáceres, Spain, designed by Justo García Rubio (Figure) (Rubio 2004). The main span is a 34 m, 120 mm thick shell, and the entire structure can be described by eight surfaces consisting of hyperboloids and truncated cones (Egea 2004).

Figure 2.10: Doka SK175 self-climbing formwork, applied to 150 m high Kalinin cooling tower, Russia, 2010.

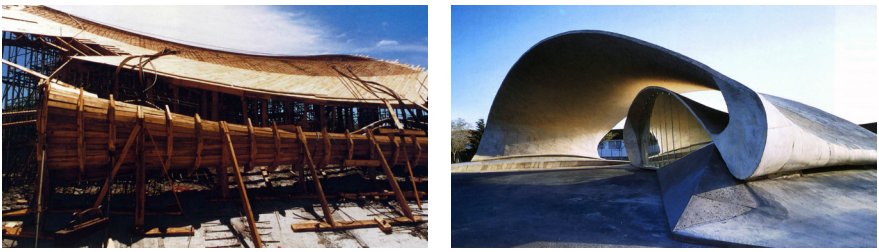

Figure 2.11: Bus station in Casar de Cáceres, Spain, 2004.

2.1.2 Conoids and cylindroids

Together with the hyperbolic paraboloid, conoids and cylindroids are classified as Catalan surfaces. These are ruled surfaces whose ruling is parallel to a fixed plane. This ruling, a straight generatrix, moves along two directrices in space. If both directrices are also straight lines, then the surface is a hyperbolic paraboloid. If one directrix is curved, then the surface is a conoid. Examples are circular, elliptic, paraboloid and sinusoidal conoids. If the conoid's straight directrix is perpendicular to the aforementioned fixed plane, then it is called a right conoid. If both directrices are curved, then the surface is a cylindroid. Early examples in concrete are the (possibly parabolic or hyperbolic) conoid roofs of the 1926 Magasin général de Saint-Pierre-des-Corps, by Eugène Freyssinet (1879–1962) (Figure 2.12)

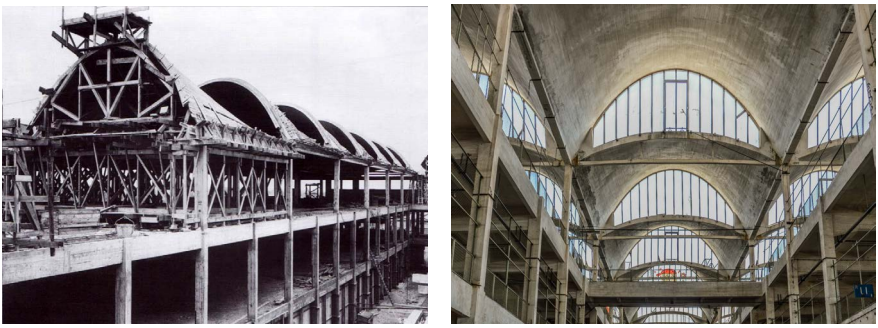

Figure 2.12: Post-war rebuilding in 1948 of the Magasin général de Saint-Pierre-des-Corps, France, 1926.

2.1.3 Generalized translational and other surfaces

Generalized translational surfaces may have a generatrix that no longer moves perpendicular to a fixed plane, or its shape can vary depending on the position of the generatrix. The generatrix and directrices can be the same type of curve, resulting in elliptical, paraboloid or sinusoidal surfaces.

The unrealized 1955 design for the Táchira Club in Caracas, Venezuela, by Eduardo Torroja y Miret (1899–1961), for example, had a trigonometric directrix, consisting of three sinusoidal terms, and a catenary generatrix (Figure 2.13). The shell's boundaries were defined by parabolas and higher-order polynomials (Escrig & Sánchez 2005). The second phase of the project, which included this shell, was never built due to the 1958 Venezuelan coup d'état, which effectively ended lavish public spending by the previous dictatorship. The complicated nature of the shell's mathematical definition blurs the lines between mathematical and freeform shapes, and the Táchira Club has indeed been referred to as the latter (Section 2.4). The same is true for some of Heinz Isler's shells, which were derived from circular curves of varying radii and referred to as freeform as well (Chilton 2000).

Beyond translational surfaces, there are other, in fact endless ways in which to aggregate and combine analytical shapes to obtain new ones.

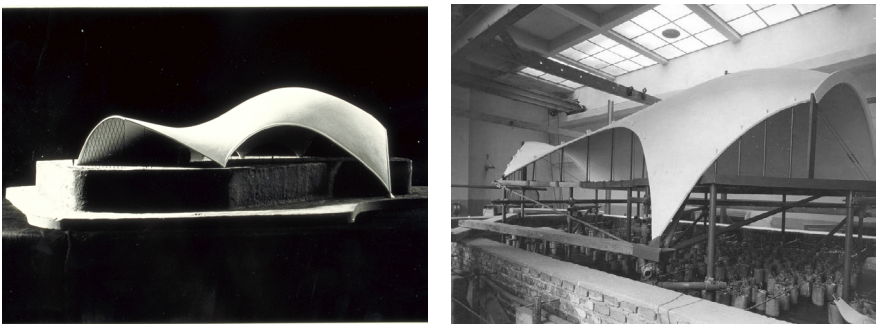

Figure 2.13: Scale models for the unbuilt Táchira Club, Caracas, Venezuela, 1955.

2.2 Physical form finding

In 1959, Heinz Isler presented his seminal paper, titled "New Shapes for Shells" at the very first Congress of the, then, International Association for Shell Structures (IASS) in Madrid. He introduced three physical methods for shaping shells and also mentioned one more during the subsequent discussion (Isler 1960):

- the freely shaped hill;
- the membrane under pressure;
- the hanging cloth reversed; and,
- soap skins.

This event is generally regarded as a watershed moment in the design of shells, creating awareness of alternatives to mathematical shapes.

In the case of the freely shaped hill, Isler mentions the idea of small models, but presents only one example of a free-standing shell; a small atomic shelter, built in 1955 (Figure 2.58). Here, the hill, or earthen formwork, is not only a direct method of design, but the construction method as well (Section 2.5.4). As the bunker's shape was designed to be semi-spherical (Isler 1956), the hill was only a construction mould, so Isler conflated the two purposes. So, given the lack of firm examples, the utility of the freely shaped hill as a form-finding method is questionable.

This section discusses each of the other methods, with the hanging cloth preceded by a section on hanging chain models, and the soap skins, or soap films, followed by additional subsections on rubber membrane models (which typically produce self-stressed, but not necessarily minimal surfaces like soap films do). The final

subsections illustrate the introduction of pneumatic and hydraulic pressure to the membrane. Built projects used as examples in this chapter include masonry vaults as well as tensioned cable-net and membrane roofs, as only few structures designed by form finding were executed as concrete shells.

2.2.1 The hanging chain

The earliest recorded suggestion of physical modelling to derive a structural shape is the hanging chain by Robert Hooke (1635–1703). He published ten "Inventions" in the form of anagrams of Latin phrases in order to protect his ideas (Hooke 1676). The third invention would later become known as Hooke's law of elasticity for which he is most known. The second (Figure 2.14), describing 'the true Mathematical and Mechanical form of all manner of arches for building' is given as: "abcccddeeeeefggiiiiiiiillmmmmnnnnnooprrsssttttttuuuuuuuux".

The solution to this architectonic riddle was posthumously published by the secretary of the Royal Society, Waller (1705), and read "Ut pendet continuum flexile, sic stabit contiguum rigidum inversum", or "As hangs the flexible line, so but inverted will stand the rigid arch". The idea is simple: invert the shape of the hanging chain, which by definition is in pure tension and free of bending, to obtain the equivalent arch that acts in pure compression.

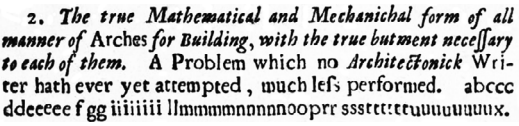
2. *The true Mathematical and Mechanichal form of all manner of* Arches *for Building, with the true butment necessary to each of them.* A Problem which no *Architectonick* Writer hath ever yet attempted, much less performed. abccc ddeeeee f gg iiiiiiii llmmmmnnnnnooprr ssstttttuuuuuuuux.

Figure 2.14: Robert Hooke's anagram on the means to find the ideal compression-only geometry for a rigid arch (Hooke 1676)

Hooke published his work while collaborating with Christopher Wren (1632–1723) on the design of St. Paul's Cathedral in London. Their attempt to find the ideal shape of its structural, interior dome, led Wren to define the section as a cubic parabola, where $y = ax^3$, although the eventual dome was conical to account for the heavy roof lantern at the top, and incorporated iron chains to resist ring forces (Figure 2.15). The correct expression for the catenary, $y = \cosh(x/a)$, was established soon after by others (Heyman 1998).

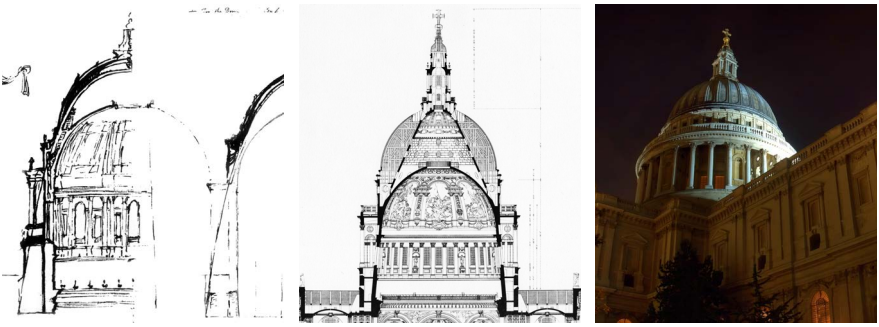

Figure 2.15: St. Paul's Cathedral, London, UK, with study for a dome with a cubic parabola as curve, drawn by Christopher Wren, c. 1690, cross-section revealing final conical design, drawn by Arthur Poley, 1927, and recent photo of exterior.

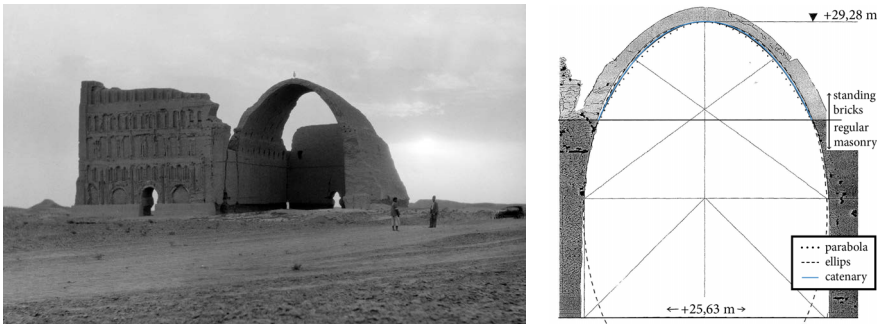

Figure 2.16: Great Hall of the Palace of Taq-i Kisra, Ctesiphon, sixth century BCE, located in Iraq, 1932. Single point load introduced at midspan. Comparison of the structure with an ellipse, parabola and catenary, revealing the latter to best describe the shape.

Knowledge of the catenary is likely to have existed as early as the sixth century BCE, as evidenced by the 26 m span, 30 m high catenary shaped vault of Taq-i Kisra at the ancient Sassanid city of Ctesiphon, located in Iraq. Photogrammetric measurements made in 1966 have supported this assertion (Figure 2.16) (Trautz 1998). This structure would later inspire James Waller (1884–1968) to develop a patented system of flexibly formed, corrugated, catenary shaped vaults and domes, called Ctesiphon (Section 3.2.2). In turn, "Ctesiphon" vaults have become synonymous with Spanish catenary shaped roofs in general, which were particularly popular in the 1950s (Rabasco 2011).

Hooke's idea led to the use of simple hanging models for designing and calculating arches and bridges in eighteenth century England, and more famously by Giovanni Poleni (1683–1761) in the 1740s to assess the safety of St. Peter's cathedral in Rome.

The concept of an interior, catenary shaped dome was later implemented for the Panthéon (originally called Ste. Geneviève) in Paris, completed in 1790 and designed Jean Baptiste Rondelet (1734–1829). The catenary appears elsewhere in several openings adjacent to the dome. Rondelet had incorrectly spoken against the final design of St. Paul's, while uncritically propagating the catenary. Trautz (1998) argues that cracks in the structure cannot be explained solely by material strength and settlement, but, ironically, are also due to the inappropriate shape of the dome given the weight of the roof lantern.

2.2.2 Hanging chain models

By the nineteenth century, the inverted hanging chain had become more widely known throughout continental Europe via a range of textbooks (Tomlow 2002).

Wilhelm Tappe (1769–1823) recognized the catenary as an ideal shape, but preferred pointed or elliptical arches for other reasons. He indicated that the shape of the catenary could be altered by changing the weights along the chain model. In effect, he proposed the principle of weighted chains for design rather than analysis as in Poleni's case. He built an experimental, elliptical hut in 1818 (Figure 2.17), and applied his designs to at least one other instance (Tomlow 2002). Based on his ideas, Tappe proposed a new type of architecture with catenary or elliptical arches and domes (Huerta 2006, Tappe 1818-1823), which Tomlow (2002) refers to as proto-Gaudinism (Figure 2.17).

Heinrich Hübsch (1795–1863) designed several churches using hanging models, using multiple strings with weights corresponding to the real structure. Hübsch (1838), lamenting existing, time-consuming approaches, published the method and claimed its invention: " I finally thought up a graphical method, which is not a strict geometric construction, but is as easy as it is infallible". He was able to apply the approach for example, to the 1837 St. Cyriakus church in Bulach, near Karlsruhe, Germany (Figure 2.18).

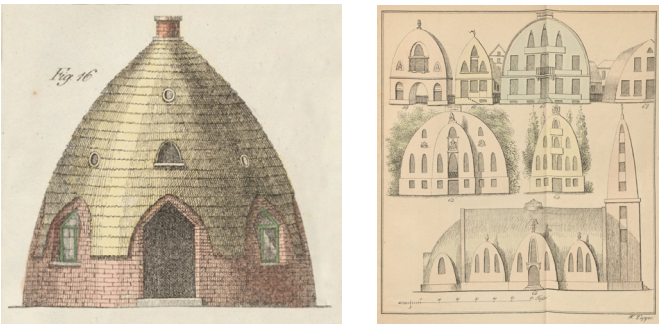

Figure 2.17: Experimental hut, similar to an 1818 house for the Fürstin-Regentin von der Lippe (Tomlow 2002) and catenary architecture proposed by Tappe (1818-1823).

Carl-Anton Henschel (1780–1861) designed a 16 m dome for his own foundry in Germany, also completed in 1837, now part of the University of Kassel (Figure 2.18). Its thickness varies from 320 down to 175 mm, to approximate a nearly semi-spherical shape, while keeping the thrust line within the geometry. Based on a reconstruction by Tomlow (1993), Henschel is thought to have used a hanging model, possibly three-dimensional, but certainly one that accounted for ring forces. It is likely that Henschel was aware of Poleni's and Hübsch' work (Tomlow 1993, 2002).

Similarly, the line of thrust of the internal dome of San Gaudenzio (Figure 2.18), completed in 1887, designed by Alessandro Antonelli (1798–1888), is perfectly contained within the masonry section of the dome (Corradi et al. 2009). Its unique shape and performance has led Trautz (1998) to hypothesize that Antonelli, who was aware of Rondelet's work, had used a three-dimensional hanging model in its design process, which had initially started from a catenary around 1855.

By the late nineteenth century Germany, hanging models were recommended and used for design and analysis of arches and vaults. This culminated in publications on the idea of three-dimensional hanging models by Friedrich Gösling (1837–1899) (Figure 2.19) and Karl Mohrmann (1875–1937). Gösling was likely familiar with Tappe's work, as both men had worked in Detmold (Graefe 2012). Mohrmann proposed the following thought experiment in his 1890 revised edition of Ungewitter: "One can best imagine its form, when one imagines a hanging net underneath the vault, whose nodes are loaded just like those of the upper vault. This net will assume a shape which is a faithful mirror image of a bar system corresponding to the vault." Mohrmann proceeded to discuss graphical methods, but recommended the construction of actual 1:10 three-dimensional hanging models in special cases.

Figure 2.18: Structures designed with hanging models: Stiftskirche St. Cyriakus, Bulach, Germany, 1837; Gießhaus (foundry) of firma Henschel, Kassel, Germany, 1837; and, Basilica San Gaudenzio, Novara, Italy, 1887.

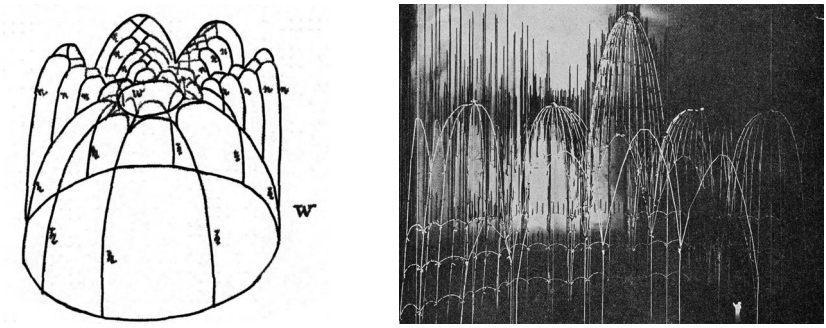

Figure 2.19: Earliest known depiction of a three-dimensional hanging model by Friedrich Gösling, 1895 (Graefe 2012), and earliest known three-dimensional hanging model by Antoni Gaudí (Ráfols 1929).

It is probable that Antoni Gaudí would have been educated on these principles (Addis 2014, Huerta 2006). He used the hanging chain, along with graphic statics, for the design of catenary shaped arches like those for the 1912 Milà House in Barcelona, Spain. Gaudí constructed a first three-dimensional hanging model around 1898 (Figure 2.19). He applied this technique soon after, when he was commissioned to design the Church of Colònia Güell (Tomlow 2002, 2011). Unfortunately, only the crypt was built and left in this incomplete state from 1914 onward. The model itself was lost but was reconstructed at the institute of Frei Otto (1925–2015), the Institut

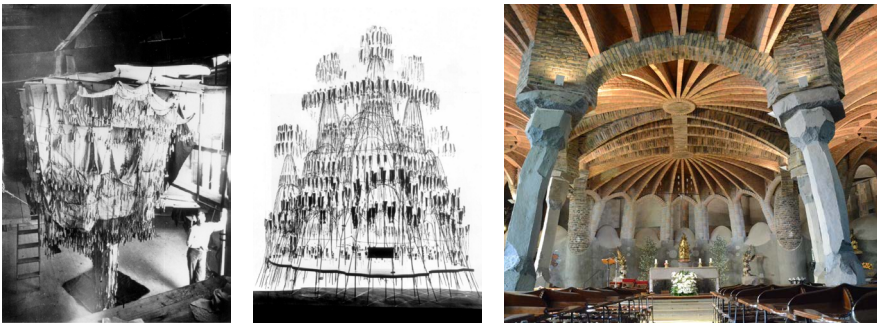

Figure 2.20: Original hanging model, 1898-1908, and reconstruction, 1983, and the crypt of the Church of Colònia Güell, Santa Coloma de Cervelló, Spain, 1917.

für leichte Flächentragwerke (IL) in Stuttgart, Germany (Figure 2.20) (Graefe et al. 1983, Tomlow et al. 1989*b*). Gaudí's work was revolutionary, when compared to his predecessors, because he used hanging models as a means to design entirely novel, yet sound structures.

Discrete hanging models in general had become a subject of study at IL. These followed in the footsteps of an early 1960-1961 study by John Koch (Otto et al. 1973), and Otto's work on early hanging chain models for a gridshell prototype in Berkeley, at the 1962 World Conference on Shell Structures at the University of California (Happold & Liddell 1975, Otto 1964). This was followed by a 17 m span gridshell in Essen, Germany, that same year, and two 18 m ones for the German Pavilion at the 1967 Expo in Montreal, Canada (Hennicke et al. 1974). The work at IL culminated in the hanging model used for the design of the 1974 Multihalle gridshell in Mannheim, Germany, built as part of the Federal Horticultural Show (Bundesgartenschau). After an initial 1:300 model establishing the general design, a 1:98.9 scale model was constructed and measured with photogrammetry (Figure 2.21). This data was then used for further numerical analysis and constrained form finding (Figure 2.43) (Addis 2014, Happold & Liddell 1975).

2.2.3 Hanging surface models

The idea of hanging a fabric, casting concrete and inverting it to obtain a funicular shell was patented as early as 1932 and developed on a large scale in the late 1950s (see Section 3.2.3).

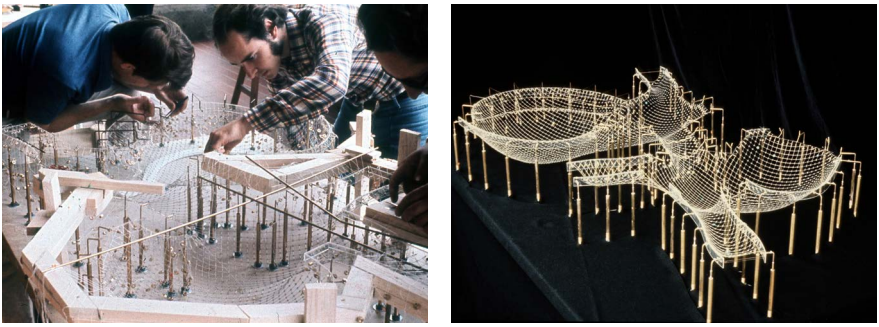

Figure 2.21: Hanging model for the Multihalle gridshell in Mannheim, Germany, 1974.

Otto et al. (1973) mention "sail shells", "thin bending- and compression-resistant structures that are shaped like a sail [that] are efficient under uniformly distributed positive loads". Otto undertook a series of experiments with cloth and plaster in 1946-1949 to determine their shape (Hennicke et al. 1974). In his doctoral thesis, Otto (1954) writes that "from the inversion of this hanging roof form, which is readily investigated with static modelling, one can easily determine a favorable form for a shell dome along a few points." Further experiments were undertaken in 1958 at Washington University in St. Louis. In this case, a rubber membrane was suspended, loaded with weights, plastered, inverted and then hardened with plaster and a GFRP resin. A later experiment with six rather than four corner supports is depicted in Figure 2.22. Otto then moved on to discrete models for gridshells (see previous section).

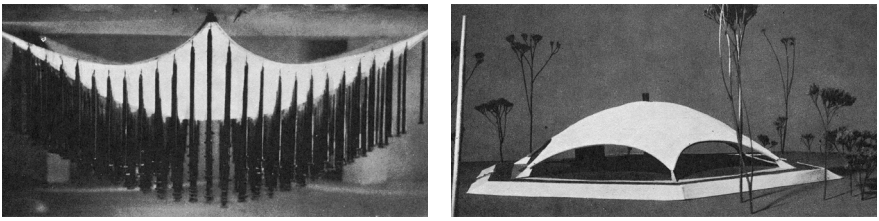

Figure 2.22: Hanging model of an unbuilt hexagonal river pavilion for a scout camp in Mississippi.

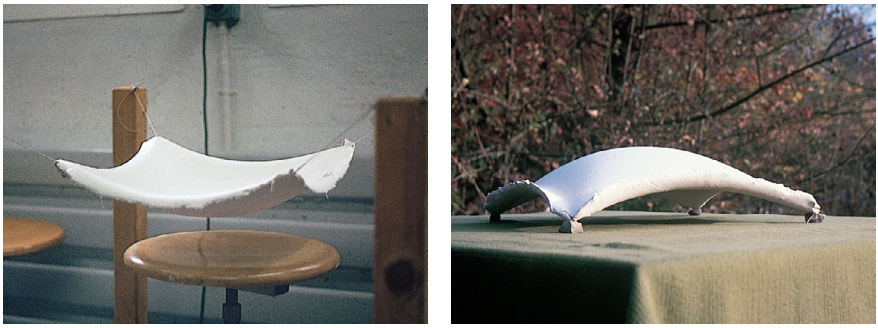

Figure 2.23: Hanging model and inverted form by Heinz Isler.

As mentioned, it was Isler who proposed this approach as a general design method rather than a construction method, claiming it was "for three-dimensional problems, what the catenary line is for two-dimensional arches" (Figure 2.23) (Isler 1960). He did so based on observations made in 1955 of how wet hanging cloth would freeze in winter (Ramm & Schunk 2002), but it is unknown if the correlation with the catenary was established later, or influenced his thinking beforehand.

Figure 2.24: Hanging model and built structure of the Sicli Company Building, Geneva, Switzerland, 1970.

Isler would succesfully be responsible for at least twenty projects consisting of 72 individual shell structures whose design was based on hanging models (Table 2.2) (Chilton 2000, Ramm & Schunk 2002). In particular, Isler enjoyed great success with the construction of tennis hall roofs. With the exception of the Broadland Sports Village in the UK, these were built in Switzerland, mostly with 47-48 m span, and generally 90-100 mm thick (Table 2.2).

Figure 2.25: Construction for Isler's tennis halls, and Sportscentre Heimberg, Switzerland, 1978.

Many of these shells were built with contractor W. Bösiger in Langenthal, who kept a stock of reusable curved glulam beams that formed the shuttering profiles of Isler's shells. The shuttering consisted of insulation boards and timber laths, and the entire system was supported by a standard shoring system.

project and location	year	span	thickness
Motorway Service Station (2), Deitingen, Switzerland	1968	31.6	90
Sicli Factory, Geneva, Switzerland	1969	30	100
Open-air theatre, Stetten auf den Fildern, Germany	1976	27.2	
Open-air theatre, Grötzingen, Germany	1977	28	90-120
Swimming pool, Heimberg, Switzerland	1978	32.5	90
Ballet Salon, Stetten auf den Fildern, Germany	1979	22	
Brugg Swimming Pool, Aarepark, Switzerland	1981	35	90
Aircraft Museum (4), Dübendorf, Switzerland	1987	51.7	
Broadland Sports Village Aquapark, Norwich, UK	1991	35	100
Tennis-Sport Düdingen (3)	1978	48.5	90-100
Sportscentre Heimberg (4)	1978-1979	47-48	90-100
Tennis Club La Chaux-de-Fond (2)	1978	47-48	90-100
Tennis Halls Grenchen (4,2)	1978, 1993	47-48	90-100
Crissier Halls (5)	1980	47-48	90-100
Tennis Halls Burgdorf (4)	1980	47-48	90-100
Dreilinden Tennis Centre, Langenthal (4)	1980	47-48	90-100
Emmen Tennis Centre, Lucerne (4)	1981	47-48	90-100
Brühl Sports Centre (6), Solothurn	1982	47-48	80
Paradies Tennis Centre (4), AllSchwil	1982	47-48	90-100
La Thène Sports Centre(4), Marin-Epagnier	1983	47-48	90-100
Sports Centre Les Iles, Sion (4)	1983	47-48	90-100
Broadland Sports Village (9), Norwich, UK	1988	47-48	90-100

Table 2.2: List of projects by Heinz Isler, designed using hanging models. Tennis hall roofs in second part. Number of shells in brackets. Sicli Factory and Sportscentre Heimberg shown in Figures 2.24 and 2.25 respectively.

2.2.4 Soap films and rubber membranes

Robert Le Ricolais (1894-1977) has been referred to as the "father of spatial structures" (Motro 2007). During his tenure at the University of Pennsylvania, he and his students carried out many experiments, including the use of soap bubbles and soap films around 1958-61 for the design of new structures (Figure 2.26).

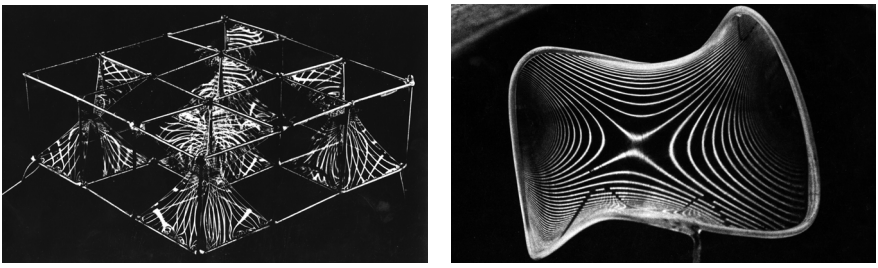

Figure 2.26: Soap film models with polarized light, identified as "soap film structure" and "hyperboloid", by Robert Le Ricolais, University of Pennsylvania, 1958-61.

Meanwhile, Frei Otto and his team also experimented with soap films and bubbles at IL. Earlier experiments with elastic rubber threads and membranes began around 1953, and fundamental studies on soap films and bubbles took place between 1958 and 1965 (Bach et al. 1988). Otto had met Le Ricolai in Philadelphia and knew of his work. He thought they may have "mutually benefited from each other to a certain extent, but that's it" (Songel 2010).

Figure 2.27: Soap film model and final structure of the 1979 King Abdul Aziz Stadium, Jeddah, Saudi Arabia.

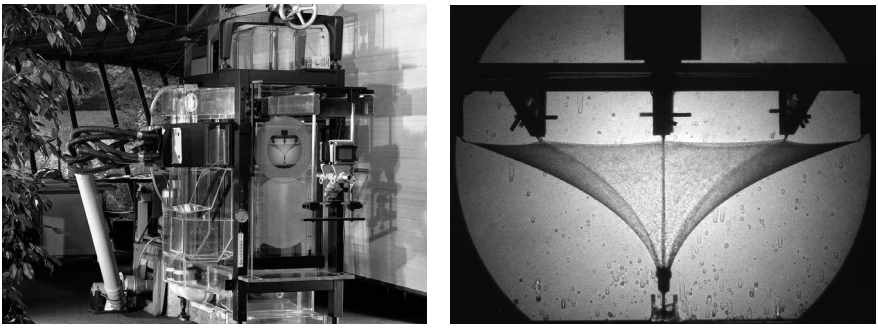

Figure 2.28: Soap film machine with an umbrella canopy model inside for the 1977 Pink Floyd US concert tour, at IL, University of Stuttgart, Germany.

Otto used soap film models for the design of several tensile membrane structures (Figure 2.27). For this purpose, a soap film machine was developed and built at IL in the period 1967-1973. The machine featured a climate chamber, lighting and photography to study, measure and record models (Figure 2.28) (Bach et al. 1988).

Primarily occupying himself with lightweight tensile systems, it was only at the end of his life that Otto employed a soap film model for a reinforced concrete shell. Ingenhoven Architects approached him to design the thin-shell platform canopy as part of the overhaul of Stuttgart's main station and tracks, better known as the Stuttgart 21 project. The 28 supports, spanning a distance of 36 m with a thickness of 350 mm, are referred to Kelchstütze (chalice supports) due to their open shape, which allows for daylight entry. At his own studio, Atelier Warmbronn, Otto used both soap films and meshes to develop the design. Buro Happold measured and digitized the final model, as the starting point for further refinement of the design. Controversially, Otto quit the project in 2009, citing geotechnical safety concerns, not long after both Buro Happold and engineering firm Leonhardt, Andrä und Partner were released from the project. A mockup of the formwork was recently completed, and consisted of standard scaffolding, props and timber trusses, with milled plastic foam.

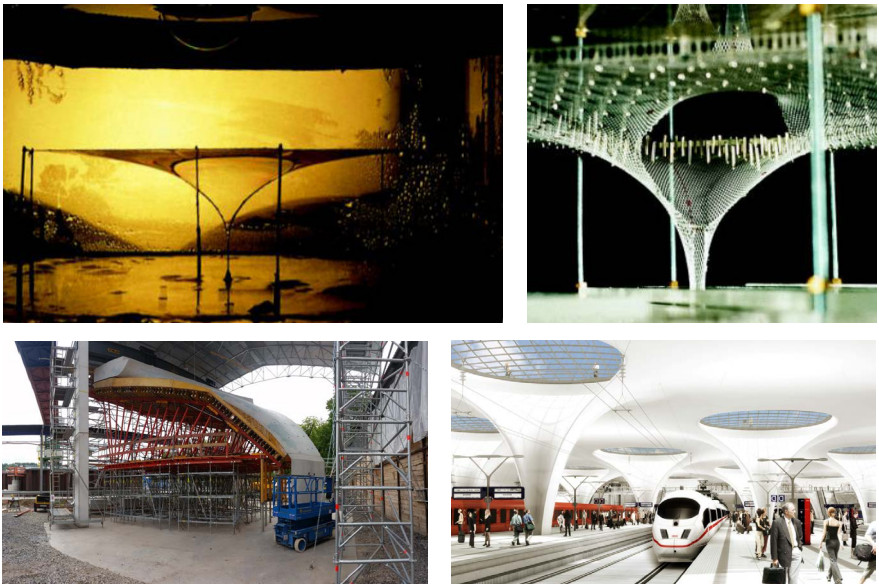

Figure 2.29: Soap film and mesh models, c. 2000, formwork mockup, 2016 and render of the train station platform canopy, Stuttgart 21 project, Germany, 2000.

Sergio Musmeci (1926-1981) used stretched rubber membrane and soap film models to design large-span bridges: the Tiber Bridge in Tor di Quinto, Rome, 1959 (Figure 2.30); and the Lao Bridge in Conzensa, 1964. He had also experimented with hanging models for the 1956 design of the Astico Bridge, close to Vicenza (Figure 2.30).

While Musmeci knew of Le Ricolais, at the time he was unaware "that Frei Otto was embarking on similar experiences with tensile structures in the same years." All three projects were never built, but soon after he was able succesfully propose the Basento Bridge, also known as the Musmeci Bridge (Figures 2.31 and 2.32) (Adriaenssens et al. 2015, Ingold & Rinke 2015).

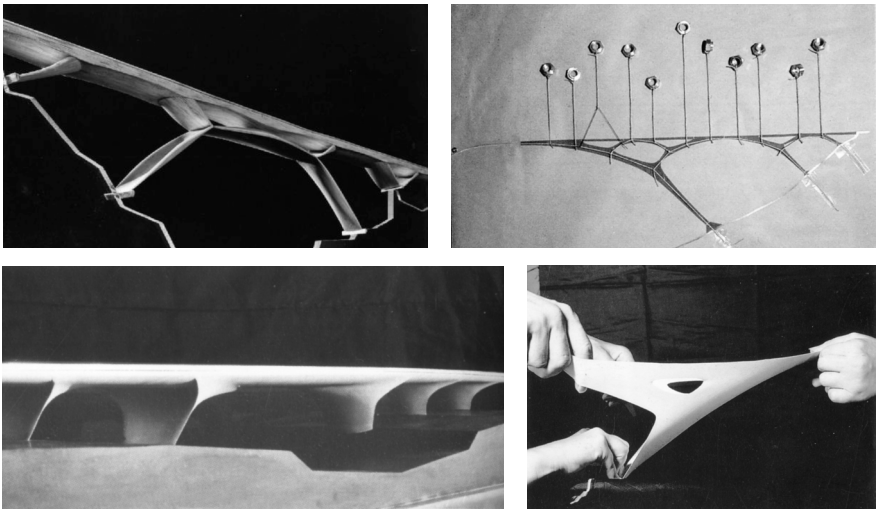

Figure 2.30: Form-finding models for the unbuilt Astico Bridge, 1956, and Tiber Bridge in Tor di Quinto, Rome, 1959.

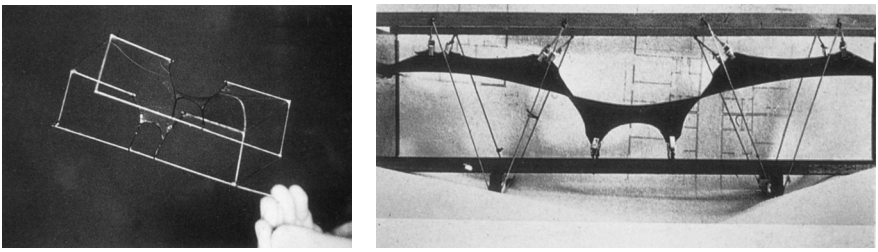

Figure 2.31: Form-finding models for the Basento Bridge in Potenza, Italy, 1975.

The bridge consists of four 69 m spans, and the shell structure supporting the deck has a nominal thickness of 300 mm. The design work started in 1967, with construction taking place between 1971 and 1975. The formwork consisted of timber and standardized shoring. Above the river the formwork was supported by large struts radiating from the abutments. The complexity of the geometry and subsequent delays plagued the project, with construction costs spiraling from 490 to 920 million liras (Giovannardi 2010). However, given the sheer size of the Basento Bridge, this cost, even by today's standards, seems modest.

Figure 2.32: Basento Bridge, Potenza, Italy, 1975.

In the US, only one year after Isler's conference presentation, Kolbjørn Saether (1925–2007) published a paper on designing funicular shells, or "structural membranes", by analogy with elastic membranes (Saether 1961). "If a complete stress reversal is assumed the shape of an elastic membrane under tension would be ideally suited for a concrete structure under compression." He argued that funicular shapes were too complex to physically measure or analyze, and advocated their approximation with mathematical shapes. The model shown in Figure 2.33, for example, was approximated by connected conoids and hyperbolic paraboloids. Most of his other physical models included air pressure (Section 2.2.5). Saether (1995) mentions traditional and earthen formworks as possible methods of construction.

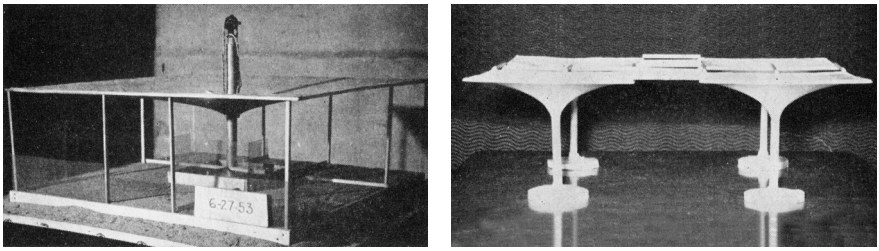

Figure 2.33: Rubber membrane models for one- and four-column structure (Saether 1961).

Citing Otto and Saether, Willard August Oberdick (1922–1982) suggested using soap films and elastic membranes for the design of plastic funicular shells, but also as a direct means of construction, referring to the method as a "form-giving device". This is possibly the earliest realization that the method of design and method of construction can be the same, though this idea is already implicit in some of Otto's and Isler's earlier work.

Two prototypes were built at the University of Michigan, both 24 ft square in plan consisting of four umbrella shells, one with four high points, the other inverted (Oberdick 1965*a*,*b*). They were made by impregnating a 1 in reticulated flexible foam with urethane resin, stretching it into a frame, curing it and then spraying glass fibre reinforced polyester resin, with the initial shell removed for use as a template formwork for the other umbrellas (Figure 2.34). Oberdick (1965*b*) also considered hanging models, which were deemed problematic to invert at larger scales, leading him to bending-active formworks (Section 3.5).

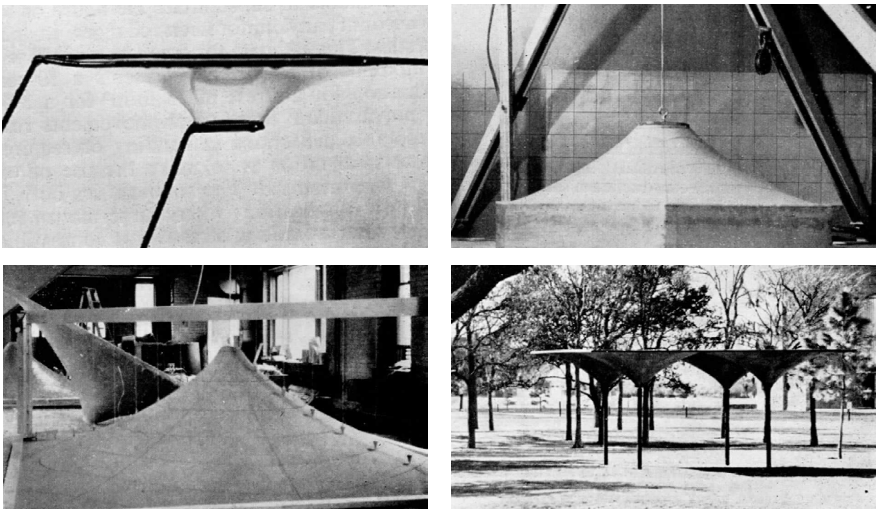

Figure 2.34: Soap film and flexible polyurethane foam membrane models, 12 ft square measurement model and inverted prototype (Oberdick 1965*a*).

Rein Jansma used a stretched rubber membrane to design the Extended Waalbridge (Figure 2.35) (Torsing et al. 2012), although further requirements from the client required the shape to be substantially altered. These changes were made through a computational form-finding model. The bridge has two larger 79 m spans and its lower surface is 300-500 mm thick. Although the bridge was initially envisioned

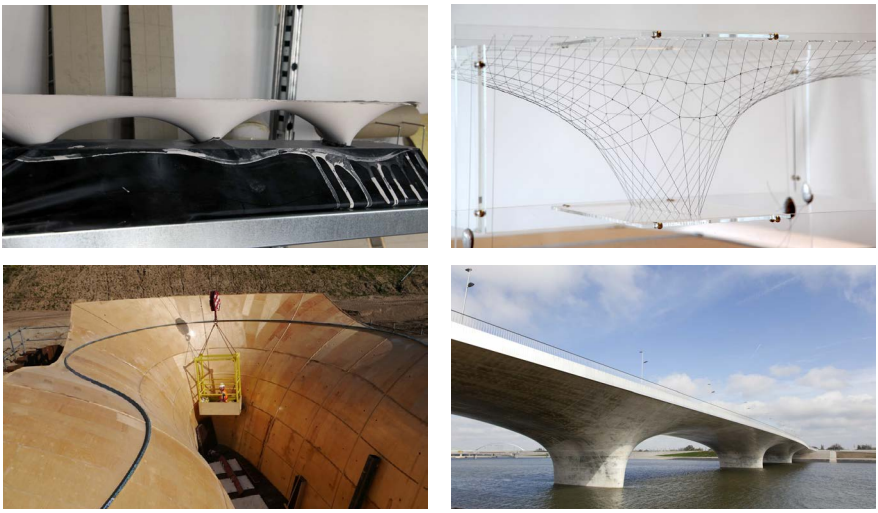

Figure 2.35: Plaster model using rubber membrane, wire model, timber formwork and final structure of the Extended Waalbridge, Nijmegen, Netherlands, 2015.

as a shell, the final design has vertical diaphragm walls throughout, connecting the lower surface with the upper deck. The construction was carried out in full timber formwork, but prior to tendering the idea of a fabric formwork had been suggested. Søndergaard et al. (2014) report that CNC milling was prohibitively ineffective for this scale and not economically competitive with the more traditional approach that was chosen.

Toyo Ito designed the Taichung Metropolitan Opera House, Taiwan, built 2005-14, based on an earlier proposal with Andrea Branzi for his firm's competition entry for the Ghent Forum for Music, Dance and Visual Culture in 2004 (Figure 2.36) (Motosugi & Mizunuma 2011). Some physical concept models were used to generate a continuous spatial structure, but final design was done by computationally generating the catenoid minimal surfaces within given boundaries. The challenging nature of the project led to a protracted tendering process, failing four times to find a suitable contractor. Ultimately, a stay-in-place formwork was chosen instead of a doubly curved formwork. In this case, shotcrete was sprayed against the reinforcement and an expanded metal mesh that served as a backstop. A final mortar coating provided a smooth finish. The structure clearly relies on bending rather than membrane action, so in this thesis, it is not strictly classified as a shell.

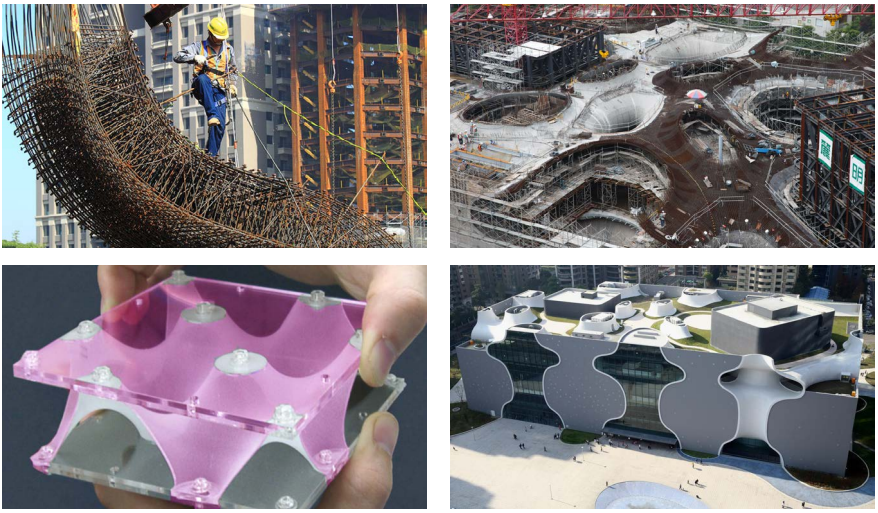

Figure 2.36: Taichung Metropolitan Opera House, Taiwan, 2014, and earlier stretched model for the design of the Forum for Music, Dance and Visual Culture, Ghent, Belgium.

2.2.5 Pneumatic form finding

As mentioned, Isler presented the idea of shaping shells through inflating and measuring rubber membrane models in 1959. Some years earlier, in 1954, he had designed his first shell in this manner and later his commercially successful bubble shell, or Buckelschale (Chilton 2000), which was constructed on a rigid formwork instead (Figure 2.37). Isler (1967) initially suggested that pneumatic formwork was a logical method of construction for such shapes, but that they still presented many technical difficulties. He would in fact proceed to use air-inflated formworks a decade later (Section 3.4.1).

Around the same time, Saether (1961) also experimented with air-inflated rubber membranes. These models were also measured, but not used as a direct means of design. Instead, measurements were compared to known geometrical shapes such as the elliptical paraboloid, hyperbolic paraboloid and logarithmic elliptoids, in order to establish analytical functions for further use (Figure 2.38). He concluded that "there is no apparent limit to the number of different elastic membranes which can

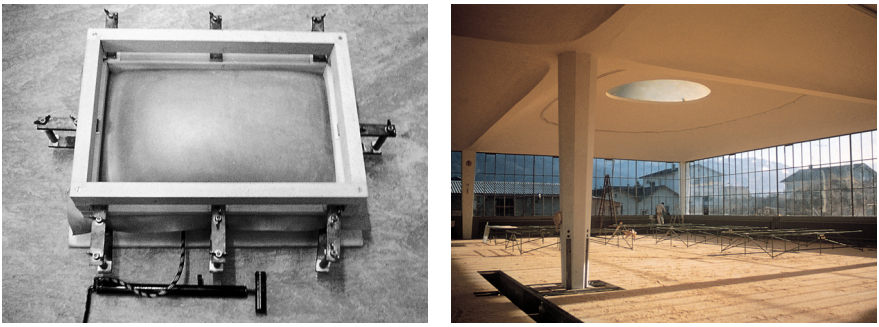

Figure 2.37: Original inflated rubber membrane model and interior of Eschmann Company, Thun, Switzerland, 1958.

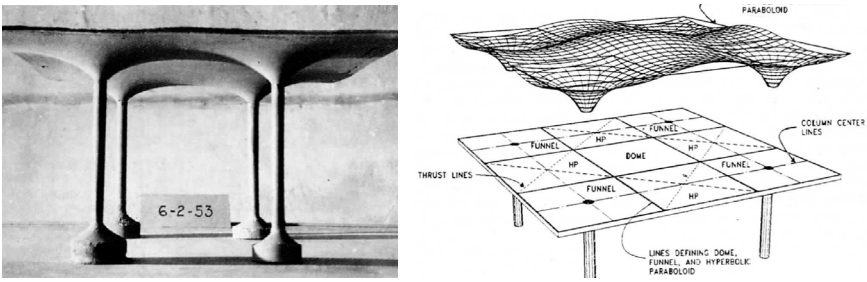

Figure 2.38: Model cast from inflated rubber membrane and analytical approximation (Saether 1995).

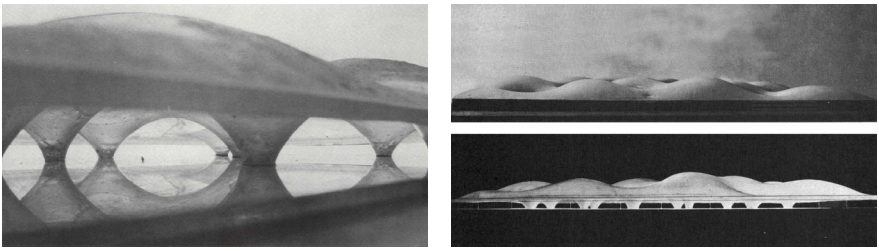

Figure 2.39: Inflated model of shell with internal drainage points, hardened with GFRP (Otto & Stromeyer 1962).

be approximated in this manner", eliminating the "problem of physically measuring or analyzing a funicular shape" (Saether 1961). He published about this approach again in the 90s, but no longer discussing the physical modelling in any particular detail (Saether 1995).

Otto & Stromeyer (1962) show several inflated membrane models, mostly as literal scale models of air-inflated structures, but also intended as structures that are stiffened by applying GFRP (Figure 2.39), or, in other words, as air-inflated formworks (Section 3.4.1).

2.2.6 Hydrostatic form finding

João Francisco Lobo Fialho used both experimental and analytical work for the design of the 55m long Vilar Dam, spanning the Távora river in Portugal (Lobo Fialho 1956). The funicular dam was designed using a hydrostatic form-finding model, such that membrane stresses would not exceed 5 MPa anywhere (Figure 2.40). Measurement of the boundary conditions on site and shape of model were used to establish approximate analytical expressions for the boundaries, generatrix and directrices. The varying thickness was also expressed analytically to improve the stress distribution. The work was carried out at the Laboratório Nacional de Engenharia Civil (LNEC) in Lisbon, and mentioned at Isler's lecture in 1959 by the laboratory's director, Ferry Borges. An interesting parallel are tension-loaded, funicular cable-net dams, proposed by Otto et al. (1973), and as early as 1954.

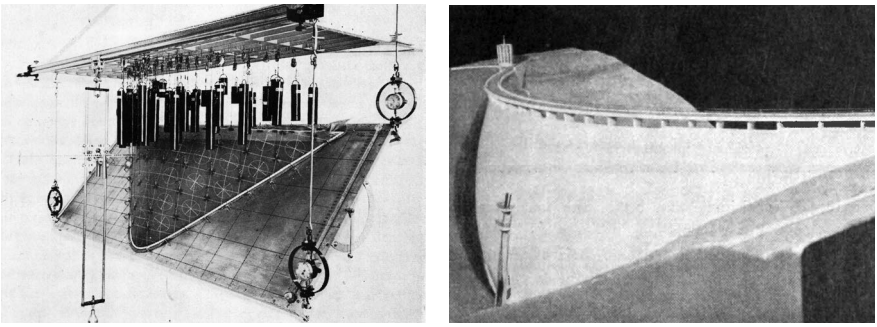

Figure 2.40: Hydrostatic form-finding model and scale model of the funicular design for the Vilar Dam, Portugal (Lobo Fialho 1956, 1966).

In 1965, the Vilar Dam was inaugurated, but by then designed and constructed as a conventional earthen dam. A major reason to decide against an arch dam had been the alarming 1959 accident at the Malpasset Dam, near Fréjus, France, which resulted in 423 fatalities after the dam had broken due to geological instabilities. Nevertheless, Lobo Fialho & Rodrigues (1965*a*,*b*,*c*) presented and advocated the design again (Figure 2.40). Based on a comparative study of different types of dams

for this location, they argued that the funicular dam was the best and most affordable option, though they acknowledged that for this site, extensive geological studies would be required. Akbari et al. (2011) provide an overview of developments in the shape optimization of arch dams since, which have typically included additional loading conditions, material behaviour and soil stability, to derive a shape.

2.3 Numerical form finding

Even though Frei Otto was skeptical of computers and their role in design (Songel 2010), it was his work that was instrumental to the development of all types of numerical form-finding methods: stiffness matrix methods and force density methods through their development for the Munich Olympia Park (Figure 2.41), and dynamic relaxation through its use during his many collaborations with Ted Happold (1930–1996). These methods are digital analogues to the physical form-finding methods presented in the previous section.

Figure 2.41: Munich Olympic Park, Germany, with stadium (top), sports hall (right) and swimming pool (bottom), completed in 1972

Since the 1960s, and with the advent of the computer age, research focused on developing these numerical form-finding methods, initially applied to the design and analysis of prestressed and hanging cable-net roofs (Figure 5.1). This coincided with what is now considered to be the golden age of the finite element method, 1962-1972 (Felippa 2013). These earliest form-finding or shape-finding methods assumed an initial, unloaded geometry, or cutting pattern. This was relevant as it is practical to erect cable-net roofs from given, uniformly spaced meshes. In essence, these were finite element methods for structural analysis with large displacements, but in the context of form finding have been referred to as stiffness matrix methods.

Two seminal form-finding methods were developed around this time; the force density method by Klaus Linkwitz, Hans-Jörg Schek and Lothar Gründig from 1968 onwards at the University of Stuttgart, Germany; and dynamic relaxation by Michael Barnes, David Wakefield and Manolis Papadrakakis from 1971 onwards at the City University London, UK. The force density method was developed in competition with stiffness matrix methods.

2.3.1 Force density and stiffness matrix methods

Physical models were used to determine the shape of the roofs of the 1972 Munich Olympic stadium. Initially, photogrammetric measurements of these models were used to derive cutting patterns, but these were not sufficiently accurate (Figure 2.42).

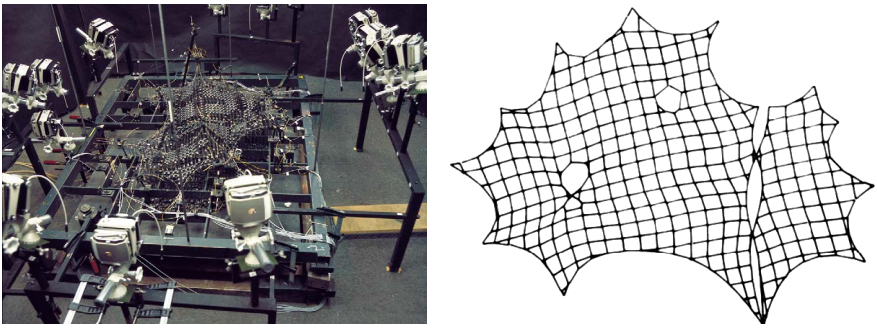

Figure 2.42: Photogrammetric measurements of the Olympic Swimming Pool model, and numerical shape finding model (colours inverted) (Argyris et al. 1974).

As a result, least squares methods were used to establish a digital model in static equilibrium under constraints of unstressed equal mesh width (Gründig et al. 2000, Linkwitz & Schek 1971), an approach that is referred to here as constrained form finding (Chapter 6). The work was accelerated by the pressure of completing the stadium roofs on time, and the fact that Prof. Linkwitz' group was in competition with that of Prof. Argyris, also at the University of Stuttgart.

In parallel, Argyris & Angelopoulos (1972) developed a method which assumed an initial geometry and material properties. They realized the initial lengths could be changed afterwards to optimize the resulting prestresses without influencing the final equilibrium shape. Ultimately, the western stadium roofs were calculated using Linkwitz' least squares method, while the roofs of the Olympic Swimming Pool, Olympic Hall and the unbuilt eastern stadium roofs used Argyris' (Figure 2.41).

Argyris et al. (1974) soon realized that "it is possible to develop a shape finding method [..] which does not consider the elastic properties of the structure", citing Siev (1963) and Schek (1974). The latter, the force density method, was able to produce general networks in static equilibrium by solving only one system of linear equations, requiring no further iteration. The equilibrium shape could now be found geometrically, and any cutting patterns could be derived afterwards. Later, this would become increasingly relevant for tensioned membrane roofs where cutting patterns are not obvious to specify in advance.

During the period 1972-1995, further development was funded by the German Research Foundation, as part of the interdisciplinary research groups Sonderforschungsbereiche (SFB) 64 "Lightweight Tension Structures" (Linkwitz et al. 1984) and 230 "Natural Constructions, Lightweight Structures in Nature and Engineering".

As a result, the constrained force density method was later applied to the timber gridshell roofs of the Multihalle in Mannheim (Figure 2.43), and the Solemar-Therme in Bad Dürrheim, both in Germany (Gründig 1988, Gründig & Schek 1974). The unconstrained, linear method was used for the latter project as a starting point.

The unconstrained force density method was first applied to the cable-nets of the 1979 King Abdul Aziz Stadium, Jeddah, Saudi Arabia (Figure 2.27), and the 1986 Hannover Aviary, Germany. The first tensioned membrane project was the Olympic Roof in Montreal, completed in 1987, although intended for the 1976 Olympic Games. Widespread application of the unconstrained force density method was found through its implementation in software such as EASY by Technet from 1989 onwards for the design and engineering of tensioned membrane and air-inflated structures.

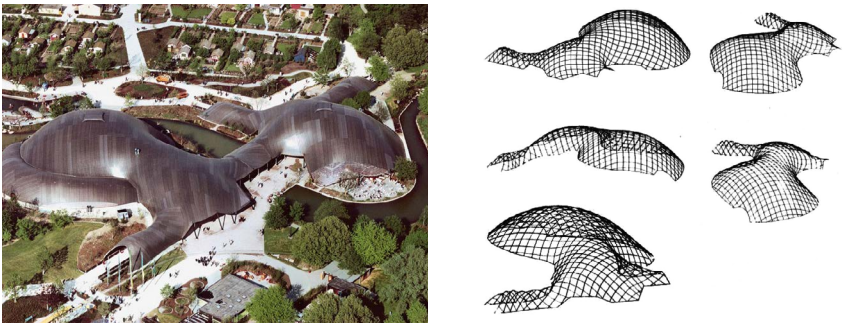

Figure 2.43: Multihalle, Mannheim, Germany and numerical constrained form-finding model (Gründig & Schek 1974).

A large number of methods have been presented since, as extensions or generalizations of the original force density method, such as the geometric stiffness method (Haber & Abel 1982), the updated reference strategy (Bletzinger & Ramm 1999) and the natural force density method (Pauletti & Pimenta 2008). A recent method, thrust network analysis, combines the force density method with principles of graphic statics for the form finding of funicular shells (Block 2009). Early work was applied to the Mapungubwe National Park Interpretive Centre, South Africa (Ramage et al. 2010), and a range of structural prototypes and pavilions since (Figure 2.44) (Rippmann 2016).

Figure 2.44: Freeform Catalan thin-tile vault, Zurich, Switzerland (Davis et al. 2012), and the Armadillo Vault at the 2016 Venice Biennale of Architecture, Italy (Rippmann et al. 2016).

A number of extended force density methods has been published in China in recent years (see Chapter 5.2). Indeed, a 2006 special issue of the Journal of the International Association for Shell and Spatial Structures on spatial structures in China cites four hundred membrane structures built each year and growing (see also Section 3.9).

Due to today's wide availability of finite element software, the stiffness matrix method has been applied to the form finding of shell structures more often than the force density method. In these cases, the elastic stiffness is set a value close to zero. The following three examples each used the finite element program Sofistik for this purpose.

The renovation of the Palacio de Cibeles (Cybele Palace), formerly the Palacio de Comunicaciones, in Madrid, included a steel gridshell covering the inner courtyard, completed in 2009 (Figure 2.45). The shape, designed by Arquimática, was derived from an inflated balloon, constrained by the highly irregular plan of the courtyard. Although the engineers, Schlaich Bergermann und Partner, initially made attempts to rationalize the shape as a quadrangulated, translational surface, the final triangulated gridshell was modelled as a hanging membrane using numerical form finding (Schlaich et al. 2009, Schober 2015). They had taken a similar approach for the 2007 Odeon Munich roof by Ackermann and Partner.

The Elephant House at the Zurich Zoo, Switzerland, by Markus Schietsch Architekten and Walt + Galmarini, was completed in 2014. This filigree timber shell has 540 mm thick ribs spanning up to 80 m (Figure 2.45). Starting from a flat pattern, form finding was carried out as a hanging model while adhering to constraints on the maximum building height and deformations along the open edges at the perimeter (Kübler 2014).

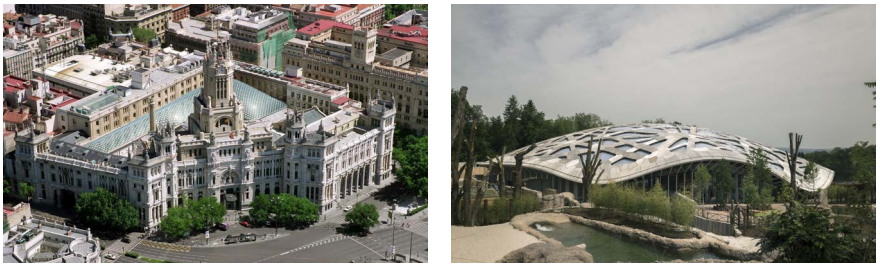

Figure 2.45: Palacio de Cibeles, Madrid, Spain, 2009, and the Zurich Zoo Elephant House, Switzerland, 2014.

2.3.2 Dynamic relaxation

The dynamic relaxation (DR) method was initially proposed for the structural analyis of portal frames by Day (1965). In 1966, Barnes had completed his Master's thesis on cable-net analysis, and started using DR after reading a 1969 internal paper by Day and Bunce for the engineering firm Arup, soon publishing about its application to cable networks himself (Barnes 1971). In 1975, while lecturing at the City University London, Barnes invited his students Wakefield, Topping and Papadrakis to undertake doctoral studies under his supervision and suggested their topics in the area of DR and tension structures, before completing his own (Barnes 1977).

Barnes met with Ian Liddell and Ted Happold from engineering firm Buro Happold while presenting at conferences in Stuttgart and Montreal in 1976. This began a series of projects, all involving Frei Otto and Buro Happold, in which Barnes undertook analysis and patterning for the contractors on behalf of the engineering firm Ingenieurplanung Leichtbau (IPL). Many of these occurred during the late 1970s construction boom in Saudi Arabia, resulting from the ongoing global energy crisis (see also Section 3.4.1).

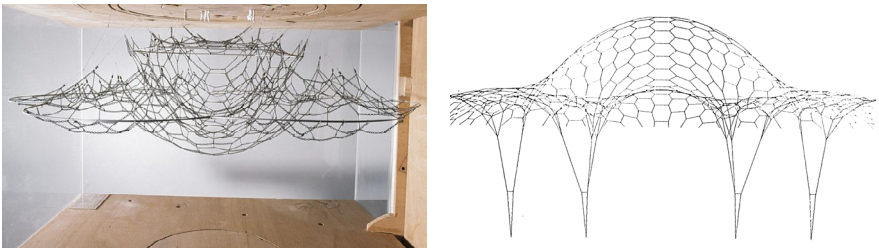

Figure 2.46: King's Office, Council of Ministers and Majlis Al Shura (KOCOMMAS) project of Frei Otto and Buro Happold, hanging model and numerical form-finding model (Barnes 1977).

The first and highly ambitious application of DR was the hexagonal lattice shell for the King's Office, Council of Ministers and Majlis Al Shura (KOCOMMAS) (Figure 2.46). The project started in 1974, involving Ove Arup as well, but was cancelled after the death of King Khalid in 1982 (Walker & Addis 2005).

The second was the analysis of the cable network for the King Abdul Aziz University Sports Hall in Jeddah, Saudi Arabia; the first built structure analyzed using DR, following initial hanging chain and soap film studies (Figure 2.27). As mentioned, it was also the first built structure using the unconstrained force density method.

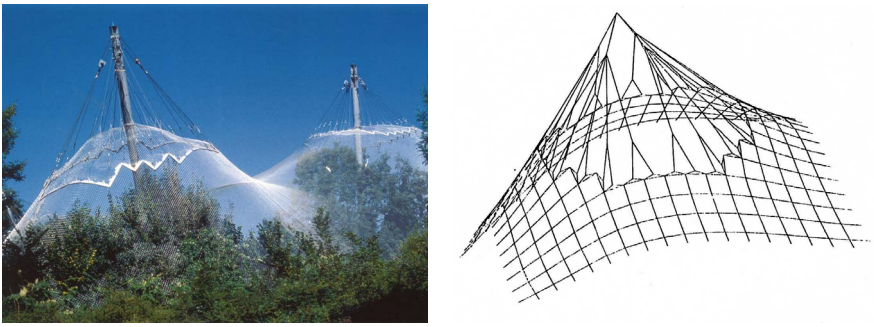

Figure 2.47: Munich Zoo Aviary and numerical form-finding model (Barnes & Wakefield 1984).

This project was soon followed in 1980 by the cable-net enclosure of the Munich Zoo Aviary (Figure 2.47) and the 1985 Diplomatic Club for the Diplomatic Quarters in Riyadh, Saudi Arabia (Figure 2.48). The latter project consisted of three membrane structures, two cable networks, and another cable network with stained glass as the central focus of the complex (Barnes 1988).

Like the force density method, wider use of dynamic relaxation was found through software. Buro Happold's in-house program Tensyl was developed from 1980 onwards, and when Wakefield left to co-found Tensys with Barnes, this was followed by Tensys' in-house program inTENS from 1990 onwards. Several built examples of tensioned and air-supported membrane structures from both firms are shown by Barnes (1994) and Wakefield (1999).

DR has been applied to the analysis and mesh relaxation (but not the form finding) of gridshells such as the 2000 Great Court roof of the British Museum (Figure 1.3) and the 2002 Downland Gridshell, both in the UK (Harris et al. 2003, Williams 2001). It was finally used for the form finding of the gridshell roof of the 2011 Dutch National Maritime Museum in Amsterdam (Figure 2.49), designed by Ney+Partners (Adriaenssens et al. 2009) and again (using finite element program GSA) for the 2015 terminal of Arnhem Central Station in the Netherlands, by UN Studio and Arup (Figure 2.50). This terminal was designed by establishing boundary conditions based on a knot, and then "tuning the surface and edge stresses and applying surface pressure at specific locations" (Van de Straat et al. 2015). The resulting "minimal surface" was intended to optimize the span and organize pedestrian flow through the terminal (Wallisser 2009). The tendering of the entire project failed in 2008 after five parties had withdrawn and a sixth bid came in at twice the budget. Individual

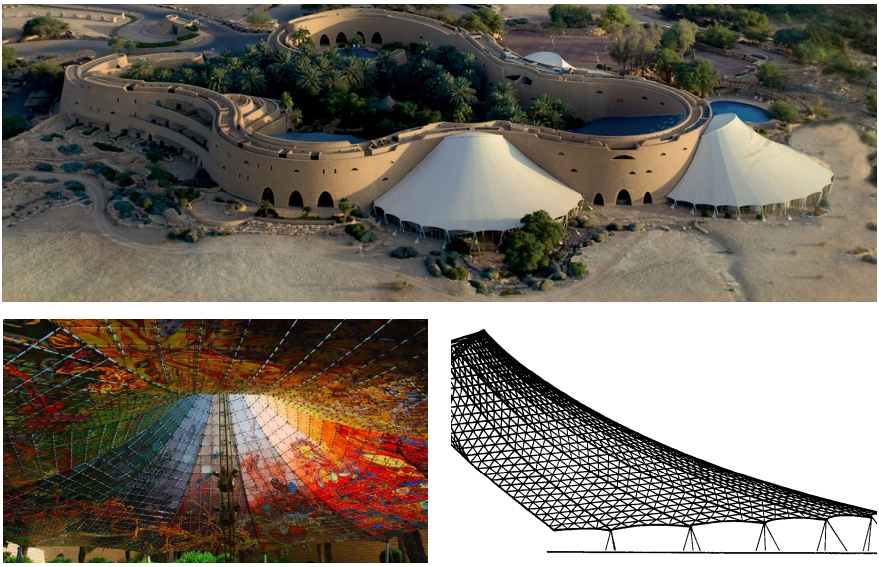

Figure 2.48: Diplomatic Club (now Tuwaiq Palace), with stain glass cable network at the centre, Riyadh, Saudi Arabia, 1985, and form-finding model of outer membrane structure, or Banqueting Roses (Barnes 1988).

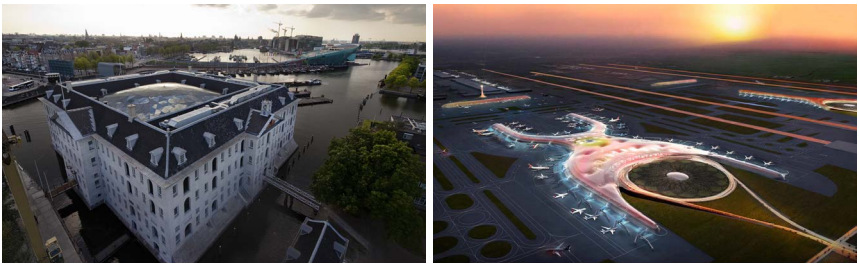

Figure 2.49: Dutch National Maritime Museum, Amsterdam, 2011; and design for the new Mexico City international airport, c. 2014.

parts such as the terminal were then separately tendered out. Although originally envisioned as a concrete shell, the roof and most complex parts were ultimately built in steel by shipbuilder Centraal Staal (now CIG) (Figure 2.50) (van Dijk et al. 2013). Coincidentally, the curved concrete cladding panels of the roof were cast on a flexible mould (Hoppermann et al. 2015).

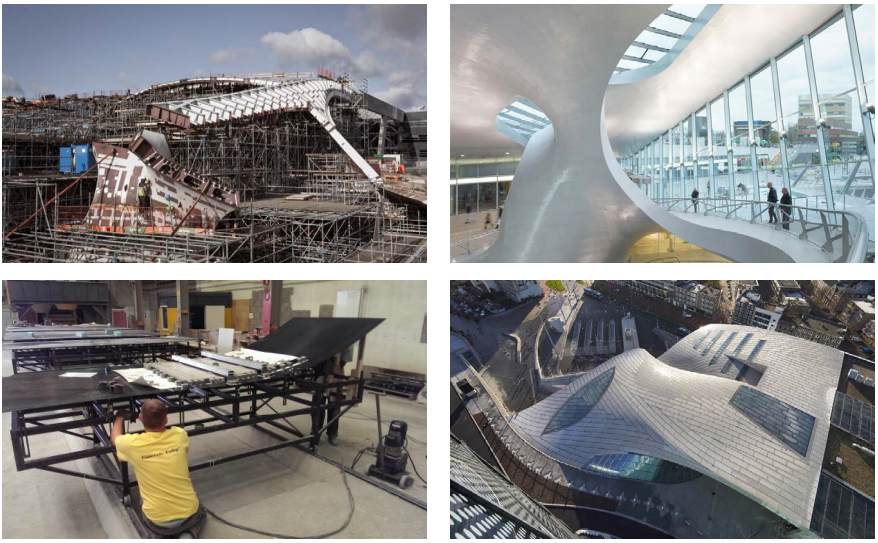

Figure 2.50: Steel elements for the shell and flexible mould for the cladding of Arnhem Central Station, Netherlands, 2015.

Particle-spring form finding is a recent approach combining the idea of Gaudí's hanging models with principles similar to dynamic relaxation (Kilian 2004, Kilian & Ochsendorf 2005). Both methods were implemented in Kangaroo, a plugin for Grasshopper, which has been applied to the new international airport for Mexico City, designed by Foster+Partners. The structure is a large, double-layered steel gridshell, or spaceframe (Figure 2.49).

2.4 Freeform shapes

The unbuilt Táchira Club by Fruto Vivas and Eduardo Torroja has been considered to be one of the first freeform shell designs, even though it can still be defined as a generalized translational surface, based on only two equations (Figure 2.13, Section 2.1.3). It was also developed with structural considerations in mind, and using models for analysis along the way (Escrig & Sánchez 2005). Whatever the case, Andrés (2009) points out that Torroja anticipated a paradigm shift in shell design: "And thus it is

possible to build successfully forms so varied [...] that is only the announcement and proclamation of the revolution that is approaching in the field of architecture, whose vocabulary of plastic forms is opening and widening with rapidity and imaginative fecundity unknown in all the history of Construction [sic]."

Figure 2.51: Construction and final interior of TWA Flight Center, New York, US, 1962.

The 1962 Trans World Airlines (TWA) Flight Center (Figure 2.51), designed by Eero Saarinen (1910–1961) and Associates and engineered by Amman & Whitney, is perhaps the earliest realized freeform concrete shell (Sasaki (2005), although considering it a personal favorite, objects to even calling it a shell). Rather than being mathematically defined, or resulting from physical form finding, its shape was the outcome of a purely sculptural design process. The terminal was intended to resemble a bird in flight. A series of clay models and cardboard forms were used to arrive at the final design. The surface was then rationalized as four individual surfaces, generated by translating two intersecting arcs along a longitudinal curve of varying, but smoothly transitioning arcs. The shells have clear spans of 67 and 91 m with minimum thicknesses of 178 and 279 mm. The formwork consisted of steel scaffolding with adjustable jacks, supporting timber shuttering and boards (Figure 2.51) (Anderson et al. 1964).

The freeform Eastman Kodak Pavilion for the 1964-1965 New York World's Fair was a 5'600 m^2 shell with "undulating surfaces, not definable geometrically" and was referred to as the "Flying Carpet" (Figure 2.52). Conceived as a lunar landscape, it was designed by Will Burtin using a sculptured plastic model, and developed by architectural firm Kahn and Jacobs. The shell spans up to 34 m and has a thickness of 152 to 356 mm, averaging 279 mm (Zetlin 1964, 1966).

More recently, Sasaki (2014) has been involved in five freeform concrete shell structures. He was frustrated with the design process of the unbuilt 1998 National Grand Theater in Beijing China, with Arata Isozaki: "there is very little merit in just using repeated trial-and-error to structurally analyze a particular shape provided by an architect, and so just doing it all again would be an immense waste of effort". He then

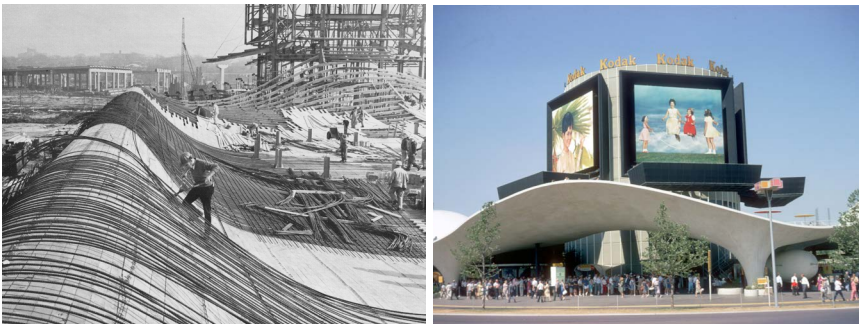

Figure 2.52: Eastman Kodak Pavilion, World's Fair, New York, 1964-1965.

developed an optimization method which minimizes the strain energy of a doubly curved surface by changing the position of the nodes or control points. Sasaki sees this method, which he calls "sensitivity analysis", as a modern replacement to Gaudí's experimental models (Sasaki 2005). He applied it to another project with Isozaki: the 2005 Kitagata Community Centre in Gifu, Japan (Figure 2.53). The 25 m span, 150 mm thick shell, was built using the reinforcement bars as stay-in-place formwork.

Figure 2.53: Kitagata Community Centre in Gifu, Japan, 2005.

Three subsequent projects were all built with doubly curved timber formwork on a system of steel shoring, not unlike the TWA Flight Center. These are the 70 m span, 400 mm thick 2005 Island City Park "Gringrin", in Fukuoka, Japan; the 20 m span, 200 mm thick 2006 Kakamigahara Crematorium in Gifu, Japan; and, the 80 m span, 400 mm thick 2009 Rolex Learning Centre in Lausanne, Switzerland. Sensitivity analysis was applied to each of these, including an early design for the Rolex Learning Centre (Sasaki 2005). Further structural design and engineering was carried out by Bollinger + Grohmann Ingenieure (Grohmann et al. 2009).

An earthen formwork was used for the fifth project, the 2010 Teshima Art Museum in Kagawa, Japan. This 43 m span, 250 mm thick shell was imagined as a water droplet, and optimized using sensitivity analysis. The earthen formwork was coated with mortar and its shape controlled through measurements, before casting and eventually excavating the shell (Figure 2.54) Sasaki (2014).

Figure 2.54: Teshima Art Museum in Kagawa, Japan, 2010.

Figure 2.55: Spencer Dock Bridge, Dublin, Ireland, 2010.

The 2010 Spencer Dock Bridge, spanning the Royal Canal in Dublin, Ireland, was designed by Amanda Levete Architects and engineered by Arup. Its fluid, free-form shape was inspired by the manta ray. The concrete bridge was constructed on a CNC-milled EPS formwork, supported by scaffolding. The EPS foam blocks, produced by Nedcam, were coated with layers of polyurea and their seams were filled with epoxy putty (Lavery 2013). The intention was to reuse or recycle the EPS foam. Upon removal of the formwork, the foam was too damaged and dirty to reuse. Furthermore, separating the foam from the polyurea coating was deemed too costly to allow for recycling (Verhaegh 2010).

2.5 Formwork systems

Throughout this chapter, figures have shown the formwork method of construction for many past shell structures. The concrete is poured or sprayed, and this can be done in-situ or for prefabrication, but requires some kind of formwork regardless. Here, the types of formwork methods are categorized and additional information is given where needed. The emerging technology of 3D printing is also discussed as it applies to shell structures. Beyond these methods, Chapter 3 provides a comprehensive overview of instances in which flexible surfaces were used to construct shells.

2.5.1 Timber formworks

As seen throughout this chapter, the earliest and still most common solution to form shell structures is the use of timber formworks. Early shoring and scaffolding was made of timber as well. Today, these have been replaced by steel or aluminium prefabricated, modular and adjustable systems. This falsework supports a system of timber shuttering and sheeting. Timber shuttering is typically made of I-beams, but for curved surfaces, timber trusses and curved glulam beams have been used as well. Formwork companies such as Doka and Peri market their expertise in this approach as a product rather than a service; DokaShape and Freeform Formwork respectively. While traditional formworks for hyperbolic paraboloids and hyperboloids rely on straight timber following their generator lines, developments in digital fabrication now allow mass customized timber formwork for freeform shapes. Specialist consultancy DesignToProduction, for example, has worked on such formworks for the Rolex Learning Centre, mentioned in Section 2.4, and the 2006 Mercedes-Benz Museum in Stuttgart, Germany, designed by UN Studio.

2.5.2 Slipforms

Slipforms are efficiently used for vertical concrete structures such as cores of high-rises, and in terms of shells, for cooling towers (Figure 2.10) and arch dams (Figure 2.56). These systems are so widely required, that they have been developed as standardized products by formwork companies such as Doka, Meva and Ulma.

Figure 2.56: Doka D34 dam formwork, applied to the Sarvsfossen dam of the Skarg power station, Norway, 2014.

2.5.3 Stay-in-place formworks

If substantial enough, the shell's reinforcement can act as a self-supporting formwork system. The reinforcement cage would generally be too coarse and thus requires a steel mesh or some other form to hold the concrete. These meshes or forms can be attached directly or suspended from the reinforcement. If the mesh is the predominant reinforcement material, and any rebars serve more as a skeletal cage to hold the mesh in place, the resulting composite is referred to as ferrocement. In the context of sprayed concrete, or shotcrete, such a mesh might be referred to as a backstop. Unfortunately, there is no consistent term for this type of formwork system.

Examples in this chapter include the 1926 Zeiss Planetarium in Jena, Germany (Figure 2.2), the 2005 Kitagata Community Centre in Gifu, Japan (Figure 2.53) and the 2014 Taichung Metropolitan Opera House (Figure 2.36). In addition, as many as ninety earth houses, designed by Peter Vetsch, have been built in Switzerland using this type of formwork technique (Figure 2.57). At ground level, the concrete is sprayed, while at roof level it is poured. Due to the use of sprayed concrete, stay-in-place formworks require additional finishing.

Figure 2.57: Earth house under construction in Giswil, Switzerland, 2006, and earth houses in Dietikon, Switzerland, 1993.

2.5.4 Earthen formworks

As mentioned at the start of Section 2.2, Isler (1956, 1960) built an atomic shelter on an earthen mould in 1955 (Figure 2.58). He continued experimenting with 6 m polyester shells, constructed on sand mounds, for use in modular storage buildings of the Swiss military (Chilton 2000).

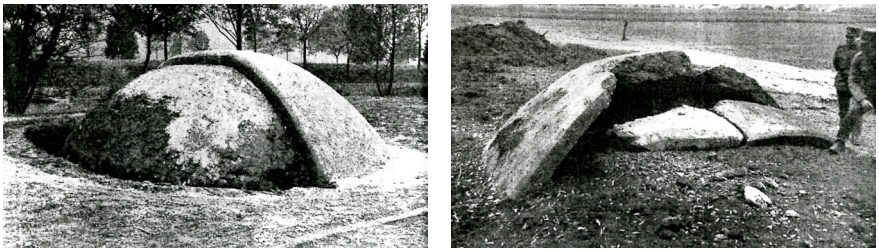

Figure 2.58: Atomic shelter under construction and after testing, built as 4 m span, 200 mm thick spherical and semi-spherical domes, Germany, 1955.

Ulrich Müther (1934–2007) designed lifeguard houses, made from two halves prefabricated on an earthen mould (Figure 2.59). They were built in Binz auf Rügen, Germany; first in 1975 (demolished in 1993) and again in 1981. Coincidentally, Müther continued building shells well into the 1980s and early 1990s, but he is not often mentioned alongside Isler as a succesful shell builder beyond the golden era.

Figure 2.59: Lifeguard station, 70-165 mm thick, Binz, Germany, 1975.

Other examples of earthen formworks include the 1958 Philips Pavilion (Figure 2.8) and the 2010 Teshima Art Museum (Figure 2.54). The latter is particularly remarkable considering its scale when compared to the other examples, which are limited to either small structures, or modular and prefabricated segments.

2.5.5 Foam formworks

A recent alternative to timber sheeting has been to use high density foam. The foam is still supported by a system of timber shuttering and steel scaffolding, but allows CNC machining of this lightweight, affordable material.

An early large-scale application is the 2006 Cliffs of Moher Visitor Centre in Ireland (Figure 2.60). This 25 m span, 750 mm thick subterranean dome has a central roof light, and featured double curvatures deemed too complex for traditional timber. Instead, the 907 m^2 surface area was covered by about three hundred high-density EPS formers, provided by Cordek. They were covered by bonded rubber mats before pouring concrete (Seaton 2007).

The 2010 Spencer Dock Bridge (Figure 2.55) has become a standard reference when discussing disadvantages of CNC milled foam formworks, and proposing alternatives. Despite earlier intentions, the EPS foam could not be recycled; a problem pointed out by Verhaegh (2010) and addressed by Oesterle et al. (2012) who developed a reusable wax for robotic milling, or "zero-waste formwork". Robotic hot-wire cutting has been suggested by Filipe Martins et al. (2015), to address the issue of extensive

Figure 2.60: Cliffs of Moher Visitor Centre, Ireland, 2006.

milling times, although wire cutting is limited to ruled surfaces. To circumvent this drawback, Søndergaard et al. (2014) and Rust et al. (2016) have investigated the bending or hanging of the wire during cutting, to allow for greater geometric freedom.

2.5.6 3D printed formworks and shells

Recent years have been dominated by developments in 3D printing, also in construction. In terms of shell construction, there are three ways in which 3D printing could be used: printing the formwork, printing reinforcement as stay-in-place formwork, or directly printing the shell.

Printed lost formworks for straight and singly curved wall construction were proposed around the turn of the century by Khoshnevis (2004), as part of his 3D printing technology referred to as "contour crafting". Similar formworks have been printed by companies such as Winsun in China, and CyBe in the Netherlands. Others with large printers are: D-Shape, Italy; Eindhoven University of Technology, Netherlands; Loughborough University, UK; REX|LAB, Austria; TotalKustom, US; and, XtreeE, France. These machines use cementitious printing materials, with the exception of D-Shape which uses a magnesium-based binder.

Printed, stay-in-place formwork, referred to as "mesh mould" was proposed by Hack & Lauer (2014) for the construction of doubly curved walls. A similar formwork was developed by the company Branch Technology in the US, with their technique called "cellular fabrication". They recently organized a design competition to use their technology (Figure 2.61) (Dezeen 2016). Yet another similar technology using welding steel instead of polymers is "anti-gravity additive manufacturing" by Novikov et al. (2014).

Figure 2.61: Proposals for 3D printed thin curved slab or shell houses: Landscape House by Universe Architecture using D-Shape printer, 2013; Curve Appeal by WATG's Urban Architecture Studio using segmented cellular fabrication, 2016.

Tam et al. (2015) directly printed small shell models along their principal stress lines, but their process, called "stress line additive manufacturing", still required a milled wooden formwork. A proposal for a 3D printed house featuring curved surfaces using a D-Shape printer (Figure 2.61) (Dezeen 2013*a*), has recently progressed to produce a scale model prototype. In this case, the house is printed in the powder bed, which in a way can be seen as an earthen formwork. ESA and Foster+Partners proposed printing a shell for a lunar base directly onto an air-inflated formwork (Figure 2.62) (Dezeen 2013*b*).

To avoid the need for formwork, Khoshnevis (2004) already suggested the direct printing of a shell using Nubian vaulting techniques. Here, bricks are placed in layers at an angle against a back wall. The Great Hall of the Palace of Taq-i Kisra in Figure 2.16 is a historical example in traditional masonry. His recent joint proposal with NASA for a lunar base uses the same principle (Figure 2.62) (Khoshnevis 2012). In the context of this proposal, they printed a small model of a dome in staggered layers. The same technique was suggested for the winning entry of NASA's 2015 3D-Printed Habitat Challenge, but printed in ice (Figure 2.62) (NASA 2015).

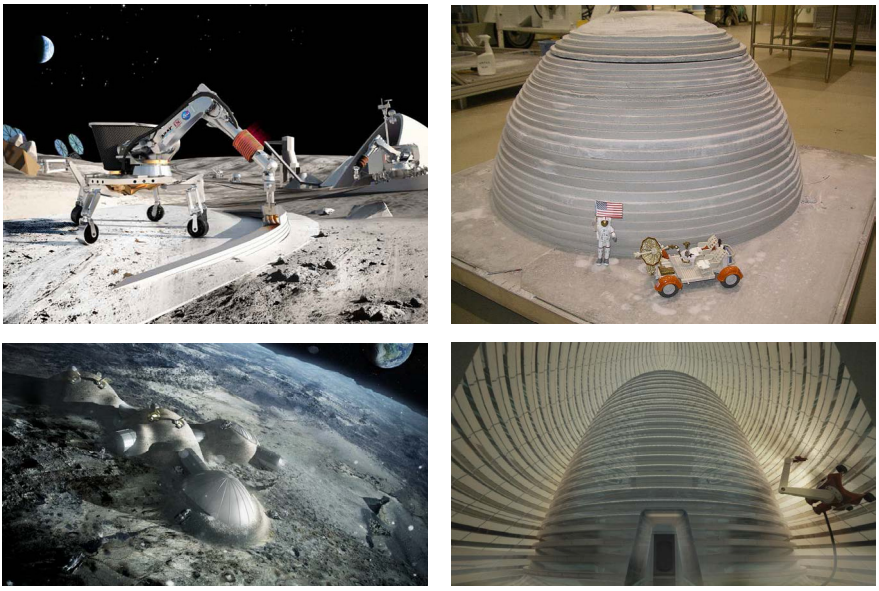

Figure 2.62: Proposals for 3D printed extraterrestrial bases: NASA and University of Southern California, using contour crafting with Nubian vaulting or staggered layering, 2012; ESA and Foster+Partners using D-Shape printer with air-inflated formwork, 2013; and, winning entry of NASA's 3D-Printed Habitat Challenge, 2015.

2.5.7 Cost of formwork

Historical and recent cost estimates have been converted to cost in 2016 currency for a UK/US construction market in this section. The cost of formwork can be 35 % up to as much as 60 % of the total cost of a general concrete work (Johnston 2008), and for traditional applications is between 21 and 71 €/m^2 (van Dijk et al. 2013).

For shell structures, this generally seems to lie between 20 and 50 %, given the following references.

For the largest ever concrete dome and shell, the 1958 CNIT shell shell in Paris, France, and the 1976 Kingdome in Seattle, US (Figure 8.3), this was likely around 50 %. In the former case, Nicolas Esquillan (1902–1989) commented that in his experience in France, formworks amounted to half of the shell's cost, also accounting for reuse (Isler 1960). In the latter, Chistiansen (1988) gives an example estimate for a smaller version of one of the segments of the Kingdome, although for his later work on the

identically constructed 1990 Sundome in Washington, US, this went up to an outlier of 73 % (Randall & Smith 1991). The same proportion of 50/50 is true for the 1962 TWA Flight Center in New York, US (Figure 2.51) (Anderson et al. 1964), and the 2013 Centro Ovale in Chiasso, Switzerland (Figure 2.3) (Muttoni et al. 2013).

Chistiansen (1988) quotes savings between 31 % and 48 %. This is based on having built c. 139'000 m^2, and using estimates of square and saddle hypar roofs, with formwork that can be reused up to four times. Isler (1960) claimed that, based on having built c. 13'000 m^2 thus far, the cost of formwork represented between 20 and 25 % of the total cost of the shell, up to 30 % in other countries, depending on local prices. The low relative cost of Isler's system can be attributed to the reuse of standardized glulam shuttering profiles, and use of insulation boards as lost shuttering (Chilton 2000).

Table 2.3 shows absolute costs for shell construction excluding foundations and finishing, corrected for inflation. The percentage of that cost for the formwork is also given. Both Ketchum (1964) and Chistiansen (1988) claim reuse of five to six or at least more than four times is necessary for economical formworks, so their formwork cost has been multiplied by five, under the assumption that they included such reuse in their estimates. Overall, the formwork for vaults costs 170–300 €/m^2 and for hyperbolic paraboloids 110–420 €/m^2. By comparison, the formwork for the freeform TWA Flight Center came at an exorbitant cost of about 725 €/m^2.

Based on correspondence with Zwarts & Jansma Architects (Verbeek 2015) and a formwork contractor regarding the Extended Waalbridge, SO-IL Architects regarding an undisclosed shell project (Lamyuktseung 2015) and a formwork contractor regarding the NEST HiLo project (Chapter 12), more recent estimates were obtained. The formwork contractors have to remain anonymous. A doubly curved one-sided custom timber formwork will cost 400-500 (Verbeek 2015) up to 600-800 €/m^2 from low to high curvature and including shoring , or 550 €/m^2 excluding shoring (Lamyuktseung 2015). A doubly curved one-sided milled foam formwork for the same projects will cost 800 €/m^2 including shoring (Verbeek 2015), or 820 excluding shoring (Lamyuktseung 2015). Smaller, moderately curved elements would cost 440 €/m^2 in our experience, or, according to Schipper & Grünewald (2014), about 300-560 €/m^2.

An upper limit for the cost of any particular formwork for a doubly curved surface may be 1'000-1'200 €/m^2 (van Dijk et al. 2013).

type	span		infl.				formwork		source
		[$/sqft]	[-]	[$/sqft]	[€/sqft]	[€/m^2]	excl. reuse	[€/m^2]	
vaults									
barrel vault	30–100 ft	2.31	10.39	23.96	21.56	232.07	26% × 5	301.96	Ketchum (1964)
barrel vault	80 ft	1.26	41.56*	52.46	47.21	508.19	33%	169.99	Chatterjee (1964)
catenary arches	120 ft	2.00	41.56*	83.12	74.81	805.23	22%	174.47	Chatterjee (1964)
parabolic arches	190 ft	2.53	17.20	43.52	39.17	421.58	41%	171.45	Whitney (1950)
parabolic arches	300 ft	7.47	17.20	128.51	115.66	1'244.94	21%	259.41	Whitney (1950)
hyperbolic paraboloid									
umbrella	36 ft	3.20	2.34	7.47	6.72	72.39	31% × 5	112.96	Chistiansen (1988)
umbrella	30–60 ft	2.03	10.39	21.09	18.98	204.33	30% × 5	301.96	Ketchum (1964)
umbrella	80 ft	1.25	41.56*	51.95	46.76	503.27	25%	127.49	Chatterjee (1964)
saddle	120 ft	5.98	2.34	13.96	12.57	135.27	47% × 5	319.04	Chistiansen (1988)
dome segment	320 ft	7.26	2.34	16.95	15.26	164.22	51% × 5	422.47	Chistiansen (1988)
dome segment (Sundome)	270 ft	13.98	2.03	28.38	25.54	274.93	73%	200.88	Randall & Smith (1991)
freeform									
TWA Flight Center		14.80	10.39	138.39	138.39	1489.67	49%	724.70	Anderson et al. (1964)

Table 2.3: Cost in 2015 €/m^2 for conventionally formed shells, converted from original reference, using current exchange rate of 0.90. Inflation factor (infl.) based on average between real and skilled labour value (Williamson & Officer 2016). *Incl. construction cost index to convert from India to UK/US (Moore & Riley 2012).

However, while the above costs were provided by formwork contractors and that cost would likely double for the entire shell, subsequent initial bids from five construction managers and general contractors, for two of the mentioned projects, actually came in at average of 3'800 €/m^2 with a standard deviation of 1'100 €/m^2. This reflects the perceived risk and complexity of such structures today, rather than the actual cost. It might explain why recent projects such as Arnhem Central Station (Figure 2.50) and the Taichung Metropolitan Opera House (Figure 2.36) failed to tender as concrete shells made with timber formworks, and instead were realized as a steel shell and as a concrete shell with stay-in-place formwork (which is basically building a steel structure, to be covered by concrete).

In summary, the cost of timber formworks for shells has been about 110-420 up to 725 €/m^2 for complex curvatures. Today, this range has moved to 400-800 €/m^2, depending on the curvature. For milled foam formworks the cost is similarly at about 300-800 €/m^2, though dependent on scale rather than curvature. An upper limit for any type might be 1'000-1'200 €/m^2, but perceived risk and complexity may lead to even higher prices during tendering. No information was found for stay-in-place and earthen formworks.

2.6 Discussion

The historical overview of shells, their method of design and method of construction, has revealed few examples of thin concrete shells designed through form finding: twenty projects by Heinz Isler, the Basento Bridge by Sergio Musmeci and the Stuttgart 21 canopies by Frei Otto. The latter two, initially designed through soap films, are globally anticlastic. Isler's shells, designed using hanging models, are generally synclastic, but along edges, or where multiple shells join, may feature negative curvature. Perhaps surprisingly, there is no known instance of a thin concrete shell designed using numerical form finding. This is explained by the fact that form finding, and certainly computational equivalents, developed directly after the golden era of concrete shells came to an end.

Figure 2.63 shows that during the 1970s the German term "Formfindung" was introduced and increasingly used, due to the works by Frei Otto. Initially, it was translated to "formfinding", which remained popular for the duration of the German research programs and early applications of numerical form finding to tensioned membrane structures. The term "form finding" picked up, and overall use of such terminology increased again halfway through the 1990s, presumably tracking advances in computer aided-design and architectural trends such as blobitecture.

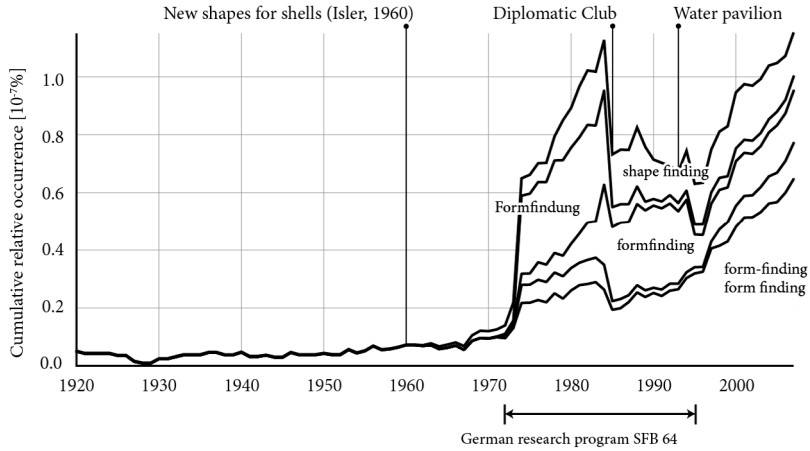

Figure 2.63: Relative, historical occurence in English literature of the term "form finding" and synonyms, plotted cumulatively (Ngrams 2016). Diplomatic Club and Water pavilion shown in Figures 2.48 and 1.1 respectively.

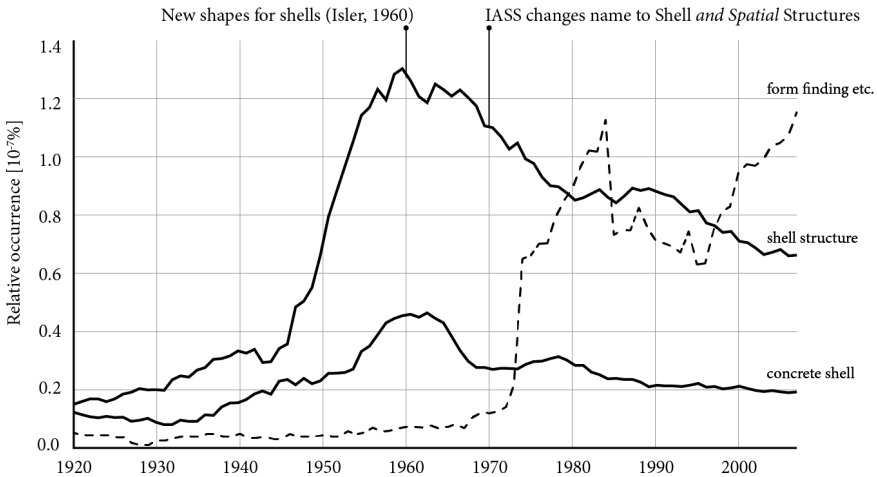

Figure 2.64: Relative, historical occurence in English literature of the terms "shell structure", "concrete shell", versus "form finding" and its synonyms (Ngrams 2016).

Figure 2.64 compares the historical use of the term "form finding" and its synonyms against that of "shell structure" and "concrete shell". The International Association for Shell Structures (IASS) added the words "and spatial" to its name in 1970, signaling the shifting interests from shell structures to other systems such as gridshells,

spaceframes, cable nets and membranes. In essence, concrete shells missed the boat on developments in both physical and numerical form finding for the generation of efficient, natural shapes. This begs the question to what extent they might have benefited, or might still benefit, from these design techniques.

On the other hand, alternative structural systems in timber or steel have also been designed as mathematical or freeform shapes, with only few examples found using form finding (Table 2.4).

project	year	type	method
Multihalle, Mannheim	1974	timber gridshell	hanging model
Solemar-Therme, Bad Dürrheim	1987	timber gridshell	force density method (custom)
Toskana Therme, Bad Sulza	1999	timber gridshell	
Odeon, Munich	2007	steel gridshell	stiffness matrix method (Sofistik)
Cybele Palace, Madrid	2009	steel gridshell	stiffness matrix method (Sofistik)
Mapungubwe National Park Interpretive Centre	2009	masonry shells	graphic statics, thrust network analysis (custom)
National Maritime Museum, Amsterdam	2011	steel gridshell	dynamic relaxation (custom)
Elephant House, Zurich	2014	timber shell	stiffness matrix method (Sofistik)
Arnhem Central Station	2015	steel shell	dynamic relaxation (GSA)
Chadstone Shopping Centre	2016	steel gridshell	dynamic relaxation (custom)

Table 2.4: List of permanent shell projects, designed using form finding, other than concrete shells.

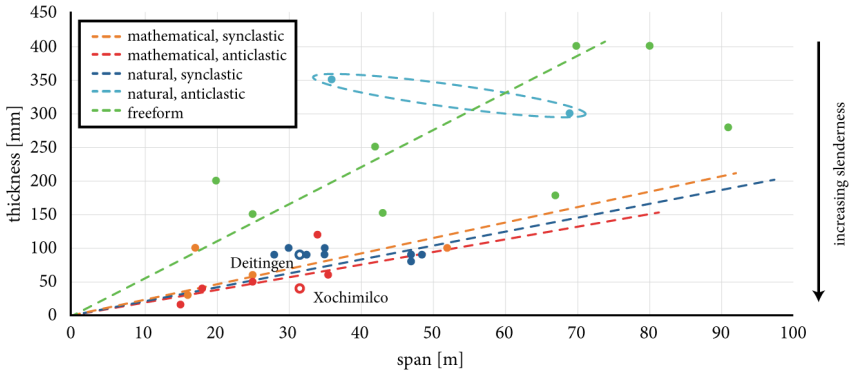

Figure 2.65: Span versus thickness (slenderness) of thin concrete shells mentioned in this chapter. Grouped by method of generation and type of curvature.

Figure 2.65 shows the rise and thickness of the thin concrete shells mentioned throughout this chapter for which the data was available. Isler's Deitingen gas station and Candela's Xochimilco Los Manantiales restaurant are highlighted as seminal references for what are considered to be an efficient synclastic and anticlastic shell structure.

Mathematical or natural synclastic shapes seem to have or be capable of similar slenderness. One would expect the synclastic shapes of Isler to be more slender. The efficiency in his designs appears to translate more in the lack of edge beams and lower requirements for reinforcement than overall slenderness.

For anticlastic shells, Tomás & Martí (2010*b*) show that it is possible to optimize even Candela's shells when departing from the hyperbolic paraboloid shape. However, the only natural anticlastic shapes, the Basento Bridge and Stuttgart 21, have not been able to capitalize on this supposed efficiency of natural shapes, although both are large infrastructural projects, rather than purely shell roofs, so the comparison is not entirely fair.

The most obvious conclusion from Figure 2.65 is the apparent material inefficiency of purely freeform shapes, although they are compared to some of the thinnest known shells.

2.7 Conclusion

Based on this chapter and its references, the following observations are made regarding thin concrete shells and their design:

- mathematical shapes have virtually dominated the design of shell structures, and were the only type until the late 1960s;
- mathematically, most of these doubly curved shapes can be classified as quadrics or conoids;
- natural shapes, resulting from physical form finding, were only applied by Heinz Isler to twenty of his projects, and by Sergio Musmeci and Frei Otto to one project each;
- the projects of Frei Otto were instrumental in the development of all three common types of numerical form finding, despite, ironically, his own misgivings;

- no thin concrete shell designed by numerical form finding was found, which could largely be due to the disappearance of such structures at a time when form finding was first developed;
- freeform shapes, often inspired by animal or other natural form, have been built around 1970 and in the past decade by Mutsuro Sasaki, but such shapes have not approached the slenderness achieved by mathematical and natural shapes; and,
- there is ambiguity in the definition of "free form" which has been applied to complex mathematical shapes as well.

Apart from concrete shells, surprisingly only ten permanent shell structures in timber or steel were found that derived their shape from some physical or numerical form-finding process.

On a side note, literature on form finding often refer to Isler's, Otto's and Antoni Gaudí's works without providing context, suggesting they were isolated in a way. However, both Isler and Otto refer to catenary or hanging models associated with Gaudí, which, through nineteenth century German and eighteenth century English textbooks can be traced back to Hooke's original hanging chain.

Regarding the construction of thin concrete shells, the following observations are made:

- timber formworks and stay-in-place formworks have dominated the construction of shells and are the default methods even today, though in the former case milled foam has replaced timber sheeting in some instances;
- even when correcting for inflation, the cost of timber formworks has increased, partially explaining the decline in concrete shell construction;
- milled foam formworks seem to be less competitive to timber formworks, although multiple developments are underway to improve upon the use of milling or the foam;
- perceived risks and complexity of concrete shells made with timber or foam formworks has led to protracted or failed tendering processes in several recent instances;
- earthen formworks have been used in a few cases, generally to produce prefabricated segments of a shell;

- 3D printing can be used in three ways to construct shells, and has mostly been proposed for extraterrestrial application; and,
- there is no substantial prototype for a 3D printed shell yet, though one is likely to appear within the next few years, given the momentum in the development of the technology.

The main conclusion is that at this point, timber or milled foam formworks cannot bring back concrete shells in a substantial manner. Furthermore, freeform shapes may lead to uneconomic designs, even if they are post-rationalized through structural optimization. Instead, if shells are to return in large numbers, they should be generated through traditional mathematics or form finding. Form finding allows for a greater variety in shape, and may thus still accommodate contemporary tastes for complex geometry. To address the subsequent problem of construction, the reader is referred to Willard Oberdick's notion of a "form-giving device", where the method of construction is derived from how the design is generated through form finding. Otto and Isler implied the same in their experiments on air-inflated models. These construction methods are referred to as "flexible formworks", discussed in the next chapter.

Therefore we should not permit [concrete] *shells to vanish, but rather give them a future, give the role back to them they had in the past. There is no reason, why it should not be possible to develop manufacturing techniques for shells which suit the requirements of today, in order to build with them economical light shells. Certainly this would also result in new and interesting shell geometries.*

After all we have today at our disposal not only the conventional wooden falsework and shuttering [...]. *If we add all that with phantasy* [sic] *and with the desire to build light and versatile, concrete shells will definetely* [sic] *enjoy a come-back.*

— Jörg Schlaich, 1985

Why not accept that in recent years concrete shells have lost ground [...] *but that fortunately new materials have stimulated a revival.* [...] *No question, the future of shells is steel grids, glass cover and textile membranes but not concrete.*

— Jörg Schlaich, 2013

CHAPTER THREE

Flexible formworks for shells

The use of fabrics and meshes to create concrete structures can be traced back as far as the turn of the nineteenth century; the latter part of the Industrial Revolution. Necessary conditions for the development of fabric formwork were the industrial production of textiles, the rediscovery of concrete and the invention of reinforced concrete. Moreover, it was the abundance, quality, low cost and widespread availability of their ingredients: natural fibres, cement and steel. Among many of these early flexible formwork concepts, the Ctesiphon system of construction for barrel vaults and the Airform system for domes were the most successful.

At the end of the golden era of concrete shells, from the 1960s onward, the cost of labour, steel and particularly timber dramatically increased. This made traditional timber formworks unattractive, and briefly led to academic experimentation with flexible formworks, such as the use of gridshells and cable nets as falsework. The arrival of affordable synthetic fibres in the same period proved crucial to the further development and use of air-inflated (pneumatic) formworks for concrete domes, with tens of thousands having been built since.

More recently, the seminal work since the early 1990s by Prof. Mark West at the Centre for Architectural Structures and Technology (CAST), University of Manitoba, in Winnipeg, Canada, coincided with the arrival of the internet, and thus was widely disseminated. His work received a great deal of attention and created awareness of the broad potential and rich history of fabric formworks. In turn, this has led to both academic and professional interest in the topic, including their application to the construction of shells.

This chapter presents an overview of flexible formworks as they were applied in particular to the construction of thin-shell structures[1]. More general, comprehensive historical overviews of fabric formwork can be found in Veenendaal et al. (2011) and Veenendaal (2016). Schipper (2015) provides an overview of related flexible surface moulds, supported on a bed of actuators.

Section 3.1 reviews possible categorizations of fabric or flexible formworks. The first sections place an emphasis on fabric formworks: hanging formworks including inverted systems, and prestressed formworks are discussed in Sections 3.2 and 3.3 respectively; pneumatic formworks in Section 3.4. The remaining sections discuss alternatives to fabrics: bending-active formworks, or gridshells, in Section 3.5; mesh formworks in Section 3.6; and discrete tensile systems such as cable-net falseworks in Section 3.7. The literature study ends with a technical summary and historical analysis in Sections 3.8 and 3.9, before drawing some conclusions in Section 3.10.

3.1 Categorization

Abdelgader et al. (2008) distinguish four categories of fabric formworks, grouped by common applications: mattresses, sleeves, shuttering and open troughs. However, fabric-formed shells do not fit in any of these categories, as the formworks are always defined as being filled.

A broader categorization was suggested in Veenendaal et al. (2011), based on the question if and how the fabric is (pre-)stressed and supported, and whether the concrete is applied as a thin layer, or by filling the formwork. This results in ten types of formwork, each with a unique kind of geometry for the resulting concrete (Figure 3.1).

Yet another categorization was offered by Pronk & Dominicus (2011, 2012) in the form of eighty-five ways to manipulate a flexible formwork: a prestressed or air-inflated surface can have different types of curvature, different ratios of prestress, can interact with other such surfaces as well as rigid objects, and can undergo different loading conditions to help shape it further.

[1]This chapter is partially based on Veenendaal et al. (2011) and Veenendaal (2016).

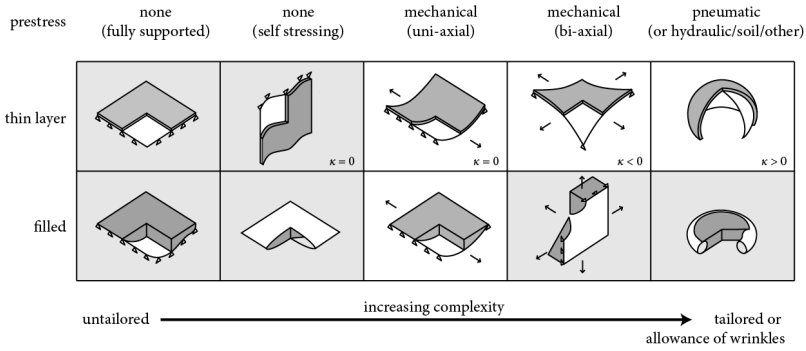

Figure 3.1: Taxonomy of fabric formwork and formwork liners. Types in this chapter against white background. Adapted from Veenendaal et al. (2011).

3.2 Hanging fabric formworks

A flexible membrane will deflect substantially under any load that is perpendicular to its surface. To counteract or avoid this effect, prestress in its plane or some kind of opposite pressure is required. The simplest, therefore, is to allow the membrane to hang under its own weight, which is perhaps why this is the earliest type of fabric formwork to be invented and used. At first, such hanging formworks were used to construct floors. This was soon followed by the idea of casting shells on them, either directly, or by inverting the resulting form; a literal translation of Hooke's hanging chain.

3.2.1 Floor systems

On September 8th, 1897, Gustav Lilienthal (1849–1933) obtained a patent for a fire-proof ceiling in the German Empire, followed by other patents in Switzerland, the United States and the United Kingdom. It is the first known instance of fabric formwork.

His invention, doubling as a floor system, consisted of "spreading some pliable but sufficiently impermeable fabric, [cardboard] or paper over the beams intended to carry the ceiling that is to be built, of covering the fabric with wire-netting [or vice versa], and of pouring concrete on the top of the covering thus formed" (Lilienthal 1899). The fabric is "not tightly strained but [is] allowed to hang in catenary form between the beams" and covered with wire netting (Figure 3.2) (Lilienthal 1898).

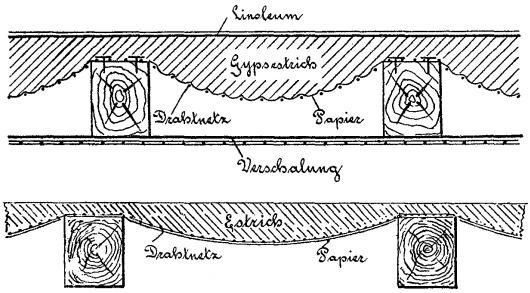

Figure 3.2: Lilienthal's fireproof ceiling, consisting of wire netting ('Drahtnetz') and a layer of paper ('Papier') or suitable fabric, with a concrete screed ('Estrich') (Lilienthal 1898).

This shape causes a relatively uniform stress in the wire mesh when the floor is loaded, and Lilienthal therefore claimed a significant increase in strength of the floor. He also presented a variation where the paper is on top of the netting, "thus forming a surface similar to that of a sofa-cushion" (Lilienthal 1899).

The ceiling was later marketed under the name Terrast Decke. The system was used in Berlin, in several houses as well as in the Königin-Elisabeth-Hospital, in 1909, where it was applied to most of the 2'000 m^2 of ceilings. In order to repurpose the long abandoned hospital, a structural survey determined the floor's capacity to be an impressive 10 kN/m^2 still (Vogdt & Djahani 2000). Nonetheless, in 2013, the building was entirely demolished.

Similar incarnations of this system were patented throughout the twentieth century (Figure 3.3) (Veenendaal 2016), but no further large-scale applications of these singly curved floor systems are known to exist.

The engineer James Hardress de Warenne Waller (1884–1968) had one of these patents. He was perhaps the most prolific inventor of fabric formworks, having patented various ideas for fabric formwork construction. One such idea was stretching hessian over timber frames to form wall panels; a system he called Nofrango. For a new type

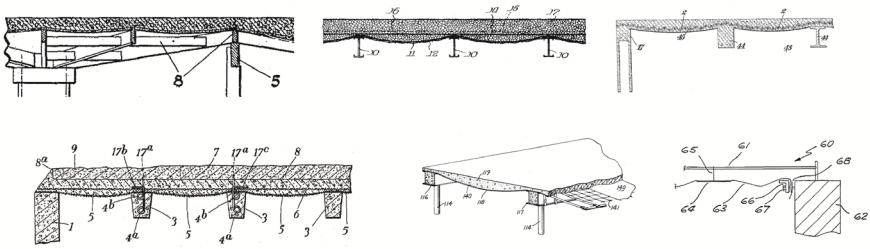

Figure 3.3: Inventions of the fabric-formed floor by Fletcher (1917), Govan & Ashenhurst (1928), Waller (1934), Farrar et al. (1937), Parker (1971) and Redjvani (1999).

of concrete hut, the Patrick portable hut, this hessian continued onto the roof. The fabric hung under the weight of the applied concrete, no more than 1 in, forming a 2 ft wide precast unit. At the corners, this created a strong double curvature. These units were then bolted together to form the hut (Anon. 1941).

3.2.2 Corrugated vaults

James Waller was also the first to apply fabrics to the construction of thin-shell structures. He was inspired during his visit to the vaulted Palace of Taq-i-Kisra at the ancient city of Ctesiphon, while stationed in Iraq (Figure 2.16). He developed the "Ctesiphon system", which started from reusable, lightweight falsework arches, made of steel or timber, catenary in profile, and placed in parallel. The fabric could be jute, coir, sisal or burlap, but typically hessian. The slightly prestressed fabric was tacked to the arches and, under the weight of the applied cement mortar, sagged in between the falsework arches to form corrugations, acting as a lost formwork (Figure 3.4). The thickness of the first thin coat of cement, the prestress in the fabric and the spacing between the arches would determine the depth of the corrugations, and thus the stiffness of the shell. Typically, two more layers of cement were then applied. The arched ribs had an inverted catenary shape, so that the resulting form was in compression and required a minimum amount of reinforcement to mainly deal with thermal expansion and contraction.

About fifty military huts were built using this system during the 1942–1943 period of feverish construction of the American camps in preparation for D-Day (Mallory & Ottar 1973), as well as the ends of blister hangars, a type of arched, portable aircraft hangar. Waller patented a specific system in 1955 for spans of up to 150 m using prefabricated trussed arches from which to suspend the fabric. Co-developer Kurt

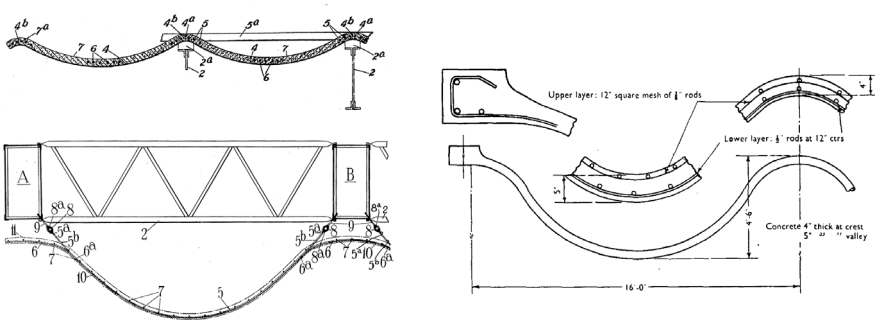

Figure 3.4: Sections of the Ctesiphon system with girder arches and fabric (Waller 1952*b*), or, for 100-500 ft spans, with external lattice box girder arches and fabric or expanded metal (Waller 1952*a*), up to 5 in concrete and two reinforcement meshes for a 310 ft span (Waller & Aston 1953).

Billig noted that there appeared to be "no reason why corrugated shell roofs should not be built to span freely several hundred feet with a shell thickness not exceeding 4-5 inches" (Billig 1963) (Figure 3.4). The system was also competitive as it reduced the cost of moulds and scaffolding, and required no skilled labour (Billig 1946).

An unusual Ctesiphon structure was the Church of Christ The King and St. Peter, in Lawrence Weston, Gloucestershire, Bristol, England (Figure 3.5). The building had a 40 ft span, 2.5 in thick vault over the nave and another 30 ft span annex. Unfortunately, it has since been demolished.

Figure 3.5: Church of Christ The King and St. Peter with 30 and 40 ft span, 2.5 in thick Ctesiphon vaults in Bristol, England, c. 1950 (demolished).

Two of the last and largest structures were the Chivas Distillery Warehouses in Paisley, Scotland, still in use by Chivas today. The two structures, 100 ft and 150 ft long, each feature three 100 ft spans (Figure 3.6). The shell has a thickness of 2.5 in including a 2 in structural layer of concrete, with a 7-day cube compressive strength of 3'850 psi, c. C20/25. Instead of hessian, expanded metal, weighing 5.5 lbs/sq yd yard, was draped between the arches, spaced at 100 in distances. The thin metal sheeting was used as lost formwork and tensile reinforcement (Anon. 1959).

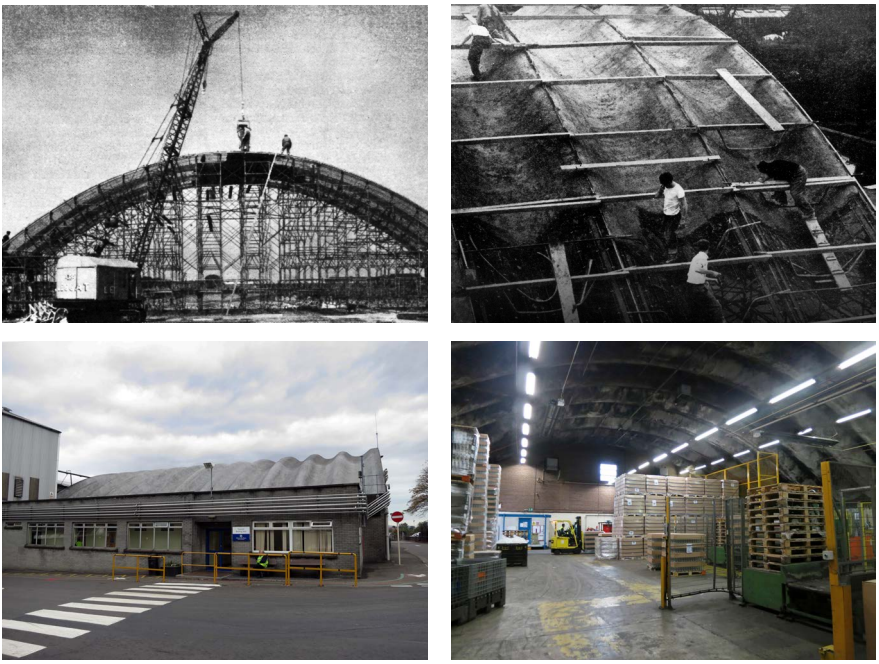

Figure 3.6: Chivas Distillery Warehouses with 100 ft spans, 2.5 in thick Ctesiphon vaults in Paisley, Scotland, c. 1959.

The largest known complex built with fabric is a former jute factory in Umtali, Southern Rhodesia (now Mutare, Zimbabwe). It consists of seven adjoining 44 ft span barrel vaults and another separate one. Constructed with almost entirely local labour, the 100'000 sqft jute mill and store was deemed to perform very well in terms of insulation, ventilation, construction cost and maintenance (Figure 3.7) (Vandenbergh & Partners 1952). The structure still stands today in its entirety.

Figure 3.7: Jute factory with 44 ft span Ctesiphon vaults in Umtali, Southern Rhodesia (now Mutare, Zimbabwe), 1948.

Even larger spans of 112-115 ft Ctesiphon shells were built in Spain (Billig 1961), but it is unknown whether they were built using fabric or expanded metal.

The success of the system was partially attributed to the rising demand for unobstructed covered spaces with increased clearances in addition to global shortages at the time of the "modern wonder material, steel", as well as timber (Waller & Aston 1953). The Ctesiphon system by James Waller and Kurt Billig would also have significant influence on two shell builders in particular: Félix Candela and Guruvayur Ramaswamy.

The first, renowned concrete shell builder Félix Candela Outeriño (1910–1997), was greatly inspired by the Ctesiphon system in his early work. Candela graduated in 1935 from the Escuela Técnica Superior de Arquitectura de Madrid (ETSAM), Spain, but was forced to move to Mexico after the Spanish Civil War. There, he spent the greater part of the 1940s rigorously devoting himself to literature on shell design, analysis and construction, coming across the work of Waller and Billig: "This was copying a system they were using in England at the time; I copied everything I could" (Rabasco 2011). Candela's first shell, an experimental vault with a 6 m span in San Bartolo, Mexico City, used the Ctesiphon system. He used this approach again for a rural school in Santa Librada near Ciudad Victoria, Tamaulipas in 1951 (Figure 3.8), before moving on to other geometries, such as conoids and hyperbolic paraboloids, which required other approaches to construction (Faber 1963). The latter structure is still standing.

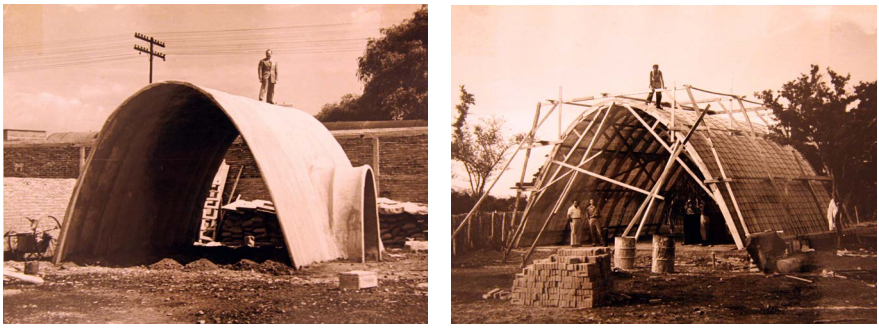

Figure 3.8: Experimental 6 m span vault, San Bartolo, Mexico City, 1949 and rural school, Santa Librada, Mexico, 1951, both by Félix Candela.

The second, Guruvayur Subramanian Ramaswamy (1923–2002), became head of the Structures Division of the Central Building Research Institute (CBRI) in Roorkee, India, in 1956, while Billig had been appointed director of the CBRI four years earlier. Ramaswamy described, and was possibly involved with the Ctesiphon shells built there at Billig's initiative (Ramaswamy 1963). Ramaswamy's work is discussed further in the next section.

By the end of the 1970s, the Ctesiphon system had been employed in over five hundred shells in one form or another around the globe. Before his death, Waller sold his Ctesiphon patents to Seagrams, for whom he had designed the Chivas Distillery Warehouses (Figure 3.6). Seagrams never used the patents after Waller's death (Williams 1996). Other factors may have contributed to the disappearance of this building system. Specific problems were the necessity of proper supervision (Waller 1953), the likelihood of cracking at the top of the ribs (Anon. 1960) and instances of poor thermal quality (Naidu 1963). Another reason may be the architectural novelty of the catenary form wearing off. For example, catenary shells (initially Ctesiphon shells) were developed and adopted in Spain by several renowned Spanish architects (Rabasco 2004, 2011). However, already by 1959, one of them, Rafael de La-Hoz Arderius, while lauding Candela's later achievements, referred to his first catenary shaped vaults (Figure 3.8) as being cautious and conservative (Candela et al. 1959).

3.2.3 Inverted vaults

By 1932, Waller had patented the idea of inverting a hanging fabric to obtain "ceilings, domes or roofs having curved surfaces of catenary form" (Waller 1932), but it is unknown if he was able to apply it.

While working at the CBRI, Ramaswamy developed and patented a method of casting unreinforced, small-sized modular shells in fabric and inverting them as a flooring system of doubly curved shells (Figure 3.9) (Ramaswamy 1986, Ramaswamy et al. 1958, Ramaswamy & Chetty 1958). Each module was 4×4 ft, and 1 in thick, so it could be handled by four men. The savings in cost, cement and steel compared to traditional means were estimated to be around 25, 49 and 46 % respectively (Ramaswamy & Chetty 1960, Williams et al. 1958).

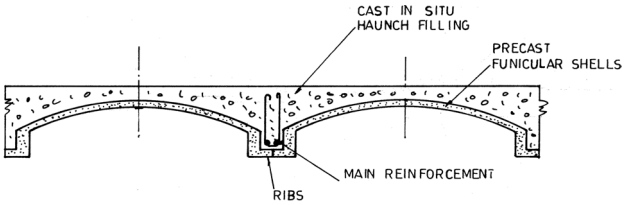

Figure 3.9: Section of the funicular waffle shell roof (Ramaswamy 1986).

Application of the floor system started with a large scale housing project of nearly 45'000 m^2 in Punjab (Figure 3.10) (Ramaswamy & Chetty 1960). These funicular shell floors would be adopted in the construction of thousands of buildings in India and abroad according to Parameswaran (2002), possibly because the patent was released free of charge.

Since the late 1970s, academic work has continued at Shiraz University, and later Sharif University of Technology in Iran (Vafai et al. 2005, Vafai & Farshad 1979, Vafai et al. 1997). Later work investigated the inclusion of wire-mesh reinforcement, and the most recent that of 2 % steel-fibre reinforcement. So far, this particular work has not seen any industrial application. Funicular shell roofs in general are still advocated and built in India, but using other construction methods like earthen moulds.

Ramaswamy's inverted floor system predates Heinz Isler's (1926–2009) famous conference lecture on new shell shapes, which included the notion of generating funicular shapes through the use of inverted hanging models (Isler 1960). Isler had started his experimentation on non-geometric shell shapes back in 1954, and would use this

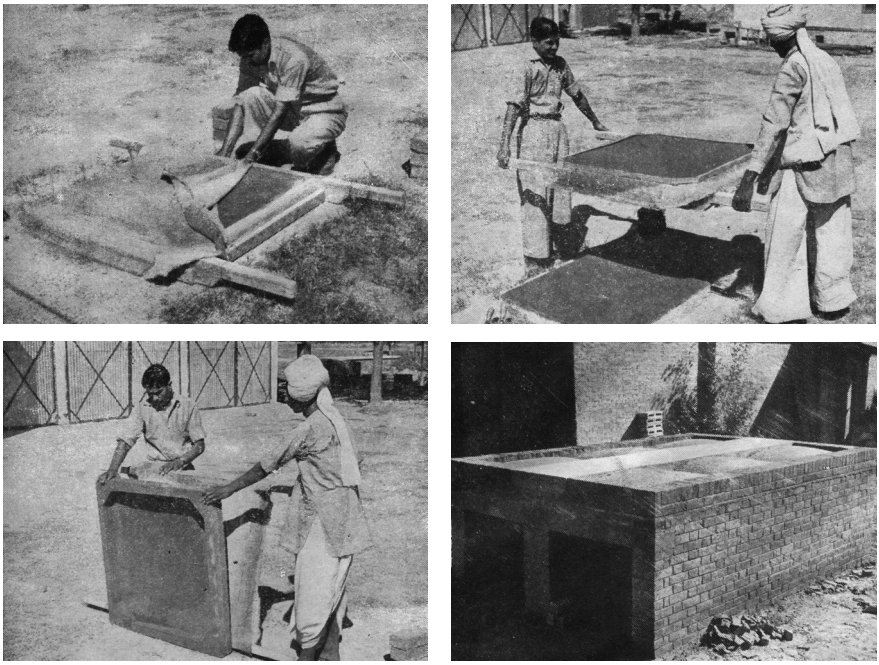

Figure 3.10: Sequence of construction for Ramaswamy's inverted floor system, subjected to 16.6 kN/m^2 for seven months without distress, Punjab, India (Ramaswamy & Chetty 1960).

particular approach to great effect for many of his shell designs (Isler 1980). These were large-span roofs, which renders the inversion of a hanging shell impractical. As such, they were generally built using laminated timber for rigid formworks, although pneumatic formworks were also used in several of Isler's projects (Section 3.4.1).

The use of an inverted shell resurfaced in 2004. Inspired by Isler, and essentially scaling up his ideas, Mark West developed a prototype at CAST (Figure 3.11). In this case, a rigid formwork was made by spraying glass-fibre reinforced concrete (GFRC) against a flat sheet of geotextile hung from a steel frame. Then, after being inverted, the formwork served to produce a single 2.5 m GFRC barrel vault; a unique example of a singly curved, inverted vault (West et al. 2011). Similar to Ramaswamy's floor system, CAST also developed two rectangular panels, with the second version cast at a Lafarge precast factory (Figure 3.11). This, in turn, led to three more highly prestressed versions, with one using a mould itself made as an inverted vault (Section 3.3.3).

Figure 3.11: Barrel vault and doubly curved vault, both produced at the Lafarge Building Materials precast factory, Winnipeg, Canada, 2004 and 2007.

At the University of Edinburgh, three fabric-formed prototype shells were built (Pedreschi 2013). The first was defined by two plywood catenary curves of equal span but differing rises, and is similar to the Ctesiphon system (Section 3.2.2). The second prototype is discussed in Section 3.3.1. The third, a dome, is the only one classified as an inverted shell. It was assembled from individually fabric-formed segments, each cast in hanging form, then placed upright.

Two pavilions were developed by Supermanoeuvre architects (Maxwell & Pigram 2014). One was built together with students of the Institut d'Arquitectura Avancada de Catalunya (IAAC), Barcelona, Spain, and the other with students of the University of Technology Sydney (UTS), Australia, at their respective institutes (Figure 3.12). These 4.85 m and 6 m span shells, designed using dynamic relaxation, consisted

of 83 and 193 individually fabric-formed segments respectively. Each segment was cast using a hanging formwork, reminiscent of Ramaswamy's system, by applying about 8 mm of gypsum-based plaster to a cotton lycra. The segments were placed on cardboard scaffolding and joined with additional plaster.

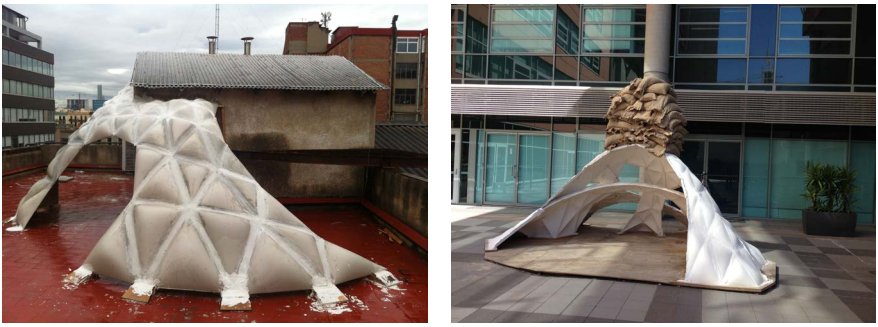

Figure 3.12: Gaudi's Puffy Jackets pavilions, produced at IAAC, Barcelona, Spain and UTS, Sydney, Australia, 2013.

A range of prototype shells were produced using impregnated carbon fibre textile instead of concrete, starting from work at the Architectural Association School of Architecture, London, UK, in 2008, and continued later at the Technion Israel Institute of Technology, Haifa (Blonder 2015, Blonder & Grobman 2015*a*,*b*). The method, called FABRICation, consists of hanging and manipulating the textile, then impregnating it with resin, before it is cured in an oven and finally inverted. The largest fibre-reinforced polymer (FRP) prototype thus far had an 8 m span, 2 m width and 1 m rise (Figure 3.13).

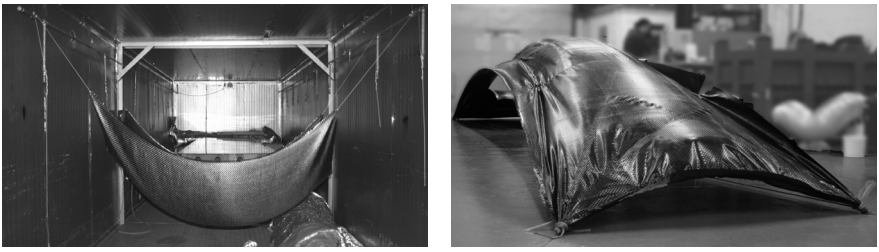

Figure 3.13: FABRICation prototypes, membrane curing in oven, and inverted 8 m span shell, both at the Gurit factory, Isle of Wight, UK, 2008.

3.3 Prestressed fabric formworks

The previous examples did not rely on any, or only on a very minor amount of prestress. By increasing the initial pretension, combined with proper boundary conditions, it is possible to avoid sagging of the fabric resulting in negatively curved shapes. These geometries are generally modelled after and approximate traditional shell shapes such as hyperbolic paraboloids or catenoids. Of course, by using a flexible fabric, a much wider range of shapes is in fact possible, and some further examples indeed defy any straightforward mathematical definition.

3.3.1 Hyperbolic paraboloids

By the 1970s, shell building had fallen out of favor. "The expense of the formwork necessary for construction caused [the] demise [of concrete shells]. Now, hypar structures can be constructed easily and simply without forms." Joseph Kersavage (1936–2005) of the University of Tennessee spoke of the system he patented to cast the surface of a hyperbolic paraboloid (or hypar) using prestressed fabric (Figure 3.14). In previous decades, Candela had famously used timber planks as shuttering, following the hypar's straight generator lines. Kersavage's idea was to follow those same lines using strips of fibreglass or metal insect screening, and later fabric. These were then bonded by applying a semi-rigid material such as acrylic plastic (Kersavage 1975), or by brushing or spraying a mix of latex, cement and sand, or Latex Modified Concrete (LMC), to a thickness of only 1 cm (Knott & Nez 2005, Stepler 1980). Like the Ctesiphon system, it required low- to unskilled labour with little or no supervision. Kersavage's main interest was the hypar itself and not its formwork system in particular, so later work focused more on arrangements of multiple hypars, their use as solar collectors and military applications.

Others continued to develop the formwork system further, in particular George Nez, an engineer for the US Park Service, with further engineering expertise by Albert Knott (Knott & Nez 2005). Starting with a workshop roof at the Rocky Mountain Park in 1977, their involvement led to a string of about twenty projects in developed and developing countries, most of which feature arrangements of several hypar shells, each referred to as a Latex Concrete Habitat (LCH). Each unit is typically 10 ft square in plan. Four units are assembled to form a 20 ft square gabled roof. The LMC is not reinforced other than the fibreglass screening itself. Coincidentally, Knott & Nez (2005) also proposed a system similar to Ctesiphon.

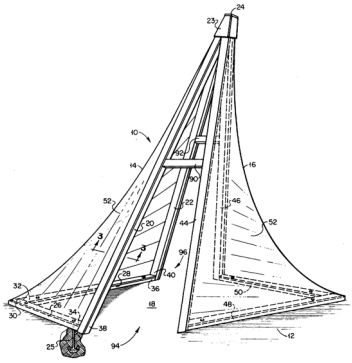

Figure 3.14: Patented formwork system for hypars by Kersavage (1975)

Their work also inspired others to found a company, TSC Global, in 2010, with the most recent projects involving hypars, marketed as Thin Shell Composite Hyperbolic Paraboloids (TSC HyPars), being completed in 2011 in Bangladesh and Haiti (Figure 3.15). The latter project, built with a local construction partner, has since been criticized for flooding when it rains, despite patches, tarps and other fixes (Katz 2015).

Although TSC Global still operates, it no longer actively promotes TSC HyPars, favouring other formwork techniques for traditional construction instead. Still, these roofs have attracted some recent academic interest, investigating the seismic behaviour of these structures (Balding 2013), and the properties of polymer modified concrete (PMC) (Carlton 2013). Concrete strengths range between C20/25 and C30/37, depending on the water-cement ratio and use of sand aggregate.

In 2006, several experiments at Eindhoven University of Technology demonstrated a construction method using fabric and shotcrete (Figure 3.16), as a means to reconstruct the Philips Pavilion, designed for the 1958 World Expo in Brussels by the office of Le Corbusier (Figure 2.8). This method was suggested as an alternative to the earthen formworks used to cast the nine hypars that made up the original structure.

Figure 3.15: Model HyPar roofs for Building Back Better Communities (BBBC), in Zoranje, Haiti, 2011.

A 7 m high, 2.5 m wide prototype with a thickness of 7 cm was constructed (Figure 3.16). The project concluded that the construction method would be feasible in a developed country, but that the surface could have deviations as a result of the application of shotcrete, up to several centimetres (Pronk et al. 2007*b*). A follow-up feasibility report shows an additional experiment replacing the fabric by a stiffer metal mesh to resolve the issue of form control, and mentions the use of a cable net with rebar for the actual proposed construction method (Pronk & Dominicus 2012).

A 4.5 m high, 6.2 m wide prototype with a thickness of 3 to 7 cm was similarly constructed at the Institute for Membrane and Shell Technologies, Building and Real Estate (IMS), Anhalt University of Applied Sciences, Dessau, Germany (Duerr & Off 2014). This followed an earlier 3 × 3 m prototype which suffered from ponding

Figure 3.16: Early and final prototype for reconstruction of the Philips Pavilion, Eindhoven, Netherlands, 2007.

due to insufficient prestress and uneven spraying thickness (Figure 3.17). The larger version was executed in three layers of steel fibre-reinforced shotcrete with open mesh fabric. At each step, the geometry was 3D scanned while perimeter cable forces were monitored and adjusted.

Another independent physical experiment was carried out at the University of Edinburgh, as part of a student project, to investigate constructional aspects of the fabric forming of a hypar shell. In this case, two layers of woven fabric were stretched between timber edge beams (Figure 3.18) (Pedreschi 2013). The lower structural fabric, a greenhouse netting, acted as shuttering, while the upper elastic cotton fabric produced a smooth finish of the concrete.

A considerably larger 7.5 m span, 120-150 mm thick hypar was built by Infinity & Beyond Building Solutions (Figure 3.19) (Mathur 2015). The shell was hand rendered using M25 (C20/25) concrete, applied in two layers. The technique uses 50-100 mm strips of fabric, produced from waste from the textile industry. Contrary to the roofs

Figure 3.17: Early and final prototype of the membrane shell, Dessau, Germany, 2014.

Figure 3.18: Hypar shell, University of Edinburgh, 2012.

by TSC Global, the strips roughly follow principal curvatures, rather than straight lines. The final form is then "reinforced with binding wire from underneath, tied into the edge piping, that helps [to hold] the weight of the concrete". Figure 3.19 shows the pipe frame runs along the edges, and along three internal lines, subdividing the surface into six fabric-formed segments. Mathur (2015) claims a 38-42 % cost reduction for a 50 m^2 shell compared to a conventional timber formwork. Tolerances were measured at the tips and centre (coinciding with the pipe frame) and were less than 10 mm.

Figure 3.19: RSPL Poolside Canopy shell by Infinity & Beyond Building Solutions in Bangalore, India, 2015.

3.3.2 Catenoids

In Brussels, a series of thirteen prototypes were constructed from a prestressed fabric using shotcrete (Cauberg 2009, Cauberg et al. 2012). The final shells had a thickness of 5 cm and a 2 m span (Figure 3.20). Both traditional steel reinforcement and glass-fibre mat reinforcement were compared. The form-found shape, using the force density method, did not exactly have uniform prestress. This means the resulting shape is approximately, but not exactly a catenoid, although it is referred to as a minimal surface.

After applying the shotcrete, the deformed shape of eight out of thirteen shells was measured and compared to a numerical model. Deviations from an expected deflection of 15 mm ranged between 5 and 58 %, to more than 100 % for non-coated fabrics. These errors were attributed to several causes: tolerance of the applied concrete thickness; incorrect stiffness of the membrane edges; erroneous swapping of warp and weft direction; slip at the fixation points; and, the dynamic effects of the shotcreting (Cauberg 2009).

3.3.3 Non-analytical shapes

Continuing from earlier prototypes (Section 3.2.3), three more doubly curved shells were produced at CAST. Figure 3.21 shows a 5.3 m span, 3 cm thick shell, reinforced with a carbon grid (West & Araya 2009).

Figure 3.20: Catenoid-like prototypes by the Belgian Building Research Institute, Centexbel and the Vrije Universiteit Brussels, 2007-8.

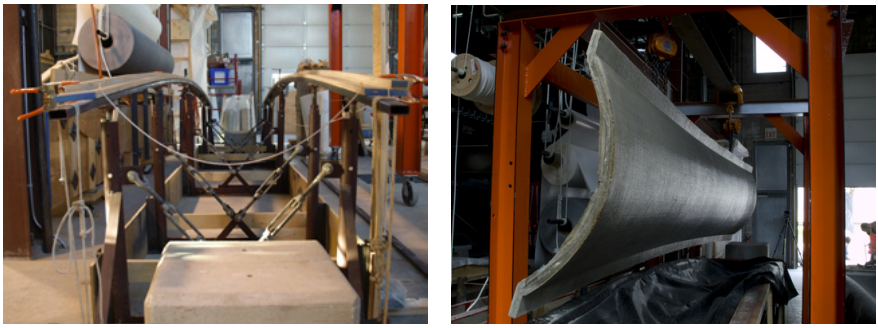

Figure 3.21: Negatively curved vault, produced at CAST, 2009.

Another, a 3 cm lenticular shell, was cast from two flat sheets of fabric. These sheets were fixed to an outer frame along three of their edges, with the remaining adjoining edges sandwiched along the centre of the formwork by two layers of plywood. This 'keel', along with the rest of the frame, controls the longitudinal shape and curvature (Figure 3.22). As before, a carbon grid was used as reinforcement. Details on this prototype have not been published.

A final 6 m prototype was a 'flayed beam', integrating a central tension tie to resist horizontal thrust from the overall shell. The formwork used a custom fabric, Fabrene W756, designed at CAST together with PGI-Fabrene. This is a standard high strength, woven, coated PE fabric, but with a welded, fuzzy non-woven backing. By casting GFRC against the fuzzy side facing upward, then inverting, a fabric-formed rigid mould, with a smooth, coated surface was made. The design was highly corrugated,

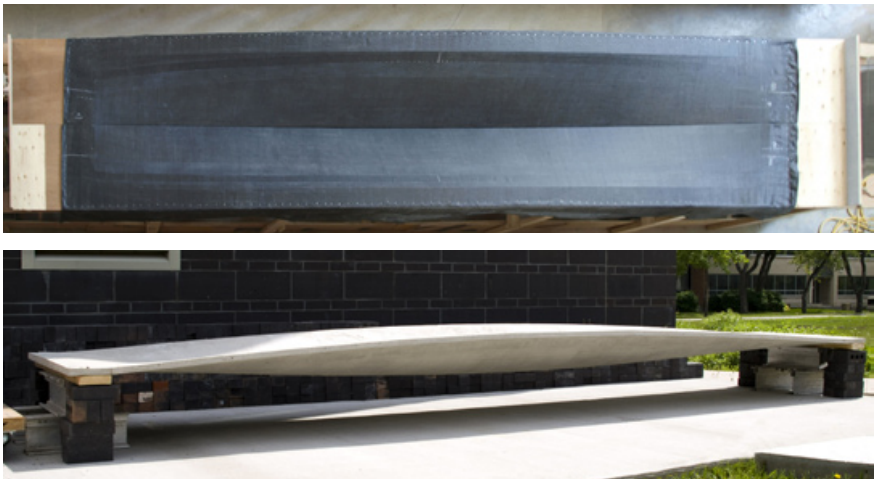

Figure 3.22: Lenticular shell prototype, produced at CAST, 2009.

or 'buckled', by selectively prestressing the fabric at both ends. As each previous prototype made at CAST, the formwork used only flat sheets, meaning the reinforcement could be made from flat meshes as well, requiring no complicated cutting patterns. The fabric was sufficiently elastic to allow for double curvature. Instead of a carbon grid, alkaline-resistant (AR) glassfibre scrim was used in the shell, with steel reinforcing along the centre and edges (Figure 3.23) (West et al. 2011).

Figure 3.23: Flayed shell prototype, produced at CAST, 2009.

A 48 m^2 pavilion was built at the entrance of the BMS College of Engineering in Bangalore, India, 2011, as part of the AA Visiting School (Figure 3.24). Utsav Mathur, mentioned in Section 3.3.1, was one of the participating students. The anticlastic shell was designed using particle-spring form finding (Bhooshan & El Sayed 2012, Bhooshan et al. 2014). The fabric acted more as a guidework than a formwork, serving to describe the complex geometry of the steel reinforcement bars and mesh, which in turn carried the weight of the applied concrete.

Figure 3.24: Hyperthreads shell with fabric guidework, 6 m span, 8 cm thick shell, Bangalore, India, 2011.

Belton (2012*a*,*b*) constructed a 1.22 m square fabric-formed minimal surface (Figure 3.25). The shape was inspired by the work of Frei Otto, but novel as it was a non-orientable surface. Spandex with PVC along the edges, was stretched into a metal frame, before spraying up to 20 mm of plaster. His work includes designs and proposed sequencing for a larger structure enclosing a chapel.

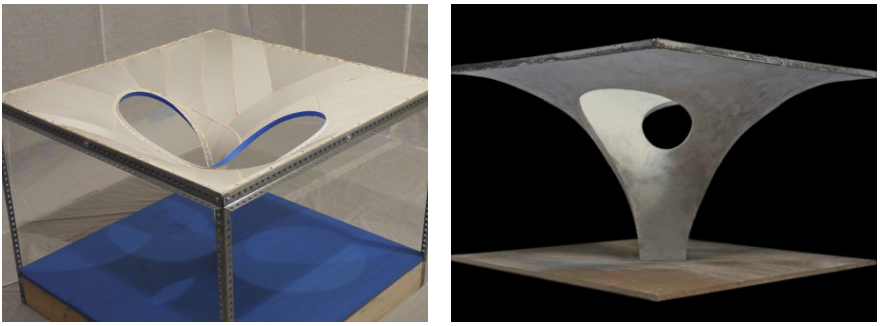

Figure 3.25: Bow-tie column, Florida, US, c. 2012.

3.3.4 Double-layered formworks

In the examples thus far, the formworks have been open, with concrete applied to the exterior of one side. By using two layers of fabric or membrane, tying them together at regular intervals, it is possible to inject the formwork by pumping concrete and create a mattress. This concept has been widely applied to fabric formworks from the late 1960s onward, to create mattresses as river or coastal revetments. By placing the formwork vertically, it is possible to cast concrete walls instead, as has been done since the 1990s in several cases (Veenendaal 2016).

By making the boundaries of such a formwork non-planar, opportunities arise to create doubly curved surface structures. A student project from Eindhoven University of Technology used a double layered formwork, combined with cables to create a surface structure in this manner (Section 3.7.2, Figure 3.46).

The ties can also be replaced by larger plywood clamps, to create open cellular wall structures, which has attracted some academic interest (Dominicus et al. 2011, Pedreschi 2013, Pronk et al. 2011). A parallel student project from Eindhoven (Dielemans et al. 2016), and an earlier student project from the University of Michigan (Holzwart et al. 2010), used this technique to create doubly curved, cellular structures (Figure 3.26) .

3.4 Pneumatic formworks

In the previous sections, the stress in the formwork was generated through weight or pressure exerted by the concrete, combined with varying levels of prestress. Air pressure can be used to inflate the formwork, creating positive curvature and carry part of the weight of the concrete.

Using air-inflated formwork for hollowcore, concrete constructions is patented as far back as 1907, by James M. Boyle. In the 1940s, such formworks were applied to the construction of concrete domes. From the 1970s onward, the rise of tensioned membrane structures, and subsequently that of air-inflated membrane roofs, led to greater opportunities for flexibly formed shells, at a time that the future of thin concrete shells was put into question (Sobek 1987). More recently, vacuum has been proposed for pneumatic formworks as well.

Figure 3.26: Student prototypes: (above) FattyShell, University of Michigan, US, 2010, (below) Organica Hyparbolica, Eindhoven University of Technology at Geelen Beton precast factory, Netherlands, 2016.

3.4.1 Air-inflated formworks

By 1940, Karl Pauli Billner (1882–1965), engineer and prolific inventor, had developed a construction system of inflated, rubberized fabric, constrained by flexible bands, and likewise pressurized from the inside by either air or water (Billner 1943). Billner had already patented a system of vacuum concrete construction to reduce the curing time of concrete (Billner 1936), and combined both ideas for a demonstration in 1940; a pillbox fort made on an air-inflated form, cured using the vacuum method to squeeze out excess water (Figure 3.27). This required an external, rigid steel form as well. The pillbox was completely finished within five hours.

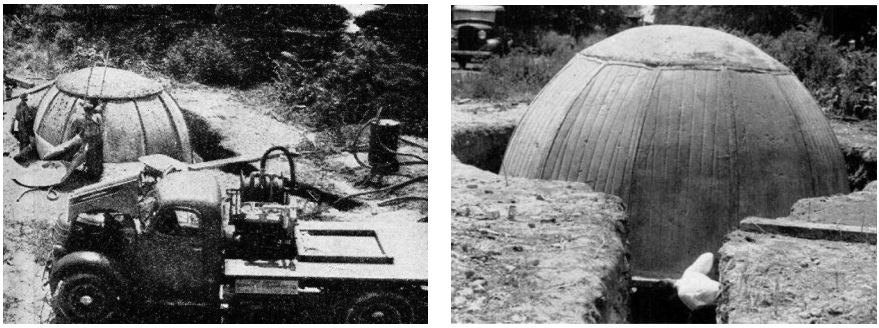

Figure 3.27: Concrete pillbox completed in five hours using vacuum concrete, Washington, US, 1940.

He patented this particular system much later, declaring that "ever since the time, many years ago, that the present inventor publicly demonstrated the use of inflatable flexible internal forms for the production of concrete structures, there have been many attempts by others to imitate and reproduce the methods and products" (Billner 1953). Indeed, since then, a long string of concepts for pneumatically formed shells were patented (Figure 3.28), as well as for other applications. One interesting patent by Bird et al. (1964), for example, describes a system of parallel, inflated, semi-circular tubes to cast a corrugated shell, reminiscent of Ctesiphon. The University of Maine developed a similar system in which the carbon and glass FRP tubes, or sleeves, are inflated, cured with resin, and then filled with concrete to form arches for a bridge structure (Dagher et al. 2012).

Wallace Neff (1895–1982) is widely credited as the first inventor, having patented the concept of an inflatable dome as a formwork for concrete bubble houses in 1942, using neoprene-impregnated nylon fabrics (Neff 1942). Neff himself acknowledged Billner as being the first, though criticized specific aspects of his system (Kanner & Neff 2005). His Airform system used only an internal form, with concrete applied from the top down using a cement gun. The concrete is mixed at the nozzle, i.e. guniting (Figure 3.29). This presented a low-cost way of quickly erecting dome shells by reducing the need for materials and labour. Neff envisaged this as a solution to the housing crisis in the 1940s, but also emphasized its aesthetic appeal, saying that "beautiful flowing lines and curves come into being without effort [...] The absolute absence of girders, columns and jigsaw trusses startles the imagination". In October of 1941, construction began on twelve bubble houses in Falls Church, Virginia, US. In the following two decades, around 2'500 Airform shells were constructed worldwide, although few remain.

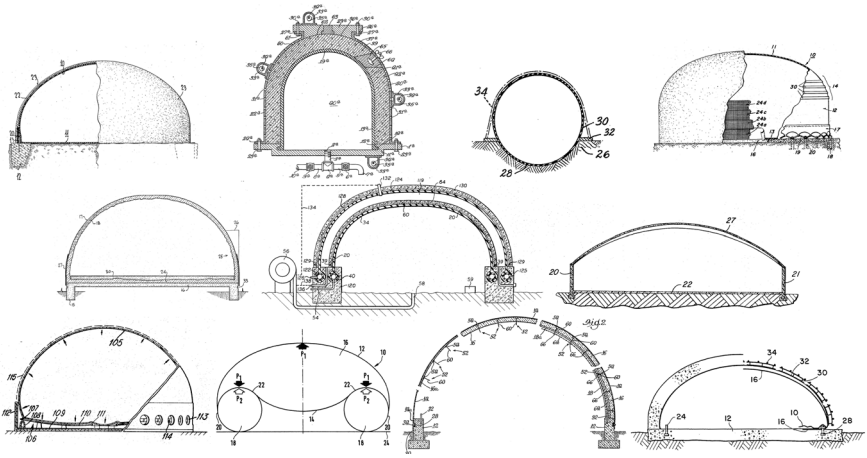

Figure 3.28: Inventions of the air-inflated formwork for concrete domes (from left to right, top to bottom) by Neff (1942), Baily (1942), Billner (1953), Bird et al. (1959), Turner (1966), Bini (1969), Harrington (1971), Heifetz (1972), Prouvost (1978), South & South (1979) and Hale (1988).

Figure 3.29: Airform construction, 1941, and completed Goodyear Balloon House, Litchfield Park, Arizona, US, 1945.

During the late 1960s until the 1980s, academic interest in inflatable structures and formworks grew, as evidenced by the 1967 IASS colloquium and the 1972 IASS conference dedicated to pneumatic structures, and the 1986 special issue of Concrete International devoted to pneumatically formed domes.

This interest paralleled the commercial success enjoyed by those that followed in Neff's footsteps. Father and son Haim and Raphael Heifetz successfully built many shells in Israel during the 1960s using PVC-coated fabrics (Heifetz 1972). Their system is still represented by Raphael Heifetz' company YSM-for-Building, which asserts that more than 40'000 Domecrete structures have been built since. Heifetz (2016) claims that Domecrete may save 50-60 % in cost for the full envelope, resulting in 20-25 % savings for the finished building, compared to traditional construction. Around the same time, over 1'600 shells were constructed by Dante Bini and at least a hundred by Horrall Harrington in the US, both of which offered geometric and/or constructional variations on the principle of pneumatically formed shells (Bini 1969, Harrington 1971, Sobek 1987). Bini's approach deviates considerably, as the formwork is inflated after the concrete is applied. Like Heifetz, Bini's work is being continued by his son Nicoló Bini at Binishells. Horrall Harrington's Air Shells and HP Domes, however, no longer operate. This is possibly related to the former never becoming profitable, a copyright infringement lawsuit between both companies in 1988, which was dismissed, and the aftermath of the collapse of one of HP Domes' storage domes in 1992, which was attributed to design flaws.

Many other people and companies employed these systems, notably the shell builder Heinz Isler, who studied Heifetz' work.

Isler had used inflatables for form-finding models (Section 2.2.5). He co-founded the company Bubble System AG in 1976, along with François Prouvost (see Figure 3.28) and others. They developed pneumatic formworks for 7-8 m domes; the first buildings were made in Langenthal and Aarwangen, Switzerland, then twelve in Ponthierry, France (Sobek 1987). Due to the rising oil prices of the 1970s energy crisis, a construction boom occurred in Saudi Arabia (see also Section 2.3.2). During this period Bubble System built as many as forty-three shells in Riyadh in 1977 (Figure 3.30) and another eighty in Al Baha in 1984.

Pneumatic formworks continue to provide a market for specialist companies like YSM-for-Building and Binishells. Four more companies, Domtec (80 domes built), Dome Technology (600 domes built), PIRS (150 domes built) and Monolithic Constructors (4'000 domes built) all construct shells by spraying foam and concrete on the inside of the formwork following Harrington's system, leaving the formwork as waterproofing. Yet another approach was recently developed at TU Vienna, called the pneumatic wedge method, in which segments of hardened concrete are lifted by an inflatable before being connected (Kromoser & Kollegger 2015*a*,*b*). All in all, Hennik & Houtman (2008) claim over 70'000 shells have been built using pneumatic formwork around the world. The largest is the 330 ft diameter Climax Molybdenum Mine by Dome Technology (Figure 3.31).

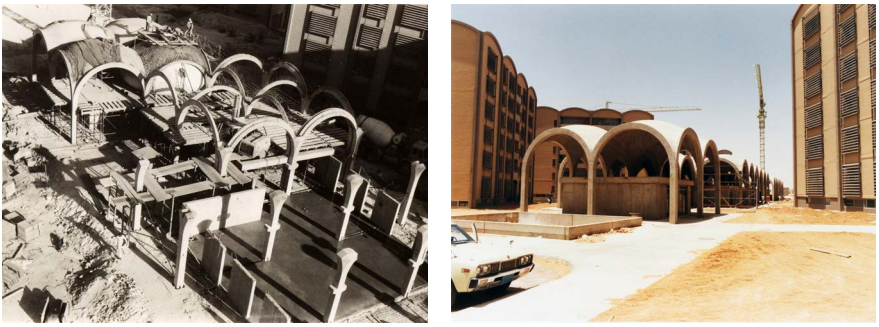

Figure 3.30: Market with forty-three shell roofs, 6×6 m in plan, by Bubble System, Riyadh, Saudi Arabia, 1977.

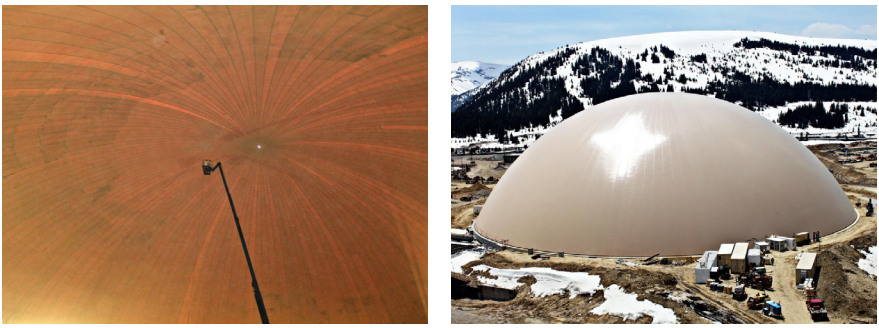

Figure 3.31: Climax Molybdenum Mine with 330 ft diameter formwork, shown prior to PU foam spraying, built in four months, Leadville, Colorado, US, 2011.

The examples thus far concentrated on spherical domes. Other geometries are possible, but certainly not as common. Heifetz (2016) has built cylindrical, ellipsoidal and toroidal shapes, for instance. Otto et al. (1973) show an unusual and large experimental structure in Essen, Germany, built in 1962, where an inflatable was coated with sprayed GFRP. They also show a large pneumatically formed model with multiple internal supports, hardened by applying a GFRP resin (Figure 2.39). Schlaich & Sobek (1986) and Hennik & Houtman (2008) discuss what the greater potential is of pneumatic formworks for more irregularly shaped shells.

The British company Concrete Canvas manufactures an impregnated fabric, that can be inflated before applying water to quickly construct concrete shelters. These shelters have a somewhat arbitrary, barrel vaulted shape.

Another unusual system was recently built by BB-Con (Figure 3.32), following a prototype with Eindhoven University of Technology in the Netherlands. It combines a catenary form with the use of inflatables as a formwork. The 260 mm thick shell was constructed in three layers of either polymer or steel fibre reinforced shotcrete. The project was completed after BB-Con went bankrupt, but the company has since restarted under the name BetonBallon Technology, promoting the same system.

Figure 3.32: Mettler Autodemontage office building, 11×11 m in plan, with 260 mm thick shell, Schijndel, Netherlands, 2012.

A long string of experimental work has been undertaken by Arno Pronk et al. at the Eindhoven University of Technology. Pronk had supported BB-Con's prototype and developed the shotcreted hypars shown in Figure 3.16 (Pronk et al. 2007*b*). He supervised two parallel student projects, using double-layered fabric formworks to cast shells (Figure 3.26 and 3.46).

Other prototypes explored the combination of inflatables within prestressed wire mesh or PVC-coated polyester to produce unusually shaped concrete or GFRP pavilions (Figure 3.33) (Pronk et al. 2007*a*, 2003) and wrapping an inflatable with rubber cooling tubes to create an ice pavilion (Pronk & Osinga 2005). Citing Isler's experiments in creating hanging ice shells (Chilton 2000), recent work using air-inflated formworks has resulted in the largest ever ice dome with a 30 m span (Pronk et al. 2014*a*) and the highest ever ice dome with a height of 30 m, inspired by the Sagrada Família (Belis et al. 2015, Pronk et al. 2015). Both projects combined an inflated formwork with ropes and cables, and used ice reinforced with wood fibres (also known as pykrete) (Pronk et al. 2014*b*).

Figure 3.33: Blob mesh prototype with 5 cm sprayed concrete on formwork using inflatables and nets, Netherlands, 2007.

3.4.2 Double-layered, air-inflated formworks

Zimmermann (2007) proposed the combination of inflatables with a double-layered formwork (see also Section 3.3.4), allowing for an unconventional, synclastic, open cellular shell. Depending on the openings, such a shell could be considered as a gridshell. Tomlow et al. (1989*a*) already show a scale model of the same concept, produced at ILEK in Stuttgart, Germany.

Such a structure, the STGILAT pavilion, was actually recently completed. The student project was a collaboration between architectural firm Cloud 9 from Barcelona, Spain, and the ArtCenter's Environmental Design Department in Pasadena, California, US (Figure 3.34). The structure was built by pumping concrete into a fabric formwork with rounded plywood plugs, supported on an air-inflated ellipsoidal balloon. All elements were pre-fabricated in the US, before being shipped and installed onsite in Begur, Spain.

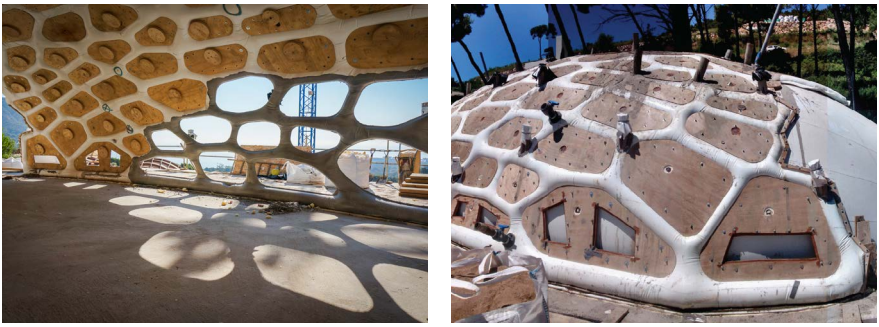

Figure 3.34: STGILAT Pavilion during construction, Begur, Spain, 2015.

3.4.3 Vacuumatic formworks

Another related development is the use of pressure below atmospheric pressure, or vacuum, to create deflated structures. The earliest occurrence is at the Queen's University Belfast in 1970, where several students explored vacuumatic structures. Other researchers experienced in pneumatic formworks such as Schlaich & Sobek (1986) have suggested it as a formwork for concrete, and recently Huijben (2014) revisited the idea, making various small-scale prototypes. Possible formworks systems are a vacuumatic exterior mould, to cast concrete on top, or a direct vacuum injection mould (Figure 3.35).

Figure 3.35: Experiments at Eindhoven University of Technology, Netherlands, on vacuumatics as formwork, 2012, or infused with concrete, 2015.

3.5 Bending-active formworks

The use of bending for a formwork system can be traced back to Roman times. Architect and engineer Vitruvius proposed bending tied reeds and applying sand mortar for the construction of vaults (Vitruvius 1914). Vaults around the Mediterranean can be found showing impressions of the reed (Veenendaal et al. 2011).

Today, rebar is often bent to form a skeletal structure as lost formwork, for example for complex concrete surface structures, artworks and boats. In general, we may assume that the steel is plastically deformed, meaning that any bending is permanent, or "passive" or that individual straight segments are combined to form a rigid gridshell. Examples are the Taichung Metropolitan Opera House (Section 2.2.4) and the Zeiss-Diwidag construction method (Section 2.1.1) respectively.

Instead, bending-active structures derive their geometry from elastic deformation. These initially straight or planar, elastically bent elements, also called spline elements, interact with each other, or with other connecting elements, preventing them from taking their original shape. This creates a stable, prestressed structural system (Lienhard et al. 2013, Van Mele et al. 2013). Such systems can be used as a reusable formwork, and a few examples exist.

The earliest known example is the Lift-Shape process for the construction of shells (Evans & Marsh III 1962, Marsh III 1962, 1964). In this system, a pattern of reinforcement bars, covered with a galvanized diamond mesh lath, is lifted. The supports are then pulled to their final position by using chain ratchets, before spraying concrete. The concrete's 28-day compressive strength was 2'400 psi, c. C17/20.

Several paraboloid shaped structures were built based on designs that were refined using physical models. The largest were 50 ft span shells, supported on six points (Figure 3.36): one on the campus of the Texas A & M (today in Hensel Park); the Medo Camera Shop for the 1964-1965 New York World's Fair, in front of the Eastman Kodak Pavilion (Figure 2.52); and, two for the Little Rock Zoo in Arkansas. Compared with an estimate for a traditional timber formwork, the Lift-Shape method allowed for a 23 % theoretical cost saving.

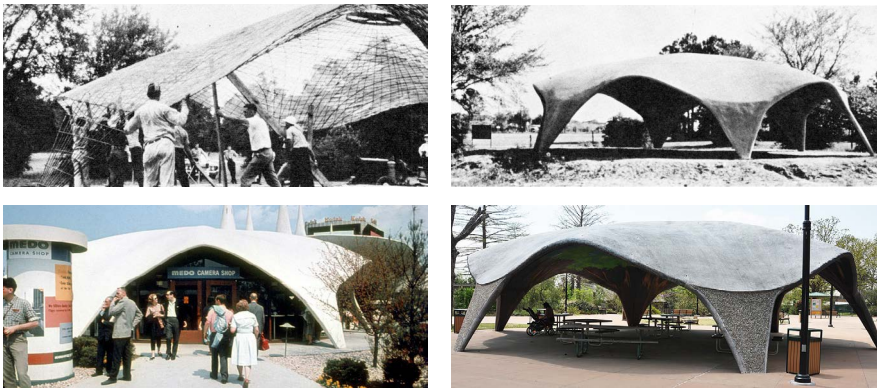

Figure 3.36: Erected steel armature as formwork, or Lift-Shape, for 21 ft square polyurethane shell, Texas A & M, College Station, US, 1961; the Medo Camera Shop, World's Fair, New York, US, 1964-1965; and Little Rock Zoo, Arkansas, US, 1964.

Around the same time, artist and inventor James Buchanan "Buck" Winn Jr. (1905–1979) constructed a small hangar at his own ranch in Wimberley, Texas. This shell structure, inspired by primitive use of reed and mud, also used an armature of steel rods, successively coated until a desired thickness was reached (Figure 3.37) (Winn 1962). Although Winn also taught in Texas, at the University of Texas School of Architecture, both he and Marsh presented independently at a 1961 conference, suggesting their work was not related.

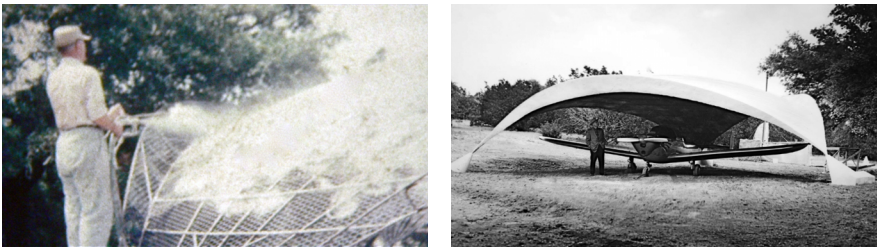

Figure 3.37: Steel armature as formwork for hangar, Wimberley, Texas, US, c. 1961.

A few years later, in 1964, Oberdick (1965*a*,*b*) constructed a 16 ft and a 27 ft square wooden lattice grid with stapled-on nylon-reinforced paper skin, as a formwork for a 4 in thick, sprayed polyurethane foam shell, at the University of Michigan (Figure 3.38).

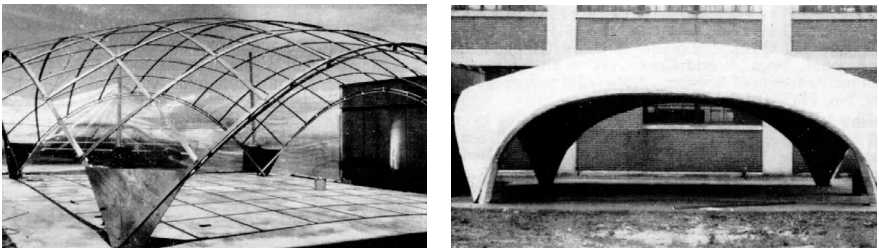

Figure 3.38: Erected wood armature as formwork for 21 ft square polyurethane shell, University of Michigan, 1964.

The idea of using a gridshell as formwork reappeared when it was proposed by Tang (2012, 2015), who built two small prototypes of different spans, using the same formwork (Figure 3.39). The system used elliptical PVC electrical pipes for the grid, and PP fabric as shuttering.

Figure 3.39: Deployable gridshell formwork and two resulting size vaults, University of Edinburgh, 2014.

Researchers from the École Nationale des Ponts et Chaussées (ENPC) built a 10 m^2 prototype for a "hybrid structural skin" (Figure 3.40) (Cuvilliers et al. 2017). A gridshell was covered with concrete, referring to the gridshell as formwork and the concrete as roofing. This leaves the level of composite behaviour between both systems ambiguous.

Figure 3.40: Deployable gridshell as lost formwork for a hybrid system, ENPC, 2016.

3.6 Mesh formworks

The use of wire mesh as shuttering is relatively common, for example, in ferrocement construction, where it acts as reinforcement in the final structure. In such cases, the mesh is supported by a skeletal frame of rods like rebar, by timber formwork, or through some other means. A more unconventional approach is to suspend or prestress the mesh. Many of the patents in the previous sections suggest both fabrics and meshes as possible alternatives for their specific concept of a flexible formwork, but actual use of meshes is rare.

However, examples do exist, and some have already been mentioned: the Chivas Distillery Warehouses, built around 1958, replaced the earlier hessian fabric with expanded metal (Figure 3.6); and Pronk et al. (2007*a*) combined inflatables with steel nets (Figure 3.33) as well as proposed and built a prestressed mesh formwork, replacing a previous version featuring a coated fabric (Pronk & Dominicus 2012) (Figures 3.16).

The idea of spraying concrete onto a tensile network to create a rigid shell, or "membranal structure", existed as early as 1953, as part of a series of studies in Raleigh, North Carolina, US (Caminos 2012, 1959). They considered the problem of finding the correct shape when stretched, and proposed three measures for construction: cutting patterns of the membrane, made from flat pieces; segmenting the surface, assembled from smaller moulded pieces; and replacing the membrane by a network of cables, rods or wires. The option of using a fabric was never mentioned, though many small models were made with fabric. They proceeded with a 50 in diameter model with wire elements connected with washers at the nodes, another model

with metal lath, then finally a 120 in diameter model using metal lath and sprayed concrete (Figure 3.41). The outer ring and the internal supports were maintained in the final structure, requiring no further formwork. Interestingly, shell builders Eduardo Torroja and Pier Luigi Nervi acted as consultants for the project.

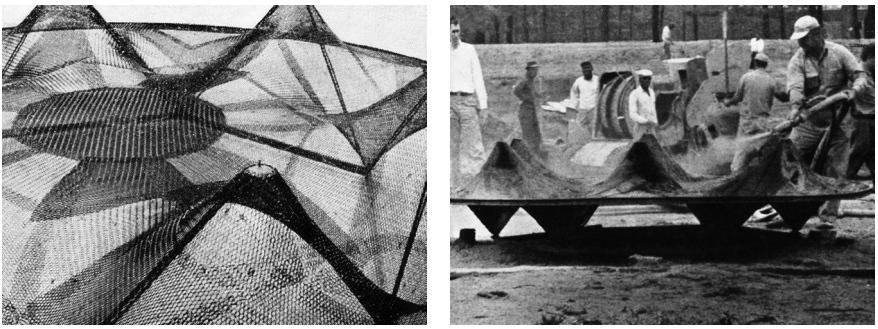

Figure 3.41: Model with 120 in diameter, prior and during concrete spraying with gunite, State College Raleigh, North Carolina, US, c. 1953.

In 1972, Aleksandra Kasuba described a method of sandwiching a membrane guidework between honeycomb elements, then applying plaster on the interior, and concrete and cladding on the exterior (Kasuba 2011). A self-described environmental artist, Kasuba has a long history of creating fabric structures and art installations. She had intended to use this new construction method to the Millay Colony project, in Steepletop, New York, US, but the project was in the hands of others by 1978.

She revisited and further developed the method around 2000, calling it the "K-method". A group of prototype shell dwellings were built in New Mexico, Manzano Mountains, 2002-3, using chicken wire mesh between wooden frames, before applying PU foam, expanded metal lath, stucco render, and finally aluminium roof cladding (Figure 3.42). No other applications followed, but a large variety of design studies were carried out. Among the chief advantages were bypassing the fabrication of disposable and custom shaped metal or wooden formwork, and, interestingly enough, avoiding "the use of computer design methods that replicate sculpted curvatures or simulate tensile surface configurations".

Figure 3.42: Shell dwellings, built using the K-method, New Mexico, US, 2003.

3.7 Cable-net and wire falseworks

An alternative tensile formwork system is to replace the fabric or mesh by discrete elements. As mentioned, Caminos (1959) suggested a network of cables, rods or wires, although for the final concrete prototype had used a metal lath. As with the fabric formworks, the simplest imaginable use of cables for falsework would be to suspend them. A few years earlier, in his thesis on hanging roofs, Otto (1954) in fact suggested to cover and insulate such a roof with a thin 15–20 mm layer of concrete (Figure 3.43). Here, the cable net is still the structural system.

The 1950s actually saw the construction of many hanging roofs, some in the form of suspended reinforced concrete shells. This popularity led to a dedicated 1962 IASS colloquium. Here, Liudkovsky (1962) commented that most suspended concrete shells were erected using cast-in-place concrete (with formwork), and only a few exceptions used precast elements, which avoided the need for scaffolding.

Possibly the first example of the latter is the 95 m span, 50 mm thick circular 1956 Cilindro Municipal in Montevideo, Uruguay. Engineer Leonel Viera (1913–1975) also worked on a hyperbolic paraboloid version, the church of San Antonio María Claret, which unfortunately collapsed during construction in 1967. Another example, also a hyperbolic paraboloid, is the 1958 Philips Pavilion (Figure 2.8). The largest hyperbolic paraboloid shell is the 122 m span, 600 mm thick, 1983 Scotiabank Saddledome, formerly the Olympic Saddledome. It was built from 6'400 precast panels suspended from post-tensioned cables for the 1988 Winter Games in Calgary, Canada.

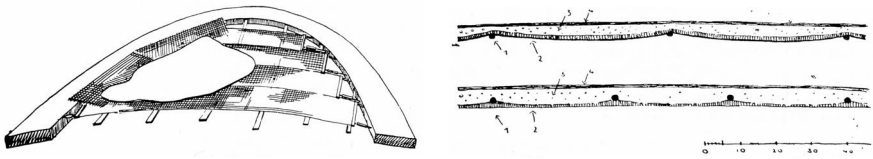

Figure 3.43: Proposal for a cable-net roof with concrete cover (Otto 1954).

3.7.1 Hanging cables

The only example found of a hanging roof with cast-in-place concrete without scaffolding is St. Stephen's Lutheran Church in Northglenn, Colorado, US. Charles A. Haertling designed this church that was built in 1963 (Figure 3.44). Steel cables were hung from four 2 ft wide by 2 to 8 ft high, catenary shaped, prestressed concrete beams. Two main beams were 83 ft long, the other 50 ft. Ribbed metal lathing was placed on the cables, on which the 2.5 in thick concrete roof was placed (Anon. 1966).

Figure 3.44: St. Stephen's Lutheran Church in Northglenn, Colorado, US, 1963.

3.7.2 Generator lines

When constructing a flexible cable-net or wire falsework for a hypar shell, the initial reaction may be to follow generator lines. However, since a straight line cannot support a load at any angle to its axis, tensions would theoretically need to be infinite in order to maintain the shape. Nonetheless, some smaller models have been built in this manner. The earliest, around 1960, is shown in Figure 3.49.

Another shell was built in 1976-7 as part of a student project at the University of Illinois at Chicago (Figure 3.45). Four connected hypars cover 40 m^2 and rise up to 7 m above ground. Steel strands, 1/8 in diameter, formed a 300×300 mm grid within a tubular steel frame. The grid seems to coincide with the generator lines of the hypars, and in turn supported wire mesh. Concrete was applied using shotcrete to an approximate thickness of 20 mm, though this was difficult to control (Naaman 2000).

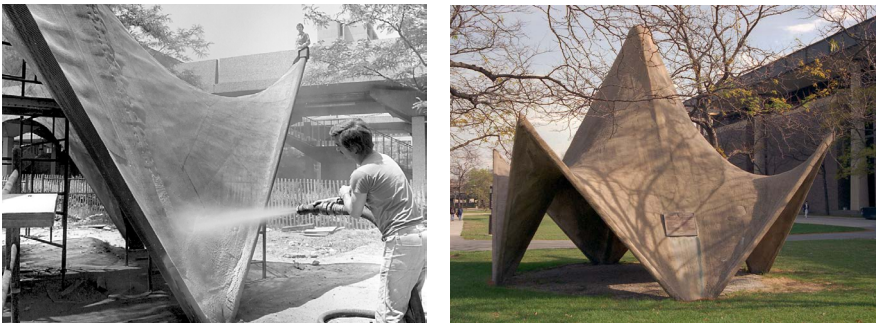

Figure 3.45: Hyperbolic paraboloid shell, University of Illinois at Chicago, US, 1977.

A recent project for a 2.4×2.4 m shell (Figure 3.46) included a double-layered fabric (see also Section 3.3.4), but suffered significant deflections, and subsequent failure of seams, forcing casting to be seized (Claessens et al. 2016). The deflections of the generator lines were likely exacerbated by the lack of appreciable prestress in the cables and insufficient stiffness of the timber frame. The project was carried out in tandem with another, similar student project, shown in Figure 3.26.

3.7.3 Offset generator lines

A construction method, called the offset wire method, was developed by Waling & Greszczuk (1960) at Purdue University, Indiana, US, and avoided the need for "a forest of falsework". Initially, they observed that placing the wires along the straight-line generators of the hypar would require "excessively high tension" (Ziegler 1961). Thus, they offset the wires from the straight lines, slightly curving them as a result. In addition, the method used two layers of wires to sandwich a layer of extruded polystyrene (XPS) tiles as shuttering. The cable net and XPS acted as lost formwork for traditionally placed concrete.

Figure 3.46: Concrete shell prototype, by Eindhoven University of Technology at Geelen Beton precast factory, Netherlands, 2016.

Early prototypes are described by Waling & Greszczuk (1960). After building a 37 ft 7/8 in square small-scale model with a rise of 9.22 in, they proceeded with a large-scale 20 ft square laboratory model with a rise of 7 ft (Figure 3.47). The prototype had 3 in thick XPS designed for a 2 in thick concrete cover, deviating by 2.7 in from a true hypar at its centre under equivalent loading. A coating of mortar reduced deflections to 0.4 in, but showed cracking above 80 % of the applied load. The wires, spaced 12 in apart, were prestressed between 0.9–2.7 kN using standard prestressing equipment.

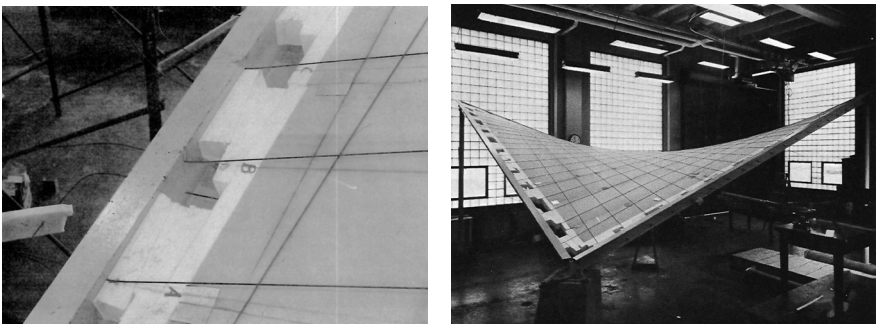

Figure 3.47: Large-scale laboratory model with steel frame, two layers of wires, XPS foam boards and wedges, 20 ft square, at the School of Civil Engineering at Purdue University, Lafayette, Indiana, US, c. 1959.

Two larger, identical 64 ft square structures were built around 1960-1962: the Bay Service Station, in Midland, Michigan, US (Maddex 2007), now the Auto Perfection car repair shop; and, a clubhouse at the Purdue Golf Course in West Lafayette, Indiana, US (Waling et al. 1964), demolished in the mid-1990s. Both were assemblies of four hypars (Figures 3.48 and 9.4). The Purdue shell had two layers of 0.135 in wires, 6 ft offset from the straight-line generators. The bottom wires were spaced 12 in apart, the top layer 24 in apart. The bottom wires had an initial camber of about 4 in to account for the weight of the XPS boards.

The hypars are 6.5 in thick, consisting of 3 in concrete, 0.5 in mortar, and 3 in XPS. The average cylinder compression strength of the concrete was measured to be 7415 psi after 28 days, or 51 MPa, close to a C45/55.

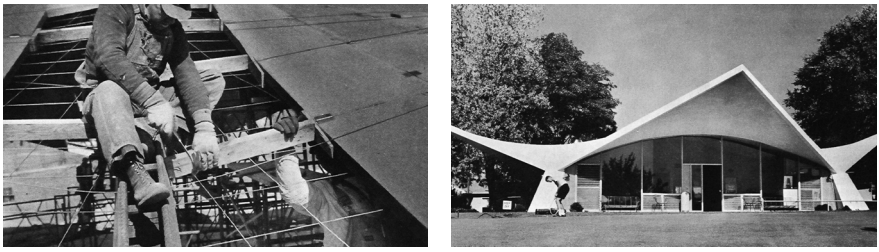

Figure 3.48: Construction of the Purdue Golf Course clubhouse, Indiana, US, 1960–1962.

3.7.4 Catenary lines

A London City Council school assembly hall consisting of five 73 ft hypars, in Southwark, Newington, London, now the Ark Global Academy, was built around 1960 (Flint & Low 1960). The 1300 m^2 complex is pentagonal in plan. The hypars are 4 in thick consisting of 1 in mortar, 1 in woodwool, 2 in sprayed concrete (gunite).

An earlier 1:8 prototype is described by Flint (1961) (Figure 3.49). PVC sheathed generator wires of high tensile steel were anchored in the frame, with adjustable screws for tensioning at one end. The wires were covered with strips of light expanded metal lathing, overlain by building paper. The largest predicted movements were about 10 in at full-scale during guniting, later confirmed on the full-scale shells. A final test loaded the prototype up to 170 psf.

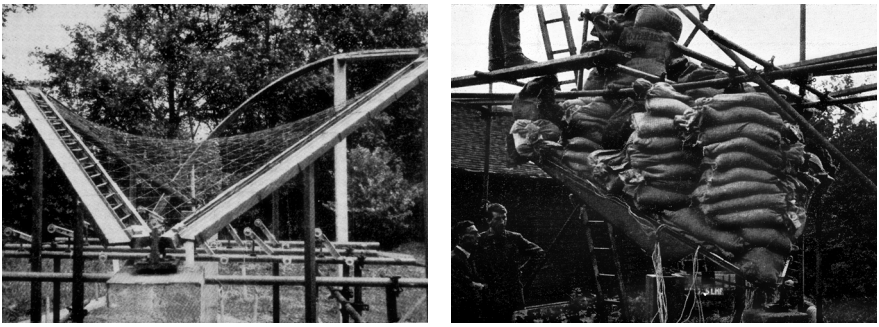

Figure 3.49: Prototype for Pentagon Hall at scale 1:8.

For the full-scale structure (Figures 3.50 and 9.5), a third set of catenary wires were added to avoid substantial deformations. All steel wires were 0.276 in and the generator wires were sheathed to allow post-tensioning. The shuttering consisted of the mesh reinforcement and wood-wool insulation. Remarkably, the sprayed mortar was applied from underneath. The cube compression strength of the mortar was measured to be more than 9000 psi after 28 days, or 62 MPa, close to a C50/60. A final comparison showed the cost of the shell to be potentially 20 % lower than a similar project built using timber formwork. The latter did not include insulation and mullions, which were an inherent part of the wire formwork system. The Pentagon Hall also used a final coat of gunite as a cost-effective means of finishing the interior surface.

3.7.5 Lines of principal curvature

Both Waling et al. (1964) and Flint & Low (1960) realized that the generator lines require too much tension to reduce deviations from the intended shape, and solved this by offsetting them or adding a third direction respectively. Another approach is to follow the highest, i.e. principal, curvatures. Since the applied load is equal to tension times curvature: the higher the curvature, the lower the tension. By following principal curvature, we obtain the lowest requirements for the amount of pretension in a discrete formwork. Depending on the shape, these lines of curvatures may converge or diverge, so a compromise has to be made if a minimum or maximum spacing in the network is required.

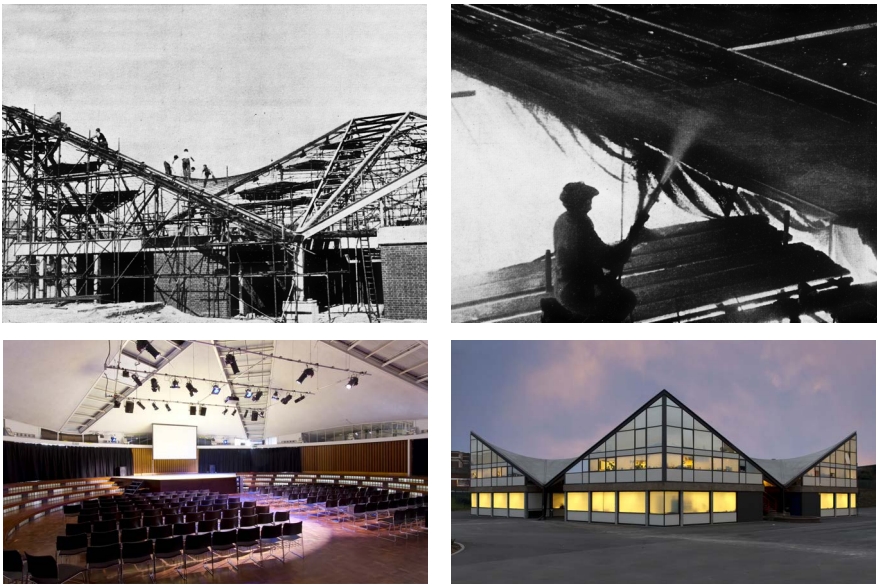

Figure 3.50: Pentagon Hall, Ark Globe Academy, formerly a London City Council school assembly hall, UK, 1960.

Mollaert & Hebbelinck (2002) proposed a network of edge chains and adjustable belts. The network seems to be approximately oriented with principal curvatures. A prototype formwork, based on this concept, was built at the Vrije Universiteit Brussels, Belgium (Figure 3.51). It is briefly described by De Bolster et al. (2009), but details of this work by Hebbelinck remain unpublished. The network of belts was covered with expanded polystyrene (EPS) tiles before applying FRP on either side. The system is labour-intensive, but allowed for a range of shallow to highly curved hypar shapes of varying spans.

As part of the present work, two 1.8 m square hypar cable-net and fabric-formed prototypes were built in 2013-4 based on this approach, and reusing much of the same formwork system (Veenendaal & Block 2014*a*) (Chapter 9). The system was proposed for an unbuilt 81.5 m span wildlife crossing (Torsing et al. 2012).

Figure 3.51: Adaptable and reusable discrete falsework, Brussels, Belgium, c. 2009.

Three cable-net and fabric-formed shell prototypes were built by Escobedo Construction. The final two, designed and constructed with support from, and based on the work by, Van Mele & Block (2011), followed principal curvatures. The final, uniquely shaped shell was hand rendered and reinforced with a carbon grid. The curved edges were offset from the digitally fabricated, custom timber frame, and their thickness controlled by profiles clamped to the cable net. The timber frame was supported and braced by standard shoring and scaffolding elements (Figure 3.52).

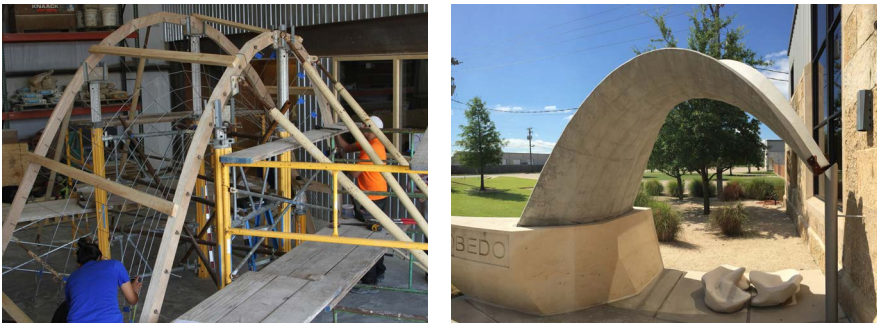

Figure 3.52: Cable-net and fabric formed thin shell by Escobedo Construction and the Block Research Group, ETH Zurich, Buda, Texas, US, 2014.

3.8 Technical summary

This is a summary of technical information found in the historical and contemporary references on flexibly formed shells, discussed in the previous sections. This includes span, rise and thickness of built examples, overviews of concrete, reinforcement and formwork materials, and reported costs.

3.8.1 Geometry

Pneumatically formed domes have been constructed up to 100 m, and proposals for even larger ones exist. The largest fabric-formed Ctesiphon barrel vault has a span of 34 m, while the largest flexibly formed hypar is the 38 m span Pentagon Hall (noted as having a 22 m span for each of its five segments). According to Candela, the upper economical limit for shells is about 30 m (Cassinello et al. 2010), presumably based on the use of timber formworks. Isler suggested large spans in excess of 90 m are not appropriate (Isler 1994).

Figure 3.53 shows the rise and thickness of precedent, flexibly formed shells relative to their span. Examples cast on rigid timber formworks, by Isler (synclastic) and Candela (anticlastic), are added for reference. The rise of Ctesiphon shells increases logarithmically relative to the span, with the Chivas Distillery Warehouses as an outlier, being relatively shallow. These warehouses were supported on 10 ft high buttressed walls, so the total height is comparable to other Ctesiphon shells of similar span. The much shallower flexibly formed hypars follow a linear relation between span and rise. Pneumatically formed domes like the Domecrete system were generally semi-spherical, so with a fixed rise-to-span ratio of 1:2. Binishells, and other systems have been shallower as well.

The Ctesiphon shells have a roughly linear relation between thickness and span, so maintaining similar slenderness, regardless of size. There is no strong relation for the hypars, with the RSPL Poolside Canopy shell being particularly heavy. The LCH and Pentagon Hall have the same slenderness as Candela's work, which is regarded as the standard for very slender shells. It is noted that the RSPL Poolside Canopy shell used C20/25 concrete, the Purdue shell C50/60 and the most slender, Pentagon Hall, used C60/75. Pneumatically formed domes tend to be relatively thick, possibly due to the decreasing post-buckling capacity of domes in general.

Overall, the most shallow and slender examples found are anticlastic hypars.

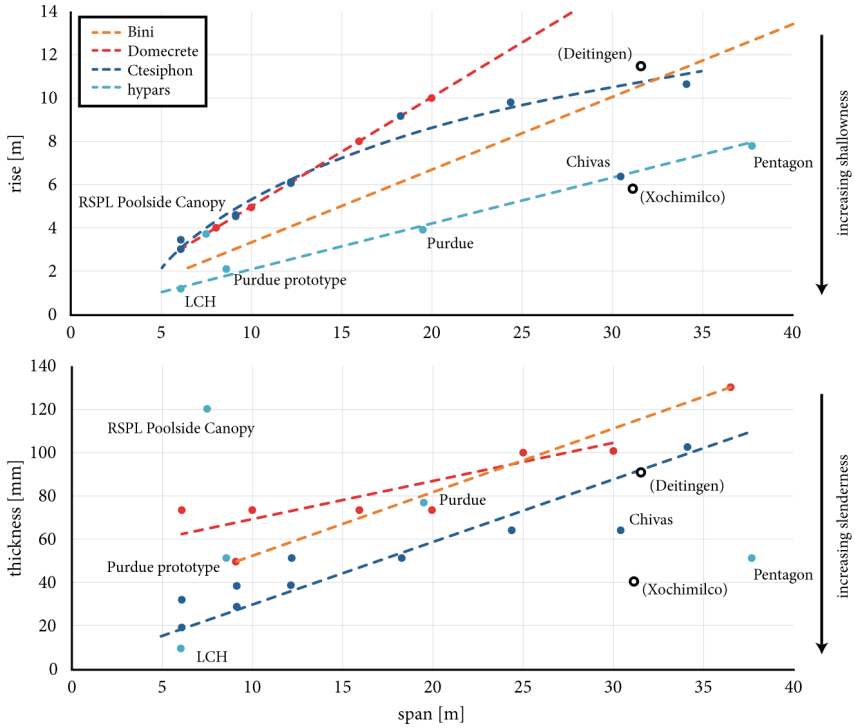

Figure 3.53: Span versus rise (shallowness) and thickness (slenderness) of precedent, flexibly formed shells. Isler's Deitingen gas station and Candela's Xochimilco Los Manantiales restaurant, constructed on timber formworks, included between brackets for reference.

3.8.2 Material

Application of concrete has been done by spraying for the pneumatic domes and the Pentagon Hall. Waller & Aston (1953) also recommended the use of gunite for the larger Ctesiphon shells, although most seem to have been hand-rendered. Flint & Low (1960) specifically argued the use of gunite as a final finish in order to save on cost. In the Pentagon Hall, it was applied from underneath, demonstrating the clearances a flexible formwork can afford. Most contemporary airformed domes are sprayed from the inside as well, including the insulation foam. Concrete for smaller Ctesiphon and LCH shells were applied by brushing and hand-rendering. The Purdue and RSPL Poolside Canopy shells were also done by hand.

The strength of concrete has varied, with concrete as low as C25/30 for Ctesiphon and LCH shells, and up to C60/75 for Pentagon Hall. Whenever reported, maximum aggregate sizes were small (about 1 mm) and water-cement ratios were about 0.40 (typical for early gunite and contemporary shotcrete as well). Other materials have been used instead of concrete: ice, or reinforced ice (pykrete); PU foam; and carbon FRP.

Short-span Ctesiphon and LCH shells are unreinforced, apart from the fabric or mesh shuttering left behind. Larger shells have all been traditionally steel reinforced with steel reinforcement meshes and bars. The Pentagon Hall is noteworthy for its additional use of the wire formwork to post-tension the roof.

Recent prototypes have included newer reinforcement materials and types, including the use of polymer fibre grids, textiles and mats as well as steel and polymer fibres.

3.8.3 Formwork system

Early and existing commercial systems are mostly lost formworks, with fabrics, wires and cables left behind. With the exception of Harrington's system and its current following in the US, pneumatic formworks are deflated and recovered. Heifetz (2016) claims each form can be reused 200 times, and upon repair up to another 150 times. Ctesiphon shells used organic fabrics like hessian, and later expanded metal lath. Pneumatic formworks started with rubberized fabrics, and today use PVC coated polyester or nylon fabrics. Prototypes have been built with a wide range of coated and uncoated polymer fabric, including polyester, nylon, polypropylene and polyethylene. The cable-net systems have relied on steel cables or wires, with XPS foam or woodwool insulation as shuttering. Some examples have even used paper as shuttering. More recent prototypes all propose and emphasize removable and potentially reusable systems.

3.8.4 Cost

Historical and recent cost estimates have been converted to cost in 2015 currency for a UK/US construction market (Table 3.1). Of course, these conversions are increasingly inaccurate, the further back in time the original estimate was made ("confidence" in Table 3.1). Nevertheless, this should give some sense of whether these systems are financially prohibitive when placed in a modern construction context.

The cost for the Ctesiphon system is about 150-390 €/m^2 depending on the span (Billig 1946). An additional 40 and 25 % will include the floor and foundations (Billig 1955). The affordability can be explained by the repetition in the shape of these shells, allowing reuse of design and engineering works, as well as the falsework arches. The use of unskilled labour would also have contributed.

An estimate for the Pentagon Hall roof comes to 380 €/m^2 with 34 % for the concreting (Flint & Low 1960). For the Purdue golf clubhouse shell, the cost is about 510 €/m^2 with 20 % spent on concreting, shoring and reinforcement (Waling et al. 1964). An additional 33 % includes the roof finishes, floor and foundations. For the finished building this cost is more than doubled (×2.18). The difference in cost between these two contemporary systems is due to the steelwork and the insulation: the steel edge and ridge members were custom fabricated, and its XPS insulation foam was experimental at the time.

Mathur (2015) cites the cost at 150 €/m^2 for a 50 m^2 shell, but based on having used his system up to a span of 5.5 m at the time.

Heifetz (1970) quotes 430 €/m^2 for a 99 ft span, pneumatically formed dome, indicating a comparable cost to the contemporary Purdue and Pentagon cable-net formed shells. For smaller spans, down to 20 ft, the cost is a low as 170 €/m^2. Today, for pneumatic formworks, Monolithic Constructors quotes 625 €/m^2 for a shell and integrated concrete floor, and slightly more than double for the finished shell (×2.17). South (1990) cites two specific projects at the finished cost of about 775-910 €/m^2. PIRS' two largest projects cost 1'100 €/m^2 in total, similar to Monolithic.

Torsing et al. (2012) mention that, based on cost estimates for a competion design, an 81.5 m span hypar shell including the foundations and using a cable-net and fabric formwork would cost about 1286 \$/m^2, with 31 % due to the formwork.

In summary, the cost of a flexibly formed shell of spans between 1 and 5 m may be as low as 150 €/m^2, and 400-500 €/m^2 between 5 and 40 m. An additional 33 to 65 % will take the floor and foundation into account. Multiplying the total by a factor of up to 2.2 on top of that indicates the total cost of a finished building.

Compared to traditionally formed shell structures, cost savings have been claimed between 20 and 25 % for the funicular shell floors, the Domecrete system, the Lift-Shape process and Pentagon hall, up to 40 % by Mathur (2015) for his RSPL Poolside Canopy shell.

type	span			infl.		exch.			conf.	source
			[cost/sqft]	[-]	[cost/sqft]	[-]	[€/sqft]	[€/m^2]		
fabric-formed barrel vault (Ctesiphon)										
shell only	20 ft	£	0.17	65.75	10.96	1.28	14.03	150.97	±81%	Billig (1946)
shell only	89 ft	£	0.43	65.75	28.49	1.28	36.47	392.52	±81%	Billig (1946)
fabric-formed hypar										
shell only		$	-	4*	-	0.90	-	149.90	-	Mathur (2015)
cable-net formed hypar										
shell only	124 ft	£	0.83	33.25	27.57	1.28	35.28	379.79	±61%	Flint & Low (1960)
shell only	64 ft	$	4.90	10.75	52.70	0.90	47.43	510.56	±80%	Waling et al. (1964)
pneumatically formed dome										
shell only	20 ft	$	2.30	7.05	16.20	0.90	14.58	156.97	±60%	Heifetz (1970)
shell only	99 ft	$	6.35	7.05	44.74	0.90	40.26	433.38	±60%	Heifetz (1970)
shell and floor	36 ft	$	60.00	1.08	64.50	0.90	58.05	624.85	±2%	Monolithic, 2013
finished building	60 ft	$	40.00	2.00	80.00	0.90	72.00	775.00	±27%	South (1990)
finished building	180 ft	$	47.00	2.00	94.00	0.90	84.60	910.63	±27%	South (1990)
finished building	61.4 m	$	-	-	-	-	-	1'094.25	-	PIRS, 2014

Table 3.1: Cost in 2015 €/m^2 for flexibly formed shells, converted from original reference, using current exchange rates (exch.). Inflation factor (infl.) based on average between real and skilled labour value, and confidence (conf.) based on one standard deviation in these two and two more possible inflation measures: historical opportunity cost and economic cost (Williamson & Officer 2016). *Construction cost index to convert from India to UK/US (Moore & Riley 2012).

3.9 Historical analysis

This analysis summarizes the historical development of flexible formworks for shell structures, against the backdrop of major political and economic events, and changing value of steel, concrete, timber, textiles and labour. Throughout this analysis, some publically available US statistics are used as they go back to the early twentieth century. It is assumed that due to increased globalization, effects seen in the US economy are sufficiently valid to draw more general conclusions.

Innovations in flexible formworks for shells were initially motivated by housing crises following the Great Depression and the Second World War, and later by the looming end to the golden era of concrete shells.

Wallace Neff devised the Airform system for pneumatically formed shells in response to the 1940s housing crisis, building 2'500 of them in the following two decades. Across the Atlantic, low-cost housing was also the motivation for James Waller's Nofrango system. Figure 3.54 shows that cost of concrete and steel were highly volatile during this time. After the war, his Ctesiphon system was presented at the 1954 International Exhibition on Low-Cost Housing in India (Billig 1955). Over five hundred Ctesiphon corrugated barrel vaults and domes were built, attributed to increasing demand for covering of large unobstructed spaces, and to global shortages of steel and timber (Waller & Aston 1953). Ramaswamy's low-cost funicular shell roof and floor were also developed due to post-war shortages in steel and cement in India (Ramaswamy 1968).

However, conventional rigid formwork systems were still competitive as Félix Candela "could not charge owners what [his umbrella shells] cost. They were so inexpensive that it would undermine the industrial building market" (Ketchum 2016).

During the 1960s, the cost of conventional timber formwork became the main incentive to explore flexible formworks, as the price of timber had steadily risen up to the 1950s (Figure 3.54). This caused a first wave of academic experiments on flexible formworks (1960-1975). New concepts were the use of gridshells by Marsh III (1964) and Oberdick (1965*a*) or discrete networks by Flint & Low (1960) and Waling et al. (1964). The first two both cite minimizing the need for prefabrication as another advantage, possibly due to negative views on the quality of prefabricated components at the time. Flint & Low (1960) also mention that conventional formwork has difficulty to produce shapes other than true hyperbolic paraboloids. Waling et al. (1964) go as far as suggesting the cost of formwork acted as a deterrent to engineers that were even considering a shell structure in their projects.

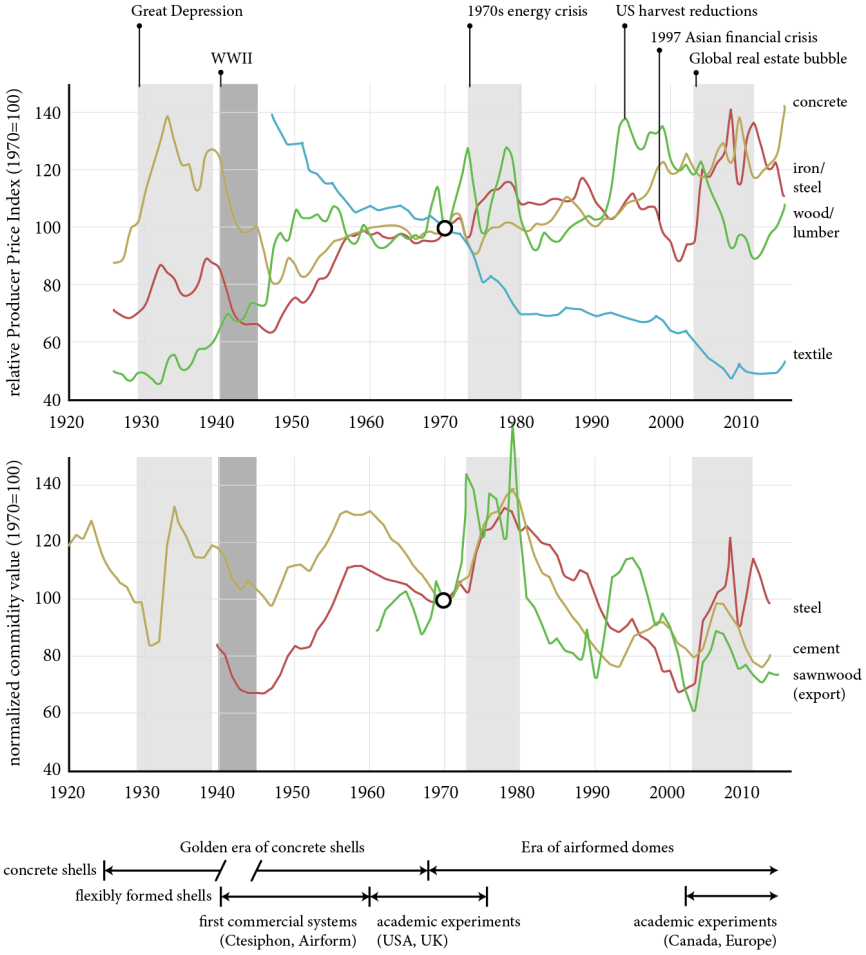

Figure 3.54: Historical Relative Producer Price Index (PPI) (at producer level) (USBLS 2016), and commodity (Kelly et al. 2013) or export (FAOSTAT 2016) value per metric ton (at consumer level) in the US of building materials for concrete shells. Values corrected for inflation, and both measures normalized to 1970 (=100).

By the 1970s, the era of concrete shells was considered to be over by many, including Kersavage (1975). He explored fabric formworks for hypars as a possible solution, but his system only later found application in developing countries, many in the last decade. The 1970s energy crisis was the death knell for concrete shells, as the cost of concrete, steel and particularly timber reached new highs (Figures 3.54). In 1969, a distraught Candela said: "I am out of place in today's world and I do not know what to do nor if I am worth anything" (Cassinello et al. 2010).

Around that same time, Dante Bini, Horrall Harrington and Haim Heifetz all commercially constructed airformed domes and secured patents. Meanwhile, the earliest patents expired, naturally leading to more competition. Pneumatically formed domes continued their success, with over 70'000 claimed to have been built since, due to the increasing availability and affordability of synthetic fibres for coated, woven fabrics. In general, the relative price of textiles has decreased, seemingly undisturbed by larger global and economic events (Figure 3.54). The other main factor of cost, labour, accounts for only 10 % of cost in pneumatic formworks (South 1990). Furthermore, relative labour costs were also constant, as increased income equality caused wages to stagnate from 1970 onward (Figure 3.55).

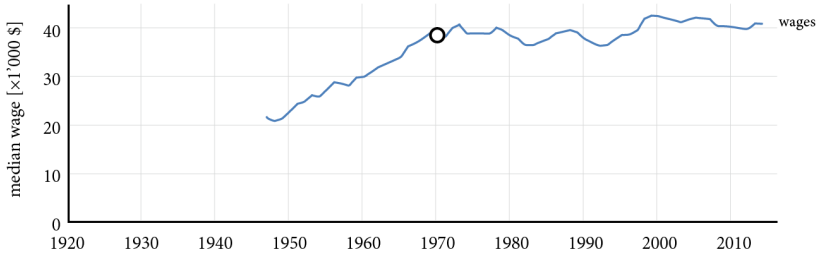

Figure 3.55: Historical median wage and salary income for males in the US in 2014 dollars (Bureau 2016).

The 1980s seems to have been a promising economical period for conventional shell construction to recover, but it never did. Chistiansen (1988) showed hyperbolic paraboloid construction to be cheaper than wood framing, but depending on the use of moveable, reusable forms, and after taking long-term mortgage and insurance costs into account. Among other reasons, Isler (1995) attributed the rise of prefabrication and mass production for the continued decline of shells. The 1990s saw the cost of timber increase again due to federal reductions in forest harvests, making traditional formworks more expensive.

The current revival of flexible, particularly fabric, formworks could be attributed to the Internet, and growing awareness between those active in this area, and exposing those who might be interested. The work carried out at CAST, founded in 2002, generated great interest among architectural firms and academic institutions. This also coincided with the general trend of complex, doubly curved geometry in contemporary architecture and construction, and associated struggles to devise affordable and practical fabrication methods. These trends might have been fueled by the global real estate bubble (Figure 3.54).

This began a second wave of experiments (2002–present) in flexible formworks for shells, carried out at CAST as well as other academic institutions and their collaborators: Eindhoven University of Technology, Netherlands; University of Edinburgh, Scotland, UK; Vrije Universiteit Brussel, Belgium; Anhalt University of Applied Sciences, Germany; and, ETH Zurich, Switzerland. The International Society of Fabric Forming (ISOFF) was founded, and dedicated international conferences (ICFF) have been held, the first in 2008 at CAST in Winnipeg, Canada, followed by others in Bath, UK and in Amsterdam, Netherlands.

3.10 Conclusions

Based on this chapter and its references, the following observations are made:

- thoughout the twentieth century, various competing concepts for fabric-formed floors and pneumatically formed domes have been patented;
- multiple flexible formwork systems for shell structures have enjoyed commercial success in the past, specifically for roof and floor units, barrel vaults and domes, with the latter maintaining its success to the present;
- motivations for developing these systems initially were a high demand for low-cost housing; later, post-war shortages of steel, cement and timber, followed by the further rising cost of timber and labour;
- a first wave of academic experiments (1960-1975) tackling the increased cost of formwork was unable to avert the general decline of concrete shells;
- during this period, emphasis was placed on the use of new materials, such as polymer foams;

- a second wave of academic experiments (2002-present) is still motivated by the cost of formwork, but also contemporary trends in architecture (related to developments in computation), and sustainability (due to global warming); and,
- further emphasis is placed on new reinforcement strategies and reusable formworks.

In terms of advantages of flexible formworks for shells, these references claim that:

- they are affordable as
  - fabrics are inexpensive and widely available;
  - these systems require little or no falsework; and,
  - little or no skilled labour is needed (if properly supervised);
- they allow unobstructed access to the formwork from underneath, offering opportunities to spray concrete and insulation under controlled conditions, and otherwise continue construction and operation;
- they allow the construction of non-standard shell shapes that can provide renewed architectural interest, and are potentially more efficient;
- they are lightweight systems, saving on transportation, handling, and storage; and,
- they do not require release agents or chemicals for demoulding, and result in improved surface quality of the concrete, depending on the permeability of the chosen fabric.

There is evidence that flexible formworks offer a competitive means to construct thin concrete shells in today's construction industry:

- several sources have quoted 25-40 % cost savings for finished shells when using flexible formworks compared to timber formworks;
- cost estimates for fabric and cable-net formed shells, corrected for inflation, are comparable to those for airformed domes, which sustain several businesses today;

- those estimates are below quoted costs for conventional timber and milled foam formworks (Section 2.5.7), representing savings of up to about 40 %;
- the cost of textiles has been declining for decades, while wages have stagnated since 1970; and,
- the cost of steel, cement and sawnwood at the consumer level are comparable or lower than pre-1970 levels.

Part III

Numerical methods

Mechanics without finite elements is like rock 'n' roll without electricity.

— Juan Carlos Simo, from Carstensen & Wriggers (2009)

CHAPTER FOUR

Discretization

Numerical methods for structural form finding and analysis find approximate solutions to boundary value problems for partial differential equations. An essential part of this is subdividing the problem into a discrete assembly of smaller constituent parts, or finite elements, that locally approximate the original problem.

This chapter explains how topological and geometrical information on finite elements and their assemblies is represented in the context of this thesis[1]. This is then used in the next chapters on form finding and constrained form finding, Chapters 5 and 6. The chosen representation appears often in the field of form finding, particularly for the force density methods and related work. It is highly suitable for systems with only linearly interpolated elements allowing for simple vector-matrix notation. On the other hand, it does not extend well to higher-order elements and, likely as a result of that, it is rare in the general field of structural mechanics.

Section 4.1.1 introduces branch-node matrices that define the connectivity between branches and nodes in a network. Section 4.1.2 shows how these, together with nodal coordinates, can be used to compute coordinate differences, branch lengths and triangular surface areas. Section 4.2 explains how, together with mechanical information such as forces, stresses and strains, so-called force densities are determined for different elements. Derivatives for force densities with respect to coordinates are given, required in Chapter 5 to form stiffness matrices. Section 4.2.5 discusses different coordinate systems for triangle elements appearing in literature. Section 4.2.6 explains that constant forces, force densities, extended force densities, stresses, or stress densities lead to networks or surfaces with different minimum geometric properties. Section 4.3 cites various conflicting opinions on the performance of higher-order elements in form finding, compared to linear elements.

[1]This chapter is partially based on Veenendaal & Block (2012*b*, 2018).

4.1 Networks

A discrete assembly of finite elements such as line and surface elements is called a mesh. It is possible to convert quantities within the plane of triangular surface elements to linear properties along its element edges. In this way, we may view this assembly as a network rather than a mesh. Topological concepts from graph theory can then be used to deal with descriptions of the overall assembly, required to solve our numerical problem.

4.1.1 Topology

A sparse branch-node matrix $\bar{\mathbf{C}}$ is used here to describe the topology of a network of branches and nodes. The transpose of $\bar{\mathbf{C}}$ is defined as the incidence matrix in graph theory (Bondy & Murty 1976).

Fenves & Branin Jr. (1963) and Connor (1976) applied such matrices to the structural analysis of frames, and Schek (1974) first introduced the use of branch-node matrices in form finding, applied to the force density method (Linkwitz & Schek 1971). Other form-finding methods have also been formulated in this manner (Veenendaal & Block 2012*b*, 2018). Argyris (1964) already extended their use to include triangle elements (using the term difference matrix), and Singer (1995) to tetrahedral elements. The use of the incidence matrix was compared favourably by Christensen (1988) to then-standard approaches in the finite element method to assemble a stiffness matrix from its explicitly computed, constituent element stiffness matrices (see also equation (4.55) and subsequent discussion).

For a network with m branches and n nodes, the branch-node matrix $\bar{\mathbf{C}}$ is of size $[m \times n]$, where the entries of the ith row and jth column,

$$\bar{C}_{ij} = \begin{cases} +1 \text{ if node } j \text{ is the head of branch } i, \\ -1 \text{ if node } j \text{ is the tail of branch } i, \text{ and} \\ \ \ 0 \text{ otherwise.} \end{cases} \tag{4.1}$$

Note that the direction of the branch vectors may be chosen arbitrarily. For a line element, consisting of one branch and two nodes, and a triangle element, consisting of three branches or edges, and three nodes (Figure 4.1),

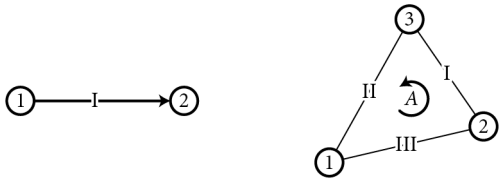

Figure 4.1: Line and triangle elements with conventional side and node numbering

$$\bar{\mathbf{C}} = \begin{bmatrix} -1 & 1 \end{bmatrix} \text{ and } \bar{\mathbf{C}} = \begin{bmatrix} 0 & -1 & 1 \\ 1 & 0 & -1 \\ -1 & 1 & 0 \end{bmatrix}.$$

Strictly speaking, the order and direction of the branch vectors in the triangle element are also arbitrary, but are chosen here to conform with conventions in structural mechanics (as a result, the strain-displacement matrix in equation (4.55) will have the same structure as in literature).

Figure 4.2 shows the branch-node matrix for a larger network with multiple line and triangle elements. The example is based on a similar one appearing in Schek (1974) and Block (2009).

For convenient use in problems involving three-dimensional networks, Singer (1995) used a $[3m \times 3n]$ matrix, such that for a single line and triangle,

$$\bar{\mathbf{C}} = \begin{bmatrix} -\mathbf{I} & \mathbf{I} \end{bmatrix} \text{ and } \mathbf{C} = \begin{bmatrix} \mathbf{0} & -\mathbf{I} & \mathbf{I} \\ \mathbf{I} & \mathbf{0} & -\mathbf{I} \\ -\mathbf{I} & \mathbf{I} & \mathbf{0} \end{bmatrix}, \tag{4.2}$$

where $\mathbf{I}$ is an identity matrix and $\mathbf{0}$ is a null matrix, both of size $[3 \times 3]$. For an entire network, we can generalize equation (4.2) to

$$\mathbf{C} = \bar{\mathbf{C}} \otimes \mathbf{I}. \tag{4.3}$$

where $\otimes$ is the Kronecker product. The matrix $\mathbf{C}$ is also referred to as the augmented branch-node incidence matrix, or connectivity matrix (Connor 1976, p. 124). Linkwitz (1999) also uses such a $[3m \times 3n]$ connectivity matrix but with a different ordering (by dimension first, then triangle element, then triangle side, instead of dimension last).

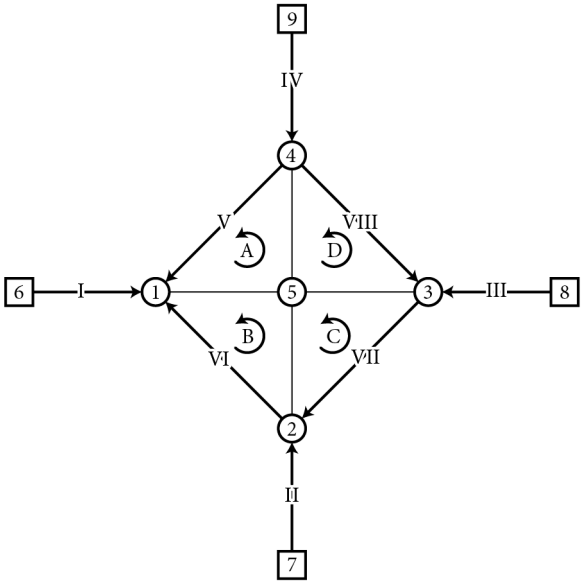

Figure 4.2: Graph and branch-node matrix for network with eight lines (I-VIII), four triangle elements (A-D), five free nodes (1-5) and four fixed nodes (6-9).

$$
\bar{\mathbf{C}} = \begin{array}{c}
\\ \bar{\mathbf{C}}_b \\ \\ \\ \\ \\ \\ \\ \\ \bar{\mathbf{C}}_t \\ \\ \\ \\ \\ \\ \\ \\
\end{array}
\begin{array}{c}
\begin{array}{ccccc|cccc} 1 & 2 & 3 & 4 & 5 & 6 & 7 & 8 & 9 \end{array} \\
\left[\begin{array}{ccccc|cccc}
1 & . & . & . & . & -1 & . & . & . \\
. & 1 & . & . & . & . & -1 & . & . \\
. & . & 1 & . & . & . & . & -1 & . \\
. & . & . & 1 & . & . & . & . & -1 \\
1 & . & . & -1 & . & . & . & . & . \\
1 & -1 & . & . & . & . & . & . & . \\
. & 1 & -1 & . & . & . & . & . & . \\
. & . & 1 & -1 & . & . & . & . & . \\
\hline
0 & . & . & -1 & 1 & . & . & . & . \\
1 & . & . & 0 & -1 & . & . & . & . \\
-1 & . & . & 1 & 0 & . & . & . & . \\
0 & 1 & . & . & -1 & . & . & . & . \\
1 & -1 & . & . & 0 & . & . & . & . \\
-1 & 0 & . & . & 1 & . & . & . & . \\
. & 0 & 1 & . & -1 & . & . & . & . \\
. & 1 & -1 & . & 0 & . & . & . & . \\
. & -1 & 0 & . & 1 & . & . & . & . \\
. & . & 0 & 1 & -1 & . & . & . & . \\
. & . & 1 & -1 & 0 & . & . & . & . \\
. & . & -1 & 0 & 1 & . & . & . & .
\end{array}\right] \\
\bar{\mathbf{C}}_i \qquad\qquad\qquad\qquad \bar{\mathbf{C}}_f
\end{array}
\begin{array}{c}
\\ \mathrm{I} \\ \mathrm{II} \\ \mathrm{III} \\ \mathrm{IV} \\ \mathrm{V} \\ \mathrm{VI} \\ \mathrm{VII} \\ \mathrm{VIII} \\ \\ \mathrm{A} \\ \\ \\ \mathrm{B} \\ \\ \\ \mathrm{C} \\ \\ \\ \mathrm{D} \\ \\
\end{array}
$$

4.1.2 Geometry

For each of the three dimensions in the global Cartesian coordinate system (X, Y, Z), there are n nodal coordinates:

$$\begin{aligned}\bar{\mathbf{x}} &= (X_1, X_2, \ldots, X_n)^{\mathrm{T}},\\ \bar{\mathbf{y}} &= (Y_1, Y_2, \ldots, Y_n)^{\mathrm{T}} \text{ and}\\ \bar{\mathbf{z}} &= (Z_1, Z_2, \ldots, Z_n)^{\mathrm{T}}.\end{aligned}$$

These $3n$ nodal coordinates are assembled in two different ways, depending on their use. Either they are horizontally stacked as an $[n \times 3]$ nodal coordinate matrix,

$$\mathbf{X} = \begin{bmatrix} \bar{\mathbf{x}} & \bar{\mathbf{y}} & \bar{\mathbf{z}} \end{bmatrix}, \tag{4.4}$$

or vertically arranged as a $[3n \times 1]$ nodal coordinate vector by vectorization of $\mathbf{X}^{\mathrm{T}}$, meaning that

$$\mathbf{x} = (X_1, Y_1, Z_1, X_2, \ldots, Z_n)^{\mathrm{T}}. \tag{4.5}$$

The n nodes are declared to be either interior (i.e. free) or fixed nodes, with $n = n_{\mathrm{i}} + n_{\mathrm{f}}$. Note that this may differ in each direction if, for example, a node is fixed in x direction but free to move in y direction. In our case, the nodes are assumed to be either interior or fixed in all directions.

The n and $3n$ columns of the branch-node matrices $\bar{\mathbf{C}}$ and $\mathbf{C}$ and the n and $3n$ rows of the nodal coordinate matrix $\mathbf{X}$ and vector $\mathbf{x}$ are resequenced accordingly. The branch-node matrices

$$\bar{\mathbf{C}} = \begin{bmatrix} \bar{\mathbf{C}}_{\mathrm{i}} \mid \bar{\mathbf{C}}_{\mathrm{f}} \end{bmatrix} \text{ and } \mathbf{C} = \begin{bmatrix} \mathbf{C}_{\mathrm{i}} \mid \mathbf{C}_{\mathrm{f}} \end{bmatrix}, \tag{4.6}$$

where $\bar{\mathbf{C}}_{\mathrm{i}}$ and $\mathbf{C}_{\mathrm{i}}$ are $[m \times n_{\mathrm{i}}]$ and $[3m \times 3n_{\mathrm{i}}]$ branch-node matrices for the interior nodes, and $\bar{\mathbf{C}}_{\mathrm{f}}$ and $\mathbf{C}_{\mathrm{f}}$ are $[m \times n_{\mathrm{f}}]$ and $[3m \times 3n_{\mathrm{f}}]$ branch-node matrices for the fixed nodes (Figure 4.2). The coordinates

$$\mathbf{X} = \begin{bmatrix} \mathbf{X}_{\mathrm{i}} \\ \mathbf{X}_{\mathrm{f}} \end{bmatrix} \text{ and } \mathbf{x} = \begin{bmatrix} \mathbf{x}_{\mathrm{i}} \\ \mathbf{x}_{\mathrm{f}} \end{bmatrix}, \tag{4.7}$$

where $\mathbf{X}_\mathrm{i}$ and $\mathbf{x}_\mathrm{i}$ are an $[n_\mathrm{i} \times 3]$ matrix and $[3n_\mathrm{i} \times 1]$ vector of the interior node coordinates and $\mathbf{X}_\mathrm{f}$ and $\mathbf{x}_\mathrm{f}$ are an $[n_\mathrm{f} \times 3]$ matrix and $[3n_\mathrm{f} \times 1]$ vector of the fixed node coordinates.

To further distinguish between properties of branches and triangle edges, the m and $3m$ rows of the branch-node matrices are split into $m = m_\mathrm{b} + m_\mathrm{t}$ and $3m = 3m_\mathrm{b} + 3m_\mathrm{t}$ rows (Figure 4.2),

$$\bar{\mathbf{C}} = \left[\begin{array}{c|c} \bar{\mathbf{C}}_{\mathrm{i,b}} & \bar{\mathbf{C}}_{\mathrm{f,b}} \\ \hline \bar{\mathbf{C}}_{\mathrm{i,t}} & \bar{\mathbf{C}}_{\mathrm{f,t}} \end{array}\right] \text{ and } \mathbf{C} = \left[\begin{array}{c|c} \mathbf{C}_{\mathrm{i,b}} & \mathbf{C}_{\mathrm{f,b}} \\ \hline \mathbf{C}_{\mathrm{i,t}} & \mathbf{C}_{\mathrm{f,t}} \end{array}\right]. \tag{4.8}$$

The coordinate differences, or edge vectors, are

$$\begin{bmatrix} \bar{\mathbf{u}} & \bar{\mathbf{v}} & \bar{\mathbf{w}} \end{bmatrix} = \bar{\mathbf{C}}\mathbf{X} \text{ and } \mathbf{u} = \mathbf{C}\mathbf{x}, \tag{4.9}$$

and the $[3m \times m]$ coordinate difference matrix

$$\mathbf{U} = \begin{bmatrix} \bar{\mathbf{U}} & \bar{\mathbf{V}} & \bar{\mathbf{W}} \end{bmatrix}^\mathrm{T}, \tag{4.10}$$

with $\bar{\mathbf{U}}$, $\bar{\mathbf{V}}$ and $\bar{\mathbf{W}}$, the diagonal matrices of $\bar{\mathbf{u}}$, $\bar{\mathbf{v}}$ and $\bar{\mathbf{w}}$. This matrix is reordered by branch, so that

$$\mathbf{U} = \begin{bmatrix} U_1 & V_1 & W_1 & 0 & 0 & 0 & \dots & 0 & 0 & 0 \\ 0 & 0 & 0 & U_2 & V_2 & W_2 & & 0 & 0 & 0 \\ \vdots & & & & & & \ddots & & & \vdots \\ 0 & 0 & 0 & 0 & 0 & 0 & \dots & U_m & V_m & W_m \end{bmatrix}^\mathrm{T}.$$

The $[m \times m]$ branch lengths

$$\mathbf{L} = \left(\bar{\mathbf{U}}^2 + \bar{\mathbf{V}}^2 + \bar{\mathbf{W}}^2\right)^{\frac{1}{2}} = \left(\mathbf{U}^\mathrm{T}\mathbf{U}\right)^{\frac{1}{2}} \tag{4.11}$$

and the squared lengths $\mathbf{L}^\mathrm{T}\mathbf{L} = \mathbf{U}^\mathrm{T}\mathbf{U}$ and $\mathbf{L}^\mathrm{T}\mathbf{l} = \mathbf{U}^\mathrm{T}\mathbf{u}$, where vector $\mathbf{l}$ is the diagonal of matrix $\mathbf{L}$.

For a triangle with three edge lengths $\mathbf{l}$, the surface area can be expressed algebraically using Heron's formula (Buchholz 1992)

$$16A^2 = \mathbf{l}^{\mathrm{T}}\mathbf{L}\mathbf{N}\mathbf{L}\mathbf{l}, \text{ so that } A = \frac{1}{4}(\mathbf{l}^{\mathrm{T}}\mathbf{L}\mathbf{N}\mathbf{L}\mathbf{l})^{\frac{1}{2}}, \tag{4.12}$$

where

$$\mathbf{N} = \begin{bmatrix} -1 & 1 & 1 \\ 1 & -1 & 1 \\ 1 & 1 & -1 \end{bmatrix}. \tag{4.13}$$

4.2 Finite elements

The simplest approximations in a finite element mesh are carried out by linear elements, which interpolate any physical properties linearly between the element nodes. When including material behaviour, line and surface elements are referred to as bar or truss and membrane elements respectively. The bars are meant to carry only tensile force, and hence can also be called cable elements.

There is no concensus, but some evidence that higher-order, quadratic interpolation would offer better performance (Section 4.3). In this thesis, and indeed most sources on form finding, linear line and linear triangular surface elements are used. The use of branch-node matrices may also not be straightforward when combined with quadratic interpolation (Section 4.4).

The following sections define force densities and their derivatives with respect to coordinates for each element type. These equations are summarized in Table 4.1. Subscripts b and t are used to distinguish between branches, representing line and bar elements, and triangles, representing triangle and membrane elements. For legibility, these subscripts are omitted for any variables except the force densities.

4.2.1 Line element

The branches have length $\mathbf{l}$ and forces $\mathbf{f}$. Their ratios

$$\mathbf{q}_{\mathrm{b}} = \mathbf{L}^{-1}\mathbf{f}, \tag{4.14}$$

type	force densities $\mathbf{q}$		coordinate derivative $\partial\mathbf{q}/\partial\mathbf{x}_i$			
line[a]	$\mathbf{L}^{-1}\mathbf{f}$	(4.14)		$-\mathbf{L}^{-1}\bar{\mathbf{Q}}_b\mathbf{L}^{-1}\mathbf{U}^T\mathbf{C}_i$		(4.17)
line[b]	$\mathbf{q}$	(4.14)				
line[c]	$4\mathbf{L}^2\mathbf{w}_b$	(4.15)		$8\mathbf{W}_b\mathbf{U}^T\mathbf{C}_i$		(4.18)
spring	$\mathbf{L}^{-1}\mathbf{K}_s(\mathbf{l}-\mathbf{l}_0)$	(4.19)	$\mathbf{L}^{-1}\mathbf{K}_s\mathbf{L}^{-1}\mathbf{U}^T\mathbf{C}_i$	$-\mathbf{L}^{-1}\bar{\mathbf{Q}}_b\mathbf{L}^{-1}\mathbf{U}^T\mathbf{C}_i$		(4.23)
bar	$\mathbf{L}^{-1}\mathbf{EAe} =$					
	$\mathbf{L}^{-1}\mathbf{L}_0^{-1}\mathbf{EA}(\mathbf{l}-\mathbf{l}_0)$	(4.20)	$\mathbf{L}^{-1}\mathbf{L}_0^{-1}\mathbf{EAL}^{-1}\mathbf{U}^T\mathbf{C}_i$	$-\mathbf{L}^{-1}\bar{\mathbf{Q}}_b\mathbf{L}^{-1}\mathbf{U}^T\mathbf{C}_i =$		(4.23)
			$\mathbf{L}^{-1}\mathbf{L}^{-1}\mathbf{EAL}^{-1}\mathbf{U}^T\mathbf{C}_i$			(4.22)
triangle	$At\mathbf{H}^{-T}\boldsymbol{\sigma} =$	(4.33)		$-At\mathbf{H}^{-T}\boldsymbol{\sigma}\boldsymbol{\sigma}_0^T\mathbf{H}^{-1}\mathbf{U}^T\mathbf{C}_i$	$+\frac{t}{4A}\mathbf{NU}^{*T}\mathbf{S}\boldsymbol{\lambda}_T\mathbf{C}_i =$	
	$\frac{t}{8A}\mathbf{NU}^{*T}\mathbf{Su}^*$	(4.35)		$-\frac{1}{A}\mathbf{q}_t\mathbf{q}_{t,m}^T\mathbf{U}^T\mathbf{C}_i$	$+\frac{t}{4A}\mathbf{NU}^{*T}\mathbf{S}\boldsymbol{\lambda}_T\mathbf{C}_i$	(4.43)
triangle[d]	$\frac{1}{8A}\mathbf{NL}^T\mathbf{l}$	(4.38)		$-\frac{1}{A}\mathbf{q}_{t,m}\mathbf{q}_{t,m}^T\mathbf{U}^T\mathbf{C}_i$	$+\frac{1}{4A}\mathbf{NU}^T\mathbf{C}_i$	(4.44)
triangle[e]	$\frac{1}{4}\mathbf{NLl}$	(4.46)			$\frac{1}{2}\mathbf{NU}^T\mathbf{C}_i$	(4.47)
membrane	$At\mathbf{H}^{-T}\mathbf{D}\boldsymbol{\varepsilon} =$					
	$\frac{1}{2}At\mathbf{H}^{-T}\mathbf{H}^{-1}(\mathbf{Ll}-\mathbf{L}_0\mathbf{l}_0)$	(4.53)	$At\mathbf{H}^{-T}\mathbf{DH}^{-1}\mathbf{U}^T\mathbf{C}_i$	$-At\mathbf{H}^{-T}\boldsymbol{\sigma}\boldsymbol{\sigma}_0^T\mathbf{H}^{-1}\mathbf{U}^T\mathbf{C}_i$	$+\frac{t}{4A}\mathbf{NU}^{*T}\boldsymbol{\lambda}_T\mathbf{SC}_i$	(4.54)

Table 4.1: Overview of force densities and their derivative with respect to coordinates for each element type. Line for minimal constant[a], quadratic/squared[b] and quartic[c] sum of lengths. Triangle for minimal constant[d] or quadratic/squared[e] sum of element areas.

are known as force densities (Schek 1974) or tension coefficients (Barnes 1977) (Figure 4.3), where either forces or the force densities themselves are prescribed. The use of the term *density* refers to the linear density rather than the area or volumetric density of a physical property; here, force instead of, more typically, mass. Miki & Kawaguchi (2010) prescribe so-called extended force densities $\mathbf{w}_\mathrm{b}$, such that

$$\mathbf{q}_\mathrm{b} = \mathbf{L}^{-1}\mathbf{f} = 4\mathbf{L}^2\mathbf{w}_\mathrm{b}. \tag{4.15}$$

In their particular approach, these extended force densities are said to generate more practical designs for systems with both tension and compression, such as tensegrity structures and tension structures with support struts.

Block (2009) introduced the use of graphic statics, specifically reciprocal form and force diagrams, as a means to define force densities. This method, thrust network analysis, allows for the interactive design of compression/tension-only shell structures.

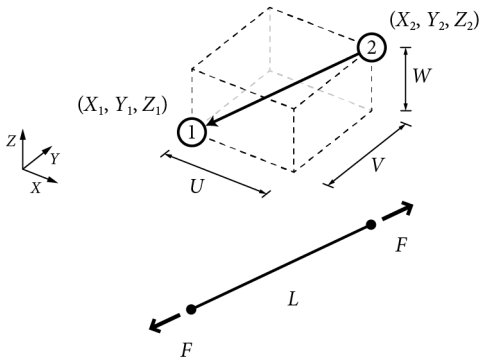

$$L = \sqrt{U^2 + V^2 + W^2}$$

$$Q = \frac{F}{L}$$

Figure 4.3: Single line element in space with force density Q and length L calculated from force F and coordinates (X_1, Y_1, Z_1) and (X_2, Y_2, Z_2).

Tensile forces and force densities have a positive sign. In the linear force density method, the force densities are prescribed and constant. If this is not the case, some methods require their derivative with respect to coordinates. With the partial derivative already given by Schek (1974), and using the reciprocal rule,

$$\frac{\partial \mathbf{l}}{\partial \mathbf{x}_\mathrm{i}} = \mathbf{L}^{-1}\mathbf{U}^\mathrm{T}\mathbf{C}_\mathrm{i} \text{ and } \frac{\partial \mathbf{l}^{-1}}{\partial \mathbf{x}_\mathrm{i}} = -\mathbf{L}^{-2}\frac{\partial \mathbf{l}}{\partial \mathbf{x}_\mathrm{i}} = -\mathbf{L}^{-3}\mathbf{U}^\mathrm{T}\mathbf{C}_\mathrm{i}, \tag{4.16}$$

the derivative of force densities with respect to coordinates becomes

$$\frac{\partial \mathbf{q}_\mathrm{b}}{\partial \mathbf{x}_\mathrm{i}} = \mathbf{F}\frac{\partial \mathbf{l}^{-1}}{\partial \mathbf{x}_\mathrm{i}} = -\mathbf{L}^{-1}\bar{\mathbf{Q}}_\mathrm{b}\mathbf{L}^{-1}\mathbf{U}^\mathrm{T}\mathbf{C}_\mathrm{i}, \tag{4.17}$$

where $\bar{\mathbf{Q}}_\mathrm{b}$ is the diagonal matrix belonging to $\mathbf{q}_\mathrm{b}$.

Reciprocal rule of differentiation
Given a function that is the inverse, or reciprocal, of another differentiable function,

$$f(x) = \frac{1}{g(x)},$$

with $g = g(x)$, the derivative of that function is

$$\frac{d}{dx}\left(\frac{1}{g}\right) = -\frac{1}{g^2}\frac{dg}{dx}.$$

For the extended force densities in equation (4.15),

$$\frac{\partial \mathbf{q}_\mathrm{b}}{\partial \mathbf{x}_\mathrm{i}} = 4\mathbf{W}_\mathrm{b}\frac{\partial \mathbf{L}^2}{\partial \mathbf{x}_\mathrm{i}} = 8\mathbf{W}_\mathrm{b}\mathbf{U}^\mathrm{T}\mathbf{C}_\mathrm{i}. \tag{4.18}$$

4.2.2 Spring and bar elements

In spring systems, the forces $\mathbf{f}$ are governed by Hooke's law (Barnes 1999, Bhooshan et al. 2014),

$$\mathbf{q}_\mathrm{b} = \mathbf{L}^{-1}\mathbf{K}_\mathrm{s}(\mathbf{l} - \mathbf{l}_0) = \mathbf{k}_\mathrm{s} - \mathbf{L}^{-1}\mathbf{K}_\mathrm{s}\mathbf{l}_0, \tag{4.19}$$

where $\mathbf{K}_\mathrm{s}$ is a diagonal matrix of spring constants $\mathbf{k}_\mathrm{s}$, and $\mathbf{l}_0$ are the initial, or rest, lengths of the springs. For zero-length springs proposed by Harding & Shepherd (2011), where $\mathbf{l}_0 = \mathbf{0}$, equation (4.19) reverts to $\mathbf{q}_\mathrm{b} = \mathbf{k}_\mathrm{s}$, meaning their method is identical to the linear force density method in terms of its elements.

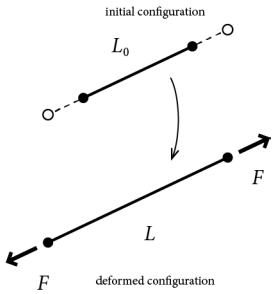

$$Q = \frac{F}{L} = k_s \frac{L - L_0}{L} = \frac{EA}{L_0} \frac{L - L_0}{L}$$

Figure 4.4: Single spring or bar element with the force F calculated from the spring constant k_s or axial stiffness EA and the initial and current lengths L_0 and L.

For linear elastic bars in stiffness matrix methods and dynamic relaxation,

$$\mathbf{q}_b = \mathbf{L}^{-1}\mathbf{E}\mathbf{A}\mathbf{e} = \mathbf{L}^{-1}\mathbf{L}_0^{-1}\mathbf{E}\mathbf{A}(\mathbf{l} - \mathbf{l}_0) = \mathbf{E}\mathbf{A}(\mathbf{l}_0^{-1} - \mathbf{l}^{-1}), \tag{4.20}$$

where $\mathbf{E}$ are the Young's moduli, $\mathbf{A}$ the cross-sectional areas of the bars, $\mathbf{L}_0$ a diagonal matrix of the initial lengths $\mathbf{l}_0$, and where we have assumed small strains, or Cauchy strains (Argyris et al. 1974, Tabarrok & Qin 1992),

$$\mathbf{e} = \mathbf{L}_0^{-1}(\mathbf{l} - \mathbf{l}_0) \tag{4.21}$$

Comparing equations (4.19) and (4.20), it is clear that spring constants $\mathbf{k}_s$ are the ratios of axial stiffnesses $\mathbf{EA}$ and initial lengths $\mathbf{l}_0$. With this relation, $\mathbf{K}_s = \mathbf{L}_0^{-1}\mathbf{E}\mathbf{A}$, the derivatives are (Linkwitz 1999)

$$\begin{aligned}\frac{\partial \mathbf{q}_b}{\partial \mathbf{x}_i} = -\mathbf{K}_s\mathbf{L}_0 \frac{\partial \mathbf{l}^{-1}}{\partial \mathbf{x}_i} &= \mathbf{L}^{-1}\mathbf{L}^{-1}\mathbf{K}_s\mathbf{L}_0\mathbf{L}^{-1}\mathbf{U}^T\mathbf{C}_i \\ &= \mathbf{L}^{-1}\mathbf{L}^{-1}\mathbf{E}\mathbf{A}\mathbf{L}^{-1}\mathbf{U}^T\mathbf{C}_i,\end{aligned} \tag{4.22}$$

which, given that from equation (4.19) it follows that $\mathbf{L}^{-1}\mathbf{K}_s\mathbf{L}_0 = \mathbf{K}_s - \mathbf{Q}_b$, we can rewrite it to (Veenendaal & Block 2012*b*)

$$\begin{aligned}\frac{\partial \mathbf{q}_b}{\partial \mathbf{x}_i} &= \mathbf{L}^{-1}\mathbf{K}_s\mathbf{L}^{-1}\mathbf{U}^T\mathbf{C}_i - \mathbf{L}^{-1}\mathbf{Q}_b\mathbf{L}^{-1}\mathbf{U}^T\mathbf{C}_i \\ &= \mathbf{L}^{-1}\mathbf{L}_0^{-1}\mathbf{E}\mathbf{A}\mathbf{L}^{-1}\mathbf{U}^T\mathbf{C}_i - \mathbf{L}^{-1}\mathbf{Q}_b\mathbf{L}^{-1}\mathbf{U}^T\mathbf{C}_i,\end{aligned} \tag{4.23}$$

which we will use later to derive stiffness matrices as they appear in Haug & Powell (1972) and Knudson & Scordelis (1972). We would also have arrived here, by taking the derivative of equation (4.20) using the product rule, requiring equation (4.17) and the derivative of equation (4.21),

$$\begin{aligned}\frac{\partial \mathbf{q}_\mathrm{b}}{\partial \mathbf{x}_\mathrm{i}} &= \mathbf{L}^{-1}\mathbf{E}\mathbf{A}\frac{\partial \mathbf{e}}{\partial \mathbf{x}_\mathrm{i}} + \mathbf{F}\frac{\partial \mathbf{l}^{-1}}{\partial \mathbf{x}_\mathrm{i}} \\ &= \mathbf{L}^{-1}\mathbf{L}_0^{-1}\mathbf{E}\mathbf{A}\mathbf{L}^{-1}\mathbf{U}^\mathrm{T}\mathbf{C}_\mathrm{i} - \mathbf{L}^{-1}\mathbf{Q}_\mathrm{b}\mathbf{L}^{-1}\mathbf{U}^\mathrm{T}\mathbf{C}_\mathrm{i}.\end{aligned} \tag{4.24}$$

Product rule of differentiation
Given a function that is the product of two other differentiable functions,

$$f(x) = g(x) \cdot h(x), \tag{4.25}$$

with $g = g(x)$ and $h = h(x)$ its derivative is

$$\frac{d}{dx}(g \cdot h) = g \cdot \frac{dh}{dx} + h \cdot \frac{dg}{dx}. \tag{4.26}$$

Instead of Cauchy strains in equation (4.21), we can assume large strains, or Green strains (Pauletti & Pimenta 2008), which can be split into their linear parts, corresponding to Cauchy strains, and their nonlinear, or quadratic, parts,

$$\begin{aligned}\mathbf{e} &= \frac{1}{2}\mathbf{L}_0^{-2}(\mathbf{L}\mathbf{l} - \mathbf{L}_0\mathbf{l}_0) \\ &= \mathbf{L}_0^{-1}(\mathbf{l} - \mathbf{l}_0) &&+ \frac{1}{2}\mathbf{L}_0^{-2}(\mathbf{L} + \mathbf{L}_0)(\mathbf{l} - \mathbf{l}_0) \\ &= \mathbf{L}_0^{-2}(\mathbf{L}_0\mathbf{l} - \mathbf{L}_0\mathbf{l}_0) &&+ \frac{1}{2}\mathbf{L}_0^{-2}(\mathbf{L}\mathbf{l} - 2\mathbf{L}_0\mathbf{l} - \mathbf{L}_0\mathbf{l}_0) \\ &= \mathbf{L}_0^{-2}(\mathbf{U}_0\mathbf{u} - \mathbf{U}_0\mathbf{u}_0) &&+ \frac{1}{2}\mathbf{L}_0^{-2}(\mathbf{U}\mathbf{u} - 2\mathbf{U}_0\mathbf{u} - \mathbf{U}_0\mathbf{u}_0).\end{aligned} \tag{4.27}$$

The force densities

$$\mathbf{q}_\mathrm{b} = \mathbf{L}^{-1}\mathbf{E}\mathbf{A}\mathbf{e} = \frac{1}{2}\mathbf{L}^{-1}\mathbf{L}_0^{-2}\mathbf{E}\mathbf{A}(\mathbf{L}\mathbf{l} - \mathbf{L}_0\mathbf{l}_0) \tag{4.28}$$

and their derivatives

$$
\begin{aligned}
\frac{\partial \mathbf{q}_\mathrm{b}}{\partial \mathbf{x}_\mathrm{i}} &= \mathbf{L}^{-1}\mathbf{E}\mathbf{A}\frac{\partial \mathbf{e}}{\partial \mathbf{x}_\mathrm{i}} + \mathbf{F}\frac{\partial \mathbf{l}^{-1}}{\partial \mathbf{x}_\mathrm{i}} \\
&= \mathbf{L}^{-1}\mathbf{L}_0^{-2}\mathbf{E}\mathbf{A}\mathbf{U}_0^\mathrm{T}\mathbf{C}_\mathrm{i} + \mathbf{L}^{-1}\mathbf{L}_0^{-2}\mathbf{E}\mathbf{A}(\mathbf{U}-\mathbf{U}_0)^\mathrm{T}\mathbf{C}_\mathrm{i} - \mathbf{L}^{-1}\mathbf{Q}_\mathrm{b}\mathbf{L}^{-1}\mathbf{U}^\mathrm{T}\mathbf{C}_\mathrm{i} \\
&= \mathbf{L}_0^{-1}\mathbf{L}^{-1}\mathbf{E}\mathbf{A}\mathbf{L}_0^{-1}\mathbf{U}^\mathrm{T}\mathbf{C}_\mathrm{i} - \mathbf{L}^{-1}\mathbf{Q}_\mathrm{b}\mathbf{L}^{-1}\mathbf{U}^\mathrm{T}\mathbf{C}_\mathrm{i}. \qquad (4.29)
\end{aligned}
$$

4.2.3 Triangle element

Typically, in literature on form finding, a membrane surface is discretized using triangle elements, and occasionally using quadrilaterals. These triangle elements are no different from those used in the finite element method for structural analysis, where they are referred to as linear, three-node triangular elements (TRIA3) or constant strain triangles (CST). In form finding, the descriptions of triangular elements vary in detail and mathematical form. They are not always identified under a common name, but equivalent nonetheless. Section 4.2.5 summarizes different coordinate systems that are used, which apart from notation, largely explain these different descriptions.

The surface is governed by membrane stresses, which defined in the local (x, y) coordinate system are, in tensor or, using Voigt notation, in vector form

$$
\boldsymbol{\sigma} = \begin{bmatrix} \sigma_{xx} & \sigma_{yy} & \sigma_{xy} \end{bmatrix}^\mathrm{T} = \begin{bmatrix} \sigma_x & \sigma_y & \tau_{xy} \end{bmatrix}^\mathrm{T}. \qquad (4.30)
$$

The natural stresses, i.e. the stresses along the triangle sides, can be written as a function of the local Cartesian stresses, and vice versa:

$$
\mathbf{s} = \boldsymbol{\Psi}^{-\mathrm{T}}\boldsymbol{\sigma}, \qquad \boldsymbol{\sigma} = \boldsymbol{\Psi}^\mathrm{T}\mathbf{s}, \qquad (4.31)
$$

where,

$$
\boldsymbol{\Psi} = \begin{bmatrix} c_1^2 & s_1^2 & c_1 s_1 \\ c_2^2 & s_2^2 & c_2 s_2 \\ c_3^2 & s_3^2 & c_3 s_3 \end{bmatrix} = \begin{bmatrix} l_1 & . & . \\ . & l_2 & . \\ . & . & l_3 \end{bmatrix}_0^{-2} \begin{bmatrix} u_1^2 & v_1^2 & u_1 v_1 \\ u_2^2 & v_2^2 & u_2 v_2 \\ u_3^2 & v_3^2 & u_3 v_3 \end{bmatrix} = \mathbf{L}_0^{-2}\mathbf{H}, \qquad (4.32)
$$

with the direction cosines $c_i = \cos\theta_i = u_i/l_i$ and $s_i = \sin\theta_i = v_i/l_i$, and angles as in Figure 4.5.

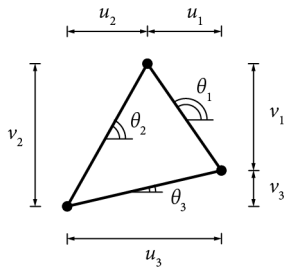

Figure 4.5: Transformation angles θ_i of a triangle element.

The membrane stresses can be converted to force densities acting along the triangle sides (Pauletti & Pimenta 2008, Singer 1995),

$$\mathbf{q}_{\mathrm{t}} = At\mathbf{H}^{-\mathrm{T}}\boldsymbol{\sigma} \tag{4.33}$$

also referred to as natural force densities, where A is the triangle surface area according to equation (4.12), t is the thickness, and

$$\mathbf{H}^{\mathrm{T}} = \frac{1}{4A^2}\begin{bmatrix} -v_2v_3 & -u_2u_3 & v_2u_3 + u_2v_3 \\ -v_3v_1 & -u_3u_1 & v_3u_1 + u_3v_1 \\ -v_1v_2 & -u_1u_2 & v_1u_2 + u_1v_2 \end{bmatrix}, \tag{4.34}$$

defined in the local coordinate system (x, y). Similar expressions are given by Barnes (1999) and Li & Chan (2004).

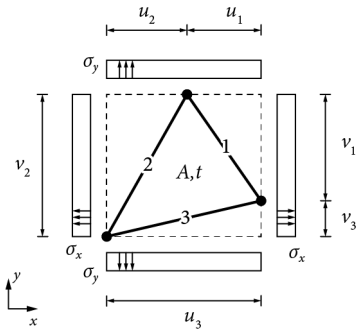

$$\begin{bmatrix} Q_1 \\ Q_2 \\ Q_3 \end{bmatrix} = At \begin{bmatrix} u_1^2 & v_1^2 & u_1 v_1 \\ u_2^2 & v_2^2 & u_2 v_2 \\ u_3^2 & v_3^2 & u_3 v_3 \end{bmatrix}^{-T} \begin{bmatrix} \sigma_x \\ \sigma_y \\ \tau_{xy} \end{bmatrix}$$

$$= \frac{t}{4A} \begin{bmatrix} -v_2 v_3 & -u_2 u_3 & v_2 u_3 + u_2 v_3 \\ -v_3 v_1 & -u_3 u_1 & v_3 u_1 + u_3 v_1 \\ -v_1 v_2 & -u_1 u_2 & v_1 u_2 + u_1 v_2 \end{bmatrix} \begin{bmatrix} \sigma_x \\ \sigma_y \\ \tau_{xy} \end{bmatrix}$$

Figure 4.6: Triangle element with three force densities Q_i calculated from stresses $\boldsymbol{\sigma}$, area A, thickness t and coordinate differences u_i and v_i.

For larger networks, $\mathbf{H}$ is a $[3m \times 3m]$ block diagonal matrix, where each $[3 \times 3]$ block corresponds to equation (4.34), and similarly, $\boldsymbol{\sigma}$ is a $[3m \times 1]$ vertically stacked vector. Strictly speaking, each area and thickness would have to be repeated three times, $A \otimes \mathbf{I}_3$ and $t \otimes \mathbf{I}_3$, and then assembled to a $[3m \times 3m]$ block diagonal matrix as well.

An equivalent formulation to equation (4.33), proposed here, is

$$\mathbf{q}_{\mathrm{t}} = \frac{t}{8A} \mathbf{N} \mathbf{U}^{*\mathrm{T}} \mathbf{S} \mathbf{u}^* \tag{4.35}$$

where $\mathbf{N}$ is according to equation (4.13), $\mathbf{u}^*$ and $\mathbf{U}^*$ are defined in local coordinates and of size $[2m \times 1]$ and $[2m \times m]$,

$$\mathbf{u}^* = \begin{bmatrix} u_1 & v_1 & u_2 & v_2 & u_3 & v_3 \end{bmatrix}^{\mathrm{T}}, \mathbf{U}^* = \begin{bmatrix} u_1 & v_1 & . & . & . & . \\ . & . & u_2 & v_2 & . & . \\ . & . & . & . & u_3 & v_3 \end{bmatrix}, \tag{4.36}$$

and

$$\mathbf{S} = \mathbf{I}_3 \otimes \begin{bmatrix} \sigma_y & -\tau_{xy} \\ -\tau_{xy} & \sigma_x \end{bmatrix}, \tag{4.37}$$

For the specific case of minimal surfaces, the corresponding stresses are uniform and isotropic, $\boldsymbol{\sigma}_0 = [\sigma_0, \sigma_0, 0]^{\mathrm{T}}$ with $\sigma_0 > 0$. For simplicity, $\sigma_0 = 1$ and $t = 1$. Using equation (4.11), equation (4.35) then simplifies to (Singer 1995),

$$\mathbf{q}_{\mathrm{t,m}} = \frac{\sigma_0 t}{8A}\mathbf{N}\mathbf{U}^{*\mathrm{T}}\mathbf{u}^* = \frac{1}{8A}\mathbf{N}\mathbf{L}^{\mathrm{T}}\mathbf{l}. \tag{4.38}$$

We notice that this definition is independent of the chosen coordinate system.

Chain rule of differentiation
Given a function that is the composition of two other differentiable functions

$$f(x) = g(h(x)), \tag{4.39}$$

and writing $g = g(h(x)) = g(u)$, where $u = h(x)$, its derivative

$$\frac{dg}{dx} = \frac{dg}{du}\frac{du}{dx}. \tag{4.40}$$

With the derivative of area with respect to edge lengths, the reciprocal rule, and the chain rule,

$$\frac{\partial A}{\partial \mathbf{l}} = \frac{1}{8A}\mathbf{l}^{\mathrm{T}}\mathbf{L}\mathbf{N}\mathbf{L}, \qquad \frac{\partial A^{-1}}{\partial \mathbf{l}} = -A^{-2}\frac{\partial A}{\partial \mathbf{l}} \text{ and,} \tag{4.41}$$

$$\frac{\partial A^{-1}}{\partial \mathbf{x}_{\mathrm{i}}} = -A^{-2}\frac{\partial A}{\partial \mathbf{l}}\frac{\partial \mathbf{l}}{\partial \mathbf{x}_{\mathrm{i}}} = -\frac{1}{8A^3}\mathbf{l}^{\mathrm{T}}\mathbf{L}\mathbf{N}\mathbf{U}^{\mathrm{T}}\mathbf{C}_{\mathrm{i}}, \tag{4.42}$$

the derivative of the force densities with respect to coordinates,

$$
\begin{aligned}
\frac{\partial \mathbf{q}_\mathrm{t}}{\partial \mathbf{x}_\mathrm{i}} &= \frac{t}{8A}\mathbf{N}\frac{\partial \mathbf{U}^{*\mathrm{T}}\mathbf{S}\mathbf{u}^*}{\partial \mathbf{x}_\mathrm{i}} + \frac{t}{8}\mathbf{N}\mathbf{U}^{*\mathrm{T}}\mathbf{S}\mathbf{u}^*\frac{\partial A^{-1}}{\partial \mathbf{x}_\mathrm{i}} \\
&= \frac{2t}{8A}\mathbf{N}\mathbf{U}^{*\mathrm{T}}\mathbf{S}\frac{\partial \mathbf{u}^*}{\partial \mathbf{u}}\frac{\partial \mathbf{u}}{\partial \mathbf{x}_\mathrm{i}} - \frac{t}{8^2A^3}\mathbf{U}^\mathrm{T}\mathbf{S}\mathbf{u}\mathbf{l}^\mathrm{T}\mathbf{L}\mathbf{N}\mathbf{U}^\mathrm{T}\mathbf{C}_\mathrm{i} \\
&= \frac{t}{4A}\mathbf{N}\mathbf{U}^{*\mathrm{T}}\mathbf{S}\boldsymbol{\lambda}_\mathrm{T}\mathbf{C}_\mathrm{i} - \frac{1}{A}\mathbf{q}_\mathrm{t}\mathbf{q}_{\mathrm{t,m}}^\mathrm{T}\mathbf{U}^\mathrm{T}\mathbf{C}_\mathrm{i} \text{ or,} \\
\frac{\partial \mathbf{q}_\mathrm{t}}{\partial \mathbf{x}_\mathrm{i}} &= \frac{t}{4A}\mathbf{N}\mathbf{U}^{*\mathrm{T}}\mathbf{S}\boldsymbol{\lambda}_\mathrm{T}\mathbf{C}_\mathrm{i} - At\mathbf{H}^{-\mathrm{T}}\boldsymbol{\sigma}\boldsymbol{\sigma}_0^\mathrm{T}\mathbf{H}^{-1}\mathbf{U}^\mathrm{T}\mathbf{C}_\mathrm{i}.
\end{aligned} \tag{4.43}
$$

where $\boldsymbol{\lambda}_\mathrm{T}$ is the coordinate transformation matrix between the local and global coordinate system (Rao 2004, p. 361-3). This derivative will be used later to define a non-symmetric geometric stiffness matrix as it appears in Spillers et al. (1992) and is discussed in Pauletti & Pimenta (2008). For the simpler case of minimal surfaces (Singer 1995), $\mathbf{S}$ becomes an identity matrix, so that

$$
\begin{aligned}
\frac{\partial \mathbf{q}_{\mathrm{t,m}}}{\partial \mathbf{x}_\mathrm{i}} &= \frac{1}{8A}\mathbf{N}\frac{\partial \mathbf{L}\mathbf{l}}{\partial \mathbf{x}_\mathrm{i}} + \frac{1}{8}\mathbf{N}\mathbf{L}\mathbf{l}\frac{\partial A^{-1}}{\partial \mathbf{x}_\mathrm{i}} \\
&= \frac{2}{8A}\mathbf{N}\mathbf{L}\frac{\partial \mathbf{l}}{\partial \mathbf{x}_\mathrm{i}} - \frac{1}{8^2A^3}\mathbf{N}\mathbf{L}\mathbf{l}\mathbf{l}^\mathrm{T}\mathbf{L}\mathbf{N}\mathbf{U}^\mathrm{T}\mathbf{C}_\mathrm{i} \\
&= \frac{1}{4A}\mathbf{N}\mathbf{U}^\mathrm{T}\mathbf{C}_\mathrm{i} - \frac{1}{A}\mathbf{q}_{\mathrm{t,m}}\mathbf{q}_{\mathrm{t,m}}^\mathrm{T}\mathbf{U}^\mathrm{T}\mathbf{C}_\mathrm{i} \text{ or,} \\
\frac{\partial \mathbf{q}_{\mathrm{t,m}}}{\partial \mathbf{x}_\mathrm{i}} &= \frac{1}{4A}\mathbf{N}\mathbf{U}^\mathrm{T}\mathbf{C}_\mathrm{i} - At\mathbf{H}^{-\mathrm{T}}\boldsymbol{\sigma}_0\boldsymbol{\sigma}_0^\mathrm{T}\mathbf{H}^{-1}\mathbf{U}^\mathrm{T}\mathbf{C}_\mathrm{i},
\end{aligned} \tag{4.44}
$$

which will lead to a symmetric geometric stiffness matrix.

Maurin & Motro (1997, 2001) developed the surface stress density as an analogue to the force density for line elements. The surface stress density is defined as

$$
Q_\mathrm{s} = \frac{\sigma_0}{A}. \tag{4.45}
$$

For constant surface stress densities, this generates a geometry that minimizes the sum of squared element areas (Section 4.2.6). This can be expressed as force densities along the triangle sides (Veenendaal & Block 2018),

$$
\mathbf{q}_{\mathrm{t,s}} = \frac{1}{4}\mathbf{N}\mathbf{L}\mathbf{l}, \tag{4.46}
$$

which is identical to equation (4.35) if $Q_s = 2$ and $t = 1$, suggesting equation (4.45) should be redefined to $Q_s = \sigma_0/2A$. The derivatives of the force densities with respect to coordinates,

$$\frac{\partial \mathbf{q}_{t,s}}{\partial \mathbf{x}_i} = \frac{1}{4}\mathbf{N}\frac{\partial \mathbf{Ll}}{\partial \mathbf{x}_i} = \frac{2}{4}\mathbf{NL}\frac{\partial \mathbf{l}}{\partial \mathbf{x}_i} = \frac{1}{2}\mathbf{NU}^{\mathrm{T}}\mathbf{C}_i. \tag{4.47}$$

4.2.4 Membrane element

For an isotropic, linear elastic material, with plane stress, the constitutive equation (material law),

$$\boldsymbol{\sigma} = \mathbf{D}\boldsymbol{\varepsilon}, \tag{4.48}$$

where the strains,

$$\boldsymbol{\varepsilon} = \begin{bmatrix} \varepsilon_x & \varepsilon_y & \gamma_{xy} \end{bmatrix}^{\mathrm{T}}. \tag{4.49}$$

and the constitutive matrix (Barnes 1999, Tabarrok & Qin 1992)

$$\mathbf{D} = \frac{E}{1-\nu^2}\begin{bmatrix} 1 & \nu & 0 \\ \nu & 1 & 0 \\ 0 & 0 & (1-\nu)/2 \end{bmatrix}, \tag{4.50}$$

with Young's modulus E and Poisson's ratio ν.

The natural strains, i.e. the strains along the triangle sides, can be written as a function of the local Cartesian strains, and vice versa:

$$\mathbf{e} = \boldsymbol{\Psi}\boldsymbol{\varepsilon}, \qquad \boldsymbol{\varepsilon} = \boldsymbol{\Psi}^{-1}\mathbf{e}. \tag{4.51}$$

The natural strains can be expressed in the form of Green strain, equation (4.27), which is typically used for large deformations (Pauletti & Pimenta 2008, Singer 1995), such that

$$\boldsymbol{\varepsilon} = \boldsymbol{\Psi}^{-1}\mathbf{e} = \frac{1}{2}\mathbf{H}^{-1}\mathbf{L}_0^2\mathbf{L}_0^{-2}\left(\mathbf{Ll} - \mathbf{L}_0\mathbf{l}_0\right) = \frac{1}{2}\mathbf{H}^{-1}\left(\mathbf{Ll} - \mathbf{L}_0\mathbf{l}_0\right), \tag{4.52}$$

with $\mathbf{H}^{-\mathrm{T}}$ already given in equation (4.34). The force densities

$$\mathbf{q}_{\mathrm{t}} = At\mathbf{H}^{-\mathrm{T}}\boldsymbol{\sigma} = At\mathbf{H}^{-\mathrm{T}}\mathbf{D}\boldsymbol{\varepsilon} = \frac{1}{2}At\mathbf{H}^{-\mathrm{T}}\mathbf{D}\mathbf{H}^{-1}\left(\mathbf{L}\mathbf{l} - \mathbf{L}_0\mathbf{l}_0\right). \tag{4.53}$$

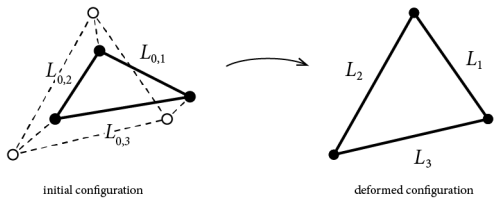

Figure 4.7: Membrane element with force densities according to equation (4.53) due to deformations between the initial and deformed configurations.

The derivatives of the force densities due to changes in $\mathbf{L}\mathbf{l} - \mathbf{L}_0\mathbf{l}_0$,

$$\frac{\partial \mathbf{q}_{\mathrm{t}}}{\partial \mathbf{x}_{\mathrm{i}}} = \frac{1}{2}At\mathbf{H}^{-\mathrm{T}}\mathbf{H}^{-1}\frac{\partial \mathbf{L}\mathbf{l} - \mathbf{L}_0\mathbf{l}_0}{\partial \mathbf{x}_{\mathrm{i}}} = At\mathbf{H}^{-\mathrm{T}}\mathbf{D}\mathbf{H}^{-1}\mathbf{U}^{\mathrm{T}}\mathbf{C}_{\mathrm{i}}. \tag{4.54}$$

The derivatives of A and $\mathbf{H}^{-\mathrm{T}}$ with respect to the coordinates were already derived in equation (4.43), and have been omitted here for brevity.

On a side note, it is possible to rewrite

$$\mathbf{B}\boldsymbol{\lambda}_{\mathrm{T}} = \mathbf{H}^{-1}\mathbf{U}^{\mathrm{T}}\mathbf{C}_{\mathrm{i}}, \tag{4.55}$$

where $\mathbf{B}$ and $\boldsymbol{\lambda}_{\mathrm{T}}$ are known as the (linear) *strain-displacement* matrix and the coordinate transformation matrix respectively, both common in literature on finite elements. Matrix $\mathbf{B}$ is also explicitly given for a single membrane element by Haber & Abel (1982), Tabarrok & Qin (1992) and Nouri-Baranger (2002). Matrix $\boldsymbol{\lambda}_{\mathrm{T}}$, for transformations between local element and global system coordinates is explained by (Rao 2004, p. 361-3), as cited by Tabarrok & Qin (1992).

The $[3 \times 6]$ matrix $\mathbf{B}$ and $[6 \times 9]$ $\boldsymbol{\lambda}_{\mathrm{T}}$ are defined per element, for later assembly into a global stiffness matrix. On the other hand, $\mathbf{H}^{-1}$ and $\mathbf{U}^{\mathrm{T}}$ are $[m \times m]$ and $[m \times 3m]$ block matrices, representing all elements. Together with the $[3m \times 3n_{\mathrm{i}}]$ branch-node matrix $\mathbf{C}_{\mathrm{i}}$ they can immediately describe the entire system.

4.2.5 Triangle coordinate systems

Existing form-finding methods vary in their use of numbering conventions of the triangle sides as well as coordinate systems to express element equations. The differences in coordinate system do not change the method in any fundamental way, only their presentation. In each case, we start from an imposed local stress field and the final system of equations to be solved is always expressed in the global coordinate system. The intermediate quantities differ: natural or side stresses, forces or force densities; intrinsic stresses or forces; and/or local nodal forces. This obscures the fact that many, seemingly independent methods are in fact analogous or even identical. The following coordinate systems have been used in form finding (Figure 4.8):

- global and local Cartesian element coordinates from finite element analysis, using shape functions and strain-displacement matrices (Haber & Abel 1982, Nouri-Baranger 2002, Tabarrok & Qin 1992);
- local, natural element coordinates (Barnes 1977, Barnes & Wakefield 1984, Pauletti & Pimenta 2008, Singer 1995, Tan 1989), with expressions for forces or force densities parallel to the triangle sides;
- intrinsic coordinates (Maurin & Motro 1998), defining forces perpendicular to the triangle sides; and,
- curvilinear coordinates from differential geometry, using co- and contravariant base vectors (Bletzinger & Ramm 1999, Oelkuch & Dieringer 2011, Tabarrok & Qin 1992).

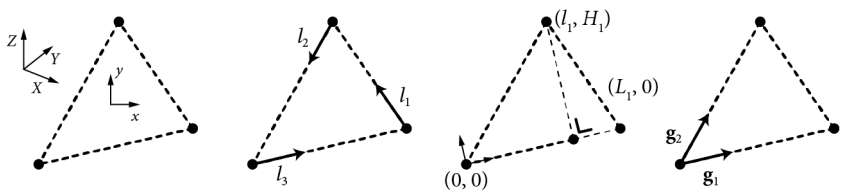

Figure 4.8: Cartesian, natural, intrinsic and curvilinear coordinate systems, as adopted by various references, for triangle or membrane elements.

Brew & Lewis (2003*b*) have expressed the method of dynamic relaxation both in the original form and using intrinsic coordinates. The reader is referred to Meek (1991) for more on all of these coordinate systems, and transformations between them.

4.2.6 Minimal sum of element lengths and areas

It is possible to view uniform forces and surface stresses as properties of minimal length and minimal surface networks, or rather networks with a minimal p-norm of lengths and areas, where $p = 1$ (Schek 1974, Singer 1995).

Similarly, uniform force and surface stress densities are properties of networks with a minimal p-norm of lengths and areas, where $p = 2$. Schek (1974) states that "each equilibrium state of an unloaded network structure with [constant] force densities q_j is identical with the net, whose sum of squared way lengths weighted by q_j is minimal." Maurin & Motro (1997) presented the surface strain density method (SSDM) as an extension of this to surfaces: "a surface performed with identical surface stress density coefficients minimizes the sum of squared element areas."

Miki & Kawaguchi (2010) extended this logic to use $p = 4$ for line elements with "extended force densities", but maintaining $p = 2$ for surface elements.

Table 4.2 summarizes these types of quantities and the geometric property their use leads to.

Sum	**p-norm**	**Lengths**	**Areas**
constant	1	force (Schek 1974)	uniform stress (Singer 1995)
quadratic	2	force density (Schek 1974)	surface stress density (Maurin & Motro 1997)
cubic	3	–	–
quartic	4	extended force density (Miki & Kawaguchi 2010)	–

Table 4.2: Constant quantity to minimize the varying degrees of sum of lengths or element areas. E.g. constant *force density* leads to minimum *quadratic* sum of *lengths*.

4.3 Higher-order elements

The dominant choice for linear triangular elements is probably due to their simplicity in terms of representation and implementation. For example, the fact that these elements exhibit constant strain means that no integration procedure is required. The bilinear quadrilateral element, even though it is still linear, already requires

integration along the surface. For most higher-order elements, stiffness matrices cannot be conveniently expressed in closed form, and are provided in integral form only. Section 4.4 adds that their combination with branch-node matrices is not obvious.

Tabarrok & Qin (1992) assert that due "to the greater geometric nonlinearity of membrane structures, it is preferable to use a dense mesh of primitive elements rather than a coarse mesh made up of higher order isoparametric elements", an opinion echoed by Barnes (1999). Gosling & Lewis (1996) used quadratic quadrilateral elements (QUAD8), but report no clear advantages.

By contrast, Haber & Abel (1982) offer the opinion that "curved isoparametric elements should perform better". In addition, Oelkuch & Dieringer (2011) have shown the form finding of a catenoid to be faster and more accurate when comparing a coarse mesh of higher-order elements (TRIA6, QUAD8, QUAD9) with the solution of a dense mesh of simple triangles or quadrilaterals (TRIA3, QUAD4), concluding that "the use of elements with quadratic shape functions [..] with relatively coarse meshes can be recommended", and noting no significant improvement beyond quadratic elements.

More recent sources have combined form finding with newer forms of parameterization such as cubic splines (Brew & Lewis 2003*a*, 2007), and isogeometric elements based on NURBS (Alic & Persson 2016, Philipp et al. 2014). They report higher accuracy per iteration, but do not mention computational effort.

4.4 Limitations of branch-node matrices

The use of branch-node matrices is standard in literature on the force density method and related form-finding methods. However, its use in structural analysis is rare with most references already given in Section 4.1.1.

Instead, finite elements are generally expressed with shape functions, which describe how deformations in local Cartesian directions are interpolated within an element, as a function of the deformations at the nodes. Especially if the shape functions are of a higher order, the use of branch-node matrices is no longer obvious. To illustrate this, an attempt is made to derive branch-node matrices for a one-dimensional linear and quadratic element in Table 4.3, starting from shape functions and subsequent procedure as they appear in finite element literature.

linear	**quadratic**
Shape functions $\mathbf{N}$	
$\begin{bmatrix} \frac{1}{2}(1-\xi) & \frac{1}{2}(1+\xi) \end{bmatrix}$	$\begin{bmatrix} \frac{\xi}{2}(\xi-1) & \frac{\xi}{2}(\xi+1) & 1-\xi^2 \end{bmatrix}$
Strain-displacement matrix $\mathbf{B} = \frac{\partial \mathbf{N}}{\partial \xi}\frac{\partial \xi}{\partial x} = \frac{2}{L}\frac{\partial \mathbf{N}}{\partial \xi}$	
$\frac{1}{L}\begin{bmatrix} -1 & 1 \end{bmatrix}$	$\frac{2}{L}\begin{bmatrix} \xi-\frac{1}{2} & \xi+\frac{1}{2} & -2\xi \end{bmatrix}$
Stiffness matrix $\mathbf{K} = \int_{-1}^{1} \mathbf{B}^{\mathrm{T}} EA\mathbf{B}\frac{L}{2}d\xi$	
$\frac{EA}{L}\begin{bmatrix} 1 & -1 \\ -1 & 1 \end{bmatrix}$	$\frac{EA}{3L}\begin{bmatrix} 7 & 1 & -8 \\ 1 & 7 & -8 \\ -8 & -8 & 16 \end{bmatrix}*$
Branch-node matrix $\bar{\mathbf{C}}$ if $\mathbf{K} = \frac{EA}{L}\bar{\mathbf{C}}^{\mathrm{T}}\bar{\mathbf{C}}$	
$\begin{bmatrix} -1 & 1 \end{bmatrix}$	$\sqrt{\frac{2}{3}}\begin{bmatrix} -\frac{3}{2} & -\frac{1}{2} & 2 \\ -1 & 1 & 0 \\ \frac{1}{2} & \frac{3}{2} & -2 \end{bmatrix}$

Table 4.3: Comparison of the 1D linear and quadratic bar element, to derive a branch-node matrix. *The quadratic element requires integration, in our case Simpson's rule of integration, as $\mathbf{B} = \mathbf{B}(\xi)$.

It is noticed that the derivative of linear shape functions with respect to natural coordinates leads us to the branch-node matrix used here. For the quadratic element, the derivates of the shape functions can be integrated using Simpson's rule of integration to produce a closed-form solution as well. However, the results is a weighted branch-node matrix, with edges that have multiple vertices (a hypergraph). In doing so, the elegance of using branch-node matrices is lost.

Simpson's rule of integration
A definite integral can be approximated by evaluation at three points,

$$\int_a^b f(x)dx \approx \frac{b-a}{6}\left[f(a) + 4f(\frac{a+b}{2}) + f(b)\right], \tag{4.56}$$

and the approximation will be exact if $f(x)$ is a polynomial of degree three or less.

4.5 Conclusions

This chapter formulates force densities for line and triangle elements for all form-finding methods. The derivative of these force densities with respect to coordinates have been defined, and will be used to construct geometric stiffness matrices in the next chapter.

Structural analysis as well as several form-finding methods include material properties. Force densities for spring, bar and membrane elements have been defined for these purposes. Corresponding derivatives with respect to coordinates have an additional term due to the presence of strain. These will be used to construct material stiffness matrices in the next chapter.

The following observations are made:

- branch-node matrices are standard in force density and related form-finding methods, but no longer used in literature on structural analysis;
- they provide an elegant means to describe systems of linear elements, but are not obvious to combine with quadratic or elements of an even higher order;
- there is no concensus, but some evidence that quadratic elements perform better in the context of form finding;
- there are many definitions for the linear triangle element, but these have been found to be equivalent; and,
- a line element with a constant force density is identical to a zero-length spring with a spring constant.

Over the course of this thesis, the following contributions have been made:

- a trivial force density formulation for the spring element (Bhooshan, Veenendaal & Block 2014);
- a force density formulation and its coordinate derivative for the triangle element;
- a force density formulation and its coordinate derivative for the triangle element with constant surface stress density (Veenendaal & Block 2018); and,
- a branch-node formulation for the spline element (Van Mele, De Laet, Veenendaal, Mollaert & Block 2013), not included in this thesis.

The ropes [in a hanging model] *respond to the static requirements. To pretend that the architectural shapes directly follow from the ropes is childish, since they are only a means of verifying stability, to be used at an appropriate moment. Before stability, there are other aspects to satisfy* [...] *it's like pretending that a barometer tells you the upcoming weather, or that the thermometer tells you how warm is it (when the sensation of warmth is a made up of temperature, humidity, wind, etc).*

— Antoni Gaudí, from Tomlow (2011)

CHAPTER FIVE

Form finding

The principle of *form follows force* is particularly relevant in structures that transfer their loads purely through axial forces or in-plane stresses. In these cases, where no bending occurs, shape is determined by forces and vice versa. These form-active shapes are not known in advance, and therefore require a *form-finding* process. Examples of structures that require form finding are cable nets, shells, gridshells, tensegrity structures and tensioned or air-supported membrane structures. Numerical form-finding methods have been applied to each of these types of structures (Figure 5.1).

This chapter provides an overview of form-finding methods, and presents a general formulation based on these references[1]. This formulation can be viewed as a generic form-finding method.

Section 5.1 defines the concept of form finding. Section 5.2 provides a description of existing form-finding methods for tension structures, and suggests four categories in which to divide them. Based on these methods, Section 5.3 describes a generic form-finding method that may or may not include material properties and uses Newton's method for its solution. Specific differences are highlighted, and the resulting distinct methods are compared. References to other iterative methods that have been used in form finding are also given. Section 5.4 continues this generic form-finding method by applying integration methods as solvers, which, apart from Newton's method, have been popular in form finding. Section 5.5 discusses viewing iterative and integration methods as solvers, rather than unique categories of form-finding methods. Section 5.6 compares the performance of distinct, existing methods as applied to a selection of benchmark problems, before drawing conclusions in Section 5.7.

[1]This chapter is partially based on Veenendaal & Block (2012*b*, 2018) and Bhooshan, Veenendaal & Block (2014).

5.1 Definition

Possible definitions of *form finding*, or *shape finding*, are:

> "finding an (optimal) shape of a [form-active structure] that is in (or approximates) a state of static equilibrium,' (Lewis 2003); or,

> "a forward process in which parameters are explicitly/directly controlled to find an 'optimal' geometry of a structure which is in static equilibrium with a design loading" (Adriaenssens et al. 2014*b*).

The parameters mentioned will include mechanical ones such as forces, force densities, stresses or stress densities, discussed in the previous chapter.

Definitions such as those above are broadly accepted and used, but have been criticized in the past by Haber & Abel (1982) for not acknowledging the fact that in many cases the stresses cannot be imposed and are, like the shape, also unknown. Instead, they suggest calling the problem of form finding the *initial equilibrium problem*. Sensitive to this issue, recent works by Bletzinger et al. typically offer variations of the following, narrower definition of form finding:

> "finding a shape of equilibrium of forces in a given boundary with respect to a certain stress state."

5.2 Categorization

A large number of form-finding methods exist, with seminal methods originating from the early 1970s, but most having been presented in the last two decades (Table 5.1). Three particular methods are often listed as the main, or most common ones: the stiffness matrix method (SM) or nonlinear finite element method (FEM), the force density method (FDM), and dynamic relaxation (DR) (Lewis 2003, Li & Chan 2004). These correspond to three main families or categories in which all methods can be divided (Bletzinger 2011, Veenendaal & Block 2012*b*). These categories also derive from a strong historical basis (Section 2.3). Lewis (2003) mentions another method, by Buchholdt et al. (1968), described as "non-linear gradient vector methodologies, [...] based on the minimization of the total potential energy of the system." This and other similar methods belong to a fourth category proposed here: minimization methods.

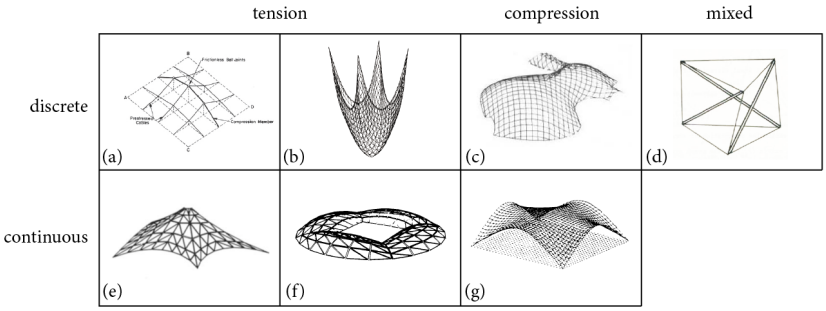

Figure 5.1: Early applications of computational form finding to (a) prestressed cable nets (Siev 1963), (b) loaded cable nets (Argyris et al. 1974), (c) gridshells (Gründig & Schek 1974), (d) tensegrity (Motro 1984), (e) tensioned and (f) air-supported membrane structures (Haber & Abel 1982) and (g) shells (Ramm & Mehlhorn 1991).

Stiffness matrix methods are based on using the standard elastic and geometric stiffness matrices. These methods are among the oldest form-finding methods, and are adapted from structural analysis. They may either assume a relevant initial geometry or use a fictitious material stiffness and/or the updated Lagrangian formulation. If the real material stiffness is used, we may view these methods simply as nonlinear (large-displacement) finite element methods.

Geometric stiffness methods are material independent, with only a geometric stiffness matrix. In several cases, starting with the force density method, the ratio of force to length is a central parameter in the mathematics. Several later methods are presented as generalizations, independent of element type, or extensions to surface elements, often prescribing forces or stresses, rather than force densities.

Minimization methods emphasize the formulation of a functional or energy to be minimized, using a Quasi-Newton or gradient descent solver, which avoids the need to construct or invert a stiffness matrix. Elastic energy may or may not be included. Most of these are presented as being novel methods or extensions, but they may also be regarded as specific solvers applied to the first two categories.

Dynamic equilibrium methods solve the problem of dynamic equilibrium to arrive at a steady-state solution, equivalent to the solution of static equilibrium, by using an integration scheme. Methods that use explicit integration schemes avoid the need to construct and invert stiffness matrices. Like minimization methods, we may regard these as applying a specific iterative solver to the first two categories.

Type	Name	Acronym	Reference
stiffness matrix methods (SM)			
	natural shape finding**		Haug & Powell (1972),Argyris et al. (1974),Meek & Xia (1999)
	nonlinear displacement analysis approach		Wu et al. (1988)
	nonlinear finite element method*		Tan (1989),Tabarrok & Qin (1992),Li & Chan (2004)
geometric stiffness methods (GSM)			
	grid method**		Siev (1961, 1963)
	force density method	FDM	Linkwitz & Schek (1971), Schek (1974), Singer (1995)
	assumed geometric stiffness method,		
	iterative smoothing technique, and	GSM	Haber & Abel (1982)
	stress ratio method	SRM	Nouri-Baranger (2002)
	surface stress density method	SSDM	Maurin & Motro (1997, 1998)
	updated reference strategy	URS	Bletzinger & Ramm (1999)
	natural force density method	NFDM	Pauletti (2006), Pauletti & Pimenta (2008)
	modified force density method		Zeng & Ye (2006),Ye et al. (2012)
	multi-step force density method		
	with force/stress adjustment	MFDF/MFDS	Sánchez et al. (2007)
	improved nonlinear force density method	INFDM	Xiang et al. (2010)
	extended updated reference strategy	X-URS	Dieringer et al. (2013)
	nonlinear force density method		Koohestani (2014)
	modified nonlinear force density method	MNFDM	Xu et al. (2015)
minimization methods			
	energy method*		Buchholdt et al. (1968)
	energy minimization*		Zhang & Tabarrok (1999) using Brakke (1992)
	minimum potential energy method		Yousef et al. (2003*a*,*b*)
	shape minimization*		Arcaro & Klinka (2009)
	extended force density method	EFDM*	Miki & Kawaguchi (2010)
	functional minimization*		Bouzidi & Levan (2013) using Brakke (1992)
dynamic equilibrium methods			
	dynamic relaxation method	DR/DRM	Barnes (1977, 1988, 1999)
	particle-spring systems	PS	Kilian & Ochsendorf (2005),Bhooshan et al. (2014)
	vector form intrinsic finite element method	VFIFE	Zhao (2012)
	finite particle method	FPM	Yang et al. (2014)

Table 5.1: Overview of existing, unconstrained form-finding methods for tension/compression-only structures per category. Minimization methods below dashed lines. *No explicit name given in literature. **Name coined by citing literature.

The existing category of stiffness matrix methods is not well defined, with no consensus on name and principal sources. The term "stiffness matrix methods", used here, was coined by Lewis (1989). Similar classifications of these methods are, in chronological order: nonlinear network computation (Schek 1974); computer erecting (Linkwitz 1976); Newton-Raphson iteration (Barnes 1977); nonlinear displacement analysis (Haber & Abel 1982); and, transient stiffness method (Lewis 2003). Each of these classifications refer to at least one reference by Haug et al., published in the period 1970-1972, e.g. Haug & Powell (1972), and one by Argyris, Angelopoulos et al., published in the period 1970-1974, e.g. Argyris et al. (1974).

Some minimization methods include material deformations and minimize potential energy (Bouzidi & Levan 2013, Buchholdt et al. 1968, Yousef et al. 2003*a*), while other do not and minimize a functional that is not dependent on strain, often defined geometrically (Arcaro & Klinka 2009, Miki & Kawaguchi 2010, Zhang & Tabarrok 1999).

Table 5.2 illustrates these categories of form-finding methods, as they depend on the inclusion of material law and use of a specific type of solver.

solver	**material and geometric**	**geometric**
Newton-Rhapson	stiffness matrix methods (e.g. nonlinear FEM)	geometric stiffness methods (e.g. FDM)
Quasi-Newton Gradient descent	minimization methods	
Integration	dynamic equilibrium methods (e.g. DR)	

Table 5.2: Categories of form-finding methods, depending on inclusion of material law and on the type of solver.

Figure 5.2 shows the form-finding methods, as listed in Table 5.1, plotted against time. Research on newer types of parameterization within these methods has been included as well (Alic & Persson 2016, Philipp et al. 2014). The early developments clearly relate to projects that involved Frei Otto, with several key projects in Saudi Arabia. These projects were part of a local construction boom, that resulted from the 1970s global energy crisis (Section 2.3). Many recent papers originate from China, which in turn reference an even larger body of Chinese publications on existing form-finding methods and software. China has seen large economic growth in recent decades, and underwent a real estate bubble in the late 2000s, as part of a wider global crisis. This growth is illustrated by a marked increase in the number of membrane structures built since 2002 (Lan & Liu 2006).

(1) **Select element type(s)** (Section 4.2),

geometric						**material**	
line			triangle			bar	membrane
force	force density	extended force density	uniform stress	surface stress density	stress	strain	strain
$p = 1$	$p = 2$	$p = 4$	$p = 1$	$p = 2$	$\boldsymbol{\sigma}$	e	$\mathbf{e}$
F	Q (FDM)	W (EFDM)	σ_0	Q_s (SSDM)	$\sigma_x, \sigma_y, \tau_{xy}$	E, A, L_0	$E, t, \nu, \mathbf{L}_0$

(2) **assemble the problem**, and

↓

(3) **solve the nonlinear system**,

$\mathbf{x}_{n+1} = \mathbf{x}_n + \Delta\mathbf{x}$, with

Newton's method (Section 5.3.4)	**integration methods**		**iterative methods** (Section 5.3.6)	
$\Delta\mathbf{x} = \mathbf{K}^{-1}\mathbf{r}$	$\Delta\mathbf{x} = \Delta t(\mathbf{v}(\mathbf{r}) + \Delta\mathbf{v})$	$\Delta\mathbf{x} = \Delta t\mathbf{v}(\mathbf{r})$	$\Delta\mathbf{x} = h\mathbf{d}(\mathbf{r})$	$\Delta\mathbf{x} = \mathbf{B}^{-1}\mathbf{r}$ where $\mathbf{B}^{-1} \approx \mathbf{K}^{-1}$
	implicit (Section 5.4.7)	explicit (Section 5.4.3)	gradient descent	Quasi-Newton
• keep nonlinear terms constant, i.e. modified Newton (SM) • remove nonlinear terms (GSM) • interpolate w/nonlinear terms (URS) • remove in-plane components (X-URS)	• Backward Euler (PS)	• semi-explicit Euler • Leapfrog (DR) • Störmer-Verlet (FPM/VFIFE) • RK4 (PS)	• steepest descent • CG	• L-BFGS-B
(Section 5.3.3)	with damping strategy and mass matrix $\mathbf{M}$.		possibly with a pre-conditioner $\mathbf{M}$.	

and solve the linear system for $\Delta\mathbf{x}$ or $\Delta\mathbf{v}$ using

- direct methods (e.g. Gaussian elimination, Cholesky decomposition),
- stationary methods (e.g. Jacobi, Gauss-Seidel), or
- iterative methods (e.g. CG).

Felippa (1991) and Feng (2006) explain under what conditions DR is equivalent to PCG (Section 5.5.1).

geometric stiffness methods, or **stiffness matrix methods** (Section 5.3)	**dynamic equilibrium methods** (Section 5.4)	**minimization methods** (Section 5.5.2)

Figure 5.3: Selection of element type(s), defining the problem, and possible solvers to find the solution. Some elements or solvers are associated with specific form-finding methods in brackets.

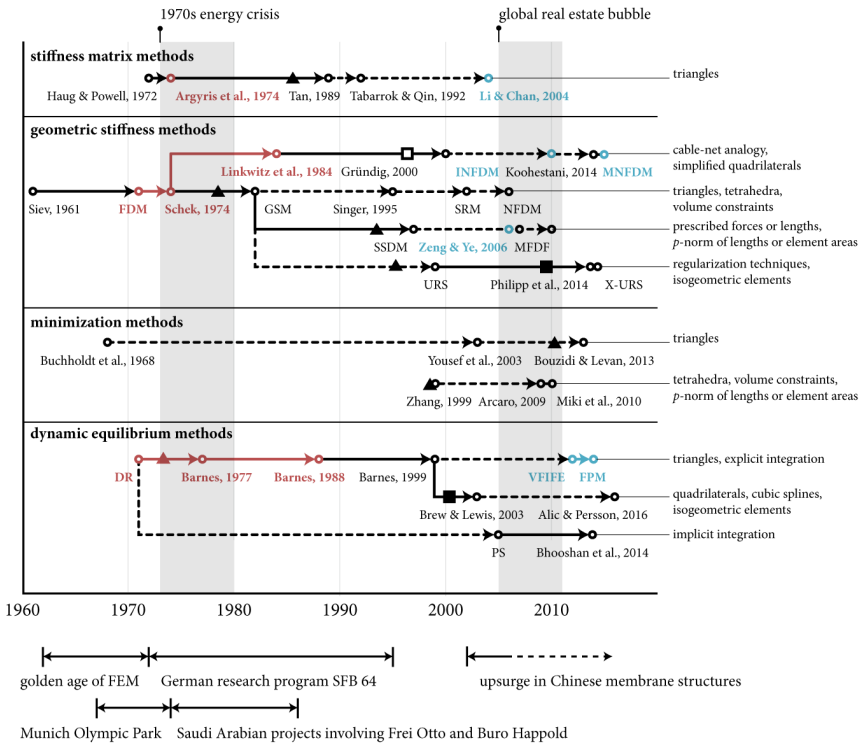

Figure 5.2: Historical development and categorization of unconstrained form-finding methods. Type of contributions on the right. Arrows denote lineage and dotted lines denote independent but related methods. Triangles and squares indicate first use of triangular or quadrilateral elements. Red indicates publications regarding projects involving Frei Otto. Blue indicates publications originating from China.

Table 5.3 shows three consecutive steps in any form-finding process: first, the selection of elements; second, the assembly of them into a single problem; and, third, the decision for a solver with which to find the solution. New form-finding methods have introduced the use of an element or application of another solver, and may have become associated with them. Table 5.3 identifies these instances.

It is important to realize that only the assembly of elements and the input for their driving parameters (forces, force densities, stress, stress densities, and strains) determine the unique problem and thus its solution. The solver only determines how accurate the approximate solution is, and how long it took to get there.

We may assemble a problem consisting of all these element types, which no longer belongs to any specific form-finding method. For this reason, this chapter presents a generic form-finding method instead, based on Table 5.3. The topic of choosing a solver is dealt with by presenting Newton's method in Section 5.3 and integration methods in Section 5.4. Rao (2009) provides more details on the iterative methods used by minimization methods to solve nonlinear systems. Section 5.6 then compares the performance of these solvers for several benchmark problems.

5.3 Static equilibrium methods

The following generic form-finding method describes the general approach taken by stiffness matrix (SM) and geometric stiffness methods (GSM), and highlights any differences between specific methods. These equations have already been discretized, using the finite elements described in Chapter 4.

Section 5.3.1 expresses static equilibrium, which is the end goal of any form-finding method. Deriving this equilibrium equation from the principles of virtual work and minimum total potential energy has been shown in general by Haber & Abel (1982) and Bletzinger & Ramm (1999) in the context of form finding. Section 5.3.2 linearizes the nonlinear system of equilibrium equations using a first-order Taylor expansion. The linearized system of equations contains derivatives of the internal forces, or stiffness matrices, which are given in Section 5.3.3 for both SM and GSM. Some emphasis is placed on nonlinear geometric terms that are traditionally neglected, but used by the more recent updated reference strategy (URS). These additional terms are also provided for the specific cases of minimal surfaces (Singer 1995) and for the surface stress density method (SSDM) (Maurin & Motro 1997). The latter would allow us to combine URS with SSDM. Section 5.3.4 solves the linearized system of equations using Newton's method and the convergence criteria from Section 5.3.7, and provides references to alternative solvers. Without the nonlinear geometric terms, the system of equations can be reduced in size, as shown in Section 5.3.8. After finding our solution, the reaction forces can be calculated according to Section 5.3.9.

5.3.1 Static equilibrium

A network is in a state of equilibrium if the sum of the external forces $\mathbf{p}$ and internal forces at all nodes is zero. The internal forces are expressed in terms of the vectors $\mathbf{g}$ as a function of the coordinates $\mathbf{x}$,

$$\mathbf{C}^{\mathrm{T}}\mathbf{g}(\mathbf{x}) - \mathbf{p} = \mathbf{0}. \tag{5.1}$$

Linkwitz (1999) expresses the internal forces as a function of coordinate differences $\mathbf{u}$, which is equivalent, as from equation (4.9) we know that $\mathbf{u} = \mathbf{Cx}$. The external forces are grouped by interior and fixed nodes as in equation (4.8),

$$\mathbf{P} = \begin{bmatrix} \mathbf{P}_{\mathrm{i}} \\ \mathbf{P}_{\mathrm{f}} \end{bmatrix} \text{ or } \mathbf{p} = \begin{bmatrix} \mathbf{p}_{\mathrm{i}} \\ \mathbf{p}_{\mathrm{f}} \end{bmatrix}, \tag{5.2}$$

where $\mathbf{P}_{\mathrm{i}}$ or $\mathbf{p}_{\mathrm{i}}$ are an $[n_{\mathrm{i}} \times 3]$ matrix and $[3n_{\mathrm{i}} \times 1]$ vector of external loads, and $\mathbf{P}_{\mathrm{f}}$ or $\mathbf{p}_{\mathrm{f}}$ are an $[n_{\mathrm{f}} \times 3]$ matrix and $[3n_{\mathrm{f}} \times 1]$ vector of reaction forces. Reducing the system to the internal forces and external loads acting on the unknown coordinates $\mathbf{x}_{\mathrm{i}}$, we obtain

$$\mathbf{C}_{\mathrm{i}}^{\mathrm{T}}\mathbf{g}(\mathbf{x}) - \mathbf{p}_{\mathrm{i}} = \mathbf{0}. \tag{5.3}$$

The forces $\mathbf{g}(\mathbf{x})$ are vectors where the magnitudes are the m element forces $\mathbf{f}$. These can be related through the direction vectors, or *direction cosines*, $\mathbf{UL}^{-1}$, so that $\mathbf{g}(\mathbf{x}) = \mathbf{UL}^{-1}\mathbf{f}$. By substituting equation (4.14) and then (4.9) into (5.3), these forces can be written as

$$\mathbf{g}(\mathbf{x}) = \mathbf{UL}^{-1}\mathbf{f} = \mathbf{Uq} = \mathbf{Qu} = \mathbf{QCx} \tag{5.4}$$

so that static equilibrium is (Schek 1974),

$$\mathbf{C}_{\mathrm{i}}^{\mathrm{T}}\mathbf{UL}^{-1}\mathbf{f} = \mathbf{C}_{\mathrm{i}}^{\mathrm{T}}\mathbf{Uq} = \mathbf{C}_{\mathrm{i}}^{\mathrm{T}}\mathbf{Qu} = \mathbf{C}_{\mathrm{i}}^{\mathrm{T}}\mathbf{QCx} = \mathbf{p}_{\mathrm{i}}, \tag{5.5}$$

where $\mathbf{Q} = \bar{\mathbf{Q}} \otimes \mathbf{I}$ and $\mathbf{Q}$ is the diagonal matrix belonging to $\mathbf{q}$.

Taylor series

A Taylor series is the representation of a function $f(x)$ as an infinite sum of terms that are calculated from the values of the function's derivatives around the point of interest x_0. The first few terms can serve as an approximation of that function, in order to solve an otherwise unsolvable problem.

$$f(x) = f(x_0) + \frac{f'(x_0)}{1!}(x - x_0) + \frac{f''(x_0)}{2!}(x - x_0)^2 + \dots. \tag{5.6}$$

The higher-order terms become negligible, if $\Delta x = x - x_0$ is sufficiently small. The function is linearized if we only take a first-order approximation.

$$f(x) \approx f(x_0) + \frac{f'(x_0)}{1!}\Delta x. \tag{5.7}$$

5.3.2 Linearization

The system of equilibrium equations (5.1) is nonlinear and can be solved by linearization. The system is approximated by the first-order term of its Taylor expansion.

As a result, the system of equilibrium equations (5.1) is linearized, and we have a new linear system with the changes in positions $\mathbf{x}_i$, $\Delta\mathbf{x}$, as its variables (Linkwitz 1999):

$$\mathbf{C}_i^T \mathbf{g}(\mathbf{x}) - \mathbf{p}_i + \mathbf{C}_i^T \frac{\partial \mathbf{g}(\mathbf{x})}{\partial \mathbf{x}_i} \Delta\mathbf{x} = \mathbf{0} \tag{5.8}$$

$$\mathbf{C}_i^T \frac{\partial \mathbf{g}(\mathbf{x})}{\partial \mathbf{x}_i} \Delta\mathbf{x} = \mathbf{p}_i - \mathbf{C}_i^T \mathbf{g}(\mathbf{x}) \tag{5.9}$$

where $\partial\mathbf{g}(\mathbf{x})/\partial\mathbf{x}_i$ is the Jacobian of the branch forces $\mathbf{g}$ with respect to the nodal coordinates $\mathbf{x}_i$. By convention the resulting LHS matrix and RHS vector in equation (5.9) are called the stiffness matrix and the (residual) force vector,

$$\mathbf{K} = \mathbf{C}_i^T \frac{\partial \mathbf{g}(\mathbf{x}_0)}{\partial \mathbf{x}_i} \text{ and } \mathbf{r} = \mathbf{p}_i - \mathbf{C}_i^T \mathbf{g}(\mathbf{x}_0), \tag{5.10}$$

respectively, arriving at the linear system

$$\mathbf{K}\Delta\mathbf{x} = \mathbf{r}. \tag{5.11}$$

5.3.3 Differentiation

In order to define the stiffness matrix $\mathbf{K}$, we need to differentiate the Jacobian in the linear system (5.9), which expresses how the internal forces change with respect to the coordinate positions. Combining equation (5.4) with the partial derivative

$$\frac{\partial \mathbf{u}}{\partial \mathbf{x}_i} = \mathbf{C}_i, \tag{5.12}$$

and assuming for the moment that the stresses, and thus the force densities remain constant, the *geometric stiffness* or *initial stress* matrix,

$$\mathbf{K}_{g,l} = \mathbf{C}_i^T \frac{\partial \mathbf{g}(\mathbf{x})}{\partial \mathbf{x}_i} = \mathbf{C}_i^T \mathbf{Q} \frac{\partial \mathbf{u}}{\partial \mathbf{x}_i} = \mathbf{C}_i^T \mathbf{Q} \mathbf{C}_i. \tag{5.13}$$

Haber & Abel (1982) also call this the updated Lagrangian geometric stiffness matrix. They refer to the *updated Lagrangian formulation*, in which variables correspond to the *current* configuration, which is then assumed to be the new updated *reference* configuration. The assumption is made that the 2nd Piola-Kirchhoff stresses in the reference configuration are prescribed, remain constant (Bletzinger & Ramm 1999), and are equal to the actual Cauchy stresses (Haber & Abel 1982). Bletzinger & Ramm (1999) add that this is true if the current and reference configuration are identical. This occurs as we converge towards static equilibrium, as the changes $\Delta\mathbf{x}$ and residual forces $\mathbf{r}$ tend to zero. Setting the continuum mechanics aside, this simply means the variables $\mathbf{x}_i$ are always updated.

Without these assumptions, meaning that the force densities are not constants,

$$\mathbf{K}_g = \mathbf{C}_i^T \frac{\partial \mathbf{g}(\mathbf{x})}{\partial \mathbf{x}_i} = \mathbf{C}_i^T \mathbf{Q} \frac{\partial \mathbf{u}}{\partial \mathbf{x}_i} + \mathbf{C}_i^T \mathbf{U} \frac{\partial \mathbf{q}}{\partial \mathbf{x}_i} = \mathbf{C}_i^T \mathbf{Q} \mathbf{C}_i + \mathbf{C}_{i,b}^T \mathbf{U} \frac{\partial \mathbf{q}_b}{\partial \mathbf{x}_i} + \mathbf{C}_{i,t}^T \mathbf{U} \frac{\partial \mathbf{q}_t}{\partial \mathbf{x}_i} \tag{5.14}$$

where we have split the derivatives for the line and the triangle elements. From Table 4.1, the force densities for these elements,

$$\mathbf{q} = \begin{bmatrix} \mathbf{q}_\mathrm{b} \\ \mathbf{q}_\mathrm{t} \end{bmatrix} = \begin{bmatrix} \mathbf{L}^{-1}\mathbf{f} \\ At\mathbf{H}^{-\mathrm{T}}\boldsymbol{\sigma} \end{bmatrix}, \tag{5.15}$$

and substituting the corresponding derivatives into equation (5.14), the stiffness matrix

$$\begin{aligned} \mathbf{K}_\mathrm{g} &= \mathbf{C}_\mathrm{i}^\mathrm{T}\mathbf{Q}\mathbf{C}_\mathrm{i} - \mathbf{C}_\mathrm{i,b}^\mathrm{T}\mathbf{U}\mathbf{L}^{-1}\bar{\mathbf{Q}}_\mathrm{b}\mathbf{L}^{-1}\mathbf{U}^\mathrm{T}\mathbf{C}_\mathrm{i,b} \\ &\qquad - At\mathbf{C}_\mathrm{i,t}^\mathrm{T}\mathbf{U}\mathbf{H}^{-\mathrm{T}}\boldsymbol{\sigma}\boldsymbol{\sigma}_0^\mathrm{T}\mathbf{H}^{-1}\mathbf{U}^\mathrm{T}\mathbf{C}_\mathrm{i,t} + \frac{t}{4A}\mathbf{C}_\mathrm{i,t}^\mathrm{T}\mathbf{U}\mathbf{N}\mathbf{U}^{*\mathrm{T}}\boldsymbol{\lambda}_\mathrm{T}\mathbf{S}\mathbf{C}_\mathrm{i,t} \\ &= \mathbf{K}_\mathrm{g,l} \qquad + \mathbf{K}_\mathrm{g,nl}. \end{aligned} \tag{5.16}$$

This assembled geometric stiffness matrix is valid for the entire network and in global coordinates. Its constituent parts are equivalent to the element stiffness matrices provided for bars in global coordinates by Haug & Powell (1972) and Knudson & Scordelis (1972), and for triangles in local coordinates by Spillers et al. (1992). The latter is non-symmetric.

For minimal surfaces with the corresponding force densities from Table 4.1 (Singer 1995), and for simplicity assuming constant force densities for the line elements, equation (5.16) changes to

$$\mathbf{K}_\mathrm{g} = \mathbf{C}_\mathrm{i}^\mathrm{T}\mathbf{Q}\mathbf{C}_\mathrm{i} - \frac{1}{A}\mathbf{C}_\mathrm{i,t}^\mathrm{T}\mathbf{U}\mathbf{q}_\mathrm{t}\mathbf{q}_\mathrm{t}^\mathrm{T}\mathbf{U}^\mathrm{T}\mathbf{C}_\mathrm{i,t} + \frac{1}{4A}\mathbf{C}_\mathrm{i,t}^\mathrm{T}\mathbf{U}\mathbf{N}\mathbf{U}^\mathrm{T}\mathbf{C}_\mathrm{i,t}, \tag{5.17}$$

which is symmetric again.

The surface stress density method (SSDM) produces a surface with a minimal (weighted) sum of squared element areas (see also Section 4.2.6). With the corresponding force densities from Table 4.1, equation (5.16) simplifies to

$$\mathbf{K}_\mathrm{g} = \mathbf{C}_\mathrm{i}^\mathrm{T}\mathbf{Q}\mathbf{C}_\mathrm{i} + \frac{1}{2}\mathbf{C}_\mathrm{i,t}^\mathrm{T}\mathbf{U}\mathbf{N}\mathbf{U}^\mathrm{T}\mathbf{C}_\mathrm{i,t}. \tag{5.18}$$

While SSDM is an extension of FDM in this sense, the resulting system of equations is no longer linear like FDM, as the force densities are now dependent on the geometry. For the extended force density method, with extended force densities $\mathbf{w}_\mathrm{b}$ for the line elements,

$$\mathbf{K}_{\mathrm{g}} = \mathbf{C}_{\mathrm{i}}^{\mathrm{T}}\mathbf{Q}\mathbf{C}_{\mathrm{i}} + 8\mathbf{C}_{\mathrm{i,b}}^{\mathrm{T}}\mathbf{U}\mathbf{W}_{\mathrm{b}}\mathbf{U}^{\mathrm{T}}\mathbf{C}_{\mathrm{i,b}} + \frac{1}{2}\mathbf{C}_{\mathrm{i,t}}^{\mathrm{T}}\mathbf{U}\mathbf{N}\mathbf{U}^{\mathrm{T}}\mathbf{C}_{\mathrm{i,t}}. \tag{5.19}$$

The nonlinear terms $\mathbf{K}_{\mathrm{g,nl}}$ in equations (5.16) to (5.19) may cause the matrix $\mathbf{K}_{\mathrm{g}}$ to be singular, meaning it can no longer be inverted. This is why early stiffness matrix methods relied on modified Newton's method (keeping the stiffness matrix constant) (Haug & Powell 1972) and applying incremental loads to maintain convergence (Argyris et al. 1974), parallel to its use at the time in the finite element method (Bathe et al. 1975). Later stiffness matrix methods and the geometric stiffness methods removed these terms entirely, using the linear part $\mathbf{K}_{\mathrm{g,l}}$ only (Haber & Abel 1982, Singer 1995, Tabarrok & Qin 1992).

Another option was proposed by Bletzinger & Ramm (1999) in the updated reference strategy (URS), which starts in the same manner, but increasingly interpolates with the original problem, using the parameter λ_{h}. The resulting algorithm is more accurate per iteration. This process, called *homotopy mapping*, calculates the *modified* stiffness matrix as

$$\mathbf{K}_{\mathrm{mod}} = (1 - \lambda_{\mathrm{h}})\mathbf{K}_{\mathrm{g,l}} + \lambda_{\mathrm{h}}\mathbf{K}_{\mathrm{g}} \tag{5.20}$$

$$= \mathbf{K}_{\mathrm{g,l}} + \lambda_{\mathrm{h}}\mathbf{K}_{\mathrm{g,nl}} \tag{5.21}$$

where in equation (5.21) we have assumed that the reference configuration is always updated. In URS, this is not necessarily the case, resulting in separate initial and reference configurations for the two terms in equation (5.20). This means that the residual forces $\mathbf{r}$ also need to be interpolated in the same way. Numerical studies did not show an advantage for the latter approach (Veenendaal & Block 2012*b*).

An alternative to homotopy mapping was proposed by Dieringer et al. (2013) and (Dieringer 2014) in the extended updated reference strategy (X-URS). In this approach the in-plane components of $\mathbf{K}_{\mathrm{g,nl}}$ are removed by using a transformation matrix $\mathbf{T}$. This matrix relates the global coordinates to local nodal coordinates that are oriented perpendicularly to the surface, and zeroes out the in-plane components. Then,

$$\mathbf{K}_{\mathrm{mod}} = \mathbf{K}_{\mathrm{g,l}} + \mathbf{T}^{\mathrm{T}}\mathbf{K}_{\mathrm{g,nl}}\mathbf{T}, \tag{5.22}$$

where $\mathbf{T}$ is explained in Veenendaal & Block (2018).

For bar and membrane elements, which include material deformation, the force densities

$$\mathbf{q} = \begin{bmatrix} \mathbf{q}_\mathrm{b} \\ \mathbf{q}_\mathrm{t} \end{bmatrix} = \begin{bmatrix} \mathbf{L}^{-1}(\mathbf{f} + \mathbf{EAe}) \\ At\mathbf{H}^{-\mathrm{T}}(\boldsymbol{\sigma} + \mathbf{D}\boldsymbol{\varepsilon}) \end{bmatrix}. \tag{5.23}$$

The additional terms include strains, and substituting the corresponding derivatives from Table 4.1, into equation (5.14) the stiffness matrix is

$$\mathbf{K} = \mathbf{K}_{\mathrm{g,l}} + \mathbf{K}_{\mathrm{g,nl}} + \mathbf{K}_\mathrm{e}, \tag{5.24}$$

where the elastic stiffness matrix $\mathbf{K}_\mathrm{e}$ can be split into its linear and nonlinear parts, similar to Tabarrok & Qin (1992) and Nouri-Baranger (2002), so that

$$\begin{aligned} \mathbf{K}_\mathrm{e} &= \mathbf{C}_{\mathrm{i,b}}^\mathrm{T}\mathbf{U}_0\mathbf{L}_0^{-1}\mathbf{L}^{-1}\mathbf{EAL}_0^{-1}\mathbf{U}_0^\mathrm{T}\mathbf{C}_{\mathrm{i,b}} + \mathbf{C}_{\mathrm{i,b}}^\mathrm{T}(\mathbf{U}-\mathbf{U}_0)\mathbf{L}_0^{-1}\mathbf{L}^{-1}\mathbf{EAL}_0^{-1}(\mathbf{U}-\mathbf{U}_0)^\mathrm{T}\mathbf{C}_{\mathrm{i,b}} \\ &\quad + At\mathbf{C}_{\mathrm{i,t}}^\mathrm{T}\mathbf{U}_0\mathbf{H}^{-\mathrm{T}}\mathbf{DH}^{-1}\mathbf{U}_0^\mathrm{T}\mathbf{C}_{\mathrm{i,t}} + At\mathbf{C}_{\mathrm{i,t}}^\mathrm{T}(\mathbf{U}-\mathbf{U}_0)\mathbf{H}^{-\mathrm{T}}\mathbf{DH}^{-1}(\mathbf{U}-\mathbf{U}_0)^\mathrm{T}\mathbf{C}_{\mathrm{i,t}} \\ &= \mathbf{K}_{\mathrm{e,l}} + \mathbf{K}_{\mathrm{e,nl}}. \end{aligned}$$

Some earlier references use only Cauchy strain for the bar elements (Barnes 1999, Linkwitz 1999, Tabarrok & Qin 1992), while Pauletti & Pimenta (2008), for example, consistently formulate Green strain for both bar and membrane elements. In the former case, the elastic stiffness matrix simplifies to,

$$\mathbf{K}_\mathrm{e} = \mathbf{C}_{\mathrm{i,b}}^\mathrm{T}\mathbf{UL}^{-1}\mathbf{L}_0^{-1}\mathbf{EAL}^{-1}\mathbf{U}^\mathrm{T}\mathbf{C}_{\mathrm{i,b}} + At\mathbf{C}_{\mathrm{i,t}}^\mathrm{T}\mathbf{UH}^{-\mathrm{T}}\mathbf{DH}^{-1}\mathbf{U}^\mathrm{T}\mathbf{C}_{\mathrm{i,t}}, \tag{5.25}$$

while in the latter,

$$\mathbf{K}_\mathrm{e} = \mathbf{C}_{\mathrm{i,b}}^\mathrm{T}\mathbf{UL}_0^{-1}\mathbf{L}^{-1}\mathbf{EAL}_0^{-1}\mathbf{U}^\mathrm{T}\mathbf{C}_{\mathrm{i,b}} + At\mathbf{C}_{\mathrm{i,t}}^\mathrm{T}\mathbf{UH}^{-\mathrm{T}}\mathbf{DH}^{-1}\mathbf{U}^\mathrm{T}\mathbf{C}_{\mathrm{i,t}}. \tag{5.26}$$

Table 5.3 summarizes this section, by showing the stiffness terms that the geometric stiffness methods, the updated reference strategy and the stiffness matrix methods use. Of course, these methods can be mixed by combining line and triangle elements (governed by prescribed forces, stresses, etc.) with bar and membrane elements (governed by material deformation). This is done by further subdividing the corresponding force densities, branch-node matrices and other related vectors and matrices.

Method	Acronym	$\mathbf{K}_{g,l}$	$\mathbf{K}_{g,nl}$	$\mathbf{K}_{e,l}$	$\mathbf{K}_{e,nl}$
All geometric stiffness methods,	GSM	✓			
except updated reference strategy	URS/X-URS	✓	✓*		
All stiffness matrix methods	SM	✓	✓**	✓	✓***

Table 5.3: Stiffness terms used by methods. *Partially used. **Used for line elements only. ***Used for triangle elements only.

5.3.4 Solution

The system of equations (5.11), assuming it is nonlinear, can be solved using Newton's method (also known as Newton-Rhapson's method).

Newton's method

The first-order Taylor approximation of function $f(x)$ in Eq. (5.7) can be rewritten to Newton's method, to find its root by iterative approximation, starting from guess x_0 and with $\Delta x = x_1 - x_0$,

$$f(x_0) + \frac{f'(x_0)}{1!}\Delta x = 0,$$
$$x_1 = x_0 - \frac{f(x_0)}{f'(x_0)}$$

and continuing,

$$x_{i+1} = x_i - \frac{f(x_i)}{f'(x_i)}, \tag{5.27}$$

until a sufficient accuracy is achieved.

For one iteration, we obtain

$$\mathbf{x}_{\mathrm{i},i+1} = \mathbf{x}_{\mathrm{i},i} + \mathbf{K}^{-1}\mathbf{r}. \tag{5.28}$$

For the geometric stiffness methods, and, to simplify notation, setting $\mathbf{D}_\mathrm{i} = \mathbf{C}_\mathrm{i}^\mathrm{T}\mathbf{Q}\mathbf{C}_\mathrm{i}$ and $\mathbf{D}_\mathrm{f} = \mathbf{C}_\mathrm{i}^\mathrm{T}\mathbf{Q}\mathbf{C}_\mathrm{f}$, we obtain (Schek 1974),

$$\begin{aligned}\mathbf{x}_{\mathrm{i},i+1} &= \mathbf{x}_{\mathrm{i},i} - (\mathbf{C}_\mathrm{i}^\mathrm{T}\mathbf{Q}\mathbf{C}_\mathrm{i})^{-1}(\mathbf{C}_\mathrm{i}^\mathrm{T}\mathbf{Q}\mathbf{C}\mathbf{x} - \mathbf{p}_\mathrm{i}),\\ \mathbf{x}_{\mathrm{i},i+1} &= \mathbf{x}_{\mathrm{i},i} - \mathbf{D}_\mathrm{i}^{-1}(\mathbf{D}_\mathrm{i}\mathbf{x}_{\mathrm{i},i} + \mathbf{D}_\mathrm{f}\mathbf{x}_\mathrm{f} - \mathbf{p}_\mathrm{i}),\end{aligned} \tag{5.29}$$

which can be further simplified and written as a fixed point iteration (Koohestani 2014)

$$\mathbf{x}_{\mathrm{i},i+1} = \mathbf{D}_\mathrm{i}^{-1}(\mathbf{p}_\mathrm{i} - \mathbf{D}_\mathrm{f}\mathbf{x}_\mathrm{f}). \tag{5.30}$$

This leads to the identical expression for the linear force density method (FDM) (Schek 1974), where the force densities are assumed to be prescribed constants. In that case, the system of equations is in fact linear, requiring no further iteration, and its solution is independent of the initial coordinates $\mathbf{x}_{\mathrm{i},i}$. Thus, it is possible to find a solution in equilibrium knowing only the force densities and coordinates of the fixed nodes. Haber & Abel (1982) indeed remarked that although equation (5.30) "has the form of a standard stiffness equation [as in equation (5.28)], the unknowns are the equilibrium nodal coordinates rather than nodal displacements", so $\mathbf{x}_{\mathrm{i},i+1}$ rather than $\Delta\mathbf{x} = \mathbf{x}_{\mathrm{i},i+1} - \mathbf{x}_{\mathrm{i},i}$.

To solve the linear system of equations (once, if force densities are constant, otherwise at each iteration), particularly dealing with matrix inversion, Cholesky decomposition has been used in this thesis. Haug & Powell (1972) also use a direct solver; Gaussian elimination in their case. Iterative solvers have been used in the past in form finding, such as Jacobi (Haber & Abel 1982), Gauss-Seidel (Gründig & Schek 1974, Haber & Abel 1982, Linkwitz & Schek 1971) and the conjugate gradient (CG) method (Baraff & Witkin 1998, Nouri-Baranger 2002, Singer 1995), but most sources do not identify the specific solver used. Linkwitz & Schek (1971) refer to Gauss-Seidel as "Nekrasov-Seidel". Saad (2003) provides more details on these and other iterative methods including preconditioners.

5.3.5 Definition of force densities

For the linear force density method, the value of force densities is typically set to 1, but it remains difficult to anticipate the outcome for any set of given force densities. Either trial and error or some form of optimization is needed to establish suitable, final values. Block & Ochsendorf (2007), Block (2009) and Rippmann (2016) use graphic statics as a means to define force densities, in order to interactively design compression/tension-only structures.

If forces or lengths are known in advance and can be prescribed, the force densities can be automatically updated. After each iteration, the force densities for line elements are updated based on prescribed forces $\mathbf{f}$ (Maurin & Motro 1997, Sánchez et al. 2007, Zeng & Ye 2006),

$$\mathbf{q}_{i+1} = \mathbf{F}_i^{-1}\mathbf{F}\mathbf{q}_i = \mathbf{L}_i^{-1}\mathbf{f}, \tag{5.31}$$

or prescribed lengths $\mathbf{l}$ (Veenendaal & Block 2012*b*, Zeng & Ye 2006),

$$\mathbf{q}_{i+1} = \mathbf{L}^{-1}\mathbf{L}_i\mathbf{q}_i = \mathbf{L}^{-1}\mathbf{f}_i, \tag{5.32}$$

though care has to be taken that these requirements allow for practical or feasible results. Otherwise, a nonlinear force density method (Linkwitz & Veenendaal 2014, Schek 1974) has to be used where constraints are introduced. The resulting constrained minimization problems require other types of solvers such as least-squares methods (Chapter 6).

5.3.6 Iterative methods

To solve the overall nonlinear system (when force densities are not constant), apart from Newton's method, explained in Section 5.3.4 and applied by most sources, alternative iterative solvers can be used. These are gradient descent and Quasi-Newton methods, which avoid the need to construct or invert the matrix $\mathbf{K}$. Examples in form finding are the use of steepest descent (Buchholdt et al. 1968, Miki & Kawaguchi 2011, Yousef et al. 2003*a*), CG (Brakke 1992, Maurin & Motro 2001), and L-BFGS (Arcaro & Klinka 2009). Rao (2009) provides more details on these iterative methods under the name "indirect search methods".

Dynamic equilibrium methods that use explicit integration, can be counted among these strategies, as they do not require a stiffness matrix. This is not true for methods that use implicit integration (see Section 5.4).

5.3.7 Convergence criteria

To determine convergence, typical criteria are (Lewis 2003):

1. small values of residual forces ($||\mathbf{r}|| < \varepsilon$) (absolute error);
2. small variations in the displacements between successive iterations ($||\mathbf{x}_{i+1} - \mathbf{x}_i|| < \varepsilon$) (relative error); or the
3. maximum number of iterations; or,
4. maximum duration of computational time reached,

where ε is a prescribed tolerance. For practical implementations of stiffness matrix and geometric stiffness methods, references suggest a fixed number of iterations, roughly between four and nine (Pauletti & Pimenta 2008, Tabarrok & Qin 1992).

5.3.8 Reduced system

For geometric stiffness matrix methods except the updated reference strategy, we notice there is no need for a $[3n_\mathrm{i} \times 3n_\mathrm{i}]$ stiffness matrix $\mathbf{K}_{\mathrm{g,l}}$. Instead, we can write the stiffness as an $[n_\mathrm{i} \times n_\mathrm{i}]$ matrix

$$\mathbf{K}_{\mathrm{g,l}} = \bar{\mathbf{C}}_\mathrm{i}^\mathrm{T} \bar{\mathbf{Q}} \bar{\mathbf{C}}_\mathrm{i}, \tag{5.33}$$

suggesting that computational effort for these methods is lower as the system of equations to be solved is three times smaller. The iteration (5.29) changes to

$$\mathbf{X}_{\mathrm{i},i+1} = \mathbf{X}_{\mathrm{i},i} - (\bar{\mathbf{C}}_\mathrm{i}^\mathrm{T} \bar{\mathbf{Q}} \bar{\mathbf{C}})^{-1} (\bar{\mathbf{C}}_\mathrm{i}^\mathrm{T} \bar{\mathbf{Q}} \bar{\mathbf{C}} \mathbf{X} - \mathbf{P}_\mathrm{i}), \tag{5.34}$$

and (5.30) to

$$\mathbf{X}_{\mathrm{i},i+1} = \bar{\mathbf{D}}_\mathrm{i}^{-1} (\mathbf{P}_\mathrm{i} - \bar{\mathbf{D}}_\mathrm{f} \mathbf{X}_\mathrm{f}). \tag{5.35}$$

5.3.9 Reaction forces

Once the system is solved and an equilibrium configuration is found, reaction forces are typically needed for further design of the structure's supports, connections and foundations. The reaction forces

$$\mathbf{p}_f = \mathbf{C}_f^T \mathbf{Q} \mathbf{C}_i \mathbf{x}_i + \mathbf{C}_f^T \mathbf{Q} \mathbf{C}_f \mathbf{x}_f = \mathbf{C}_f^T \mathbf{Q} \mathbf{C} \mathbf{x}, \tag{5.36}$$

or in reduced form,

$$\mathbf{P}_f = \bar{\mathbf{C}}_f^T \bar{\mathbf{Q}} \bar{\mathbf{C}} \mathbf{X}. \tag{5.37}$$

5.4 Dynamic equilibrium methods

This section is a continuation of the generic form-finding method established in 5.3, which used Newton's method to solve the system of equations. For dynamic equilibrium methods, explicit and implicit integration schemes are used to solve them instead.

As mentioned, dynamic relaxation was a method developed specifically for numerical computation in structural analysis (Day 1965). In this *pseudo-dynamic* process, "static equilibrium of a structure under a system of applied forces may be found by following the movement of the structure from its initial, un-deformed and un-loaded, position until all vibrations resulting from its subsequent loading have died out." A related method, particle-spring form finding, was applied to computational hanging models by Kilian & Ochsendorf (2005), based on cloth animation in computer graphics Baraff & Witkin (1998). A full description in the context of form finding was given by Bhooshan et al. (2014). Implementations typically, but not necessarily, use implicit integration. More recently, Zhao (2012) and Yang et al. (2014) proposed the vector form intrinsic finite element method (VFIFE) and the finite particle method (FPM) for form finding respectively.

5.4.1 Dynamic equilibrium

In a dynamic system, equilibrium exists according to Newton's Second Law,

$$\mathbf{C}_{\mathrm{i}}^{\mathrm{T}}\mathbf{g}(\mathbf{x}) + \mathbf{D}\frac{d\mathbf{x}_{\mathrm{i}}}{dt} - \mathbf{p}_{\mathrm{i}} = \mathbf{M}\frac{d^2\mathbf{x}_{\mathrm{i}}}{dt^2}, \tag{5.38}$$

where compared to static equilibrium (5.3) we have a term dependent on damping matrix $\mathbf{D}$ with velocities $d\mathbf{x}_{\mathrm{i}}/dt$ and a term dependent on mass matrix $\mathbf{M}$ with accelerations $d^2\mathbf{x}_{\mathrm{i}}/dt^2$. Assuming the damped motion arrives at a steady-state equilibrium, velocities and accelerations become zero, both terms disappear, and we obtain static equilibrium.

The forces $\mathbf{g}(\mathbf{x})$ are defined as before in equation (5.4), as are the residuals forces $\mathbf{r}$ from equation (5.10). We refer to the additional damping term, as the damping forces

$$\mathbf{d} = \mathbf{D}\frac{d\mathbf{x}_{\mathrm{i}}}{dt}. \tag{5.39}$$

Second-order ordinary differential equation (ODE)

A second-order ODE has the form

$$y''(t) = f(t, y, y') \tag{5.40}$$

which together with initial conditions

$$y(t_0) = y_0 \text{ and } y'(t_0) = y'_0 \tag{5.41}$$

forms an initial value problem (IVP). This second-order ODE can be converted to two first-order ODEs to simplify the problem, by defining a new variable $v = y'$,

$$\begin{aligned} v' &= f(t, y, v) \quad &&\text{and } v(t_0) &&= y'_0, \\ y'(t) &= v &&\text{and } y(t_0) &&= y_0. \end{aligned} \tag{5.42}$$

5.4.2 Simplification

Newton's Second Law can be rewritten to a more familiar form, by expressing the residual and damping forces in equation (5.38) as a function,

$$\mathbf{M}\frac{d^2\mathbf{x}_\mathrm{i}}{dt^2} = \mathbf{f}(\mathbf{x}_\mathrm{i}, \frac{d\mathbf{x}_\mathrm{i}}{dt}), \tag{5.43}$$

which is a second-order differential equation.

We introduce velocities $\mathbf{v}_\mathrm{i} = d\mathbf{x}_\mathrm{i}/dt$, to form two first-order ODEs,

$$\frac{d\mathbf{v}_\mathrm{i}}{dt} = \mathbf{M}^{-1}\mathbf{f}(\mathbf{x}_\mathrm{i}, \mathbf{v}_\mathrm{i}), \tag{5.44}$$

$$\frac{d\mathbf{x}_\mathrm{i}}{dt} = \mathbf{v}_\mathrm{i}, \tag{5.45}$$

or in block form,

$$\frac{d}{dt}\begin{pmatrix} \mathbf{v}_\mathrm{i} \\ \mathbf{x}_\mathrm{i} \end{pmatrix} = \begin{bmatrix} \mathbf{M}^{-1}\mathbf{f}(\mathbf{x}_\mathrm{i}, \mathbf{v}_\mathrm{i}) \\ \mathbf{v}_\mathrm{i} \end{bmatrix}, \tag{5.46}$$

with initial conditions

$$\mathbf{v}_\mathrm{i}(t_0) = \frac{d\mathbf{x}_{\mathrm{i},0}}{dt} \text{ and } \mathbf{x}_\mathrm{i}(t_0) = \mathbf{x}_{\mathrm{i},0}. \tag{5.47}$$

5.4.3 Explicit integration

The system of first-order ODEs (5.46) can be solved with integration, the most basic method being Euler's method. Apart from Euler's method, the following explicit integration methods have been used in form finding and are discussed in this section: semi-explicit Euler (Bhooshan et al. 2014); Leapfrog (Barnes 1999); fourth-order Runge-Kutta (Kilian & Ochsendorf 2005); and, Störmer-Verlet (Yu & Luo 2009, Zhao 2012). Yang et al. (2014) claim to use a method similar to Euler's method, but in fact use the Jacobi method, also given here. The Jacobi method is not an integration method and typically not applied to a system of nonlinear equations.

Euler's method for numerical integration

Numerical methods for ordinary differential equations (ODE) are methods used to find numerical approximations to the solutions of ODEs. Their use is also known as *numerical integration*, although this term applies more specifically to the computation of integrals. The integral in question follows from the first-order ODE,

$$y'(t) = f(t, y(t)) \text{ with } y(t_0) = y_0, \tag{5.48}$$

is rewritten as an integral

$$y(t+h) = y(t) + \int_t^{t+h} y'(t)dt. \tag{5.49}$$

This is approximated with a first-order Taylor expansion,

$$y(t+h) \approx y(t) + \frac{y'(t)}{1!}h, \tag{5.50}$$

which leads us to Euler's method,

$$y_{n+1} = y_n + h \cdot f(t_n, y_n). \tag{5.51}$$

To simplify notation, we define $\mathbf{v}_t := \mathbf{v}(t)$ and $\mathbf{x}_t := \mathbf{x}(t)$. Furthermore, we use the forward difference form $\Delta\mathbf{v} = \mathbf{v}_{\mathrm{i},t+\Delta t} - \mathbf{v}_{\mathrm{i},t}$ and $\Delta\mathbf{x} = \mathbf{x}_{\mathrm{i},t+\Delta t} - \mathbf{x}_{\mathrm{i},t}$. The explicit *forward* Euler method applied to equation (5.46) approximates $\Delta\mathbf{v}$ and $\Delta\mathbf{x}$ as

$$\begin{pmatrix} \Delta\mathbf{v} \\ \Delta\mathbf{x} \end{pmatrix} = \Delta t \begin{bmatrix} \mathbf{M}^{-1}\mathbf{f}(\mathbf{x}_{\mathrm{i},t}, \mathbf{v}_{\mathrm{i},t}) \\ \mathbf{v}_{\mathrm{i},t} \end{bmatrix}, \tag{5.52}$$

or, solving for the current velocity and position,

$$\begin{pmatrix} \mathbf{v}_{\mathrm{i},t+\Delta t} \\ \mathbf{x}_{\mathrm{i},t+\Delta t} \end{pmatrix} = \begin{bmatrix} \mathbf{v}_{\mathrm{i},t} + \Delta t\mathbf{M}^{-1}\mathbf{f}(\mathbf{x}_{\mathrm{i},t}, \mathbf{v}_{\mathrm{i},t}) \\ \mathbf{x}_{\mathrm{i},t} + \Delta t\mathbf{v}_{\mathrm{i},t} \end{bmatrix}. \tag{5.53}$$

More commonly, the slightly different, *semi-explicit* Euler method is used, where

$$\begin{pmatrix} \mathbf{v}_{\mathrm{i},t+\Delta t} \\ \mathbf{x}_{\mathrm{i},t+\Delta t} \end{pmatrix} = \begin{bmatrix} \mathbf{v}_{\mathrm{i},t} + \Delta t \mathbf{M}^{-1}\mathbf{f}(\mathbf{x}_{\mathrm{i},t}, \mathbf{v}_{\mathrm{i},t}) \\ \mathbf{x}_{\mathrm{i},t} + \Delta t \mathbf{v}_{\mathrm{i},t+\Delta t} \end{bmatrix}. \tag{5.54}$$

The step size Δt must be small enough to ensure stability when using this method. Note that equation (5.54) is equivalent to equations for dynamic relaxation (DR). A minor distinction between the two is that DR states the velocity in central difference form $\Delta \mathbf{v} = \mathbf{v}_{\mathrm{i},t+\Delta t/2} - \mathbf{v}_{\mathrm{i},t-\Delta t/2}$, rather than forward difference form, leading to Leapfrog integration,

$$\begin{pmatrix} \mathbf{v}_{\mathrm{i},t+\Delta t/2} \\ \mathbf{x}_{\mathrm{i},t+\Delta t} \end{pmatrix} = \begin{bmatrix} \mathbf{v}_{\mathrm{i},t-\Delta t/2} + \Delta t \mathbf{M}^{-1}\mathbf{f}(\mathbf{x}_{\mathrm{i},t}, \mathbf{v}_{\mathrm{i},t}) \\ \mathbf{x}_{\mathrm{i},t} + \Delta t \mathbf{v}_{\mathrm{i},t+\Delta t/2} \end{bmatrix}. \tag{5.55}$$

Particle-spring systems have used the classic fourth-order Runge-Kutta method (RK4),

$$\begin{pmatrix} \mathbf{v}_{\mathrm{i},t+\Delta t} \\ \mathbf{x}_{\mathrm{i},t+\Delta t} \end{pmatrix} = \begin{bmatrix} \mathbf{v}_{\mathrm{i},t} + \Delta t \sum_{i=1}^{4} b_i \mathbf{k}_i \\ \mathbf{x}_{\mathrm{i},t} + \Delta t \mathbf{v}_{\mathrm{i},t+\Delta t} \end{bmatrix}, \tag{5.56}$$

where

$$\begin{aligned}
b_1\mathbf{k}_1 &= \tfrac{1}{6}\mathbf{M}^{-1}\mathbf{f}(\mathbf{x}_{\mathrm{i},t}, && \mathbf{v}_{\mathrm{i},t}), \\
b_2\mathbf{k}_2 &= \tfrac{1}{3}\mathbf{M}^{-1}\mathbf{f}(\mathbf{x}_{\mathrm{i},t} + \Delta t \tfrac{1}{2}\mathbf{v}_{\mathrm{i},t}, && \mathbf{v}_{\mathrm{i},t} + \Delta t \tfrac{1}{2}\mathbf{k}_1), \\
b_3\mathbf{k}_3 &= \tfrac{1}{3}\mathbf{M}^{-1}\mathbf{f}(\mathbf{x}_{\mathrm{i},t} + \Delta t \tfrac{1}{2}(\mathbf{v}_{\mathrm{i},t} + \Delta t \tfrac{1}{2}\mathbf{k}_1), && \mathbf{v}_{\mathrm{i},t} + \Delta t \tfrac{1}{2}\mathbf{k}_2), \\
b_4\mathbf{k}_4 &= \tfrac{1}{6}\mathbf{M}^{-1}\mathbf{f}(\mathbf{x}_{\mathrm{i},t} + \Delta t(\mathbf{v}_{\mathrm{i},t} + \Delta t \tfrac{1}{2}\mathbf{k}_2), && \mathbf{v}_{\mathrm{i},t} + \Delta t \mathbf{k}_3).
\end{aligned}$$

The finite particle method (FPM) for form finding by Yang et al. (2014) uses an undefined scheme without any damping, suggested to be similar to Euler's method,

$$\mathbf{x}_{\mathrm{i},t+1} - \mathbf{x}_{\mathrm{i},t} = -\omega \mathbf{M}^{-1}\mathbf{r}, \tag{5.57}$$

where $\omega = \frac{\Delta t}{2} S$ is a step size. We continue to rewrite to

$$
\begin{aligned}
\mathbf{x}_{\mathrm{i},t+1} &= \mathbf{x}_{\mathrm{i},t} - \omega\mathbf{M}^{-1}(\mathbf{D}_{\mathrm{i}}\mathbf{x}_{\mathrm{i},t} - \mathbf{p}_{\mathrm{i}}) \\
&= (\mathbf{I} - \omega\mathbf{M}^{-1}\mathbf{D}_{\mathrm{i}})\mathbf{x}_{\mathrm{i},t} + \omega\mathbf{M}^{-1}\mathbf{p}_{\mathrm{i}} \\
&= \mathbf{M}^{-1}((1-\omega)\mathbf{M} - \omega\mathbf{R})\mathbf{x}_{\mathrm{i},t} + \omega\mathbf{M}^{-1}\mathbf{p}_{\mathrm{i}} \\
&= (1-\omega)\mathbf{x}_{\mathrm{i},t} + \omega\mathbf{M}^{-1}(\mathbf{p}_{\mathrm{i}} - \mathbf{R}\mathbf{x}_{\mathrm{i},t}),
\end{aligned} \tag{5.58}
$$

where $\mathbf{R} = \mathbf{D}_{\mathrm{i}} - \mathbf{M}$. The resulting equation is known as a weighted Jacobi method, if $\mathbf{M}$ is the diagonal of $\mathbf{D}_{\mathrm{i}}$. Yang et al. (2014) actually use physical masses for $\mathbf{M}$, rather than fictitious mass derived directly from stiffness $\mathbf{D}_{\mathrm{i}}$. However, their factor ω is in the order of only 10^{-2} to 10^{-3}, while their densities are the same magnitude smaller than their stiffnesses, meaning they cancel each other out.

The Jacobi method is a standard stationary method to iteratively solve systems of linear equations. It is in fact used for that purpose by Haber & Abel (1982). It is not an integration method for dynamic problems, and has no velocities or equivalent vectors, making FPM's place among dynamic equilibrium methods debatable. On the other hand, the original work on FPM (Yu & Luo 2009) as well as the vector form intrinsic finite element method (VFIFE) (Zhao 2012) both use Störmer-Verlet integration, although they do not identify it as such:

$$
\mathbf{x}_{\mathrm{i},t+1} = 2\mathbf{x}_{\mathrm{i},t} - \mathbf{x}_{\mathrm{i},t-1} + \Delta t^2\mathbf{M}^{-1}\mathbf{f}(\mathbf{x}_{\mathrm{i},t}, \mathbf{v}_{\mathrm{i},t}). \tag{5.59}
$$

5.4.4 Mass

As mentioned, FPM, but also VFIFE use physical mass to define a lumped diagonal mass matrix $\mathbf{M}$. However, since our interest lies not with the actual dynamic behaviour of the structure, the most optimal values with respect to convergence can be chosen, even if they are fictitious. Implementations of particle-spring systems (PS) have used unity masses, meaning $\mathbf{M} = \mathbf{I}$. For dynamic relaxation (DR), the masses correspond to the diagonal of the stiffness matrix, which for the form finding of simple bar networks can be simplified to (Veenendaal & Block 2012*b*):

$$
\mathbf{m} = \frac{\Delta t^2}{2}|\bar{\mathbf{C}}_{\mathrm{i}}^{\mathrm{T}}|\mathbf{q}. \tag{5.60}
$$

Han & Lee (2003) define the mass for a triangular membrane element as well.

The mass matrix $\bar{\mathbf{M}}$ is the diagonal matrix belonging to $\mathbf{m}$, and $\mathbf{M} = \bar{\mathbf{M}} \otimes \mathbf{I}$. This definition corresponds to viewing $\mathbf{M}$ as a Jacobi preconditioner. This is the simplest type of preconditioner for solving linear systems of the form $\mathbf{Ax} = \mathbf{b}$, which is defined as the diagonal matrix of $\mathbf{A}$.

5.4.5 Viscous damping

At this point, we have not yet defined the damping and time step. Day (1965) mentions that the "main disadvantage of the method is the derivation of the time interval and damping factor. The easiest way to ascertain these quantities is by trial and error [...]". Barnes (1988) relates the damping matrix to the mass matrix,

$$\mathbf{d} = -\mathbf{D}\mathbf{v}_{\mathrm{i},t} = -\frac{1}{\Delta t} C' \mathbf{M} \mathbf{v}_{\mathrm{i},t} \tag{5.61}$$

As a result,

$$\begin{pmatrix} \mathbf{v}_{\mathrm{i},t+\Delta t} \\ \mathbf{x}_{\mathrm{i},t+\Delta t} \end{pmatrix} = \begin{bmatrix} (1 - C')\mathbf{v}_{\mathrm{i},t} + \Delta t \mathbf{M}^{-1} \mathbf{r}(\mathbf{x}_{\mathrm{i},t}) \\ \mathbf{x}_{\mathrm{i},t} + \Delta t \mathbf{v}_{\mathrm{i},t+\Delta t} \end{bmatrix}, \tag{5.62}$$

or rewriting to conform to conventions in DR, such as damping constants A' and B', and centred finite difference form, $\Delta \mathbf{v} = \mathbf{v}_{\mathrm{i},t+\Delta t/2} - \mathbf{v}_{\mathrm{i},t-\Delta t/2}$,

$$\mathbf{d} = -\frac{1}{\Delta t} C' \mathbf{M} \frac{\mathbf{v}_{\mathrm{i},t+\Delta t/2} + \mathbf{v}_{\mathrm{i},t-\Delta t/2}}{2}, \tag{5.63}$$

so that

$$\begin{pmatrix} \mathbf{v}_{\mathrm{i},t+\Delta t/2} \\ \mathbf{x}_{\mathrm{i},t+\Delta t} \end{pmatrix} = \begin{bmatrix} A' \mathbf{v}_{\mathrm{i},t-\Delta t/2} + B' \Delta t \mathbf{M}^{-1} \mathbf{r}(\mathbf{x}_{\mathrm{i},t}) \\ \mathbf{x}_{\mathrm{i},t} + \Delta t \mathbf{v}_{\mathrm{i},t+\Delta t/2} \end{bmatrix}. \tag{5.64}$$

where $A' = (1 - C'/2)/(1 + C'/2)$ and $B' = (1 + A')/2$.

Yu & Luo (2009) and Zhao (2012) also use viscous damping, the latter referring explicitly to DR,

$$\mathbf{x}_{\mathrm{i},t+1} = 2B' \mathbf{x}_{\mathrm{i},t} - A' \mathbf{x}_{\mathrm{i},t-1} + B' \Delta t^2 \mathbf{M}^{-1} \mathbf{r}(\mathbf{x}_{\mathrm{i},t}). \tag{5.65}$$

5.4.6 Kinetic damping

Instead of viscous damping, Barnes (1999) suggests an approach in which the algorithm resets every time a peak in kinetic energy is detected, called *kinetic damping*. This maximum in kinetic energy corresponds to a minimum in potential energy. Here, viscous damping factors are removed, or $A' = 1$ and $B' = 1$. The kinetic energy

$$E_{\text{kin}} = \frac{1}{2}\mathbf{v}_{\text{i}}^{\text{T}}\mathbf{M}\mathbf{v}_{\text{i}}. \tag{5.66}$$

Once this value decreases, following a kinetic energy peak, velocities are set to zero, $\mathbf{v}_{\text{i},0} = \mathbf{0}$. Thus, for the first iteration and after each energy peak, or re-initialization,

$$\mathbf{v}_{\text{i},\Delta t/2} = \frac{1}{2}\Delta t\mathbf{M}^{-1}\mathbf{r}(\mathbf{x}_{\text{i},0}). \tag{5.67}$$

After detecting an energy peak, coordinates will have been projected to time $t + \Delta t$. But, the true kinetic energy peak will have occurred at some earlier time t^*. To determine the coordinates at time t^*, a quadratic function can be fitted through the current (F) and two previous total kinetic energy values (D and E) in Figure 5.4.

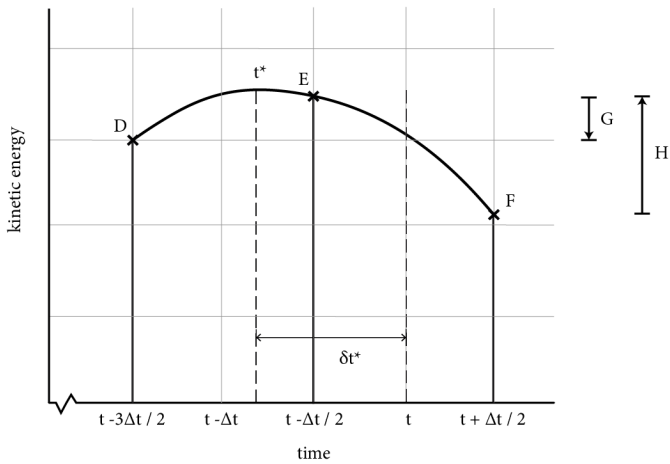

Figure 5.4: Time of kinetic energy peak t^* approximated by a quadratic function through points D, E and F, with time difference δt^* as a function of changes in energy G and H (Adriaenssens et al. 2014*a*).

It is convenient for computation to keep records of the difference between the previous and current kinetic energies G and H. We define the elapsed time t^* since the energy peak in terms of these differences

$$\delta t^* = \Delta t \frac{E}{E - D} = \Delta t \cdot q, \tag{5.68}$$

where $G = D - E$ and $H = E - F$.

Since coordinates have been updated using average velocities (at mid-points of time intervals), they should be reset according to the same scheme. Thus, using equations (5.64) and (5.68),

$$\begin{aligned} \mathbf{x}_{\mathrm{i},t^*} &= \mathbf{x}_{\mathrm{i},t+\Delta t} - \Delta t \mathbf{v}_{\mathrm{i},t+\Delta t} + \delta t^* \mathbf{v}_{\mathrm{i},t-\Delta t} \\ &= \mathbf{x}_{\mathrm{i},t+\Delta t} - \Delta t(1+q)\mathbf{v}_{\mathrm{i},t+\Delta t} + q\Delta t \mathbf{M}^{-1}\mathbf{r}(\mathbf{x}_{\mathrm{i},t}). \end{aligned} \tag{5.69}$$

An alternative is to assume that the peak occurs at $t - \frac{\Delta t}{2}$ and hence $q = \frac{1}{2}$ in equation (5.69).

5.4.7 Implicit integration

The use of implicit rather than explicit integration methods in particle-spring systems was presented by Baraff & Witkin (1998) and later adopted by Kilian & Ochsendorf (2005) for application to structural form finding of discrete networks. Although it has not been previously used for form finding of surfaces, it finds widespread use for cloth animation in computer graphics.

Backward Euler method

Whereas forward Euler method is defined at time t_n,

$$y_{n+1} = y_n + h \cdot f(t_n, y_n), \tag{5.70}$$

backward Euler method is defined at time $t_n + 1$

$$y_{n+1} = y_n + h \cdot f(t_n + 1, y_n + 1), \tag{5.71}$$

The implicit *backward* Euler method approximates $\Delta\mathbf{v}$ and $\Delta\mathbf{x}$ by

$$\begin{pmatrix} \Delta\mathbf{v} \\ \Delta\mathbf{x} \end{pmatrix} = \Delta t \begin{bmatrix} \mathbf{M}^{-1}\mathbf{f}(\mathbf{x}_{\mathrm{i},t} + \Delta\mathbf{x}, \mathbf{v}_{\mathrm{i},t} + \Delta\mathbf{v}) \\ \mathbf{v}_{\mathrm{i},t} + \Delta\mathbf{v} \end{bmatrix}. \qquad \begin{matrix} (5.72\mathrm{a}) \\ (5.72\mathrm{b}) \end{matrix}$$

Compared to the equation (5.52), derived with Euler's method, $\mathbf{f}$ is now evaluated at unknown coordinates and velocities. To resolve this, a Taylor series expansion is applied and the first-order approximation is used:

$$\mathbf{f}(\mathbf{x}_{\mathrm{i},t} + \Delta\mathbf{x}, \mathbf{v}_{\mathrm{i},t} + \Delta\mathbf{v}) = \mathbf{f}_t + \frac{\partial\mathbf{f}}{\partial\mathbf{x}_{\mathrm{i}}}\Delta\mathbf{x} + \frac{\partial\mathbf{f}}{\partial\mathbf{v}}\Delta\mathbf{v}, \tag{5.73}$$

where the derivatives

$$\frac{\partial\mathbf{f}}{\partial\mathbf{x}_i} = \mathbf{K}, \quad \frac{\partial\mathbf{f}}{\partial\mathbf{v}} = -\Delta t^{-1}C'\mathbf{M},. \tag{5.74}$$

Substituting the Taylor approximation and equation (5.72b) into (5.72a), then reordering, yields the linear system

$$\left(\mathbf{I} - \Delta t\mathbf{M}^{-1}\frac{\partial\mathbf{f}}{\partial\mathbf{v}} - \Delta t^2\mathbf{M}^{-1}\frac{\partial\mathbf{f}}{\partial\mathbf{x}_i}\right)\Delta\mathbf{v} = \Delta t\mathbf{M}^{-1}\left(\mathbf{f}_t + \Delta t\frac{\partial\mathbf{f}}{\partial\mathbf{x}_i}\mathbf{v}_{\mathrm{i},t}\right), \tag{5.75}$$

where $\mathbf{I}$ is an $[3n_i \times 3n_i]$ identity matrix. Solving for $\Delta\mathbf{v}$ and multiplying the entire equation by $\mathbf{M}$, we obtain

$$\begin{pmatrix} \mathbf{v}_{\mathrm{i},t+\Delta t} \\ \mathbf{x}_{\mathrm{i},t+\Delta t} \end{pmatrix} = \begin{bmatrix} \mathbf{v}_{\mathrm{i},t} + \Delta t\left(\mathbf{M} + C'\mathbf{I} - \Delta t^2\mathbf{K}\right)^{-1}\left(\mathbf{r}_t + \Delta t\mathbf{K}\mathbf{v}_{\mathrm{i},t}\right), \\ \mathbf{x}_{\mathrm{i},t} + \Delta t\left(\mathbf{v}_{\mathrm{i},t} + \Delta\mathbf{v}\right) \end{bmatrix}. \tag{5.76}$$

5.4.8 Reduced system

As with GSM, using DR would allow us to reduce the size of the above systems of equations by using equation (5.33), mass matrix $\bar{\mathbf{M}}$ and replacing $[3n_i \times 1]$ vectors $\mathbf{x}$, $\mathbf{v}$ and $\mathbf{r}$ with $[n_i \times 3]$ matrices $\mathbf{X}$, $\mathbf{V}$ and $\mathbf{R}$. However, in its above formulation, it would be possible to combine DR with SM or URS, effectively solving their equations using an integration method.

5.5 Discussion

Dynamic equilibrium and minimization methods have been presented here as unique categories of form-finding methods. However, Section 5.3.6 suggests that we might perceive them merely as solvers. They would then fall within the categories of stiffness matrix or geometric stiffness methods, depending on whether material deformations are included or not. Although no actual stiffness (matrix) has to be defined, they all require some kind of vector, whether they are velocities $\mathbf{v}$, gradient descent directions $\mathbf{d}$ or approximated gradients $\mathbf{B}^{-1}\mathbf{r}$. Section 5.5.1 provides references that compare and equate dynamic relaxation methods to the conjugate gradient method. Section 5.5.2 discusses the equivalence of problem formulations as they appear in minimization methods versus those in stiffness matrix or geometric stiffness methods that use Newton's method.

5.5.1 Dynamic relaxation as an iterative solver

Dynamic equilibrium methods using explicit integration schemes can be considered purely as iterative solvers for linear systems of the form $\mathbf{Ax} = \mathbf{b}$.

In particular, DR has been compared to CG in the past on several occassions. Felippa (1996) claims that for linear problems, DR is not competitive with the best preconditioned iterative and semi-iterative methods, such as CG, and argues the same is to be expected for nonlinear problems. On the other hand, Felippa (1991) and Feng (2006) demonstrate under what conditions preconditioned CG (PCG) and DR with viscous damping are equivalent. This is the case if the time-step and damping parameters are automatically adjusted, and if a Jacobi preconditioner is used. Papadrakakis (1981) shows examples of linear problems, where CG is superior to DR, but vice versa, if automatic adaptation of step size and damping parameters is introduced. Typically, in form-finding applications, DR does not feature such adaptive time-stepping or damping, but does include Jacobi preconditioning.

5.5.2 Minimization methods versus Newton's method

References on minimization methods emphasize the minimization of some scalar function, using a gradient descent or Quasi-Newton method. Although Maurin & Motro (2001) describe their approach as a "mixed formulation", others do not explicitly relate their work to form-finding methods that traditionally use Newton's method as a solver. Newton's method is often described as a means to find the root of

a function. Here, we show that minimization and root finding are equivalent means of solving the form-finding problem. Both can employ Newton's method, and do so in the same manner, although the measure of convergence may differ. Switching to a gradient descent or Quasi-Newton method then also produces the same result.

Table 5.4 summarizes the different language that may be used. Either a scalar function $f(x)$ is minimized, meaning its stationary point is sought, such that its gradient $f'(x)$ is zero, or the root of a vector function $g(x)$ is sought, meaning it should be equal to zero as well.

	scalar	**vector**	**matrix**
	function	gradient	Hessian
minimization	minimize $f(x)$	$f'(x) = 0$	$f''(x)$
		function	Jacobian
root finding		find the root of $g(x) = 0$	$g'(x)$
	$\frac{1}{2}\mathbf{x}^{\mathrm{T}}\mathbf{A}\mathbf{x} - \mathbf{x}^{\mathrm{T}}\mathbf{b}$	$\mathbf{A}\mathbf{x} - \mathbf{b} = -\mathbf{r}$	$\mathbf{A}$
	potential energy	residual forces	stiffness

Table 5.4: Alternative mathematical views on the linearized form-finding problem: minimizing and finding the stationary point of a scalar function f, or finding the root of a vector function g.

If the scalar function $f(x)$ to be minimized includes material deformations, it is referred to as *potential energy* (Bouzidi & Levan 2013, Yousef et al. 2003*a*); otherwise, it is defined as a specific geometrical property or a *functional* (Arcaro & Klinka 2009, Maurin & Motro 2001, Miki & Kawaguchi 2010, Singer 1995, Zhang & Tabarrok 1999). This scalar is often expressed as a (nonlinear) quadratic function, in the form shown in Table 5.4. Its gradient $f'(x)$ must be zero, arriving at a system of equations of the form $\mathbf{A}\mathbf{x} = \mathbf{b}$. Applying Newton's method in the optimization means that for each iteration,

$$x_{n+1} = x_n - \frac{f'(x_n)}{f''(x_n}).$$

Most methods describe a vector function $g(x)$ that must be zero to obtain static equilibrium, or in other words, for which we seek the root. Whether this function includes material deformation or not, the vector is referred to as the *residuals*, or the *residual*, *unbalanced* or *out-of-balance* forces. This again leads to a system of equations

of the form $\mathbf{Ax} = \mathbf{b}$. In many cases, it is no longer thought of as minimizing the non-zero potential energy or functional, but rather the norm of the residuals themselves, $\mathbf{r}^{\mathrm{T}}\mathbf{r} = (\mathbf{b} - \mathbf{Ax})^{\mathrm{T}}(\mathbf{b} - \mathbf{Ax})$, which approaches zero as it converges. Applying Newton's method to find the root of a function means that for each iteration,

$$x_{n+1} = x_n - \frac{g(x_n)}{g'(x_n)}.$$

This means that in either case, referring to Table 5.4, it follows that for each iteration,

$$\mathbf{x}_{n+1} = \mathbf{x}_n + \mathbf{A}^{-1}\mathbf{r}. \tag{5.77}$$

Other solving methods, such as gradient descent or Quasi-Newton, or explicit integration methods, avoid forming and inverting the matrix $\mathbf{A}$ through a form of approximation. Again, the first two types can be classified as minimization methods, and the third as dynamic equilibrium methods.

5.6 Comparison

Despite almost half a century of literature on numerical form-finding methods, thorough comparisons remain rare. Consequently, it is generally unclear to what extent these methods differ and in which cases one may be preferable over another. Compounding this problem is the apparent divide between researchers focusing on particular methods, in spite of their setting similar goals. Comparison is not straightforward as a variety of nomenclatures, mathematical structuring and notation is used. The generic form-finding method presented in this chapter, addresses these issues and provides a framework for comparison (Veenendaal & Block 2011, 2012*b*, 2018).

5.6.1 Existing reviews

Reviews of form-finding methods can be found (Barnes 1977, Basso & Del Grosso 2011, Haber & Abel 1982, Lewis 2008, Linkwitz 1976, Meek & Xia 1999, Nouri-Baranger 2004, Tan 1989, Tibert & Pellegrino 2003). They differ in scope, for example focusing on tension structures or tensegrity, and many have become dated. Some do not

Type	Criticism	Reference	Rebuttal
stiffness matrix methods (SM)			
	The inclusion of material properties is unnecessary, computationally costly, and may lead to difficulty in control of (stable) convergence	Barnes (1977), Haber & Abel (1982), Lewis (2008), Nouri-Baranger (2004)	They are relevant if information on the initial geometry is available.
geometric stiffness methods (GSM)			
	Linear force densities produce results that are not constructionally practicable and can serve only as a preliminary result.	Barnes (1977)	This depends on how the values are determined, or whether they are arbitrary.
	Linear force densities are dependent on mesh density and anisotropy. Additional iterations are necessary for uniform or geodesic networks or shape dependent loading.	Barnes (1977), Haber & Abel (1982), Lewis (2008), Tan (1989)	This is inherent to these particular applications and not a disadvantage of the method.
	Linear force densities are not meaningful or intuitive quantities, making it difficult to predict the outcome for a prescribed set of force densities.	Haber & Abel (1982), Nouri-Baranger (2004), Tan (1989)	Most methods focus on strategies to deal with this, prescribing forces rather than force densities, or determining them by some other means.
dynamic equilibrium methods			
	Too many parameters are required to control stability and convergence.	Nouri-Baranger (2004)	This can be reduced to a single damping parameter and often to a trivial value for the time step $\Delta t = 1$.
	The mass and damping parameters are also fictitious, and have no physical representation and may therefore not be meaningful.	Nouri-Baranger (2004)	For dynamic relaxation, the masses are in fact the Jacobi preconditioner of the stiffness matrix. The damping is also determined based on the stiffnesses.

Table 5.5: Common criticisms of various form-finding methods, and author's rebuttal.

offer critical comments and serve purely as non-comparative reviews (Basso & Del Grosso 2011, Linkwitz 1976, Meek & Xia 1999). In other cases, they only serve as an introduction for a method put forward by the author(s), again without comparison (Haber & Abel 1982, Lewis 2008, Nouri-Baranger 2004).

A summary of existing criticisms found in literature is provided in Table 5.5, by category, including a rebuttal.

5.6.2 Existing comparisons

There are very few sources that compare the actual performance and results of different methods. Barnes (1977) compared the storage and operation requirements of dynamic relaxation and stiffness matrix methods per iteration and quotes required numbers of iterations, concluding dynamic relaxation to be favourable in the case of cable networks. This was further demonstrated by Lewis (1989, 2003) who compared several configurations of loaded cable nets (Figure 5.5). The conclusion was that the stiffness matrix method did not converge for one of the examples and that dynamic relaxation had lower total computational cost for examples with many degrees of freedom.

For stiffness matrix methods, Lewis (1989) mentions that they "show a strong exponential relationship [$O(c^n)$] between the CPU time and the size of the problem considered", and "for a structure with 189 degrees of freedom, any realistic limits of computer time would have been exceeded, unless steps to treat the numerical ill-conditioning are taken". While the comparison ignores the fact that stiffness matrix methods indeed deal with divergence through the use of modified Newton's method and/or incremental loading, it does illustrate why such steps may be necessary.

dof's	3	6	12	36	45	189
SM_{TLF}	**1.00** (**3**)	1.57 (**7**)	**1.00** (**4**)	2.20 (**6**)	4.49 (**5**)	N/A
DR_{vis}	1.46 (34)	**1.00** (35)	1.62 (113)	**1.00** (176)	**1.00** (132)	**1.00** (**262**)
DR_{kin}	4.69 (46)	2.03 (39)	3.52 (148)	2.30 (263)	2.18 (139)	1.95 (329)
t_{min} [s]	0.13	0.30	0.33	3.62	3.50	23.70

Table 5.6: Normalized duration of form finding and number of iterations in parentheses, best result in **bold**

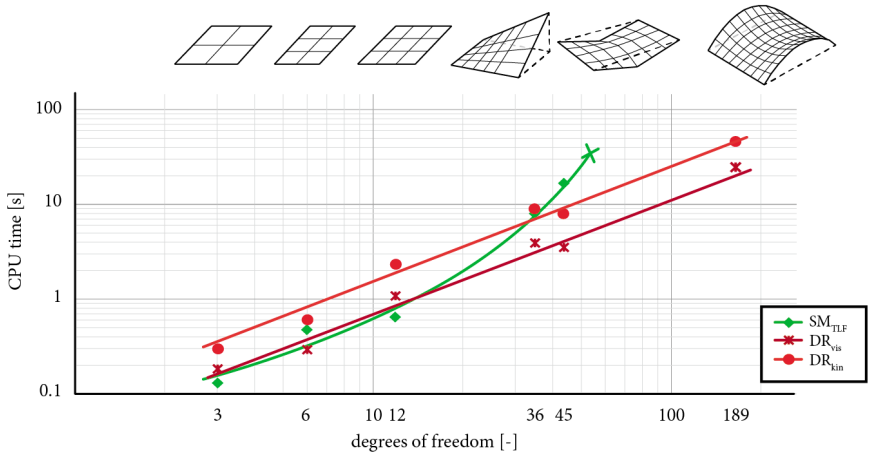

Figure 5.5: Comparison of the efficiency of methods. Adapted from (Lewis 1989).

Maurin & Motro (2001) compared the force density method for constant forces and surface strain density method for minimal surfaces when using either Newton's method or nonlinear conjugate gradient (CG) methods on five problems (6, 243, 243, 483 and 450 dof's). The computational performance was very similar, with Newton's method performing slightly better on average.

5.6.3 Uniform force networks

To compare the performance of different methods, a saddle shape with constant forces $\mathbf{f} = \mathbf{1}$ and fixed boundaries is sought (Figure 5.6). A network with constant forces is equivalent to a minimal length net (Section 4.2.6).

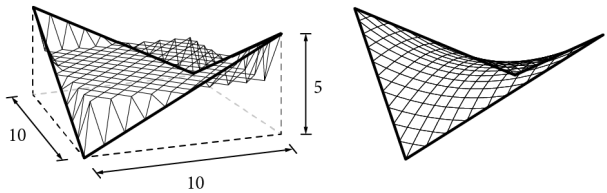

Figure 5.6: Initial and resulting geometry of form finding of saddle with 543 degrees of freedom.

The following ten methods were compared:

- stiffness matrix method with
  - total Lagrangian formulation (SM_{TLF}) and,
  - updated Lagrangian formulation (SM_{ULF});
- geometric stiffness method starting with
  - force densities $\mathbf{q} = \mathbf{1}$ (MFDF) or
  - forces $\mathbf{f} = \mathbf{1}$ (GSM);
- updated reference strategy with homotopy mapping (URS_{HM});
- dynamic relaxation with
  - viscous damping (DR_{vis}), and
  - kinetic damping (DR_{kin}); and,
- particle-spring systems with,
  - viscous damping and RK4 ($PS_{RK4,vis}$),
  - spring damping and RK4 (PS_{RK4}), and
  - spring damping and backward Euler (PS_{BE}).

For SM, the updated or total Langrangian formulation refer to updating the initial geometry every iteration or not.

dof's	75	183	339	543
SM_{TLF}	1.25 (**8**)	N/A	N/A	N/A
SM_{ULF}	1.44 (13)	4.22 (16)	6.26 (18)	9.93 (17)
MFDF	**1.00** (14)	**1.00** (16)	**1.00** (18)	**1.00** (17)
GSM	1.52 (16)	2.64 (15)	3.77 (14)	3.73 (13)
URS_{HM}	1.38 (10)	3.13 (**8**)	4.31 (**9**)	5.36 (**8**)
DR_{vis}	1.22 (**8**)	5.40 (34)	15.54 (63)	24.66 (96)
DR_{kin}	1.41 (16)	5.19 (32)	10.36 (42)	13.16 (50)
$PS_{RK4,vis}$	1.78 (17)	3.68 (22)	6.74 (28)	11.30 (50)
PS_{RK4}	4.10 (39)	6.58 (39)	13.57 (60)	22.73 (67)
PS_{BE}	6.31 (37)	11.30 (32)	14.44 (30)	20.33 (30)
t_{min} [s]	0.007	0.015	0.026	0.040
$\Sigma\mathbf{L}$ [m]	117.66	176.16	235.11	293.47

Table 5.7: Normalized duration of form finding and number of iterations in parentheses, best result in **bold**

For DR, for each element, the stiffness $EA = 0$. For PS, the spring constant k_s, damping factor k_d and drag coefficient b were all set to 0.5 (Veenendaal & Block 2012*b*). The time step $\Delta t = 1$, except for PS_{RK4} where $\Delta t = 0.2$ and masses $\mathbf{m} = \mathbf{1}$, except $PS_{RK4,vis}$ where $\mathbf{m} = \mathbf{2}$. The exceptions were made to avoid instability.

The convergence criterium was a fixed sum of branch lengths, in order to objectively compare the convergence of the methods for a result of equal geometric accuracy. The fixed sum of branch lengths was chosen such that at least one method had small residual values $\|\mathbf{r}\| \leq \varepsilon$ or normal strains $\|\mathbf{L}_0^{-1}\mathbf{l} - \mathbf{1}\| \leq \varepsilon$, where tolerance $\varepsilon = 10^{-3}$ and $\mathbf{L}_0$ are the lengths in the reference configuration.

Table 5.7 shows the time and iterations required to solve the problem, for increasing degrees of freedom (dof's). Note that the resulting durations have been normalized with respect to the minimum solving time t_{min}.

Figure 5.7 shows the computational time needed depending on the degrees of freedom, plotted on a log-log scale. Appearing as lines, the required time for all methods seems to exhibit polynomial growth $O(n^c)$ with $c > 0$, almost linear in some cases, though the number of data points is limited.

For SM, the standard method did not converge for 183 dof's and above (see Table 5.7), which agrees with Lewis (1989) (Section 5.6.2). Effectively, this is the standard finite element method without any convergence control. After introducing an elasticity $EA = 1$ for each element and an updated Lagragian formulation (ULF), the adapted method SM_{ULF} showed polynomial growth $O(n^c)$ as well. Surprisingly, it is superior to DR in this case and requires a roughly constant number of iterations. PS, with either explicit RK4 or implicit backward Euler, did not show faster convergence

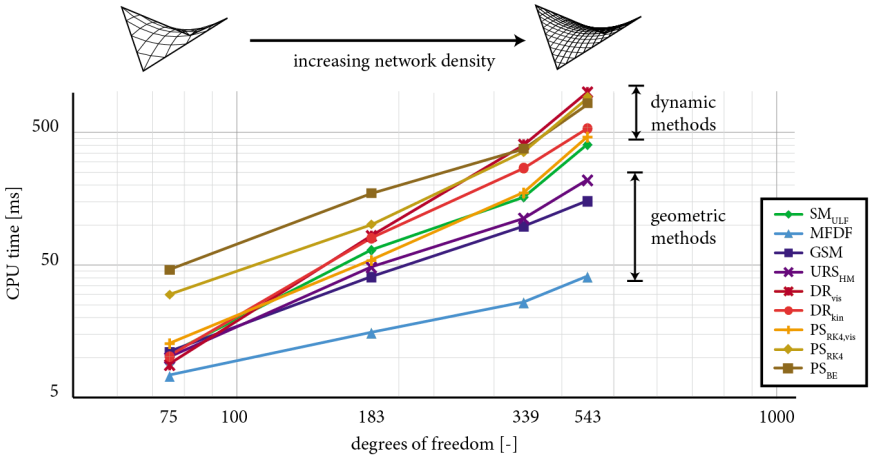

Figure 5.7: Comparison of the efficiency of methods (Veenendaal & Block 2012*b*).

for these small examples. From Figure 5.7 it can be seen that the latter does start overtaking other dynamic methods at higher dof's. This is consistent with Baraff & Witkin (1998), who report implicit solvers to be faster than explicit ones, based on examples of 7806 dof's or more.

Based on these results, MFDF is the fastest method for the form finding of minimal-length nets in this range of dof's. Its advantage is explained by the fact that it automatically starts with one force density-controlled iteration before becoming force-controlled (proceeding as GSM would after the first iteration). The other methods start directly from the prescribed forces, meaning they are dependent on the initial geometry, in our case a flat net (Figure 5.6).

In terms of iterations, all methods that use stiffness matrices exhibit nearly constant iterations: SM_{ULF}, MFDF, GSM, URS_{HM} and PS_{BE}. URS_{HM} requires the lowest number of iterations.

5.6.4 Minimal surfaces

The previous example consisted of line elements. To further compare the performance of different methods, a catenoid and a pseudo-Scherk's first surface with uniform stress and fixed boundaries is sought (Figures 5.8 and 5.9), modelled using triangle elements. The second example, pseudo-Scherk's first surface is also referred to as a box surface. An actual Scherk's first surface cannot be bounded along straight edges, hence the 'pseudo'.

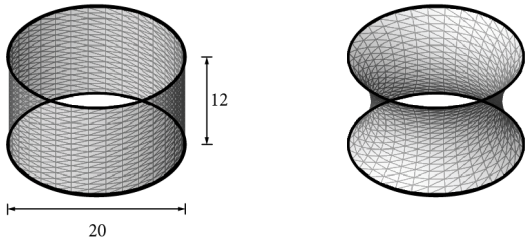

Figure 5.8: Initial and resulting geometry of form finding of catenoid.

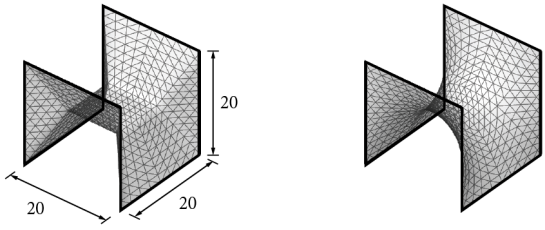

Figure 5.9: Initial and resulting geometry of form finding of pseudo-Scherk's first surface.

The following seven methods were compared:

- stiffness matrix method, using an updated Lagrangian formulation (SM_{ULF});
- geometric stiffness method (GSM);
- surface stress density method and its specific 'minimal surface approach' ($SSDM_{MSA}$);
- updated reference strategy with
  - homotopy mapping (URS_{HM}), and
  - extended URS (X-URS); and,

- dynamic relaxation with,
  - viscous damping (DR_{vis}), and
  - kinetic damping (DR_{kin}).

In addition, the following variations in solvers were compared with Newton's method for GSM and Leapfrog integration for DR:

- modified Newton's method, updated every two or ten iterations;
- conjugate gradient method (CG);
- low-memory Broyden-Fletcher-Goldfarb-Shanno (L-BFGS-B);
- classic fourth-order Runge-Kutta method (RK4); and,
- backward Euler.

Two convergence criteria are used:

- the relative error in change in total surface area $|(A_{t+1} - A_t)/A_t| < \varepsilon = 0.001$; or,
- the absolute error in the norm of residuals $||\mathbf{r}|| < \varepsilon = 0.01$.

The former is less dependent on the density of the mesh, and therefore better to plot performance of each method for increasing degrees of freedom. The latter is best suited to compare the accuracy and convergence of each method for a specific case. For X-URS, $||\mathbf{r}|| < \varepsilon = 0.001$, as otherwise the relative convergence was not reached yet (the absolute error decreases too fast, and no further data would be obtained for comparison). The method also starts with one GSM iteration for the pseudo-Scherk's first surface, as the sharp angles in the initial geometry caused problems. For $SSDM_{MSA}$ the procedure is altered to initially converge such that $||\mathbf{r}|| < \varepsilon = 0.1$, before continuing as GSM would (instead of after just 1 iteration).

For SM, the Young's modulus $E = 0.001$ and Poisson's ratio $\nu = 0.3$. For URS_{HM}, $\lambda_{h,i=1,2,3\ldots} = 0, 0.5, 0.9$, etc. For DR, time step $\Delta t = 1.0$ and damping constant $C' = 0.5$ except for RK4 ($C' = 1.0$). Kinetic damping does not require any damping constants. Both CG and L-BFGS-B solvers use the actual Jacobian matrix, and not an approximation.

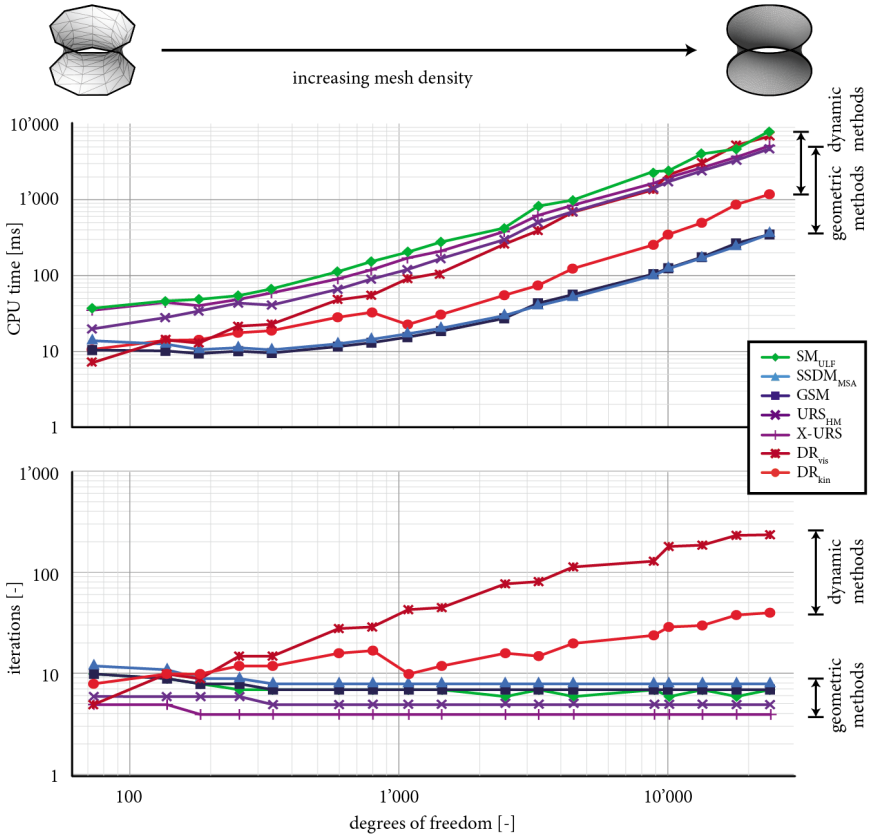

Figure 5.10: Comparison of the efficiency of methods for a catenoid. Criterion is relative error in surface area.

The results from Figure 5.10 show that in terms of computational time and relative convergence, GSM performs the best, followed by SSDM. The slowest are SM and both types of URS. In terms of iterations, X-URS is the best, followed by URS. Again, the required number of iterations for the geometric stiffness methods is virtually constant. Convergence for DR with kinetic damping is erratic.

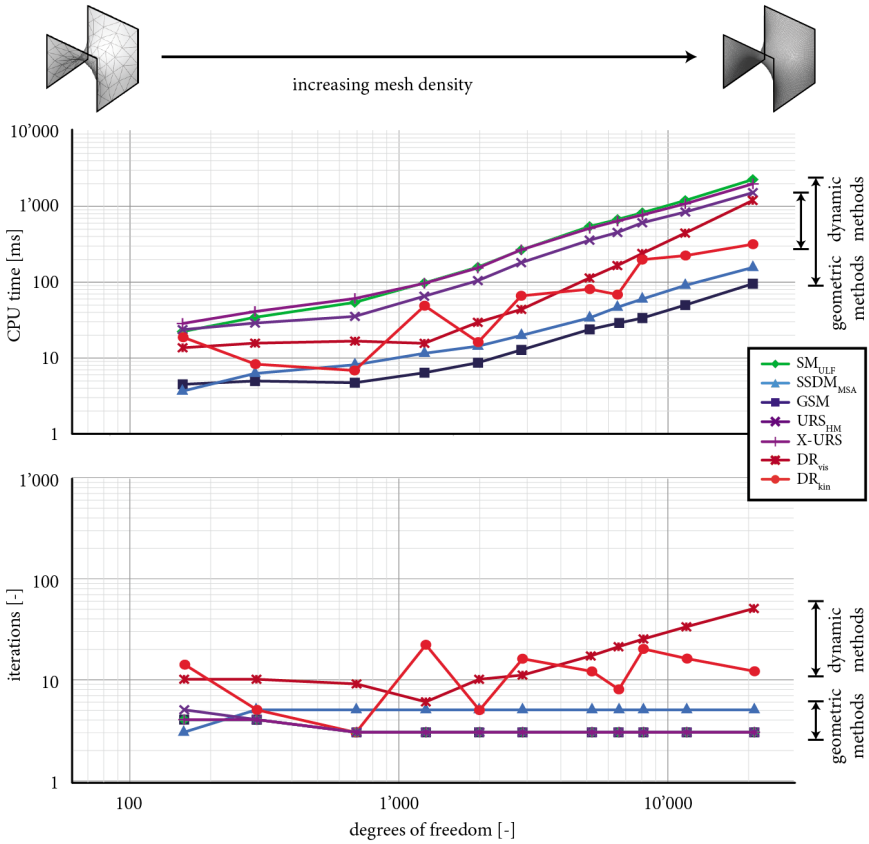

Figure 5.11: Comparison of the efficiency of methods for a pseudo-Scherk's first surface. Criterion is relative error in surface area.

The results from Figure 5.11 confirm many of the previous observations. There is even less to no difference in the number of required iterations for SM and the geometric stiffness methods. The behaviour of DR with kinetic damping is even more erratic.

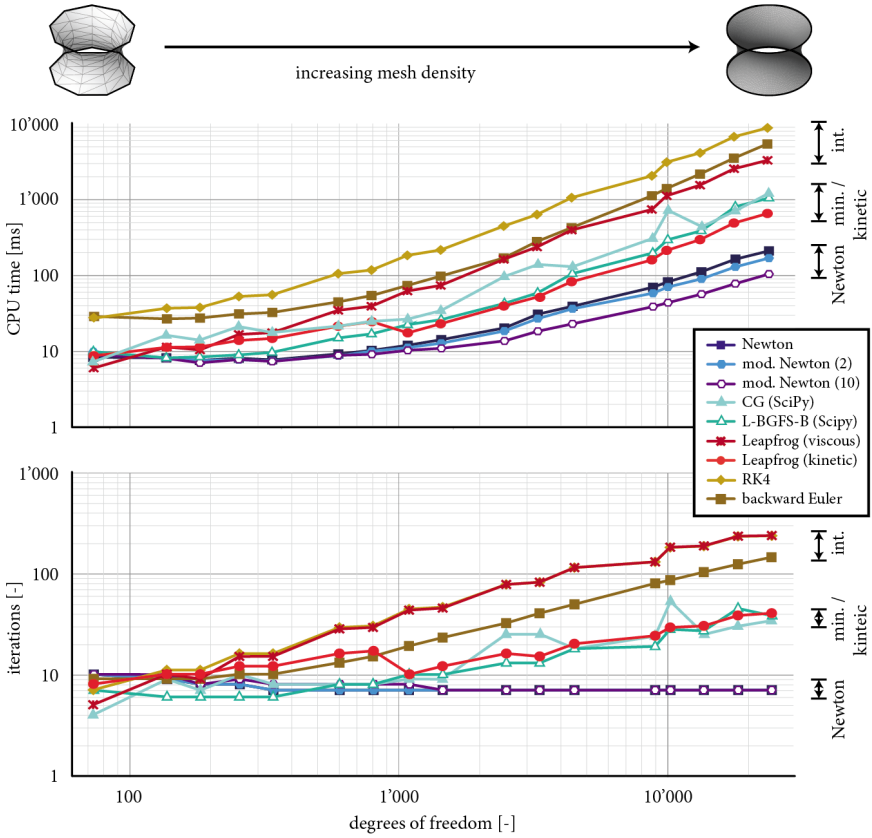

Figure 5.12: Comparison of solvers for CPU time [ms] and number of iterations against increasing degrees of freedom for a catenoid. Criterion is relative error in surface area.

The results from Figure 5.12 show that the nonlinear iterative solvers CG and L-BFGS are unable to improve GSM's performance, while modified Newton's method is. Neither RK4 nor BE can improve the performance of DR's standard Leapfrog integration.

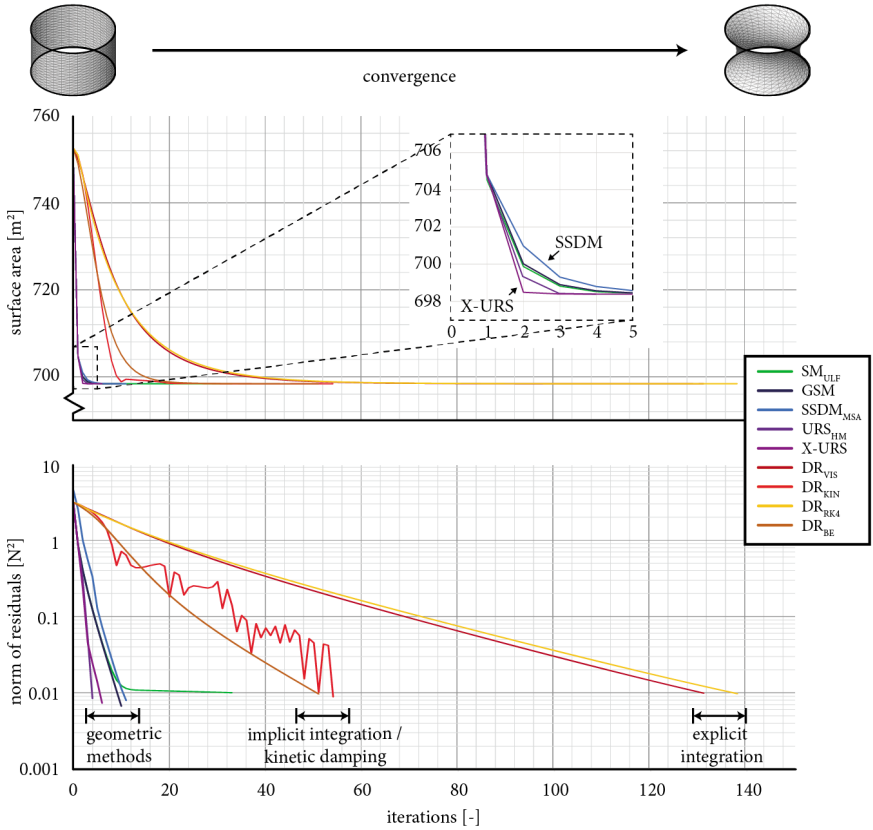

Figure 5.13: Convergence of implemented methods, as well as different integration schemes for DR. Criterion is absolute error in norm of residual forces.

The absolute error in the norm of residuals $||\mathbf{r}|| < \varepsilon = 0.01$ is used as the convergence criterion to compare the accuracy of the methods. Figure 5.13 shows the convergence for a catenoid with 1440 dof's.

Backward Euler and DR_{kin} have higher accuracy than the other two explicit integration methods. In fact, the accuracy of BE is so improved that we have found absolute convergence is reached sooner at higher dof's at well (2000+). Again, this is consistent with Baraff & Witkin (1998), who report implicit solvers to be faster than explicit ones, for examples of 7806 dof's or more.

The accuracy of all geometric stiffness methods is superior than the dynamic ones, with the second iteration revealing the improvements yielded by URS_{HM} over GSM, and in turn X-URS over URS_{HM}.

5.7 Conclusions

This chapter presents an overview of existing form-finding methods for tension structures. As a result, a generic form-finding method is presented that encompasses them. This method is presented using consistent notation and language, and has been implemented in a single computational framework. This generic method and its framework provide for three functions:

- a *didactic instrument* allowing better understanding of various methods and how they relate;
- an *objective comparison* of performance, enabling more informed decisions when choosing between methods, elements, solvers and so on; and,
- *development of new and hybrid methods*, by identifying opportunities, preventing needless repetition and allowing future research to be directed to entirely new discoveries.

The following general observations are made:

- early, seminal form-finding methods were developed in the 1970s and were applied to projects involving Frei Otto;
- many more form-finding methods have been presented, particularly in the past three decades, often presented as generalizations or extensions of previously existing methods;
- methods distinguish themselves from each other depending on
  - whether material deformation is involved or not;
  - what mechanical or geometrical objectives are defined (forces, stress, or weighted p-norm of lengths and areas);
  - element type and definition; and ,
  - solver type (and how ill-conditioning is avoided); and

- these methods can be divided into four categories based on the first and last distinctions: stiffness matrix methods, geometric stiffness methods, dynamic equilibrium methods and minimization methods.

By presenting methods in the same manner and carrying out an extensive review of literature, the following specific observations were made:

- the references for SM are largely equivalent;
- the references for GSM are largely equivalent, except for
  - element definitions that minimize some weighted p-norm of lengths or areas (FDM, SSDM and EFDM); and
  - methods that include nonlinear geometric stiffness matrices while avoiding ill-conditioning (URS, X-URS);
- GSM, SSDM and DR allow a system of equations to be solved that is three times smaller than that of SM or URS, as the three coordinates can be decoupled;
- SSDM can be described in terms of traditional force densities along triangle edges;
- SSDM's and EFDM's nonlinear geometric stiffness matrices have been defined, allowing their combination with URS' homotopy mapping;
- integration methods have been formulated such that they can be combined with SM, URS and SSDM, in the same way that DR can be considered a combination of GSM with an integration scheme as a solver;
- integration and solving methods used in recent form-finding methods developed in China have been identified as existing ones (Störmer-Verlet and Jacobi).

Through the examples, some additional insights were possible:

- GSM is generally the most efficient numerical method;
- X-URS and URS are generally the most accurate numerical methods;
- geometric stiffness methods require a constant number of iterations, consistent with practical advice given by Tabarrok & Qin (1992) and Pauletti & Pimenta (2008) to terminate at four to nine iterations;

- integration schemes for dynamic equilibrium and iterative solvers are generally unable to compete with Newton's method applied to static equilibrium;
- the use of modified Newton's method seems to improve the speed of convergence;
- Leapfrog integration with kinetic damping has comparable performance to CG and L-BFGS-B; and,
- the advantages of starting with force densities (MFDF) do not carry over to surfaces (SSDM) in terms of performance.

Ultimately, it is possible to formulate a single form-finding problem that transcends the four proposed categories. Imagine a problem that includes different elements, where some elements are governed by material deformation, while others have various stress states or geometrical objectives. Now that this problem is defined, its solution must be as well. The remaining choice, the solver, will only determine how fast we reach an approximate solution or how accurate that approximation is.

For normally sized problems (up to 10^4 dof's), and modern computers, where storage of such problems is no longer an issue, Newton methods perform well. The advantage of not having to construct or invert a stiffness matrix (as in minimization and explicit integration methods) has therefore become overrated. At low dof's of freedom, less than 500, the performance of L-BFGS-B may offer some improvement. We may then conclude the decision for a solver to be a trivial one; an opinion not previously held, but now afforded to us by modern computing power. Then, the meaning of the proposed categories is lost in the light of such a general problem and the arbitrary means by which it is solved.

On the other hand, it is emphasized that the individual methods, while possibly producing the same results, differ in how they were originally derived and presented, and as such, one may find them to be intuitive or meaningful in varying degrees. Similarly, the overall proposed categorization can be helpful in initially structuring and understanding form-finding methods and their specific concepts and features.

There is no discovery that one cannot claim for oneself by saying that one had found the same thing some years previously; but if one does not supply the evidence by citing the place where one has published it, this assertion becomes pointless and serves only to do a disservice to the true author of the discovery. [...] .

— Adrien-Marie Legendre, 1809 (referring to Carl Fiedrich Gauss and their dispute on who discovered the method of least squares)

CHAPTER SIX

Constrained form finding

This chapter describes the application of the method of least squares to constrained form finding, and specifically the problem of flexible formworks for concrete shells as it has been used for subsequent chapters[1]. The term *constrained* refers to constraints additional to those of static equilibrium and imposed boundary conditions, that are inherent in form finding. In such cases, a compromise has to be found between form and forces. The chapter is also intended to relate variations of the least-squares method as they were presented by Linkwitz et al. in the 1970s, most of which were published in German, as well as more recent publications, which are primarily based on one such version by Schek (1974).

The method of least squares was first published by Adrien-Marie Legendre (1752–1833) in order to fit equations to a dataset, and developed further by Carl Friedrich Gauss (1777–1855) for applications in statistics as well. The name "least squares" refers to the fact that the method minimizes a squared sum of variables, usually the unknowns or the residuals. In essence, a least-squares method solves systems of equations in which the number of equations and the number of variables is not equal, so systems $\mathbf{Ax} = \mathbf{b}$, where the left-hand side matrix $\mathbf{A}$ is no longer square.

Section 6.1 provides the main references regarding least-squares methods in form finding, and cites projects that were designed with them. Section 6.2 outlines the basic least-squares problem and how it applies to flexible formworks. Sections 6.3 and 6.4 explain linear and nonlinear least squares, including their regularized or damped form respectively. Section 6.5 describes application to problems that can be defined in two different sets of variables, specifically the force densities $\mathbf{q}$ and coordinates $\mathbf{x}$. The possible addition of further constraints is briefly discussed in Section 6.6, before drawing conclusions in Section 6.7.

[1]This chapter is partially based on Linkwitz & Veenendaal (2014).

6.1 Least squares in form finding

In 1972, at the IASS Pacific Symposium in Tokyo and Kyoto, three least-squares methods for cable networks were independently presented: Linkwitz; Knudson & Scordelis; and, Ohyama & Kawamata. The latter two methods attempt to find forces of a given geometry in equilibrium. They are restricted to vertical equilibrium and orthogonal grids. Both discuss the additional prescription of forces, but point out that this could result in an inability to find equilibrium. Haber & Abel (1982) generalized their work to apply to arbitrary geometries and three-dimensional loads.

The least-squares method by Linkwitz & Schek (1971) was developed for the Munich Olympic stadium, in an attempt to reconcile inaccurate photogrammetric and force measurements of Frei Otto's physical hanging models, while constraining the initial mesh to be square (Figures 2.41 and 2.42). Their work was published in English by Linkwitz (1972), Schek (1974) and Gründig & Schek (1974), though it is generally remembered for another part of it: introducing the unconstrained, linear force density method in the seminal paper by Schek (1974). At more than 600 citations and counting, it is arguably the most significant scientific paper in the field of form finding.

More recently, Van Mele & Block (2010, 2011) published a least-squares method to determine the equilibrium of a given cable net under load, initially for the purpose of developing a flexible formwork for anticlastic, thin concrete shells, and later by Van Mele et al. (2014) to determine equilibrium for vaulted structures of given geometry for static and other loads. Tamai (2013, 2015), Lachauer & Block (2014) and Lachauer (2015) published least-squares methods to determine equilibrium for discrete structures with both tension and compression of given geometry, subject to bounds on the force densities.

Table 6.1 lists known projects that were optimized using a least-squares method. Tamai (2015) describes an application to the 2015 Art Rotana Hotel in Bahrain, United Arab Emirates, on behalf of contractor Waagner Biro, but the project was awarded to another company.

project	year	type	constraints
Olympic Stadium, Munich	1972	cable net	coordinates, force densities, unstressed lengths (Linkwitz et al. 1974)
Multihalle, Mannheim	1974	timber gridshell	coordinates, force densities, lengths (Gründig & Schek 1974)
Solemar-Therme, Bad Dürrheim	1987	timber gridshell	coordinates, force densities (Gründig 1988)

Table 6.1: List of projects, optimized using constrained form finding based on least-squares methods, with original references. Additional details found in Linkwitz & Veenendaal (2014)

6.2 Least squares for flexible formworks

Having established a form through freeform modelling, mathematical definition or form finding, the next problem is to establish the force distribution when the load of concrete is applied to the flexible formwork. In other words, we wish to find the required prestressing forces such that, under given loads of the wet concrete, the resulting concrete shell takes the form of the target shape. The initial shape, prior to casting, is still an unknown at this point.

The solution to this problem is to calculate the unknown force densities $\mathbf{q}$ as a function of coordinates $\mathbf{x}$ of a known geometry and applied loads $\mathbf{p}$. Referring to equation (5.5), our system of equations is

$$\mathbf{C}_{\mathrm{i}}^{\mathrm{T}}\mathbf{U}\mathbf{q} = \mathbf{p}_{\mathrm{i}}, \tag{6.1}$$

or in reduced form,

$$\bar{\mathbf{C}}_{\mathrm{i}}^{\mathrm{T}}\bar{\mathbf{U}}\mathbf{q} = \mathbf{P}_{\mathrm{i}}, \tag{6.2}$$

both of the general form $\mathbf{A}\mathbf{x} = \mathbf{b}$.

The left hand side matrices $\mathbf{C}_{\mathrm{i}}^{\mathrm{T}}\mathbf{U}$ and $\bar{\mathbf{C}}_{\mathrm{i}}^{\mathrm{T}}\bar{\mathbf{U}}$ are of size $[3n_{\mathrm{i}} \times m]$ and $[n_{\mathrm{i}} \times m]$. This means that if $3n_{\mathrm{i}} \neq m$ or $n_{\mathrm{i}} \neq m$, neither matrix is square, and neither can be inverted. The system has n_{i} or $3n_{\mathrm{i}}$ equations and m unknowns. Depending on the specific number of nodes and branches, these systems are either under- or overdetermined systems (number of equations < or > number of unknowns respectively). An un-

determined system has either no or infinitely many solutions. An overdetermined system typically has no solution, unless some of the equations are identical or linearly dependent. The method of (linear) least squares finds the approximate solution of such systems.

Table 6.2 summarizes differences in terminology and solutions for both types of systems, as they appear in the following sections.

System	**Underdetermined**	**Overdetermined**
equations and unknowns	$m < n$	$m > n$
problem	least-squares problem	least-squares approximation problem
solution	none (inconsistent) or infinitely many (consistent)	none (only approximate)
normal equations		$(\mathbf{A}^{\mathrm{T}}\mathbf{A})\mathbf{x} = \mathbf{A}^{\mathrm{T}}\mathbf{p}$
Moore-Penrose pseudoinverse	right inverse $\mathbf{A}^{\mathrm{T}}(\mathbf{A}\mathbf{A}^{\mathrm{T}})^{-1}$	left inverse $(\mathbf{A}^{\mathrm{T}}\mathbf{A})^{-1}\mathbf{A}^{\mathrm{T}}$
minimizes	$\mathbf{q}^{\mathrm{T}}\mathbf{q}$ subject to $\mathbf{A}\mathbf{q} = \mathbf{p}$	$(\mathbf{p} - \mathbf{A}\mathbf{q})^{\mathrm{T}}(\mathbf{p} - \mathbf{A}\mathbf{q})$
weighted	$\mathbf{Q}^{-1}\mathbf{A}^{\mathrm{T}}(\mathbf{A}\mathbf{W}_1^{-1}\mathbf{A}^{\mathrm{T}})^{-1}$	$(\mathbf{A}^{\mathrm{T}}\mathbf{W}_2\mathbf{A})^{-1}\mathbf{A}^{\mathrm{T}}\mathbf{W}_2$
minimizes	$\mathbf{x}^{\mathrm{T}}\mathbf{W}_1\mathbf{x}$ subject to $\mathbf{A}\mathbf{q} = \mathbf{p}$	$(\mathbf{p} - \mathbf{A}\mathbf{q})^{\mathrm{T}}\mathbf{W}_2(\mathbf{p} - \mathbf{A}\mathbf{q})$
Gauss-Newton (nonlinear)	$\mathbf{J}^{\mathrm{T}}(\mathbf{J}\mathbf{J}^{\mathrm{T}})^{-1}$	$(\mathbf{J}^{\mathrm{T}}\mathbf{J})^{-1}\mathbf{J}^{\mathrm{T}}$
Tikhonov regularisation	$\mathbf{A}^{\mathrm{T}}(\mathbf{A}\mathbf{A}^{\mathrm{T}} + \delta\mathbf{I})^{-1}$	$(\mathbf{A}^{\mathrm{T}}\mathbf{A} + \delta\mathbf{I})^{-1}\mathbf{A}^{\mathrm{T}}$
minimizes	$\mathbf{x}^{\mathrm{T}}\mathbf{x} + \delta(\mathbf{p} - \mathbf{A}\mathbf{q})^{\mathrm{T}}(\mathbf{p} - \mathbf{A}\mathbf{q})$	
weighted	$\mathbf{W}_1^{-1}\mathbf{A}^{\mathrm{T}}(\mathbf{A}\mathbf{W}_1^{-1}\mathbf{A}^{\mathrm{T}} + \mathbf{W}_2^{-1})^{-1}$	$(\mathbf{A}^{\mathrm{T}}\mathbf{W}_2\mathbf{A} + \delta\mathbf{W}_1)^{-1}\mathbf{A}^{\mathrm{T}}\mathbf{W}_2$
minimizes	$\mathbf{x}^{\mathrm{T}}\mathbf{W}_1\mathbf{x} + \delta(\mathbf{p} - \mathbf{A}\mathbf{q})^{\mathrm{T}}\mathbf{W}_2(\mathbf{p} - \mathbf{A}\mathbf{q})$	
Levenberg-Marquardt (nonlinear)	$\mathbf{J}^{\mathrm{T}}(\mathbf{J}\mathbf{J}^{\mathrm{T}} + \delta\mathbf{I})^{-1}$	$(\mathbf{J}^{\mathrm{T}}\mathbf{J} + \delta\mathbf{I})^{-1}\mathbf{J}^{\mathrm{T}}$

Table 6.2: Least-squares terminology for systems with more or less m equations than n unknowns, in linear and nonlinear, and regularized form. Partially based on (Schek & Eggensperger 1977).

The matter is complicated by allowing only specific values of the force densities $\mathbf{q}$, for instance requiring that they are non-zero (tension only) or limited (prestress and stress limits), leading to non-negative and bounded least squares. Furthermore, additional constraints may be placed on the geometry, leading to nonlinear least squares.

In this chapter, to simplify notation $\mathbf{C}_i^{\mathrm{T}}\mathbf{U}\mathbf{q} = \mathbf{C}_i^{\mathrm{T}}\mathbf{U}\mathbf{L}^{-1}\mathbf{f} = \mathbf{C}_i^{\mathrm{T}}\mathbf{Q}\mathbf{C}_i\mathbf{x} = \mathbf{p}_i$ will be written as $\mathbf{A}\mathbf{q} = \mathbf{B}\mathbf{f} = \mathbf{D}_i\mathbf{x} = \mathbf{p}$.

6.3 Ordinary least squares

The system may be underdetermined or overdetermined, resulting in either a *least-squares problem* or a *least-squares approximation problem* (Boyd & Vandenberghe 2004). The former is a constrained problem that appears in the references on the nonlinear force density and other constrained form-finding methods. The latter is an unconstrained problem that is more common to literature on linear least squares. In the context of constrained form finding, Haber & Abel (1982) refer to the solution to both problems as the *underdetermined least squares method* and *overdetermined least squares method*.

Undetermined problems occur in the work of Linkwitz & Schek (1971) Linkwitz (1972) and Gründig & Schek (1974), where both coordinates and forces are unknowns. The same is done in the context of this thesis (Veenendaal & Block 2014*b*, 2015). Schek (1974) also adds that the number of constraints, i.e. equations, is usually less than the number of unknowns.

Overdetermined problems feature in Knudson & Scordelis (1972), Ohyama & Kawamata (1972) and Van Mele & Block (2010, 2011). In these cases, the number of unknowns is limited because the structures are orthogonal and only one force or force density along each cables is sought. Block & Lachauer (2014) identify possible sets of independent variables in an automated fashion, citing an approach by Pellegrino & Calladine (1986).

6.3.1 Least-squares problem

The nonlinear force density method has been presented in the form of minimization problems, specifically simple *equality-constrained quadratic programs*:

$$\begin{aligned} \text{min. } & \mathbf{q}^{\mathrm{T}}\mathbf{W}_1\mathbf{q} \\ \text{subject to } & \mathbf{A}\mathbf{q} = \mathbf{p}, \end{aligned} \tag{6.3}$$

where $\mathbf{p}$ is often referred to as the *observations* in least squares, and in our case generally is a vector of applied loads, and $\mathbf{W}_1$ is an optional weighting matrix.

Method of Lagrange multipliers

Given an optimization problem

$$\begin{aligned} \text{max. } & f(x) \\ \text{subject to } & g(x) = 0, \end{aligned} \tag{6.4}$$

where f and g are differentiable with respect to x. By introducing a new variable called a Lagrange multiplier λ, a Lagrange function, or Lagrangian, can be defined as

$$\Lambda(x, \lambda) = f(x) \pm \lambda \cdot g(x), \tag{6.5}$$

for which a stationary point is sought.

Applying the method of Lagrange multipliers, we introduce the Lagrangian

$$\Lambda(\mathbf{q}, \boldsymbol{\lambda}) = \mathbf{q}^{\mathrm{T}}\mathbf{W}_1\mathbf{q} - \boldsymbol{\lambda}^{\mathrm{T}}(\mathbf{A}\mathbf{q} - \mathbf{p}), \tag{6.6}$$

which we solve by finding the minimum of Λ, i.e. $\nabla\Lambda(\mathbf{q}, \boldsymbol{\lambda}) = 0$. We take the partial derivatives, or *optimality conditions*,

$$\frac{\partial \Lambda}{\partial \mathbf{q}} = 2\mathbf{q}^{\mathrm{T}}\mathbf{W}_1 - \boldsymbol{\lambda}^{\mathrm{T}}\mathbf{A} = 0, \tag{6.7}$$

$$\frac{\partial \Lambda}{\partial \boldsymbol{\lambda}} = -(\mathbf{A}\mathbf{q} - \mathbf{p}) = 0, \tag{6.8}$$

or in block matrix form,

$$\begin{bmatrix} 2\mathbf{W}_1 & -\mathbf{A}^{\mathrm{T}} \\ -\mathbf{A} & \mathbf{0} \end{bmatrix} \begin{bmatrix} \mathbf{q} \\ \boldsymbol{\lambda} \end{bmatrix} = \begin{bmatrix} \mathbf{0} \\ -\mathbf{p} \end{bmatrix}. \tag{6.9}$$

From the first condition, we obtain

$$\mathbf{q} = \frac{1}{2}\mathbf{W}_1^{-1}\mathbf{A}^{\mathrm{T}}\boldsymbol{\lambda}, \tag{6.10}$$

which, substituted in the second condition, gives

$$\boldsymbol{\lambda} = 2\left(\mathbf{A}\mathbf{W}_1^{-1}\mathbf{A}^{\mathrm{T}}\right)^{-1}\mathbf{p}, \tag{6.11}$$

and, if the weighting $\mathbf{W}_1 = \mathbf{I}$, back into the first condition results in:

$$\mathbf{q} = \mathbf{W}_1^{-1}\mathbf{A}^{\mathrm{T}}\left(\mathbf{A}\mathbf{W}_1^{-1}\mathbf{A}^{\mathrm{T}}\right)^{-1}\mathbf{p} \tag{6.12}$$

$$= \mathbf{A}^{\mathrm{T}}\left(\mathbf{A}\mathbf{A}^{\mathrm{T}}\right)^{-1}\mathbf{p} = \mathbf{A}^{+}\mathbf{p}, \tag{6.13}$$

where $\mathbf{A}^{+}$ is the so-called Moore-Penrose pseudoinverse.

To avoid computing the inverse of $\mathbf{A}\mathbf{A}^{\mathrm{T}}$ directly, Gründig & Schek (1974) applied the iterative conjugate gradient (CG) method to the normal equations (CGNE) (Saad 2003) for the Multihalle project. Similarly, Van Mele et al. (2014) applied a Cholesky factorization and performed triangular substitutions (Nocedal & Wright 2000).

6.3.2 Least-squares approximation problem

The method of least squares is usually explained by the following premise: instead of finding the solution $\mathbf{q}^*$ (which is not unique, or does not exist), we wish to find an approximate value $\mathbf{q}$ such that $\mathbf{A}\mathbf{q}$ is the best approximation of $\mathbf{p}$. The errors $\mathbf{e}^*$ of our approximations are not known, since we do not know $\mathbf{q}^*$, but can be related to the *residuals* $\mathbf{r}$, which we can compute:

$$\mathbf{e}^* = \mathbf{q}^* - \mathbf{q}, \tag{6.14}$$

$$\mathbf{A}\mathbf{e} = \mathbf{A}\mathbf{q}^* - \mathbf{A}\mathbf{q}$$

$$= \mathbf{p} - \mathbf{A}\mathbf{q} = \mathbf{r}. \tag{6.15}$$

The smaller the distances $\|\mathbf{p} - \mathbf{A}\mathbf{q}\|^2$, the better the approximation. Finding $\mathbf{q}$ in this context is the least-squares problem, where "least squares" refers to the fact that the overall solution minimizes the sum of the squares of the errors (or residuals), in the results of every single equation in the system. A least-squares problem is an optimization problem with no constraints and has an objective which is a sum of squares,

$$\text{min.} \ (\mathbf{p} - \mathbf{A}\mathbf{q})^{\mathrm{T}} \mathbf{W}_2 (\mathbf{p} - \mathbf{A}\mathbf{q}), \tag{6.16}$$

where $\mathbf{W}_2$ is a weighting matrix. The objective can be written out as function

$$f(\mathbf{q}) = \mathbf{q}^{\mathrm{T}}\mathbf{A}^{\mathrm{T}}\mathbf{W}_2\mathbf{A}\mathbf{q} - 2\mathbf{p}^{\mathrm{T}}\mathbf{W}_2^{\mathrm{T}}\mathbf{A}\mathbf{q} + \mathbf{p}^{\mathrm{T}}\mathbf{p}, \tag{6.17}$$

which can be solved by finding the minimum of f,

$$\nabla f(\mathbf{q}) = 2\mathbf{A}^{\mathrm{T}}\mathbf{W}_2\mathbf{A}\mathbf{q} - 2\mathbf{A}^{\mathrm{T}}\mathbf{W}_2\mathbf{p} = 0. \tag{6.18}$$

Rewriting, we obtain the solution of a least-squares problem, the normal equations:

$$(\mathbf{A}^{\mathrm{T}}\mathbf{W}_2\mathbf{A})\mathbf{q} = \mathbf{A}^{\mathrm{T}}\mathbf{W}_2\mathbf{p}. \tag{6.19}$$

The normal equations have the analytical solution, and if the weighting $\mathbf{W}_2 = \mathbf{I}$,

$$\mathbf{q} = (\mathbf{A}^{\mathrm{T}}\mathbf{W}_2\mathbf{A})^{-1}\mathbf{A}^{\mathrm{T}}\mathbf{W}_2\mathbf{p} \tag{6.20}$$

$$= (\mathbf{A}^{\mathrm{T}}\mathbf{A})^{-1}\mathbf{A}^{\mathrm{T}}\mathbf{p} = \mathbf{A}^{+}\mathbf{p}, \tag{6.21}$$

similar to equation (6.13), but not identical as the Moore-Penrose pseudoinverse for overdetermined systems is $(\mathbf{A}^{\mathrm{T}}\mathbf{A})^{-1}\mathbf{A}^{\mathrm{T}}$ instead of $\mathbf{A}^{\mathrm{T}}(\mathbf{A}\mathbf{A}^{\mathrm{T}})^{-1}$ for underdetermined systems (Schek & Eggensperger 1977).

These steps are sometimes omitted by simply stating that both sides of the linear system $\mathbf{A}\mathbf{q} = \mathbf{p}$ can be multiplied by $\mathbf{A}^{\mathrm{T}}$, thus obtaining a square left-hand side *normal matrix* $\mathbf{A}^{\mathrm{T}}\mathbf{A}$ and a set of linear equations, the normal equations.

In the context of this thesis, the above solution already works for simple problems. In cases where the geometry with coordinates $\mathbf{x}$ is viable, and loads $\mathbf{p}$ are modest such that force densities remain in tension, no further work is needed.

6.3.3 Regularization

Depending on the problem, it is possible to find approximations where both the solution $\mathbf{q}$ and their residuals are small (Boyd & Vandenberghe 2004). Schek & Eggensperger (1977) introduced the most common form of such regularized approximations, Tikhonov regularization, for application to the problem of cable nets. The objective function is

$$\text{min. } (\mathbf{p} - \mathbf{A}\mathbf{q})^{\mathrm{T}} \mathbf{W}_2 (\mathbf{p} - \mathbf{A}\mathbf{q}) + \mathbf{q}^{\mathrm{T}}\mathbf{W}_1\mathbf{q} \tag{6.22}$$

Tthe objective can be written out as function

$$f(\mathbf{q}) = \mathbf{q}^{\mathrm{T}}\mathbf{A}^{\mathrm{T}}\mathbf{W}_2\mathbf{A}\mathbf{q} - 2\mathbf{p}^{\mathrm{T}}\mathbf{W}_2\mathbf{A}\mathbf{q} + \mathbf{p}^{\mathrm{T}}\mathbf{W}_2\mathbf{p} + \mathbf{q}^{\mathrm{T}}\mathbf{W}_1\mathbf{q}, \tag{6.23}$$

which can be solved by finding the minimum of f,

$$\nabla f(\mathbf{q}) = 2\mathbf{A}^{\mathrm{T}}\mathbf{W}_2\mathbf{A}\mathbf{q} - 2\mathbf{A}^{\mathrm{T}}\mathbf{W}_2^{\mathrm{T}}\mathbf{p} + 2\mathbf{W}_1\mathbf{q} = 0. \tag{6.24}$$

where often $\mathbf{W}_2 = \mathbf{I}$ and $\mathbf{W}_1 = \delta\mathbf{I}$.

The analytical solution, for overdetermined systems, then is

$$\mathbf{q} = \left(\mathbf{A}^{\mathrm{T}}\mathbf{W}_2\mathbf{A} + \mathbf{W}_1\right)^{-1} \mathbf{A}^{\mathrm{T}}\mathbf{W}_2\mathbf{p} \tag{6.25}$$

$$= \left(\mathbf{A}^{\mathrm{T}}\mathbf{A} + \delta\mathbf{I}\right)^{-1} \mathbf{A}^{\mathrm{T}}\mathbf{p}. \tag{6.26}$$

For underdetermined systems,

$$\mathbf{x} = \mathbf{W}_1^{-1}\mathbf{A}^{\mathrm{T}} \left(\mathbf{A}\mathbf{W}_1^{-1}\mathbf{A}^{\mathrm{T}} + \mathbf{W}_2^{-1}\right) \mathbf{p} \tag{6.27}$$

$$= \mathbf{A}^{\mathrm{T}} \left(\mathbf{A}\mathbf{A}^{\mathrm{T}} + \delta\mathbf{I}\right)^{-1} \mathbf{p}. \tag{6.28}$$

If we wish to minimize distances to given values $\mathbf{q}_0$, the objective function is

$$\text{min. } (\mathbf{p} - \mathbf{A}\mathbf{q})^{\mathrm{T}} \mathbf{W}_2 (\mathbf{p} - \mathbf{A}\mathbf{q}) + (\mathbf{q} - \mathbf{q}_0)^{\mathrm{T}} \mathbf{W}_1 (\mathbf{q} - \mathbf{q}_0) \tag{6.29}$$

The objective can be written out as function

$$f(\mathbf{q}) = \mathbf{q}^{\mathrm{T}}\mathbf{A}^{\mathrm{T}}\mathbf{W}_2\mathbf{A}\mathbf{q} - 2\mathbf{p}^{\mathrm{T}}\mathbf{W}_2\mathbf{A}\mathbf{q} + \mathbf{p}^{\mathrm{T}}\mathbf{W}_2\mathbf{p} + \mathbf{q}^{\mathrm{T}}\mathbf{W}_1\mathbf{q} + 2\mathbf{q}_0^{\mathrm{T}}\mathbf{Q}\mathbf{q} + \mathbf{q}_0^{\mathrm{T}}\mathbf{W}_1\mathbf{q}_0 \quad (6.30)$$

which can be solved by finding the minimum of f,

$$\nabla f(\mathbf{q}) = 2\mathbf{A}^{\mathrm{T}}\mathbf{W}_2\mathbf{A}\mathbf{q} - 2\mathbf{A}^{\mathrm{T}}\mathbf{W}_2^{\mathrm{T}}\mathbf{p} + 2\mathbf{W}_1\mathbf{q} - 2\mathbf{W}_1\mathbf{q}_0 = 0. \quad (6.31)$$

we obtain the analytical solution

$$\begin{aligned}
\mathbf{q}^* &= \left(\mathbf{A}^{\mathrm{T}}\mathbf{W}_2\mathbf{A} + \mathbf{W}_1\right)^{-1}\left(\mathbf{A}^{\mathrm{T}}\mathbf{W}_2\mathbf{p} + \mathbf{W}_1\mathbf{q}_0\right) && (6.32)\\
&= \left(\mathbf{A}^{\mathrm{T}}\mathbf{A} + \delta\mathbf{I}\right)^{-1}\left(\mathbf{A}^{\mathrm{T}}\mathbf{p} + \delta\mathbf{q}_0\right) && (6.33)\\
&= \mathbf{q}_0 + \left(\mathbf{A}^{\mathrm{T}}\mathbf{A} + \delta\mathbf{I}\right)^{-1}\left(\mathbf{A}^{\mathrm{T}}(\mathbf{p} - \mathbf{A}\mathbf{q}_0)\right). && (6.34)
\end{aligned}$$

6.4 Nonlinear least squares

If $\mathbf{A}$ in the system of equations $\mathbf{A}\mathbf{q} = \mathbf{p}$ is itself a function of $\mathbf{q}$, it needs to be recomputed after finding an initial solution. In other words, the problem is now a nonlinear least-squares problem. Writing the system as a function

$$\mathbf{g}(\mathbf{q}) = \mathbf{A}\mathbf{q} - \mathbf{p} = \mathbf{0}, \quad (6.35)$$

the first step is to then linearize the problem according to Newton-Raphson's method

$$\begin{aligned}
\mathbf{g}(\mathbf{q}) &= \mathbf{g}(\mathbf{q}_0) + \frac{\partial \mathbf{g}(\mathbf{q})}{\partial \mathbf{q}}\Delta\mathbf{q} && (6.36)\\
&= \mathbf{A}\mathbf{q}_0 - \mathbf{p} + \frac{\partial \mathbf{A}\mathbf{q}}{\partial \mathbf{q}}\Delta\mathbf{q} = 0, && (6.37)
\end{aligned}$$

assuming that $\mathbf{p}$ is not dependent on $\mathbf{q}$. By introducing the first derivative, or Jacobian, $\mathbf{J}$, and residuals $\mathbf{r}$, the problem is rewritten as the linearized system of equations

$$
\begin{aligned}
\frac{\partial \mathbf{Aq}}{\partial \mathbf{q}} \Delta \mathbf{q} &= \mathbf{p} - \mathbf{Aq}_0 \\
\mathbf{J} \Delta \mathbf{q} &= \mathbf{r}_0 .
\end{aligned}
\tag{6.38}
$$

We are still solving a linear system $\mathbf{J}\Delta\mathbf{q} = \mathbf{r}_0$ of the form $\mathbf{Aq} = \mathbf{p}$ to which we can apply normal equations, but instead of finding $\mathbf{q}$ directly, we now have iterations, in which $\mathbf{q}$ is updated using $\Delta\mathbf{q}$,

$$
\begin{aligned}
\Delta \mathbf{q} &= \left(\mathbf{J}^{\mathrm{T}}\mathbf{J}\right)^{-1} \mathbf{J}^{\mathrm{T}} \mathbf{r}_0 = \mathbf{J}^{+} \mathbf{r}_0 \\
\mathbf{q} &= \mathbf{q}_0 + \mathbf{J}^{+} \mathbf{r}_0 ,
\end{aligned}
\tag{6.39}
$$

with respect to given values $\mathbf{q}_0$ (Schek & Eggensperger 1977)

$$
\Delta \mathbf{q} = \left(\mathbf{J}^{\mathrm{T}}\mathbf{J}\right)^{-1} \mathbf{J}^{\mathrm{T}} \left(\mathbf{r}_0 - \mathbf{J}\Delta\mathbf{q}_0\right) . \tag{6.40}
$$

This iterative procedure is commonly known as Gauss-Newton's method, as applied in most of the cited references. In regularised form it is

$$
\Delta \mathbf{q} = \left(\mathbf{J}^{\mathrm{T}}\mathbf{J} + \delta \mathbf{W}\right)^{-1} \mathbf{J}^{\mathrm{T}} \mathbf{r}_0 , \tag{6.41}
$$

which is commonly known as Levenberg-Marquardt, as used by Schek & Eggensperger (1977) and Van Mele & Block (2010, 2011). Regularizing with respect to given values $\mathbf{q}_0$, leads to

$$
\Delta \mathbf{q} = \left(\mathbf{J}^{\mathrm{T}}\mathbf{J} + \delta \mathbf{I}\right)^{-1} \left(\mathbf{J}^{\mathrm{T}} \mathbf{r}_0 + \delta \Delta \mathbf{q}_0\right) . \tag{6.42}
$$

The *damping matrix* or *scaling matrix* $\mathbf{W}$ is often an identity matrix $\mathbf{I}$ or the diagonal matrix of $\mathbf{J}^{\mathrm{T}}\mathbf{J}$.

There are other options to define the *damping parameter* δ and damping matrix $\mathbf{W}$. For example, Schek (1974) mentions either a "diagonal weighting matrix" $\mathbf{P}^{-1}$ or $\mathbf{P}^{-1}\mathbf{R}^2$ for "large changes in the force densities or in the shape, where $\mathbf{R}$ is a diagonal matrix of the residuals. Schek & Eggensperger (1977) suggest either $p\mathbf{R}^2$, where some guidance is given on determining p, or $\delta = p\mathbf{r}^{\mathrm{T}}\mathbf{r}$ and $\mathbf{W} = \mathbf{I}$.

Schek & Eggensperger (1977) and Linkwitz & Veenendaal (2014) distinguish between strong and weak least squares, or hard and soft constraints, by observing that convergence for the above equations may be very slow or that divergence may occur. In such cases, the minimization towards $\mathbf{q}_0$ is relaxed by defining $\Delta\mathbf{q}$ as $\mathbf{q}_{i+1} - \mathbf{q}_i$ rather than $\mathbf{q}_{i+1} - \mathbf{q}_0$.

6.5 Multivariate least squares

The term "multivariate least squares" normally refers to solving systems of the form $\mathbf{AX} = \mathbf{B}$, appearing in regression analysis.

Here, it is used to mean the least-squares problems where the left-hand side of the system of equations and any constraints can be written in forms corresponding to different sets of variables, $\mathbf{Ax} = \mathbf{Cy} = \mathbf{b}$.

This was relevant for the Olympic Park in Munich (Linkwitz 1972, Linkwitz & Schek 1971), and the Multihalle in Mannheim (Gründig & Schek 1974), where measurements produced approximate values for both coordinates and forces. The least-squares method then was only intended to reconcile both measurements. In the later case of the Solemar Therme in Bad Dürheim, an initial linear form-finding step provided this information, and the introduction of additional constraints required them to deviate from this equilibrated geometry (Gründig 1988, Linkwitz & Veenendaal 2014). The approach was used in this thesis in cases where ordinary least squares were unable to immediately provide a viable solution (Veenendaal & Block 2014*b*). In each of these cases, the systems of equations were underdetermined, hence the following procedure.

The objective function is

$$\begin{aligned} \text{min. } & \mathbf{q}^{\mathrm{T}}\mathbf{q} + \mathbf{x}^{\mathrm{T}}\mathbf{x} \\ \text{subject to } & \mathbf{Aq} = \mathbf{Dx} = \mathbf{p}. \end{aligned} \tag{6.43}$$

The corresponding Lagrangian is

$$\Lambda(\mathbf{q}, \mathbf{x}, \boldsymbol{\lambda}) = \mathbf{q}^{\mathrm{T}}\mathbf{q} + \mathbf{x}^{\mathrm{T}}\mathbf{x} - \boldsymbol{\lambda}^{\mathrm{T}}(\mathbf{Aq} + \mathbf{D}_{\mathrm{i}}\mathbf{x} - 2\mathbf{p}) \tag{6.44}$$

which we solve by finding the stationary point of Λ, i.e. $\nabla\Lambda(\mathbf{q}, \mathbf{x}, \boldsymbol{\lambda}) = 0$. The optimality conditions are

$$\frac{\partial \Lambda}{\partial \mathbf{q}} = 2\mathbf{q}^{\mathrm{T}} - \boldsymbol{\lambda}^{\mathrm{T}}\mathbf{A} = \mathbf{0}, \tag{6.45}$$

$$\frac{\partial \Lambda}{\partial \mathbf{x}} = 2\mathbf{x}^{\mathrm{T}} - \boldsymbol{\lambda}^{\mathrm{T}}\mathbf{D}_{\mathrm{i}} = \mathbf{0}, \tag{6.46}$$

$$\frac{\partial \Lambda}{\partial \boldsymbol{\lambda}} = -(\mathbf{A}\mathbf{q} + \mathbf{D}_{\mathrm{i}}\mathbf{x} - 2\mathbf{p}) = \mathbf{0}, \tag{6.47}$$

or in block matrix form,

$$\begin{bmatrix} 2\mathbf{I} & \mathbf{0} & -\mathbf{A}^{\mathrm{T}} \\ \mathbf{0} & 2\mathbf{I} & -\mathbf{D}_{\mathrm{i}}^{\mathrm{T}} \\ -\mathbf{A} & -\mathbf{D}_{\mathrm{i}} & \mathbf{0} \end{bmatrix} \begin{bmatrix} \mathbf{q} \\ \mathbf{x} \\ \boldsymbol{\lambda} \end{bmatrix} = \begin{bmatrix} \mathbf{0} \\ \mathbf{0} \\ -2\mathbf{p} \end{bmatrix}. \tag{6.48}$$

From the first two conditions, we obtain

$$\begin{bmatrix} \mathbf{q} \\ \mathbf{x} \end{bmatrix} = \frac{1}{2}\begin{bmatrix} \mathbf{A} & \mathbf{D}_{\mathrm{i}} \end{bmatrix}^{\mathrm{T}} \boldsymbol{\lambda} = \frac{1}{2}\begin{bmatrix} \mathbf{A}^{\mathrm{T}} \\ \mathbf{D}_{\mathrm{i}}^{\mathrm{T}} \end{bmatrix} \boldsymbol{\lambda}, \tag{6.49}$$

which, substituted in the third condition, gives

$$\boldsymbol{\lambda} = 2\left(\begin{bmatrix} \mathbf{A} & \mathbf{D}_{\mathrm{i}} \end{bmatrix}\begin{bmatrix} \mathbf{A} & \mathbf{D}_{\mathrm{i}} \end{bmatrix}^{\mathrm{T}}\right)^{-1}\mathbf{p} = 2\left[\mathbf{A}\mathbf{A}^{\mathrm{T}} + \mathbf{D}_{\mathrm{i}}\mathbf{D}_{\mathrm{i}}^{\mathrm{T}}\right]^{-1}\mathbf{p}, \tag{6.50}$$

and back into the first condition results in:

$$\begin{bmatrix} \mathbf{q} \\ \mathbf{x} \end{bmatrix} = \begin{bmatrix} \mathbf{A}^{\mathrm{T}} \\ \mathbf{D}_{\mathrm{i}}^{\mathrm{T}} \end{bmatrix}\left[\mathbf{A}\mathbf{A}^{\mathrm{T}} + \mathbf{D}_{\mathrm{i}}\mathbf{D}_{\mathrm{i}}^{\mathrm{T}}\right]^{-1}\mathbf{p} = \begin{bmatrix} \mathbf{A} & \mathbf{D}_{\mathrm{i}} \end{bmatrix}^{+}\mathbf{p}. \tag{6.51}$$

In nonlinear form, we start with the nonlinear function (Linkwitz & Schek 1971):

$$\mathbf{g}(\mathbf{q}, \mathbf{x}) = \mathbf{A}\mathbf{q} - \mathbf{p} = \mathbf{D}\mathbf{x} - \mathbf{p} = \mathbf{0}, \tag{6.52}$$

and then linearize it with respect to both variables,

$$\mathbf{g}(\mathbf{q},\mathbf{x}) = \mathbf{g}(\mathbf{q}_0,\mathbf{x}_0) + \frac{\partial \mathbf{g}(\mathbf{q},\mathbf{x})}{\partial \mathbf{q}}\Delta\mathbf{q} + \frac{\partial \mathbf{g}(\mathbf{q},\mathbf{x})}{\partial \mathbf{x}}\Delta\mathbf{x} \tag{6.53}$$

$$= \mathbf{A}\mathbf{q}_0 - \mathbf{p} + \frac{\partial \mathbf{A}\mathbf{q}}{\partial \mathbf{q}}\Delta\mathbf{q} + \frac{\partial \mathbf{D}\mathbf{x}}{\partial \mathbf{x}}\Delta\mathbf{x} = 0. \tag{6.54}$$

As before, we might introduce first derivatives, or Jacobians, $\mathbf{J}_x$ and $\mathbf{J}_y$, but (Linkwitz & Schek 1971) simplify the derivatives to $\frac{\partial \mathbf{A}\mathbf{q}}{\partial \mathbf{q}} = \mathbf{A}$ and $\frac{\partial \mathbf{D}\mathbf{x}}{\partial \mathbf{x}} = \mathbf{D}_\mathrm{i}$ (ignoring derivatives of $\mathbf{A}$ and $\mathbf{C}$ with respect to $\mathbf{q}$ and $\mathbf{x}$ respectively) to obtain the following linearized system of equations

$$\begin{aligned} \frac{\partial \mathbf{A}\mathbf{q}}{\partial \mathbf{q}}\Delta\mathbf{q} + \frac{\partial \mathbf{D}\mathbf{x}}{\partial \mathbf{x}}\Delta\mathbf{x} &= \mathbf{p} - \mathbf{A}\mathbf{q}_0 \\ \mathbf{A}\Delta\mathbf{q} + \mathbf{D}_\mathrm{i}\Delta\mathbf{x} &= \mathbf{r}_0, \end{aligned} \tag{6.55}$$

or in block form,

$$\begin{bmatrix} \mathbf{A} & \mathbf{D}_\mathrm{i} \end{bmatrix} \begin{bmatrix} \Delta\mathbf{q} \\ \Delta\mathbf{x} \end{bmatrix} = \mathbf{r}_0, \tag{6.56}$$

with the solution

$$\begin{bmatrix} \Delta\mathbf{q} \\ \Delta\mathbf{x} \end{bmatrix} = \begin{bmatrix} \mathbf{A}^\mathrm{T} \\ \mathbf{D}_\mathrm{i}^\mathrm{T} \end{bmatrix} \left[\mathbf{A}\mathbf{A}^\mathrm{T} + \mathbf{D}_\mathrm{i}\mathbf{D}_\mathrm{i}^\mathrm{T}\right]^{-1} \mathbf{r}_0 = \begin{bmatrix} \mathbf{A} & \mathbf{D}_\mathrm{i} \end{bmatrix}^+ \mathbf{r}_0. \tag{6.57}$$

Linkwitz & Schek (1971) use a weighted form to either emphasize the importance of the required force densities, or required coordinates.

6.6 Constrained least squares

Additional constraints may be imposed on the problem. In the context of a flexible formwork, such constraints could be given forces along the perimeter to limit the effort in prestressing, or given initial, unstressed lengths related to practical cutting patterns. Ultimately, such constraints were not applied in this thesis, but the general approach is provided for potential future work.

In the multivariate case of both unknown force densities $\mathbf{x}$ and coordinates $\mathbf{q}$, Sections 6.3 and 6.4 already mention how to impose given values. Additionally, Linkwitz et al. (1974) and Gründig & Schek (1974) explain how to constrain initial and stressed lengths respectively.

The function $\mathbf{g}(\mathbf{q}, \mathbf{x})$ representing static equilibrium is still linearized as in equation (6.54), leading to the system of equations in equation (6.56). Then, any additional constraint function $\mathbf{g}_i(\mathbf{q}, \mathbf{x})$ is also linearized with respect to force densities $\mathbf{q}$ and coordinates $\mathbf{x}$, and simply added to this same system.

Assuming here that the constraint function has a Jacobian $\mathbf{G}$ that is only a function of $\mathbf{x}$, and $\mathbf{s}$ is the residual of this function, then

$$\begin{bmatrix} \mathbf{A} & \mathbf{D}_\mathrm{i} \\ \mathbf{0} & \mathbf{G} \end{bmatrix} \begin{bmatrix} \Delta\mathbf{q} \\ \Delta\mathbf{x} \end{bmatrix} = \begin{bmatrix} \mathbf{r}_0 \\ \mathbf{s}_0 \end{bmatrix}, \tag{6.58}$$

leading to the solution of the form (Linkwitz et al. 1974):

$$\begin{bmatrix} \Delta\mathbf{q} \\ \Delta\mathbf{x} \end{bmatrix} = \begin{bmatrix} \mathbf{A}^\mathrm{T} & \mathbf{0} \\ \mathbf{D}_\mathrm{i}^\mathrm{T} & \mathbf{G}^\mathrm{T} \end{bmatrix} \begin{bmatrix} \mathbf{A}\mathbf{A}^\mathrm{T} + \mathbf{D}_\mathrm{i}\mathbf{D}_\mathrm{i}^\mathrm{T} & \mathbf{D}_\mathrm{i}\mathbf{G}^\mathrm{T} \\ \mathbf{D}_\mathrm{i}\mathbf{G}^\mathrm{T} & \mathbf{G}\mathbf{G}^\mathrm{T} \end{bmatrix}^{-1} \begin{bmatrix} \mathbf{r}_0 \\ \mathbf{s}_0 \end{bmatrix}. \tag{6.59}$$

For unknown force densities only, Schek (1974) explains constraints on initial and stressed lengths as well as internal forces. Van Mele & Block (2010, 2011) describe imposing coordinates, and Malerba et al. (2012) reaction forces. Instead of

$$\mathbf{g}_i(\mathbf{q}, \mathbf{x}) = 0, \tag{6.60}$$

Schek (1974) writes any constraint as a function solely of the force densities, so that

$$\mathbf{g}_i^*(\mathbf{q}) = \mathbf{g}(\mathbf{x}(\mathbf{q}), \mathbf{q}) = \mathbf{0}. \tag{6.61}$$

Linearizing this with respect to force densities $\mathbf{q}$ and using the chain rule,

$$\mathbf{g}_i^*(\mathbf{q}) = \mathbf{g}_i^*(\mathbf{q}_0) + \frac{\partial \mathbf{g}_i^*(\mathbf{q})}{\partial \mathbf{q}} \Delta\mathbf{q} \tag{6.62}$$

$$= \mathbf{g}_i^*(\mathbf{q}_0) + \frac{\partial \mathbf{g}_i(\mathbf{q}, \mathbf{x})}{\partial \mathbf{x}} \frac{\partial \mathbf{x}}{\partial \mathbf{q}} \Delta\mathbf{q} + \frac{\partial \mathbf{g}_i(\mathbf{q}, \mathbf{x})}{\partial \mathbf{q}} \Delta\mathbf{q} = 0, \tag{6.63}$$

where

$$\frac{\partial \mathbf{x}}{\partial \mathbf{q}} = \mathbf{D}_{\mathrm{i}}^{-1}\mathbf{A}, \tag{6.64}$$

to obtain the linearized system of equations

$$\begin{aligned} \left[\frac{\partial \mathbf{g}_i(\mathbf{q},\mathbf{x})}{\partial \mathbf{x}} \mathbf{D}_{\mathrm{i}}^{-1}\mathbf{A} + \frac{\partial \mathbf{g}_i(\mathbf{q},\mathbf{x})}{\partial \mathbf{q}} \right] \Delta\mathbf{q} &= \mathbf{g}_i^*(\mathbf{q}_0) \\ \mathbf{G}\Delta\mathbf{q} &= \mathbf{r}_0. \end{aligned} \tag{6.65}$$

Gründig & Schek (1974) preferred the former approach due to the large computational cost of the latter, related to the inversion of matrix $\mathbf{D}_{\mathrm{i}}$.

6.7 Conclusions

This chapter presents an overview of least-squares methods for constrained form-finding problems. These methods can be directly applied to form-found results from the preceding Chapter 5, meaning that for a prescribed, form-found geometry of a network of linear and triangular finite elements, the internal force distribution can be found or approximated of that network subjected to an additional load. Ordinary, nonlinear, and multivariate least squares have been applied in subsequent chapters to the problem of flexible formworks. Constrained least squares have not been applied, but can be relevant if constraints are placed on prestressing forces or geometry of cutting patterns. It has been observed that the approach by Schek (1974) to use the force densities as the only variables has not been compared to that of surrounding literature where both coordinates and force densities are variables. Specifically, Gründig & Schek (1974) criticizes the former approach due to inversion of a large matrix requiring too much computer memory. On the other hand, four decades later, Van Mele et al. (2014) are able to apply Cholesky decomposition without any issue. On a wider note, this chapter may serve as a primer on existing work in this area, which has thus far been mostly published in German.

Part IV

Design methodology

I should have to so design buildings that they would not only be appropriate to materials but design them so the machine that would ***have*** *to make them could make them surpassingly well.*

— Frank Lloyd Wright, 1932

CHAPTER SEVEN

Design process

This chapter sets out to present a design and engineering process required for an anticlastic thin concrete shell, constructed on a flexible formwork, whilst taking into account its fabrication constraints[1]. To fully realize the structural efficiency of a flexibly formed shell, it is crucial to both design an optimal shell within the project's constraints and to control the cable forces such that its form, despite the formwork's flexibility and the weight of the wet concrete, is exactly as required in the end. A computational approach to realize this goal was developed and is explained here in more detail. The procedure consists of eight steps (Figure 7.1):

1. generating the shell geometry by
    - establishing boundary conditions or domain,
    - generating the surface (possible using form finding; see Chapter 5), and
    - determining the thickness;
2. verifying and (possibly) optimizing the concrete shell geometry;
3. patterning and flattening the formwork surface;
4. calculating loads due to weight of the fresh concrete (and some selfweight of the fabric and shuttering);
5. determining cable forces or fabric stresses due to those loads (using least squares; see Chapter 6);
6. materializing the cables and/or fabric, i.e. choosing materials and cross sections, in order to determine the initial geometry;
7. determining cable forces or fabric stresses prior to loading; and
8. generating and analyzing the formwork frame.

[1]This chapter is partially based on Veenendaal & Block (2014*b*, 2015).

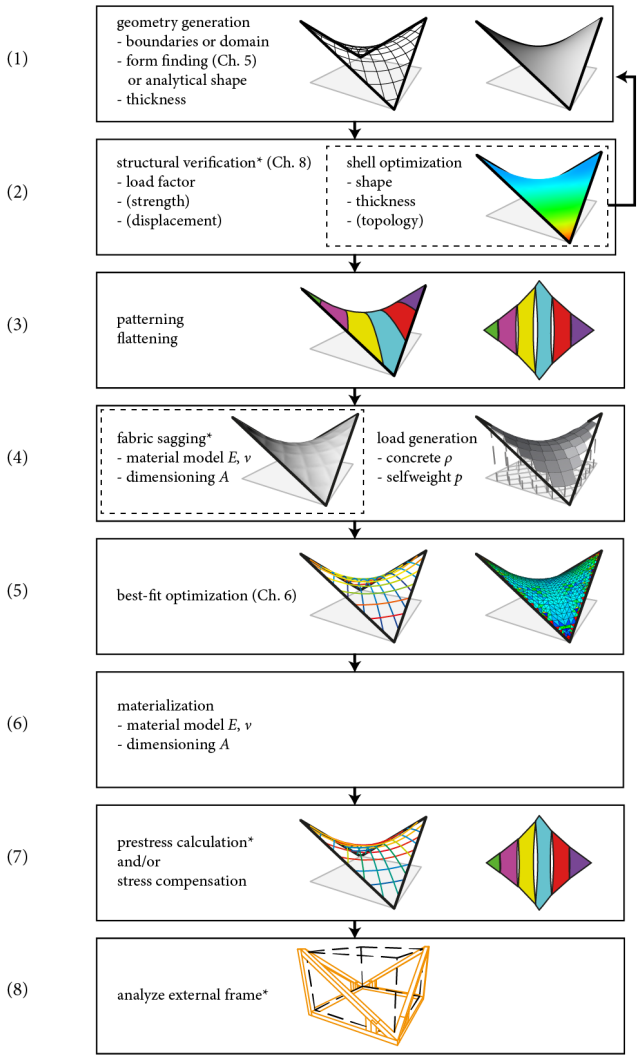

Figure 7.1: Design process for flexible formwork and resulting shell. Based on similar flowcharts in Veenendaal & Block (2014*b*, 2015) and Veenendaal et al. (2015, 2017). * indicates that finite element analysis is required.

At each step, the computational cost should be modest. This would allow either a real-time process where the designer can interactively evaluate many designs, or an optimization in which a multitude of designs need to be generated. Some suggestions are made throughout to minimize this cost. For the same reason, the design process does not integrate all possible or required loads and load combinations. Rather, these have to be checked afterwards. The formwork, for example, is only evaluated for selfweight, and loads due to the applied concrete.

This chapter is divided into eight sections corresponding to each step in the design process, before drawing conclusions in the ninth and final section.

7.1 Geometry generation

The establishment of a shell geometry can be done through:

- analytical expressions within a domain (Section 2.1);
- physical or numerical form finding (Sections 2.2, 2.3 and Chapter 5);
- numerical finite element analysis with large displacements; or,
- freeform design and modelling (Section 2.4).

The first two approaches can be controlled easily to produce only anticlastic shapes. Form finding is particularly suited to generating feasible flexible formworks because, in the absence of applied loads, the resulting shapes are guaranteed to be anticlastic, but have a wider range than those produced by analytical expressions. The resulting mesh can also be the same geometry used for optimization and subsequent steps (see also Chapter 12. The last two approaches are only briefly discussed, and are otherwise outside the scope of this thesis.

Analytical expressions

Analytical expressions for shells usually define the height, or vertical coordinate, as a function of the horizontal coordinates. They might be valid within an infinite domain (perhaps locally asymptotic), and therefore, the shape of the shell has to be bounded. This may be a simple rectangular domain, meaning the horizontal coordinates have lower and upper limits. The boundaries can also be governed by functions themselves, such as the unbuilt Táchira Club in Caracas, Venezuela (Section 2.1.3) (Escrig & Sánchez 2005). Examples of anticlastic shapes are hyperbolic paraboloids and hyperboloids.

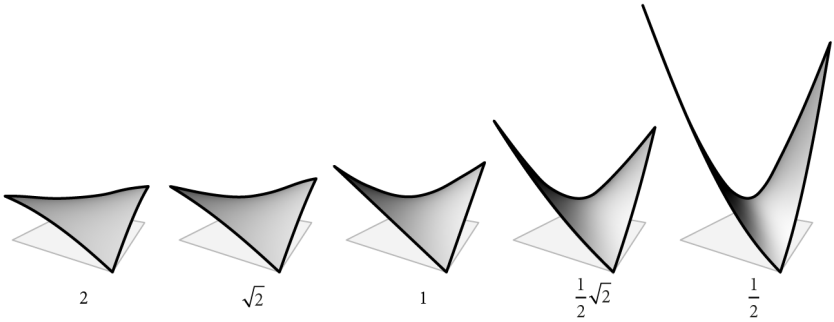

Figure 7.2: Hypars with varying values γ, and equal domain, span and rise at midspan.

Figure 7.2 shows a small, square hypar (dimensions $w \times l \times h = 1.8{\times}1.8{\times}0.6$ m). It is defined by equations (11.1), (11.5) and (11.7), with plan proportion $\alpha = w/l = 1.0$, shallowness $\beta = s/h = 3$ and factor $\gamma = a/b$, such that $a = \gamma \cdot b$. Maintaining the same domain and the same rise at midspan, while varying only $\gamma = 1/2\sqrt{2}, 1/2, 1, \sqrt{2}, 2$, produces a range of hypars with different edge curves. An even larger variety of shapes is possible by establishing different cutting planes (the domain) and inclinations, and aggregating multiple hypars. Such strategies were expertly exploited by Candela in his designs (Faber 1963, Schober 2015).

Form finding

Form finding, whether physical or numerical, requires the definition of boundary conditions in advance. These might be fixed points or edges. If the boundary conditions are not entirely in one plane, and no external forces are introduced, the resulting shape will always be anticlastic. In other words, by prescribing only internal forces or stresses and not applying any loads, a wide variety of anticlastic shapes can be generated. In the past, physical form finding has required photogrammetry to digitize the model, to then compute a more precise shape using least squares.

Figure 7.3 shows the ability of form finding to produce a variety of anticlastic shapes for given boundary conditions. The force density and natural force density methods were used to prescribe ratios of forces and stresses respectively. In the former case, equation (5.31) was used to iteratively update the force densities, introduced in equation (4.14). In the latter case, the orientation of the elements is iteratively changed to always follow principal stresses, making the problem less dependent on the initial mesh. The natural force densities were defined in equation (4.33).

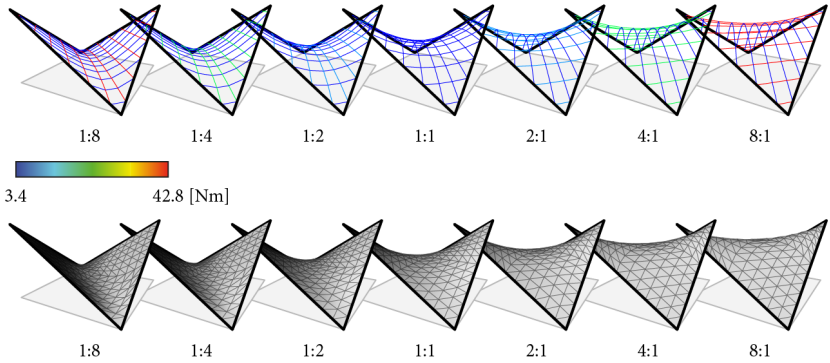

Figure 7.3: Saddle shapes of varying ratio of either forces or stresses in two directions. The stresses are continuously defined along the directions of principal stress.

Large-displacement analysis

Geometry generation can also be done by keeping the flexible formwork, rather than the resulting shell in mind. For a tensioned fabric roof, its surface is normally created to have an as uniform stress state as possible and avoid any wrinkling by tailoring appropriate cutting patterns. In fabric formworks, avoiding wrinkling is not a necessary requirement. Instead of tailoring, one could allow for wrinkles and maximize the use of large, flat sheets of fabrics, as was the case for projects at CAST (Section 3.3.3).

Such shapes would be difficult to find using numerical form finding, since the stress field has specific areas of uni- and bi-axial stress. Instead, large-displacement analysis could be performed for prescribed initial patterns of flat fabric for given material properties and boundary conditions.

Freeform design

Freeform design is an umbrella term for any kind of design process that does not (initially) involve mathematical expressions or methods of form finding. Such shapes would have to be post-rationalized using some kind of functions approximating their shape for subsequent modelling and analysis. Examples are describing a physical model by translational surfaces, or meshing a NURBS-surface for finite element analysis.

7.2 Geometry optimization

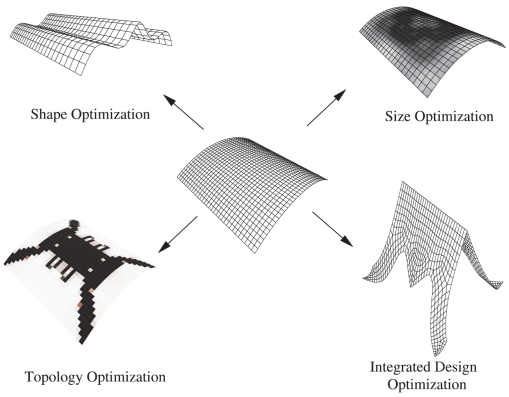

Figure 7.4: Various optimization results for a cylindrical shell by Lee & Hinton (2000*a*).

However the shape is initially generated, it can then be optimized further. The geometry can be optimized by changing the shape, thickness and topology of the surface (Figure 7.4). The latter, topology optimization, is outside the scope of this thesis. Early applications to barrel vaults and conoidal shells can be found in Lee & Hinton (2000*b*).

The definition of what constitutes an "optimal" shell depends on the objectives. For shell structures, typical objectives are maximizing stiffness or buckling resistance whilst minimizing weight or volume. Ramm et al. (1993) mention a few more possible objectives and constraints in shell design.

These objectives may compete, requiring the designer to either convert some to constraints with a desired value (e.g. a given volume) or decide on a trade-off. Such a compromise can be found through weighting factors (e.g. weighted least squares in Section 6.5). One can also visually inspect a Pareto front, which plots the objectives against each other, effectively revealing many different weightings (e.g. Figure 12.19).

Pugnale et al. (2014) show, using a genetic algorithm, that optimizing a simple shell for displacements has local optima, related to reversals of curvature. This suggests that a sufficiently constrained model that does not allow such reversals, could be optimized using gradient-based approaches. In fact, several built shells by

Sasaki (2014) (Section 2.4) were optimized for strain energy, using a gradient-based approach, called sensitivity analysis (Ebata et al. 2003, Sasaki 2005). Presumably, this was appropriate if allowable deviations from the freeform architectural starting point were limited to an extent that only a local optimum could be found.

Any optimization is complicated further by including multiple load cases as well as material and geometric nonlinearities. The nonlinearities in particular require resource-intensive calculations. For this reason, Chapter 8 details the use of reduction factors to include these nonlinearities at early design stages.

In addition, other objectives might be included to account for spatial, functional, building physical and other goals. For this reason, genetic algorithms were used as a standard approach in this thesis.

7.2.1 Shape optimization

The optimization of shell structures requires a method of generating geometry in which design variables allow for their variation. For analytical shapes, such as hyperbolic paraboloids, one can vary the domain and coefficients of their functions as a shape generator. Although some of the thinnest known shell structures are hypars, both Tomás & Martí (2010*b*) and Sasaki (2014) indicate that slight changes, deviating from the hypar, can drastically improve their structural behaviour. This implies that conventional analytical shapes have their limits in structural optimization, and that other parameterizations should be used. Design variables can be:

- coefficients and other parameters of a function (e.g. Tomás & Martí (2010*a*,*b*) ;
- nodal coordinates of a mesh (e.g. Sasaki (2014)), possibly requiring some method of filtering (Bletzinger & Ramm 2014);
- control points or key points of a surface, or its defining curves (e.g. Pugnale et al. (2014), Ramm et al. (1993), Sasaki (2014));
- weighting factors for a linear combination of shapes (e.g. Michalatos & Kaijima (2014) using eigenmodes as shapes);
- external loads for form finding; and/or,
- internal forces for form finding.

Figure 7.5 shows two shapes that were optimized for strain energy, using either control points or force densities as design variables, arriving at similar form. The former shape was used in Veenendaal & Block (2014*b*) to obtain the shape for two prototypes, discussed in Chapter 10. The latter approach, using form finding as a shape generator by varying internal forces, is adopted for Chapter 12.

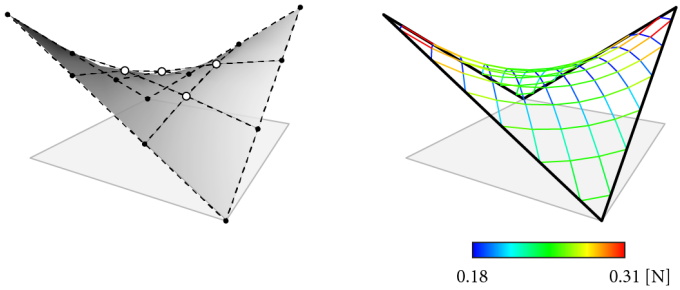

Figure 7.5: Saddle shapes with uniform thickness, and control points or internal force densities as shape variables.

Bletzinger et al. (2005) already used form finding as a shape generator for optimization, specifically by varying the loads (distribution of selfweight) as the degrees of freedom. Following the experimental work by Cauberg (2009) (Section 3.3.2), Guldentops et al. (2009) and Tysmans et al. (2011) used form finding to generate flexibly formed, anticlastic shells, using the force density method and dynamic relaxation respectively. Both examples reduced the shape generation to a single degree of freedom. In the former case, a ratio between a set of two force densities (corresponding to the two orthogonal directions) was varied manually until the resulting shape approximated that of a hyperboloid. In the latter, a fictitious elastic stiffness (identical for all links) was iterated until a required height at midspan was reached. Méndez Echenagucia & Block (2015) used thrust network analysis to generate funicular vaults, optimized for acoustic performance, with sets of force densities as variables (see also Section 6.3). A similar compromise between the full or single degrees of freedom was suggested in Veenendaal et al. (2015). Here, the design variables are force densities at key locations of the shell, and some kind of interpolation between these locations is used (Figure 12.9).

Figure 7.6 shows that varying a single ratio of force densities can produce a large variety of anticlastic shapes. The range of shapes is equivalent to that of varying ratios of forces or stresses in Figure 7.3, but does not require iterative solving, as explained in Section 5.3.4. It is therefore more suitable for parametric design or shape generation, provided that there is no particular need to enforce certain forces or stresses. However, Figure 7.6 also illustrates that any ratio of force densities will produce a hypar if the network coincides with straight lines and in the absence of external loads. This means some care is necessary in generating the topology and orientation of the network, which should follow expected lines of principal curvature.

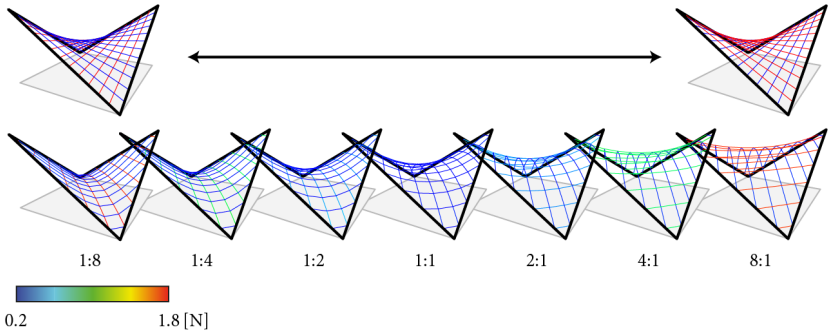

Figure 7.6: Saddle shapes of varying ratio of force densities, using the linear force density method.

7.2.2 Shape and thickness optimization

Lee & Hinton (2000*a*) showed that optimizing shells for strain energy (stiffness) with only shape or thickness variables may produce shapes with a lower buckling resistance. Optimizing for both variables did lead to improvements in the buckling load, but they ultimately concluded that the geometrically nonlinear buckling load must still be calculated and verified. Reitinger & Ramm (1995) compared the results of maximizing stiffness versus maximizing the load factor, with and without imperfections for shells of given volume. The load factor is the multiplier by which the applied load has to be factored to obtain the load at which buckling occurs. The buckling load for the optimization with imperfections was considerably higher than those for the other optimizations. The resulting shell shape for both types of objectives was quite different, while the inclusion of imperfections mostly affected the thickness rather than the shape. Both studies used a linear elastic material model, which would likely overestimate the buckling load if a reduction factor is not included.

As design variables, Reitinger & Ramm (1995) used two thickness parameters, with some kind of interpolation along the surface. Ramm et al. (1993) and Arnout et al. (2012) used the Kresge Auditorium as a case study for shape and thickness optimization, with the latter using free parameter optimization (each nodal thickness is a variable). Chapter 12 also uses free parameterization.

As these references all applied to synclastic shells, a small study was carried out for an anticlastic shell with fixed boundaries, to verify some of the above conclusions. Figure 7.7 shows several results when optimizing for strain energy or load factor, and when including imperfections or not. The shape variable c, determines the force densities in both directions, 2^{-c} and 2^{c}. The thickness variables, limited between 10 and 50 mm, are the thicknesses t_1, t_9 and t_2, at the tips, centre and corners of the shell respectively. Interpolation is done using quadratic Lagrangian polynomials (like in a quadrilateral, quadratic finite element), while keeping the total volume constant.

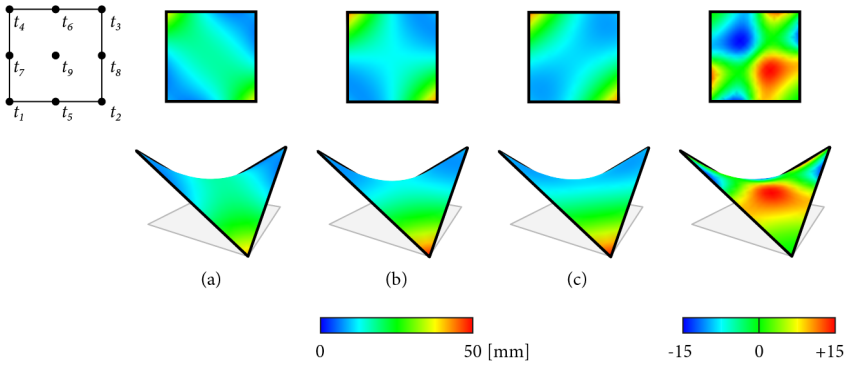

Figure 7.7: Saddle shapes with variable thickness, optimized for (a) strain energy E_{se} or (b,c) load factor λ, (a,b) without or (c) with imperfections. The first buckling mode, on the right, is taken as the shape imperfection.

	variables				performance		
	c	t_1	t_9	t_2	E_{se}	λ	λ_{imp}
	[-]	[mm]	[mm]	[mm]	10^3·[Nm]	[-]	[-]
hypar	0.00	15	15	15	42	169	159
uniform	-0.22	15	15	15	**36**	132	126
variable	-0.19	10	17	42	**15**	406	397
variable	-0.09	10	13	50	17	**440**	372
variable	-0.17	10	11	50	30	422	**407**

Table 7.1: Reference hypar and saddle shapes, optimized for shape and thickness variables, for different objectives indicated in bold.

Table 7.1 shows that, compared to a hypar of uniform thickness, the load factor λ can substantially be improved, more than a factor of 2.5. Without including thickness variables, the load factor actually reduces when optimizing for strain energy, in agreement with Lee & Hinton (2000*a*). The load factor does not proportionally increase when including imperfections, in agreement with Reitinger & Ramm (1995) as well.

7.3 Patterning and flattening

The next step, having settled on the required shape of the shell, is to map a cable net or fabric onto the intrados (interior surface) of the shell. Figure 7.8 shows different patterns for either a fabric or a cable-net formwork.

Several criteria govern the design of the fabric patterning:

- the fabric seam lines should follow geodesics to minimize the amount of cutting waste;
- the weave should align with the principal stresses, such that the cutting patterns are not distorted by stress compensation for shear stresses;
- the strip width should:
  - be as wide as possible, close to the maximum roll width, to reduce the number of total strips; but,
  - be as narrow as possible, such that the developable patterns can approximate the doubly curved surface.

These criteria largely coincide with those for tensioned fabric roofs, though the alignment with principal stresses is of greater importance. This is because stresses are usually uniform or smoothly graded in fabric roofs, while in fabric formworks, they are governed by the distribution of the concrete loads leading to greater variation.

Several criteria govern the design of the cable-net topology:

- the valency of the cable net should ideally be even to allow continuous cables, simplifying details within the net;
- continuous cables should:
  - terminate at the boundaries to allow for more convenient prestressing (and thus control) throughout, rather than terminate or loop within the mesh;

  - follow principal curvatures of the surface to reduce the amount of prestressing required, as the cables' load capacity is proportional to prestress and curvature; and,
  - have as low geodesic curvature as possible for two reasons:
    * to double as seam lines for secondary fabric strips (thus reducing material waste); and,
    * to reduce out-of-plane forces, and corresponding shear in the cross clamps at the nodes;
- the density of the mesh should:
  - be fine enough such that the demands on the secondary fabric or shuttering are low (in terms of strength, prestressing and patterning requirements); and,
  - be coarse enough, such that the total length of cable, the number of intersections and the amount of prestressing work (thus material and labour cost) are reduced.

If all cables follow geodesics, their principal normals coincide with the surface normals. This means that without any external load, there is no out-of-plane force, and no theoretical need for cross clamps to connect intersecting cables. Any out-of-plane force, produced by the subsequent applied concrete load, is precisely the force that the cross clamps need to resist, particularly in steep areas where the vertical load vector does not coincide with the normals. Note that the wire formworks in Sections 3.7.3 and 3.7.4 roughly followed geodesics, were relatively shallow, and therefore did not require any cross clamps, at most some simple ties at regular intervals.

Given these above criteria, a starting point would be a quadrilateral mesh, or patches of such meshes, roughly oriented along lines of principal curvature. The mesh that was produced during form finding and/or shape optimization, could already have been generated with some or all of these criteria in mind (as in Chapter 12). Geodesic lines can be plotted between the end points of continuous lines in the mesh to update the mesh, or as suggested by Barnes (1999), found during the initial form finding. Then, the end points can be shifted such that the distribution of mesh widths becomes more uniform (Figure 7.9). The patterns in Figure 7.8 were generated in this manner.

The fabric surface is then unrolled, using a geometric, area-preserving approach, by simple subdivision, triangulation and flattening. The degree of subdivision is increased until the difference between surface areas of the flattened pattern and the original doubly curved surface are within a certain tolerance (Figure 7.8). For a fabric formwork, the cutting patterns must be compensated to account for the amount of

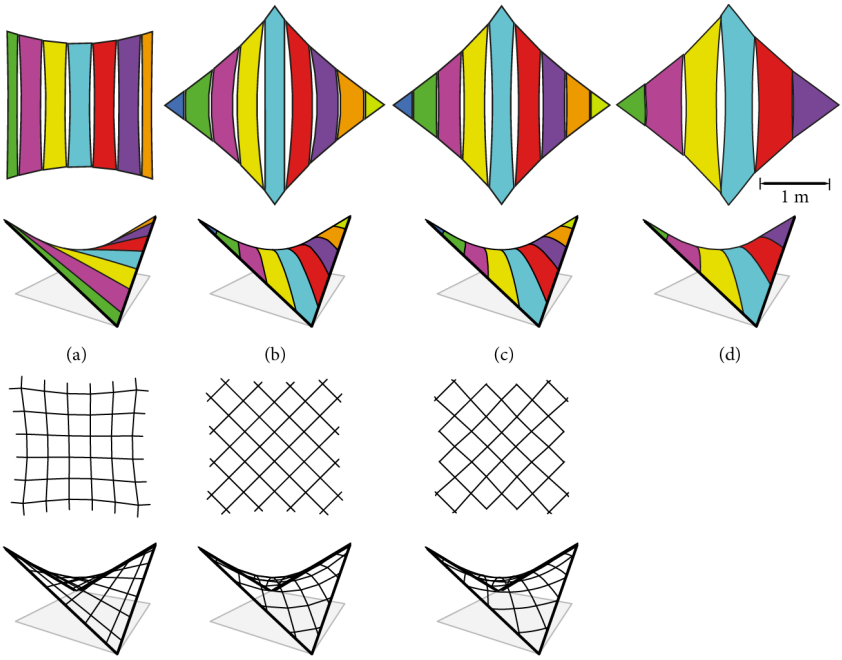

Figure 7.8: Saddle shapes with fabric or cable-net cutting patterns, (a) along straight line generators, (b) along 45 degrees, (c) along geodesics and (d) coarser version used for the prototype in Chapter 10.

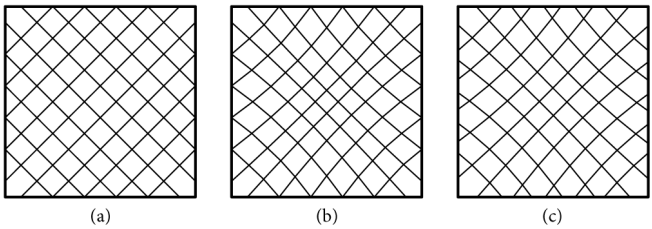

Figure 7.9: Mesh generated as orthogonal, quadrilateral mesh, redrawn along geodesics and optimized for average mesh width.

stretch, which can be done once a material model for the fabric is chosen (Section 7.6). Moncrief & Topping (1990) and Bletzinger et al. (2009) discuss more precise constrained and mechanical patterning methods used to define the fabric strips, to develop them and compensate them for stresses.

For a hybrid cable-net and fabric formwork, the fabric strips can be aligned along the arching cables (rather than the hanging ones). In this way, the strips can simply be placed over the cable net without the possibility of sliding down. Stress compensation is not necessary, if the fabric is simply laid onto the cable net and allowed to sag.

If sagging is not preferred, then no amount of prestressing of the fabric itself will entirely avoid this. Instead, an additional finishing layer is required after removing the formwork, or concrete has to be applied from both sides (see Section 3.7.3). Alternatively, the fabric can be replaced or infilled by another material that can be shaped, such as foam (see Section 3.7.4).

7.4 Target loads

To determine the forces in the formwork surface, the applied concrete loads are approximated by point loads, applied to vertices of a mesh. The mesh represents the cable net or fabric surface. The vertices may coincide with the actual nodes in the net (as in Chapter 12). Each load is assumed to correspond to the tributary area of its associated vertex. The tributary areas are based on the dual diagram of the mesh. Each face of the dual is planarized, and then extruded by the required thickness of the shell (Figure 7.10).

For a cable-net and fabric formwork, the fabric will sag between the cables, locally increasing the shell's thickness. This additional concrete can be considered non-structural, but adds to the loads on the formwork. Modelling the sag requires further refinement of the mesh, and, since the cutting patterns and their orientations are given, some form of large-displacement finite element analysis. This can be computationally expensive, especially for parametric design or in an optimization process. Figure 7.10 shows such a model, in which an attempt was made to reduce computational cost using a simplified spring mesh (Van Gelder 1998) instead of constant strain triangle elements. Ultimately, it was decided to avoid this step entirely, by simply adding an additional weight to the target loads, as an average representation of the weight due to sagging. This was a reasonable assumption due to the relatively uniform spacing of the cables.

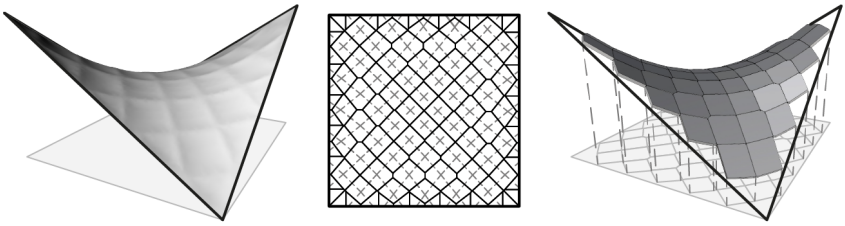

Figure 7.10: Saddle surface with fabric sagging between cables due to the applied concrete, dual diagram of the cable network and approximate target loads per cable node.

7.5 Least squares fitting

For the given formwork surface geometry and applied concrete loads, a least squares method, or best-fit optimization is then used to find the unknown internal forces or stresses (Chapter 6). If an exact answer cannot be found, the best possible fit is accepted. If the geometry deviates too much, the original analysis has to verify whether the performance of the shell has changed too much. In Section 12.2.6 the fitting itself was an additional objective in the overall optimization. This was done to maintain a computationally less costly bounded linear least squares calculation, rather than use nonlinear least squares. The underlying assumption was that a more reasonable fit produced by linear least squares would already give an indication of geometries that are more easily constructed using a flexible formwork.

Figure 7.11 shows forces under concrete load for the same surface, but with different cable-net geometries, to validate some of the criteria in Section 7.3. They are an orthogonal net, one based on the offset wire method (Section 3.7.3), and one approximately aligning with principal curvatures, with the latter revealing the lowest required forces, to generate the same shape. The orthogonal net would have infinite forces on a hypar, but the optimized shape (Figure 7.5) has a slight curvature, allowing us to find a solution.

For a fabric formwork, the stresses can be calculated immediately, once the local orientation of the elements is mapped from the geometrically flattened patterns to those on the three-dimensional surface. The mesh has to be refined in order to produce a reasonable resolution (Figure 7.12). However, triangle elements along the boundaries that have two fixed vertices produced illogical stress results. This is because the triangle edge between those fixed vertices can have an arbitrary natural force density. Furthermore, the results were found to be highly sensitive to the quality

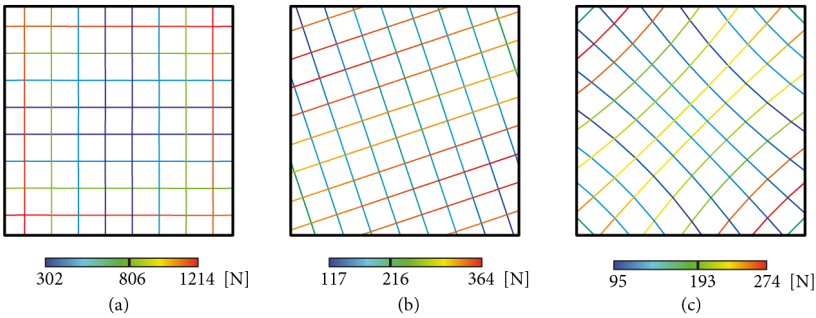

Figure 7.11: Saddle shapes with forces after casting from best-fit optimization, for (a) orthogonal, (b) offset, and (c) principal curvatures net.

and uniformity of the particular mesh. As a result, the fabric stresses in Chapter 11 are derived from a discrete network of elements, using the cable-net analogy (Gründig et al. 2000, Ströbel 1995). This approach is substantially faster, suitable for early design stages, and is fairly common practice in the engineering of tensioned membrane roofs.

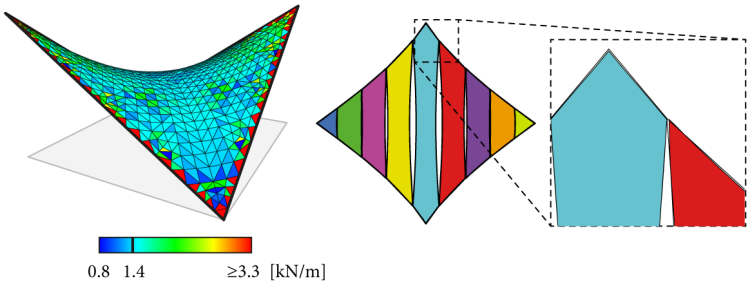

Figure 7.12: Saddle with fabric stresses after casting and compensated cutting patterns for construction.

7.6 Materialization

Having determined the forces or stresses after casting, we wish to know the forces or stresses prior to casting in order to construct and prestress our formwork. This is only possible by relating both states, before and after casting, through material deformation. By choosing material and section properties, it is possible to calculate the initial geometry of the cables and fabric, allowing us to compensate for the prestress.

From equations (4.14) and (4.20), we know that for a linear elastic cable

$$\mathbf{q} = \mathbf{L}^{-1}\mathbf{f} = \mathbf{EA}(\mathbf{l}_0^{-1} - \mathbf{l}^{-1}). \tag{7.1}$$

After choosing a material and cross-section, with an axial stiffness EA, the initial lengths $\mathbf{l}_0$ can directly be computed from the forces $\mathbf{f}$ and lengths $\mathbf{l}$ in the final state (Linkwitz 1999):

$$\mathbf{l}_0 = \left(\mathbf{I} + (\mathbf{EA})^{-1}\mathbf{F}\right)^{-1}\mathbf{l}, \tag{7.2}$$

where $\mathbf{I}$ is an identity matrix of size m, and $\mathbf{EA}$ and $\mathbf{F}$ are diagonal matrices of all stiffnesses EA and the forces $\mathbf{f}$ respectively.

For an isotropic, linear elastic fabric, the constitutive model is given by equation (4.48) with (4.50). The strain is given by equation (4.52) with (4.53). Rewriting equation (4.53), the squared initial lengths are

$$\mathbf{L}_0\mathbf{l}_0 = \mathbf{Ll} - \frac{2}{A}\mathbf{HD}^{-1}\mathbf{H}^{\mathrm{T}}\mathbf{q}, \tag{7.3}$$

and by taking the square root, we have found the initial lengths $\mathbf{l}_0$, which allow us to calculate the compensated cutting patterns and also deform to the prestressed state.

Galliot & Luchsinger (2009) discuss symmetric and non-symmetric orthotropic constitutive matrices that are more often used for the analysis of tensioned membrane structures. They also present their own orthotropic constitutive matrix, which is nonlinear with respect to the ratio of warp and weft stresses. Notice that any material

model, no matter how complicated, can be introduced instead of the orthotropic model to compute the initial lengths, at very little cost. The real computational cost occurs in the next step if other loading states, such as the prestressed, initial state, are calculated.

7.7 Prestress calculation and compensation

From the final state geometry, and the prescribed material model and resulting initial lengths, it is now possible to compute the intermediate geometry and forces or stresses prior to casting. This is the actual geometry that is to be constructed. In this situation, the fresh concrete has not been applied yet, so assuming the selfweight of the formwork to be negligible compared to the prestresses, we simply remove the loads when computing the residual forces and attempt to find a new equilibrium shape. This requires finite element analysis that allows for the prescription of initial geometry or corresponding strains. Figure 7.13 shows that the range of forces has decreased for the unloaded, initial state. At this point, the cables can be dimensioned.

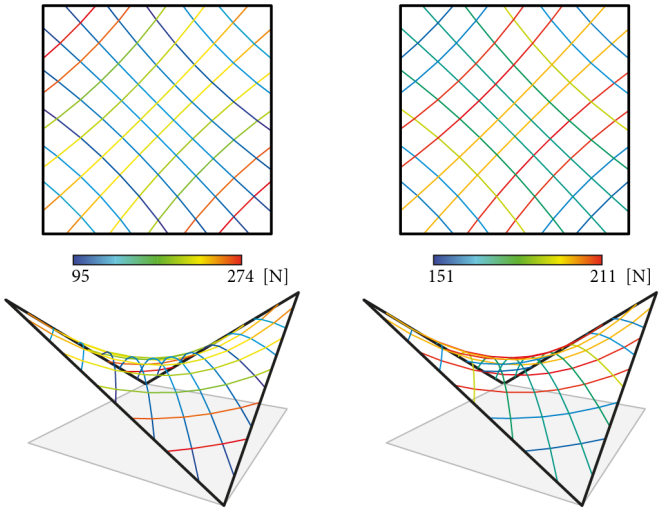

Figure 7.13: Saddle shape with cable forces after and before casting. The former state is also shown in Figure 7.11. The range of prestresses is smaller in the latter state.

For a fabric, the patterns can be compensated for the stress (Figure 7.12). At this point, discrepancies occur between the geometry and orientation of the elements in the flattened two-dimensional and the three-dimensional states, and Bletzinger et al. (2009) discuss the resulting deviations between the actual stresses and those prescribed during form finding. These deviations are neglected in engineering practice for tensioned membrane roofs, but Bletzinger et al. (2009) propose to iteratively couple form finding and patterning in a manner that reduces these deviations.

7.8 External frame

Finally, the external frame can be designed and analyzed by applying the reaction forces from the least-squares fitting and the prestress calculation as two load cases. These correspond to the formwork system before and after applying concrete. The reaction forces can be calculated according to equation (5.36) for any given set of force densities $\mathbf{q}$ and nodal coordinates $\mathbf{x}$ that describe a network in equilibrium.

The entire process assumes that the concrete can be applied relatively quickly and uniformly, otherwise intermediate states should be checked including the effect on the resulting shape. It would have been possible to include the frame in the earlier form-finding process, but this is outside the scope of the present thesis. Such a combination of form finding and structural analysis is not unusual in the design of tensioned membrane roofs in which the fabric is not materialized yet, but steelwork at the boundaries is.

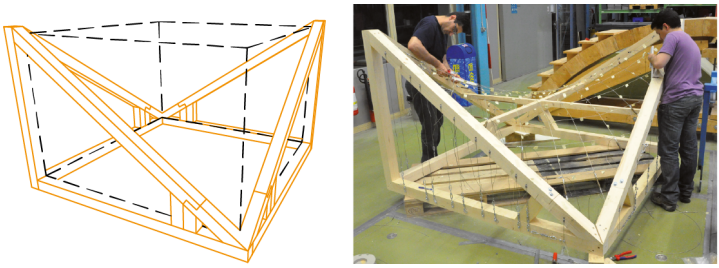

Figure 7.14: External frame design and construction of prototype (see Chapter 10).

7.9 Conclusions

This chapter has outlined a computational design process to develop a thin concrete shell structure, and to compute the stress states and cutting patterns of a flexible fabric and/or cable-net formwork for that shell geometry and corresponding concrete weight. The process includes form finding for shape generation (Chapter 5), least squares to determine forces under load of the concrete (Chapter 6), and simplified reduction factors to include geometric and material nonlinearities during shape optimization (to be discussed in Chapter 8). The initial mesh geometry from shape generation can, if adhering to proposed design criteria for the formwork, be maintained (possibly subdivided) throughout the entire process, all the way to producing the final reaction forces on the external frame. This simplifies the amount of data that is produced and transferred while avoiding reparameterization. This concept is applied to Chapters 11 and 12.

Specific contributions are :

- the formulation of design criteria for the fabric and/or cable-net topology and geometry;
- the concept of calculating prestresses in the final state, and materializing before finally calculating prestresses prior to casting; and,
- the observation that conclusions drawn by Lee & Hinton (2000*a*) and Reitinger & Ramm (1995) for synclastic shells apply to anticlastic ones as well:
  - without including thickness variables the load factor λ can actually reduce when optimizing for strain energy, and
  - when including imperfections and optimizing for the load factor λ_{imp}, the corresponding load factor without imperfections λ can actually reduce, meaning the two do not necessarily correlate.

Structural engineering is the art of moulding materials we do not wholly understand into shapes we cannot fully analyse, so as to withstand forces we cannot really assess, in such a way that the community at large has no reason to suspect the extent of our ignorance.

— Alexander Robert Dykes, 1976, paraphrasing Brown (1967)

CHAPTER EIGHT

Structural engineering

Shell structures have been defined as "constructed systems described by thin, three-dimensional, curved surfaces, in which one dimension is significantly smaller compared to the other two" (Adriaenssens et al. 2014*b*). Structural shells exhibit membrane behaviour when they resist (out-of-plane) loading through in-plane stresses rather than bending stresses. Such membrane action is achieved through sufficient curvature. These curvatures can be monoclastic (e.g. barrel vaults), synclastic (e.g. domes), anticlastic (e.g. hypars), or a combination thereof. In pure membrane action, the entire section of the shell is used. This makes for efficient use of material, particularly if the shape and thickness of the curved shell is optimized to maximize this behaviour everywhere.

However, Bletzinger & Ramm (2014) warn that optimized systems become "extremely sensitive to a change of these parameters or even other circumstances not considered. Optimization often is a generator of instabilities and imperfection sensitivities." The structural rigidity of shells in fact prevent them from visibly deforming, giving little warning prior to sudden buckling failure. For this reason, Ramm & Schunk (2002) have referred to shells as the "prima donna" of all structures.

In light of these sensitivities, the International Association for Shells and Spatial Structures (IASS) issued recommendations for the structural analysis of shells (Medwadowski et al. 1979), here referred to as "IASS 1979". This chapter lays out the procedure from IASS 1979, mostly based on surrounding literature and relevant building codes, as the recommendations themselves provide insufficient information. The main purpose is to provide a complete mathematical model to allow for parametric implementation and thus design of thin concrete shell structures.

Section 8.1 lists details and references on collapsed shell structures, summarizing common causes for failure. Section 8.2 establishes ranges of typical dimensioning values for shell structures. Section 8.3 briefly explains serviceability and ultimate limit states. These concepts are central to limit state design (LSD), which is the common approach in contemporary engineering. Another state, the critical limit state, is proposed in order to incorporate IASS 1979 recommendations, which are still based on outdated allowable stress design (ASD). Sections 8.4 and 8.5 present the factor of safety λ_s and knockdown factor γ_k, which are traditionally used in shell design to safely account for various nonlinear effects, by applying them to the linear critical buckling load, discussed in Section 8.6. Section 8.7 discusses the overall stability analysis according to IASS 1979, which individually considers each type of nonlinear effect, together determining the knockdown factor. Based on typical values, a lower limit of the safety and knockdown factor is given in Section 8.8, before drawing conclusions in Section 8.9.

8.1 Failures

Literature on failed shell structures is sparse. Ramm (1987) lists known failures of reinforced concrete shells. These and other references generally indicate that creep, imperfections, wind or some combination thereof are primary causes for failure (Table 8.1). Godoy (1996) in fact devotes an entire book to the significance and influence of imperfections in shells. This underlines the need to carefully consider these effects during the analysis of a shell.

For this thesis, failed hypar roofs are particularly relevant to consider. Gallegos-Cazeres & Schnobrich (1988) claim that the examples shown in Figure 8.2 collapsed due to creep, exacerbated by their shallow design.

Project, location	Type	Year	Age [yrs]	Causes and effects	Reference
single-curved					
Cottbus, Germany	barrel vault	1934		creep	Hines & Billington (2004)
Terminal 2E, Charles De Gaulle Airport, Paris, France	elliptical vault	2004		creep, thermal expansion of embedded steel	Raphael et al. (2012*a*)
domes					
Fairvale High School, Sydney, Australia	airformed dome	1975	0	thermal gradients, creep	
Pittwater High School, Sydney, Australia	airformed dome	1986	10	imperfections due to deflation during construction, cracking, thermal gradients, reinforcement failure	Bini (1991), Grad (1991)
Nucor iron ore plant, LA, US	airformed dome	2013	0		
ellipsoid					
Hungary	concrete shell	1954	2	creep or shrinkage, snow	Csonka (1956)
Latin America	concrete shell	1975	0	imperfections, concrete quality	Ballesteros (1969)
Sporthalle or "Knick-Ei", Halstenbek, Germany	steel gridshell	1997, 1998	0	imperfections	Baitsch (2003)
hypars					Gallegos-Cazeres & Schnobrich (1988)
Dallas, TX, US	inverted umbrella	1960	0.4	creep	ENR (1960)
Tucker High School, Henrico County, VA, US	gabled roof	1970	8	creep	ENR (1970)
Airport terminal, Cheyenne, WY, US	saddle shell	1975	15	creep	ENR (1975)
Kongresshalle, Berlin, Germany		1980	23	reinforcement corrosion, design flaws, construction defects	Buchhardt et al. (1984)
cooling towers					Bamu & Zingoni (2005)
Ferrybridge Power Station, Yorkshire, UK	three hyperboloids	1965		incorrect wind loading, reinforcement failure, inadequate factor of safety	
Ardeer Nylon Works, Scotland, UK	hyperboloid	1973		moderate wind, reinforcement yielding, imperfections	
Centrale thermique de Bouchain, France	hyperboloid	1979	10	minimal wind, imperfections, deterioration	
Fiddlers Ferry Power Station, Lancashire, UK	hyperboloid	1985	0	wind, imperfections	

Figure 8.1: List of structural failures and causes of shell structures.

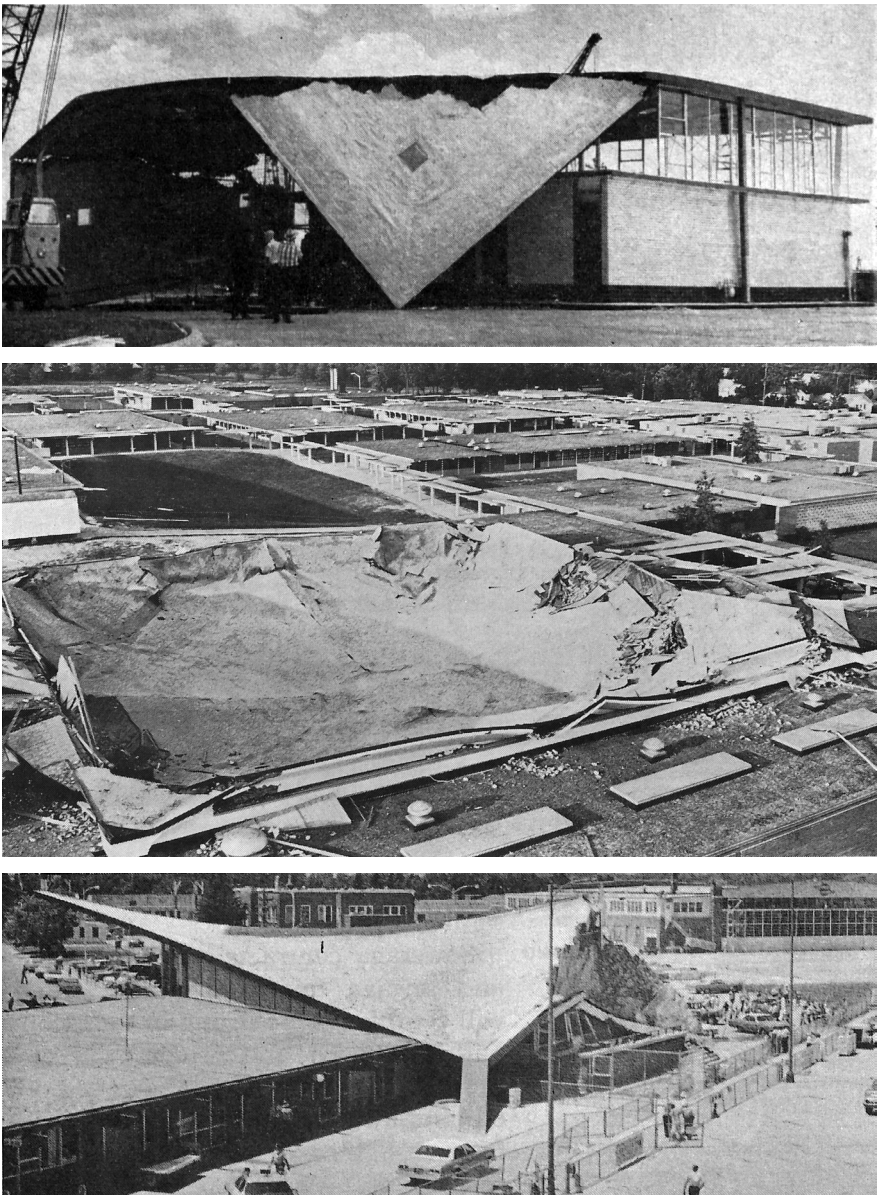

Figure 8.2: Collapsed hypar roofs, injuring 0, 8 and 18 people respectively (ENR 1960, 1970, 1975), attributed to creep by Gallegos-Cazeres & Schnobrich (1988).

8.2 Dimensions

Based on existing shell structures, building codes, recommendations and other literature, it is possible to define typical ranges of dimensioning values. This section discusses the thickness, rise, span of shells, their ratios, slenderness and shallowness, and reinforcement ratios. These ranges are used in Section 8.8 and for computational results in Chapter 11.

8.2.1 Span

As mentioned in Section 3.8.1, Félix Candela and Heinz Isler believed the upper economical limit for the span of thin concrete shells to be between s = 30 and 90 m. Pneumatically formed domes have been constructed up to 100 m (Figure 3.31). The largest built concrete shell is the double-layered shell roof for the Centre des Nouvelles Industries et Technologies (CNIT) in La Défense, Paris, France, with a span of 218 m (Figure 8.3). The 1976 Kingdome in Seattle, US, was the largest ever concrete dome with a span of 201 m (Figure 8.3). The ribbed dome consisted of 127 mm thick, hyperbolic paraboloid segments. By the 1990s, its location was economically undesirable, and combined with roof leaks and collapsing ceiling tiles, the decision was made to demolish the unpopular Kingdome in 2000.

8.2.2 Thickness

In absolute terms, Candela constructed some of the thinnest shells, often 40 mm, and, in the case of the hyperbolic paraboloid segments of the Cosmic Rays Pavilion, as little as 15 mm (Figure 8.4). Flexibly formed shells have been constructed between 10 and 135 mm. IASS 1979 mentions that shells as thin as 25 mm have been constructed, but suggest 50 to 100 mm as a practical range for placing and covering reinforcement. For shells thinner than 80 mm, it recommends to subtract 10 mm in the calculations to account for construction errors.

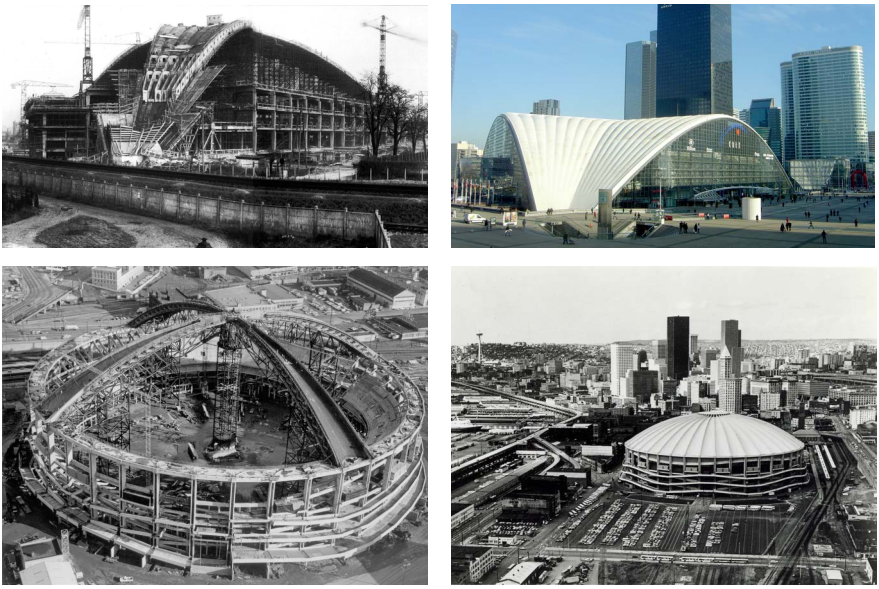

Figure 8.3: Longest span concrete dome and concrete shell: the 218 m span CNIT shell, Paris, France, 1958; and the 201 m span Kingdome, Seattle, Washington, US, 1976–2000.

Figure 8.4: The 15 mm thick, 10.75 m span Cosmic Rays Pavilion, Mexico City, 1951.

8.2.3 Slenderness

Although there is no official rule as to how thin a thin shell has to be, Chen (2014) suggests a ratio of span to thickness s/t between 30 and 4000. Figure 3.53 shows s/t for flexibly formed concrete shells to be between c. 50 and 750. The globally mono- or synclastic Ctesiphon shells and the synclastic shells by Isler have a ratio of about $s/t = 360$, while the thinnest hypars and the anticlastic shells by Candela about $s/t = 750$.

8.2.4 Shallowness

The ratio of span to rise s/h, or shallowness, for flexibly formed shells is between 2 and 5 (Figure 3.53). In the context of hypar roofs, Gallegos-Cazeres & Schnobrich (1988) define shallowness by two criteria,

$$\frac{s_2}{h} \geq 5 \tag{8.1}$$

and

$$\frac{s_1}{t} \cdot \frac{s_2}{h} < \begin{cases} 1000/3 & \text{for saddle roofs or umbrellas, and} \\ 800 & \text{for gable roofs,} \end{cases} \tag{8.2}$$

where h is the rise, t is the thickness, s_1 is the first, larger span, and s_2 is the second, smaller span. The second criterion in fact is a combination of shallowness and slenderness. Gallegos-Cazeres & Schnobrich (1988) suggest that shallow shells with edge beams cannot be accurately modelled by membrane theory, and are more susceptible to creep and shrinkage. Note that the flexibly formed shells in Figure 3.53 do not meet these criteria for shallowness.

8.2.5 Reinforcement ratio

IASS 1979 recommends that the minimum area of reinforcement in one direction is $\mu_{rc} = 0.20$ %, and the minimum sum of areas of both directions is 0.60 %. The maximum reinforcement ratio,

$$\mu = \begin{cases} 0.6 \cdot \dfrac{f_{ck}}{f_y} & \text{for } f_{ck} < 28 \text{ N/mm}^2; \\ \dfrac{16.8}{f_y} & \text{for } f_{ck} \geq 28 \text{ N/mm}^2. \end{cases} \tag{8.3}$$

For ferrocement shells, Naaman (2000) recommends a much higher minimum total volume fraction of $\mu_{rc} = 1.80$ %. Based on the above proportions, the minimum area of reinforcement in one direction could be $\mu_{rc} = 0.60$ %. Alternatively, he suggests a minimum reinforcement ratio,

$$\mu_{rc} = \frac{1}{f_y/f_{ctm} + 1 - n}, \tag{8.4}$$

where f_y is the ultimate strength of the reinforcement, assumed here to be equal to the yield strength, f_{ctm} is the cracking tensile strength of the concrete, assumed to be the mean value, and the ratio of Young's moduli for the steel and concrete,

$$n_{rc} = \frac{E_s}{E_{cr}}, \tag{8.5}$$

where E_{cr} is a reduced modulus due to creep according to equation (8.32). According to Eurocode EN 1992-1-1:2004,

$$f_{ctm} = \begin{cases} 0.30\,(f_{ck})^{2/3} & \text{for } f_{ck} \leq 50 \text{ N/mm}^2, \text{ and} \\ 2.12 \ln\left(1 + \dfrac{f_{ck} + 8}{10}\right) & \text{for } f_{ck} > 50 \text{ N/mm}^2. \end{cases} \tag{8.6}$$

8.3 Limit states

Limit state design (LSD) is a standard design approach used in structural engineering. Beyond a limit state, a structure no longer satisfies certain design criteria. Eurocode EN 1990:2002 defines two types of limit states. Here, a third limit state for shell structures is also defined, based on IASS 1979. Each is discussed in the following subsections.

The recommendations are still based on allowable stress design (ASD), an engineering approach that has been largely replaced by LSD. The third limit state is a temporary, conservative measure, to be used until these recommendations are conformed to LSD. An update of IASS 1979 could be done on the basis of EN 1993-1-6:2007, a Eurocode for the design of thin steel shell structures.

Generally, it does not make sense to combine both approaches, and would lead to the most conservative result. However, due to the lack of an accepted contemporary engineering practice for shells, ASD or a mixed approach is the current state-of-the-art, applied to built concrete shells such as the Rolex Learning Center in Lausanne, Switzerland (Grohmann et al. 2009), the Centro Ovale in Chiasso, Switzerland (Muttoni et al. 2013), and the Teshima Art Museum in Japan (Sasaki 2014) (see Section 8.4.1). On the other hand, the Oceanografic Centre in Valencia, Spain, simply applied LSD based on Spanish building code (Domingo et al. 1999, 2004).

8.3.1 Serviceability limit state

The serviceability limit state (SLS) concerns "the functioning of the structure or structural members under normal use, the comfort of people, and the appearance of the construction works". In SLS, a structure needs to meet criteria for deformations. This includes the crack width of concrete. Partial factors for loads and material strength are generally 1. IASS 1979 claims that given the large variety of possible shell geometries, no universally allowable displacements can be defined. Instead, it recommends to avoid unsightly sagging, prevent cracking, ensure connection tolerances and proper drainage.

8.3.2 Ultimate limit state

The ultimate limit state (ULS) concerns "the safety of people, and/or the safety of the structure". In ULS, a structure needs to meet criteria for stability, strength, fatigue and (excessive) deformations. Both load and material factors are taken into account, and unlike ASD, material strength is assessed beyond elastic limits. For steel shells, EN 1993-1-6:2007 defines four ultimate limit states: one to assess plasticity; two for types of cracking due to cyclic loading; and, a fourth for buckling. The buckling limit is based on imperfections and buckling reduction factors specific to the geometry

and material of thin steel shell structures, so its application to thin concrete shells is not immediately obvious. For now, the next section proposes a new limit state based on IASS 1979 to deal with stability of the shell, referred to as the critical limit state (CLS).

8.3.3 Critical limit state

IASS 1979 requires the structural engineer to perform a stability analysis, based on unfactored loads p and material properties. An initial buckling load is calculated and then modified through several reduction factors to obtain a critical load (capacity) $p_{\mathrm{cr}}^{\mathrm{plast}}$. The resulting factor of safety,

$$\lambda_{\mathrm{s}} = \frac{p_{\mathrm{cr}}^{\mathrm{plast}}}{p}, \tag{8.7}$$

effectively means the factor by which an SLS load combination can be multiplied before significant loss of stability occurs. This definition is very similar to that of the (buckling) load factor λ, explained in 7.2.2. While the factor of safety assumes that certain nonlinear effects have been taken into account, the term load factor is ambivalent and already applies to critical loads obtained by linear buckling analysis. The factor of safety can also be viewed as a partial factor or safety factor for a new limit state,

$$\lambda_{\mathrm{s}} \cdot p \leq p_{\mathrm{cr}}^{\mathrm{plast}}, \tag{8.8}$$

to simply verify that the critical load capacity has not been reached. Note that the load has to be applied incrementally in a nonlinear analysis to obtain a realistic view of the shell's load capacity. IASS 1979 in fact uses both meanings for the factor of safety interchangeably: it can be the load factor that the structure actually achieves, as in equation (8.7), but also a safety factor that the structure has to meet, as in equation (8.8). Here, the former will be referred to as the load factor λ, and the latter as factor of safety λ_{s}.

The load p is referred to as the "real load" or "shell load" in IASS 1979, but is not further explained. This creates a significant gap in understanding, as one might think this is the shell's weight, possibly including any dead loads. A first hint is provided by Dulácska (1981), who denotes this load as $p_{\mathrm{cr}}^{\mathrm{real}}$, implying it is some kind of critical load. Furthermore, an example calculation by Kollár & Dulácska (1984) includes both self-weight and snow load, revealing that p is likely meant to be, or can be interpreted as, any governing SLS load combination.

8.4 Factor of safety

According to IASS 1979, the value of the factor of safety λ_{s} in equation (8.7) is 1.75 if the critical load increases in the post-buckling range, and a minimum of 3.50 if post-buckling behaviour governs (Figure 8.5). Section 8.4.2 discusses how to establish behaviour.

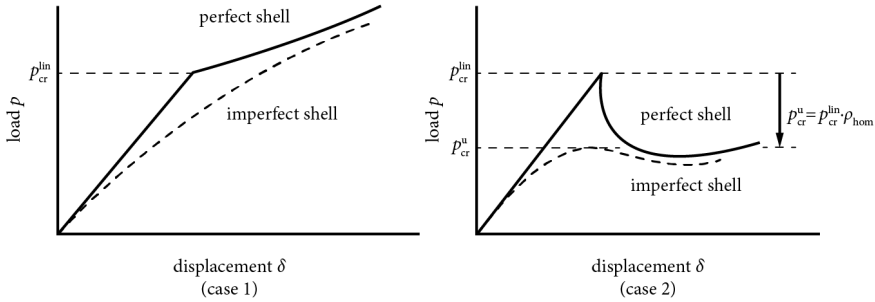

Figure 8.5: Post-buckling behaviour with increasing (case 1) and decreasing (case 2) capacity of the shell after buckling. Adapted from IASS 1979.

The underlying literature by Kollár & Dulácska (1984) as well as subsequent recommendations for revision of IASS 1979 by Dulácska (1981, 1986) and Dulácska & Kollár (1995) describe lower factors of safety (Table 8.1). Dulácska (1986) clarifies that IASS adopted slightly more conservative values from the 1972 German code DIN 1045.

The factor of safety for shells with decreasing post-buckling capacity is based on experimental data on axially compressed cylinders or radially compressed spheres. For shells that decrease at a lower rate, Dulácska (1981) recommends to interpolate between the values in Table 8.1, so that

reference	increasing λ_{incr}	constant λ_{const}	decreasing λ_{decr}
Kollár & Dulácska (1984)	1.75	2.50	3.00
IASS 1979	1.75	-	3.50
Dulácska (1981)	1.75	2.50	3.00
Dulácska (1986), Dulácska & Kollár (1995)	1.50	2.35	3.00

Table 8.1: Factor of safety according to IASS1979 and surrounding literature, depending on whether post-buckling capacity increases, is constant or decreases.

$$\lambda_{\text{s}} = \lambda_{\text{const}} + (\lambda_{\text{decr}} - \lambda_{\text{const}}) \frac{1 - \rho_{\text{hom},0.5}}{0.75}, \tag{8.9}$$

where factor $\rho_{\text{hom},0.5}$ is explained in Section 8.7.1.

Alternatively, Dulácska & Kollár (1995) suggest that the factor of safety can be determined by the ratio between the plastic failure load under central compression, without buckling, and the critical linear buckling load $p_{\text{p}}/p_{\text{cr}}^{\text{lin}}$. This means that if plastic failure occurs much sooner than buckling, $p_{\text{p}}/p_{\text{cr}}^{\text{lin}} \approx 0$, and the safety factor $\lambda_{\text{s}} = 1.50$, or vice versa, if $p_{\text{p}}/p_{\text{cr}}^{\text{lin}} = \infty$, then $\lambda_{\text{s}} = 3.00$. Dulácska & Kollár (1995) provides a table with a few intermediate values. A curve fit of these values, proposed here, is the following generalized sigmoid function,

$$\lambda_{\text{s}} = \lambda_{\text{decr}} - (\lambda_{\text{decr}} - \lambda_{\text{incr}}) \cdot \frac{1}{1 + (1.17 \cdot p_{\text{p}}/p_{\text{cr}}^{\text{lin}})^{1.88}}. \tag{8.10}$$

where,

$$p_{\text{p}} = \frac{1.6 \cdot f_{\text{ck,cube}} \cdot t}{R}, \tag{8.11}$$

Depending on the situation, either approach may yield a lower factor of safety than the other.

8.4.1 Recent projects

For reference, Table 8.2 shows achieved margins of safety for several recent thin concrete shells. The factor for Tomás & Martí (2010*b*) was calculated by dividing the reported values for the linear and nonlinear buckling load factors of 8.7 and 2.6.

The Centro Ovale is implied to meet IASS 1979 requirements, but Muttoni et al. (2013) and correspondence with Fernández Ruiz (2016) do not provide sufficient information to verify this independently. It is not immediately clear whether the other structures satisfy IASS 1979 and the revision by Dulácska (1981), because, apart from Sasaki (2014), they do not report the required minimum factor of safety, and, apart from Grohmann et al. (2009), they do use load combinations including both permanent and variable load.

Sasaki (2014) determines the load factor in two ways, both of which may not actually conform to IASS1979, likely owing to confusion surrounding its (lack of) definition of the "real load" p to which the load factor applies (see Section 8.3.3).

On a similar note, Grohmann et al. (2009) did not use IASS1979, but were recommended to achieve a load factor of 3.0 by engineer Jörg Schlaich, presumably based on Dulácska (1981). Their resulting argument for accepting a factor λ of 2.8, "due to the high percentage of permanent loads compared to the variable loads" is actually not valid, since the factor of safety λ_s does not distinguish between both types of loads (although perhaps it should). However, a factor of safety of 3.0 is based on the imperfection sensitivity of a sphere or axially loaded cylinder, whereas a laterally loaded cylinder might me more apt to approximately describe the geometry of the Rolex Learning Centre. This results in a factor of safety $\lambda_s = 2.7 < 2.8$, meaning the structure does in fact satisfy IASS 1979.

8.4.2 Post-buckling behaviour

The factor of safety λ_s according to equation (8.9) requires us to establish the type of post-buckling behaviour, but IASS 1979 offers no guidance on how to do this.

Kollár (1969) and Kollár & Dulácska (1984) establish the behaviour by transforming a load-deflection diagram of an imperfect shell to a Southwell-plot, introduced by Southwell (1932). This method was originally developed to determine the theoretical buckling load of a perfect column, based on experimental load-deflection data on imperfect columns. The graph plots the ratio of the deflection over the load, δ/p,

Project	Load factor	Safety	Load	Reference
L'Oceanogràfic Entrance (ACHypar), Valencia, Spain, 2003	3.3		λ·self-weight	Tomás & Martí (2010*b*) (Figure 2.7)
Rolex Learning Centre, Lausanna, Switzerland, 2009	2.8	2.7*	λ·(permanent+variable)	Grohmann et al. (2009)
Teshima Art Museum, Kagawa, Japan, 2010**	5.2	3.0	λ·static	Sasaki (2014) (Figure 2.54)
	3.1	3.0	λ·seismic+static	
Centro Ovale, Chiasso, Switzerland, 2013**		1.75	λ·(permanent+variable)	Fernández Ruiz (2016) (Figure 2.3)
RWTH Aachen TRC Pavilion, Germany	9.1		λ·permanent	Scholzen (2014)

Table 8.2: Load factors λ, applied to load combination p, subject to factors of safety λ_s, for existing projects. *Factor of safety calculated here. **Explicitly used IASS 1979.

against the deflection δ. This normally produces a straight line whose slope is the theorical buckling load, but will deviate if post-buckling capacity increases or decreases, a phenomenon observed by Roorda (1967) and soon exploited by Kollár (1969) to establish factors of safety (Figure 8.6).

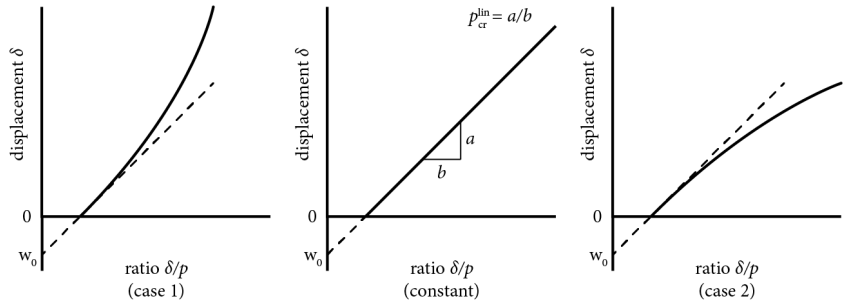

Figure 8.6: Southwell-plot for structures with increasing (case 1), constant and decreasing (case 2) post-buckling behaviour. Adapted from Kollár & Dulácska (1984).

Alternatively, the factor of safety λ_s according to equation 8.10, based on Dulácska & Kollár (1995), requires us the calculate the linear buckling load and the point at which plastic failure occurs. This could be done by evaluating the stress at the linear buckling load, and comparing that against the material's yield strength.

By comparison, the latter strategy is more suitable to parametric design, as the computational demand of calculating the linear buckling load and evaluating the corresponding stress is much lower than performing an incremental load analysis with third-order nonlinearity (post-buckling) of an imperfect shell shape.

Another theoretical option, which would still be computationally demanding, is to calculate the first several eigenvalues. A series of closely spaced eigenvalues is typically seen as an indication that a structure is imperfection sensitive (Chen 2014, Hoogenboom 2005). The implication that post-buckling capacity increases in that case still has to be verified. Moreover, there is no rule at present on how to distinguish post-buckling behaviour on this basis, but it is imaginable that the standard deviation of the eigenvalues, which indicate how closely spaced they are, could be used for such a purpose.

Finally, for early design purposes, one could simply assume whether post-buckling capacity is increasing, constant or decreasing based on similarity to known shell shapes.

8.5 Knockdown factor

Originally, without the aid of computers, it was only possible to calculate the theoretical linear buckling load of a perfect structure $p_{\mathrm{cr}}^{\mathrm{lin}}$. However, experimentally obtained critical buckling loads turned out to be far lower. Extensive experiments such as those carried out at NASA led to the definition of "correlation factors" to relate these theoretical and experimental values (Weingarten et al. 1968). Based on such observations, shell design manuals came to recommend the use of the following buckling formula (Arbocz 1987):

$$p \leq \frac{\gamma_{\mathrm{k}}}{\lambda_{\mathrm{s}}} p_{\mathrm{cr}}^{\mathrm{lin}}, \tag{8.12}$$

where γ_{k} reduces the theorical buckling loads, and is more commonly referred to as the knockdown factor. Dulácska & Kollár (1995) suggests that "the actual critical load of the shell is obtained in the following form":

$$p_{\mathrm{cr}}^{\mathrm{plast}} = p_{\mathrm{cr}}^{\mathrm{lin}} \cdot \rho_{\mathrm{hom}} \cdot \rho_{\mathrm{crp}} \cdot \rho_{\mathrm{rc}} \cdot \rho_{\mathrm{pl}}, \tag{8.13}$$

where $p_{\mathrm{cr}}^{\mathrm{lin}}$ is the linear critical buckling load, and the reduction factors:

ρ_{hom}	accounts for geometric imperfections;
ρ_{crp}	for creep of concrete;
ρ_{rc}	for cracking of concrete and the influence of the reinforcement; and,
ρ_{pl}	for plasticity.

If we accept equation (8.8), and then compare it to (8.12) and (8.13), we obtain

$$\gamma_{\mathrm{k}} = \frac{p_{\mathrm{cr}}^{\mathrm{plast}}}{p_{\mathrm{cr}}^{\mathrm{lin}}} = \rho_{\mathrm{hom}} \cdot \rho_{\mathrm{crp}} \cdot \rho_{\mathrm{rc}} \cdot \rho_{\mathrm{pl}}. \tag{8.14}$$

This would allow us to compute a preliminary knockdown factor γ_{k} as a composite factor of reduction factors ρ, without relying on experiments, or on a complex nonlinear analysis to directly compute $p_{\mathrm{cr}}^{\mathrm{plast}}$, instead computing only the linear critical buckling load $p_{\mathrm{cr}}^{\mathrm{lin}}$. This is relevant in an early design and optimization stage,

in which repeated nonlinear analyses might be too computationally demanding. Note that the final structural analysis should still rely on experimental or nonlinear analysis to assess the shell's strength and stability, as the knockdown factor has not been verified for arbitrary shell geometries.

8.6 Linear critical buckling load

Kollár & Dulácska (1984) offer equations to directly compute $p_{\mathrm{cr}}^{\mathrm{lin}}$ for domes, hypars and hyperboloids supported along their edges under uniform load. These can be used as benchmarks for numerical analysis, before applying it to arbitrary geometries, loading and boundary conditions.

For a spherical shell, subjected to radial pressure,

$$p_{\mathrm{cr}}^{\mathrm{lin}} = \frac{2}{\sqrt{3\left(1-\nu^2\right)}} \frac{E_{\mathrm{cr}} t^2}{R^2}. \tag{8.15}$$

For a square hypar under uniform load this load is the same, but multiplied by a factor ρ, which is a function of the slenderness a/t, and $\rho \approx 1$ for $a/t \geq 25$ which covers most conventional cases. If two or all four edges are only vertically supported, and no longer laterally, the linear critical buckling load decreases, where Kollár & Dulácska (1984) offer equations with coefficients in tabular form.

8.7 Stability analysis

Adopting IASS 1979 requires us to do one of two things: either calculate the initial buckling load, or critical load $p_{\mathrm{cr}}^{\mathrm{lin}}$, then modifying this load using the knockdown factor γ_{k}; or, directly calculate $p_{\mathrm{cr}}^{\mathrm{plast}}$ using a sufficiently refined computer model. In either case, the knockdown factor or model refinements should take into account the effects of

- geometric nonlinearity due to large displacements;
- deviations from the idealized shape (imperfections); and,
- material nonlinearity due to
  - plasticity of the concrete,

- creep (and shrinkage), and
- the effect of reinforcement and cracking.

In addition, the importance of including relevant thermal actions is stressed.

IASS 1979 establishes two cases depending on whether post-buckling behaviour governs or not, which determines the safety factor (Figure 8.5). For case 2, in which post-buckling behaviour governs, the effect of geometric imperfections and large displacements is taken into account by modifying the initial buckling load

$$p_{\mathrm{cr}}^{\mathrm{u}} = p_{\mathrm{cr}}^{\mathrm{lin}} \cdot \rho_{\mathrm{hom}}. \tag{8.16}$$

For case 1, $\rho_{\mathrm{hom}} = 1$. Then, to account for the effects of creep as well as reinforcement and cracking,

$$p_{\mathrm{cr}}^{\mathrm{u,reinf}} = p_{\mathrm{cr}}^{\mathrm{u}} \cdot \rho_{\mathrm{crp}} \cdot \rho_{\mathrm{rc}} = p_{\mathrm{cr}}^{\mathrm{lin}} \cdot \rho_{\mathrm{hom}} \cdot \rho_{\mathrm{crp}} \cdot \rho_{\mathrm{rc}}. \tag{8.17}$$

Finally, to account for the plasticity of concrete,

$$p_{\mathrm{cr}}^{\mathrm{plast}} = p_{\mathrm{cr}}^{\mathrm{u,reinf}} \cdot \rho_{\mathrm{pl}} = p_{\mathrm{cr}}^{\mathrm{lin}} \cdot \rho_{\mathrm{hom}} \cdot \rho_{\mathrm{crp}} \cdot \rho_{\mathrm{rc}} \cdot \rho_{\mathrm{pl}}, \tag{8.18}$$

arriving at equation 8.13 as defined by Dulácska & Kollár (1995). In the following sections, the individual reduction factors are discussed, as well as the effect of shrinkage, which IASS 1979 treats as a load case.

8.7.1 Effect of large displacements and imperfections

The reduction factor ρ_{hom}, which accounts for geometric nonlinearity and imperfections due to large displacements, is determined by calculating the ratio of the magnitude of the initial imperfection w_0 and the shell thickness t, and then applying the appropriate design curve (Figure 8.7). The initial imperfection w_0 consists of the calculable imperfection, or deflection, w_0' and accidental imperfection, or shape deviation, w_0''.

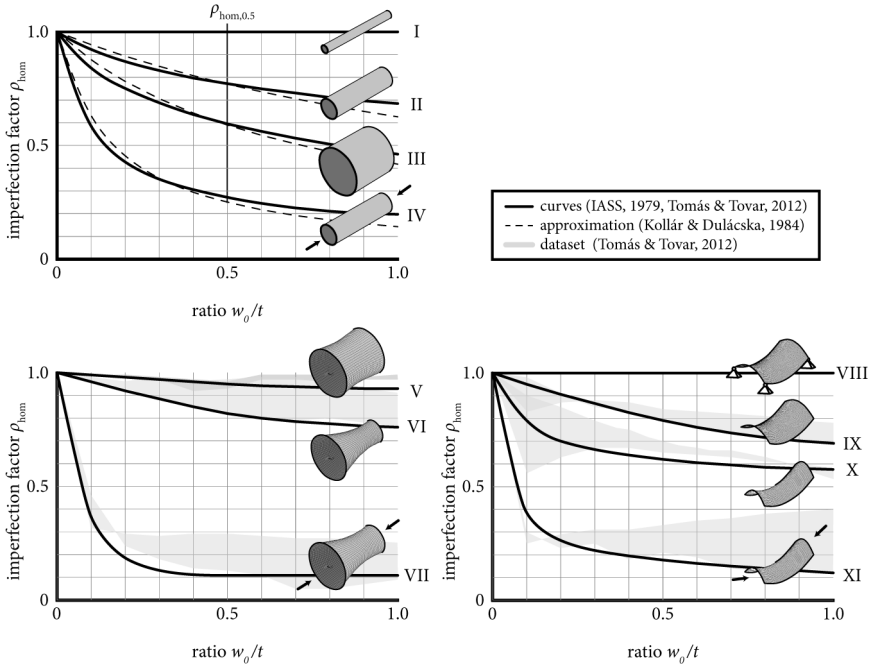

Figure 8.7: Curves to determine factor ρ_{hom} to account for geometric imperfection sensitivity of domes, cylinders (IASS 1979), hyperboloids and hypars (Tomás & Tovar 2012). See Table 8.3

The choice for a specific curve depends on the shape and boundary conditions of the shell, and IASS 1979 mentions that they are available in literature for a large number of shell geometries and configurations. In absence of other information, the lowest of the curves, the one corresponding to an axially compressed cylinder, is to be chosen, though Tomás & Tovar (2012) conclude this to be too conservative. Instead, they generated additional curves for circular barrel vaults, shallow domes, hyperbolic paraboloids and hyperboloids.

For a mathemical expression of reduction factor ρ_{hom}, Kollár & Dulácska (1984) claim that for $w_0/t \leq 1$ the curves can be "closely approximated" using

$$\rho_{\text{hom}} = \frac{1}{1 + 2\left(\frac{1}{\rho_{\text{hom},0.5}} - 1\right)\frac{w_0}{t}} \tag{8.19}$$

where the value of ρ_{hom} at $w_0/t = 0.5$,

$$\rho_{\text{hom},0.5} = \begin{cases} 1.00 & \text{for laterally compressed long cylinders,} \\ 0.77 & \text{for medium cylinders,} \\ 0.59 & \text{for short cylinders, and} \\ 0.25 & \text{for spheres and axially compressed cylinders.} \end{cases} \tag{8.20}$$

Figure 8.7 shows dotted lines based on equation (8.19) which only roughly approximate the actual curve, so new approximations are proposed here, both for the three curves from IASS 1979, and the curves for hyperboloids and hyperbolic paraboloids with governing boundary conditions by Tomás & Tovar (2012). The approximations are either exponential equations of the form

$$\rho_{\text{hom}} = a + b \cdot e^{c \cdot w_0/t}, \tag{8.21}$$

or sigmoidal equations of the form

$$\rho_{\text{hom}} = a + \frac{b - a}{1 + \left(\frac{w_0/t}{c}\right)^d}, \tag{8.22}$$

with parameters a, b, c and d defined in Table 8.3.

For vertical hyperboloids, not shown here, the curves are similar to that of a short cylinder. For hyperbolic paraboloids with clamped supports at the corners, a common boundary condition, $\rho_{\text{hom}} \approx 1$, suggesting that they are not sensitive to imperfections. Although Hoogenboom (2005) and Chen (2014) remark that hypars and negatively curved shells are less sensitive to imperfections, and become insensitive with sufficient curvature, the work by Tomás & Tovar (2012) does not seem to support this. A more thorough study of post-buckling behaviour of anticlastic shell geometries of increasing curvature would be required to answer this matter.

Calculable imperfection amplitude

The calculable imperfection w_0' is the calculated bending deflection of the shell or "computed or measured normal displacement before buckling".

Dulácska (1978) defines this imperfection for positively curved shells as

	geometry	load	coefficients				
		compression	a	b	c	d	$\rho_{\text{hom},0.5}$
I	long cylinder		1.00	0	0		1.00
II	medium cylinder	lateral	0.65	0.35	-2.25		0.77
III	short cylinder	lateral	0.45	0.55	-2.68		0.59
IV	cylinder	axial	0.23	0.77	-6.37		0.25
IV	sphere	radial	0.23	0.77	-6.37		0.25
V	medium hyperboloid	lateral	0.90	0.10	-1.42		
VI	long hyperboloid	lateral	0.70	0.30	-1.83		
VII	hyperboloid	axial	0.11	0.89	-12.14		
VIII	corner supports		1.00	0	0		
IX	wide hypar	lateral	0.62	0.38	-1.36		
X	narrow hypar	lateral	0.45	1.01	0.14	0.63	
XI	axial hypar	axial	0.05	1.01	0.04	0.80	

Table 8.3: Exponential or sigmoidal functions, with three or four parameters respectively, fit to curves from Figure 8.7 to account for geometric imperfection sensitivity. Long, medium and short cylinders and hyperboloids have $\frac{L^2}{Rt}$ = 10'000, 1'000 and 100 respectively. Wide and narrow hypars not defined by Tomás & Tovar (2012).

$$c\frac{R_2}{R_1}t, \tag{8.23}$$

where R_1 and R_2 are the radii of principal curvatures, and c is found in Table 8.4 and depends on the presence of lateral pressure in addition to uniform loading, and the boundary conditions. The shell with a square plan has edges that are supported by vertical diaphragms that still allow horizontal movement, so no lateral pressure develops. The dome is laterally supported at ground level, or has a tension ring that is not fully rigid.

boundaries	square plan	dome	dome
	without lateral pressure	with lateral pressure	with tension ring
hinged	0.2	0.1	0.2
clamped	0.1333	0.067	0.1333

Table 8.4: Coefficient c for calculable imperfection according to Dulácska (1978).

Alternatively, if the displacement is not known, the SLS deflection limits from code can be used as a very conservative estimate. For example, using Swiss code SIA 260:2003, deflections should be less than 1/500th of the span L or 1/300th of twice the length of a cantilever.

Accidental imperfection amplitude

The accidental imperfection w_0'' is due to erection inaccuracies and is the "amplitude of shape deviation" (Medwadowski et al. 1979, Tomás & Tovar 2012). If it is not specified by the contractor, Dulácska & Kollár (1995) suggest it is between $0.25t$ and $0.75t$, and Kollár & Dulácska (1984) that it is $R/3500$. Kollár & Dulácska (1984) also propose an equation that Medwadowski (2004) later revised (first term was $0.05t$) to

$$w_0'' = 0.1t + \frac{t\alpha_f}{2\left(1+\beta_s^{-2}\right)}, \tag{8.24}$$

where t is the shell thickness, the radius of curvature

$$R = \sqrt{R_1 R_2} = \sqrt{\frac{1}{\|K\|}}, \tag{8.25}$$

where K is the Gaussian curvature,

$$\beta_s = \frac{R/1000}{t}, \text{ and} \tag{8.26}$$

parameter α_f accounts for the type of formwork, with

$$\alpha_f = \begin{cases} 1 & \text{for rigid forms,} \\ 6 & \text{for slipforms, and} \\ 12 & \text{for air-supported forms.} \end{cases} \tag{8.27}$$

Initial imperfection amplitude

The combined effect of both imperfections is given in several forms: by IASS 1979 as $w_0' + w_0''$; by Dulácska (1981) as the maximum of $0.8w_0' + w_0''$ and $w_0' + 0.8w_0''$; and, by Kollár & Dulácska (1984) as the maximum of the latter and w_0''. The most recent recommendations by Kollár (1993) reflect the low probability that both imperfections occur at the same location on the shell, so that

$$w_0 = \sqrt{(w_0')^2 + 1.4w_0'w_0'' + (w_0'')^2}. \tag{8.28}$$

Imperfection shape

For numerical analysis, instead of a reduction factor, it is necessary to assume a shape of the imperfect shell with the imperfection as its amplitude. Ramm & Stegmüller (1982) suggest that "the geometrical imperfection can be based upon the buckling mode at the bifurcation load, on any postbuckling mode, on a combination of several modes or on realistic deviations of the ideal geometry occurring during the manufacturing process". Typically, buckling modes are used.

8.7.2 Effect of creep

Gallegos-Cazeres & Schnobrich (1988) claim that gabled roofs with shallow hyperbolic parabolas are particularly sensitive to time-dependent deformation, citing three specific instances of such structural failures (Section 8.1). They add that including creep and shrinkage can lead to 25-50 % reduction in load-carrying capacity and may increase in displacements by a factor of 4 to 8. For shells in general, IASS 1979 already mentions a factor of 2 to 3.

Dulácska & Kollár (1995) explain that

$$\rho_{\mathrm{crp}} = \frac{1}{1 + \zeta \cdot \varphi}, \tag{8.29}$$

where φ is the creep coefficient and ζ, introduced here in accordance with IASS 1979, is the ratio of long term loads p_0 to all loads. Kollár & Dulácska (1984) include some contribution of the short term stresses, rewritten here as loads p_t, such that

$$\zeta = \frac{p_0 + k_{\mathrm{crp}} \bar{\rho} p_t}{p_0 + p_t}, \tag{8.30}$$

with $\bar{\rho}$ between 0.5 and 1.0, but conservatively set to 1.0, and k_{crp} at time t is approximated here as

$$k_{\mathrm{crp}} = 0.5 + \frac{1.3}{2^{t/22.08}} \tag{8.31}$$

based on three values given by Kollár & Dulácska (1984).

The creep coefficient φ is the ratio of the increase in strain due to creep, or creep strain, to the initial strain. The modulus of elasticity of concrete E_c reduces accordingly,

$$E_{\mathrm{cr}} = \frac{E_{\mathrm{c}}}{1 + \zeta \cdot \varphi}, \tag{8.32}$$

where according to Eurocode EN 1992-1-1:2004,

$$E_{\mathrm{c}} = 22'000 \left(\frac{f_{\mathrm{cm}}}{10} \right)^{0.3} = 22'000 \left(\frac{f_{\mathrm{ck}} + 8}{10} \right)^{0.3}. \tag{8.33}$$

IASS 1979 defines the creep coefficient as

$$\varphi = 4 - 2 \log f_{\mathrm{c}}, \tag{8.34}$$

where f_{c} is the strength of concrete at the time of loading.

Alternatively, according to SIA 262:2003, art. 3.1.2.5.3, and EN 1992-1-1:2004, the creep coefficient at time t, and time at first loading t_0,

$$\varphi = \varphi_{\mathrm{RH}} \cdot \beta_{\mathrm{fc}} \cdot \beta_{\mathrm{t}} \cdot \beta_{\mathrm{c}}, \tag{8.35}$$

where

$$\varphi_{\mathrm{RH}} = \left(1 + \frac{1 - RH/100}{0.1\sqrt[3]{h_0}} \cdot \alpha_1 \right) \cdot \alpha_2, \tag{8.36}$$

$$\beta_{\mathrm{fc}} = \frac{16.8}{\sqrt{f_{\mathrm{cm}}}}, \tag{8.37}$$

$$\beta_{\mathrm{t}} = \frac{1}{0.1 + (t_0)^{0.20}}, \tag{8.38}$$

$$\beta_{\mathrm{c}} = \left(\frac{t - t_0}{\beta_{\mathrm{H}} + t - t_0} \right)^{0.3}, \tag{8.39}$$

with relative humidity RH in percent, the 28-day cylinder compressive strength $f_{\mathrm{ck}} = f_{\mathrm{cm}} + 8$, and the notional size of the cross-section

$$h_0 = \frac{2A}{l} = \frac{2 \cdot w \cdot t}{2 \cdot w} = t, \tag{8.40}$$

with concrete cross-section A, perimeter length of the part that is exposed to drying l, width of the cross-section w and shell thickness t,

$$\beta_{\mathrm{H}} = 1.5\left(1 + (0.012 \cdot RH)^{18}\right) h_0 + 250 \cdot \alpha_3 \leq 1500 \cdot \alpha_3, \tag{8.41}$$

and

$$\alpha_1 = \left(\frac{35}{f_{\mathrm{cm}}}\right)^{0.7}, \quad \alpha_2 = \left(\frac{35}{f_{\mathrm{cm}}}\right)^{0.2}, \quad \alpha_3 = \left(\frac{35}{f_{\mathrm{cm}}}\right)^{0.5}, \tag{8.42}$$

where each $\alpha_i \leq 1$.

8.7.3 Effect of shrinkage

The effect of shrinkage is imposed by calculating a shrinkage strain. IASS 1979 suggests that for design purposes, the shrinkage strain

$$\varepsilon_{\mathrm{cs}} = \frac{90 - RH}{80000}, \tag{8.43}$$

where RH is the relative humidity in percent. Alternatively, according to EN 1992-1-1:2004, the shrinkage strain is the sum of strains due to drying and due to autogeneous shrinkage at time t, and time at the start of drying t_s,

$$\varepsilon_{\mathrm{cs}} = \varepsilon_{\mathrm{cd}} + \varepsilon_{\mathrm{ca}}. \tag{8.44}$$

There are multiple conflicting views on this approach from Eurocode.

According to SIA 262:2003, only the drying shrinkage is taken into account, and increased autogeneous shrinkage for concrete with low water-cement ratios is only mentioned. Instead, it recommends to perform testing if the influence of shrinkage on the structure is of particular importance.

CIRIA C660 suggests that "when considering long-term deformation, autogeneous shrinkage is ignored beyond 28 days, except in cases where high strength, low [water-cement] ratio is used under conditions where moisture loss, and hence drying shrinkage, will be prevented." In this case, autogeneous shrinkage is applied for no more than 28 days as well as an overall stress relaxation factor of 0.65.

By contrast, Raphael et al. (2012*b*) suggest both types of strain are applied, and factored with 1.203 to 1.355 (RH = 40-60 % to 60-85 %) for long-term behaviour and C40-80 concrete.

Drying shrinkage

The strain due to drying

$$\varepsilon_{\mathrm{cd}} = \beta_{\mathrm{ds}} \cdot k_{\mathrm{h}} \cdot \varepsilon_{\mathrm{cd},0}, \tag{8.45}$$

where

$$\beta_{\mathrm{ds}} = \frac{t - t_{\mathrm{s}}}{t - t_{\mathrm{s}} + 0.04\sqrt{h_0^3}}, \tag{8.46}$$

and, interpolated from EN 1992-1-1:2004,

$$k_{\mathrm{h}} = 2.5 \cdot 10^{-6} \cdot h_0^2 - 2.25 \cdot 10^{-3} \cdot h_0 + 1.2 \tag{8.47}$$

with $1.0 \geq k_{\mathrm{h}} \geq 0.7$,

$$\varepsilon_{\mathrm{cd},0} = 0.85\left(\left(220 + 110 \cdot \alpha_{\mathrm{ds1}}\right) \cdot e^{\left(-\alpha_{\mathrm{ds2}} \cdot f_{\mathrm{cm}}/10\right)}\right) \cdot 10^{-6} \cdot \beta_{\mathrm{RH}} \tag{8.48}$$

with α_{ds1} and α_{ds2} depending on the cement class S, N or R (slow, normal or rapidly hardening, with α_{ds1} = 3, 4 or 6 and α_{ds1} = 0.13, 0.12 or 0.11, respectively), and

$$\beta_{\mathrm{RH}} = 1.55\left(1 - \left(RH/100\right)^3\right). \tag{8.49}$$

Autogeneous shrinkage

The autogeneous shrinkage

$$\varepsilon_{\mathrm{ca}} = \beta_{\mathrm{as}} \varepsilon_{\mathrm{ca}}\left(\infty\right), \tag{8.50}$$

where

$$\beta_{\mathrm{as}} = 1 - e^{-0.2t^{0.5}}, \tag{8.51}$$

and

$$\varepsilon_{\mathrm{ca}}(\infty) = 2.5\,(f_{\mathrm{ck}} - 10) \cdot 10^{-6}, \tag{8.52}$$

with concrete cylinder compression strength f_{ck}.

8.7.4 Effect of reinforcement and cracking

The effect of reinforcement and cracking is taken into account by a factor ρ_{rc}. IASS 1979 uses two graphs to determine ρ_{rc} using the ratios of the Young's moduli n_{rc} and cross-section of the reinforcement steel and the concrete, or reinforcement ratio μ_{rc} (Section 8.2.5).

Instead of graphs, Kollár & Dulácska (1984) has three equations for ρ_{rc}, with their choice depending on the ratio of the eccentricity to shell thickness e_0/t. Here, a single equation is proposed for one of its parameters, ρ_{c}, such that ρ_{rc} can also be defined using only one of these three expressions,

$$\rho_{\mathrm{rc}} = \frac{1+\psi_0}{2}\rho_{\mathrm{c}} + \psi_\infty\left(\rho_{\mathrm{hom}} - \rho_{\mathrm{c}}\right) \leq 1.00, \tag{8.53}$$

where the specific effect of cracking is redefined here as a Gaussian function,

$$\rho_{\mathrm{c}} = a \cdot e^{-(e_0/t+b)^2/(2c^2)}, \tag{8.54}$$

with

$$\begin{aligned}
a &= 8.904 - 13.944 \cdot \frac{e_0}{w_0} + \quad 7.2\left(\frac{e_0}{w_0}\right)^2, \\
b &= \quad 0.381 - 0.198 \cdot \frac{e_0}{w_0} + 0.089\left(\frac{e_0}{w_0}\right)^2, \text{ and} \\
c &= \quad 0.131 + 0.138 \cdot \frac{e_0}{w_0} - \quad 0.05\left(\frac{e_0}{w_0}\right)^2.
\end{aligned}$$

The proportion between the eccentricity and imperfection $e_0/w_0 = 1.00$ for cylinders, 0.67 for domes and 0.50 for hypars and hyperboloids (Dulácska 1981, Kollár & Dulácska 1984).

The factors ψ_0 and ψ_∞ account for buckling rigidity in the uncracked state,

$$\psi_0 = \sqrt{(1 + n_{\mathrm{rc}}\mu_{\mathrm{rc}})\left(1 + 3n_{\mathrm{rc}}\mu_{\mathrm{rc}}(1 - 2\eta)^2\right)}, \tag{8.55}$$

and the cracked state of the concrete,

$$\psi_\infty = \sqrt{12\left(n_{\mathrm{rc}}\mu_{\mathrm{rc}} + \xi\right)\left(\frac{\xi^3}{3} + \frac{n_{\mathrm{rc}}\mu_{\mathrm{rc}}}{2}\left(1 + 2\xi^2 + 2\eta^2 - 2\xi - 2\eta\right)\right)}, \tag{8.56}$$

where

$$\xi = n_{\mathrm{rc}}\mu_{\mathrm{rc}}\left(\sqrt{1 + \frac{1}{n_{\mathrm{rc}}\mu_{\mathrm{rc}}}} - 1\right), \tag{8.57}$$

n_{rc} is defined by equation (8.5) and $\eta = 0.2$ for reinforcement on both sides of the shell, and 0.5 for reinforcement on only one side.

There are some contradictory approaches as Dulácska & Kollár (1995) apply only ρ_{c} accounting only for cracking, while Kollár & Dulácska (1984) use ρ_{rc}, which can be greater than 1 for small eccentricities, actually having an improving effect due to reinforcement. IASS 1979 refers to the German edition of the latter, but its graphs clarify that $\rho_{\mathrm{rc}} \leq 1.0$, which was adopted in equation (8.53) as an upper limit.

8.7.5 Effect of concrete plasticity

For design purposes, the effect of plasticity is taken into account with the aid of the semi-quadratic Dunkerley interaction formula (IASS 1979),

$$\left(\frac{p_{\mathrm{cr}}^{\mathrm{plast}}}{p_{\mathrm{pl}}}\right)^2 + \frac{p_{\mathrm{cr}}^{\mathrm{plast}}}{p_{\mathrm{cr,reinf}}^{\mathrm{u}}}, \tag{8.58}$$

which Kollár & Dulácska (1984) rewrite, using equation (8.18), to

$$\rho_{\mathrm{pl}} = \frac{p_{\mathrm{pl}}}{p^{\mathrm{u}}_{\mathrm{cr,reinf}}} \sqrt{\frac{1}{4}\left(\frac{p_{\mathrm{pl}}}{p^{\mathrm{u}}_{\mathrm{cr,reinf}}}\right)^2 + 1} - \frac{1}{2}\left(\frac{p_{\mathrm{pl}}}{p^{\mathrm{u}}_{\mathrm{cr,reinf}}}\right)^2, \tag{8.59}$$

where it is implied that the plastic failure load

$$p_{\mathrm{pl}} \approx p_{\mathrm{p}} \frac{1}{1 + 3 \cdot e_0/t}, \tag{8.60}$$

if $e_0/t \leq 1$, where p_{p} is defined in equation (8.11), and shell thickness t should be reduced by 10 mm if $t < 80$ mm. Alternatively, Kollár & Dulácska (1984) suggest

$$p_{\mathrm{pl}} \approx p_{\mathrm{p}} \left(1 - \frac{2e_0}{t}\right), \tag{8.61}$$

but this may result in negative values, depending on the assumed eccentricity.

8.8 Limit of safety and knockdown factors

To have an idea of how much the linear critical buckling load potentially would have to be reduced, a parametric study is carried out to obtain a limit based on realistic design values.

The following values are fixed:

density	ρ	=	25	kN/m^3;
yield strength	f_{y}	=	435	N/mm^2;
Young's modulus	E_{s}	=	210′000	N/mm^2;
reinforcement parameter	η	=	0.2;	
reference period	t	=	50	years;
time at loading	t_0	=	28	days;
variable load	p_t	=	1	kN/m^2;
permanent load	p_0	=	$\rho \cdot t$	where $\rho = 25$ kN/m^3.

Several parameters are varied within the following bounds:

cylinder compressive strength	$20 \leq$	f_{ck}	≤ 90 N/mm^2;
span	$5 \leq$	s	≤ 100 m;
shell thickness	$15 \leq$	t	≤ 100 mm;
shallowness	$2 \leq$	s/h	≤ 5;
slenderness	$50 \leq$	s/t	≤ 750;
ratio	$0.50 \leq$	e_0/w_0	≤ 1.00;
ratio of reinforcement	$0.002 \leq$	μ_{rc}	$\leq$ eq. (8.3);
relative humidity	$25 \leq$	RH	≤ 100 %);
formwork factor	$1 \leq$	α_{f}	≤ 12.

Furthermore, the imperfection sensitivity is evaluated for curves I ($\rho_{\mathrm{hom}} = 1.00$) and IV (spheres and axially loaded cylinders) from Figure 8.7. The latter is recommended by IASS 1979 for unknown cases (note that Tomás & Tovar (2012) show a few specific cases that are even worse). The linear critical buckling load is calculated according to equation (8.15). The radius of curvature is assumed to be that of an arc, based on the chosen span s and the rise h following from the chosen shallowness, and identical in both directions,

$$R = \frac{1}{8}\frac{4h^2 + s^2}{h}. \tag{8.62}$$

Based on this, the lower and upper limits for the reductions factors are (with values in brackets for $\rho_{\mathrm{hom}} = 1.00$):

$$\begin{aligned} 0.23 \leq \quad & \rho_{\mathrm{hom}} && \leq 0.36(1.00) \\ 0.22 \leq \quad & \rho_{\mathrm{crp}} && \leq 0.63 \\ 0.02 \leq \quad & \rho_{\mathrm{rc}} && \leq 0.60(1.00) \\ 0.22(0.03) \leq \quad & \rho_{\mathrm{pl}} && \leq 1.00 \end{aligned} \tag{8.63}$$

The plasticity factor ρ_{pl} has an inverse relation with the other factors. As a result, the lowest combination found was $\gamma_{\mathrm{k}} = 0.0024$ ($0.23 \cdot 0.50 \cdot 0.02 \cdot 1.00$) along with a safety factor of 3.00, for C90/105 concrete, minimum reinforcement, maximum span, shallowness and slenderness, ratio $e_0/w_0 = 0.5$, $RH = 25$ % and $\alpha_{\mathrm{f}} = 12$, and imperfection curve IV. The highest found was $\gamma_{\mathrm{k}} = 0.33$ ($1.00 \cdot 0.63 \cdot 0.60 \cdot 0.88$) with a safety factor of 2.35.

As a result, the theoretical linear critical buckling load might be reduced by a factor $\lambda_{\mathrm{s}}/\gamma_{\mathrm{k}}$ in the order of 10 to 1000.

8.9 Conclusions

Shells are extremely efficient structures, but as a result, can be very sensitive and suffer from buckling phenomena. Any structural evaluation of a shell needs to account for geometric nonlinearity due to large displacements, imperfections, plasticity, cracking, reinforcement, creep, shrinkage and thermal action. This requires a highly nonlinear and demanding computational analysis, or traditionally, the calculation of a knockdown factor γ_k, which takes these effects into account. The latter is suitable for early design and optimization where computational time is preferably kept to a minimum. Only a linear critical buckling load has to be calculated. The final design should still be verified with a sufficiently refined model, particularly for non-standard shell geometries.

An overview has been presented allowing the parametric implementation of the IASS 1979 recommendations for the stability analysis of thin concrete shells. This requires us to calculate a knockdown factor from four individual factors ρ_{hom}, ρ_{crp}, ρ_{rc} and ρ_{pl}, as well as a factor of safety λ_s for a sufficient margin. The recommendations do not provide sufficient information themselves, and recent shell structures reflect the confusion in applying IASS 1979. To resolve this, they need to be viewed in conjunction with surrounding literature by Kollár Lajos (1926–2004), Dulácska Endre, Stefan Jerzy Medwadowski and others. Graphs and tables have been replaced by equations fit through their data, specifically equations (8.10), (8.21), (8.22), (8.31), (8.47) and (8.54). Conflicting information has been noted wherever found. European and Swiss building codes are used as well to fill in any gaps, but local codes should be adopted for any specific project. Effects of shrinkage and temperature need to be added as actions on the structure.

Furthermore, these recommendations are still based on outdated allowable stress design (ASD); an approach that has been replaced by limit state design (LSD) in contemporary practice. Since the present demand for thin concrete shells is low, it is unlikely that dedicated building codes will be developed. Instead, IASS 1979 should be updated to conform to LSD, and a starting point could be Eurocode EN 1993-1-6:2007, intended for thin steel shells.

The great liability of the engineer compared to men of other professions is that his works are out in the open where all can see them. [...] *He cannot bury his mistakes in the grave like the doctors. He cannot argue them into thin air or blame the judge like the lawyers. He cannot, like the architects, cover his failures with trees and vines.*

— Herbert Hoover, 1954

CHAPTER NINE

Construction process

During the development of the computational approach presented in Chapter 7, three prototype shells were built as a proof-of-concept of this approach. The prototypes themselves were part of the development of the NEST HiLo project (Chapter 12) and the unbuilt Amant Arts Gallery (Veenendaal & Block 2015). These prototypes were intended to evaluate the design process, investigate constructional details and verify construction tolerances. Experimental results on these tolerances can be found in Chapter 10.

This chapter provides photo documentation of details and construction steps of the three prototypes. In addition, details from some reference projects are mentioned at times, particularly the wire-net falseworks shown in Sections 3.7.3, 3.7.4 and 3.7.5: the 1959 Purdue University prototype, 1962 Purdue Golf Course clubhouse and 1962 Bay Gas Station (Figures 3.47 and 3.48); and, the 1960 Pentagon Hall and its prototypes (Figure 3.50). Some useful references are recommended for more information on detailing and construction: West (2016) for fabric formworks, Seidel (2009) for tensioned membrane roofs, and Naaman (2000) for ferrocement shells.

The chapter is ordered by logical construction sequencing. Section 9.1 details the external frame, including drawings from the reference projects. Section 9.2 details the cable net and it various connections. Section 9.3 lists the fabric used for each prototype, and Section 9.4 reports the concrete mix used for all prototypes.

A flexible formwork for thin concrete shells consists of an external frame that largely replaces a conventional shoring system. The shuttering, which is prestressed or hung from this frame, is a fabric or cable net. The traditional definition of shuttering is broadened to encompass materials other than timber. The cable-net shuttering has to be covered by a fabric or some type of formwork sheeting or lining.

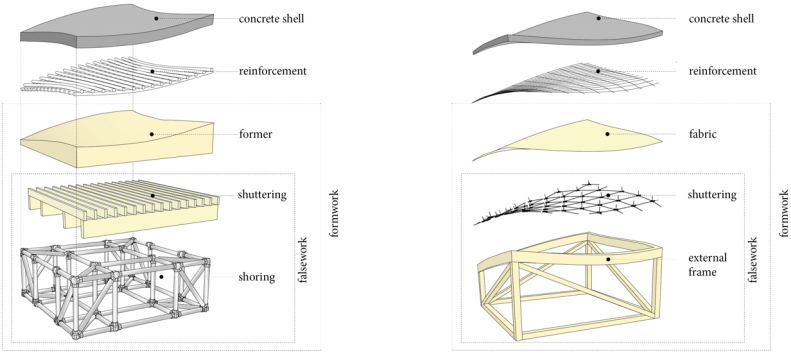

Figure 9.1: Nomenclature for traditional and flexible formworks of doubly curved concrete shells.

9.1 External frame

Traditional shoring systems are usually made from timber, steel or aluminium, and thus far, external frames for flexibly formed shells have been made from timber and steel. Some examples have used the frame as lost formwork, to become part of the composite edge and ridge beams of the final shell structure.

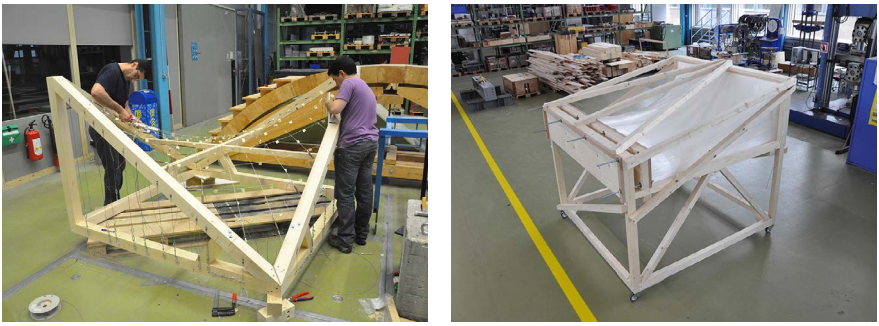

Figure 9.2: Timber frame of a cable-net formwork and a fabric formwork prototype.

Three prototype shells were built using flexible, either a cable-net or a fabric, formwork (Figure 9.2).

The frame for the prototype cable-net formwork used square 90 mm fir elements, and was designed such that the upper part would be removable for demoulding, whilst the lower part would support the two bottom corners of the shell. A tension tie connected the two bottom corners to resist the horizontal thrust from the shell. The frame was first stiffened by a timber cross (Figure 9.2) and later by a top member to allow access for measurements of the cable net (Figure 10.4).

The frame for the prototype fabric formwork used 60 × 80 mm fir elements, locally reinforced with 30 × 50 mm beech along the edges connected to the fabric (Figure 9.2). The frame was built such that the fabric was in an elevated position to allow access for 3D scanning measurements.

The cable-net and fabric formwork prototype at Escobedo Construction in Buda, Texas had digitally fabricated, custom curved timber edge beams (Figure 3.52). In contrast to the other examples in this section, a separate edge detail was clamped to the cable net to form the edges of the shell. The space between the edge beams and edge detail was used to accommodate turnbuckles for prestressing.

The timber frames each feature horizontal struts to internally resolve the horizontal components of the prestress in the cable net or fabric. The following historical examples of steel frames do not, and resist these forces through bending of the frame. At these larger scales, any horizontal strut would have to contend with buckling, made worse by eccentricities due to increasing sag.

The 20 ft square laboratory model at Purdue University, Indiana, USA had edges of rolled 6 in steel Z-sections and 4 in steel pipe columns (Figures 3.47 and 9.3) (Waling & Greszczuk 1960).

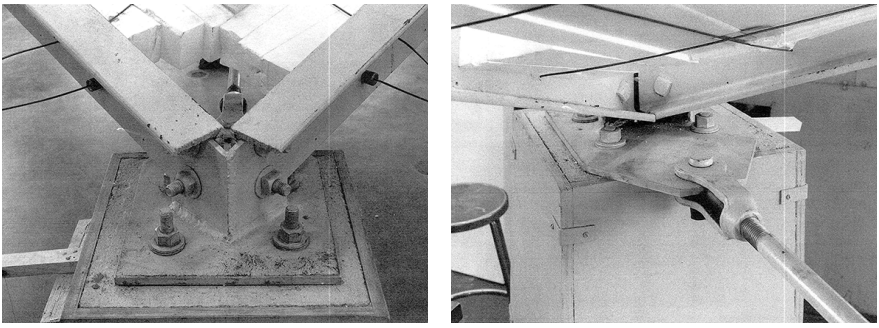

Figure 9.3: Connections of the edge beams and tie-rod to the abutment of the laboratory model in Figure 3.47 (Greszczuk 1959).

The full-scale 64 ft square structures used custom edge and ridge members, formed from 5/16 in and 3/8 in steel plate respectively (Figures 3.48 and 9.4).

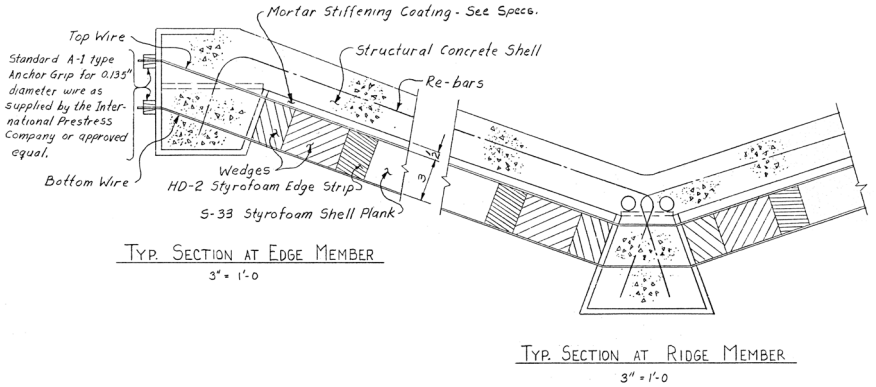

Figure 9.4: Sections and shell materials of edge and ridge members for Auto Perfection, formerly the Bay Gas Station, 1960–1962.

The Pentagon Hall largely consists of 12 × 4 in steel channel sections along the edges, vertical tapered I-sections, cut from 18 × 8 in sections, as well as 5 × 3 in I-sections for the mullions (Figures 3.50 and 9.5). A prototype was built using a steel frame, but Flint (1961) does not describe the dimensions of its sections (Figure 3.49).

These examples have used straight steel sections, but curved sections can be used such as the L-section used for the circular edges of the catenoid-like prototypes produced in Belgium (Figure 3.20). Similarly, a custom curved tubular steel edge beam was proposed at an early stage of the NEST HiLo project (Section 12.3).

Apart from the above strategies, it is interesting to point out early formwork prototypes at Eindhoven University of Technology, Netherlands, and at Anhalt University of Applied Sciences in Dessau, Germany, that were in fact relatively conventional membrane structures (Figures 3.16 and 3.17). Although they did not produce fin-

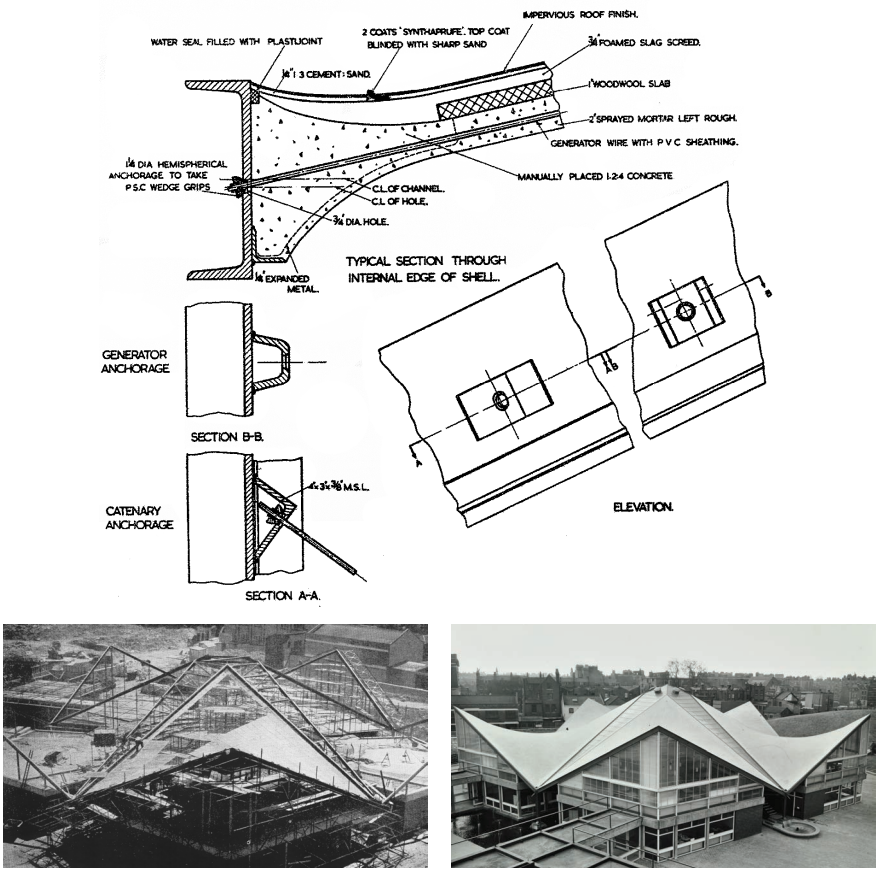

Figure 9.5: Sections of edge members and steel frame of Pentagon Hall, UK (Flint & Low 1960).

ished concrete shells, they introduce two valuable concepts: both feature edge cables instead of edge beams; with the former's cables terminating at struts and ties, instead of a rigid frame. This minimizes the need for rigid external framing. Possible drawbacks are the concentration of forces at the foundations and higher flexibility of the formwork, leading to greater deviations.

9.2 Cable net

Once the frame is erected, the cable net can be installed (Figure 9.6).

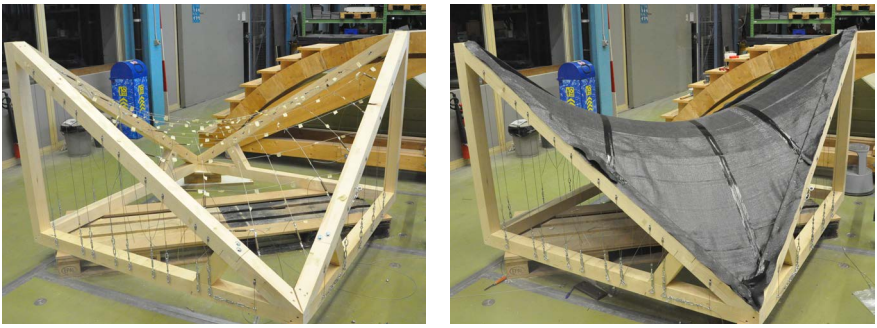

Figure 9.6: Prestressed cable net, covered with Propex 60-7041 geotextile.

The prototypes had a 230 mm spacing. Historical examples of cable-net formed hypar shells had a cable-net spacing of about 300 mm for the offset wire method for the 19.5 m span Purdue Golf Clubhouse and 390 mm for the catenary wires for the 22 m span Pentagon Hall (Sections 3.7.3 and 3.7.4). Hanging roofs, generally made by suspending concrete panels from cables, may be designed for similar conditions, and can serve as further source of details and dimensions (Section 3.7).

For the prototype, the cable net was made from 2 mm stainless steel cable. Pentagon Hall used 7 mm wire with an ultimate strength of about 1379 N/mm^2, while Purdue Golf Clubhouse used 3.4 mm prestressing wire with a strength of 1758 N/mm^2. The former had PVC sheathing to allow for post-tensioning.

For the first prototype, nodes were fixed by simple wire ties. For the second, cross clamps were used instead (Figure 9.7), which also served as measuring points for photogrammetry. Purdue Golf Clubhouse did not require ties or clamps, as the cables followed nearly straight lines, and were held in friction with the insulation boards. Pentagon Hall similarly had no clamps, only some ties at regular intervals. Section 7.3 also discusses the fact that geodesic lines reduce the need for node connections.

At the ends, the cables were guided through the timber frame along cringles, terminating at eyebolts using crimp sleeves. At one end of each of the twenty cables, a turnbuckle was used to introduce prestress (Figures 9.8 and 10.2).

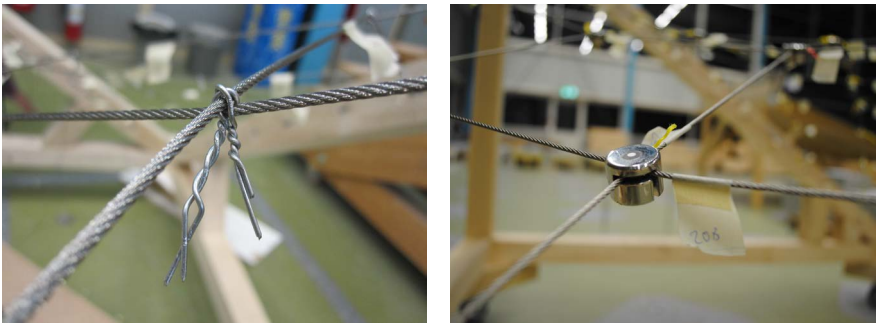

Figure 9.7: Node connection with wire or cross clamp.

Figure 9.8: Turnbuckles and threaded bolts used for prestressing the cable-net and the fabric formwork respectively

Figure 9.9 shows the smaller and larger Purdue prototypes, which used either screws or wedge grips. Initially, a Gifford-Udall pocket jack was used for prestressing, but found to be inaccurate in controlling the level or pretension. It was then changed to a simple lever with a spring at its end, described to be similar to a "pipe clamp used in furniture making" (Figure 9.10) (Greszczuk 1959). According to Waling et al. (1964), this custom device was used at large scale as well. The generator wires of the Pentagon Hall, sheathed in PVC, were anchored at one end by tapered pins and attached to adjustable screws for tensioning at the other.

For shuttering, the prototypes used a fabric, as discussed in the next section. The Purdue Golf Clubhouse used 9 × 2 × 1/4 ft Styrofoam boards with foam wedges along the edge beams (see also Figure 9.4). The Pentagon Hall prototype used a "suspended mesh [...] covered with a light expanded metal lathing in discontinuous

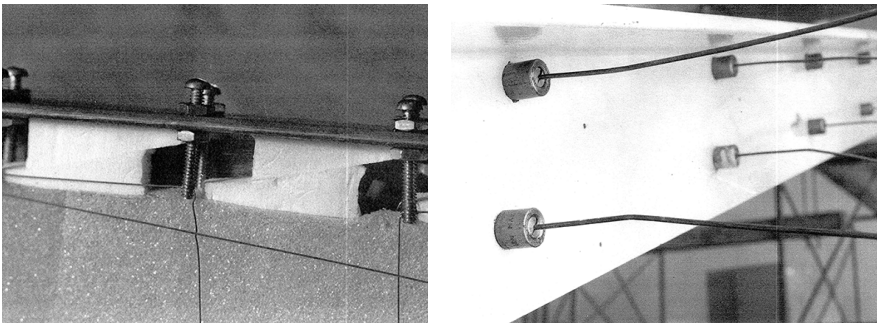

Figure 9.9: Typical connections of the wires to the edge beams (Greszczuk 1959).

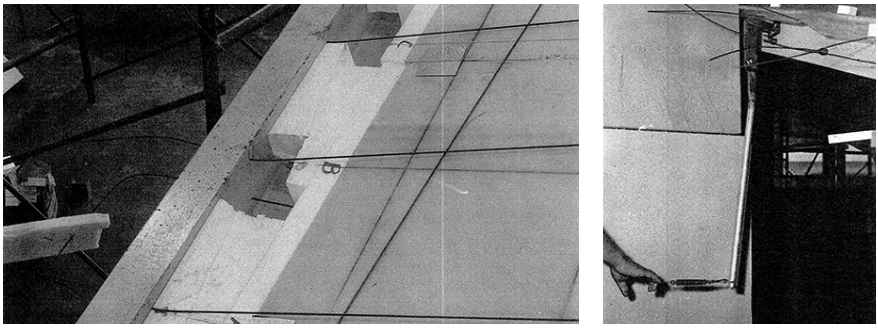

Figure 9.10: Wedges in position and custom device used in pretensioning of wires (Greszczuk 1959)

strips, overlain by building paper and blocked off to the required clearance by steel spacers" (Flint 1961), and the actual structure a layer of light mesh reinforcement, laid on mortar blocks resting on the lower generator wires. This was then covered by 1 in thick woodwool and polyethylene sheets (Flint & Low 1960) (Figure 9.5).

9.3 Fabric

The first fabric placed on the cable net was a PP geotextile, Propex 60 – 7041, with a tensile strength of 42 kN/m, and a 5.2 m roll width (Figure 9.6). The geotextile was chosen purely for its similarity in terms of weight, strength and hydraulic properties to the North American Propex 315ST, used by Prof. Mark West in many of his

experiments at CAST. The second fabric was a PP Proserve F0899 with a tensile strength of 54–60 kN/m, and 3.6 m roll width, used for underwater fabric formworks. While the first prototype used duct tape along the seams of the cutting patterns, the second was properly sown (Figure 9.11). The third fabric used was a PVC Ferrari STAM 7002 with a tensile strength of 30 kN/m, used for inflatables. The cutting and welding of the fabric was done by the company Luft & Laune (Figure 9.11).

Figure 9.11: Sown and welded seam lines for the second and third prototypes

The first fabric was simply tacked onto the timber frame. The second fabric was also clamped to the frame with an additional timber profile to control the edge geometry. The third prototype used existing keder rail profiles (Figure 9.12).

Figure 9.12: Keder rail with fabric connection, attached to the timber frame along the perimeter.

9.4 Concreting

After prestressing the formwork, concrete can be applied. The historical examples of the Purdue Golf Clubhouse and Pentagon Hall demonstrate that concrete can be either cast or sprayed.

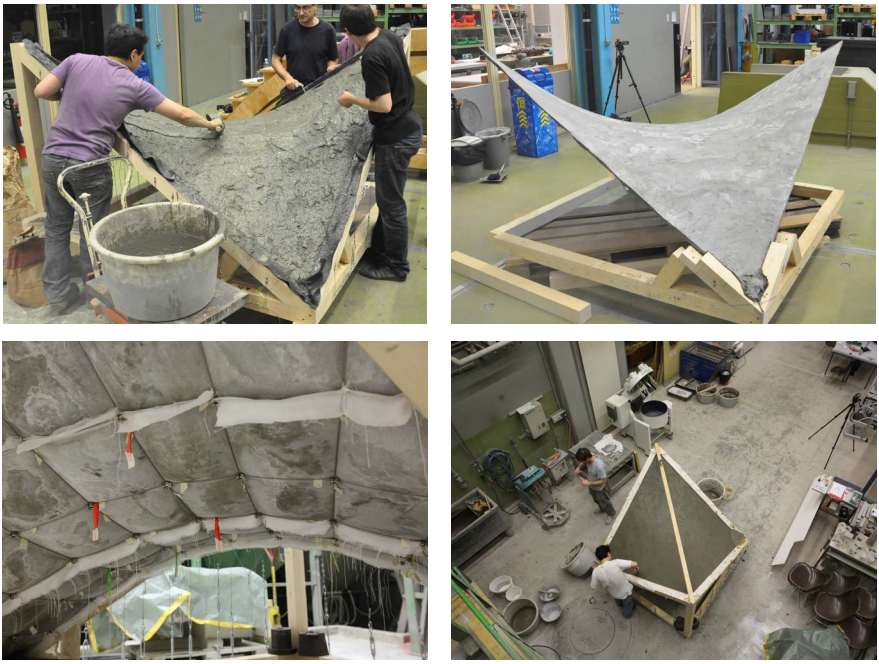

Figure 9.13: Casting of the first and second prototypes.

The first prototype was hand-rendered with a 9 to 29 mm (24 mm average) PVA-fibre reinforced cement mortar. The second shell was cast while continuously measuring the thickness for better control, by distributing the concrete accordingly (Figure 9.13). It was also fitted with an additional layer of AR-glass textile reinforcement. The third prototype was again only fibre reinforced (Figure 9.14). An interesting detail was that one of the workers lost his balance. The fabric carried his full weight without any distress.

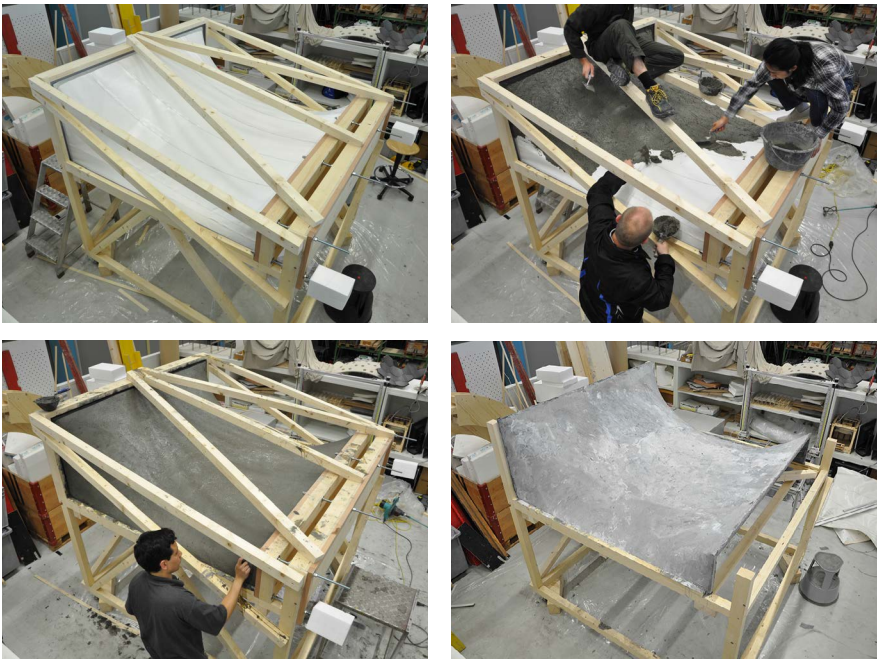

Figure 9.14: Casting of the third prototype.

The mix design and choice of fibre reinforcement was adapted from Máca et al. (2012), based on further discussion and availability of materials at the concrete lab. The mix design was outside the scope of this thesis, so the only immediate criteria were to obtain a mixture with high slump, resistance to shrinkage cracking, and tensile capacity. The proportions by weight were:

- 1 kg cement (Holcim Normo 5R, CEM I 52.5)
- 0.1 kg microsilica (Elkem Grade 971-U)
- 0.7 kg fine sand/aggregate (0/4mm)
- 0.015 kg PVA fibres (Kuralon K-II 6/12 mm)
- 0.24 l water
- 0.010–0.015 l plasticizer (BASF Glenium ACE 30)
- 0.015 kg stabilizer (Sika 4R)

9.5 Conclusions

This chapter serves mostly as photo documentation for those interested in the specific materials and details that were used in the construction of the prototypes. Some related information on the reference projects, particularly regarding the external frame, is provided as it is not easily available, and can also serve as inspiration.

Part V

Results and applications

[I have] *done all shape-finding for new shells merely by physical experiments or by design.* [...] *Someday computers may be helpful in the creative process of shell design, but only when the structures they propose have been built and monitored over a period of time.*

— Heinz Isler, 1994

CHAPTER TEN

Experimental results

Three prototype shell structures were cast from flexible formworks[1]. The first one was built as a constructional proof-of-concept for the cable-net and fabric formwork, and to develop an appropriate digital design process. The second one was constructed to reduce differences between computational model and physical result. The third one was built as a constructional proof-of-concept for a purely fabric formwork.

The first two prototype shell structures were built using much of the same cable-net and fabric formwork. Their shape has straight edges, and slightly deviates from a hypar. The midpoint is slightly higher which reduces maximum deflection. The 25 mm thick shells were 1.8 × 1.8 m in plan, and had a height of 1.2 m (Figure 10.1). Both shells acted as prototypes for the NEST HiLo project (Chapter 12).

The third, fabric-formed shell is based on a minimal surface between straight edges, and is a 1:4 model of one of the roofs of the Amant project (Veenendaal & Block 2015). The 30 mm thick shell was 1.73 × 1.83 m in plan, and had a height of 0.65 m (Figure 10.1).

To establish construction deviations for these prototypes, both geometry and forces had to be measured. To measure geometry and deformations, traditional rulers, meters or gauges as well as more advanced photogrammetry, 3D scanning or digital image correlation can be used. Existing methods to measure cable force are strain gauges or extensometers, hydraulic force transducers, vibrating wire sensors and three-point bending measurements with tension meters. Methods to measure fabric stress are less common. Although strain gauges are used for bi-axial material testing of fabrics, Seidel (2009) notes that they are impractical for on-site measurement of

[1]This chapter is partially based on Veenendaal & Block (2014*b*) and Veenendaal, Bezbradica, Novak & Block (2014).

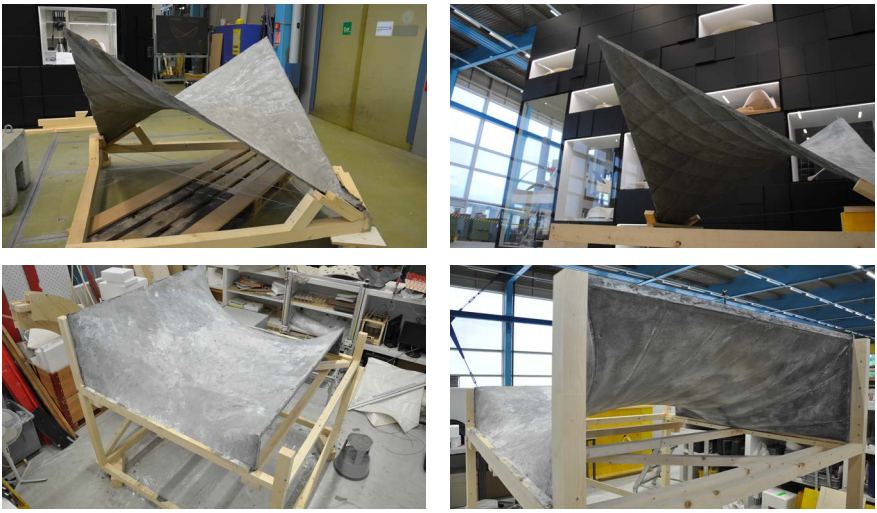

Figure 10.1: Two cable-net and fabric-formed prototype shells, April 2013 and February 2014, and third fabric-formed prototype shell, June 2015, built at ETH Zurich, Switzerland.

membrane roofs. Possible alternatives are an oscilloscope to measure the spread of waves through the fabric, a circular "plate-shaped device" that applies a defined pressure, and a "ring force measuring device" with two potentiometers that applies a defined point load (Seidel 2009). However, it is unknown whether such devices, developed for tensioned membrane roofs, would give accurate predictions for fabrics under (concrete) load.

Different measuring strategies were applied to the prototypes, as summarized in Table 10.1 and explained in Sections 10.1, 10.2 and 10.3, both for measurement of geometry and forces. The geometry after the application of concrete or an equivalent load was then checked against the geometry of the design model. Measurements are compared with precedent studies for which data has been published in Section 10.4. The cost of the prototypes is compared to that of existing flexible and traditional formwork in Section 10.5. Some conclusions are drawn in Section 10.6.

	geometry	forces
prototype 1		
initial, prestressed state	tape measure	springs (20)
final, loaded state	tape measure and laser meter (13)	springs (20)
estimated error	± 5 mm	± 11.6 N
prototype 2		
initial, prestressed state	photogrammetry (60)	tension meter (140)
final, loaded state	photogrammetry (60)	tension meter (140)
estimated error	± 0.8 mm	± 22 N
prototype 3		
initial, prestressed state	portable 3D scanner	
final, loaded state	portable 3D scanner	
estimated error	± 0.3 mm/m	

Table 10.1: Equipment used for measuring geometry or forces in various stages (number of measurements in brackets).

10.1 First prototype

The first prototype was primarily intended to develop constructional details and verify the computational design process. Nonetheless, some measurements were taken to quantify the formwork's total deviations, and inform further improvements.

10.1.1 Force measurements

In order to measure forces, the cable net was fitted with springs (Federtechnik No. 50885.01) at twenty locations, one for each continuous cable (Figure 10.2). The springs act as simple extensometers. The springs were selected to have the highest (most sensitive) spring rate k while still fitting within the mesh of the cable net at maximum load. The measured force F could then be calculated using Hooke's law, $F = k \cdot u$, where the spring rate k = 11.6 N/mm according to the manufacturer and u is the measured elongation of the spring. Assuming a measuring error of ± 1 mm, the error in measured prestress F would be ± 11.6 N, or 4-12 % full scale, given that the maximum prestresses were calculated to range between 93 and 262 N. The springs were then used to verify the required prestressing forces prior to casting.

Figure 10.2: Cable-net and fabric formwork, using springs to measure forces via elongation.

10.1.2 Geometry measurements

After the concrete had cured, thirteen measurements were taken at nodes of the cable net (specifically, the imprint of those nodes left on the concrete shell) to see how much the actual prototype deviated from the computer model.

The top surface of the lower timber members, corresponding to the bottom side of the hypar's bounding box, was taken as a reference level $z = 0$. Measurements in the horizontal xy-plane were taken using a tape measure with an error of ±5mm (due to limited accessibility underneath the shell), and in vertical z-direction with a laser meter (Leica Disto Classic 5) with an error ±5mm (due to the high local curvatures around the node locations on the shell surface). Measurements revealed an average deviation of $\mu = 22.1$ mm with a standard deviation $\sigma = 0.7$ mm.

Afterwards, the shell was cut and the thickness of the section was measured. The actual prototype had a thickness varying between 10–30 mm, averaging c. 24 mm, rather than the uniform thickness of 25 mm in the computational model.

10.1.3 Interpretation

The deviations in the geometry are attributed to the assumed properties of the springs used for measurement, causing an inaccuracy of 40-50% in the measured forces. Two reserve springs were load tested to check the specifications of the manufacturer. These showed that the actual spring rate varied between 13.4-24.0 N/mm, instead of 11.6 N/mm, exhibiting nonlinear behaviour for the first 15 kg applied.

The approximate loads from the concrete and the assumed cable stiffness ($E = 195$ kN/mm^2) are both ruled out as major sources of inaccuracy:

- For a uniform thickness of ± 5 mm, the position of the nodes in the computational model varies by less than 1 mm, less than our error in measurement.
- For a higher E-modulus of 210 kN/mm^2 (another common value for steel) forces differed no more than in the order of 0.1 N (less than the accuracy of our measuring devices), and the maximum difference in cable length was in the order of only 10^{-3} mm.

10.2 Second prototype

To understand and control the relatively large differences between the actual and designed loaded states in the first prototype, the second prototype focused on alternative strategies to measure both force and geometry. Forces were measured using a tension meter, while geometry was measured using photogrammetry.

After prestressing the cable net to correspond to desired force values, it was loaded and measured again. The loads from the wet concrete were simulated by discrete weights applied at the nodes, allowing access and transparency for both types of measurement. The loads were 1.5 L PET bottles filled with sand with an error of ± 1 g. The equivalent uniform thickness of the shell was modelled to be 15 mm such that no more than one bottle per node was required. This meant a range of 1'545-2'146 g per node, or an accuracy of 0.05-0.06 % full scale. After the measurements were completed, the bottles were removed, fabric was applied and the shell was cast (Figure 10.3).

10.2.1 Force measurements

Instead of springs, a compact and portable aircraft cable tension meter (Tensitron ACX-250-M) was used for the forces, which takes three-point bending measurements (Figure 10.4). When properly calibrated, it has an accuracy of 2 % full scale. With an upper limit of 250 lbs, or 1'112 kN, this means an error of ±22.2 N. This is more than the theoretical accuracy of the springs. However, the tension meter was assumed to be more reliable, faster, would leave no imprint on the concrete, and allowed a larger set of 140 measurements, one for each cable segment.

Figure 10.3: Second prototype shell after demoulding.

10.2.2 Geometry measurements

Both the loaded and unloaded state were measured by photogrammetry at each of the sixty nodes. Photography was done using a specially calibrated Nikon D3200 camera, using coded targets from the Australis Photometrix software package. Photographs were taken from a static platform, while rotating the model on the ground. Rotating the model allowed the three-dimensional reconstruction of the nodal points while the camera is in the same position. The reconstruction was executed in the software program PhotoModeler Scanner and resulted in a point cloud model (Figure 10.5).

10.2.3 Interpretation

The point cloud data from photogrammetry was compared to the design model. Multiple comparisons were then made between the design model and the as-built result (see Table 10.2).

Figure 10.4: Cable-net and fabric formwork with dummy loads, using tension meter to measure forces, both in the prestressed and loaded states.

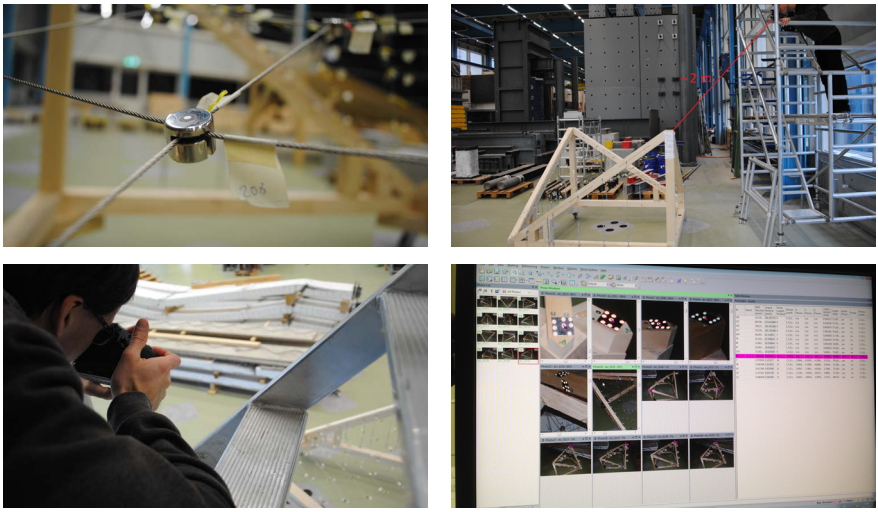

Figure 10.5: Cable-net and fabric formwork with dummy loads, using photogrammetry to measure geometry.

1. First, the distances between design and measured nodal coordinates were calculated.

2. Second, the measured boundaries did not exactly match that of the digital model, presumably due to construction deviations and deformations of the timber frame. The digital model was therefore remapped to exactly fit the measured boundary, and nodal distances were recalculated.

3. Third, the measured nodal points were projected to a mesh of the design model, to find corresponding closest points. The distances between the measurements and their projections on the target surface were then calculated. This quantity reflects how deviations would be checked against tolerances in practice.

Table 10.2 reveals that most of the deviations were already accumulated in the pre-stressed state. The table also shows that when conforming the digital design model to the measured boundary, the deviations are reduced more in the unloaded state than in the loaded state. This suggests that deformation of the timber frame has a large influence, and the edges cannot be considered as fixed. Excluding this effect reduces the final average deviation from 10.0 mm to 7.0 mm.

Furthermore, in-plane nodal deviations are higher than the out-of-plane deviations. The latter, the distances between the measured points and the target surface, are of greater interest when comparing structural behaviour of the as-built shell with that of the digital model. Arguably, they are also of greater importance for any client. By excluding in-plane deviations, the average deviation normal to the target surface is 2.0 mm instead of the total of 7.0 mm (Table 10.2).

The measured forces $\mathbf{f}$ and lengths $\mathbf{l}$ are not in exact equilibrium, and the residual forces can be regarded as errors in the measurements. To post-process the measurements, static equilibrium was recalculated using the force density method (Section 5.3.4) with the individual force densities derived from the measured forces and lengths, $\mathbf{q} = \mathbf{L}^{-1}\mathbf{f}$. By equilibrating the measured cable net, thus attempting to exclude measurement errors or variation in these measurements, the average deviation is reduced from 2.0 mm to $\mu = 1.3$ mm with a standard deviation $\sigma = 0.8$ mm (Table 10.2).

type	no.	prestressed state		loaded state	
		$\mu \pm \sigma$ [mm]	min.-max. [mm]	$\mu \pm \sigma$ [mm]	min.-max. [mm]
node-to-node distance	1	7.8 ± 2.5	3.5-13.0	10.0 ± 2.6	5.3-16.0
with remapped boundaries	2a	7.0 ± 3.1	1.1-14.2	7.0 ± 3.3	1.6-15.0*
and recomputed equilibrium	2b			2.6 ± 1.0	0.5-4.5
node-to-surface distance					
with remapped boundaries	3a	2.6 ± 1.4	0.0-5.5	2.0 ± 1.5	0.0-6.7
and recomputed equilibrium	3b			1.3 ± 0.8	0.0-3.1

Table 10.2: Comparisons between photogrammetric measurements and design model for both unloaded and loaded state. Values are mean ± standard deviation, and minimum to maximum.

Figure 10.6 visualizes the deviations, which show a correlation with the prestressing sequence. Turnbuckles were installed at one end of each continuous cable. The cable net was installed by placing nodes, measuring lengths and prestresses, while working from edge *AB* towards the opposite edge *CD* where the turnbuckles were. This could have introduced a cumulative error, which would explain the asymmetry of the deviations. It is assumed that the remaining deviations are due to construction errors, with this asymmetry being the main cause.

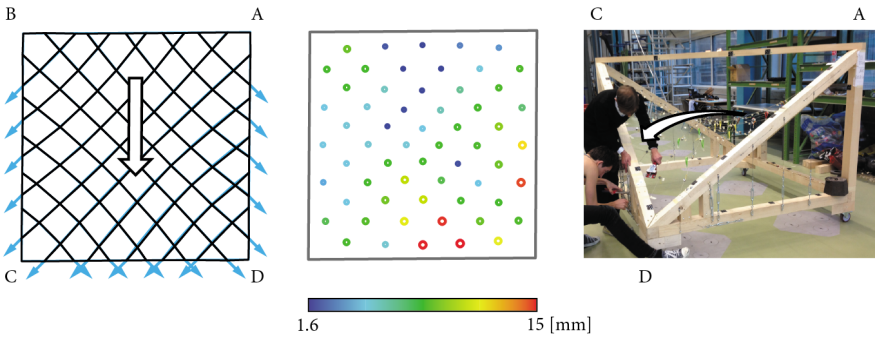

Figure 10.6: Position of turnbuckles, asymmetric distribution of deviations (2a) from Table 10.2, and direction of installing and prestressing the cable net.

The last results (3b) from Table 10.2 are assumed to be the final deviations of the second prototype. As mentioned, these deviations exclude those due to the timber frame, and measure deviations normal to the surface.

10.3 Third prototype

The third, fully fabric-formed prototype, required other strategies to measure forces and geometry. For the third prototype, only geometry was measured, as measuring stresses in a fabric, certainly during concrete casting, is not straightforward.

10.3.1 Geometry measurements

A Creaform Go!SCAN 50 portable 3D scanner was used to measure geometry (Figure 10.7). The scanner has a reported accuracy of 0.3 mm/m and operates on a maximum area of 380 × 380 mm. The software registers reference points on the frame and produces a dense surface mesh. A global registration, based on 116 target points on the rigid frame, produced an average point-distance of 0.4 ± 0.34 mm with respect to the design.

Figure 10.7: Fabric formwork using portable 3D scanner to measure geometry.

Figure 10.8 shows the results of the measurements, compared to the original design model. The average and maximum deviations were 19.6 and 52.0 mm respectively. The deviations also reveal the influence of the seam lines.

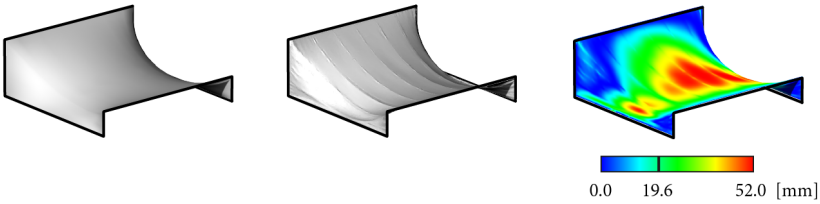

Figure 10.8: Design model, scanned model, and deviations between the two.

10.3.2 Interpretation

The fabric-formed shell deviated substantially from the intended design. There are global and local effects. The overall shape deviates due to insufficient prestress, meaning that the cutting patterns were either incorrectly produced, or the material model did not accurately reflect its real behaviour. At the recommendation of the supplier, the material model was based on the properties of V700 fabric Galliot & Luchsinger (2009), due to its similarity, in terms of tested properties, weave and coating, to the STAM 7002 fabric that was actually used. Locally, the welded seam lines are closer to the target surface as their stiffness is twice that of the rest of the fabric. This effect, though obvious in hindsight, was not anticipated. To alleviate this, further work should consider alternative detailing, for example by staggering cutting patterns, such that the thickness of the fabric is more uniform throughout.

The true causes of the deviations is ultimately difficult to ascertain, as methods to measure stresses in fabrics were not available.

10.4 Construction tolerances

Partial safety factors in building codes will typically account for some construction deviations without jeopardizing structural safety. The allowable tolerances should be specified according to the local building code.

For instance, in Eurocode EN 13670:2009, tolerances are ±5-10 mm for the depth of a concrete slab or plate less than 150 mm thick, and ±5-10 mm for concrete cover. Similarly, for a shell less than 80 mm thick, IASS 1979 recommends to subtract 10 mm for structural calculations.

These tolerances do not relate to the overall shape of a shell and its possible geometric imperfection. Eurocode EN 1993-1-6:2007 defines imperfections specific to steel shell structures and EN 13670:2009 defines eccentricities for (concrete) walls and columns. For example, EN 13670:2009 defines eccentricities of ±15-30 mm for walls and columns, as well as deviations of up to ±50 mm for multi-storey buildings with an inclination. Unfortunately, no guidance is given for concrete shells. Instead, an acceptable tolerance can be based on the accidental imperfection in IASS 1979, explained in Section 8.7.1 and equation (8.24).

Figure 10.9 and Table 10.3 show an overview of the present two cable-net and fabric-formed prototypes as well as precedent studies on flexible formworks for which data was published. Here, the total difference between design model and final loaded state is compared, where the difference is the sum of deformations δ due to loading of the formwork and additional deviations Δ from the predicted geometry. Waling & Greszczuk (1960) measured deviations Δ from a true hypar, but prior to loading the formwork. Additional deformations δ due to loading were measured as well, and have been added here. Cauberg (2009) reports calculated deformations δ and additional measured deviations Δ of the formwork for six prototypes. Figure 10.9 illustrates that the design model for the present prototypes already included deformations, and that the initial, unloaded state was accordingly prestressed, or precambered.

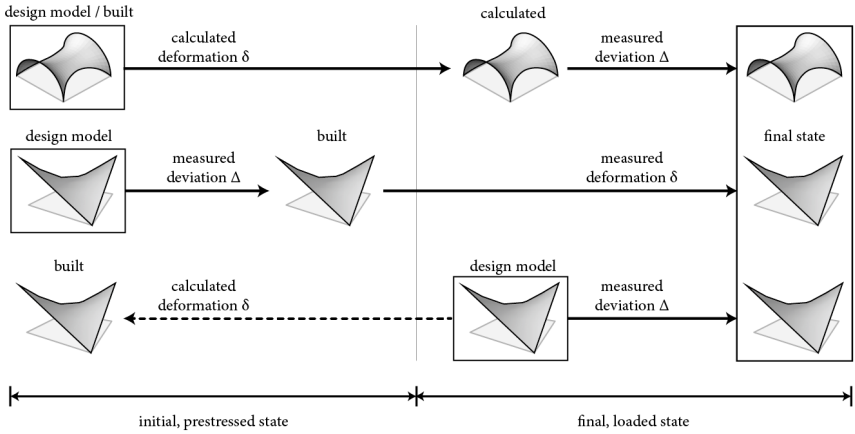

Figure 10.9: Sequence of differences from design model to final built state for Cauberg (2009), Waling & Greszczuk (1960) and the present study, with data in Table 10.3.

The total construction errors are the sum of deformations and deviations. These can be compared with the accidental imperfections w_0'', which are considered here to be the allowable tolerances. The accidental imperfections in Table 10.3 have been calculated according to Medwadowski (2004):

$$w_0'' = 0.1e + \frac{e\alpha_f}{2(1+\beta_s^{-2})}, \tag{8.24}$$

where shell thickness e is taken from Table 10.3, factor $\alpha_f = 12$ for air-inflated forms (assumed to be valid for flexible forms in general), the radius of curvature

type reference name	**surface**	**plan**	**span** s [m]	**rise** h [m]	**thickness** e [mm]	**def.** δ [mm]	**dev.** Δ [mm]	**total** [mm]	**≤ accid. imperf.** w_0'' [mm]
fabric-formed pseudo-catenoids (Cauberg 2009)									
A3	PVC coated PES	2×2	2	**0.5	50	18.0	**-1.8**	16.2	5.2
A5	⋮	⋮	⋮	⋮	⋮	16.1	**0.7**	16.8	⋮
A6	⋮	⋮	⋮	⋮	⋮	17.6	-5.6	12.0	⋮
A7	⋮	⋮	⋮	⋮	50	25.5	-9.4	16.1	5.2
A8	PVC coated PES	⋮	⋮	⋮	35	10.7	**1.0**	11.7	3.8
A9	uncoated fabric	2×2	2	**0.5	50	32.1	-17.3	14.8	5.2
cable-net formed hypars (Waling & Greszczuk 1960)									
small scale model	cable + EPS-foam	1×1	1.4	0.1	*35	17.6	5.1	22.7	4.4
laboratory model	cable + EPS-foam	6.1×6.1	8.6	1.1	*40	68.6	**12.7**	81.3	17.6
	+ mortar	6.1×6.1	8.6	1.1	*40	10.9	**12.7**	23.6	16.6
cable-net and fabric-formed pseudo-hypars (Veenendaal et al. 2014)									
prototype 1	cable + uncoated PP	1.8×1.8	2.5	0.6	24	N/A	22.1	22.1	3.6
prototype 2	cable + uncoated PP	1.8×1.8	2.5	0.6	*15	N/A	***1.3	**1.3**	3.4

Table 10.3: Comparison of deformations of the formwork and additional deviations, in flexible formworks. Deviations in bold meet accidental imperfections if deformations are excluded. Total values in bold meet accidental imperfection. *Thickness in equivalent amount of concrete to applied load in sand. **Rise not given, and estimated here.

$$R = \sqrt{R_1 R_2} = \sqrt{\frac{1}{K}}, \tag{8.25}$$

where R_1 and R_2 are the radii of principal curvatures and K is the Gaussian curvature, and

$$\beta_s = 0.001\frac{R}{e}. \tag{8.26}$$

The radius of curvature for the catenoids by Cauberg (2009) is estimated by assuming that at the edges, $R_1 = \frac{1}{2}s$, and that in the other direction the shape is also semi-circular, such that

$$R_2 = \frac{1}{8}\frac{4h^2 + s^2}{h}, \tag{10.1}$$

where span s and rise h are taken from Table 10.3.

The Gaussian curvature for the hypars by Waling & Greszczuk (1960) is assumed to be (Weisstein 2016)

$$K = -\frac{4a^6 b^6}{a^4 b^4 + 4b^4 x^2 + 4a^4 y^2}, \tag{10.2}$$

where, for a square hypar,

$$a = b = \frac{1}{2}s\sqrt{\frac{1}{h}}, \tag{10.3}$$

with span s taken from Table 10.3 and assuming the lowest curvature, located at the tips, where

$$x = y = \frac{1}{4}\sqrt{2}s. \tag{10.4}$$

Table 10.3 shows that the second prototype is the only flexible formwork that has deviations within the limit of accidental imperfections. This is partly because precedent studies did not include deformations in their design model. Instead, they constructed their formwork to reflect the design *prior* to loading, meaning any load immediately

represents a deviation. By considering their result as if they had followed the present approach of recalculating prestresses, we can exclude the deformations from their total error. In that case, the deviations for the laboratory model by Waling & Greszczuk (1960) and three out of six prototypes by Cauberg (2009) actually also fall within acceptable limits of the accidental imperfections.

Alternatively, the deviations can be accounted for by assuming larger imperfections in the stability analysis. If, for instance, we assume the imperfections to be $w_0'' = 0.75e$ (Dulácska & Kollár 1995), then more, but not all, flexible formworks in Table 10.3 have deviations below that limit. Of course, these higher construction deviations still need to be acceptable for reasons of serviceability.

10.5 Cost estimation

Table 10.4 shows the materials and their costs for the first prototype formwork. The cost of the formwork is CHF 527.79, or CHF 162.90 per plan square meter with nearly 60 % due to the timber frame. The relative cost is expected to go down at larger spans, where the ratio of surface area to edge perimeter is higher. This is more likely if the falsework system supporting the edge transfers its loads through supporting struts and ties rather than through bending of the edge itself. The relative cost will also go down for multiple use of the formwork. Indeed, much of the first prototype could be reused for the second one, reducing the average cost.

component	**type**	**qty.**	**cost per unit** [CHF/unit]	**total excl.** [CHF]	**total cost** [CHF]
timber	1 m 100×100 mm fir	25	11.50	287.50	310.50
fabric	1 m^2 Propex 60 – 7041	9	0.71	6.39	7.60
tacks	1 kg 1.8×20 mm	0.5	26.10		13.05
cable	1 m INOX V4a 2.0 mm	100	0.52	52.29	58.10
wire	steel wire 1 mm			12.00	12.96
cringle	6 mm	60	0.62	37.26	40.24
turnbuckle	M5	20	2.00	40.00	43.20
crimp sleeve	2 mm	60	0.09	5.49	5.93
quick link	4 mm	40	0.56	22.32	24.11
eye screw	M6×40	20	0.56	11.20	12.10
total					**527.79**

Table 10.4: List of materials, quantities and cost in Swiss francs for the first formwork.

Apart from the initial woodwork, construction involved only unskilled labour. The various activities are summarized in Table 10.5 for both prototypes.

activity	cable-net and fabric formwork				fabric formwork		
	no.		formwork	shell	no.	formwork	shell
	1	2	max.	avg.	3	max.	avg.
woodwork	8	1	8		1	1	
carpentry	39	15	39		16	16	
patterning	8	5	8		*	*	
installation	34	32		33	10		10
prestressing	12	14		13	1		1
concreting	22	14		18	25		25
total	123	81	55	64	62	26	36
total per unit area	**38**	**25**	**17**	**20**	**19**	**5**	**11**

Table 10.5: Labour involved in construction of prototypes and resulting shell structures in hours. Plan area is 3.2 m^2 for all prototypes. *labour included in price of membrane

The cost of formwork and shell construction can be expressed in €/m^2, by assuming an unskilled hourly rate of CHF 63, a construction cost index of 1.62 to convert from Switzerland to UK/US (Moore & Riley 2012), and an exchange rate of 0.91 from Swiss francs to €. The cost of concrete is not yet included. Naaman (2000) estimates 5.81-15.61 \$/m^2/cm for ferrocement construction in 1980, up to double that for on-site construction. The range is due to the amount and type of reinforcement. Correcting for inflation with 3.34 (Williamson & Officer 2016), and an exchange rate of 0.89 from US dollars to €, the lower limit for the cost is 33 €/m^2/cm, or 83 €/m^2 for a 25 mm thick shell.

The resulting cost for the formwork is

$$\left(\text{CHF } 63/\text{hr} \cdot 17 \text{ hr/m}^2 + \text{CHF } 162.90/\text{m}^2\right) \cdot 0.91/1.62 \approx 690 \text{ €/m}^2$$

and for the shell, it is

$$\text{CHF } 63/\text{hr} \cdot 20 \text{ hr/m}^2 \cdot 0.91/1.62 + 83 \text{ €/m}^2 \approx 790 \text{ €/m}^2.$$

The formwork cost of 690 €/m^2 is well above the 150-500 €/m^2 found for existing flexibly formed shells (Section 3.8.4), but still within the range of 400-800 €/m^2 for full-scale timber and milled foam formworks (Section 2.5.7).

The material cost of the third, fabric-formed prototype was CHF 2'380 or CHF 743.75/m^2, consisting of CHF 470 for the timber, CHF 1'650 for the membrane (incl. labour) and CHF 260 for hardware. The resulting cost for the formwork is

$$\left(\text{CHF } 63/\text{hr} \cdot 5\ \text{hr/m}^2 + \text{CHF } 743.75/\text{m}^2\right) \cdot 0.91/1.62 \approx 590\ €/\text{m}^2$$

and for the shell, it is

$$\text{CHF } 63/\text{hr} \cdot 11\ \text{hr/m}^2 \cdot 0.91/1.62 + 83\ €/\text{m}^2 \approx 470\ €/\text{m}^2.$$

Like the cost of the cable-net and fabric formworks, the cost of this fabric formwork is above that for existing flexible formworks, but comparable to that of timber and milled foam formworks.

10.6 Conclusions

Based on the historical overview in Chapter 3, including specific studies, as well as the present study in Section 10.4, possible strategies to improve accuracy of flexible formworks that have been used are:

- to reduce the applied loading by layering and curing the shell in stages, thereby creating a partially or entirely self-supporting structure as soon as possible;
- to increase the stiffness of the material (e.g. coated instead of uncoated fabrics, cable nets) and/or the prestress such that the formwork is less sensitive to the magnitude of the applied load;
- to design for the loaded state, in order to take deformations due to the applied concrete load into account when calculating prestresses, and thus exclude those deformations from the final construction errors; and,
- to accurately measure and correct these required prestresses before applying the concrete.

The approach used for the second prototype is based on the latter three: a cable net for the required prestresses in the final state are calculated, then measuring and controlling the prestresses required in the initial state.

An evaluation of the first prototype excluded modelling assumptions such as the magnitude of the loads and material stiffness as major sources of deviations.

A comparison of the present work with precedent studies in Table 10.3 demonstrates that deformations are considerable, and therefore must be taken into account in the design of flexible formworks to limit deviations. It is recommended to evaluate the influence of the stiffness of the external frame, possibly requiring the inclusion of beam elements during constrained form finding (best-fit optimization).

The second prototype offered significant improvements in deviations compared to the first and third one. Most of the remaining deviations were already present in the prestressed state. These observations underline the importance of accurate measurements of geometry and particularly forces, and subsequent control of prestresses. It is further recommended to prestress in a symmetric fashion from both ends of the cables, and prefabricate or measure the cable net in such a way that cumulative errors are avoided.

The third, fabric-formed prototype was unable to meet reasonable deviations, due to insufficient prestress and not having considered the local stiffness of the seams. It is unclear whether construction deviations or incorrect material modelling led to inadequate stress compensation of the patterns. Another difficulty, compared to cable nets, is that prestresses cannot easily be measured, or equipment to do so, is not commonly available.

The accidental imperfections need to be included in a stability analysis of the resulting shell structure according to IASS 1979. These imperfections can be calculated according to Medwadowski (2004) with $\alpha_f = 12$ (currently recommended for air-inflated forms), if best-fit optimization as well as force measurements and control are included in the design and construction process. The accuracy of the measurements and control needs to be comparable to that of the second prototype.

The cost of the prototypes is already competitive to that of full-scale, one-sided timber and milled foam formworks for concrete shells. For larger-sized, commercial versions, it is expected that economies of scale will reduce the cost, closer to that found for other, existing flexible formworks.

It's a serious problem that the majority of those who work only with computers today are incapable of seeing [...]. *One can't invent new structures by sitting in front of a computer, because the computer shows only the infinite possibilities of what has already been invented.*

— Frei Otto, 2004, from Songel (2010)

CHAPTER ELEVEN

Computational results

Based on the design process outlined in Chapter 7, a parametric study is carried out to investigate the limits and sensitivities of a flexibly formed shell. The span and slenderness of a square hyperbolic paraboloid are varied. The model outputs unity checks for deflection, strength and load factor of the shell based on a simple loading combination. The forces and stresses for the required cable-net or fabric formwork are calculated, as well as the reaction forces on the external frame. The structural analysis is linear elastic, and accounts for nonlinearities through safety and knockdown factors according to IASS 1979, as outlined in Chapter 8.

Section 11.1 outlines the parametric model, its parameters, variables, modelling assumptions, and limits placed on outputs. Section 11.2 presents results to establish limits for flexible formwork, investigate material economies, evaluate the influence of optimization on the formwork, and errors on its tolerances. Section 11.3 concludes the chapter.

11.1 Parametric model

Both a shell and its required formwork are modelled using a parametric model. The present example is a square hyperbolic paraboloid with four parameters governing its shape, two of which are kept fixed in this case: span s, proportion between width and length $\alpha = w/l = 1$, shallowness $\beta = s/h$ and a coefficient $a = 1$. A fifth parameter, slenderness s/t, determines the thickness.

11.1.1 Variables

The three parameters that are not fixed, are varied within the following bounds:

span	$5 \leq$	s	≤ 50 m;
shallowness		s/h	$= 2$ or 5;
slenderness	$50 \leq$	s/t	≤ 750.

The span is increased by 5 m increments, and slenderness by 100.

11.1.2 Loads

A simple loading combination is assumed: a live load of $p_t = 1$ kN/m^2 and the dead load $p_0 = \rho \cdot t$ where $\rho = 25$ kN/m^3. Strains due to shrinkage or temperature are not considered.

11.1.3 Material

The assumed material is a C50/60. This is a reasonable assumption, given that historical examples of cable-net formed hypar shells had a strength of about C45/55 to C50/60 regardless of whether they were cast or sprayed (Sections 3.7.3 and 3.7.4).

Additional parameters govern the structural analysis, safety and knockdown factors, as explained in Chapter 8. Based on equations (8.4) and (8.3), and Section 8.7.2, the reinforcement ratio ranges between $\mu_{rc} \approx 1.0$ and 4.0 %. Here, the assumed ratio is twice the lower limit. All parameters are:

density	ρ	=	25	kN/m^3;
yield strength	f_s	=	435	N/mm^2;
Young's modulus	E_s	=	210′000	N/mm^2;
reinforcement ratio	μ_{rc}	=	0.02;	
reinforcement parameter	η	=	0.2;	
time at loading	t_0	=	28	days;
relative humidity	RH	=	75	%.

For the cable net, the Young's modulus is 200'000 N/mm^2 and the assumed strength is 500 N/mm^2. For the fabric, the Young's modulus is 1'000 kN/m and the strength is 150 kN/m with a material factor of 5.

11.1.4 Geometry

The square hypar is defined as

$$z(x, y) = \frac{1}{2}\left(x^2 + y^2\right)\left(\frac{1}{a^2} - \frac{1}{b^2}\right) + xy\left(\frac{1}{a^2} + \frac{1}{b^2}\right). \tag{11.1}$$

If straight edges are assumed, then $b = a$, such that

$$z(x, y) = \frac{2xy}{b^2}. \tag{11.2}$$

The Gaussian curvature

$$K(x, y) = \frac{k_1^2 - k_2^2}{\left(1 + (k_1 x + k_2 y)^2 + (k_2 x + k_1 y)^2\right)^2}, \tag{11.3}$$

where

$$k_1 = \frac{1}{a^2} - \frac{1}{b^2} \text{ and } k_2 = \frac{1}{a^2} + \frac{1}{b^2}.$$

If the edges of the hypar are fixed, the span s is equal to its width, so $s = w$. For a given proportion $\alpha = w/l$, the rise of the hypar $h = -z\left(w/2, -1/\alpha \cdot w/2\right)$,

$$h = c_1 \frac{s^2}{a^2} + c_2 \frac{s^2}{b^2} \tag{11.4}$$

where

$$c_1 = \frac{1}{8}\left(-1 + \frac{2}{\alpha} - \frac{1}{\alpha^2}\right) \text{ and } c_2 = \frac{1}{8}\left(1 + \frac{2}{\alpha} + \frac{1}{\alpha^2}\right). \tag{11.5}$$

For straight edges with $b = a$, the rise simplifies to

$$h = \frac{1}{2\alpha}\frac{s^2}{b^2}. \tag{11.6}$$

For a given span s, proportion $\alpha = w/l$, shallowness $\beta = s/h$, and a given proportion $\gamma = a/b$, such that $a = \gamma \cdot b$,

$$b = \sqrt{\beta s \left(\frac{1}{\gamma^2} c_1 + c_2 \right)} \tag{11.7}$$

or, if $b = a$,

$$b = \sqrt{\frac{\beta s}{2\alpha}}. \tag{11.8}$$

The boundary conditions of the hypar are three fixed vertices at each corner, and vertical springs along the perimeter to model a structural facade (Figure 11.1). The spring constants are determined by first analyzing the shell with a fixed perimeter. The vertical reaction forces are then divided by 1/1000th times the span s, to obtain the constants. This assumes that the facade is structurally engineered to allow deflections in this order of magnitude.

The cable-net formwork is modelled by a fixed spacing of 1/10th of the span, such that the number of elements remains constant regardless of the span, and analysis does not slow down. When increasing density, the cable force per meter width was observed to stay fairly constant, showing that this assumption is acceptable. At the same time, this force per meter width can be used to represent the stress in a fabric formwork, i.e. the cable-net analogy.

11.1.5 Limits

Several potential limiting factors influence the feasibility of a flexibly formed shell. These are the allowable deflection, material strength and buckling of the shell, as well as the allowable prestress and material strength of a fabric formwork.

As cables are widely available in very large dimensions, and equipment to prestress them exists, no limit is suggested for allowable prestress or strength of the cables. Instead, the required unit weight of cable steel is used as the vertical axis to present the results from the parametric study. However, the weight of two seminal cable-net roofs, the Munich Olympic Stadium and the London Velodrome, is indicated for reference.

Deflection

The allowable deflection of the shell is set to be 1/500th of the span. The Young's modulus of concrete E_c is reduced according to equation (8.32) to account for the effect of creep in the calculation of deflections. Note that this value is not applied when calculating the buckling load factor, where it is taken into account through reduction factor ρ_{crp} (Section 8.7.2).

Concrete strength

For the "design of bending reinforcement [of shells] no satisfactory method exists. Generally, the methods copied from the design of beams seem to be used" (Medwadowski 1998). An approximation method for beam design is used here to establish the stress when both the concrete and steel have reached yield strain and become plastic. This stress is then used as an upper limit for design using linear elastic analysis.

Using the assumed reinforcement ratio μ_{rc}, the force equilibrium in the section, between the resultant compression force in the concrete compression zone and tension force in the reinforcement in the cracked zone, requires that

$$\begin{aligned} A_s/2 \cdot f_s &= 0.8x \cdot 0.95 f_{cd} \\ \mu_{rc}/2 \cdot t \cdot f_s &= 0.76 x f_{cd} \\ x &= \frac{25}{38}\mu_{rc}\frac{f_s}{f_{cd}}t \end{aligned} \tag{11.9}$$

per unit width, where x is the height of the compression zone, and 0.80 and 0.95 are factors related to an approximation that the compression zone is fully plastic. According to SIA 262:2003, the dimensioning value of the concrete strength

$$f_{cd} = \frac{1}{1.5}\eta_{fc} f_{ck}, \tag{11.10}$$

with

$$\eta_{fc}\left(\frac{30}{f_{ck}}\right)^{1/3} \leq 1.0, \tag{11.11}$$

meaning in our case, $f_{\mathrm{cd}} = 28.1\ \mathrm{N/mm^2}$. The bending moment at plastic failure, assuming the resultant of the reinforcement acts at $0.9t$ from the top, is

$$\begin{aligned} M_{\mathrm{u}} &= (0.9t - 0.4x)\, A_s/2 \cdot f_s \\ &= \left(\frac{9}{20}t - \frac{1}{5}x\right) \mu_{\mathrm{rc}} t \cdot f_s \end{aligned} \tag{11.12}$$

per unit width. The second moment of area of the cracked section is (Naaman 2000)

$$I_{\mathrm{cr}} = \frac{1}{3}x^3 + \frac{1}{2} n \mu_{\mathrm{rc}} t (0.9t - x)^2 \tag{11.13}$$

per unit width, where $n = E_{\mathrm{s}}/E_{\mathrm{cr}}$, and ignoring the contribution of the reinforcement on the compression side. The corresponding stress, which we take to be the linear elastic strength, is

$$f_{\mathrm{y}} = \frac{M_{\mathrm{u}} x}{I_{\mathrm{cr}}}, \tag{11.14}$$

which is used as an upper limit during linear elastic analysis. The linear elastic Von Mises stress is used, assuming plane stress, so that

$$\sigma_{\mathrm{v}} = \sqrt{\sigma_1^2 + \sigma_2^2 + \sigma_1 \sigma_2}. \tag{11.15}$$

Partial factors are applied to the stresses in proportion to the self-weight and the live load, to then check in the ultimate limit state (ULS) whether

$$\frac{1.2 \cdot \sigma_{\mathrm{v},0} + 1.5 \cdot \sigma_{\mathrm{v,t}}}{f_{\mathrm{y}}} \leq 1.0, \tag{11.16}$$

noting that the strength f_{y} already included a material factor of 1.5.

Buckling

The shell is checked using the buckling formula in equation (8.12), based on the linear critical buckling load factor $p_{\mathrm{cr}}^{\mathrm{lin}}/p$, divided by the safety factor λ_{s} and multiplied by the knockdown factor γ_{k}. Both factors are automatically calculated in the parametric model, by implementing all the equations of Chapter 8.

Prestress and strength

The allowable prestress of the fabric is assumed to be 9 kN/m, taken as 6 % of the fabric strength (Forster & Mollaert 2004). The allowable stress, or fabric strength, is assumed to be 30 kN/m, based on a material safety factor of 5 (Forster & Mollaert 2004).

11.2 Results

By varying span, shallowness and slenderness at regular intervals between the bounds, 160 shells and corresponding formworks were generated and analyzed. Each analysis took only eight seconds. Figure 11.1 shows a sample result for all results generated within the allowable values for span, shallowness and slenderness.

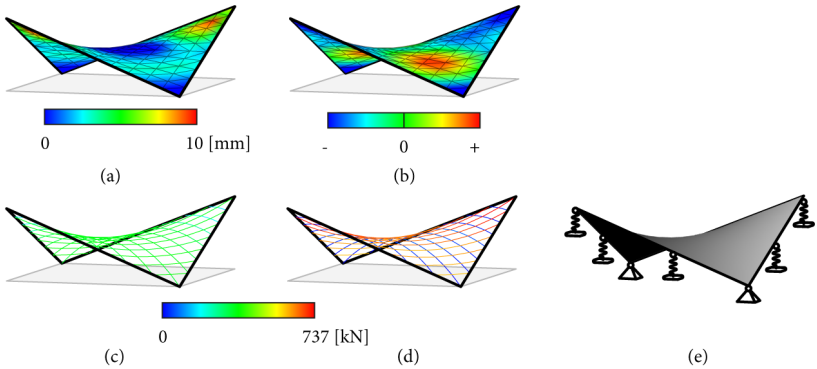

Figure 11.1: Sample result for 30 m span, shallowness of 5, and slenderness of 150. Results include (a) displacements, (b) buckling mode, cable force (c) before and (d) after casting. (e) Boundary conditions during analysis are schematically shown.

11.2.1 Mechanical limits

Figure 11.2 shows the required weight of a cable net per unit of surface area. As expected, the weight increases with the span and thickness (as the slenderness decreases).

The dimensions of two square hypars are indicated for reference: the 1968 Ostseeperle Restaurant in Glowe, Germany, by Ulrich Müther (Lämmler & Wagner 2010); and, the 1955 Chapel of Nuestra Señora de la Soledad, or El Altillo Chapel, in Mexico City by Félix Candela (Faber 1963).

The governing limit for the shell structure itself is the buckling load factor. It occurs roughly around a slenderness of 150. That this limit corresponds with a specific slenderness is not surprising when considering the critical buckling load in equation (8.15). In this equation, the buckling load is proportional to the thickness t squared over the radius of curvature R, similar to the slenderness squared. Note that many shells mentioned in Chapter 2 are considerably thinner, up to a slenderness of 750. These are aggregated hypars, suggesting that their boundary conditions allow for larger buckling load factors.

The application of a fabric formwork is limited by the allowable fabric strength and prestress, which occurs around spans of 8 to 12 m. The remaining feasible space is limited (Figure 11.2).

For a cable-net formwork, the feasible space is larger. The weight of two cable-net roofs is indicated as a possible practical limit for construction of a cable-net formwork: the 1972 Munich Olympic Stadion (Figure 2.41) and the 2011 London Velodrome (Figure 11.2). If the latter's weight is considered to be a limit, then a cable-net formwork can be applied for spans of up to 20 to 25 m. For the former reference project, this can be higher, up to 35 to 40 m.

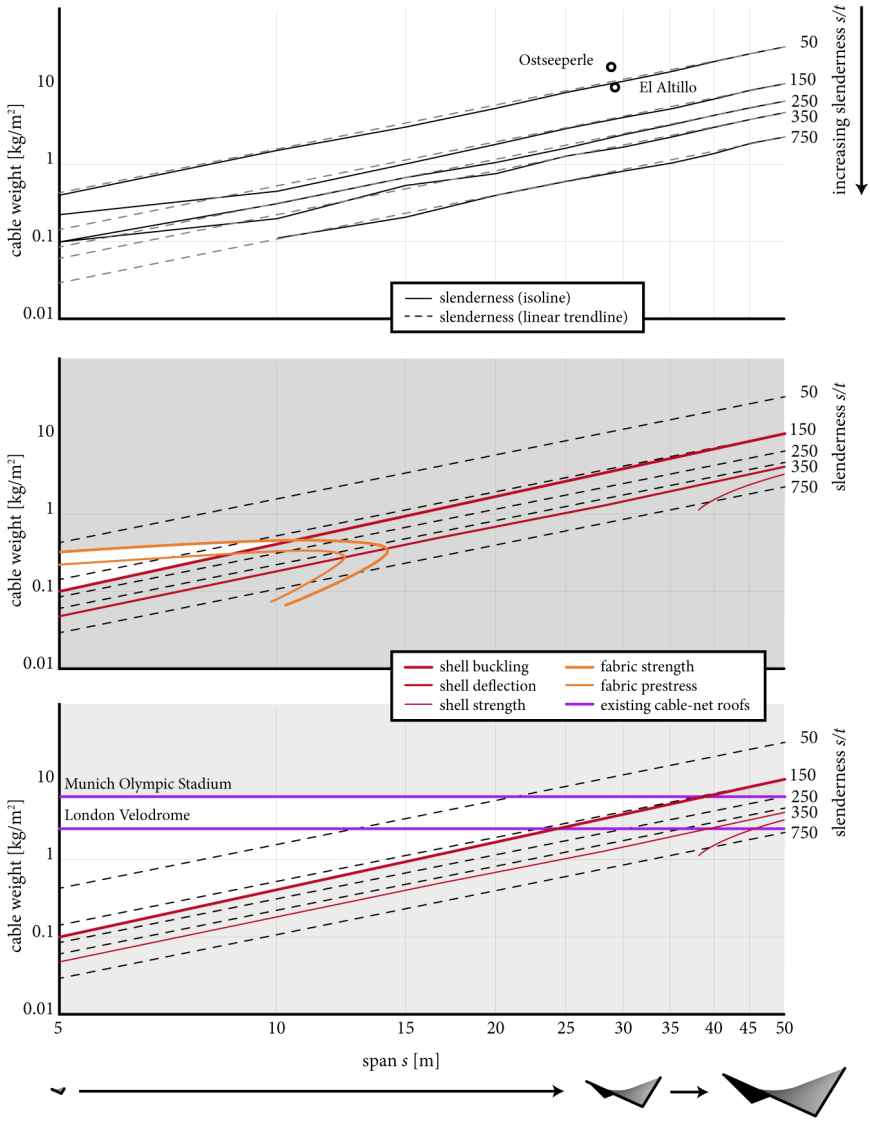

Figure 11.2: Cable weight per unit of surface area, relative to span and slenderness, for a shallowness of 5 with trendlines. The feasible space for a fabric formwork is bounded by limits of shell buckling and fabric strength, for a cable-net formwork by shell buckling and cable weight.

Surprisingly, the shallowness does not fundamentally change these findings. For instance, for a shallowness of 2, limits for the shell are similar. For most results, cable forces and fabric stresses are only 10 and 20 % lower respectively.

11.2.2 Economy of the falsework

To investigate how the external frame compares to the scaffolding for a rigid formwork, a dimensionless falsework ratio is proposed.

The structural mass of the cable-net formwork is assumed to correlate with the vertical reaction forces along the perimeter l times the average height, or the rise h of the shell. The vertical reaction force is the sum of the vertical force F_{H} per meter width and the force produced by a moment due to the horizontal force F_{V} per meter width. It is assumed that the external frame has a vertical slenderness of 1/8. As a result, our first quantity,

$$c_1 = \left(F_{\mathrm{H}} + \frac{F_{\mathrm{v}} \cdot h}{1/8 \cdot h}\right) \cdot l \cdot h = \left(F_{\mathrm{H}} + 8F_{\mathrm{H}}\right) \cdot l \cdot h. \tag{11.17}$$

The structural mass of a rigid formwork is assumed to correlate with the weight of the shell times the volume underneath the shell, so that our second quantity,

$$c_2 = \rho g \cdot t \cdot A \cdot h \tag{11.18}$$

where ρ is the concrete density, g is the gravitational constant, and A is the footprint of the shell.

Both quantities are in kNm, and their ratio c_1/c_2, is a dimensionless number. This falsework ratio turns out to be 21.3, independent of span or slenderness (Figure 11.3). This suggests that whatever the ratio of structural mass between both solutions is, it does not change when a shell is longer or thicker.

Figure 11.3: Weight indicators for the falsework for a cable-net and a rigid formwork

11.2.3 Influence of optimization

Whether structural optimization can improve the established limits is investigated by taking a shell near the reference projects in Figure 11.2: a span of 30 m, slenderness of 150, and a shallowness of 5. The optimization is performed as discussed in Section 7.2.2, using a genetic algorithm. The hypar of uniform thickness is allowed to change shape and thickness within its boundary conditions, while keeping volume constant. The minimum thickness is 40 mm. The shell is optimized for the load factor with or without an imperfection. The imperfection is the first buckling mode with an amplitude equal to the average shell thickness.

Table 11.1 shows that, in this case, neither objective produces a shell that is superior in both respects. Therefore, the shape and thickness optimization is unable to fundamentally alter the limits shown in Figure 11.2.

	variables				performance		
	c	t_1	t_9	t_2	λ	λ_{imp}	
	[-]	[mm]	[mm]	[mm]	10^3·[Nm]	[-]	[-]
hypar	0.0	200	200	200	14.8	6.8	
variable	0.9	40	40	350	**36.4**	5.7	
variable	0.0	40	60	460	10.7	**15.7**	

Table 11.1: Initial hypar of uniform thickness, optimized for shape and thickness for load factor with imperfection.

11.2.4 Sensitivities to errors

As a final result for the 30 m hypar, some of the inputs for the prestressed state are altered to investigate sensitivity to errors. The measured quantities are the maximum node deviation and maximum force deviation; quantities that can be controlled during construction. The parameters that were varied are: the initial lengths, controlling the stiffness and thus the internal forces; and, the applied concrete, controlling the external forces. The error is introduced uniformly, which is conservative. No asymmetry or distribution of errors was checked. The cable segments are 1/10th of the span, so the errors in initial length are introduced along roughly 3 m segment lengths.

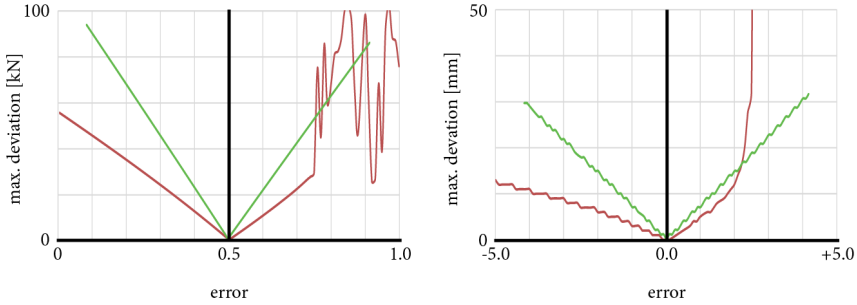

Figure 11.4: Maximum deviations in resulting force and node position, for decreasing or increasing (red) initial lengths × 1 mm and (green) applied concrete thickness × 10 mm.

Figure 11.4 shows a certain range of errors, and resulting deviations. The instability that can be observed, is due to sagging of the net, as lengths of the cable segments increase. Large errors would be difficult to observe geometrically on site, yet quickly translate into large deviations in forces. This suggests that there is substantial room for errors, but also that force measurements are the best way to register, and thus control them.

If we allow a deviation of 1/1000th of the span, while avoiding any instability, the load can be ± 40 mm and the initial geometry ± 2/3 mm/m. Alternatively, the forces have to be measured and controlled to a precision of ± 20 kN at this scale, or 3 % of the maximum force. The latter corresponds with the 2 % accuracy used for the successful construction of the second prototype in Section 10.2.

11.3 Conclusions

The design process was implemented in a parametric model. Individual results were generated within eight seconds, demonstrating its applicability to early parametric design or optimization stages. Flexibly formed shells are limited by: the buckling of the shell; and, depending on the type of formwork, the allowable fabric prestress, or practical weight of the cable net.

For the given example, a fabric formwork and a cable-net formwork can be applied to shells, with a slenderness of 150 and shallowness of 5, for spans of up to almost 10 to 15 m and up to almost 20 to 40 m, respectively. Ways to increase this range are to decrease the shallowness, but mainly to allow for greater slenderness, by

improving the buckling load factor in turn. Shape and thickness optimization of the uniform hypar was unable to achieve the latter. This means that the entire boundary conditions need to be changed, and potentially considered in the optimization, as was done for the case study in Chapter 12.

Based on a simple dimensional analysis, the structural mass of the flexible formwork's external frame is proportional to that of the weight of scaffolding and shoring of a rigid formwork, independent of span or slenderness. The proportion itself, expressed in mass, has not yet been established as this would require a full design of a rigid formwork and a flexible formwork for the same shell geometry. Reported cost savings for flexible formworks are 25 % in several cases, indeed regardless of span, which indicates that the proportion is in favour of flexible formworks (Chapter 3). In other words, this suggests that although the mass and cost may scale linearly, exponentially or however with size, the relative savings of a flexible formwork remain constant.

Errors in the initial geometry of a cable-net formwork have to be controlled through precise fabrication, and subsequent measurements and corrections of the prestress. The resulting geometry is relatively insensitive to errors in the applied loads.

[…] *very large spans in fact do not make much sense any more. A large dimension in itself is no proof of quality. Similarly, the fattest, the skinniest or the biggest woman* [or man] *is not the most attractive one.*

— Heinz Isler, 1995, about the CNIT shell.

CHAPTER TWELVE

Case study: NEST HiLo

HiLo is a research & innovation unit within the NEST building demonstrating ultra-lightweight construction and active building systems (Figure 12.1). HiLo is planned as a 16 × 9 m duplex penthouse apartment for visiting faculty of Swiss federal research institutes Empa and Eawag to be completed in 2018 in Dübendorf, Switzerland (Figure 12.2). The roof of HiLo is planned as a concrete thin-shell structure with a unique shape and modest span, constructed on a cable-net and fabric formwork, and its development was part of the present work[1].

The final design of HiLo was a collaborative effort of the Block Research Group (BRG) and the Architecture and Building Systems Group (A/S), both at the Institute of Technology in Architecture, ETH Zurich, joined by architectural offices Supermanoeuvre and ZJA Zwarts & Jansma Architects. HiLo introduces several innovations (Figure 12.3) (Block et al. 2017), and this chapter focuses on the development of the roof.

This chapter describes the geometry and structural design of the HiLo roof at the final design stage submitted in August 2015, prior to the detailed engineering and tendering (referred to as the "Bauprojekt" stage in Switzerland). Section 12.1 offers a description of the concrete shell roof structure with emphasis on unique aspects such as its open edges, sandwich section and mesh reinforcement. The form finding and optimization of the roof geometry is described in Section 12.2. Parts of that process, the parametric generation of the roof boundary and topology, were developed by ZJA as part of the collaboration (Section 12.2.1 and 12.2.2). The resulting formwork is discussed in

[1]This chapter is based on Veenendaal, Bakker & Block (2015, 2017)

Figure 12.1: NEST building as of May 2016, Dübendorf, Switzerland.

Section 12.3. More advanced structural analysis of the final roof, too computationally demanding to include in the optimization, is discussed in Section 12.4. Results from both the optimization and final analysis are presented in Section 12.5, before offering some details on their implementation in Section 12.6 and conclusions in Section 12.7.

12.1 Structural description

The roof of HiLo is an anticlastic, thin-shell structure to be constructed using a prestressed, cable-net and fabric formwork. The shell has a total concrete thickness varying between 30 and 300 mm, 80 mm on average, features spans in the range of 6-9 m and is supported on five "touch-down" points with free edges along its entire perimeter. The 157 m^2 shell is built up as a sandwich composite consisting of ferrocement or textile-reinforced concrete faces, and a rigid polyurethane (PU) core, meaning the total structural depth ranging from 30 to 415 mm, 142 mm on average.

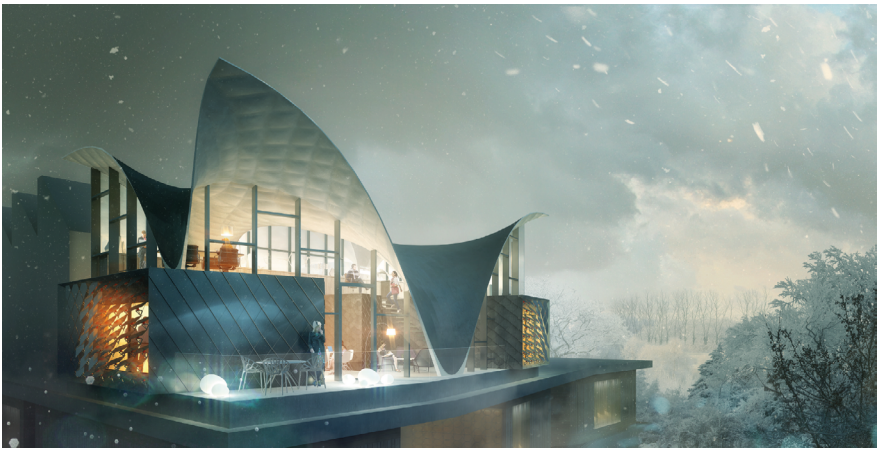

Figure 12.2: Visualisation of final design stage of HiLo on the top floor of NEST.

12.1.1 Thin, free edges

Unlike historical hypars with straight edges, HiLo's roof shell has no edge beams, but features thin edges, thickening towards the five supports. The shell is not supported by the facade mullions, which only transmit horizontal wind loads from the glazing, via the mullions, to the shell. The shell has no internal ribs, unlike traditional shells composed of multiple hypars.

For single or gabled hypar roofs, reducing or entirely removing any edge beam (possibly thickening the shell at the supports) decreases overall shell bending (Jadik & Billington 1995, Ortega & Robles 2003). Although maximum displacements may increase, they are not significant compared to serviceability limits.

Kollár & Dulácska (1984) claim, based on a synclastic model test, that shells with free edges exhibit global rather than local buckling. They may have increasing load capacity after buckling, provided that internal forces can shift to the interior and this inner part is able to carry more load than the original load paths in compression. Tomás & Tovar (2012) show results for hypars which become imperfection insensitive if only the corners instead of the edges are clamped and supported.

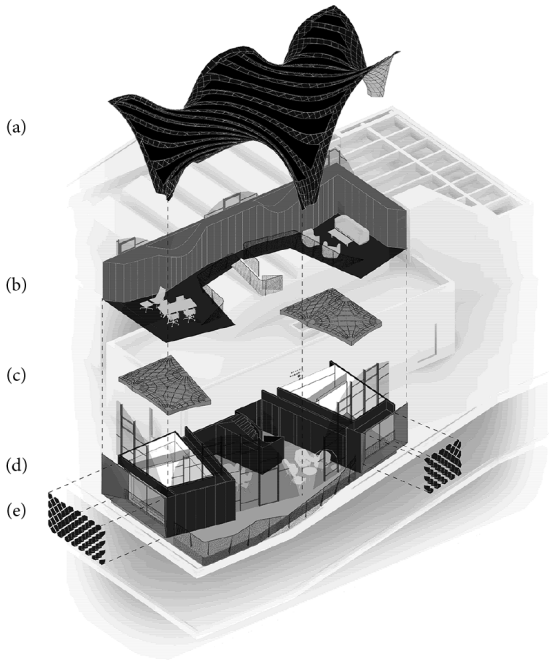

Figure 12.3: Key innovations and components of HiLo: a) the flexibly formed sandwich shell roof with photovoltaics; b) the mezzanine level; c) a funicular floor system; d) an entry level with ribbon wall concealing utilities and services; and, e) a soft-actuated adaptive solar facade.

12.1.2 Sandwich

The shell is subject to strict requirements for energy performance. The required U-value is 0.17 W/mK and the overall apartment is supposed to generate a 40-50 % annual weighted energy surplus. The roof is used as a solar collector for electrical and possibly thermal energy on the outside, and as a low energy, hydronic heating and cooling system on the inside, requiring the inside concrete surface to remain exposed.

To minimize thermal bridging, the connection between the glass facade and shell led to the present sandwich designs (Figure 12.4). Although intuitively the sandwich would seem to present only structural benefits by increasing structural depth and reducing sensitivity to external loads and imperfections, the differences in temperature and humidity on either side of the PU core lead to higher thermal loads and

differential strains due to creep and shrinkage. For this reason, but also to reduce complexity during construction, an alternative has been calculated in which the sandwich only occurs along the glass and the interior part of the shell is a single layer (Figure 12.4).

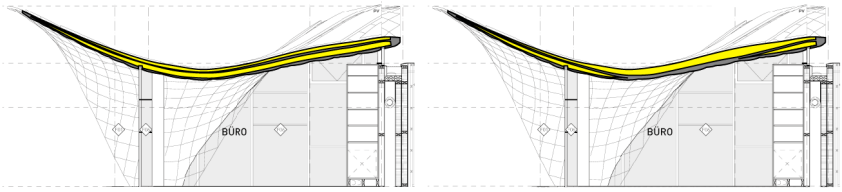

Figure 12.4: Roof section of HiLo with full sandwich, and alternative with sandwich locally along glass facade (adapted from drawing by Supermanoeuvre)

12.1.3 Reinforcement

Due to the thinness of the shell and various unfavourable load cases and combinations, the shell will locally act in bending and thus needs to be reinforced accordingly. The shell can be reinforced using woven (or welded) meshes made of ferrocement or alkali-resistant (AR) glassfibre or carbonfibre textile reinforced concrete (TRC) (Figure 12.5). This will allow us to maintain thinness, by following curvatures more easily than traditional rebar, and requiring only minimal cover of 2 mm (ACI 549R-97).

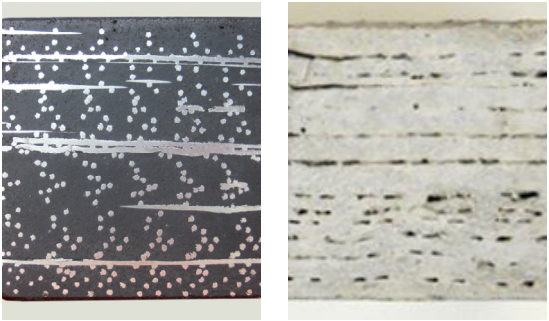

Figure 12.5: Examples of ferrocement and carbon-fibre TRC sections, 50 mm thick, showing dense mesh reinforcement (Eisenbach et al. 2014, Schneider 2011).

The decision for the final material and dimensioning of the reinforcement mesh (steel, AR-glass, or carbon) will be made in the next phase. Due to its high in-plane thermal conductivity and wide availability, ferrocement was originally favoured as reinforcement for the thermally active and innovative roof. Potentially the materials can be combined to improve thermal conductivity only for the interior part of the shell, while suppressing it at the connection to the glass facade and at the exterior.

12.2 Form finding and optimization

The design process for the roof consists of an integrated parametric model used for evolutionary optimization of the shell, and subsequent analysis of its nonlinear behaviour as well as the flexible formwork used for its construction. The number of criteria and variables changed throughout the design process, as the roof geometry and its constraints were increasingly developed and refined. The decision to shift from a single layer to a sandwich was made near the end of the design process, and was mainly dealt with in the final analysis. Figure 12.6 explains the computational design process of HiLo, consisting of form generation, structural analysis, and shape optimization.

The process consists of boundary, topology and form generation (Sections 12.2.1, 12.2.2 and 12.2.3) followed by load generation (Section 12.2.4) to allow for thickness optimization (Section 12.2.5). The shell geometry and mass is now fixed and can be evaluated for further for cable-net forces (Section 12.4) as well as the amount of glazing along its perimeter. These parameters were then used to inform the shape optimization (Section 12.2.7).

The geometry that is initially generated is maintained throughout the entire process, acting both as the layout of the cable net and the mesh of the shell itself (apart from triangulation, some nodes inserted to apply wind loads from the glass façade, and subdivision for further analysis in Section 12.4).

12.2.1 Boundary conditions

The shape of the roof is largely determined by the geometry of its boundary edges, and the topology of the generating network. The edge consists of four or five undulations, one for each support, curving between each support position to the given height h of the roof. Each half undulation is characterised by an amplitude $a = h$, period p, and sharpness s (Figure 12.7),

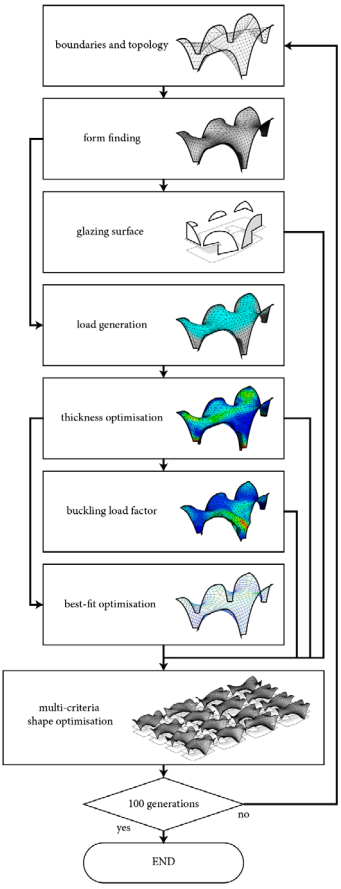

Figure 12.6: Workflow of optimization and analysis.

$$z(t) = a\cos^2\left(t(x)\frac{\pi}{2p}\right) \tag{12.1}$$

where

$$t(x) = \frac{s \cdot x + x}{s \cdot x + 1} \tag{12.2}$$

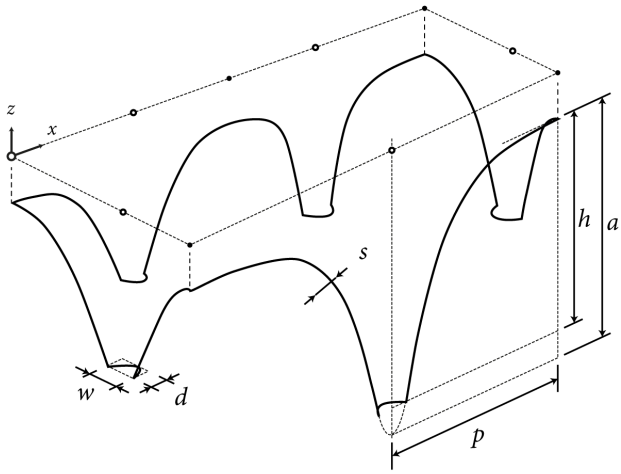

Figure 12.7: Boundary generation with vertical coordinate z from perimeter coordinate x and roof height h. Each support is a parabola with width w and depth d. Between the supports and corners, each half undulation has an amplitude a, sharpness s and period p.

In a first optimization, four or five support positions, determining p, the sharpnesses s, and the roof height h, were parameters for the optimization.

The boundary curves can extend below the foundation and can optionally be cut off. By doing this, the roof touches down on the floor with a planar, curved footprint. These are defined as parabolas with a certain width w and depth d; two additional parameters for the edge shape (Figure 12.7). The resulting space is required for the exterior insulation, drainage, connections to the thin-film photovoltaics and hydronic system, providing effective area for the supports, and ensuring that the glass facade connects to the shell at angles of ±45° to allow for proper detailing. In this case, the sharpness s can be determined from a height h, period p, width w and amplitude a

$$s = -\frac{c + \pi n}{n\left(c + 2\pi n - \pi\right)} \tag{12.3}$$

where

$$c = \arccos\left(2h/a - 1\right) \tag{12.4}$$

and

$$n = \frac{1}{2}\frac{w}{p} \tag{12.5}$$

In the final optimization, the five support positions were fixed, leaving three parameters for optimization: width w, amplitude a, depth d, i.e. fifteen variables for optimization.

12.2.2 Topology generation

The roof is then divided into five convex patches, determined by five points B_i on the shell's boundary and three interior points S_i (Figure 12.8).

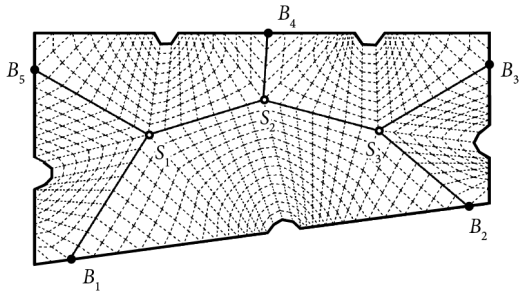

Figure 12.8: Topology generation.

Each patch is then subdivided along approximately radial and concentric directions with respect to the support positions. The interior edges of the patch are divided into an equal number of segments that are as close as possible to some desired, global edge length. This same number then subdivides the exterior edges of the patch. The resulting vertices are connected to the corresponding vertices along the interior edges. Starting at the outermost exterior vertices, concentric edges are created that follow the interior boundary of the patch, crossing all radial edges in between. For undulations that are cut off, the exterior vertices are divided evenly over the three exterior curve segments, based on their relative lengths. The parabolic segments get at least three vertices, to avoid degrading them into straight lines.

12.2.3 Form finding

From these boundary conditions, a suitable, anticlastic shape is generated using the linear force density method (Schek 1974). To minimise the number of additional variables for optimization, the force densities throughout the network are determined by interpolating nine or eleven values for four or five supports respectively (Figure 12.9). The total number of variables then varies between 18 and 26 (Table 12.1).

			single August 2014		multi May 2015
no. of supports n			4	5	5
support location	x	n	4	5	-
support sharpness	s	n	4	5	-
support width	w	n	-	-	5
support depth	d	n	-	-	5
support amplitude	a	n	-	-	5
height of roof	h	1	1	1	-
force densities	q	$2n+1$	9	11	11
total no. of variables			18	22	26

Table 12.1: Number and type of variables for optimization for four and five support points in initial stage ($4n + 2$), and five supports in final stage ($5n + 1$).

The ratio of allowable force densities is limited to 1:20, to create reasonable shapes without too abrupt changes in curvature and resulting forces. In the case of cut-off supports, the network potentially curves in on itself. This is remedied by calculating force densities of the network's triangulated projection using the linear natural force density method (Pauletti & Pimenta 2008). This tends towards a minimal surface of our projection, avoiding overlaps, and thus any inward curving. These force densities are then used in a second form-finding procedure, in which the shape is also partially constrained to the first form-found mesh.

12.2.4 Load generation

At this point, the shape for a possible roof design can be generated and must now be evaluated to allow optimization. For each shape, loads based on SIA 261:2003 are automatically generated to be applied to the roof as the starting point for structural evaluation. These loads include:

- the self-weight of the concrete (24 kN/m^3);
- dead loads from the integrated shell (0.3 kN/m^2);

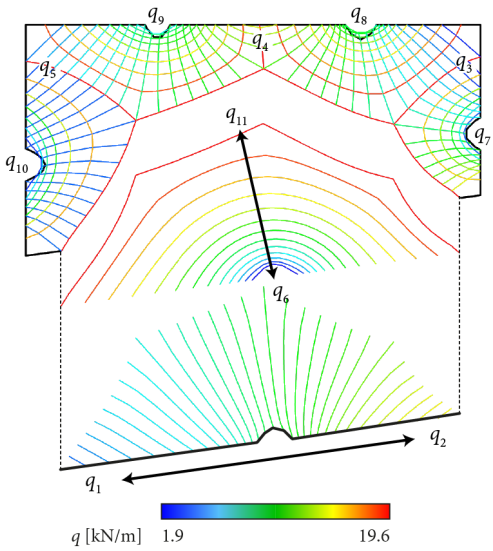

Figure 12.9: Force densities interpolated from eleven values.

- live loads for maintenance on the roof (0.4 kN/m^2);
- thermal loads due to the embedded hydronic system for a minimum temperature of 0 °C for optimization and -20 °C for final analysis (Figure 12.10);
- snow loads ($\mu_k \times 0.9$ kN/m^2 (Figure 12.11), and;
- wind loads ($C_p \times 1.07$ kN/m^2) (Figure 12.12).

Thermal loads

Thermal actions were defined on the basis of CFD models by A/S.

The initial optimization assumed a single layer shell with an ambient temperature of 0.0 °C and shell temperature of 33.0 °C due to the hydronic heating system.

Further analysis was based on the sandwich shell, which is partially insulated and also hydronically heated. The thermal expansion of concrete $\alpha_T = 10 \cdot 10^{-6}$ K^{-1} (SIA 261:2003, art. 7.1.5). Only in-plane temperature changes were considered at this stage, excluding temperature gradients along the individual layers.

The thermal actions are calculated differently for the serviceability limit state (SLS) and the ultimate limit state (ULS) (Table 12.2). In both cases, thermal conductivity for the concrete is 1.5 W/mK and 0.022 up to 0.035 W/mK for the PU (outer insulation and sandwich core). In SLS, the temperatures in the shell are calculated based on an average ambient temperature of 9.4 °C based on local weather files. In ULS, the temperatures are calculated based on an assumed extreme ambient temperature of -20 °C.

temperature	exterior	outer shell	inner shell	interior	difference
single shell (SLS)	0.0	33.0			33.0
sandwich (SLS)	9.4	17.7	27.3	21.7	9.6
sandwich (ULS)	-20.0	2.5	28.4	20.0	25.9

Table 12.2: Temperatures of the inner and outer shell for maximum PU core thickness, as inputs for thermal action in SLS and ULS.

Temperatures for the outer shell were calculated from these results for varying thickness of the sandwich insulation. The thicker the insulation, the higher the temperature difference between both concrete layer, and thus the resulting thermal action on the shell (Figure 12.10).

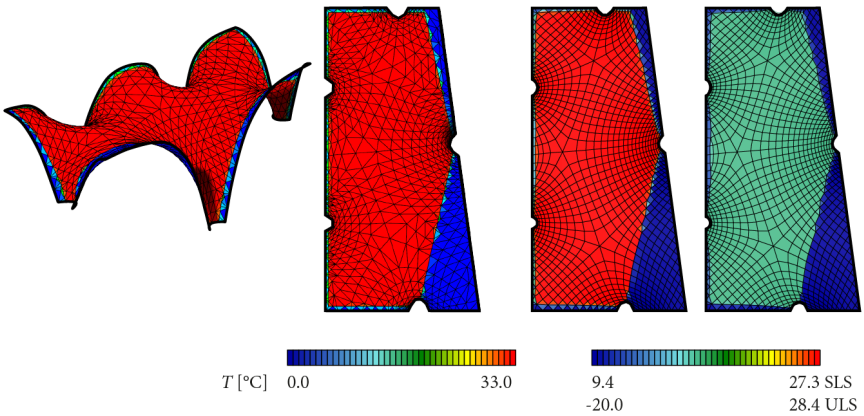

Figure 12.10: Thermal actions for single and sandwich shell.

Snow loads

The snow shape factor μ_k varies between 0 and 0.8 depending on the roof angle (SIA 261:2003) and multiplied with a snow pressure s_k = 0.8 kN/m^2 (Figure 12.11). Accumulation of snow at the supports was omitted, pending further detailing of the supports in the detailed engineering phase.

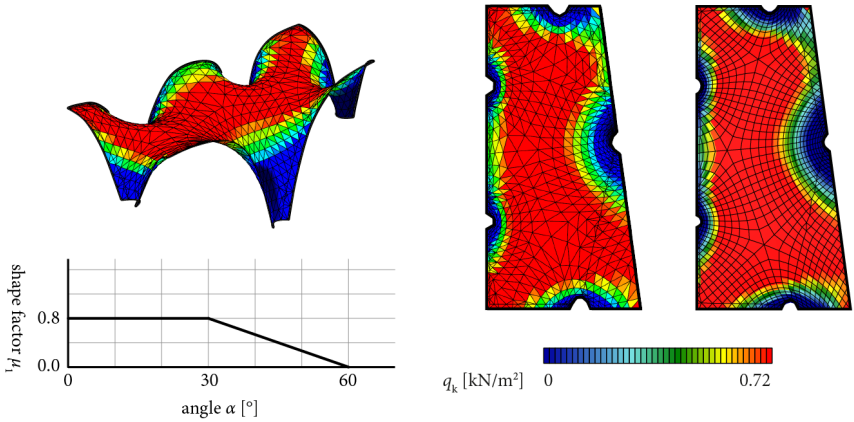

Figure 12.11: Snow loads q_k depending the shape factor $\mu_{k,1}$ according to SIA 261:2003.

Wind loads

To obtain the wind loads, the wind pressure q_p = 1.07 kN/m^2 is multiplied by shape factors, depending on the shape of the building, and the direction of the wind, and applied normal to the surface of the shell. The wind pressure assumes a Type III area, initial pressure of 0.9 kN/m^2 and building height of z = 20 m (SIA 261:2003).

Two governing wind load cases were defined: one for wind suction, one for wind pressure, both in the same direction (Figure 12.12). They assume the building is closed, as any internal pressure is not governing in our case. Half of the wind load on the glass facade is also taken into account.

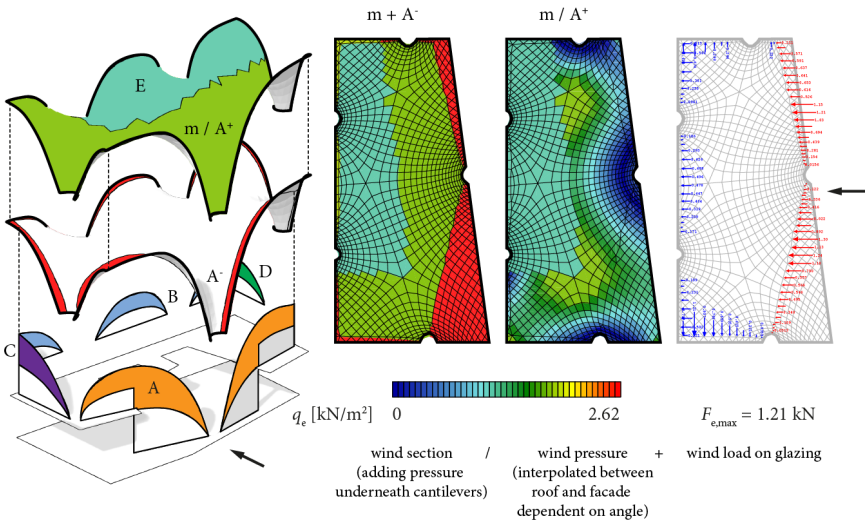

Figure 12.12: Wind pressure zones and resulting load cases.

- The wind suction load case assumes that the entire shell roof, which locally curves down to be part of the facade, is categorized as roof (Figure 12.12). Zone A is assumed to apply to the underside of the shell, outside the glass facade. The resulting local addition of shape factors m and A leads to a factor of -2.55, which is perhaps overly conservative (Table 12.3).
- The wind pressure load case assumes the steeper parts of the shell are a facade. The shape factors for facade A (now the topside of the shell) and roof m are interpolated depending on the local angle (between 10° and 90° from the horizontal plane) (Figure 12.12). The shape factors are the same as for the previous wind load case (Table 12.3).

A	B	C	D	E	m
-0.75	-0.75	0.75	-0.3	-1.05	-1.8

Table 12.3: Wind shape factors where positive load is towards (pressure) and negative load is away (suction) from the building envelope (SIA 261:2003).

Load combinations

Load combinations were defined using reduction factors ψ and load factors γ in Table 12.4 following SIA 260:2003 and assuming a category H intended for "roofs". The reduction factors for snow loads are calculated based on a height of 440 m above mean sea level for Dübendorf. Load cases are categorized as "occasional" (which are used together with a variable leading action), "frequent" (which occur more than a certain limiting value) or "quasi-permanent" (which occur at least half of the time, or as an average over time).

limit state		**self-weight**	**dead**	**thermal**	**snow**	**wind**	**live**
SLS occasional 1.0 / ψ_0		1.0	1.0 / 0	1.0 / 0.6	1.0 / 0.86	1.0 / 0.6	1.0 / 0.0
SLS frequent ψ_1 and ψ_2		1.0	1.0 / 0	0.5 / 0	0.43 / 0	0.5 / 0.0	0.0
SLS quasi-permanent ψ_2		1.0	*0.7* (1.0)	*1.0* (0)	0	0.0	0.0
ULS load factor γ		1.35 / 0.8	1.35 / 0.8	1.5 / 0	1.5 / 0	1.5 / 0.0	1.5 / 0.0
CLS safety factor λ_s				1.75			
limit state	**LC**	**self-weight**	**dead**	**thermal**	**snow**	**wind**	**live**
SLS quasi-permanent	0	1.0	0.7	0.2 / 0			
SLS occasional	1	1.0	1.0	1.0 / 0	**1.0**		
SLS occasional	2/3	1.0		1.0 / 0		**1.0**	
SLS occasional	4	1.0	1.0	1.0 / 0	0.86		**1.0**
ULS	5	1.35	1.35	0.6 / 0	**1.5**		
	6/7	0.80		0.6 / 0		**1.5**	
	8	1.35	1.35	0.6 / 0	0.86		**1.5**
	9	1.35	1.35	**1.5** / 0	0.86		

Table 12.4: Reduction factors ψ, (un)favourable load factors γ (SIA 260:2003) and safety factor λ (IASS 1979). Load combinations (LC) with and without thermal loads used. Leading action in bold.

The occasional load combinations are used for checks in the SLS against allowable deflections and crack width. They are also the starting point for limit load calculations to establish the load factor in the critical limit state (CLS). The ULS load combinations are used to check against allowable stresses.

The quasi-permanent load combination is used for the determination of creep and shrinkage effects. The dead loads and thermal loads are altered (0.7 and 1.0 instead of 1.0 and 0.0) to reflect the actual long-term load on the shell. The load is then increased to the occasional SLS or the ULS load combinations.

12.2.5 Thickness optimization

By redistributing the material in the shell, it is possible to reduce the total volume of required concrete, even though the maximum stresses stay within the same limits. The optimization tries to approach a given maximum deflection of $s/500$ = 18 mm, while reducing thicknesses throughout the structure and keeping within a 20 MPa stress limit. The linear elastic stiffness was reduced to only E = 5000 MPa to approximately account for cracking and creep in the design. The optimization is done for all SLS load combinations, as those in the ULS were found to not govern the results. The presented result has a minimum and average thickness of 30 and 80 mm, and a total weight of 29 metric tons.

12.2.6 Best-fit optimization

The cable-net forces have to be found such that, under given loads of the wet concrete, the resulting concrete shell takes the form of the target shape (Van Mele & Block 2010). The topology and shape of the cable net (Sections 12.2.2 and 12.2.3) is the basis for triangulated mesh of the shell (Section 12.2.4 and 12.2.5). To enforce reasonable bounds on these forces under load (4-50 kN along the perimeter), the resulting constrained linear least squares problem can be written as a quadratic program. Assuming the bounds have not allowed us to find an exact match with the target shape, we compute the sum of squared deviations, which are used as target for optimization. The constrained linear least squares solver offers an initial estimate of the force distribution, showing how different solutions compare, but within reasonable computational time. A more robust nonlinear algorithm, suggested by Van Mele et al. (2014), is applied to the final geometry to obtain the closest-fit fit in the detailed engineering and tendering phase, as the topology of the formwork may change depending on input from the future contractor.

12.2.7 Shape optimization

The roof was optimized in two rounds: initially, a single-criterion optimization; and then a final multi-criteria optimization. The optimization was carried out for a monolithic concrete shell, and the sandwich section was taken into account in the subsequent structural analysis (Section 12.4).

The first optimization minimized mass, proportional to the elastic bending energy E, subject to preliminary stress and deflection constraints (20 N/mm^2 and 30 mm). The energy is a function of the shape $f = f(x, s, h, q)$, with 18 or 22 variables (nine or eleven boundary parameters plus nine or eleven force density parameters, for shells with four or five supports respectively) (Table 12.1).

This stage studied different boundary conditions (positions and number of supports as well as roof height), and their relative influence on the potential to minimize the mass. The problem is to:

$$\begin{aligned} &\text{min. } E\left(f\left(x, s, h, q\right)\right) \\ &\text{subject to} \\ &\qquad \sigma \leq 20 \text{ N/mm}^2, \\ &\qquad \delta \leq 30 \text{ mm}, \\ &\qquad 0.11 \leq x_4 \leq 0.45, \\ &\qquad 0.60 \leq x_3 \leq 0.90, \\ &\qquad 1.10 \leq x_2 \leq 1.90, \\ &\qquad 2.10 \leq x_1 \leq 2.43, \\ &\qquad 3.45 \leq x_5 \leq 3.90, \\ &\qquad 0 \leq s_{1\ldots5} \leq 10, \\ &\qquad 0 \leq h \leq 5, \text{and} \\ &\qquad 1 \leq q_{1\ldots11} \leq 10. \end{aligned} \tag{12.6}$$

The bounds on variables x were determined to avoid any supports close to the corners, and keep any supports within the architecturally and functionally preferred support zones. The bounds on variable s were subjectively set to avoid extremely steep or shallow edge curves. The bounds on variable h were determined by a minimum ceiling clearance and a maximum allowable roof height.

The second and final multi-criteria optimization, subject to a preliminary stress and deflection constraints (20 N/mm^2 and 1/500th of the span L), minimized four criteria: internal elastic energy (proportional to mass) as before; the buckling load factor (lowest, positive value); deviations of the cable net to the target shape; and, surface area of glazing. A fifth measure of the amount of head clearance below

the roof was also calculated to compare results, measured as the sum of squared lengths of all nodes higher than 2.15 m. These criteria are all a function of the shape $f = f(w, d, a, q)$ with 26 variables (fifteen boundary and eleven force density parameters for a shell with five supports).

This stage determined the final design as it was submitted to the authorities for building permission (see also Sections 12.2.1-12.2.3). The problem is to:

$$
\begin{aligned}
&\text{min. } E, -\lambda, \Delta\mathbf{z}^{\mathrm{T}}\Delta\mathbf{z}, A, \\
&\text{as functions of } f\,(w, d, a, q) \\
&\quad \text{subject to} \\
&\qquad \sigma \leq 20\ \mathrm{N/mm^2}, \\
&\qquad \delta \leq s/500, \\
&\qquad 1.2 \leq w_1 \leq 2.0, \\
&\qquad 0.9 \leq w_{2\ldots5} \leq 1.2, \\
&\qquad 0.42 \leq d_1 \leq 0.82, \\
&\qquad 0.45 \leq d_{2\ldots5} \leq 0.75, \\
&\qquad 7.5 \leq a_1 \leq 9.0, \\
&\qquad 4.4 \leq a_{2\ldots5} \leq 9.0, \\
&\qquad 1 \leq q_{1\ldots5,11} \leq 20, \text{and} \\
&\qquad 1 \leq q_{6\ldots10} \leq 10.
\end{aligned}
\tag{12.7}
$$

The bounds on variables w, d and a, were set to maintain various requirements related to space for insulation and drainage on the exterior, and to angles between the shell and the glass facade on the interior.

12.3 Formwork

A feasibility check was carried out on a possible formwork frame. The frame is designed using three element types:

- tubular steel ring (S235, RO 273/2.6, E = 210 GPa);
- glulam beams (GL24h, 80x300 mm, E = 11.6 GPa): and,
- plywood plates (C24, 27 mm, E = 11 GPa).

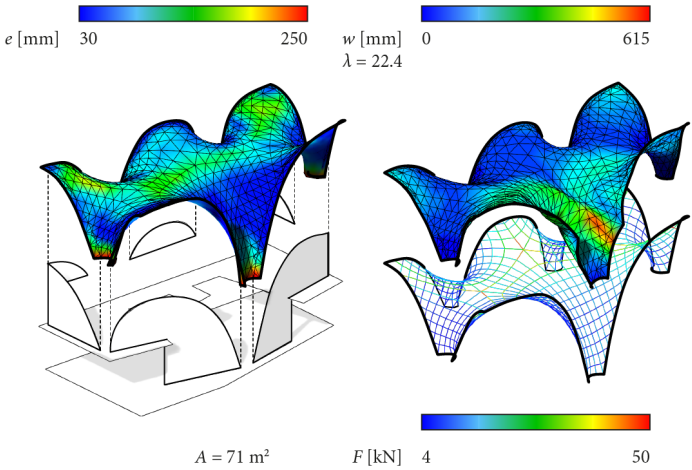

Figure 12.13: Four criteria: elastic energy (proportional to mass, shown as thickness e), buckling load factor λ for LC 0 (showing first positive buckling mode with deflection w), cable-net deviations (showing constrained forces F under load), and surface area A of clear glazing.

The elements in timber were based on typical sizes and Young's moduli provided by an earlier prospective contractor (Verhoeven Timmerfabriek).

Figure 12.14 shows the overall design of the frame. The ring follows the edge of the cable net and has two glulam struts in the middle. The ring is supported by vertical glulam members spaced no more than 2.2 m apart. Horizontal members are positioned at mezzanine and roof level. The outer ends of the frame are braced with plywood sheets. At the back the structure is supported at mezzanine level, close to the backbone slab at parapet level. Diagonal members brace the back against the backbone parapet. The analysis assumes all supports are fixed and that deflections should be 10 mm or less (in order to maintain control over the flexible formwork).

Forces from the best-fit optimisation are introduced as external point loads on the frame, meaning the structural model of the tensioned net is not coupled to that of the frame. Those forces in turn are based on the weight of the lower shell, and currently exclude the weight of the net itself. The net has been refined to an average 370 mm segment length, with forces no higher than 25 kN. The average of the 274 forces acting on the frame is 8.7 kN. The only other applied load is the self-weight of the frame, and no load factors have been applied.

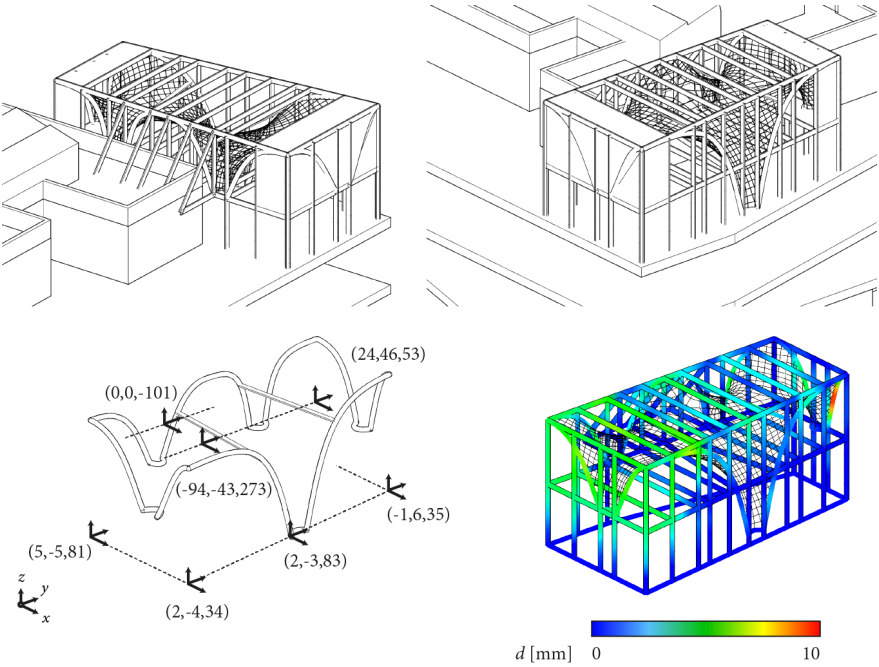

Figure 12.14: Design of the formwork frame, resulting reaction forces on the NEST building while displacements are kept within 10 mm.

The overall weight of the frame is 6.6 tons. The current concept excludes use of any scaffolding, temporary roof structure, permanent steel and timber framing inside (e.g. the mullions), leaving room to further optimise the formwork frame.

The design and materialization of the formwork has been changing substantially since the final design stage after obtaining the building permit. These ongoing developments are outside the scope and work of this thesis.

12.4 Structural analysis

The subsequent structural calculations follow a combination of building codes:

- SIA 262:2003, intended for conventional reinforced concrete, if and whenever possible;
- EN 1992-1-1:2004, which elaborates on creep and shrinkage formulas used in SIA 262:2003;
- ACI 549R-97 and ACI 549.1R-93 for aspects related to ferrocement; and
- IASS 1979, for aspects related to thin concrete shells, requiring a stability analysis (Section 8.7).

This strategy is possible in Swiss code, as SIA 260:2003, art. 0.3 allows exceptions to code, "provided they are well founded theoretically or experimentally, or justified by new developments and new knowledge".

Because the research unit will be replaced after 5-10 years, the reference period for design is conservatively put at 20 years. Load combinations are according to Section 12.2.4.

12.4.1 Boundary conditions

As mentioned, the shell is supported on five locations. Those at the rear are close to the backbone, and assumed fixed. Those in front are supported on a cantilevering, prestressed concrete floor slab, which are modelled as springs. The spring stiffnesses were provided by the structural engineers of the NEST building. One support is modelled as a horizontal spring as well to account for the local flexibility of the supporting steel frame. A linear elastic model of the shell including the cantilevering floor slab of the NEST model was used to compute a second set of spring stiffnesses, which were used as a check.

12.4.2 Limit states

The shell was checked against the following requirements in the serviceability limit state (SLS), ultimate limit state (ULS) and critical limit state (CLS):

- deflections (SLS) for occasional live loads should be less than 1/500th of the span s, i.e. 18 mm for the shell, and 1/300th of twice a cantilever, i.e. 60 mm for the cantilevering slab supporting the shell at the front (SIA 260:2003), and along the glass facade they are prescribed to be less than 10 mm;
- concrete crack widths (SLS) may not exceed 0.1 mm (ACI 549R-97) or related steel stress may not exceed 420 MPa (IASS 1979):

- stresses (ULS) should not exceed the material yield strengths or strains;
- buckling (ULS) with decreasing post-buckling capacity may not occur; and,
- load factors (CLS) should be equal or higher than a safety factor ($\lambda_s \geq 1.75$) that depends on the type of post-buckling behaviour (IASS 1979).

12.4.3 Material properties

Due to the innovative nature of the roof, it was crucial to maintain sufficient freedom for its future contractor and the design team to consider different strategies to apply and reinforce the concrete shell. For this reason, the final design of HiLo was checked for a range of concrete strengths and three types of reinforcement material.

Concrete

The concrete was modelled as a C90/105 according to SIA 262:2003 with corresponding yield strengths, but a parametric study was carried out as well for a range between C35/45 and C90/105 concrete, to inform the detailed engineering phase. The higher C90 concrete strength was primarily chosen based on the resulting creep and shrinkage behaviour according to code, and given previous experience with viscous and fine concrete mixes, which exhibit high strength (Veenendaal & Block 2014*b*). For reference, examples of cable-net formed shells from the early 1960s used concrete comparable to strength classes between C45/55 and C50/60 (Sections 3.7.3 and 3.7.4).

Table 12.5 lists relevant properties for the upper and lower limit strength classes, C35/45 and C90/105.

			C35/45	**C90/105**
E-modulus	E_c	[N/mm^2]	34'000	44'000
compressive strength	f_{cd}	[N/mm^2]	22.2 (15.8)	41.6 (40.5)
yield tensile strength	f_{ctd}	[N/mm^2]	2.91	4.55
yield strain	ε_y	[‰]	2	
ultimate strain	ε_u	[‰]	3	
Poisson's ratio	ν	[-]	0.2	
density	ρ	[kN/m^3]	24	

Table 12.5: Material properties for concrete from SIA 262:2003 with values from ACI 549R-97 in brackets for comparison.

Although the compressive strength f_{ck} can be 25 % higher after 20 years according to SIA 262:2003, or 26-48 % after 3 years according to IASS 1979, this was not (yet) taken into account. The dimensioning value of the concrete tensile strength is calculated from SIA 262:2003, art. 4.4.1.3,

$$f_{ctd} = k_t f_{ctm} = 0.91 \cdot 5 = 4.55 \text{ N/mm}^2 \tag{12.8}$$

where

$$k_t = \frac{1}{1 + 0.5t} = \frac{1}{1 + 0.5 \cdot 0.2} = 0.91 \leq 1.0 \tag{12.9}$$

and t is the smallest dimension of a tension chord in m (conservatively taken to be 200 mm, and arguably could be 30 mm).

According to code, concrete and reinforced concrete weigh 24 and 25 kN/m^3 respectively, while, according to literature, that of TRC is around 23.5 kN/m^3.

Table 12.6 shows the creep coefficients and drying shrinkage strains for the faces and core of the roof's sandwich section. These parameters were applied to the quasi-permanent load combination in forty incremental steps, simulating 20 years of creep and shrinkage. This state was then used for further application of the occasional SLS and the ULS load combinations.

For concrete, the values are calculated with equations in Sections 8.7.2 and 8.7.3. Following SIA 262:2003 (2004), autogeneous shrinkage is not included yet, pending development and testing of the actual concrete mix. The current values assume that the shell remains in the formwork while curing for 28 days, and that the average layer thickness is 50 mm. Creep and shrinkage is also dependent on relative humidity. The inner face of the sandwich is exposed on one side and has a relative humidity of 40 %, while the outer face is completely enclosed and has a relative humidity of 60 %. These values were calculated based on the required U-value of 0.17, the ambient, average relative humidity of 50-95 % for nearby Zürich Airport, and a client requirement of 30-60 % on the interior.

Polyurethane

The high density PU is modelled based on linear elastic properties from suppliers: E = 300 MPa, f_y = 20 MPa, ρ = 600 kg/m^3.

For the creep of the PU very little is known, and for now is taken from Garrido et al. (2014), who investigated rigid PU foam for sandwich panels, though of much lower density. After twenty years,

$$\varphi = 0.11 \cdot (24 \cdot t)^{0.25} = 0.11 \cdot (24 \cdot 20 \cdot 365.25)^{0.25} = 2.25 \tag{12.10}$$

where t is the time in days (see Table 12.6). The influence on the results is minor, as the stiffness of the PU is much lower than the concrete.

			inner face	**core**	**outer face**
creep coefficient	φ	[-]	1.06 (0.76–1.31)	2.25	0.81 (0.76–1.31)
shrinkage strain	ε_{cs}	[‰]	-0.19 (-0.63)	-	-0.10 (-0.38)
relative humidity	RH	[%]	40	-	60

Table 12.6: Creep and shrinkage of concrete and PU foam from SIA 262:2003, EN 1992-1-1:2004 and Garrido et al. (2014). Values from IASS 1979 in brackets for comparison.

Reinforcement

The steel type, B500A, was chosen based on its similarity to the steel properties mentioned in ACI 549.1R-93. The mesh layers are 1 mm diameter, with 13 mm spacing, so 60 mm^2/m per direction, with up to 12 layers per concrete face. Governing load cases were checked for TRC as well to inform the detailed engineering phase. Table 12.7 lists the properties for all three types of reinforcement materials. The yield strain, not provided in literature, was calculated by assuming a bi-linear stress-strain curve, and thus dividing the E-modulus by the ultimate tensile strength. The yield tensile strength was defined to be 99 % of the ultimate tensile strength, to improve convergence of the finite element program Sofistik.

			B500A	**glass**	**carbon**
E-modulus	E_s	[N/mm^2]	205'000 (200'000)	70'000	235'555
yield tensile strength	f_y	[N/mm^2]	435 (450)	455	745
ultimate tensile strength	f_{ctd}	[N/mm^2]	457	460	753
yield strain	ε_y	[‰]	2.12 (2.25)	7	3
ultimate strain	ε_u	[‰]	20	25.8	16.5
material factor		[-]	1.15	1.30	1.20
density	ρ	[kN/m^3]	78.5	19.0	28.6

Table 12.7: Material properties for steel (SIA 262:2003), glass and carbon meshes (Hegger et al. 2007, Hegger & Voss 2008). Values from ACI 549.1R-93 in brackets for comparison. Material factors for glass and carbon based on those for GFRP and CFRP (fib Bulletin No. 14 2001).

The reinforcement design is automated by Sofistik and follows the relevant limits set in Table 12.7 and Section 12.4.2. In addition, the orientation is based on the local steepest descent of the shell. The procedure determines the reinforcement based on the linear SLS and ULS load cases and the limit on crack width, selecting the governing quantity for each element. This design is then used in subsequent physically nonlinear analyses (PNL, GPNL). Both the orientation and reinforcement are very locally determined (Figure 12.15), so their distribution is unrealistic, given that the actual reinforcement will be based on larger patches related to cutting patterns. As such, these results are intended as a starting point for further reinforcement design. The outer shell is more heavily reinforced than the inner shell, suggesting that the shell is stiff enough to restrain contraction of the concrete due to the cold. The outer concrete cracks and therefore relies more heavily on reinforcement.

12.4.4 Imperfections

It is assumed that the initial imperfection has the same shape as the first positive, globally acting buckling mode (Figure 12.16), with a magnitude equal to the initial imperfection w_0.

The total imperfection is the sum of the calculable imperfection w_0' and the accidental imperfection w_0" (IASS 1979). The former is the maximum deflection obtained for a service load combination using linear elastic analysis. As an upper limit we can take the allowable deflection $w_0' = 18$ mm (Section 12.4.2). The latter is the accidental imperfection due to erection inaccuracies. Following the example of Tomás & Tovar (2012), Section 8.7.1 presents an overview of how imperfections have been calculated for shell structures, and the most conservative combination of these formulas has been taken here, such that

$$w_0 = w_0' + w_0'' = 39 \text{ mm}, \tag{8.28}$$

where

$$w_0'' = 0.1t + \frac{t\alpha_f}{2\left(1+\beta_s^{-2}\right)}, 21\text{mm}, \text{ with} \tag{8.24}$$

$$\beta_s = 0.001\frac{\sqrt{R_1R_2}}{t} = 0.13 \tag{8.26}$$

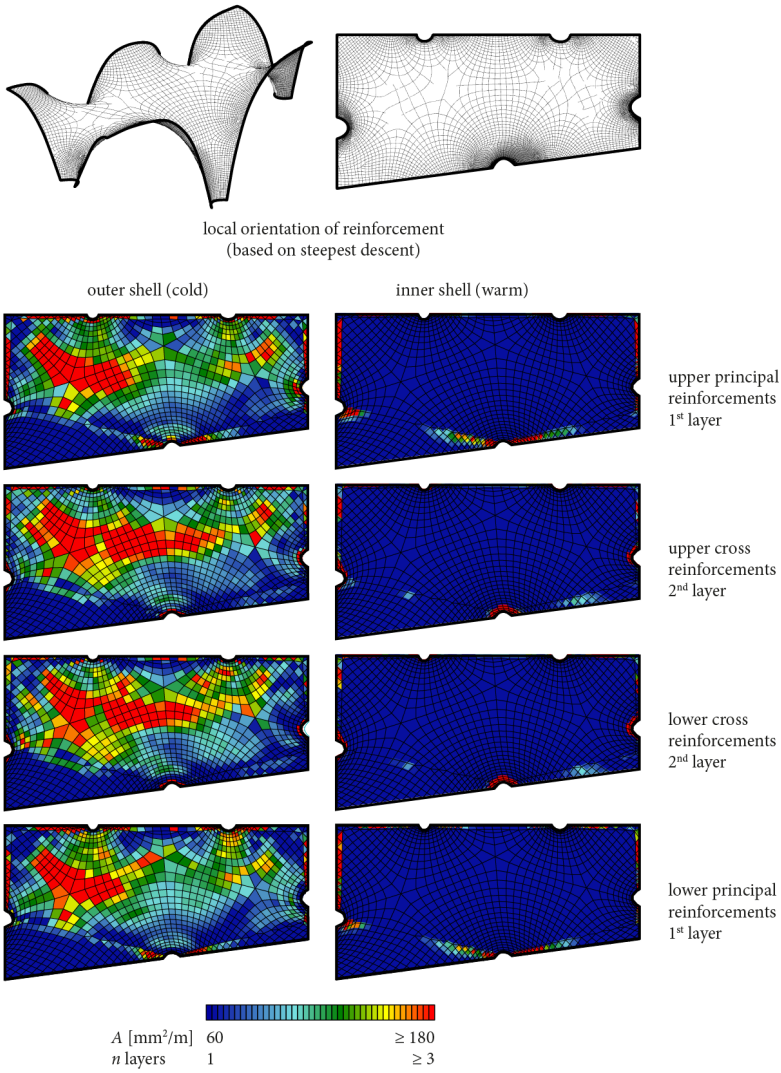

Figure 12.15: Reinforcement per layer as designed by Sofistik.

in which $\alpha_f = 6$ for a shell built using slipform (assumed to be similar to the cable-net and fabric formwork; $\alpha_f = 1$ for rigid formworks, $\alpha_f = 12$ for airforms), t is the shell thickness, and R_1 and R_2 are the principal radii of curvature of the shell. It is assumed that the (area weighted) mean values can be taken, meaning that the

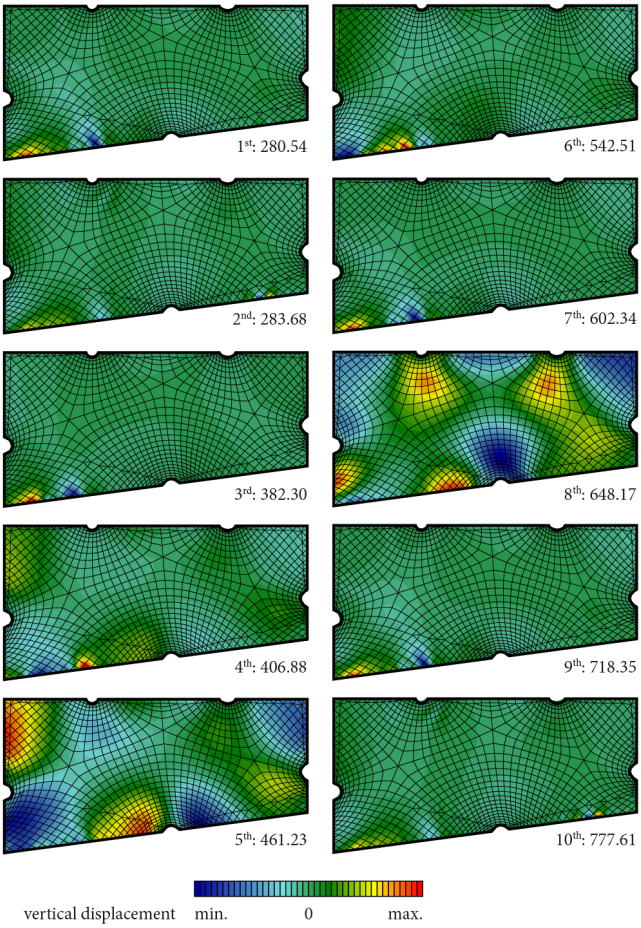

Figure 12.16: First ten positive buckling modes, with the fifth mode taken as the shape for the imperfection.

thickness of the sandwich t = 140 mm, and principal radii R_1 and R_2 are 25 m and 14 m respectively (Figure 12.17). Note that the present choice of α_f = 6 predates this thesis' final recommendation to set α_f = 12 (Section 10.6). The present result is still accepted as the total imperfection was conservatively calculated.

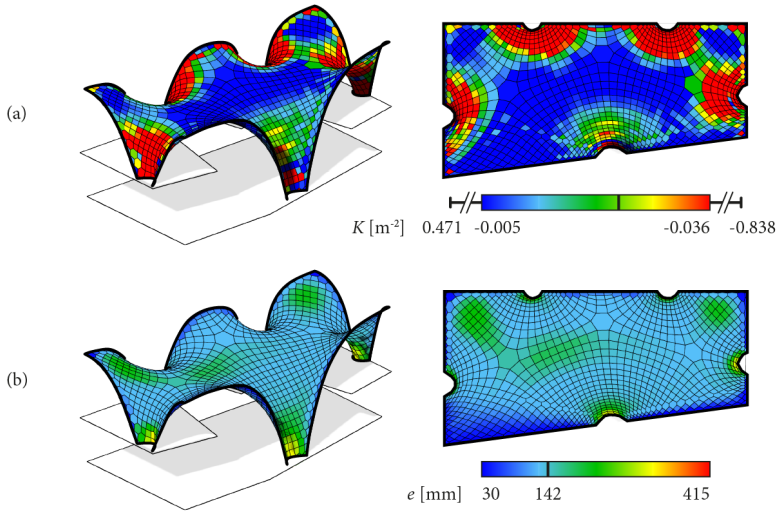

Figure 12.17: Curvatures and sandwich thickness.

12.5 Results

The two stages of design optimization led to a design which met various requirements, while staying within structural limits.

Further detailed engineering of the roof will depend on development of the specific concrete mix, method of concrete placement, more detailed reinforcement layout and so on.

Initial, single-criteria optimization

Figure 12.18 shows the results from the initial broader optimization varying position, height and number of supports, identifying greatest potential for structural and energy performance. Resulting shapes were analysed for mechanical properties (displacements, buckling load factor), geometric properties (thickness, surface area, enclosed volume, glazing surface), and total annual radiation.

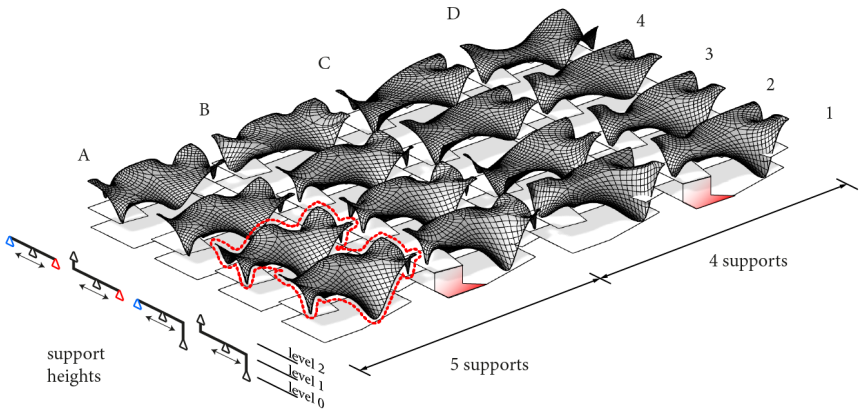

Figure 12.18: Results from sixteen early optimisations (16× 100 generations, 100 shells each), with A1 and A2 selected for further development.

Based on initial optimization results, solutions A1 and A2 were chosen as the direction for further development. Main issues were the lack of head clearance at mezzanine level and vertical position of the supports in the back. The clearance was addressed by including it as a metric for evaluation, raising the roof level, and changing the mezzanine walkways to allow more space around the supports.

The vertical position of the supports was set to be mezzanine level as in A2, to allow connection to the mezzanine and supporting building structure, and increase curvatures of the shell.

Final, multi-criteria optimization

Figure 12.19 shows the results from the final multi-criteria optimization, weighing structural and energy performance against constructional considerations. The four criteria were internal elastic energy (proportional to mass), GNL buckling load factor (lowest, positive value), deviation of cable net to target shape, and surface area of glazing. A fifth measure of the amount of head clearance below the roof was also calculated to compare results. The optimization was carried out for a monolithic concrete shell, and the sandwich section was taken into account in the subsequent structural analysis.

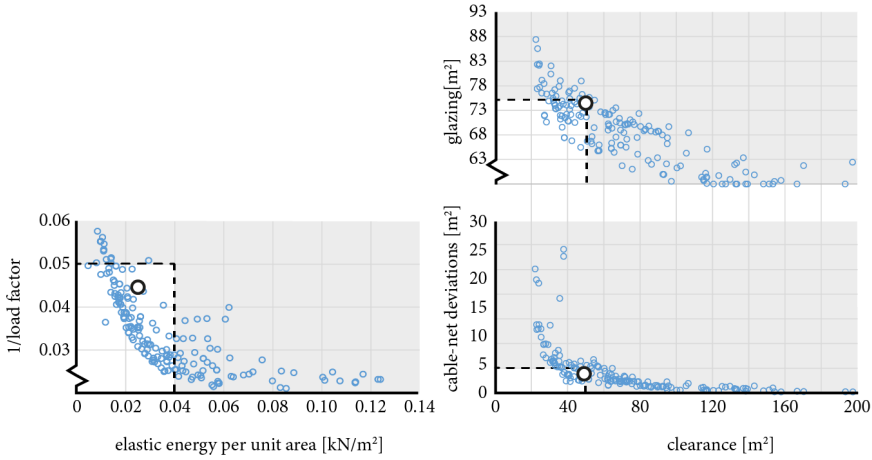

Figure 12.19: Projections of Pareto front from final multi-criteria optimization based on buckling load factor, elastic energy (proportional to mass), cable-net deviations, and glazing, showing a measure of head clearance below the roof as well. Limits on objective values shown as dotted lines.

Figure 12.20 shows the front elevation and lower floor plan of the final design, which satisfies the, sometimes conflicting, objectives seen in Figure 12.19, and was submitted to authorities for building permission.

Displacements and steel stresses

The structural capacity of the shell is limited by the steel stress in both SLS ≤ 420 MPa and ULS ≤ 457 MPa.

The sandwich causes differential temperature and humidity, and thus differential creep and shrinkage strains, as well as thermal actions. The amount of creep and shrinkage seems to be the main determinant of the shell's capacity. The shell shows very small displacements, less than 10 mm in SLS, and well below any limits. In fact, the stiffness of the shell is so substantial, that the concrete acts as in a restrained manner, with cold temperatures and subsequent contractions leading to micro-cracking throughout, rather than deformations.

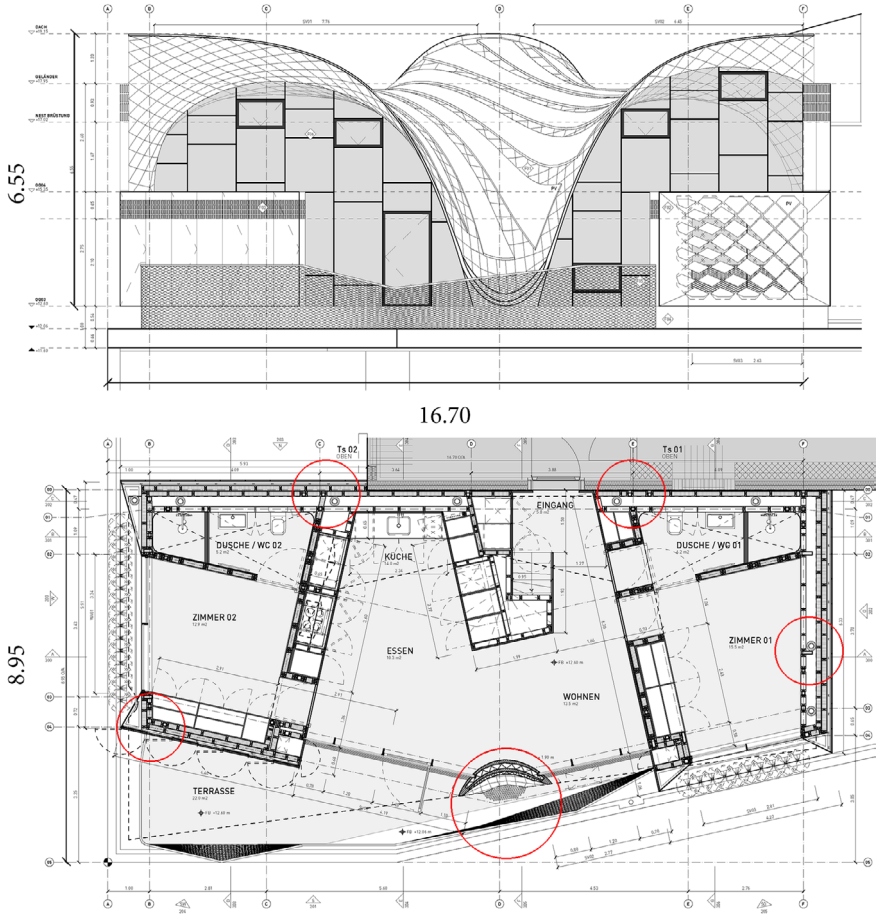

Figure 12.20: Front elevation and lower floor plan with main dimensions and location of supports in final design.

As a result, maximum steel stresses are negligible, unless thermal action (167–246 MPa in SLS, 240–438 MPa in ULS) or only creep and shrinkage is included (308–354 MPa in SLS, 330–381 MPa in ULS).

Textile reinforcement stresses

Several governing load combinations were analyzed again, but with properties for carbon or AR-glass for the reinforcement instead of B500A steel. All other parameters were kept the same, including those controlling the reinforcement design (limits on cross-sectional area, crack width, etc.).

The comparison showed that the use of carbon or AR-glass doesn't significantly influence the overall stiffness, strength or stability of the shell, as governing values from previous results stay in the same order of magnitude. The most obvious difference is the stresses and strains in the reinforcement, which differ relative to the specific material strength: for steel 354/500 = 70 %, for carbon 746/753 = 99 % and for AR-glass 138/460 = 30 %. This is likely due to the strength to stiffness ratio of these material varying as well. The stresses in the carbonfibre are close to the strength, requiring some further design optimization in order to reduce them to a comparable level as to that of the steel.

Load factor

The structural capacity of the shell is limited by a minimum load factor in CLS ≥ 1.75. Figure 12.21 plots the CLS load displacement diagrams for LC 1 and 4 with increasing nonlinearities, revealing the roughly bilinear behaviour of the shell, and the improving effect of thermal action on the load factor (Figure 12.21, blue versus red lines). This suggests the thermal action acts as a form of prestress. While the linear load capacity is in the order of 1000, the lowest load factor is only 3.0, though still more than the minimum requirement of 1.75.

The long-term effect of creep and shrinkage is more pronounced when excluding thermal action, in which case the load factor (the shell's capacity) is reduced by 17-35 %. Note that fully excluding thermal action would not be realistic, given that some thermal gradient will always exist for the roof, even if the hydronic system were to fail. Including thermal action, the opposite effect is seen in some cases, meaning the capacity actually increases. This suggests that the 25-50 % reduction due to creep observed in shallow hypars by Gallegos-Cazeres & Schnobrich (1988) is a phenomenon applicable to a much larger range of anticlastic shell shapes, including ones that do not fit the definition of shallowness (Section 8.2.4). The effect of imperfections is almost inverse, as it is most pronounced when including thermal action, reducing capacity by 15-32 %, but much lower reductions are seen when excluding thermal action. Note that the magnitude of the imperfections is conservatively chosen (Section 12.4.4).

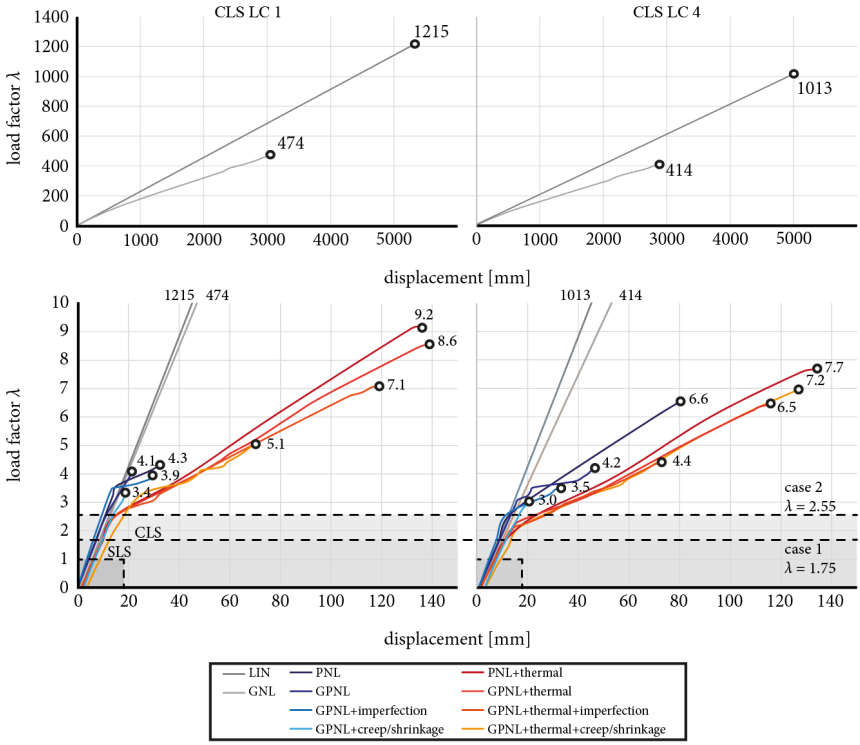

Figure 12.21: Load-deflection diagram for corner point for LC 1 and LC 4 without thermal loads, showing influence of various nonlinearities. LIN = linear, NL = nonlinear, P = physically, G = geometrically.

Concrete strength

The structural analysis so far assumed a C90, comparable to concrete used for several prototypes. However, the precise mix is to be developed in the next phase, and to allow more freedom in doing so, the influence of lowering the strength has been investigated. This has been done only for the governing load factor, so 3.0 from CLS LC 4.

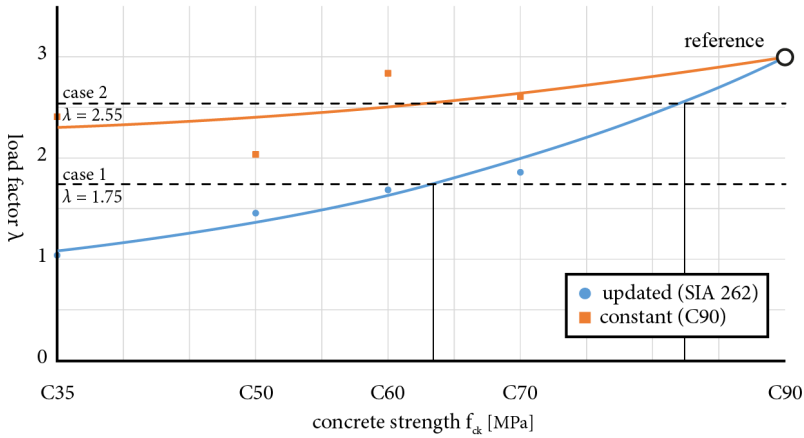

Figure 12.22: Trendlines for reducing the concrete strength while keeping the creep and shrinkage properties the same or not.

The concrete strength was lowered while updating the creep and drying shrinkage strains. In this case, it is possible to reduce to a C70. The cement supplier claimed that the creep and shrinkage properties can be tailored. As an extreme, when assuming that the total, actual shrinkage remains identical to that of drying shrinkage for C90 from SIA 262, then the concrete can be reduced to a C35. This in fact shows how sensitive the shell's capacity is to long-term effects and to a much lesser degree to the material strength.

Single shell interior

A full set of calculations was carried out on a roof shell in which the sandwich occurs only along the glass facade, and the interior is a single shell (Figure 12.4). This alternative is potentially more cost effective as it halves the number of concrete and insulation layers for a large part of the roof. Structurally speaking, the behaviour is substantially altered, not only because the structural depth is reduced, but also because the difference in thermal action, creep and shrinkage is avoided between the upper and lower part. The creep and shrinkage values for the lower sandwich shell were taken for the single shell, but the thermal actions were more smoothly graded towards the edges.

Results show that the single shell has lower or comparable stresses, and less reinforcement, but on the other hand is more susceptible to thermal actions and wind suction, leading to lower load factors. Where thermal actions had a positive effect on the load capacity of the sandwich shell, the opposite seems true for the single shell. Therefore, the single shell option has substantially less room to optimize the material properties of the concrete.

Post-buckling behaviour

As a final check on the post-buckling behaviour, Kollár (1969) and Kollár & Dulácska (1984) recommend to plot the displacement against the displacement over the load, a so-called Southwell plot. Figure 12.23 is a plot of LC 4 including thermal action and imperfection. The load P is taken to be equal to the total vertical reaction force. A straight line would indicate constant post-buckling behaviour; and an upward curving line (as in our case) indicates increasing post-buckling behaviour (referred to as "case 1" by IASS 1979). This confirms that a factor of safety λ_s of 1.75, rather than 2.55 for decreasing post-buckling capacity ("case 2") has to be achieved. The factor of 2.55 was established by following Section 8.4.

The first part of our plot (up to 12 mm displacement) is unusual and is a result from Sofistik's inability to load step thermal actions (meaning the thermal action is always included with a load factor of 1, also distorting the rest of the plot).

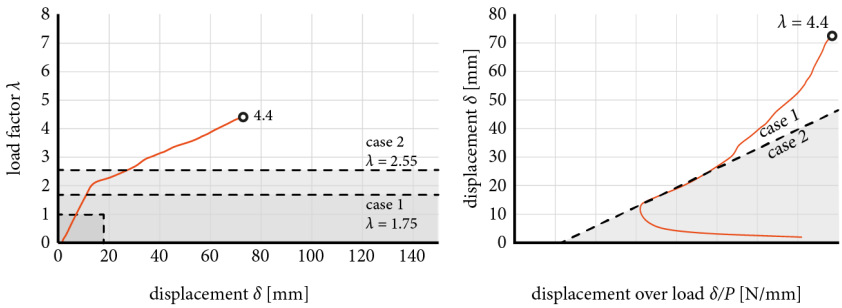

Figure 12.23: Load-deflection diagram and Southwell plot for LC 4 with imperfection, and thermal actions included, revealing increased post-buckling capacity.

12.6 Implementation

The entire design process was implemented in Grasshopper for Rhinoceros. Several plug-ins for Grasshopper were included: Karamba for structural analysis and thickness optimization, and Octopus for multi-objective optimization. Thermal actions were based on calculations carried out in Energy2D and ANSYS by A/S. Custom IronPython components were written to communicate with external CPython scripts; the shape generation of the shell and calculation of prestresses in the cable-net formwork, the latter using the CVXOPT library's QP (quadratic program) solver to solve the bounded least-squares problem.

The shell was subsequently evaluated for various additional nonlinearities in Sofistik, as the present version of Karamba does not include layered or volume elements to model the sandwich, nonlinear material models, or third-order geometric nonlinearity to evaluate post-buckling behavior. However, Sofistik is also limited as it is not capable to combine volume elements with both nonlinear material and geometric modelling, to load step thermal actions, and to model the reinforcement in more than two layers per side. The input for Sofistik is generated from Grasshopper using a custom IronPython component.

12.7 Conclusions

The structural design and geometry for the final design of a flexibly formed, mesh-reinforced sandwich shell roof, as part of the NEST HiLo project, has been presented, and was handed over to Bollinger + Grohmann Ingenieure for the detailed engineering phase. Construction details will be dependent on further development within the design team and outcome of the tendering phase.

Specific insights from the structural analysis were that

- the determination of wind loads, without the availability of wind tunnel tests or CFD models, is problematic, given the lack of guidance in building codes for doubly curved shapes;
- in general, this lack of guidance required the combination of multiple building codes and recommendations in order to deal with various aspects of this complex and innovative design;

Figure 12.24: Visualisation of the interior of the final design stage of HiLo.

- the perceived structural benefits of a sandwich shell are offset by differential creep and shrinkage behaviour due to the differences in temperature and relative humidity in the opposite concrete faces;
- a similar observation is made for thermal action and corresponding stresses, though the effect on the load factor may actually be positive;
- it is essential to check the effects of both including and excluding thermal action, as either may act negatively on the load factor;
- the effect of creep and shrinkage can significantly reduce the load factor (up to 35 %), here depending on the exclusion of thermal action, even if the shell is not considered to be shallow;
- the effect of imperfections can do the same (up to 32 %), but inversely depending on the inclusion of thermal action, noting the magnitude of the imperfection was conservatively chosen;
- the difference of ferrocement versus TRC is not structurally significant, though this is based on properties from literature, and at present there is lack of guidance from building codes for TRC; and,
- the negatively curved shell has increasing post-buckling capacity, consistent with literature on hypars.

The final design shown here is the specific result of a sequence of single- and later multi-criteria evolutionary optimization, evaluating various parameters related to structural and energy performance, as well as architectural, spatial and constructional constraints. By the end, the design space had become highly constrained as can be seen in the Pareto fronts. This was due to earlier design decisions, limitations set by the NEST building and strict requirements on energy performance. As a result, the final multi-criteria optimization was only a means to identify a solution that took all those considerations into account, rather than a design tool that allowed some freedom of choice, as had been the case for the early, single-criterion optimization.

At the same time, the optimization process and NEST HiLo's unique geometry do demonstrate the potential of greater design freedom for anticlastic shell structures that are flexibly formed. The final construction of NEST HiLo, planned for 2018, will allow the evaluation of other objectives, particularly cost efficiency and energy performance.

Part VI

Conclusion

Forming [...] *remains the great, unsolved problem of construction of concrete thin shell roofs. Any and all ideas should be explored, without prejudice. Time will tell whether significant success might emerge.*

— Stefan Jerzy Medwadowski, 1998

CHAPTER THIRTEEN

Conclusions

Thin concrete shells are efficient structural systems to cover large areas, comparable to steel gridshells in weight, though in terms of carbon footprint, far superior. Because concrete is the most widely used construction material, its cement manufacture alone still accounts for 5 % of global carbon emissions. Concrete shells offer opportunities in the aim to reduce these emissions, but since the 1970s they have not been built in any significant number.

This thesis addresses the common reason given for their disappearance, the cost of traditional rigid formworks, and proposes a prestressed cable-net and/or fabric formwork as a solution. The opportunities such a formwork affords in terms of geometry have been explored to address another reason: the formal limitations of traditional shell geometries like the hyperbolic paraboloid. The wider range of shapes possible with a flexible formwork, may better cater to current tastes for complex geometry, as contemporary architecture shows formal similarities to shell structures.

Revival of concrete shells

However, **for long-span roofs, concrete shells can undergo only a partial revival to former glory**. Contrary to the golden era of shell structures (1925–1970), concrete shells will indefinitely have to compete with prefabricated and mass-produced systems in general, and with lightweight structures such as tensioned membrane roofs and steel or timber gridshells. It is unclear whether future disruptive technologies like 3D printing are an opportunity or threat to the concrete shell.

Since a flexible formwork is defined as using some lightweight structure as formwork for concrete, the architectural program must include requirements for such a material. Otherwise, the lightweight structure, similarly capable of spanning large areas, would be the more affordable alternative. Many architectural, spatial, functional, building physical and constructional constraints may require a monolithic, continuous, smooth, fireproof and unobstructed surface that concrete naturally provides. Indeed, recent freeform projects reveal that architectural programs still exist that require doubly curved, large span monolithic surface structures.

Geometry of flexibly formed shells

Unfortunately, recent freeform concrete shell shapes have led to designs that were not as economic as historical examples, even if they were post-rationalized through structural optimization. The same is true for recent structures featuring concrete clad, steel space frames. These concerned landmark or signature buildings, and it is believed that for a wider appeal, shells should be structurally efficient.

Although some of the thinnest known structures are anticlastic hyperbolic paraboloids, it has been shown that slight changes to their shape and thickness can vastly improve their structural performance. Instead of analytical functions, form finding is an accepted means of creating efficient form. Unusually, there are no known thin concrete shells designed by numerical form finding, likely due to the problem of formwork. Here, it has been shown that **form finding can produce both the shape of a flexible formwork and its resulting concrete shell, in a way that both are structurally and constructionally informed**. This is especially true if form finding is used as a shape generator for optimization. Ideally, such an optimization should include both shape and thickness variables, and allow boundary conditions to change as well. The result is a larger vocabulary for good structural form, and a means by which to realize it.

Economy of flexible formworks

A conventional, scaffolded, rigid timber or milled foam formwork costs about 300-800 €/m^2. An upper limit may be 1000-1200 €/m^2, but, in recent examples, perceived risk and complexity has led to even higher prices during tendering. Barring major shifts in economic conditions such as the cost of labour or timber, **conventional timber or milled foam formworks will not be able to bring back concrete shells**.

By contrast, a lightweight structure may cost as little as 150-300 €/m^2, and as a formwork is the cheaper alternative to rigid ones. Savings are not immediately as high as comparing these numbers suggest. **Small-scale flexibly formed prototypes are already equally competitive to timber formworks**, as they can be constructed for 590-690 €/m^2. **For large-scale flexible formworks, reported cost savings have been 25-40 %**, and there is further evidence that while cost and weight increase with scale, these relative savings are independent of scale.

Tolerances of flexible formworks

The inherent flexibility of the proposed formwork system, raises questions about its accuracy of construction. It is demonstrated that, at least at small-scale, **construction deviations of a cable-net and fabric formwork are well within the acceptable limits**, such as so-called accidental imperfections for shell structures. **Prerequisites are to design the shell for the loaded state** to exclude deformations from the final comparison, so-called best-fit optimization, **and to accurately measure and correct the required prestresses prior to casting**. Both experimental and numerical work show that the deviations are not sensitive to errors in the assumed or applied magnitude of the loads and material stiffness. **Construction deviations are mainly determined by errors in the initial geometry and prestresses**.

13.1 Contributions

The contributions in this thesis are related to the primary objectives: to conceptualize a constructional flexible formwork system; to develop a workflow for its design; and, to establish its technical feasibility. Further contributions are divided into the specific topics of form finding, flexible formworks and shell structures.

13.1.1 Constructional proof of concept

Three prototypes were built that demonstrate the constructional feasibility of both a fabric and cable-net formwork at model scale. Several design criteria were developed for their topology and geometry, intended to reduce required prestresses and otherwise simplify construction. An extensive historical review of flexible formworks uncovered many obscure and uncited, even large-scale examples.

13.1.2 Design workflow

A conceptual, computational design process was developed that generates and evaluates a shell geometry, to then determine the prestresses required in a fabric or cable net to produce that geometry under load, as well as the reaction forces for the external falsework frame. The initial mesh geometry from shape generation is maintained throughout the entire process. Several other strategies are included to minimize computational cost. For a simple saddle-shaped shell, the final implementation required only eight seconds to compute each individual result.

13.1.3 Technical feasibility

The second prototype demonstrated that reasonable tolerances can be maintained if forces are measured and controlled. A parametric study showed that flexibly formed shells are limited by two factors: the buckling of the shell; and, depending on the type of formwork, the allowable fabric prestress or practical weight of the cable net. The study also revealed that for a square hypar with a slenderness of 150, a fabric formwork and a cable-net formwork can be applied for spans of up to 15 m and up to 40 m respectively. The final case study, the final design of NEST HiLo, was succesfully submitted and led to the approval of a building permit.

13.1.4 Form finding

Chapter 5 provides the most comprehensive review of form-finding methods for prestressed networks and surfaces thus far. Four categories are proposed: stiffness matrix methods; geometric stiffness methods; dynamic equilibrium methods; and, minimization methods. Based on this review, a generic form-finding method is presented using consistent notation, and explanations are given throughout, under what conditions it becomes a specific well known method. It also produced new force density formulations for the spring, constant strain triangle, and constant surface stress triangle elements and their coordinate derivatives. The resulting framework was used to compare the computational performance of existing methods, with geometric stiffness methods generally outperforming the rest. It also revealed identical elements and solvers, mostly among stiffness matrix methods, and in work from the past two decades.

13.1.5 Flexible formworks

Chapter 3 provides the most comprehensive review of flexible formworks for shell structures thus far, uncovering obscure and previously uncited work on systems, related or similar to the proposed cable-net and fabric formwork system. The review summarizes reported benefits including their potential cost savings.

13.1.6 Shell structures

Chapter 8 is the only known, full description of the recommendations for the stability analysis of shells (Medwadowski et al. 1979), issued by the International Association for Shells and Spatial Structures (IASS). It incorporates surrounding literature and relevant building codes, as the recommendations provide very little guidance on how to actually apply them. This description is entirely integrated in the parametric design process. This allows for fast evaluation of nonlinear effects based only on the linear critical buckling load.

This model was applied to small studies on anticlastic shells. This supported conclusions drawn in literature for synclastic shells: that shape optimizations should include thickness variables (Lee & Hinton 2000*a*); and, that optimization should be done both with and without imperfections (Reitinger & Ramm 1995). These findings carried over in the case study in Chapter 12.

Results from the case study, NEST HiLo, supported many recommendations from Medwadowski et al. (1979). Specific findings were that:

- the perceived structural benefits of a sandwich shell are offset by differential creep and shrinkage behaviour due to the differences in temperature and relative humidity in the opposite concrete faces;
- thermal action and corresponding stresses, may actually, but not necessarily improve the load factor;
- the effect of creep and shrinkage can significantly reduce the load factor (up to 35 %), even if the shell is not considered to be shallow;
- structural performance was indifferent to either the use of ferrocement or textile reinforced concrete (TRC); and,
- this unique negatively curved form has increasing post-buckling capacity, consistent with literature on hypars.

13.2 Recommendations

Based on the results, the following recommmendations are made for the design and construction of flexibly formed shells:

- deformations of the flexible formwork under the weight of the wet concrete should be taken into account by using best-fit optimization and subsequent analysis of the required prestresses;
- a strategy must be in place to measure, and ideally correct these prestresses on site, to a precision in the order of 2-3 % of the maximum prestress;
- provided these two recommendations are met, accidental imperfections can be calculated according to (Medwadowski 2004) with a formwork factor $\alpha = 12$ (currently recommended for air-inflated forms);
- for stability analysis, IASS 1979 recommendations should be updated based on contemporary limit state design (LSD), possibly using Eurocode EN 1993-1-6:2007, intended for thin steel shells, as a starting point;
- cable nets should be used in favour of fabrics, until deviations in the built geometry for the latter are resolved and demonstrated to be manageable;
- several design criteria for the formwork pattern are provided in Section 7.3; and,
- prestresses should be applied and controlled from both ends of the formwork; and,
- cutting patterns should be fabricated and measured such that cumulative errors are avoided.

13.3 Future work

The following unresolved matters may provide substance for future research.

The scope of this thesis was limited to negatively curved, i.e. anticlastic shell geometries. Regarding form, the following topics can be explored:

- anticlastic shapes can be funicular (Rippmann & Block 2013), and geometries within this overlap could be generated by combining thrust network analysis with the present work;
- similar work to this thesis can be done for locally or entirely synclastic shells, which would have to be constructed as a hanging roof, or on an invertible, or pneumatic formwork (Sections 3.7.1, 3.2.3 or 3.4), or some other method that introduces out-of-plane pressures; or,
- formworks could also use external objects (Figure 3.33), active-bent elements (Section 3.5), or some other method that introduces loads or supports into the flexible formwork surface;
- formworks can be made from flat sheets or otherwise prescribed cutting pattern, possibly manipulated to have wrinkles and folds, and requiring large-displacement analysis instead of form finding; while,
- such corrugated shell shapes may have increased buckling resistance and "this inversion of the fabric's buckling weakness into the buckling resistance of the compression shell may be something like a corollary to the fundamental geometric law of the inversion of funicular tension and compression shapes" (Section 2.2.1) (West et al. 2011), which can be investigated, for example by computing cutting patterns from optimized buckling shapes, to establish if a conventional form-finding method could have arrived at such a shape; and,
- further work can be done to investigate the validity of applying older approaches like IASS 1979, which is based on experimental analysis of analytical, mostly synclastic shapes, to unique geometries produced by form finding.

Regarding history, it would be prudent to achieve a better understanding why the observed first wave of academic experiments on flexible formworks (1960-1975) did not avert the general decline of concrete shells.

Regarding (constrained) form finding,

- it could include beam elements representing the external frame (though by itself not a novelty); and,
- additional force and initial lengths constraints for fabric cutting patterns;
- a thorough comparison should be made between the constrained nonlinear least squares approaches by Linkwitz & Schek (1971) with coordinates and forces as variables and by Schek (1974) with only forces as variables, applied to the same types of constraints; and,

- a wider comparison can be made with other constrained form-finding approaches, including those based on integration, which generally apply some type of penalty or barrier function, or use projection methods.

Regarding construction, fabric formwork could be further investigated to resolve the deviations in the third prototype, starting by finding methods to accurately measure prestresses and to produce patterns of uniform stiffness without the influence of seams. A corollary question is whether precisely tailored cutting patterns can practically produce non-uniform prestress distribution, or whether fabric formworks are more restrictive in form than cable nets where each cable segment is easily controlled.

13.4 Final remarks

There is an absolute fascination for a structural designer when it comes to thin shells. They are daring objects that, at first sight, seem to defy gravity. The idea of deriving their shape by form finding is particularly elegant. It can thus be especially surprising to realize that no concrete shell has been designed using numerical form finding. Those based on physical form finding are limited to less than a hunderd works of Heinz Isler, one more by Sergio Musmeci, and another, currently under construction, by Frei Otto. It is staggering in fact, given the sheer amount of research on form finding and shell structures by dedicated academics within the field of structural geometry; a tribe to which you might perhaps count yourself as well. The quotes throughout this thesis, offered by expert shell designers at various times in history, often remark that the problem of formwork is central to this discrepancy. The concrete shell has even been declared dead. Lives spent in its service have been thought completely wasted. It is essential to solve the problem of formwork, if we, or future architects and engineers, are to bear the fruits of all this work. The case study, NEST HiLo – the result of the knowledge and collaboration of many – aims to do just that. It should demonstrate the potential of flexible formworks and in doing so, may also (re-)acquaint many in the industry with the concrete shell. Its unique geometry already underlines the potential of greater design freedom for flexibly formed shell structures; an opportunity that you too are welcome and invited to explore. Once built, it may well be the world's first computationally form-found, permanent thin concrete shell structure. Let us hope it is not the last. So, let us end as we began by repeating after me: "There are no limits to the shape of concrete."

Figure 13.1: NEST HiLo 1:1 roof prototype, developed and constructed by the author's colleagues at the Block Research Group and their partners, August 2017, ETH Zurich, Switzerland.

Bibliography

Abdelgader, H., West, M. & Górski, J. (2008), State-of-the-art report on fabric formwork, *in* 'Proceedings of the International Conference on Construction and Building Technology', Kuala Lumpur, Malaysia.

ACI 549.1R-93 (1993), 'Guide for the design, construction, and repair of ferrocement'. (Reapproved 2009).

ACI 549R-97 (1997), 'Report on ferrocement'. (Reapproved 2009).

Addis, B. (2014), Physical modelling and form finding, *in* S. Adriaenssens, P. Block, D. Veenendaal & C. Williams, eds, 'Shell Structures for Architecture: Form Finding and Optimization', Routledge, London, pp. 32–43.

Adriaenssens, S., Barnes, M., Harris, R. & Williams, C. (2014*a*), Dynamix relaxation - design of a strained timber gridshell, *in* S. Adriaenssens, P. Block, D. Veenendaal & C. Williams, eds, 'Shell Structures for Architecture: Form Finding and Optimization', Routledge, London, pp. 88–101.

Adriaenssens, S., Block, P., Veenendaal, D. & Williams, C., eds (2014*b*), *Shell Structures for Architecture: Form Finding and Optimization*, Routledge, London.

Adriaenssens, S., Ney, L., Bodarwe, E. & Williams, C. (2009), Dutch maritime museum: Form-finding of an irregular faceted skeletal shell - Part b, *in* A. Domingo & C. Lazaro, eds, 'Proceedings of the International Association of Shells and Spatial Structures', Valencia, Spain.

Adriaenssens, S., Schmidt, K., Katz, A., Gabriele, S., Magrone, P. & Varano, V. (2015), Early form finding techniques of Sergio Musmeci revisited: the Basento Viaduct project., *in* 'Proceedings of the International Association of Shells and Spatial Structures', Amsterdam.

Aimond, F. (1936), Étude statique des voiles minces en paraboloide hyperbolique travaillant sans flexion, *in* 'IABSE congress report', Vol. 4.

Akbari, J., Ahmadi, M. T. & Moharrami, H. (2011), 'Advances in concrete arch dams shape optimization', *Applied Mathematical Modelling* **35**(7), 3316–3333.

Alic, V. & Persson, K. (2016), 'Form finding with dynamic relaxation and isogeometric membrane elements', *Computer Methods in Applied Mechanics and Engineering* **300**, 737–747.

Anderson, B. G., Tor, A. A. & Yeakel Jr., R. W. (1964), Design and construction of shell roof for the New York International Airport TWA Flight Center, *in* 'Proceedings, World Conference on Shell Structures', San Francisco, CA, US, pp. 319–328. Washington D.C., National Academy of Sciences-National Research Council Publication 1187-453.

Andrés, O. A. (2009), About the freedom of free forms, *in* A. Domingo & C. Lazaro, eds, 'Proceedings of the International Association of Shells and Spatial Structures', Valencia, Spain.

Anon. (1941), 'New type of concrete hut', *Concrete and Constructional Engineering* **36**(8), 324–327.

Anon. (1959), 'Curved roofs of large span', *Concrete and Constructional Engineering* **54**(5), 171–4.

Anon. (1960), 'Building in the tropics', *The New Scientist* p. 520.

Anon. (1966), 'A church at Denver', *Concrete and Constructional Engineering* **61**(11), 394.

Arbocz, J. (1987), Post-buckling behaviour of structures numerical techniques for more complicated structures, *in* 'Buckling and Post-Buckling: Four Lectures in Experimental, Numerical and Theoretical Solid Mechanics Based on Talks Given at the CISM-Meeting Held in Udine, Italy, September 29–October 3, 1985', Springer Berlin Heidelberg, Berlin, Heidelberg, pp. 83–142.

Arcaro, V. F. & Klinka, K. K. (2009), 'Finite element analysis for geometric shape minimization', *Journal of the International Association for Shell and Spatial Structures* **50**(161), 79–86.

Argyris, J. (1964), *Recent Advances in Matrix Methods of Structural Analysis. Progress in Aeronautical Sciences*, Pergamon Press.

Argyris, J. H. & Angelopoulos, T. (1972), 'Ein Verfahren für die Formfindung von beliebigen, vorgespannten Netzwerkkonstruktionen', *IABSE congress report* **9**, 377–384. In German.

Argyris, J. H., Angelopoulos, T. & Bichat, B. (1974), 'A general method for the shape finding of lightweight tension structures', *Computer Methods in Applied Mechanics and Engineering* **3**, 135–149.

Arnout, S., Firl, M. & Bletzinger, K.-U. (2012), 'Parameter free shape and thickness optimisation considering stress response', *Structural Multidisciplinary Optimization* **45**, 801–814.

Asadzadeh, E. & Alam, M. (2014), 'A survey on hyperbolic cooling towers', *International Journal of Civil, Architectural, Structural and Construction Engineering* **8**(10), 1022–1034.

Aste, N., Angelotti, A. & Buzzetti, M. (2009), 'The influence of the external walls thermal inertia on the energy performance of well insulated buildings', *Energy and Buildings* **41**(11), 1181–7.

Bach, K., Burkhardt, B. & Otto, F. (1988), *IL 18. Seifenblasen. Forming bubbles*, Institute for Lightweight Structures (IL), Stuttgart. In German and English.

Baily, R. (1942), 'Apparatus and method for molding concrete'. U.S. patent 2,311,358. Filed November 25, 1940, and issued February 16, 1943.

Baitsch, M. (2003), Optimierung druckbeanspruchter Stabtragwerke unter Berücksichtigung geometrischer Imperfektionen, PhD thesis, Ruhr-Universität Bochum, Germany. In German.

Balding, D. (2013), The experimental seismic testing of hypar shells, fourth-year undergraduate project, Cambridge University.

Ballesteros, P. (1969), 'Non-linear dynamic and creep buckling of elliptical paraboloidal shell', *Bulletin of the International Association for Shell and Spatial Structures* (68), 39–78.

Bamu, P. & Zingoni, A. (2005), 'Damage, deterioration and the long-term structural performance of cooling-tower shells: A survey of developments over the past 50 years', *Engineering Structures* **27**, 1794–1800.

Baraff, D. & Witkin, A. (1998), Large steps in cloth animation, *in* 'SIGGRAPH 98 Computer Graphics Proceedings', Orlando, FL, US.

Barnes, M. (1994), 'Form and stress engineering of tension structures', *Structural Engineering Review* **6**(3-4), 175–202.

Barnes, M. R. (1971), 'Pretensioned cable networks', *Construction Research and Development Journal* **3**(1), 17–22.

Barnes, M. R. (1977), Form-finding and analysis of tension space structures by dynamic relaxation, PhD thesis, City University London, United Kingdom.

Barnes, M. R. (1988), 'Form-finding and analysis of prestressed nets and membranes', *Computers and Structures* **30**(3), 685–695.

Barnes, M. R. (1999), 'Form finding and analysis of tension structures by dynamic relaxation', *International Journal of Space Structures* **14**(2), 89–104.

Barnes, M. & Wakefield, D. (1984), Dynamic relaxation applied to interactive form finding and analysis of air-supported structures, *in* 'Proceedings of Conference on the Design of Air-supported Structures', pp. 147–161.

Basso, P. & Del Grosso, A. (2011), Form-finding methods for structural frameworks: a review, *in* 'Proceedings of the International Association of Shells and Spatial Structures', London.

Bathe, K.-J., Ramm, E. & Wilson, E. L. (1975), 'Finite element formulations for large deformation dynamic analysis', *International Journal for Numerical Methods in Engineering* **9**, 353–386.

Bavarel, O., Caron, J.-F., Tayeb, F. & Du Peloux, L. (2012), 'Gridshells in Composite Materials: Construction of a 300 m^2 Forum for the Solidays' Festival in Paris', *Structural Engineering International* **22**(3), 408–414.

Belis, J., Pronk, A., Martens, K., Van Lancker, B. & Dispersyn, J. (2015), Experimental construction of a temporary church in reinforced ice, *in* 'The 2015 World Congress on Advances in Structural Engineering and Mechanics (ASEM15)', Incheon, South Korea.

Belton, S. (2012*a*), Digital formfinding. The application of mechanically prestressed fabric membranes as formwork for complex curved concrete structures using digital methods of form-finding, structural analysis, and fabrication, *in* J. Orr et al., eds, 'Proceedings of the 2nd international conference on flexible formwork', Bath, UK, pp. 54–62.

Belton, S. (2012*b*), The application of actively tensioned membranes as formwork for complex curvatures in concrete structures, *in* W. De Wilde, C. Brebbia & S. Hernández, eds, 'WIT Transactions on The Built Environment. High Performance Structure and Materials VI', Vol. 124, pp. 27–38.

Bhooshan, S. & El Sayed, M. (2012), Sub-division surfaces in architectural form finding and fabric forming, *in* J. Orr et al., eds, 'Proceedings of the 2nd international conference on flexible formwork', Bath, UK, pp. 64–74.

Bhooshan, S., Veenendaal, D. & Block, P. (2014), Particle-spring systems - design of a cantilevering concrete canopy, *in* S. Adriaenssens, P. Block, D. Veenendaal & C. Williams, eds, 'Shell Structures for Architecture: Form Finding and Optimization', Routledge, London, pp. 102–113.

Billig, K. (1946), 'Concrete shell roofs with flexible moulds', *Journal of the ICE* **25**(3), 228–231.

Billig, K. (1951), 'Corrugated concrete shell structures. new developments', *IABSE publications* **11**, 33–39.

Billig, K. (1955), 'Corrugated concrete shell roofs', *Bulletin of the Central Building Research Institute, Roorkee* **1**(3). Council of Scientific and Industrial Research, New Delhi.

Billig, K. (1961), 'Corrugated concrete shell construction', *Bulletin of the International Association for Shell Structures* .

Billig, K. (1963), *Structural Concrete*, Macmillan & Co Ltd, New York, NY, US.

Billner, K. (1936), 'Method of and apparatus for treating concrete'. U.S. patent 2,046,867. Filed, April 8, 1935, published July 7, 1936.

Billner, K. (1943), 'Building construction'. U.S. patent 2,324,554. Filed, August 12, 1940, published July 20, 1943.

Billner, K. (1953), 'Method of molding concrete structures'. U.S. patent 2,624,931. Filed February 28, 1951, and issued January 13, 1953.

Bini, D. (1969), 'Method for erecting structures'. U.S. patent 3,462,521. Filed December 12, 1966, and issued August 19, 1969.

Bini, D. (1991), 'Binishell collapse – the inventor's view', pp. 5,8.

Bird, W., Rongved, P., Strobel, P. & Zamore, D. (1959), 'Improved method of erecting shellform concrete structures'. U.S. patent 2,892,239. Filed June 19, 1952, and issued June 30, 1959.

Bird, W., Rongved, P., Strobel, P. & Zamore, D. (1964), 'Building construction'. U.S. patent 3,139,464. Filed July 22, 1960, and issued June 30, 1964.

Bletzinger, K.-U. (2011), Section 12.2: Form finding and morphogenesis, *in* I. Munga & J. F. Abel, eds, 'Fifty Years of Progress for Shell and Spatial Structures', Multi-Science, pp. 459–482.

Bletzinger, K.-U., Linhard, J. & Wüchner, R. (2009), 'Extended and integrated numerical form finding and patterning of membrane structures', *Journal of the International Association for Shell and Spatial Structures* **50**(1), 35–49.

Bletzinger, K.-U. & Ramm, E. (1999), 'A general finite element approach to the form finding of tensile structures by the updated reference strategy', *International Journal of Space Structures* **14**(2), 131–145.

Bletzinger, K.-U. & Ramm, E. (2014), Computational form finding and optimization, *in* S. Adriaenssens, P. Block, D. Veenendaal & C. Williams, eds, 'Shell Structures for Architecture. Form finding and optimization', Routledge, pp. 44–55.

Bletzinger, K.-U., Wüchner, R., Daoud, F. & Camprubí, N. (2005), 'Computational methods for form finding and optimization of shells and membranes', *Computer Methods in Applied Mechanics and Engineering* **194**, 3438–3452.

Block, P. (2009), Thrust Network Analysis: Exploring Three-dimensional Analysis, PhD thesis, Massachusetts Institute of Technology, Cambridge, MA, US.

Block, P. (2016), 'Parametricism's structural congeniality', *AD Architectural Design* **86**(2), 68–75. Special issue P. Schumacher (Ed.) - Parametricism 2.0: Rethinking Architecture's Agenda for the 21st Century.

Block, P. & Lachauer, L. (2014), 'Three-dimensional equilibrium analysis of gothic masonry vaults', *International Journal of Architectural Heritage* **8**(3), 312–335.

Block, P. & Ochsendorf, J. (2007), 'Thrust network analysis: A new methodology for three-dimensional equilibrium', *Journal of the International Association for Shell and Spatial Structures* **48**(155), 167–173.

Block, P., Schlueter, A., Veenendaal, D., Bakker, J., Begle, M., Hischier, I., Hofer, J., Jayathissa, P., Maxwell, I., Méndez Echenagucia, T., Nagy, Z., Pigram, D., Svetozarevic, B., Torsing, R., Verbeek, J., Willmann, A. & Lydon, G. (2017), 'NEST HiLo: Investigating lightweight construction and adaptive energy systems', *Journal of Building Engineering* **12**, 332–341.

Block, P. & Veenendaal, D. (2013), 'Textile Schalung - Zwischen effizienter Konstruktion und expressivem Ausdruck', *Archithese, Weak materiality - Eine Schwäche für Materialität* **3**, 38–43. In German.

Blonder, A. (2015), Full scale form-finding: Introducing fabric materiality in the fabrication of architecural [sic] FRP, *in* '20th International Conference on Composite Materials', Copenhagen, Denmark.

Blonder, A. & Grobman, Y. J. (2015*a*), Alternative fabrication process for free-form FRP architectural elements relying on fabric materiality. Towards freedom from molds and surface articulation, *in* 'The Next City: 16th International Conference CAAD Futures 2015', pp. 397–410.

Blonder, A. & Grobman, Y. J. (2015*b*), 'Design and fabrication with fibre-reinforced polymers in architecture: a case for complex geometry', *Architectural Science Review* pp. 1–12.

Boden, T., Andres, R. & Marland, G. (2013), 'Global, regional, and national fossil-fuel CO_2 emissions: 1751-2010'.

Bondy, J. A. & Murty, U. S. R. (1976), *Graph theory with applications*, Elsevier Science Publishing Co., New York.

Bouzidi, R. & Levan, A. (2013), Membrane form finding by means of functional minimization, *in* 'Textile Composites and Inflatable Structures VI – Proceedings of the 6th International Conference on Textile Composites and Inflatable Structures, Structural Membranes 2013', Munich, pp. 494–504.

Boyd, S. & Vandenberghe, L. (2004), *Convex Optimization*, Cambridge University Press, UK.

Boyle, J. (1907), 'Apparatus for molding hollow objects from cement'. U.S. patent 857,582. Filed January 23, 1907, published June 25, 1907.

Brakke, K. A. (1992), 'The surface evolver', *Experimental Mathematics* **1**(2), 141–165.

Brew, J. S. & Lewis, W. J. (2003*a*), 'Computational form-finding of tension membrane structures-non-finite element approaches - Part 1. Use of cubic splines in finding minimal surface membranes', *International Journal for Numerical Methods in Engineering* **56**, 651–668.

Brew, J. S. & Lewis, W. J. (2003*b*), 'Computational form-finding of tension membrane structures-non-finite element approaches - Part 2. Triangular mesh discretization and control of mesh distortion in modelling minimal surface membranes', *International Journal for Numerical Methods in Engineering* **56**, 669–684.

Brew, J. S. & Lewis, W. J. (2007), 'Tension membranes modelled by curvi-linear bicubic splines', *International Journal for Numerical Methods in Engineering* **72**, 1–21.

Brown, E. (1967), *Structural analysis*, Vol. 1, John Wiley & Sons, New York.

Buchhardt, F., Magiera, G., Matthees, W. & Plank, A. (1984), 'Structural investigation of the Berlin Congress Hall collapse', *Concrete International* pp. 63–68.

Buchholdt, H. A., Davies, M. & Hussey, M. J. L. (1968), 'The analysis of cable nets', *Journal of the Institute of Mathematics and Its Applications* **4**, 339–358.

Buchholz, R. (1992), 'Perfect pyramids', *Bulletin of the Australian Mathematical Society* **45**(3), 353–368.

Bureau, U. C. (2016), 'Historical income tables: People', website. Accessed March 8, 2016. **URL:** *https://www.census.gov/hhes/www/income/data/historical/people/*

Busch, D., Harte, R., Krätzig, W. B. & Montag, U. (2002), 'New natural draft cooling tower of 200 m of height', *Engineering Structures* **24**, 1509–21.

Caminos, C. H. (2012), *Horacio Caminos. Teacher. Docente.*

Caminos, H. (1959), 'Studies on models of a type of membranal structure', *Bulletin of the International Association for Shell Structures* (10).

Candela, F. et al. (1959), 'Láminas de hormigón armado', *Arquitectura* **1**(10). In Spanish.

Carlton, W. S. (2013), Material behavior of latex-modified concrete in thin hyperbolic paraboloid shells, Master thesis, University of Oklahoma.

Carpo, M. (2012), *The Digital Turn in Architecture 1992 - 2012*, Wiley & Sons.

Carstensen, C. & Wriggers, P. (2009), *Mixed Finite Element Technologies*, Springer.

Cassinello, P., Schlaich, M. & Torroja, J. (2010), 'Félix Candela. In memorian [sic] (1910-1997). From thin concrete shells to the 21st century's lightweight structures. Félix Candela. En memoria (1910-1997). Del cascarón de hormigón a las estructuras ligeras del s. XXI', *Informes de la Construcción* **62**(519), 5–26. In English and Spanish.

Cauberg, N. (2009), 'Creatieve betonconstructies door het gebruik van textiel als flexibel bekistingsmateriaal of functionele liner in bekistingen'. In Dutch.

Cauberg, N., Tysmans, T., Adriaenssens, S., Wastiels, J., Mollaert, M. & Belkassem, B. (2012), 'Shell elements of textile reinforced concrete using fabric formwork: A case study', *Advances in Structural Engineering* **15**(4), 677–689.

Chatterjee, B. K. (1964), Economics of shell roof construction in underdeveloped countries in the tropics, *in* 'Proceedings, World Conference on Shell Structures', San Francisco, CA, US, pp. 103–108. Washington D.C., National Academy of Sciences-National Research Council Publication 1187-453.

Chen, T. (2014), On introducing imperfection in the non-linear analysis of buckling of thin shell structures, Master's thesis, Technische Universiteit Delft, Netherlands.

Chilton, J. (2000), *The Engineer's Contribution to Contemporary Architecture: Heinz Isler*, Thomas Telford, London.

Chilton, J. & Tang, G. (2017), *Timber Gridshells. Architecture, Structure and Craft*, Routledge.

Chistiansen, J. V. (1988), Chapter 7. Hyperbolic Paraboloid Performance and Cost, *in* 'Special Publication', Vol. 110, American Concrete Institute, pp. 139–157.

Christensen, R. (1988), 'Network Formulation of the Finite Element Method', *International Journal of General Systems* **14**(1), 59–75.

CIRIA C660 (2007), 'Early-age thermal crack control in concrete'. Bamforth, P.B.

Claessens, R., Notemans, P., Slangen, S., Spits, G. & Vorstermans, R. (2016), 7kp2mo - design project fabric formwork. Phase 2: Design and realization of shell structure, Master's project, Eindhoven University of Technology, Netherlands.

Connor, J. J. (1976), *Analysis of Structural Member Systems*, The Ronald Press Company, New York, US.

Cook, J., Nuccitelli, D., Green, S. A., Richardson, M., Winkler, B., Painting, R., Way, R., Jacobs, P. & Skuce, A. (2013), 'Quantifying the consensus on anthropogenic global warming in the scientific literature', *Environmental Research Letters* **8**(2), 1–7.

Corradi, M., Filemio, V. & Trenetti, M. (2009), 'Antonelli's dome for San Gaudenzio: Geometry and statics', *Nexus Network Journal* **11**(2), 243–256.

Csonka, P. (1956), 'The buckling of a spheroidal shell curved in two directions', *Acta Technica Academiae Scientiarum Hungaricae* pp. 425–437.

Cuvilliers, P., Douthe, C., du Peloux, L. & Le Roy, R. (2017), 'Hybrid structural skin: Prototype of a GFRP elastic gridshell braced by a fiber-reinforced concrete envelope', *Journal of the International Association for Shell and Spatial Structures* **58**(1), 65–78.

Dagher, H. J., Bannon, D. J., Davids, W. G., Lopez-Anido, R. A., Nagy, E. & Goslin, K. (2012), 'Bending behavior of concrete-filled tubular FRP arches for bridge structures', *Construction and Building Materials* **37**, 432–439.

Damjakob, H. & Tummers, N. (2004), Back to the future of the hyperbolic concrete tower, *in* I. Mungan & U. Wittek, eds, '5th International Symposium on Natural Draught Cooling Towers', Istanbul, Turkey, pp. 3–21.

Davis, L., Rippmann, M., Pawlofsky, T. & Block, P. (2012), 'Innovative funicular tile vaulting: A prototype in Switzerland', *The Structural Engineer* **90**(11), 46–56.

Day, A. (1965), 'An introduction to dynamic relaxation', *The Engineer* pp. 218–221.

De Bolster, E., Cuypers, H., Van Itterbeek, P., Wastiels, J. & De Wilde, W. (2009), 'Use of hypar-shell structures with textile reinforced cement matrix composites in lightweight constructions', *Composites Science and Technology* **69**, 1341–1347.

Dezeen (2013*a*), 'Dutch architects to use 3D printer to build a house', website. Accessed August 22, 2016.
URL: *http://www.dezeen.com/2013/01/20/dutch-architects-to-use-3d-printer-to-build-a-house/*

Dezeen (2013*b*), 'Foster + Partners to 3D print buildings on the moon', website. Accessed August 22, 2016.
URL: *http://www.dezeen.com/2013/01/31/foster-partners-to-3d-print-buildings-on-the-moon/*

Dezeen (2016), 'WATG wins competition to design freeform 3d-printed house', website. Accessed August 22, 2016.
URL: *http://www.dezeen.com/2016/06/07/watg-urban-architecture-studio-3d-printed-house-carbon-plastic-fibre-panels-chicago-usa-competition/*

Dielemans, G., De Mooij, L., Kuzin, P., De Smet, R. & Godthelp, T. (2016), Fabric formed concrete. An art object of concrete. Design report group 1, Master's project, Eindhoven University of Technology, Netherlands.

Dieringer, F. (2014), Numerical Methods for the Design and Analysis of Tensile Structures, PhD thesis, Technische Universität München, Germany.

Dieringer, F., Wüchner, R. & Bletzinger, K.-U. (2013), The extended updated reference strategy for the form finding of tensile structures, *in* 'Textile Composites and Inflatable Structures VI – Proceedings of the 6th International Conference on Textile Composites and Inflatable Structures, Structural Membranes 2013', Munich, pp. 154–165.

Domingo, A., Lázaro, C. & Cerna, P. (1999), Design of a thin shell steel fiber reinforced concrete hypar roof, *in* 'Proceedings of the International Association of Shells and Spatial Structures. 10 Years of Progress in Shell and Spatial Structures [30th Anniversary Symposium]', Madrid, Spain.

Domingo, A., Lázaro, C. & Serna, P. (2004), Construction of JCHYPAR, a steel fiber reinforced concrete thin shell structure, *in* M. di Prisco, R. Felicetti & G. Plizzari, eds, '6th International RILEM Symposium on Fibre Reinforced Concretes', pp. 1143–52.

Dominicus, M., Khademagha, P. & Pronk, A. (2011), Modeling and producing optimal open cell structures for architecture, *in* 'Proceedings of the IABSE-IASS Symposium 2011', London, England.

Duerr, H. & Off, R. (2014), 'From membrane form to rigid shell. Applied research on material and process technology to apply and stiffen membrane structures with shotcrete', *Tensinews* (27), 14–16.

Dulácska, E. (1978), 'Die bei der Untersuchung des Beulverhaltens von Schalen in Betracht zu Ziehende Anfangsausmittigkeit', *Acta Technica Academiae Scientiarum Hungaricae* **86**(1-2), 156–167. In German.

Dulácska, E. (1981), 'Explanation of the chapter on stability of the "recommendations for reinforced concrete shells and folded plates" and a proposal to its improvement', *Bulletin of the International Association for Shell and Spatial Structures* (77), 3–18.

Dulácska, E. (1986), 'The safety factor to be applied in shell buckling analysis', *Acta Technica Academiae Scientiarum Hungaricae* **99**(1-2), 9–30.

Dulácska, E. & Kollár, L. (1995), 'Design procedure for the buckling analysis of reinforced concrete shells', *Thin-Walled Structures* **23**, 313–321.

Ebata, K., Cui, C. & Sasaki, M. (2003), Creation of free-formed shell by sensitivity analysis (application to structural design), *in* 'Proceedings of Architectural Institute of Japan 2003', pp. 269–270. In Japanese.

Egea, J. J. (2004), 'Estación de autobuses en Casar de Cáceres. Justo García Rubio', *Tectonica* **105-106**, 52–65. In Spanish.

Eisenbach, P., Vasudevan, R., Grohmann, M., Bollinger, K. & Hauser, S. (2014), 'Parapluie - realisierung einer ultraschlanken betonschale durch aktivierung einger membrantragwirkung', *Beton- und Stahlbetonbau* **109**(1), 53–59.

EN 1990:2002 (2002), 'Eurocode 0: Basis of structural design'.

EN 1992-1-1:2004 (2004), 'Eurocode 2: Design of concrete structures - part 1-1: General rules and rules for buildings'.

EN 1993-1-6:2007 (2007), 'Eurocode 3: Design of steel structures - part 1-6: Strength and stability of shell structures'.

ENR (1960), 'HP snaps, crackles, and pops ..... then collapses on gas station', p. 27.

ENR (1970), 'Students clear gym moments before roof fails', p. 11.

ENR (1975), '15 year old HP roof fails, injuring 18', p. 12.

Escrig, F. & Sánchez, J. (2005), 'La Bóveda de Hormigón del Club Táchira en Caracas (The Concrete vault of Club Táchira in Caracas)', *Informes de la Construcción* **57**(499-500), 133–144. In Spanish.

Espion, B. (2016), 'Pioneering hypar thin shell concrete roofs in the 1930s', *Beton- und Stahlbetonbau* **111**(3), 159–165.

Evans, B. H. & Marsh III, J. H. (1962), 'Lift-shape construction. A research report on a new building construction technique', report.

Faber, C. (1963), *Candela: The Shell Builder*, Reinhold Publishing Corporation, New York.

FAOSTAT (2016), 'Forestry production and trade', website. Accessed March 8, 2016.
URL: *http://faostat3.fao.org/download/F/FO/E*

Farrar, D., Davidson, J. C. F. & Harris, T. G. M. (1937), 'Construction of roofs, floors, ceilings and the like'. U.S. patent 2,096,629. Filed May 29, 1935, and issued October 19, 1937.

Felippa, C. (1991), Conjugate dynamic relaxation, *in* S. Atluri, D. Beskos, R. Jones & G. Yagawa, eds, 'Computational Mechanics '91. Theory and Applications. Proceedings of the International Conference on Computational Engineering Science', Melbourne, Australia, pp. 256–261.

Felippa, C. (1996), 'Explicit dynamic relaxation'.

Felippa, C. (2013), 'Appendix 0. the origins of the finite element method.'.
URL: *http://www.colorado.edu/engineering/CAS/courses.d/IFEM.d/IFEM.AppO.d/*

Feng, Y. (2006), 'On the discrete dynamic nature of the conjugate gradient method', *Journal of Computational Physics* (211), 91–98.

Fenves, S. J. & Branin Jr., F. H. (1963), 'Network-topological formulation of structural analysis', *Journal of the Structural Division, Proceedings of the American Society of Civil Engineers* pp. 483–514.

Fernández Ruiz, M. (2016), private communication to Veenendaal, D.

fib Bulletin No. 14 (2001), 'Externally bonded FRP reinforcement for RC structures'.

Filipe Martins, P., Fonseca de Campos, P., Nunes, S. & Pedro Sousa, J. (2015), Expanding the material possibilities of lightweight prefabrication in concrete through robotic hot-wire cutting. Form, texture and composition, *in* 'eCAADe 2015 - 33rd Annual Conference', Vol. 2, Vienna, Austria.

Fletcher, M. (1917), 'Method and means for forming concrete structural members'. U.S. patent 1,241,945. Filed May 28, 1917, and issued October 2, 1917.

Flint, A. (1961), Some model tests on shell structures as an aid to design, *in* 'Proceedings of the Symposium on Shell Research', pp. 291–301.

Flint, A. & Low, A. (1960), 'The construction of hyperbolic paraboloid type shells without temporary formwork', *Bulletin of the International Association for Shell Structures* (4), 5–18.

Forster, B. & Mollaert, M. (2004), *European Design Guide for Tensile Surface Structures*, TensiNet.

Gage, M. F. (2016), 'A hospice for Parametricism', *AD Architectural Design* **86**(2), 128–133. Special issue P. Schumacher (Ed.) - Parametricism 2.0: Rethinking Architecture's Agenda for the 21st Century.

Gallegos-Cazeres, S. & Schnobrich, W. (1988), 'Effects of creep and shrinkage on the behavior of reinforced concrete gable roof hyperbolic-paraboloids', (543). Research Grant MSM-8703352.

Galliot, C. & Luchsinger, R. (2009), 'A simple model describing the non-linear biaxial tensile behaviour of PVC-coated polyester fabrics for use in finite element analysis', *Composite Structures* **90**, 438–447.

Garrido, M., Correia, J., Branco, F. & Keller, T. (2014), 'Creep behaviour of sandwich panels with rigid polyurethane foam core and glass-fibre reinforced polymer faces: Experimental tests and analytical modelling', *Journal of Composite Materials* **48**(18), 2237–49.

Giovannardi, F. (2010), 'Sergio Musmeci. Strutture fuori dal coro'. In Italian.

Godoy, L. A. (1996), *Thin-Walled Structures with Structural Imperfections. Analysis and Behavior*, Pergamon.

Gosling, P. D. & Lewis, W. J. (1996), 'Optimal structural membrane-II. Form-finding of prestressed membranes using a curved quadrilateral finite element for surface definition', *Computers and Structures* **61**(5), 885–895.

Govan, J. & Ashenhurst, H. (1928), 'Building construction'. U.S. patent 1,671,946. Filed March, 3, 1925, and issued May 19, 1928.

Grad, P. (1991), 'Causes of accident finally public. Binishell collapse', pp. 4, 27–28.

Graefe, R. (2012), "Naturliche" Formbildungsprozesse in der Neugotik - Friedrich W.H. Gösling (1837-1899), *in* U. Hassler & C. Rauhut, eds, 'Bautechnik des Historismus. Von den Theorien über gotische Konstruktionen bis zu den Baustellen des 19. Jahrhunderts', Hirmer, pp. 144–159. In German.

Graefe, R., Tomlow, J. & Walz, A. (1983), 'Ein verschollenes Modell und seine Rekonstruktion', *Bauwelt* (15), 568–573. In German.

Greszczuk, L. B. (1959), Experiments on foamed plastic hyperbolic paraboloid shell, Master's thesis, Purdue University, US.

Grohmann, M., Bollinger, K., Weilandt, A. & Wagner, M. (2009), Form finding of the shell structures of the Rolex Learning Center in Lausanne, *in* A. Domingo & C. Lazaro, eds, 'Proceedings of the International Association of Shells and Spatial Structures', Valencia, Spain.

Gründig, L. (1988), 'Minimal surfaces for finding forms of structural membranes', *Computers & Structures* **30**(3), 679–683.

Gründig, L., Moncrieff, E., Singer, P. & Ströbel, D. (2000), A history of the principal developments and applications of the force density method in Germany 1970-1999, *in* 'Proceedings of IASS-IACM 2000 Fourth International Colloquium on Computation of Shell & Spatial Structures', Chania-Crete, Greece.

Gründig, L. & Schek, H.-J. (1974), Analytical form finding and analysis of prestressed cable networks, *in* 'International Conference on Tension Roof Structures', London, UK.

Guldentops, L., Mollaert, M., Adriaenssens, De Laet, L. & De Temmerman, N. (2009), Textile formwork for concrete shells, *in* A. Domingo & C. Lazaro, eds, 'Proceedings of the International Association for Shell and Spatial Structures (IASS) Symposium 2009', Valencia, pp. 1743–1754.

Haber, R. B. & Abel, J. F. (1982), 'Initial equilibrium solution methods for cable reinforced membranes. Part I-Formulations', *Computer Methods in Applied Mechanics and Engineering* **30**, 263–284.

Hack, N. & Lauer, W. V. (2014), 'Mesh-mould: Robotically fabricated spatial meshes as reinforced concrete formwork', *AD Architectural Design* **84**, 44–53.

Hale, L. (1988), 'Inflatable form for concrete structures'. U.S. patent 4,723,751. Filed July 21, 1986, and issued February 9, 1988.

Han, S.-E. & Lee, K.-S. (2003), 'A study of the stabilizing process of unstable structures by dynamic relaxation method', *Computers & Structures* **81**, 1677–1688.

Hansen, J., K. P., Sato, M., Masson-Delmotte, V., Ackerman, F., Beerling, D. J., Hearty, P. J., Hoegh-Guldberg, O., Hsu, S.-L. & Parmesan, C. (2013), 'Assessing "dangerous climate change": required reduction of carbon emissions to protect young people, future generations and nature', *PLOS ONE* **8**(12), 1–26.

Happold, E. & Liddell, W. I. (1975), 'Timber lattice roof for the Mannheim Bundesgartenschau', *The Structural Engineer* **53**(3), 99–135.

Harding, J. & Shepherd, P. (2011), Structural form finding using zero-length springs with dynamic mass, *in* 'Proceedings of the International Association of Shells and Spatial Structures', London.

Harrington, H. (1971), 'Method and apparatus for construction of concrete shells'. U.S. patent 3,619,432. Filed September 17, 1968, and issued November 9, 1971.

Harris, R., Romer, J., Kelly, O. & Johnson, S. (2003), 'Design and construction of the Downland Gridshell', *Building Research & Information* **31**(6), 427–454.

Haug, E. & Powell, G. H. (1972), Analytical shape finding for cable nets, *in* Y. Yokoo, ed., 'Proceedings of the 1971 IASS Pacific Symposium Part II on Tension Structures and Space Frames', Architectural Institute of Japan, Tokyo and Kyoto, Japan, pp. 83–92.

Hawkins, W., Herrmann, H., Ibell, T., Kromoser, B., Michaelski, A., Orr, J., Pedreschi, R., Pronk, A., Schipper, R., Shepherd, P., Veenendaal, D., Wansdronk, R. & West, M. (2016), 'Flexible formwork technologies: A state of the art review', *Structural Concrete* **17**(6).

Hegger, J., Horstmann, M., Voss, S. & Will, N. (2007), 'Textilbewehrter Beton - Tragverhalten, Bemessung und Anwendung', *Beton- und Stahlbetonbau* **102**(6), 362–370.

Hegger, J. & Voss, S. (2008), 'Investigations on the bearing behaviour and application potential of textile reinforced concrete', *Engineering Structures* **30**, 2050–2056.

Heifetz, H. (1970), 'Developments in inflatable forms.', *Build International* pp. 25–37.

Heifetz, H. (1972), 'Inflatable forms'. U.S. patent 3,643,910. Filed March 7, 1969, and issued February 22, 1972.

Heifetz, R. (2016), private communication to Veenendaal, D.

Hennicke, J., Matsushita, K., Otto, F., Sataka, K., Schaur, E., Shirayanagi, T. & Gröbner, G. (1974), *IL 10. Gitterschalen. Grid Shells*, Institute for Lightweight Structures (IL), Stuttgart. In German, English and Japanese.

Hennik, P. v. & Houtman, R. (2008), Pneumatic formwork for irregular curved thin shells, *in* 'Textile Composites and Inflatable Structures II', pp. 99–116.

Heyman, J. (1998), 'Hooke's cubico-parabolical conoid', *Notes and Records of the Royal Society of London* **52**(1), 39–50.

Hines, E. M. & Billington, D. P. (2004), 'Anton Tedesko and the introduction of thin shell concrete roofs in the United States', *Journal of Structural Engineering* **130**(11), 1639–1650.

Holzwart, C., Raczkowski, K. & Sturgeon, K. (2010), 'Fatty shell: Flexible formwork'. Cargo Collective. Accessed April 16, 2016.
URL: *http://cargocollective.com/fabroboticsnet/Fatty-Shell-Flexible-Formwork*

Hoogenboom, P. (2005), 'Stability of shells'.

Hooke, R. (1676), *A Description of Helioscopes, and some other Instruments*, John Martyn, London.

Hoppermann, M., Reuvers, H., Nap, P. & van Overveld, B. (2015), Design to installation of a free-form roof cladding with a flexible mould, *in* 'Proceedings of the International Association of Shells and Spatial Structures', Amsterdam.

Hübler, M. & Löschel, A. (2013), 'The EU Decarbonisation Roadmap 2050-What way to walk?', *Energy Policy* **55**, 190–207.

Hübsch, H. (1838), *Bau-Werke*, D.R. Marx'schen Buchhandlung, Karlsruhe and Baden, Germany. In German.

Huerta, S. (2006), 'Structural design in the work of Gaudí', *Architectural Science Review* **49.4**, 324–339.

Huijben, F. A. A. (2014), Vacuumatics: 3D Formwork Systems, PhD thesis, Technische Universiteit Eindhoven, Netherlands.

IASS 1979 (1979). See Medwadowski (1979).

Ingold, L. & Rinke, M. (2015), Sergio Musmeci's search for new forms of concrete structures, *in* '5th International Congress on Construction History', Chicago.

Isler, H. (1956), 'Feldmässiger Unterstand in Beton', *Technische Mitteilungen für Sappeure, Pontoniere und Mineure* **20**(4). In German.

Isler, H. (1960), 'New shapes for shells', *Bulletin of the International Association of Shell* (8).

Isler, H. (1967), Pneumatic shape for concrete shells, *in* '1st International Colloquium on Pneumatic Structures', Stuttgart, Germany, pp. 50–51.

Isler, H. (1980), Structural beauty of shells, *in* 'IABSE congress report', Vol. 11.

Isler, H. (1981), Effective use of concrete, *in* 'IABSE congress report', Vol. 36.

Isler, H. (1994), 'Concrete shells derived from experimental shapes', *Structural Engineering International* (3), 142–147.

Isler, H. (1995), Evolution of shell structures, *in* G. C. Giuliani, ed., 'Proceedings of the IASS International Symposium 1995. Spatial Structures: Heritage, Present and Future', Vol. 1, Milan, Italy, pp. 271–292.

Jadik, T. & Billington, D. (1995), 'Gabled hyperbolic paraboloid roofs without edge beams', *Journal of Structural Engineering* **121**(2), 328–335.

Johnston, D. W. (2008), Concrete construction engineering handbook, *in* 'Design and Construction of Concrete Formwork', CRC Press, pp. 7.1–7.49.

Kaethner, S. C. & Burridge, J. A. (2012), 'Embodied CO2 of structural frames', *Structural Engineer* **90**(5), 33–40.

Kanner, D. & Neff, W. (2005), *Wallace Neff and the Grand Houses of the Golden State*, Monacelli Press.

Kasuba, A. (2011), *Kasubaworks*, Blurb.

Katz, J. M. (2015), 'The king and queen of Haiti'. Politico.
URL: *http://www.politico.com/magazine/story/2015/05/clinton-foundation-haiti-117368*

Kelly, T., Matos, G. et al. (2013), 'Historical statistics for mineral and material commodities in the United States', website. U.S. Geological Survey Data Series 140. Accessed March 8, 2016.
URL: *http://minerals.usgs.gov/minerals/pubs/historical-statistics/*

Kersavage, J. A. (1975), 'Method for constructing a tensile-stress structure and resultant structures'. U.S. patent 3,927,496. Filed March 18, 1974, published December 23, 1975.

Ketchum, M. (2016), 'Milo Ketchum archive. Manuscripts by Milo Ketchum (1910-1999)', website.
URL: *http://www.ketchum.org/-milo/photos.html*

Ketchum, M. S. (1964), Economic factors in shell roof construction, *in* 'Proceedings, World Conference on Shell Structures', San Francisco, CA, US, pp. 97–102. Washington D.C., National Academy of Sciences-National Research Council Publication 1187-453.

Khoshnevis, B. (2004), 'Automated construction by contour crafting - related robotics and information technologies', *Journal of Automation in Construction - Special Issue: The best of ISARC 2002* **13**, 5–19.

Khoshnevis, B. (2012), 'ISRU-ok-based robotic construction technologies for lunar and martian infrastructures', website. Accessed August 22, 2016.
URL: *http://www.nasa.gov/directorates/spacetech/niac/2012_phaseII _fellows _khoshnevis.html*

Kilian, A. (2004), Linking digital hanging chain models to fabrication, *in* 'Fabrication: Examining the Digital Practice of Architecture: 23rd Annual Conference of the Association for Computer Aided Design in Architecture (ACADIA)', Cambridge and Toronto, Ontario, Canada, pp. 110–125.

Kilian, A. & Ochsendorf, J. (2005), 'Particle-spring systems for structural form finding', *Journal of the International Association for Shell and Spatial Structures* **46**(2), 77–84.

Knott, A. & Nez, G. (2005), *Latex Concrete Habitat*, Trafford Publishing Company, Canada.

Knudson, W. C. & Scordelis, A. C. (1972), Cable forces for desired shapes in cable-net structures, *in* Y. Yokoo, ed., 'Proceedings of the 1971 IASS Pacific Symposium Part II on Tension Structures and Space Frames', Architectural Institute of Japan, Tokyo and Kyoto, Japan, pp. 93–102.

Kollár, L. (1969), 'On the behaviour of shells in the postbuckling range', *Bulletin of the International Association for Shell and Spatial Structures* (39), 41–51.

Kollár, L. (1993), 'Modified proposal for the text of the recommendations', private communication to Medwadowski, S.J., see Medwadowski (2004).

Kollár, L. & Dulácska, E. (1984), *Buckling of Shells for Engineers*, John Wiley & Sons.

Koohestani, K. (2014), 'Nonlinear force density method for the form-finding of minimal surface membrane structures', *Communications in Nonlinear Science and Numerical Simulation* **19**, 2071–2087.

Kromoser, B. & Kollegger, J. (2015*a*), 'Application areas for pneumatic forming of hardened concrete', *Journal of the International Association for Shell and Spatial Structures* **56**(3), 187–198.

Kromoser, B. & Kollegger, J. (2015*b*), 'Pneumatic forming of hardened concrete - building shells in the 21st century', *Structural Concrete* **16**(2), 161–171.

Kübler, W. (2014), 'Das neue Elefantenhaus im Zoo Zürich', *Bautechnik* **91**(1), 51–57.

Lachauer, L. (2015), Interactive Equilibrium Modelling - A new approach to the computer-aided exploration of structures in architecture, PhD thesis, Zurich.

Lachauer, L. & Block, P. (2014), 'Interactive equilibrium modelling', *International Journal of Space Structures* **29**(1), 25–37.

Lämmler, R. & Wagner, M. (2010), *Ulrich Müther Shell Structures in Mecklenburg-Western Pomerania*, Niggli.

Lamyuktseung, K. (2015), private communication to Veenendaal, D.

Lan, T. T. & Liu, F. (2006), 'Historical review of the developments of spatial structures in China', *Journal of the International Association for Shell and Spatial Structures* **47**, 81–91.

Lavery, C. (2013), 'Spencer Dock Bridge. Casting a fluid shape using liquid stone', *Concrete International* pp. 28–31.

Lee, S. & Hinton, E. (2000*a*), 'Dangers inherited in shells optimized with linear assumptions', *Computers and Structures* **78**, 473–486.

Lee, S.J., B. J. & Hinton, E. (2000*b*), 'Shell topology optimization using the layered artificial material model', *International Journal for Numerical Methods in Engineering* **47**, 843–867.

Lewis, W. J. (1989), 'The efficiency of numerical methods for the analysis of prestressed nets and pin-jointed frame structures', *Computers and Structures* **33**(3), 791–800.

Lewis, W. J. (2003), *Tension structures. Form and Behaviour*, Thomas Telford, London.

Lewis, W. J. (2008), 'Computational form-finding methods for fabric structures', *Proceedings of the ICE - Engineering and Computational Mechanics* **161**(3), 139–149.

Li, J.-J. & Chan, S.-L. (2004), 'An integrated analysis of membrane structures with flexible supporting frames', *Finite Elements in Analysis and Design* **40**, 529–540.

Lienhard, J., Alpermann, H., Gengnagel, C. & Knippers, J. (2013), 'Active bending, a review on structures where bending is used as a self-formation process', *International Journal of Space Structures* **28**(3-4), 187–196.

Lilienthal, G. (1898), 'Decke'. German patent 100,194. Filed September 8, 1897, published December 13, 1898.

Lilienthal, L. (1899), 'Fireproof ceiling'. U.S. patent 619,769. Filed May 17, 1898, published February 21, 1899.

Linkwitz, K. (1972), New methods for the determination of cutting pattern of prestressed cable nets and their application to the Olympic Roofs Munich, *in* Y. Yokoo, ed., 'Proceedings of the 1971 IASS Pacific Symposium Part II on Tension Structures and Space Frames', Architectural Institute of Japan, Tokyo and Kyoto, Japan, pp. 13–26.

Linkwitz, K. (1976), Combined use of computation techniques and models for the process of form finding for prestressed nets, grid shells and membranes, *in* 'Proceedings of Internationalen Symposium Weitgespannte Flächentragwerke'.

Linkwitz, K. (1999), 'Formfinding by the "direct approach" and pertinent strategies for the conceptual design of prestressed and hanging structures', *International Journal of Space Structures* **14**(2), 73–87.

Linkwitz, K., Gründig, L., Hangleiter, U. & Bahndorf, J. (1984), 'SFB 64. Weitgespannte Flächentragwerke. Mathematisch-numerische Methoden der Netzberechnung Abschlußberich Teilprojekt F2'. In German.

Linkwitz, K. & Schek, H.-J. (1971), 'Einige Bemerkungen zur Berechnung von vorgespannten Seilnetzkonstruktionen', *Ingenieur-Archiv* **40**, 145–158. In German.

Linkwitz, K., Schek, H.-J. & Gründig, L. (1974), 'Die Gleichgewichtsberechnung von Seilnetzen unter Zusatzbedingungen', *Ingenieur-Archiv* **43**, 183–192. In German.

Linkwitz, K. & Veenendaal, D. (2014), Nonlinear force density method - constraints on force and geometry, *in* S. Adriaenssens, P. Block, D. Veenendaal & C. Williams, eds, 'Shell Structures for Architecture: Form Finding and Optimization', Routledge, London, pp. 142–155.

Liudkovsky, I. G. (1962), On the choice of the optimum types of suspended roofs and of their bearing contours, *in* N. Esquillan & Y. Saillard, eds, 'Hanging Roofs. Proceedings of the IASS Colloquium on Hanging Roofs, Continuous Metallic Shell Roofs and Superficial Lattice Roofs', North-Holland Publishing Company, Paris, France, pp. 83–92.

Lobo Fialho, J. (1956), Design of shells based on the experimental determination of funicular structures, *in* 'Fifth Congress. International Association for Bridge and Structural Engineering. Final Report.', Vol. 5, Lisbon, Porto, Portugal, pp. 259–280.

Lobo Fialho, J. F. (1966), *Barragens Casca. Contribuição para o seu cálculo elástico*, Fundação Calouste Gulbenkian, Lisboa, Portugal. In Portuguese.

Lobo Fialho, J. & Rodrigues, P. (1965*a*), 'Barragem de Vilar no Rio Távora. Solução abóbada (H.E.P.) (Part 1 of 3)', *Electricidade: Revista Técnica* (33), 6–15. In Portuguese.

Lobo Fialho, J. & Rodrigues, P. (1965*b*), 'barragem de Vilar no Rio Távora. Solução abóbada (H.E.P.) (Part 2 of 3)', *Electricidade: Revista Técnica* (34), 95–102. In Portuguese.

Lobo Fialho, J. & Rodrigues, P. (1965*c*), 'barragem de Vilar no Rio Távora. Solução abóbada (H.E.P.) (Part 3 of 3)', *Electricidade: Revista Técnica* (35), 174–177. In Portuguese.

Máca, P., Zatloukal, J. & Konvalinka, P. (2012), Development of ultra high performance fiber reinforced concrete mixture, *in* 'IEEE Symposium on Business, Engineering and Industrial Applications'.

Maddex, D. (2007), *Dow Alden B. Midwestern modern*, Archetype Press.

Malerba, P., Patelli, M. & Quagliaroli, M. (2012), 'An extended force density method for the form finding of cable systems with new forms', *Structural Engineering and Mechanics* **42**(2), 191–210.

Mallory, K. & Ottar, A. (1973), *Architecture of Aggression. A history of military architecture in North West Europe 1900-1945*, Architectural Press.

Markillie, P. (2012), 'The third industrial revolution'.
URL: *http://www.economist.com/node/21553017*

Marrey, B. (1992), *Nicolas Esquillan, un ingénieur d'enterprise*, Picard. In French.

Marsh III, J. H. (1962), Thin shell structures using a lift-shape erection process, *in* 'New Building Research. Spring 1961', number 986, National Academy of Sciences-Research Council, pp. 43–48.

Marsh III, J. H. (1964), Construction of thin shell structures by the "Lift-Shape" process, *in* 'Proceedings, World Conference on Shell Structures', San Francisco, CA, US, pp. 447–52.

Mathur, U. (2015), An innovative formwork and construction technique for building thin-shell RCC structures, *in* 'Proceedings of the International Association of Shells and Spatial Structures', Amsterdam.

Maurin, B. & Motro, R. (1997), 'Investigation of minimal forms with density methods', *Journal of the International Association for Shell and Spatial Structures* **38**(125), 143–154.

Maurin, B. & Motro, R. (1998), 'The surface stress density method as a form-finding tool for tensile membranes', *Engineering Structures* **20**(8), 712–719.

Maurin, B. & Motro, R. (2001), 'Investigation of minimal forms with conjugate gradient method', *International Journal of Solids and Structures* **38**, 2387–2399.

Maxwell, I. & Pigram, D. (2014), Gaudi's puffy jacket: A method for the implementation of fabric slump casting in the construction of thin-wall funicular vault structures, *in* 'Advances in Architectural Geometry', pp. 61–77.

May, R. (2015), Shell sellers, the international dissemination of the Zeiss-Dywidag system, 1923-1939, *in* '5th International Congress on Construction History', Chicago, pp. 557–564.

Medwadowski, S. (2004), 'Buckling of concrete shells: an overview', *Journal of the International Association for Shell and Spatial Structures* **45**(1), 51–63.

Medwadowski, S. J. (1998), Concrete thin shell roofs at the turn of the millenium [sic], *in* 'Current and emerging technologies of shell and spatial structures: proceedings of the colloquium held on 28-30 April 1997 in Madrid', IASS, pp. 9–22.

Medwadowski, S. J., Haas, A. M., Khaidukov, G. K., Kollár, L., Kupfer, H., Paduart, A., Popov, E. P., del Pozo, F., Rühle, H., Samartin Q., A. & Scordelis, A. C. (1979), 'Recommendations for reinforced concrete shells and folded plates'. Working group nr. 5.

Meek, J. (1991), *Computer Methods in Structural Analysis*, Chapman & Hall, London.

Meek, J. L. & Xia, X. (1999), 'Computer shape finding of form structures', *International Journal of Space Structures* **14**(1), 35–55.

Méndez Echenagucia, T. & Block, P. (2015), Acoustic optimization of funicular shells, *in* 'Proceedings of the International Association for Shell and Spatial Structures (IASS) Symposium 2015', Amsterdam.

Meyer, C. & Sheer, M. (2005), 'Do concrete shells deserve another look? Industry professionals give mixed opinions', *Concrete International* pp. 43–50.

Michalatos, P. & Kaijima, S. (2014), Eigenshells: structural patterns on modal forms, *in* S. Adriaenssens, P. Block, D. Veenendaal & C. Williams, eds, 'Shell Structures for Architecture: Form Finding and Optimization', Routledge, London, pp. 194–209.

Miki, M. & Kawaguchi, K. (2010), 'Extended force density method for form-finding of tension structures', *Journal of the International Association for Shell and Spatial Structures* **51**(4), 291–303.

Miki, M. & Kawaguchi, K. (2011), Direct minimization approaches on static problems of membranes, *in* 'Proceedings of International Conference on Textile Composites and Inflatable Structures, Structural Membranes 2011', Barcelona, Spain.

Mollaert, M. & Hebbelinck, S. (2002), Adaptent: A generating system for cable net structures, *in* 'Fifth International Conference on Space Structures', Guildford, Surrey, UK.

Moncrief, E. & Topping, B. (1990), 'Computer methods for the generation of membrane cutting patterns', *Computers & Structures* **37**(4), 441–450.

Moore, P. & Riley, M. (2012), *International Construction Cost Report*, EC Harris Research 2012.

Motosugi, S. & Mizunuma, Y. (2011), Detail Practice. Project examples of digital processes. Taichung Metropolitan Opera House in Taiwan, *in* M. Hauschild & R. Karzel, eds, 'Digital Processes. Planning, Designing, Production', Birkhauser, pp. 92–103.

Motro, R. (1984), Forms and forces in tensegrity systems, *in* 'Proceedings of the Third International Conference on Space Structures', pp. 283–288.

Motro, R. (2007), 'Robert Le Ricolais (1894-1977) "Father of spatial structures"', *International Journal of Space Structures* **22**(4), 233–238.

Musmeci, S. (1977), 'Ponte sul Basento a Potenza', *L'Industria Italiana del Cemento* (2), 77–98. In Italian.

Muttoni, A., Lurati, F. & Fernández Ruiz, M. (2013), 'Concrete shells - towards efficient structures: construction of an ellipsoidal concrete shell in Switzerland', *Structural Concrete* **14**(1), 43–50.

Naaman, A. E. (2000), *Ferrocement & Laminated Cementitious Composites*, Techno Press 3000, Ann Arbor, Michigan, US.

Naidu, M. (1963), 'Research in materials and construction', *Journal of the Institution of Engineers (India): Civil Engineering Division* **44**, 211.

NASA (2015), 'Mars ice house', website. Accessed August 22, 2016.
URL: *http://www.marsicehouse.com/*

Neff, W. (1942), 'Building construction'. U.S. patent 2,270,229. Filed April 3, 1941, and issued January 20, 1942.

Ngrams, G. (2016), 'Google books ngram viewer', website. Accessed June 18, 2016.
URL: *https://books.google.com/ngrams*

Nocedal, J. & Wright, S. J. (2000), *Numerical Optimization*, Springer.

Nouri-Baranger, T. (2002), 'Form finding method of tensile structures. Revised geometric stiffness method', *Journal of the International Association for Shell and Spatial Structures* **43**(138), 13–21.

Nouri-Baranger, T. (2004), 'Computational methods for tension-loaded structures', *Archives of Computational Methods in Engineering* **11**(2), 143–186.

Novikov, P., Jokic, S., Fraguada, L. E., Laarman, J. & Markopoulou, A. (2014), Anti-gravity additive manufacturing, *in* F. Gramazio, M. Kohler & S. Langenberg, eds, 'Fabricate2014', gta Verlag, Zurich, Switzerland.

Oberdick, W. (1965*a*), Application of minimum structure to cellular plastics, *in* 'Transactions and Journal of the Plastics Institute. Conference on Plastics in Building Structures', Pergamon Press, London, UK, pp. 277–288.

Oberdick, W. (1965*b*), 'Application of minimum structure to rigid cellular plastic structures', *Journal of Cellular Plastics* **1**(4), 503–513.

Ochsendorf, J. (2013), *Guastavino Vaulting: The Art of Structural Tile*, Princeton Architectural Press.

Oelkuch, S. W. & Dieringer, F. (2011), Formfindungsanalyse von Membrantragwerken mit der Updated Reference Strategy und Elementen mit quadratischen Ansatzfunktionen, Master's thesis, Technischen Universität München, Germany. In German.

Oesterle, S., Vansteenkiste, A. & Mirjan, A. (2012), Zero waste free-form formwork, *in* J. Orr et al., eds, 'Proceedings of the 2nd international conference on flexible formwork', Bath, UK, pp. 258–267.

Ohyama, H. & Kawamata, S. (1972), A problem of surface design for prestressed cable nets, *in* Y. Yokoo, ed., 'Proceedings of the 1971 IASS Pacific Symposium Part II on Tension Structures and Space Frames', number 1-7, Architectural Institute of Japan, Tokyo and Kyoto, Japan, pp. 103–115.

Ortega, N. & Robles, S. (2003), 'The design of hyperbolic paraboloids on the basis of their mechanical behaviour', *Thin-Walled Structures* **41**, 769Ű784.

Otto, F. (1954), *Das Hängende Dach. Gestalt und Struktur*, Verlag der Kunst Dresden, Germany. In German.

Otto, F. (1964), Shells and membranes, *in* 'Proceedings, World Conference on Shell Structures', San Francisco, CA, US, pp. 3–26. Washington D.C., National Academy of Sciences-National Research Council Publication 1187-453.

Otto, F. & Stromeyer, P. (1962), 'Pneumatic structures', *Journal of the American Institute of Architects (AIA)* pp. 101–111.

Otto, F., Trostel, R. & Schleyer, F.-K. (1973), *Tensile Structures. Volumes 1 and 2*, MIT Press. Fourth printing, March 1979.

Papadrakakis, M. (1981), 'A method for the automatic evaluation of the dynamic relaxation parameters', *Computer Methods in Applied Mechanics and Engineering* (25), 35–48.

Parameswaran, V. (2002), 'G. S. Ramaswamy (obituary)', *Current Science* **83**(3).
URL: *http://www.iisc.ernet.in/currsci/aug102002/330.pdf*

Parker, S. A. (1971), 'Concrete building'. U.S. patent 3,619,959. Filed July 7, 1968, and issued November 16, 1971.

Pauletti, R, M. (2006), An extension of the force density procedure to membrane structures, *in* 'Proceedings of IASS Symposium/APCS Conference', Beijing, China.

Pauletti, R. M. O. & Pimenta, P. M. (2008), 'The natural force density method for the shape finding of taut structures', *Computer Methods in Applied Mechanics and Engineering* **197**, 4419–4428.

Pedreschi, R. (2013), Fabric formed concrete structures and architectural elements, *in* Cruz, ed., 'Structures and Architecture: Concepts, Applications and Challenges', Taylor & Francis Group, London, pp. 896–903.

Pellegrino, S. & Calladine, C. R. (1986), 'Matrix analysis of statically and kinematically indeterminate frameworks', *International Journal of Solid and Structures* **22**(4), 409–428.

Philipp, B., Breitenberger, M., Wüchner, R. & Bletzinger, K.-U. (2014), Design of architectural membranes with isogeometric elements, *in* '11th World Congress on Computational Mechanics'.

Pizzetti, G. (1958), 'Some considerations of the past and the future of reinforced concrete', *Journal of the Boston Society of Civil Engineers* **45**(2), 151–160.

Pronk, A., Borgart, A., Hijl, J. & Pluijmen, R. (2014*a*), The calculation and construction of a 30 meter span ice dome, *in* 'Proceedings of the IASS-SLTE Symposium 2014', Brasilia, Brazil.

Pronk, A., Bullens, T. & Folmer, T. (2007*a*), A feasable [sic] way to make freeform shell structures, *in* 'Proceedings of the IASS Symposium 2007', Venice, Italy.

Pronk, A. & Dominicus, M. (2011), 85 ways to make a membrane mould, *in* 'Proceedings of International Conference on Textile Composites and Inflatable Structures, Structural Membranes 2011', Barcelona, Spain.

Pronk, A. & Dominicus, M. (2012), 'Philips-paviljoen'.

Pronk, A., Dominicus, M. & Ten Hoope, D. (2011), The production of free formed concrete elements in a flexible mould, *in* 'Proceedings of the IASS Symposium 2010', Shanghai, China.

Pronk, A., Houtman, R. & Afink, M. (2007*b*), The reconstruction of the Philips Pavilion volume 1, *in* 'Sources of Architectural Form. Theory and Practice', Kuwait City, Kuwait.

Pronk, A., Houtman, R., Hanselaar, H. & Borgart, A. (2003), A fluid pavillion [sic] by rigidizing a membrane, *in* 'Proceedings of International Conference on Textile Composites and Inflatable Structures, Structural Membranes 2005', Barcelona, Spain.

Pronk, A. & Osinga, D. (2005), Making igloos in the summer, *in* 'Proceedings of International Conference on Textile Composites and Inflatable Structures, Structural Membranes 2005', pp. 218–115.

Pronk, A., Vasiliev, N., Janssen, F. & Houben, R. (2014*b*), Spraying pykrete, *in* 'Proceedings of the IASS-SLTE Symposium 2014', Brasilia, Brazil.

Pronk, A., Verberne, T., Kern, J. & Belis, J. (2015), The calculation and construction of the highest ice dome - the Sagrada Familia in ice, *in* 'Proceedings of the International Society of Flexible Formwork (ISOFF) Symposium', Amsterdam, Netherlands.

Prouvost, F. (1978), 'Construction of houses or similar buildings by means of an inflatable structure'. U.S. patent 4,094,109. Filed February 22, 1977, and issued June 13, 1978.

Pugnale, A., Méndez Echenagucia, T. & Sassone, M. (2014), Computational morphogenesis. design of freeform surfaces., *in* S. Adriaenssens, P. Block, D. Veenendaal & C. Williams, eds, 'Shell Structures for Architecture. Form finding and optimization', Routledge, pp. 224–236.

Purnell, P. (2013), 'The carbon footprint of reinforced concrete', *Advances in cement research* **25**(6), 362–368.

Rabasco, P. (2004), La vivienda mínima en Rafael de La Hoz. Ejemplos extremos, *in* 'IV Congreso Internacional de Arquitectura Contemporánea en España. Modelos alemanes e italianos para España en los años de posteguerra', Escuela Técnica Superior de la Universidad de Navarra, Pamplone, pp. 215–24. In Spanish.

Rabasco, P. (2011), 'El sistema Ctesiphonte. Evolución de la estructura catenaria', *Informes de la Construcción* **63**(522), 43–5. In Spanish.

Ráfols, J. F. (1929), *Gaudí*, Canosa, Barcelona, Spain. In Spanish.

Ramage, M. H., Ochsendorf, J. A. & Rich, P. (2010), 'Sustainable shells: New African vaults built with soil-cement tiles', *Journal of the International Association of Shell and Spatial Structures* **51**(4), 255–261.

Ramaswamy, G. (1963), *Design and Construction of Concrete Shell Roofs*, first edn, McGraw-Hill Book Co. Inc., New York, NY, US.

Ramaswamy, G. (1968), 'Shell research in India', *Bulletin of the International Association for Shell Structures* (36), 51–54.

Ramaswamy, G. (1986), Innovative applications of funicular shells., *in* 'Shells, Membranes and Space Frames. Proceedings of the IASS Symposium', Vol. 1, Osaka, Japan, pp. 313–320.

Ramaswamy, G. & Chetty, S. (1960), 'A new form of doubly curved shell for roofs and floors', *Bulletin of the International Association for Shell Structures* (1), 49–56.

Ramaswamy, G., Chetty, S. & Bhargava, R. (1958), 'Casting and testing a shell roof unit', *Civil Engineering and Public Works Review* **53**(628), 1155–1157.

Ramaswamy, G. S. & Chetty, S. M. K. (1958), 'A new process for the manufacture of precast doubly-curved shell elements for roofs, floors and panel walls'. Indian patent 61,645. Filed September 5, 1957, specified November 16, 1957, accepted June 14, 1958.

Ramm, E. (1987), 'Ultimate load and stability analysis of reinforced concrete shells', *IABSE reports* **54**, 145–159.

Ramm, E., Bletzinger, K.-U. & Reitinger, R. (1993), 'Shape optimization of shell structures', *Bulletin of the International Association for Shell and Spatial Structures* **34**(112), 103–121.

Ramm, E. & Mehlhorn, G. (1991), 'On shape finding methods and ultimate load analyses of reinforced concrete shells', *Engineering Structures* **13**, 178–198.

Ramm, E. & Schunk, E. (2002), *Heinz Isler. Schalen*, vfd Hochschulverlag, Zurich.

Ramm, E. & Stegmüller, H. (1982), The displacement finite element method in nonlinear buckling analysis of shells, *in* E. Ramm, ed., 'Buckling of Shells. Proceedings of a State-of-the-Art Colloquium', Springer, Universität Stuttgart, Germany, pp. 201–235.

Randall, F. & Smith, A. (1991), 'Thin-shell concrete dome built economically with rotating forming and shoring system. Twenty-four-segment dome uses only six forms', *Concrete Construction* .

Rao, S. S. (2004), *The Finite Element Method in Engineering*, 4th edn, Elsevier Science & Technology Books.

Rao, S. S. (2009), *Engineering Optimization. Theory and Practice*, 4th edn, John Wiley & Sons.

Raphael, W., Faddoul, R., Feghaly, R. & Chateauneuf, A. (2012*a*), 'Analysis of Roissy Airport Terminal 2E collapse using deterministic and reliability assessments', *Engineering Failure Analysis* (20), 1–8.

Raphael, W., Faddoul, R., Geara, F. & Chateauneuf, A. (2012*b*), 'Improvements to the Eurocode 2 shrinkage model for concrete using a large experimental database', *Structural Concrete* **13**(3), 174–181.

Redjvani, A. (1999), 'Flexible formwork assembly'. U.S. patent 5,857,293. Filed November 4, 1994, and issued January 12, 1999.

Redjvani, A. & Wheen, R. (1995), 'Flexible formwork systems', *Concrete in Australia* **21**, 21–23.

Reitinger, R. & Ramm, E. (1995), 'Buckling and imperfection sensitivity in the optimization of shell structures', *Thin-Walled Structures* **23**, 159–177.

Rippmann, M. (2016), Funicular Shell Design: Geometric Approaches to Form Finding and Fabrication of Discrete Funicular Structures, PhD thesis, Zurich.

Rippmann, M. & Block, P. (2013), Funicular funnel shells, *in* C. Gengnagel, A. Kilian, J. Nembrini & F. Scheurer, eds, 'Proceedings of the Design Modeling Symposium Berlin 2013', Berlin, Germany, pp. 75–89.

Rippmann, M., Van Mele, T., Popescu, M., Augustynowicz, E., Méndez Echenagucia, T., Calvo Barentin, C., Frick, U. & Block, P. (2016), The Armadillo Vault: Computational design and digital fabrication of a freeform stone shell, *in* 'Advances in Architectural Geometry', pp. 344–363.

Roorda, J. (1967), 'Some thoughts on the Southwell plot', *Journal of the Engineering Mechanics Division. Proceedings of the American Society of Civil Engineers* **EM 6**, 37–48.

Rubio, J. G. (2004), 'Estación de autobuses, Casar (Cáceres). Bus station, Casar de Cáceres (cáceres)', *AV Monografías* **105-106**, 64–67. In Spanish.

Rust, R., Gramazio, F. & Kohler, M. (2016), Force adaptive hot-wire cutting. integrated design, simulation and fabrication of double-curved surface geometries, *in* 'Advances in Architectural Geometry (AAG)', Zurich, Switzerland.

Saad, Y. (2003), *Iterative Methods for Sparse Linear Systems*, Society for Industrial and Applied Mathematics.

Saether, K. (1961), 'The structural membrane', *Journal of the American Concrete Insitute* **32**(7), 827–850. Title No. 57-41.

Saether, K. (1995), Structural membrane approach for the design of shells, *in* G. C. Giuliani, ed., 'Proceedings of the IASS International Symposium 1995. Spatial Structures: Heritage, Present and Future', Vol. 1, Milan, Italy, pp. 409–416.

Safire, W. (2002), 'The way we live now: 12-01-02: On language; defenestration'. **URL:** *http://www.nytimes.com/2002/12/01/magazine/the-way-we-live-now-12-01-02-on-language-defenestration.html*

Sánchez, J., Serna, M. Á. & Paz, M. (2007), 'A multi-step force-density method and surface-fitting approach for the preliminary shape design of tensile structures', *Engineering Structures* **29**, 1966–1976.

Sasaki, M. (2005), *Flux Structure*, Toto Publishers, Tokyo.

Sasaki, M. (2014), Structural design of free-curved RC shells. An overview of built works, *in* S. Adriaenssens, P. Block, D. Veenendaal & C. Williams, eds, 'Shell Structures for Architecture. Form finding and optimization', Routledge, pp. 258–270.

Schek, H.-J. (1974), 'The force density method for form finding and computation of general networks', *Computer Methods in Applied Mechanics and Engineering* **3**(1), 115–134.

Schek, H.-J. & Eggensperger, R. (1977), 'Least-Squares-Lösungen und Dämpfung bei unterbestimmten nichtlinearen Gleichungssystemen', *Computing* **19**, 150–170. In Spanish.

Schipper, H. (2015), Double-curved precast concrete elements. Research into technical viability of the flexible mould method, PhD thesis, Delft University of Technology, Netherlands.

Schipper, H. & Grünewald, S. (2014), Efficient material use through smart flexible formwork method, *in* O. Wallevik, D. Bager, B. Hjartarson & J. Wallevik, eds, 'Environmentally Friendly Concrete Eco-Crete - Proceedings of the International Symposium on Eco-Crete, Reykjavik, Iceland 13.-15. August', pp. 61–68.

Schlaich, J. (1985), 'Do concrete shells have a future?', *Bulletin of the International Association of Shell* **26-3**(89), 39–46.

Schlaich, J. (2013), private communication to Veenendaal, D.

Schlaich, J. & Sobek, W. (1986), 'Suitable shell shapes', *Concrete International* pp. 41–45.

Schlaich, M., Burkhardt, U., Irisarri, L. & Goñi, J. (2009), Palacio de Comunicaciones - a single layer glass grid shell over the courtyard of the future town hall of Madrid, *in* A. Domingo & C. Lazaro, eds, 'Proceedings of the International Association of Shells and Spatial Structures', Valencia, Spain.

Schmidt, H. (2005), 'Von der Steinkuppel zur Zeiss-Dywidag-Schalenbauweise', *Beton- und Stahlbetonbau* **100**(1), 79–92. In German.

Schneider, H. (2011), 'Entwicklung von Demonstrator-Bauteilen aus textilbewehrtem Beton. Allgemeine Angaben zum beendeten Teilprojekt E4', pp. 391–415.

Schober, H. (2015), *Transparent Shells. Form Topology Structure*, Ernst & Sohn.

Scholzen, A. (2014), Flächige Tragstrukturen aus textilbewehrtem Beton: Experimentelle und numerische Charakterisierung des Tragverhaltens, Bemessung und Herstellungsmethodik, PhD thesis, Rheinisch-Westfälischen Technischen Hochschule (RWTH) Aachen, Germany. In German.

Seaton, A. (2007), 'Ireland's Cliffs of Moher Visitor Centre', *Concrete Engineering International* pp. 24–25.

Seidel, M. (2009), *Tensile Surface Structures. A Practical Guide to Cable and Membrane Construction*, Ernst & Sohn.

SIA 260:2003 (2004), 'Basis of structural design'.

SIA 261:2003 (2003), 'Actions on structures'.

SIA 262:2003 (2004), 'Concrete structures'.

Siev, A. (1961), Stability of Prestressed Suspended Roofs, PhD thesis, Israel Institute of Technology, Haifa.

Siev, A. (1963), 'A general analysis of prestressed nets', *IABSE publications* **23**, 283–292.

Singer, P. (1995), Die Berechnung von Minimalflächen, Seifenblasen, Membrane und Pneus aus geodätischer Sicht, PhD thesis, University of Stuttgart, Germany. Recently translated by Ströbel et al. (2016). In German.

Sobek, W. (1987), Auf Pneumatisch Gestützten Schalungen Hergestellte Betonschalen, PhD thesis, Universität Stuttgart, Stuttgart, Germany. In German.

Søndergaard, A., Feringa, J., Nørbjerg, T., Steenstrup, K., Brander, D., Graversen, J., Markvorsen, S., Bærentzen, A., Petkov, K., Hattel, J., Clausen, K., Jensen, K., Knudsen, L. & Kortbek, J. (2014), Robotic hot-blade cutting. An industrial approach to cost-effective production of double curved concrete structures, *in* D. Reinhardt et al., eds, 'Robotic Fabrication in Architecture, Art and Design', Springer International Publishing, pp. 151–164.

Songel, J. M. (2010), *A Conversation with Frei Otto*, Princeton Architectural Press, New York, NY, US.

South, D. B. (1990), 'Economics and the thin shell dome', *Concrete International* **12**(8), 24–29.

South, D. & South, B. (1979), 'Building structure and method of making same'. U.S. patent 4,155,967. Filed March 7, 1977, and issued May 22, 1979.

Southwell, R. (1932), 'On the Analysis of Experimental Observations in Problems of Elastic Stability', *Proceedings of The Royal Society A* pp. 601–161.

Spillers, W., Schlogel, M. & Pilla, D. (1992), 'A simple membrane finite element', *Computers and Structures* **45**(1), 181–183.

Stepler, R. (1980), 'Hypar structures. Light, easy to build, cheap — and permanent', *Popular Science* **216**(2), 73,74–77,168.

Ströbel, D. (1995), Die Anwendung der Ausgleichungsrechnung auf elastomechanische Systeme, PhD thesis, University of Stuttgart, Germany. In German.

Ströbel, D., Singer, P. & Holl, J. (2016), 'Analytical formfinding', *International Journal of Space Structures* **31**(1), 52–61.

Tabarrok, B. & Qin, Z. (1992), 'Nonlinear analysis of tension structures', *Computers and Structures* **45**(5/6), 973–984.

Tam, K.-M. M., Coleman, J. R., Fine, N. W. & Mueller, C. T. (2015), Stress line additive manufacturing (SLAM) for 2.5-D shells, *in* 'Proceedings of the International Association of Shells and Spatial Structures', Amsterdam.

Tamai, H. (2013), Advanced application of the force density method in multidisciplinary design practice by incorporating with optimization using analytical derivatives, *in* J. Obrębski & R. Tarczewski, eds, 'Proceedings of the International Association for Shell and Spatial Structures', Wroclaw, Poland.

Tamai, H. (2015), 6.3 Form-finding based on dynamic relaxation and the force density method, *in* 'Transparent Shells. Form Topology Structure', Ernst & Sohn, pp. 168–174.

Tan, K. Y. (1989), The Computer Design of Tensile Membrane Structures, PhD thesis, University of Queensland, Brisbane, Australia.

Tang, G. (2012), Deployable gridshells and their application as temporary, reuseable and flexible concrete formwork, *in* J. Orr et al., eds, 'Proceedings of the 2nd international conference on flexible formwork', Bath, UK, pp. 324–333.

Tang, G. (2015), Deployable gridshells as formwork for concrete shells, *in* 'Proceedings of the International Society of Flexible Formwork (ISOFF) Symposium', Amsterdam, Netherlands.

Tappe, W. (1818-1823), *Darstellung einer neuen äußerst wenig Holz erfordernden und höchst feuersicheren Bauart*, Essen and Duisberg, Germany. In German.

Tibert, A. G. & Pellegrino, S. (2003), 'Review of form-finding methods for tensegrity structures', *International Journal of Space Structures* **18**, 209–223.

Tomás, A. & Martí, P. (2010*a*), 'Optimality of Candela's concrete shells. A study of his posthumous design', *Journal of the International Association for Shell and Spatial Structures* **51**(1), 67–77.

Tomás, A. & Martí, P. (2010*b*), 'Shape and size optimisation of concrete shells', *Engineering Structures* **32**, 1650–1658.

Tomás, A. & Tovar, J. P. (2012), 'The influence of initial geometric imperfections on the buckling load of single and double curvature concrete shells', *Computers and Structures* **96-97**, 34–35.

Tomlow, J. (1993), 'Die Kuppel des Gießhauses der Firma Henschel in Kassel (1837). eine frühe Anwendung des Entwurfsverfahrens mit Hängemodellen', *Architectura. Zeitschrift für Geschichte der Baukunst* **23**, 151–172. In German.

Tomlow, J. (2002), The spirit of calculation in the architectural work of Antoni Gaudí, *in* 'Gaudí 2002 Miscelánea. Edición conmemorativo del Año Internacional Gaudí', Instituto de Cultura de Barcelona, pp. 176–199.

Tomlow, J. (2011), 'Gaudí's reluctant attitude towards the inverted catenary', *Engineering History and Heritage* **164**(EH4), 219–233.

Tomlow, J., Graefe, R., Otto, F. & Szeemann, H. (1989*a*), *IL 25. Experiments. Form Force Mass 5*, Institute for Lightweight Structures (IL), 34, Stuttgart. In German and English.

Tomlow, J., Graefe, R., Otto, F. & Szeemann, H. (1989*b*), *IL 34. The Model*, Institute for Lightweight Structures (IL), 34, Stuttgart.

Torsing, R., Bakker, J., Jansma, R. & Bhattacharya, A. (2015), 'Re-inventing mixed fabric and cable-net formed morphology in practice', *Next Generation Building* **2**(1), 91–110.

Torsing, R., Bakker, J., Jansma, R. & Veenendaal, D. (2012), Large-scale designs for mixed fabric and cable-net formed structures, *in* J. Orr et al., eds, 'Proceedings of the 2nd international conference on flexible formwork', Bath, UK, pp. 346–355.

Trautz, M. (1998), Zur Entwicklung von Form und Struktur historischer Gewölbe aus der Sicht der Statik, PhD thesis, Universität Stuttgart, Germany. In German.

Turner, L. (1966), 'Method of molding a building structure by spraying a foamed plastic on the inside of an inflated form'. U.S. patent 3,277,219. Filed March 27, 1961, and issued October 4, 1966.

Tysmans, T., Adriaenssens, S. & Wastiels, J. (2011), 'Form finding methodology for force-modelled anticlastic shells in glass fibre textile reinforced cement composites', *Engineering Structures* **33**, 2603–2611.

UNEP (2013), *Buildings and Climate Change*, UNEP DTIE Sustainable Consumption and Production Branch, 15 Rue de Milan, 75009 Paris, France.

Ungewitter, G. (1867), *Lehrbuch der Gotischen Konstruktionen*, 3rd edn, T.O. Weigen Nachfolger, Leipzig, Germany. In German.

USBLS (2016), 'Producer Price Index (PPI)', website. Accessed March 8, 2016.
URL: *http://www.bls.gov/ppi/data.htm*

Vafai, A., Estekanchi, H. & Javidruzi, M. (2005), 'Experimental study of prefabricated funicular shell units', *Proceedings of the Institution of Civil Engineers. Structures & Buildings.* **158**(SB3), 167–174.

Vafai, A. & Farshad, M. (1979), 'Theoretical and experimental study of prefabricated funicular shell units', *Building and Environment* **14**, 209–216.

Vafai, A., Mofid, M. & Estekanchi, H. E. (1997), 'Experimental study of prefabricated funicular shell units', *Engineering Structures* **19**(9), 748–759.

Van de Straat, R., Hofman, S., Coenders, J. & Paul, J. (2015), Digital technology impacts on the Arnhem Transfer Hall structural design, *in* 'Proceedings of the International Association of Shells and Spatial Structures', Amsterdam.

van Dijk, W., Falger, M. & Sterken, R. (2013), 'Scheepsbouwtechniek OVT. Na uitvoerig onderzoek betonnen dakconstructie en verticale componenten vervangen door staal', *Cement* (2), 34–41. In Dutch.

Van Gelder, A. (1998), 'Approximate simulation of elastic membranes by triangulated spring meshes', *Journal of Graphic Tools* **3**, 21–41.

Van Iterson, F. K. T. & Kuypers, G. (1918), 'Improved construction of cooling towers of reinforced concrete'. British patent 108,863. Applied August 9, 1917, accepted April 11, 1918.

Van Mele, T. & Block, P. (2010), A novel form finding method for fabric formwork for concrete shells, *in* 'Proceedings of the International Association for Shell and Spatial Structures Symposium 2010', Shanghai, China.

Van Mele, T. & Block, P. (2011), 'Novel form finding method for fabric formwork for concrete shells', *Journal of the International Association of Shell and Spatial Structures* **52**(4), 217–224.

Van Mele, T., De Laet, L., Veenendaal, D., Mollaert, M. & Block, P. (2013), 'Shaping tension structures by actively bent linear elements', *International Journal of Space Structures* **28**(3), 127–135.

Van Mele, T., Panozzo, D., Sorkine-Hornung, O. & Block, P. (2014), Best-fit thrust network analysis - rationalization of freeform meshes, Routledge, London, pp. 156–168.

Vandenbergh & Partners, Ltd., m. d. (1952), private communication to Messrs. Barchild Constructions Ltd.

Veenendaal, D. (2016), The history of fabric formwork, *in* M. West, ed., 'The Fabric Formwork Book. Methods for Building New Architectural & Structural Forms In Concrete', Routledge, London.

Veenendaal, D., Bakker, J. & Block, P. (2015), Structural design of the cable-net and fabric formed, ferrocement sandwich shell roof of NEST HiLo, *in* 'Proceedings of the International Association for Shell and Spatial Structures (IASS) Symposium', Amsterdam.

Veenendaal, D., Bakker, J. & Block, P. (2017), 'Structural design of the flexibly formed, mesh-reinforced sandwich shell roof of NEST HiLo', *Journal of the International Association of Shells and Spatial Structures* **58**(1), 23–38.

Veenendaal, D., Bezbradica, M., Novak, D. & Block, P. (2014), Controlling the geometry and forces of hybrid cable-net and fabric formworks, *in* 'Proceedings of the IASS-SLTE 2014 Symposium', Brasilia, Brazil.

Veenendaal, D. & Block, P. (2011), A framework for comparing form finding methods, *in* 'Proceedings of the International Association of Shells and Spatial Structures', London.

Veenendaal, D. & Block, P. (2012*a*), Computational form finding for fabric formworks: an overview and discussion, *in* J. Orr et al., eds, 'Proceedings of the 2nd international conference on flexible formwork', Bath, UK, pp. 368–378.

Veenendaal, D. & Block, P. (2012*b*), 'An overview and comparison of structural form finding methods for general networks', *International Journal of Solids and Structures* **49**, 3741–3753.

Veenendaal, D. & Block, P. (2014*a*), Comparison of form-finding methods, *in* S. Adriaenssens, P. Block, D. Veenendaal & C. Williams, eds, 'Shell Structures for Architecture: Form Finding and Optimization', Routledge, London.

Veenendaal, D. & Block, P. (2014*b*), 'Design process for a prototype concrete shells using a hybrid cable-net and fabric formwork', *Engineering Structures* **75**, 39–50.

Veenendaal, D. & Block, P. (2015), Design process of prestressed membrane formworks for thin-shell structures, *in* 'Proceedings of the International Association for Shell and Spatial Structures (IASS) Symposium', Amsterdam.

Veenendaal, D. & Block, P. (2018), 'An overview and comparison of structural form finding methods for minimal surfaces', *International Journal of Solids and Structures* . In preparation.

Veenendaal, D., West, M. & Block, P. (2011), 'History and overview of fabric formwork: using fabrics for concrete casting', *Structural Concrete - Journal of the fib* **12**(3), 164–177.

Verbeek, J. (2015), private communication to Veenendaal, D.

Verhaegh, R. (2010), Free forms in concrete. The fabrication of free-form concrete segments using fabric formwork, Master's thesis, Eindhoven University of Technology, Netherlands.

Vitruvius, P. M. (1914), 'The ten books on architecture'. Accessed September 7th, 2010. **URL:** *http://www.gutenberg.org/files/20239/20239-h/29239-h.htm*

Vogdt, F. & Djahani, M. (2000), 'Kostensenkung durch experimentellen Tragfähigkeitsnachweis', (10). Informationsblätter IEMB. In German.

Wakefield, D. (1999), 'Engineering analysis of tension structures: theory and practice', *Engineering Structures* **21**, 680–690.

Waling, J. & Greszczuk, L. (1960), Experiments with thin-shell structural models, *in* 'Proceedings, Annual Meeting, American Concrete Institute', Vol. 57, pp. 413–431.

Waling, J., Ziegler, E. & Kemmer, H. (1964), Hy-par shell construction by offset wire method, *in* 'Proceedings, World Conference on Shell Structures', San Francisco, CA, US, pp. 453–62. Washington D.C., National Academy of Sciences-National Research Council Publication 1187-453.

Walker, D. & Addis, B. (2005), *Happold. The Confidence to Build*, 2nd edn, Taylor & Francis.

Waller, J. d. W. (1932), 'Improvements in and relating to floors, roofs, walls and the like of cement, concrete and the like and method of manufacture thereof'. British patent 382,610. Filed July 15, 1931, specified April 15, 1932, accepted October 17, 1932.

Waller, J. d. W. (1934), 'Method of building with cementitious material applied to vegetable fabrics'. U.S. patent 1,955,716. Filed March 9, 1932, and issued April 17, 1934.

Waller, J. d. W. (1952*a*), 'Method of forming reinforced concrete arched structures'. U.S. patent 2,705,826. Filed November 15, 1950, and issued April 12, 1955.

Waller, J. d. W. (1952*b*), 'Method of molding in situ concrete arched structures'. U.S. patent 2,616,149. Filed December 11, 1947, and issued November 4, 1952.

Waller, J. d. W. (1953), 'Go-downs and transit sheds. A Ctesiphon system of construction', *The Dock and Harbour Authority* pp. 181–184.

Waller, J. H. d. W. W. & Aston, A. C. (1953), Corrugated concrete shell roofs, *in* 'Proceedings. The Institution of Civil Engineers. Part II', Vol. 2, pp. 153–182. Structural and Building Engineering Division Meeting. Structural Paper No. 34.

Waller, R. (1705), *The posthumous works of Robert Hooke containing his Cutlerian lectures and other discourses*, Robert Waller, London.

Wallisser, T. (2009), Other geometries in architecture: bubbles, knots and minimal surfaces, *in* M. Emmer & A. Quarteroni, eds, 'MATHKNOW', Springer.

Weingarten, V., Seide, P. & Peterson, J. (1968), 'Buckling of Thin-Walled Circular Cylinders. NASA Space Vehicle Design Criteria (Structures). NASA SP-8007'.

Weisstein, E. W. (2016), 'Hyperbolic paraboloid'. Accessed May 19th, 2016.
URL: *http://mathworld.wolfram.com/HyperbolicParaboloid.html*

West, M. (2004), 'Fabric-Formed Concrete Columns. Casa Dent showcases the capabilities of this unique formwork', *Concrete International* **26**(6), 42–45.

West, M. (2006), 'Flexible fabric molds for precast trusses. Flexible Gewebeschalungen für Fertigteilbinder', *BFT International* **72**(10), 46–52. In English and German.

West, M. (2016), *The Fabric Formwork Book. Methods for Building New Architectural & Structural Forms In Concrete*, Routledge, London.

West, M. & Araya, R. (2009), Fabric formwork for concrete structures and architecture, *in* 'Proceedings of the International Conference on Textile Composites and Inflatable Structures, Structural Membranes 2009', Stuttgart, Germany.

West, M., Araya, R., Hashemian, F. & Prakash, N. (2011), Self-forming fabric-formed funicular shells and moulds, *in* 'Proceedings of the IABSE-IASS Symposium 2011', London, England.

Whitney, C. S. (1950), 'Cost of Long-Span Concrete Shell Roofs', *Journal of the American Concrete Insitute* **46**(6), 765–776.

Williams, C. (2001), The analytic and numerical definition of the geometry of the British Museum Great Court roof, *in* M. Burry, S. Datta, A. Dawson & A. Rollo, eds, 'The Proceedings of the third International Mathematics and Design Conference M&D2001: digital, hand, eye, ear, mind', Deakin University, Geelong, Australia, pp. 434–440.

Williams, H. et al. (1958), *Central Building Research Institute. Annual Report 1957-58*, CBRI, Roorkee (U.P.), India.

Williams, J. (1996), 'An Irish genius: J H De W Waller 1884-1968', *Irish Arts Review Yearbook* **12**, 143–46.

Williamson, S. H. & Officer, L. (2016), 'Measuring worth.com', website. Accessed March 16, 2016.
URL: *https://measuringworth.com*

Winn, J. B. (1962), Development of shell structures without formwork, *in* 'New Building Research. Spring 1961', number 986, National Academy of Sciences-Research Council, pp. 87–91.

Wu, M.-T., Chen, Y.-L. & Wang, P.-H. (1988), 'Shape finding of cable system using nonlinear displacement analysis approach', *Journal of the Chinese Institute of Engineers* **11**(6), 583–294.

Xi, F., Davis, S. J., Ciais, P., Crawford-Brown, D., Guan, D., Claus Pade, T. S., Syddall, M., Lv, J., Ji, L., Bing, L., Wang, J., Wei, W., Yang, K.-H., Lagerblad, B., Galan, I., Andrade, C., Zhang, Y. & Liu, Z. (2016), 'Substantial global carbon uptake by cement carbonation', *Nature Geoscience* **9**, 880–883.

Xiang, X.-a., Tian, W., Zhao, Y. & Dong, S.-l. (2010), 'Improved nonlinear force density method accounting for 2-dimensional deformation of membrane element', *Engineering Mechanics* **27**(4), 251–256. In Chinese.

Xu, R., Li, D., Liu, W., Jiang, J., Liao, Y. & Wang, J. (2015), 'Modified nonlinear force density method for form-finding of membrane SAR antenna', *Structural Engineering and Mechanics* **54**(6), 1045–1059.

Yang, C., Shen, Y.-B. & Luo, Y.-Z. (2014), 'An efficient numerical shape analysis for light weight membrane structures', *Journal of Zhejiang University–SCIENCE A* **15**(4), 255–271.

Ye, J., Feng, R.-Q., Zhou, S. & Tian, J. (2012), 'The modified force-density method for form-finding of membrane structures', *International Journal of Steel Structures* **12**(3), 299–310.

Yousef, A. H., Atienza, J. R. & Agüero, A. (2003*a*), Analysis of cable networks by the minimum potential energy method, *in* 'Proceedings of the International Conference on Textile Composites and Inflatable Structures, Structural Membranes 2009', Barcelona, Spain.

Yousef, A. H., Atienza, J. R. & Agüero, A. (2003*b*), Form-finding for cable network, *in* 'Proceedings of the International Conference on Textile Composites and Inflatable Structures, Structural Membranes 2009', Barcelona, Spain.

Yu, Y. & Luo, Y.-z. (2009), 'Finite particle method for kinematically indeterminate bar assemblies', *Journal of Zhejiang University–SCIENCE A* **10**(5), 669–676.

Zeng, X. & Ye, J. (2006), 'The modified force-density method for form-finding of pretensioned cable roofs', *Industrial Construction* **36**(2), 72–74. In Chinese.

Zetlin, L. (1964), 'Engineering features of free-form concrete thin shell for Eastman Kodak Pavilion', *Journal of the American Concrete Insitute* **61**(10), 1249–1259. Title No. 61-62.

Zetlin, L. (1966), Engineering features of free form concrete thin shell for Eastman Kodak Pavilion of 1864-1965 New York World's Fair, *in* 'USSR IASS 1966. Symposium on Problems of Interdependence of Design and Construction of Large-Span Shells for Industrial and Civic Buildings. Theme III Manufacturing and Erection of Reinforced Concrete Shells', Leningrad, Russia.

Zhang, Y.-G. & Tabarrok, B. (1999), 'Generation of surfaces via equilibrium of forces', *Computers and Structures* **70**, 599–613.

Zhao, Y. (2012), Application of vector form intrinsic finite element method in the analysis of cable membrane structures, Master's thesis, Zhejiang University, China. In Chinese.

Ziegler, E. (1961), Foamed polystyrene in thin shell construction, *in* 'Structural Foams, BRI 1960 Fall Conference', pp. 48–53. Washington D.C.: National Academy of Sciences-National Research Council Publication 892.

Zimmermann, G. (2007), Membran Beton Gitterschalen Tragwerke. Entwicklung und Vorbemessung, PhD thesis, Universität Kassel, Germany. In German.

List of Figures

Copyright ownership is denoted by the © symbol. Creative Commons licensed material is denoted by the 🅭 symbol, with details on specific versions on their website. Material in the public domain is denoted by the 🅯 symbol. If the copyright is unclear, the original source is cited instead. In all other instances, any copyright belongs to the author.

List of Tables

List of Symbols

A few symbols represent different parameters depending on the chapter and its context: δ, t, $\mathbf{f}$ and $\mathbf{D}$. The parameterization of the NEST HiLo roof (Sections 12.2.1 and 12.2.2) also uses several duplicate symbols, which are excluded from this list.

symbol	size	unit	description
α		[-]	ratio of plan width over length
$\alpha_1, \alpha_2, \alpha_3$		[-]	coefficients for influence of concrete strength
$\alpha_{ds1}, \alpha_{dsl}$		[-]	coefficients for type of cement
α_f		[-]	parameter for formwork accuracy
α_T		[K^{-1}]	rate of thermal expansion
β		[-]	shallowness
$\beta_c, \beta_{fc}, \beta_H, \beta_t$		[-]	coefficients for creeping, concrete strength development, relative humidity and concrete aging
β_{as}, β_{RH}		[-]	coefficients for shrinkage and relative humidity
β_s		[10^{-3}]	ratio of radius over thickness
γ			a ratio or coefficient
γ_k		[-]	knockdown factor
δ		[-]	damping parameter
δ		[m]	deflection
ε			tolerance
$\varepsilon_{ca}, \varepsilon_{cd}, \varepsilon_{cs}$		[‰]	autogeneous, dying and total shrinkage strain
$\varepsilon_y, \varepsilon_u$		[‰]	yield and ultimate strain
ζ		[-]	ratio of long term load over total load
η		[-]	reinforcement parameter
θ		[rad]	angle
λ		[-]	load factor
$\lambda_{const}, \lambda_{decr}, \lambda_{incr}$		[-]	factor of safety for constant, decreasing and increasing post-buckling capacity
λ_h		[-]	continuation factor for homotopy mapping
λ_s		[-]	factor of safety
μ			mean value
μ_k		[-]	snow shape factor
μ_{rc}		[-]	reinforcement ratio
ν		[-]	Poisson's ratio

symbol	size	unit	description
ξ		[-]	reinforcement
ρ		[kg·m^{-3}]	density
$\rho_{\mathrm{crp}}, \rho_{\mathrm{hom}}, \rho_{\mathrm{pl}}, \rho_{\mathrm{rc}}$		[-]	reduction factor for influence of creep, imperfections, plasticity, and cracking and reinforcement
σ		[-]	standard deviation
σ_0		[N·m^{-2}]	uniform surface stress
σ_1, σ_2		[N·m^{-2}]	first and second principal stress
$\sigma_{\mathrm{xx}}, \sigma_{\mathrm{yy}}, \sigma_{\mathrm{xy}} = \sigma_{\mathrm{x}}, \sigma_{\mathrm{y}}, \tau_{\mathrm{xy}}$		[N·m^{-2}]	stresses in local surface coordinates
σ_{v}		[N·m^{-2}]	Von Mises stress
φ		[-]	creep coefficient
ψ		[-]	reduction factor for load combinations
ψ_0, ψ_∞		[-]	factor for buckling rigidity in the (un)cracked state
ω		[-]	step size
$\boldsymbol{\varepsilon}$		[-]	local Cartesian strains in Voigt notation
$\boldsymbol{\lambda}$		[-]	Lagrange multipliers
$\boldsymbol{\lambda}_{\mathrm{T}}$		[-]	transformation matrix (Rao 2004, p. 361-3)
$\boldsymbol{\sigma}$	$[3m \times 1]$	[N·m^{-2}]	local Cartesian stresses in Voigt notation
Λ			Lagrangian function
$\boldsymbol{\Psi}$	$[3 \times 3]$	[-]	transformation matrix, equation (4.32)
e_0			eccentricity
$f_{\mathrm{ck}}, f_{\mathrm{c}}, f_{\mathrm{cd}}$		[N·m^{-2}]	compressive strength of concrete, at time of loading, and dimensioning value
$f_{\mathrm{ctm}}, f_{\mathrm{ctd}}$		[N·m^{-2}]	cracking tensile strength of concrete, and dimensioning value
f_{y}		[N·m^{-2}]	yield strength of steel
g		[N·m^{2}kg^2	gravitational constant
h		[m]	height or rise
h_0		[mm]	notional size
i		[-]	iteration number
i, j		[-]	branch and node indices
k		[N·m^{-1}]	spring constant or rate
k_{h}		[-]	coefficient for notional size
k_{crp}		[-]	coefficient for creep
k_{t}		[-]	coefficient for dimension of the tension chord
$m, m_{\mathrm{b}}, m_{\mathrm{t}}$		[-]	number of branches, of lines, springs and/or bars, of triangle edges
n_{rc}		[-]	ratio of Young's moduli for steel and concrete
$n, n_{\mathrm{i}}, n_{\mathrm{f}}$		[-]	number of nodes, of free nodes, of fixed nodes
p		[N·m^{-2}]	real load
p_{p}		[N·m^{-2}]	plastic failure load under central compression without buckling
p_{pl}		[N·m^{-2}]	plastic failure load
$p_{\mathrm{cr}}^{\mathrm{lin}}, p_{\mathrm{cr}}^{\mathrm{u}}, p_{\mathrm{cr}}^{\mathrm{u,reinf}}, p_{\mathrm{cr}}^{\mathrm{plast}}$		[N·m^{-2}]	critical linear buckling load, increasingly modified for nonlinear effects

symbol	size	unit	description
q_p		[kN·m^{-2}]	snow pressure
q_s		[N]	surface stress density
s		[m]	span
s_k		[kN·m^{-2}]	snow pressure
t		[m]	thickness
t		[s]	time
u		[m]	elongation
u, v		[m]	coordinate difference in local directions
w		[m]	width
w_0, w_0', w_0''		[m]	initial, calculable and accidental imperfection
x, y		[m]	local coordinates
z		[m]	vertical coordinate
$\mathbf{e}$	$[m \times 1]$	[-]	natural strains along the triangle edges
$\mathbf{e}^*$	$[m \times 1]$	[-]	errors
$\mathbf{d}$	$[3n_\mathrm{i} \times 1]$	[N]	damping forces
$\mathbf{f}$	$[m \times 1]$	[N]	internal forces along branches
$\mathbf{f}$	$[3n_\mathrm{i} \times 1]$	[N]	nodal forces in global coordinates
$\mathbf{g}$	$[3m \times 1]$	[N]	internal forces in global coordinates
$\mathbf{k}_\mathrm{s}$	$[m \times m]$	[N·m^{-1}]	spring constants
$\mathbf{l}, \mathbf{l}_0$	$[m \times 1]$	[m]	lengths, initial lengths
$\mathbf{m}$	$[n_\mathrm{i} \times 1]$	[kg]	masses
$\mathbf{p}$	$[3n \times 1]$	[N]	external forces
$\mathbf{p}_\mathrm{i}$	$[3n_\mathrm{i} \times 1]$	[N]	external loads
$\mathbf{p}_\mathrm{f}$	$[3n_\mathrm{f} \times 1]$	[N]	reaction forces
$\mathbf{q}$	$[m \times 1]$	[N·m^{-1}]	force densities, or tension coefficients, of branches
$\mathbf{q}_\mathrm{b}$	$[m_\mathrm{b} \times 1]$	[N·m^{-1}]	force densities of lines, springs and/or bars
$\mathbf{q}_\mathrm{t}$	$[m_\mathrm{t} \times 1]$	[N·m^{-1}]	force densities of triangle edges
$\mathbf{q}_\mathrm{t,s}$	$[m_\mathrm{t} \times 1]$	[N·m^{-4}]	surface stress densities of triangle edges
$\mathbf{r}$	$[3n \times 1]$	[N]	residual forces, or out-of-balance forces
$\mathbf{s}$	$[3 \times 1]$	[N·m^{-2}]	natural stresses
$\mathbf{u}, \mathbf{u}_0$	$[3m \times 1]$	[m]	coordinate differences, initial values
$\mathbf{u}^*$	$[2m \times 1]$	[m]	coordinate differences in local coordinates
$\bar{\mathbf{u}}, \bar{\mathbf{v}}, \bar{\mathbf{w}}$	$[m \times 1]$	[m]	coordinate differences in global coordinates
$\mathbf{v}$	$[3n_\mathrm{i} \times 1]$	[m· s^{-1}]	nodal velocities
$\mathbf{w}_\mathrm{b}$	$[m_\mathrm{b} \times 1]$	[N·m^{-3}]	extended force densities of branches
$\mathbf{x}$	$[3n \times 1]$	[m]	coordinates
$\bar{\mathbf{x}}, \bar{\mathbf{y}}, \bar{\mathbf{z}}$	$[n \times 1]$	[m]	coordinates in global coordinates
$\mathbf{x}_\mathrm{i}$	$[3n_\mathrm{i} \times 1]$	[m]	coordinates of free nodes
$\bar{\mathbf{x}}_\mathrm{i}$	$[n_\mathrm{i} \times 1]$	[m]	coordinates of free nodes
$\mathbf{x}_\mathrm{f}$	$[3n_\mathrm{f} \times 1]$	[m]	coordinates of fixed nodes
$\bar{\mathbf{x}}_\mathrm{f}$	$[n_\mathrm{f} \times 1]$	[m]	coordinates of fixed nodes
A		[m^2]	area
A', B', C'		[-]	damping constants
C_p		[-]	wind pressure coefficient
$E_\mathrm{c}, E_\mathrm{cr}, E_\mathrm{s}$		[N·m^{-2}]	Young's modulus of concrete, due to creep and of steel

symbol	size	unit	description
E_{kin}		[J]	kinetic energy
E_{se}		[J]	strain energy
F		[N]	force
H		[m]	triangle height
I_{cr}		[m^{-3}]	moment of inertia of a cracked section
K		[m^{-2}]	Gaussian curvature
L, L_0		[m]	length and initial length or rest length
M_{u}		[Nm]	bending moment at plastic failure
Q		[$\mathrm{N{\cdot}m}^{-1}$]	force density
Q_s		[$\mathrm{N{\cdot}m}^{-4}$]	surface stress density
R		[m]	radius
RH		[-]	humidity
U, V, W		[m]	coordinate difference in global directions
X, Y, Z		[m]	coordinate in global directions
$\mathbf{A}$	$[m \times m]$	[m^2]	diagonal matrix of cross-sectional areas
$\mathbf{B}$			strain-displacement matrix
$\mathbf{C}$	$[3m \times 3n]$	[-]	branch-node matrix
$\bar{\mathbf{C}}$	$[m \times n]$	[-]	branch-node matrix
$\mathbf{C}_{\mathrm{i}}$	$[3m \times 3n_{\mathrm{i}}]$	[-]	…of free nodes
$\mathbf{C}_{\mathrm{i,b}}$	$[3m_{\mathrm{b}} \times 3n_{\mathrm{i}}]$	[-]	…of free nodes and lines, springs and/or bars
$\mathbf{C}_{\mathrm{i,t}}$	$[3m_{\mathrm{t}} \times 3n_{\mathrm{i}}]$	[-]	…of free nodes and triangle edges
$\mathbf{C}_{\mathrm{f}}$	$[3m \times 3n_{\mathrm{f}}]$	[-]	…of fixed nodes
$\mathbf{C}_{\mathrm{f,b}}$	$[3m_{\mathrm{b}} \times 3n_{\mathrm{f}}]$	[-]	…of fixed nodes and lines, springs and/or bars
$\mathbf{C}_{\mathrm{f,t}}$	$[3m_{\mathrm{t}} \times 3n_{\mathrm{f}}]$	[-]	…of fixed nodes and triangle edges
$\bar{\mathbf{C}}_{\mathrm{i}}$	$[m \times n_{\mathrm{i}}]$	[-]	…of free nodes
$\bar{\mathbf{C}}_{\mathrm{i,b}}$	$[m_{\mathrm{b}} \times n_{\mathrm{i}}]$	[-]	…of free nodes and lines, springs and/or bars
$\bar{\mathbf{C}}_{\mathrm{i,t}}$	$[m_{\mathrm{t}} \times n_{\mathrm{i}}]$	[-]	…of free nodes and triangle edges
$\bar{\mathbf{C}}_{\mathrm{f}}$	$[m \times n_{\mathrm{f}}]$	[-]	…of fixed nodes
$\bar{\mathbf{C}}_{\mathrm{f,b}}$	$[m_{\mathrm{b}} \times n_{\mathrm{f}}]$	[-]	…of fixed nodes and lines, springs and/or bars
$\bar{\mathbf{C}}_{\mathrm{f,t}}$	$[m_{\mathrm{t}} \times n_{\mathrm{f}}]$	[-]	…of fixed nodes and triangle edges
$\mathbf{D}$	$[3n_{\mathrm{i}} \times 3n_{\mathrm{i}}]$	[$\mathrm{kg{\cdot}\,s}^{-1}$]	damping matrix
$\mathbf{D}$			constitutive matrix
$\mathbf{D}_{\mathrm{i}}$	$[3n_{\mathrm{i}} \times 3n_{\mathrm{i}}]$	[$\mathrm{N{\cdot}m}^{-1}$]	geometric stiffness matrix of free nodes
$\mathbf{D}_{\mathrm{f}}$	$[3n_{\mathrm{f}} \times 3n_{\mathrm{f}}]$	[$\mathrm{N{\cdot}m}^{-1}$]	geometric stiffness matrix of fixed nodes
$\mathbf{E}$	$[m \times m]$	[$\mathrm{N{\cdot}m}^{-2}$]	diagonal matrix of Young's moduli
$\mathbf{F}$	$[m \times m]$	[N]	diagonal matrix of internal forces
$\mathbf{G}$			Jacobian matrix
$\mathbf{H}$	$[3 \times 3]$ or,$[3m_{\mathrm{t}} \times 3m_{\mathrm{t}}]$	[m^2]	transformation matrix, equation (4.32)
$\mathbf{I}$		[-]	identity matrix
$\mathbf{K}$	$[3n_{\mathrm{i}} \times 3n_{\mathrm{i}}]$	[$\mathrm{N{\cdot}m}^{-1}$]	stiffness matrix
$\mathbf{K}_{\mathrm{e}}, \mathbf{K}_{\mathrm{e,l}}, \mathbf{K}_{\mathrm{e,nl}}$	$[3n_{\mathrm{i}} \times 3n_{\mathrm{i}}]$	[$\mathrm{N{\cdot}m}^{-1}$]	elastic stiffness matrix, linear and nonlinear part
$\mathbf{K}_{\mathrm{g}}, \mathbf{K}_{\mathrm{g,l}}, \mathbf{K}_{\mathrm{g,nl}}$	$[3n_{\mathrm{i}} \times 3n_{\mathrm{i}}]$	[$\mathrm{N{\cdot}m}^{-1}$]	geometric stiffness matrix, linear and nonlinear part
$\mathbf{K}_{\mathrm{mod}}$	$[3n_{\mathrm{i}} \times 3n_{\mathrm{i}}]$	[$\mathrm{N{\cdot}m}^{-1}$]	modified stiffness matrix
$\mathbf{K}_{\mathrm{s}}$	$[m \times m]$	[$\mathrm{N{\cdot}m}^{-1}$]	diagonal matrix of spring constants
$\mathbf{L}, \mathbf{L}_0$	$[m \times m]$	[m]	diagonal matrix of lengths and of initial lengths
$\mathbf{M}$	$[3n_{\mathrm{i}} \times 3n_{\mathrm{i}}]$	[kg]	mass matrix

symbol	size	unit	description
$\bar{\mathbf{M}}$	$[n_\mathrm{i} \times n_\mathrm{i}]$	[kg]	mass matrix
$\mathbf{N}$	$[3 \times 3]$	[-]	helper matrix, equation (4.13)
$\mathbf{P}$	$[n \times 3]$	[N]	external forces
$\mathbf{P}_\mathrm{i}$	$[n_\mathrm{i} \times 3]$	[N]	external loads
$\mathbf{P}_\mathrm{f}$	$[n_\mathrm{f} \times 3]$	[N]	reaction forces
$\mathbf{Q}$	$[3m \times 3m]$	$[\mathrm{N{\cdot}m^{-1}}]$	diagonal matrix of force densities of branches
$\bar{\mathbf{Q}}$	$[m \times m]$	$[\mathrm{N{\cdot}m^{-1}}]$	diagonal matrix of force densities of branches
$\bar{\mathbf{Q}}_\mathrm{b}$	$[m_\mathrm{b} \times m_\mathrm{b}]$	$[\mathrm{N{\cdot}m^{-1}}]$	...of force densities of lines, springs and/or bars
$\mathbf{S}$	$[2m \times 2m]$	$[\mathrm{N{\cdot}m^{-2}}]$	block diagonal matrix of element stresses
$\mathbf{T}$	$[3n_\mathrm{i} \times 3n_\mathrm{i}]$	[-]	transformation matrix
$\mathbf{U}, \mathbf{U}_0$	$[3m \times m]$	[m]	coordinate differences, initial values
$\mathbf{U}^*$	$[2m \times m]$	[m]	coordinate differences in local coordinates
$\bar{\mathbf{U}}, \bar{\mathbf{V}}, \bar{\mathbf{W}}$	$[m \times m]$	[m]	diagonal matrix of global coordinate differences
$\mathbf{W}$	$[m \times m]$	[-]	damping or scaling matrix
$\mathbf{W}_1$	$[m \times m]$	[-]	weighting matrix
$\mathbf{W}_2$	$[n_\mathrm{i} \times n_\mathrm{i}]$	[-]	weighting matrix
$\mathbf{W}_\mathrm{b}$	$[m_\mathrm{b} \times m_\mathrm{b}]$	$[\mathrm{N{\cdot}m^{-3}}]$	diagonal matrix of extended force densities
$\mathbf{X}$	$[n \times 3]$	[m]	coordinate matrix
$\mathbf{X}_\mathrm{i}$	$[n_\mathrm{i} \times 3]$	[m]	coordinate matrix of free nodes
$\mathbf{X}_\mathrm{f}$	$[n_\mathrm{f} \times 3]$	[m]	coordinate matrix of fixed nodes